Titan's highly variable plasma environment: A 3D hybrid simulation study

Von der Fakultät für
Elektrotechnik, Informationstechnik, Physik
der Technischen Universität Carolo-Wilhelmina
zu Braunschweig

zur Erlangung des Grades eines
Doktors der Naturwissenschaften
(Dr. rer. nat.)

genehmigte
DISSERTATION

von

Sven Simon

aus

Goslar

---

1. Referent: Prof. Dr. Uwe Motschmann

2. Referent: Prof. Dr. Karl-Heinz Glaßmeier

eingereicht am: 26. Juni 2007

mündliche Prüfung (Disputation) am: 09. Oktober 2007

Druckjahr: 2007

Vorveröffentlichungen der Dissertation

Teilergebnisse aus dieser Arbeit wurden mit Genehmigung der Fakultät für Elektrotechnik, Informationstechnik, Physik, vertreten durch den Mentor der Arbeit, in folgenden Beiträgen vorab veröffentlicht:

Publikationen:

- S. Simon, A. Bößwetter, T. Bagdonat, U. Motschmann und K.-H. Glaßmeier. Plasma environment of Titan: a 3-d hybrid simulation study, *Annales Geophysicae*, Nr. 24 (3), Seiten 1113–1135, 2006
- S. Simon, A. Bößwetter, T. Bagdonat und U. Motschmann. Physics of the Ion Composition Boundary: A comparative 3D hybrid simulation study of Mars and Titan, *Annales Geophysicae*, Nr. 25 (1), Seiten 99–115, 2007
- S. Simon, A. Bößwetter, T. Bagdonat, U. Motschmann und J. Schüle. Three-dimensional multispecies hybrid simulation of Titan's highly variable plasma environment, *Annales Geophysicae*, Nr. 25 (1), Seiten 117–144, 2007
- S. Simon, G. Kleindienst, A. Bößwetter, T. Bagdonat, U. Motschmann, K.-H. Glaßmeier, J. Schüle, C. Bertucci und M. K. Dougherty. Hybrid simulation of Titan's magnetic field signature during the Cassini T9 flyby, eingereicht bei *Geophysical Research Letters*, 2007
- S. Simon, G. Kleindienst, A. Bößwetter, T. Bagdonat, U. Motschmann, K.-H. Glaßmeier, J. Schüle, C. Bertucci und M. K. Dougherty. Titan's magnetic field signature during the Cassini T9 flyby – Magnetometer data versus 3D multispecies hybrid simulations, eingereicht bei *Annales Geophysicae*, 2007

Tagungsbeiträge:

- S. Simon, A. Bößwetter, T. Bagdonat und U. Motschmann. Plasma environment of magnetized and unmagnetized obstacles: 3D hybrid simulation studies (Poster), *International Max-Planck Research School on Physical Processes in the Solar System and Beyond*, Max-Planck-Institut für Sonnensystemforschung, Katlenburg-Lindau, 11. November 2005
- S. Simon, A. Bößwetter, T. Bagdonat und U. Motschmann. Plasma environment of Titan: A 3D hybrid simulation study (Vortrag), *Frühjahrstagung der Deutschen Physikalischen Gesellschaft*, Heidelberg, 13.-16. März 2006
- S. Simon, A. Bößwetter, T. Bagdonat und U. Motschmann. Plasma environment of Titan: A 3D hybrid simulation study (Vortrag), *European Geosciences Union, General Assembly 2006*, Wien, 02.-07. April 2006
- S. Simon, A. Bößwetter, T. Bagdonat und U. Motschmann. Plasma environment of Titan: A 3D hybrid simulation study (Vortrag), *International Max-Planck Research School on Physical Processes in the Solar System and Beyond*, Max-Planck-Institut für Sonnensystemforschung, Katlenburg-Lindau, 17. Mai 2006

- S. Simon, A. Bößwetter, T. Bagdonat und U. Motschmann. 3D multispecies hybrid simulations of Titan's highly variable plasma environment (Vortrag), *European Planetary Science Congress*, Berlin, 18.-22. September 2006
- U. Motschmann, S. Simon, A. Bößwetter und T. Bagdonat. Plasma environment of Titan: A 3D hybrid simulation study (Poster), *European Planetary Science Congress*, Berlin, 18.-22. September 2006
- S. Simon, A. Bößwetter, T. Bagdonat und U. Motschmann. 3D multispecies hybrid simulations of Titan's highly variable plasma environment (Poster), *American Geophysical Union Fall Meeting*, San Francisco, 11.-15. Dezember 2006
- S. Simon, G. Kleindienst, A. Bößwetter, T. Bagdonat, U. Motschmann, K.-H. Glassmeier, C. Bertucci und M. K. Dougherty. 3D multispecies hybrid simulations of Titan's highly variable plasma environment: Comparison with Cassini MAG data (Poster), *European Geosciences Union, General Assembly 2007*, Wien, 15.-20. April 2007
- S. Simon, G. Kleindienst, A. Bößwetter, T. Bagdonat, U. Motschmann, K.-H. Glassmeier, C. Bertucci und M. K. Dougherty. 3D multispecies hybrid simulations of Titan's highly variable plasma environment: Comparison with Cassini MAG data (Vortrag), *International Max-Planck Research School on Physical Processes in the Solar System and Beyond*, Max-Planck-Institut für Sonnensystemforschung, Katlenburg-Lindau, 09. Mai 2007
- S. Simon, G. Kleindienst, A. Bößwetter, T. Bagdonat, U. Motschmann, K.-H. Glassmeier, C. Bertucci und M. K. Dougherty. 3D multispecies hybrid simulations of Titan's highly variable plasma environment (Vortrag), *Seminar des Instituts für Planetenforschung, Deutsches Zentrum für Luft- und Raumfahrt*, Berlin, 08. Juni 2007

Contents

Chapter 1

Introduction

On 15 October 1997, ESA and NASA scientists celebrated the successful launch of the Cassini spacecraft on board a Titan IVB/Centaur launch vehicle from Cape Canaveral Air Force Station, Florida. For the Cassini-Huygens mission, this event marked the beginning of a seven-year journey to the Saturnian system where the spacecraft arrived on 01 July 2004. During the past three years, Cassini provided an extensive source of new information on the giant planet Saturn as well as its impressive ring system and its numerous moons. The exploration of Saturn's largest satellite, Titan, has been declared one of the major scientific purposes of the mission. With a radius of $R_T = 2575\,\mathrm{km}$, this celestial body is even larger than the planets Mercury and Pluto. On 25 December 2004, the Huygens lander detached itself from the Cassini spacecraft, and – after it had been cruising towards Titan for about three weeks – finally performed a safe landing on the moon's surface on 14 January 2005. So far, Titan is the most distant world upon which a human-made space probe has landed.

Before Cassini arrived in the Saturnian system, the only available close views of Titan came from Pioneer and the two Voyager spacecraft, which had visited Saturn and Titan in the late 1970s and the early 1980s. The data collected during these missions had revealed that, except for Earth, Titan is the only body in the solar system which possesses a nitrogen-rich atmosphere. While Earth's atmosphere has evolved under the influence of life and includes carbon dioxide as the main carbon species, the atmosphere of Titan has remained in a more primitive state, is rich of methane and is assumed to bear a strong resemblance to the atmospheric composition hypothesized for the early Earth. In analogy to the Terrestrial atmosphere, Titan's upper atmosphere is ionized by solar ultraviolet radiation, leading to the formation of an extended ionosphere around the satellite. By the nominal end of the Cassini mission in the year 2008, the spacecraft will have payed more than 40 visits to Titan which will hopefully allow to gain deep insight into the physics of the satellite's atmosphere and ionosphere.

However, among the planetary satellites in our solar system, Titan is not only interesting with respect to its unique atmosphere, but also from the point of view of plasma physics. Like the planets Venus and Mars, Titan does not possess a substantial intrinsic magnetic field, so that the satellite's atmosphere and ionosphere are directly exposed to the ambient plasma flow. It is the characteristics of the impinging plasma that assign Titan an extraordinary position among the non-magnetized bodies in our solar system. Titan encircles Saturn in a distance of 1221850 kilometers, which is about 20 times the radius of Saturn. Being located in such a large distance to the giant planet, Titan and its plasma environment are strongly affected by changes in the positions of Saturn's bow shock and magnetopause. On the one hand, for average solar wind conditions, Titan is located in the outer regions of Saturn's magnetosphere, where the ambient corotating plasma flow is submagnetosonic. Nonetheless, the flow features an alfvénic Mach number that is larger than one. To date, such plasma properties have not been encountered anywhere else in our solar system. On the other hand, a reduction of Saturn's bow shock distance in times of high solar wind dynamic pressure might even allow Titan to leave the magnetosphere near the subsolar point of its orbit. In such a situation, the satellite's ionosphere could – like the ionospheres of Mars or Venus – interact directly with the unshocked solar wind. When being located inside the magnetosphere, Titan's plasma interaction is also unique in the way that the moon's dayside ionosphere is not necessarily located in the hemisphere that is exposed to the corotating magnetospheric plasma. Investigating the interaction between Titan's ionosphere and the satellite's highly variable plasma environment is the purpose of this work.

Due to advances in computing technology as well as in the development of new numerical techniques during the last decade, three-dimensional simulation codes have become the most sophisticated tool that is available for studying the interaction between a planetary obstacle and its plasma environment. Theoretical plasma physicists have a variety of fully developed simulation codes at their disposal. First of all, magnetohydrodynamic (MHD) plasma models have been developed. By applying a fluid description to the individual components of the plasma and consequently, by circumventing the necessity to store the positions and velocities of a huge number of individual particles, these models allow to gain insight into the physics of planetary plasma interaction processes while requiring only a moderate amount of storage and computing capacity. Some of these codes are able to generate a fully developed three-dimensional image of the Terrestrial or the Saturnian magnetosphere after calculating only a single day on a standard personal computer. Because of this decisive advantage, magnetohydrodynamic plasma codes currently make up the major contribution to the pallet of established simulation models. A generalization of the magnetohydrodynamic plasma description is represented by multi-fluid codes that allow to distinguish between different ion components. Nevertheless, the fluid approach features one significant disadvantage.

Applying a fluid description to the plasma environment of a planet or moon goes along with a complete elimination of individual ion dynamics from the simulation model. A magnetized plasma, such as the solar wind or the charged particle population inside a planetary magnetosphere, does not simply stream around the obstacle like water in a river, but the dynamics of individual ions are strongly affected by the local electromagnetic fields. It is well-known from basic electrodynamics that a charged particle which is inserted into a magnetic field does not perform a translation, but it is instead forced on a spiral trajectory, describing a gyration around the field lines. Covering such an effect is beyond the scope of any fluid plasma model. Nevertheless, under certain circumstances, the negligence of individual ion dynamics may be absolutely justified. For instance, the extension of the obstacle that the Terrestrial dipole field represents for the impinging solar wind flow is about several orders of magnitude larger than the gyroradii of the involved ion species. For this reason, the key features of Earth's magnetosphere are well covered within the framework of a magnetohydrodynamic treatment. However, the situation at Titan exhibits a significantly different character.

The radius of Titan is not only comparable to the gyroradii of the ions in the impinging magnetospheric plasma, but it is even clearly exceeded by the characteristic length scales defined by newly generated charged particles of ionospheric origin. After having been ionized by solar radiation, a newly generated charged nitrogen particle is affected by the electromagnetic fields in the ambient magnetospheric plasma flow and is transported away from Titan. This is the so-called *pick-up process*. The trajectory of an ionospheric ion that has been "picked up" can be considered a superposition of a straight line, i.e. the particle trajectory in an unmagnetized plasma, and a gyration of the ion around the magnetic field lines. As a result, the ion trajectory features a cycloidal shape. The spatial extensions of one arc of such a cycloid can exceed the radius of Titan by more than a factor of ten, i.e. the moon would completely "fit" into one arc of a pick-up ion's trajectory. In consequence, neither the magnetohydrodynamic nor the multi-fluid plasma description is strictly applicable to the case of Titan.

Despite this obvious inadequacy, nearly every available magnetohydrodynamic space plasma simulation code has been used to study Titan's plasma interaction during the last ten years. Although these approaches do not include any kind of ion kinetics, they provided at least a basic understanding of the physical mechanisms that are involved in the interaction between Titan's ionosphere and the impinging plasma. Since including the subfast flow inside Saturn's magnetosphere into a simulation model provides quite a challenge from the numerical point of view, most of these fluid approaches address the case of Titan being located outside the magnetosphere and hence, of being exposed to the unshocked solar wind. At the beginning of the work for the present study, only very few simulation models that offer a more realistic description of Titan's plasma interaction were existent.

The crucial question that still remains is how to include individual particle dynamics into a numerical simulation model. Of course, one could design a code that solves the equations of motion for both electrons and ions. However, the gyroradius of an electron in the plasma near Titan is more than four orders of magnitude smaller than the radius of the satellite. Thus, such an approach would waste a huge amount of storage capacity and computing time for calculating the trajectories of the electrons, without the individual dynamics of these particles having any kind of noteworthy influence on the large-scale plasma interaction process. For this reason, a compromise between the fluid approach and the full particle description of the plasma seems appropriate. This alternative is represented by the *hybrid codes*.

The hybrid model can be considered a combination of the major strengths of magnetohydrodynamic and full particle codes. The hybrid approach treats the ions of the plasma as individual particles and is therefore able to describe the influence of ion kinetic effects on the interaction between Titan and its plasma environment. Of course, a simulation model cannot cover the dynamics of every single ion. Instead, a hybrid code solves the equations of motion for so-called *macroparticles*, each of them representing a certain number of real ions. On the other hand, since the dynamics of individual electrons do not play a major role in the interaction process, the time-saving fluid description known from magnetohydrodynamic models is applied to the electrons of the plasma. Such an approach represents the optimum solution for a realistic study of Titan's plasma environment. At the beginning of the work for this thesis in 2004, only a single hybrid model of Titan's plasma interaction was available. Brecht *et al.* [30] had already successfully applied their simulation code to the interaction between the Martian ionosphere and the solar wind and presented a first hybrid study of Titan's plasma interaction in the year 2000. The necessary parallel computing capacities were provided by the NASA Ames Numerical Aerodynamic Simulation facility. However, despite the chance of analyzing the realistic Titan situation, the authors included a radical simplification into their model. By setting the temperature of the impinging Saturnian magnetospheric plasma to zero, they generated the hypothetical scenario of a supermagnetosonic magnetospheric plasma that interacts with Titan's ionosphere. Although Brecht *et al.* [30] were able to make some basic predictions about the influence of finite ion gyroradii on Titan's plasma interaction, they failed to include the high thermal velocity of the magnetospheric particles. As will be discussed in the following chapters, the necessity to neglect the finite plasma temperature may have arisen from the considerable numerical difficulties that are associated with hybrid simulations of Titan's subfast plasma environment. A subsequent study presented by Kallio *et al.* [74] also included strong simplifications of the real situation. Therefore, at the beginning of the work for this thesis, the analysis of Titan's plasma interaction by means of hybrid simulations could be considered an almost unexplored terrain.

In the late 1990s, Bagdonat and Motschmann started to develop a new kind of hybrid code at the Institute for Theoretical Physics of the University in Braunschweig, Germany. The purpose of this project was to design an analysis tool for the Rosetta mission to comet 67P/Churyumov-Gerasimenko. The code was the first of its kind and is still unique in the sense that it is not restricted to a Cartesian spatial discretization, but it can operate on an arbitrary curvilinear simulation grid. By means of this technique, a series of simulation studies has been accomplished, granting deep insight into the interaction of cometary ionospheres with the solar wind [7, 8, 9, 10, 11]. With respect to the gyroradii of the involved ion species, a cometary nucleus can be treated as a point-like obstacle. Consequentially, the next step was an application of the simulation model to the plasma interaction of a large planetary body. In the year 2004, Bößwetter *et al.* [26, 27] succeeded in applying the simulation code to the interaction between the Martian ionosphere and the solar wind. The authors achieved the first quantitative reproduction of the locations of the plasma boundaries that are formed in the vicinity of Mars. In the same year, Simon *et al.* [137, 138] presented an application of the simulation code to the plasma environment of magnetized asteroids and provided ancillary material for the interpretation of data that will be collected during Rosetta's flybys of the asteroids Steins and Lutetia in 2008 and 2010. In the framework of the analysis presented here, a modified version of this simulation code has been employed to study the interaction between Titan's ionosphere and the satellite's plasma environment.

Several modifications of the existing code have proven necessary. On the one hand, an adequate model of Titan's ionosphere had to be incorporated into the simulation code. As the ion concentration in the immediate vicinity of Titan is significantly higher than in the case of Mars, developing a new kind of boundary condition for the planetary interior has shown mandatory. On the other hand, a number of numerical problems arising from the subfast nature of the impinging magnetospheric plasma had to be overcome. However, the by far most important extension of the existing model was the inclusion of multi-component plasma flows. The original code developed by Bagdonat [7] had been designed to handle only a single upstream ion component and a single species of ionospheric origin. For an analysis of the solar wind interaction with the ionospheres of comets or Mars, this approach has shown to be absolutely sufficient. For instance, the simulation results for the Martian plasma environment achieved formidable agreement with spacecraft measurements without including the minor helium component of the solar wind. Minor species of ionospheric origin could also be safely neglected. Such an approach may not be valid for the Titan scenario, as inside the magnetosphere, the impinging plasma consists of a light and a significantly heavier component that possess comparable number densities. Furthermore, Titan's ionosphere is made up of multiple ion species as well. Of course, a multi-species hybrid model does not only allow to understand Titan's plasma interaction, but it has proven to be a valuable instrument for gaining access to basic physical processes in multi-ion plasmas as well.

In addition, the simulation model provides a useful tool for interpreting and analyzing the data collected in the vicinity of Titan by the Cassini spacecraft. In the final stage of writing this thesis, a series of about 30 Titan flybys has already been accomplished by Cassini, each of them providing a diversity of plasma and magnetic field data. Of course, the interpretation of this material is still in a very early stage. Nevertheless, quantitative comparisons between simulation results and measurements cannot only be considered an opportunity to prove the validity of the model, but the code has already shown to be a valuable tool for supporting the process of data analysis. A formal cooperation with the Cassini Magnetometer Team has been established, whereas scientific discussions with members of the Cassini Plasma Spectrometer Team are in progress and have already yielded first results.

This thesis is organized as follows: In chapter 2, the major physical properties of Titan and its plasma environment are briefly discussed. Chapter 3 deals with the simulation model itself. The discussion does not only focus on the basic assumptions and dynamic equations of the hybrid model, but it also gives at least a basic insight into the numerical concepts of the simulation code. The simulation results are presented in chapters 4 to 9 in the following way:

- In chapter 4, the physics of Titan's plasma interaction are investigated as a function of the alfvénic, sonic and magnetosonic Mach numbers of the upstream plasma flow.
- Chapter 5 deals with the dependence of the structures in Titan's plasma environment on the satellite's orbital position.
- In chapter 6, the multi-species nature of Titan's plasma interaction will be subject to an extensive discussion.
- An analysis of Cassini magnetometer data for a series of selected Titan flybys is presented in chapter 7.
- Chapter 8 will focus on the ninth close flyby of Titan (T9) by the Cassini spacecraft. The discussion will point out the unique character of this flyby scenario. Besides, the data collected during T9 by the Cassini Magnetometer and the Cassini Plasma Spectrometer will be interpreted in terms of the simulation model.
- Although not being directly related to the Titan problem, chapter 9 presents a discussion of the major properties of multi-ion shock waves. The material discussed in this chapter may be considered a concept for additional applications of the multi-species code.

Finally, chapter 10 concludes by summarizing the results obtained within this work as well as by giving an outlook to future projects. Three appendices give an overview of those numerical details which might be of importance to future users of the Titan simulation code.

Chapter 2

Titan's plasma interaction: An overview

This chapter gives an overview of the current state of knowledge on Titan. The discussion does not only focus on the moon's atmosphere and ionosphere, but the highly variable properties of the ambient magnetospheric and solar wind plasma are analyzed as well. On the one hand, identifying the key features of the plasma interaction process will allow to point out parallels and differences to other solar system bodies. On the other hand, a first rough description of Titan's plasma environment can be provided.

1 Titan: A satellite with an atmosphere

Titan, after Jupiter's satellite Ganymede the second largest moon in the solar system, was discovered by the Dutch astronomer Christiaan Huygens in March 1655. When he turned his telescope on Saturn, he spotted an additional small point of light close to the planet. When observing this point in subsequent nights, Huygens realized that it completed an entire orbit around Saturn in about 16 days. He published his finding one year later in a pamphlet entitled *De Saturni luna observatio nova*. Although the Englishman Christopher Wren as well as the German astronomer Johannes Hevelius stated that they had observed Titan through their telescopes before Huygens did, neither of them had realized the connection between the observation and Saturn. Instead, they had considered the point of light denoting the position of Titan to be a background star.

More than 250 years later, the first hint towards an atmosphere around Titan was published by José Comas Solà [36] who had observed Titan at the Fabra Observatory in Barcelona, Spain, on 13 August 1907. By using a 38 cm telescope, he was able to identify a darkening in the peripheral regions of the observed disk. Comas Solà suggested that this effect might originate from a strongly absorbing atmosphere around Titan. A better-founded hypothesis was presented by James Jeans in 1925, who had applied his *Dynamical Theory of Gases* to several satellites in the solar system, including Titan. Jeans had derived three criteria which have to be fulfilled by a celestial body in order to keep an atmosphere: On the one hand, the object's gravity should be sufficiently strong, and the gas molecules themselves must be relatively heavy. On the other hand, a sufficiently low temperature is required in order to prevent the bulk of the gas molecules from reaching escape velocity. Jeans suggested that, in the large distance where Saturn and its satellites orbit the Sun, Titan's gravity should be strong enough to retain an atmosphere for as long as the solar system has existed. However, his analysis showed that light gases, such as helium or hydrogen, would easily be able to escape. Consequentially, Jeans concluded that if Titan possessed an atmosphere, it would consist of relatively heavy components like argon, neon, nitrogen or methane. His calculations also showed that, due to the warmer regime around Jupiter, the Jovian moons would not have been able to keep an atmosphere, even if they had acquired it in the first place. The ultimate evidence of the existence of an atmosphere around Titan was presented by the Dutch-American astronomer Gerard P. Kuiper in 1944, who had recorded the spectra of the ten largest satellites in the solar system in the visible as well as in the near infrared regime [86]. The Titan spectrum contained characteristic absorption bands that could clearly be ascribed to the presence of methane gas. Titan's orange hue was also apparent in the data presented by Kuiper. Nevertheless, the spectra did not reveal that methane is far from being the most abundant species in Titan's atmosphere.

Updated information on Titan's atmospheric composition were obtained when the Voyager 1 spacecraft reached the Saturnian system in November 1980 after a journey that had lasted more than 13 years. The only Titan flyby of this mission took place on 12 November 1980. The spacecraft passed through the satellite's plasma wake and achieved a closest approach altitude of 4394 km. The combined data collected by the spacecraft's ultraviolet spectrometer and the radio occultation experiments showed that Titan's atmosphere predominantly consists of nitrogen ($85-95\%$), while despite its remarkably strong spectral signature, methane makes up only a few percent of the atmospheric gas composition. Together, methane and nitrogen exert a pressure on the surface of Titan which is about 1.5 times larger than the atmospheric pressure on Earth. Because N_2 and CH_4 molecules are being broken up by solar ultraviolet light, Titan's upper atmosphere and ionosphere exhibit a very complex chemistry.

Titan is the only satellite in the solar system with such an extended atmosphere: The atmosphere of its closest competitor, Neptune's moon Triton, is less dense by a factor of 100000. The composition of Titan's nitrogen-rich atmosphere is closer to Earth's than that of any other known planetary body with a substantial atmosphere. However, due to Titan's low surface temperature of 94 K, there are significant differences in the composition of the trace gases in the two atmospheres. Table 2.1 gives an overview of Titan's major physical and dynamical parameters.

2 Morphology of Titan's plasma interaction

For more than two decades, the data collected during the Voyager 1 flyby have provided the major source of information on Titan and its plasma environment. Since the analysis of the material collected during the first Cassini encounters is in a very early stage, most of the available theoretical models for Titan's plasma environment as well as for the satellite's atmospheric and ionospheric composition are still based on the plasma and magnetic field data from the Voyager 1 encounter. The following sections give an overview of the current state of knowledge on Titan's plasma interaction. The discussion will mainly be based on established material obtained form the analysis of the Voyager 1 data, but new insights from the Cassini mission will be included whenever it is possible. An image of Titan that was taken during the first close flyby of the Cassini spacecraft is shown in fig. 2.1. At least for this first flyby, the data set collected by the spacecraft has been published in *Science* [46, 48, 102, 133, 152].

Parameter	Numerical value
Radius (R_T)	2575 km
Mass	$1.346 \cdot 10^{23}$ kg (0.022 mass of Earth)
Mean density	1880 $\mathrm{kg/m^3}$
Surface temperature	94 K ($-179°C$)
Surface pressure	1.44 bar
Surface gravity	1.35 $\mathrm{m/s^2}$
Escape velocity	2.65 km/s
Bond albedo	0.29
Mean distance from Saturn	1.22 million km (20 Saturn radii)
Mean distance from Sun	9.539 AU (1427 million km)
Orbital period around Saturn	15.945 days
Mean orbital velocity	5.58 km/s
Orbital eccentricity	0.029

Table 2.1: Titan: Summary of dynamical and physical data. The radius of Ganymede, the largest satellite in the solar system, is only fractionally larger than Titan's radius (2634 km versus 2575 km). The bond albedo is the ratio of total reflected light intensity to total incident light intensity. The parameters have been obtained from Lorenz and Mitton [94].

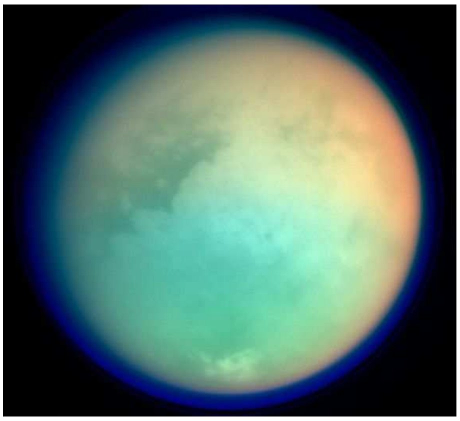

Figure 2.1: Normally hidden by a thick, hazy atmosphere, impressive features of Titan's surface appear in this false-color view. The image was recorded as the Cassini spacecraft approached its first close flyby of Titan on 26 October 2004. Here, red and green colors represent specific infrared wavelengths absorbed by Titan's atmospheric methane, while bright and dark surface areas are revealed in a more penetrating infrared band. Ultraviolet data showing the extensive upper atmosphere and haze layers are seen as blue. The image has been obtained from http://antwrp.gsfc.nasa.gov/apod/ap041028.html.

2.1 Titan in Saturn's magnetosphere and in the solar wind

With its extended neutral atmosphere, Titan encircles Saturn in a distance of 20.3 Saturn radii and with an orbital period of 15.95 days in the same direction as Saturn rotates. Titan's orbit is located in Saturn's equatorial plane. Depending on the incident solar wind conditions, the position of Saturn's bow shock has been observed to vary typically between 23.6 and 31.5 Saturn radii [90]. This value is also confirmed by various magnetohydrodynamic simulations of Saturn's magnetosphere, such as the models developed by Hansen *et al.* [58, 59] and by Gombosi *et al.* [53]. According to the calculations presented by Wolf and Neubauer [157], the subsolar point of Saturn's magnetopause is usually located in a distance between 16 and 26 Saturn radii. Therefore, in the case of average solar wind conditions, Titan's orbit is located within the outer regions of Saturn's magnetosphere. An illustration of this situation is shown in fig. 2.2. As reported by Schardt *et al.* [131] who analyzed the data from the Pioneer 11 flyby of Saturn, under extreme solar wind conditions, the distance of the bow shock can be reduced to values below 20 Saturn radii. Under these circumstances, Titan might be able to leave the Saturnian magnetosphere in the subsolar region of its orbit and interact with the shocked magnetosheath plasma or even directly with the unshocked solar wind. However, during the Voyager 1 flyby as well as during the first Cassini encounter of Titan, the satellite was located well inside the Saturnian magnetosphere [6, 119]. Recent analyses of Cassini plasma and magnetic field data presented by Achilleos *et al.* [1] and by Hendricks *et al.* [62] confirm that during the entire first series of Titan flybys (TA, TB, T3,. . .,T10), the moon was always located in the outer regions of Saturn's magnetosphere. Because so far, the case of Titan being located outside the magnetosphere has not yet been observed, the following discussion will focus on the situation inside the magnetosphere.

As suggested by Giampieri and Dougherty [51] who analyzed the magnetic field data from the Pioneer 11 and the Voyager missions, Saturn's intrinsic magnetic field can be approximated by a dipole whose magnetic moment is nearly aligned with the axis of planetary rotation. The Saturnian magnetosphere is populated by neutral atoms and plasma from several potential sources. On the one hand, Saturn's atmosphere and rings as well as the icy satellites can contribute to the plasma population inside the magnetosphere. On the other hand, plasma from Titan itself and solar wind particles are also part of the plasma population. Saturn and its neutral atmosphere rotate with a period of 10.7 hours. Due to friction with the neutral atmosphere, the planet's ionosphere is set into rotation as well. The intrinsic magnetic field rotates together with the planet and its ionosphere. Although the plasma in Saturn's inner magnetosphere is in a state of ideal corotation, such a behaviour cannot be expected for arbitrary large distances to the planet. As discussed by Hill [64], several processes occurring in a planetary magnetosphere can give rise to strong deviations from ideal corotation: radial transport of magnetospheric plasma or injection of newly generated ions impose a deceleration on a corotating flow. Based on Voyager 1 data, Eviatar and Richardson [47] have conducted an analysis of the latter process for Saturn's magnetosphere. They suggest that two observed dips in the magnetospheric plasma velocity near the orbits of the satellites Dione and Rhea can be associated with mass loading effects, for both bodies possess an icy surface and should therefore lose mass due to sputtering processes. The results of this analysis have been confirmed by Saur *et al.* [130].

In the outer regions of Saturn's magnetosphere where Titan's orbit is located, the plasma

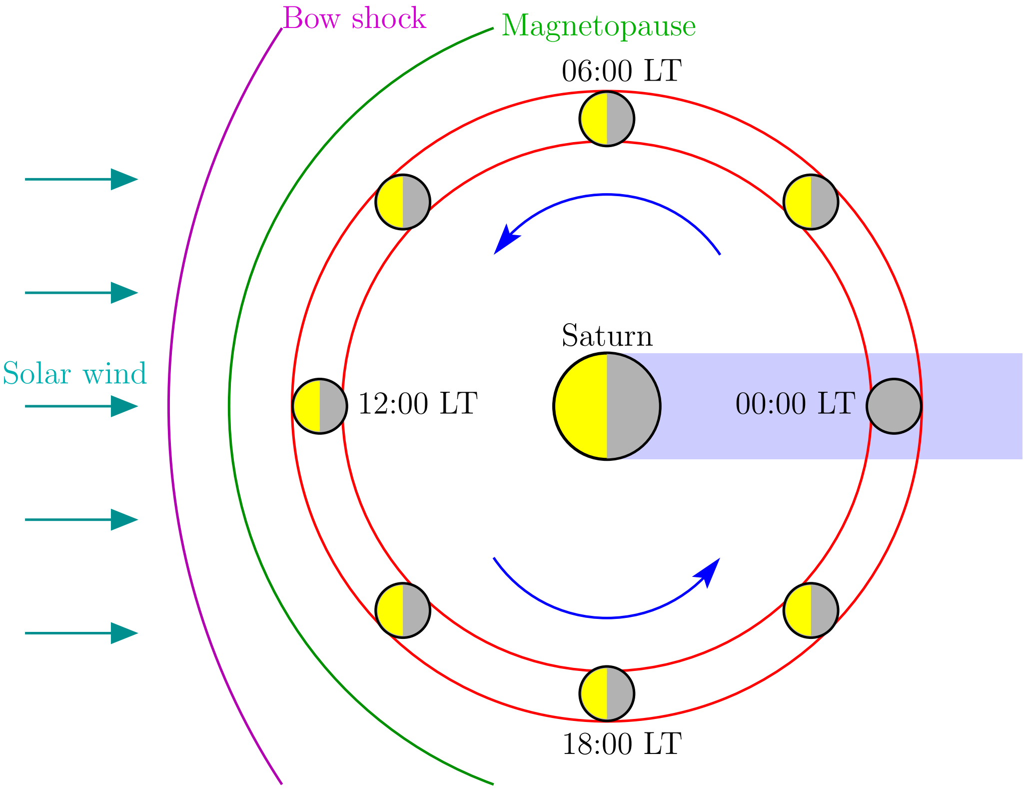

Figure 2.2: Titan's orbit in the equatorial plane of Saturn. The abbreviation "LT" in the sketch denotes the Saturnian local time at Titan. The Voyager 1 flyby of Titan took place at 13:30 local time. Titan orbits Saturn in a distance of 20.3 Saturn radii with an orbital period of 15.95 days. The moon encircles Saturn in the direction of planetary rotation. Since Titan's orbital period is significantly larger than Saturn's rotational period, Titan's atmosphere and ionosphere are permanently exposed to a flow of at least partially corotating magnetospheric plasma. The blue arrows denote Titan's rotational direction as well as the direction of the corotating plasma flow. The mean plasma velocity with respect to Titan is of the order of 120 km/s. As can be seen from the figure, Titan's dayside hemisphere is not necessarily aligned with the ram flow of the Saturnian magnetospheric plasma. This leads to a variety of different interaction scenarios. Titan's orbit is located inside the Saturnian magnetosphere for average solar wind conditions. However, when Saturn's magnetosphere is compressed due to high solar wind dynamic pressure, Titan might leave the magnetosphere in the subsolar region of its orbit. Under these circumstances, the satellite's ionosphere can interact directly with the supersonic solar wind. Such a compression of Saturn's magnetosphere was detected during the Pioneer 11 flyby [131]. The figure has been adopted from Blanc *et al.* [22].

flow speed is clearly smaller than in the case of ideal corotation [104]. If flow dynamics were strictly connected to the planetary rotation, the plasma would encircle Saturn in 10.7 hours, corresponding to a mean velocity of about 200 km/s near the orbit of Titan. However, Mac Lennan *et al.* [101] have deduced the magnetospheric flow speed in the vicinity of Titan to be of the order of only 120 km/s, thus ranging clearly below the value that would be expected for rigid corotation. Nevertheless, the magnetospheric flow speed still clearly exceeds Titan's orbital velocity, i.e. the satellite is "overtaken" by the magnetospheric plasma flow "from behind". As also displayed in fig. 2.2, the satellite therefore represents an obstacle that is embedded into the streaming magnetospheric plasma. The analysis of the resulting interaction process is the major purpose of the study presented here.

According to Neubauer *et al.* [119] who have analyzed the plasma and magnetic field data obtained during the Voyager 1 encounter, the plasma near Titan mainly consists of atomic nitrogen (N^+) and hydrogen (H^+) ions, the average number densities being $n(N^+) = 0.2\,\mathrm{cm}^{-3}$ and $n(H^+) = 0.1\,\mathrm{cm}^{-3}$, respectively. During the flyby, which took place at 13:30 Saturnian local time (cf. fig. 2.2), the ambient magnetic field of magnitude $B_0 = 5\,\mathrm{nT}$ was directed nearly perpendicular to Titan's orbital plane. Neubauer *et al.* [119] pointed out that under these ambient conditions, an upstream velocity of 120 km/s yields a unique combination of Mach numbers for the magnetospheric plasma near Titan's orbit: the flow is super-alfvénic (alfvénic Mach number $M_A = 1.87$), yet subsonic (sonic Mach number $M_S = 0.57$) and submagnetosonic (magnetosonic Mach number $M_{MS} = 0.55$). Such a set of Mach numbers has so far not been observed in the plasma environment of any other body, making Titan's plasma interaction unique among the planets and satellites in our solar system. Nevertheless, Neubauer *et al.* [119] also emphasize that the Voyager 1 encounter provided only a snapshot of the ambient plasma properties in the vicinity of Titan and that the satellite may face highly variable plasma conditions along its orbit around Saturn. Specifically, Wolf and Neubauer [157] suggest that when Titan is located in Saturn's magnetotail at 00:00 Saturnian local time, the satellite may be exposed to a *sub*-alfvénic, subsonic and submagnetosonic plasma flow. To sum up, during an entire orbit around Saturn, Titan can in principle encounter three plasma regimes that feature different combinations of Mach numbers: The satellite is exposed to

- a *sub-alfvénic*, *subsonic* and *submagnetosonic* magnetospheric plasma flow when being located in Saturn's magnetotail region.
- a *super-alfvénic*, *subsonic* and *submagnetosonic* flow when being located in the outer regions of the Saturnian magnetosphere and
- a clearly *super-alfvénic*, *supersonic* and *supermagnetosonic* flow when being able to leave the magnetosphere near noon in times of high solar wind dynamic pressure[1].

So far, the discussion has focused on the characteristics of the magnetospheric plasma in the vicinity of Titan's orbit, but the nature of the obstacle that Titan represents for the impinging flow has not been specified yet.

2.2 Intrinsic magnetic field, atmosphere and ionosphere

The interaction process between a collisionless plasma flow and a planetary obstacle is mainly determined by the question of whether the obstacle possesses a significant intrinsic magnetic field or an ionosphere. Some planets, such as Earth, feature both of these characteristics.

The simplest obstacle for a streaming plasma flow is a sufficiently large body that possesses neither an intrinsic magnetic field nor an ionosphere, as for instance the Terrestrial moon

---

[1] The transition that Titan's plasma environment undergoes when the satellite re-enters the magnetosphere and therefore encounters the shocked flow in Saturn's magnetosheath region will be briefly discussed in chapter 4 of this work.

or an unmagnetized asteroid. In such a scenario, the impinging plasma ”interacts” with the obstacle primarily by hitting its surface and being absorbed. A cavity of nearly vanishing plasma density arises in the downstream region. Nevertheless, in the case of the Terrestrial moon, this cavity possesses a quite complex magnetic field topology. The analysis of this interaction process is the major subject of the studies presented by Kallio [69], by Travnicek *et al.* [149] and by Müller [113]. If the obstacle possesses a strong intrinsic magnetic field, the key features of the interaction are governed by this field. In the case of a large planetary obstacle, such as Earth or Mercury, the interaction leads to the formation of a magnetopause that protects the body from direct penetration by the impinging plasma. The solar wind interaction of a significantly smaller magnetized obstacle, such as an asteroid, has for instance been simulated by Omidi *et al.* [120], Blanco-Cano *et al.* [23], Simon *et al.* [138] and Travnicek *et al.* [147, 148]. Despite the small size of the asteroid, it is capable of triggering a variety of different wave modes in the ambient solar wind flow [2, 14, 15, 16, 24, 54, 55, 56, 81, 153]. A quite unique example is provided by the Jovian satellite Ganymede that possesses a strong internally-generated magnetic field. Like Titan, the satellite is located inside a planetary magnetosphere. In this scenario, the interaction with the Jovian magnetospheric plasma generates some kind of ”sub-magnetosphere” around the moon [80, 124].

If the obstacle does not possess a noticeable intrinsic magnetic field, but is instead surrounded by an atmosphere and an ionosphere, the ionosphere is subject to direct interaction with the impinging plasma flow. In such a scenario, ionospheric particles are being picked up by the ambient plasma. They experience an acceleration in the plasma’s electromagnetic fields and are transported away from the obstacle, leading to an erosion of the ionosphere. The pick-up process plays a key role in the interaction of the unmagnetized planets Mars and Venus with the solar wind [27, 28, 29]. The interaction between a cometary ionosphere and the solar wind can be understood in nearly the same way, even though in that case, the size of the solid cometary nucleus is practically negligible with respect to the extension of the obstacle’s ionosphere [7, 34].

Thus, in order to understand Titan’s plasma interaction, it is mandatory to assign the satellite to one of these categories. The first who addressed the question of Titan possessing an internal magnetic field was Neubauer [117] who developed a simple model of the moon’s interior, including a metallic core. Based on cosmochemical analyses that impose constraints on the composition of Titan’s interior, as well as by considering the density and the size of the satellite, he showed that at Titan’s equator, the magnitude of a possible intrinsic magnetic field could not be larger than 100 nT. A few years later, the magnetic field data obtained during the Voyager 1 flyby allowed a significant improvement of this upper limit. Neubauer *et al.* [119] derived an upper magnetic field limit of 4.1 nT for Titan’s equatorial region, which is already smaller than the ambient magnetic field of $B_0 = 5\,\mathrm{nT}$ detected by Voyager 1. Nevertheless, the problem of Titan’s intrinsic magnetic field had not yet been resolved beyond any doubt. For instance, both Israelevich *et al.* [65] and Kabin *et al.* [67] suggested that the strong magnetic field rotations detected in Titan’s wake by Voyager 1 can only be understood by assigning the satellite a dipole-like internal magnetic field. However, the ultimate evidence of Titan being a practically unmagnetized body was presented by Backes *et al.* [6] who analyzed Titan’s magnetic field signature during the first Cassini flyby on 26 October 2004 (TA flyby). By using a magnetohydrodynamic plasma model, the authors were able to achieve an excellent reproduction of the magnetometer data without superimposing any intrinsic magnetic field. Hence, with respect to its plasma interaction, Titan can definitely be considered an unmagnetized body.

For this reason, Titan's plasma interaction is expected to bear a strong resemblance to the situation at Venus or at Mars: The satellite's atmosphere and ionosphere represent the major obstacle for the impinging magnetospheric plasma flow. Based on the data collected by the Ultraviolet Spectrometer on board Voyager 1, a variety of atmosphere models for Titan have been developed, such as the approaches described by Strobel *et al.* [143], by Owen [123], by Yung *et al.* [159, 160], by Lellouch *et al.* [92] and by Toublanc *et al.* [146]. All of these models suggest that more than 97% of the atmospheric gas near the surface consist of molecular nitrogen (N_2), whereas methane and other minor species make up the rest. In an altitude between 1700 and 2500 km, methane (CH_4) becomes the predominant constituent of the atmosphere, while at even higher altitudes, molecular hydrogen (H_2) is the major neutral species. As discussed by Waite Jr. *et al.* [152], these key features of Titan's atmosphere have been confirmed by the Ion Neutral Mass Spectrometer results from the Cassini TA flyby, i.e. the bulk composition and thermal structure of the moon's upper atmosphere do not appear to have undergone considerable changes since the Voyager 1 flyby. Figure 2.3 shows density profiles of the most abundant species in Titan's atmosphere.

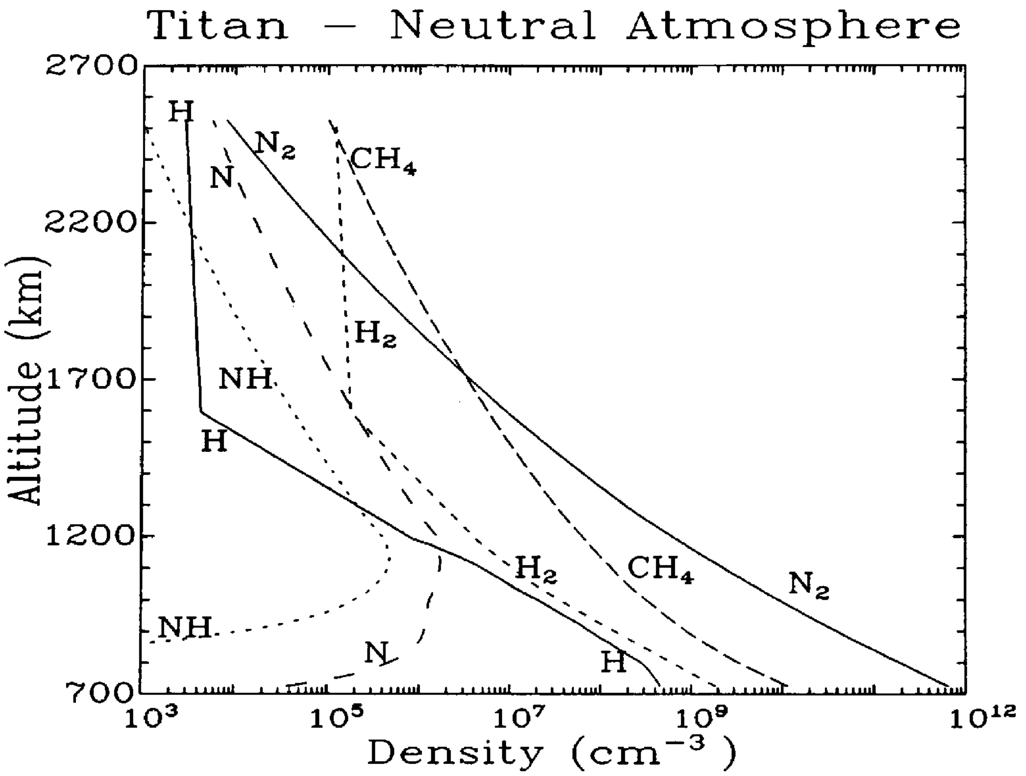

Figure 2.3: Density profiles of neutral species in Titan's atmosphere. The figure has been obtained from Keller *et al.* [77].

Various ionization sources lead to the formation of an ionosphere around Titan. Ionization of neutrals is not only caused by solar extreme ultraviolet radiation, but also due to impact of photoelectrons produced by this radiation. Magnetospheric electron impact ionization can be considered another source of newly generated charged particles. According to Capone *et al.* [33], cosmic rays as well as precipitation of protons and other ions may also make up a minor contribution to the ionosphere. By using electron flux data from an ionosphere model presented by Gan *et al.* [49], Keller *et al.* [77] found out that solar ultraviolet ionization can be considered the major source of ionization, while electron impact ionization contributes only about 20% to the total ionization rate. Keller *et al.* [77] also suggest the peak electron density of about $3 \ldots 5 \cdot 10^3\,\mathrm{cm}^{-3}$ to be located in an altitude of 1100 km above the surface. Of course, in the case of Titan being located in Saturn's magnetosheath or in the solar wind, the nature and intensity of the impact ionization source will differ significantly from the situation inside the magnetosphere.

The data obtained from a solar occultation experiment during the Voyager 1 flyby provided the fundament for a large number of ionosphere models for Titan, most of them addressing the complex ion chemistry in the satellite's upper ionosphere. Based on a one-dimensional photochemical model, Keller *et al.* [77] demonstrate that a complex chain of chemical reactions finally converts the initially ionized atmospheric particles into H_2CN^+ and long-chain hydrocarbon ions ($C_nH_m^+$). The number of ion species included into the model as well as the diversity of the possible chemical reactions has been updated several times (cf. Keller *et al.* [75] and Cravens *et al.* [41]). Because at Titan's nightside, particle impact processes are the only source of ionization, the satellite's nightside and dayside ionosphere feature significantly different properties. This aspect is discussed by Keller *et al.* [76, 78] who developed one-dimensional multi-species magnetohydrodynamic models of Titan's ionosphere that take into account the relative positions of Titan, Saturn and the Sun. The authors demonstrate that the ion and electron densities as well as the magnetic field profiles in the upper ionosphere are highly susceptible to changes in the position of the ultraviolet ionization source. Roboz and Nagy [126], who have conducted a detailed analysis of the dynamics and energetics in Titan's ionosphere, present a series of density, velocity and temperature profiles for different orbital positions of the satellite. In accordance to the calculations of other groups, their models suggest the ionospheric density peak to be located in an altitude of about 1100 km. Furthermore, the authors point out the important influence of ion chemical heating on the shape of Titan's ionosphere. Recently, a global, three-dimensional magnetohydrodynamic model of Titan's ionosphere has been presented by Backes *et al.* [6]. This model has been applied to the situation during the first three Cassini encounters by Neubauer *et al.* [118]. The authors identify photoionization to be the dominant ionization mechanism of Titan's atmosphere, whereas the energy density of impinging magnetospheric electrons is quantitatively too small to lead to a significant contribution to the ionization process.

A preliminary application of photochemical modelling to the ionospheric electron densities measured during Cassini's TA flyby was presented by Cravens *et al.* [40]. At least for this flyby, there are still controversial points of view concerning the influence of magnetospheric electron impact ionization. In order to identify the ion production mechanisms in the TA scenario, the authors considered different combinations of ionization sources. The case of an ionosphere that is generated by both solar radiation and electron impact processes is compared to alternative approaches that include only one of these two mechanisms. By comparing the resulting electron density profiles to data from the Cassini Radio and Plasma Wave Experiment, Cravens *et al.* [40] demonstrate that at least for the situation during TA, ionization by both solar radiation and by incoming electrons from Saturn's magnetosphere is required to obtain satisfactory agreement between measured and calculated electron densities. However, the model employed in the present work is based on the approaches of Keller *et al.* [77], of Backes *et al.* [6] as well as of Neubauer *et al.* [118], who assume solar ultraviolet radiation to be the major ionization source.

2.3 Comparison with other solar system bodies

The preceding sections have concentrated on identifying those characteristics of Titan itself and of the ambient magnetospheric plasma that play a crucial role in determining the shape of the satellite's plasma environment. This section will focus on the plasma interaction process itself. The discussion will not only point out the major physical effects, but it will also place emphasis on the parallels and differences to the plasma observations in the vicinity of other bodies in the solar system that possess an ionosphere, but not an intrinsic magnetic field. Of major interest is a comparison to Venus, Mars and comets.

Although Titan is not the only object in the solar system whose plasma interaction is mainly determined by its ionosphere, the characteristics of the impinging plasma have proven to be quite unique. Moreover, it is important to notice that the ionospheric properties of the side of Titan that faces the impinging magnetospheric plasma flow depend on the satellite's orbital position. In contrast to the situation at Venus or at Mars, Titan's dayside ionosphere is not necessarily located in the hemisphere that is exposed to the upstream plasma flow. Because of this high variability, it is quite difficult to draw a global picture of the interaction region. However, when Titan is located inside the Saturnian magnetosphere, several key processes should always be present.

Due to the submagnetosonic character of the ambient magnetospheric plasma flow, no bow shock evolves at the Titan's ramside. In contrast to this, the supermagnetosonic nature of the impinging solar wind gives rise to a bow shock at the ramside of Venus or Mars. In the shock front, most of the flow energy is converted into thermal energy, thus leading to an increase of entropy. Downstream of the shock front, all three Mach numbers of the decelerated solar wind are smaller than 1, which yields at least a distant analogy between the post-shock situation at Venus or Mars and the ambient flow near Titan. At Titan, the properties of the impinging magnetospheric plasma are mainly determined by its high thermal pressure, being one order of magnitude larger than the dynamic pressure nmv^2 (cf. Neubauer *et al.* [119] and Backes [6]). In the unshocked solar wind that interacts with the ionospheres of Venus or Mars, the dynamic term makes up the major contribution to the total pressure. However, at both planets, the properties of the shocked solar wind are controlled by the thermal pressure, with the plasma beta being clearly larger than 1.

By using the electron and ion measurements conducted by the Voyager 1 Plasma Science Instrument, Hartle *et al.* [61] were able to identify several key features of Titan's plasma interaction. Downstream of the satellite, a plasma wake is formed which is characterized by a more dense and colder plasma than the surrounding magnetospheric flow. Neubauer *et al.* [119] suggest the major constituents of the slow wake plasma to be N^+ ions and relatively heavy species, like N_2^+ or H_2CN^+. The density of these ions ranges between $6 - 10\,\mathrm{cm}^{-3}$ and $30 - 40\,\mathrm{cm}^{-3}$ and therefore clearly exceeds the ambient magnetospheric density of only

$0.3\,\mathrm{cm}^{-3}$. On the other hand, the wakeside flow speed of about 10 km/s is significantly smaller than in adjacent regions. Charge neutrality in the tail should be guaranteed by the presence of cold electrons with energies below 10 eV. According to Hartle *et al.* [61], these structures arise from a deflection of the magnetospheric plasma around Titan and the pick-up of newly generated exospheric ions by the ambient flow.

At Titan and Mars, the gyroradii of newly generated ionospheric ions as well as of particles in the ambient plasma are comparable to the size of the obstacle [95, 97], so that the dynamics of individual particles are likely to cause a strong hemispherical asymmetry in the structure the obstacle's induced magnetosphere[2]. Although not being completely negligible, finite gyroradius effects may play a less important role at Venus, for the gyroradii of newly generated planetary oxygen ions are of the order of only 0.06 planetary radii. Besides, while in the unshocked solar wind that impinges on the Venus ionosphere, the proton gyroradius is comparable to the planetary radius of $R_V = 6052\,\mathrm{km}$, the deceleration of the plasma and the magnetic field enhancement in the shock front go along with a reduction of the proton gyroradius. Thus, with respect to the properties of the upstream flow, finite gyroradius effects may be not play an important role either [97, 125].

According to Voyager 1 and Cassini measurements, the Saturnian magnetic field lines in the vicinity of Titan are arranged in a highly draped configuration. A bipolar magnetic lobe structure emerges downstream of the obstacle. In the two lobes, the magnetic field vectors are oriented in opposite directions, so that a central field reversal region is formed in between. At the obstacle's ramside, the draping leads to the formation of a pile-up region with enhanced magnetic field strength. A similar draping pattern has been observed at Venus and Mars as well [18, 19, 82]. However, Luhmann *et al.* [97], who have performed a comparative study of the plasma environments of non-magnetized bodies in the solar system, point out that Voyager 1 data indicate the tail diameter at Titan to be comparable to the spatial extension of the satellite, whereas the magnetotails of Mars and Venus are significantly broader than the planets themselves. Besides, at Venus and Mars, the transition between the highly draped field configuration and the non-draped region has shown to be quite smooth. In contrast to this, the magnetic field data collected during the Voyager 1 flyby of Titan showed a rather abrupt field enhancement when the spacecraft entered the satellite's magnetotail. According to Verigin *et al.* [150] who compared the magnetometer data from the Voyager 1 flyby to magnetic field measurements conducted during the Venera 9 and Venera 10 missions to Venus, there appears to be evidence of reconnection between the oppositely directed tail lobes of both bodies. Unfortunately, the data from the single Voyager 1 flyby of Titan do not allow a definite clarification of this issue, as conclusive observations like detection of heated electrons and accelerated ions are absent. So far, the problem has not been addressed during the analysis of the Cassini magnetometer data.

As discussed by Breus *et al.* [31] as well as by Sauer *et al.* [127, 129], the interaction of the Martian ionosphere with the supersonic solar wind gives rise to a set of sharply pronounced plasma boundaries. Especially, an *Ion Composition Boundary* is formed, separating the shocked solar wind flow from the cold plasma population of ionospheric origin. However, in the vicinity of Titan, a similar boundary layer has neither been detected by Voyager 1

---

[2] Since the analysis of these effects is the major purpose of the study presented here, the discussion will not dwell on the details in this introductory chapter.

nor during the first Cassini encounters. Finding an answer to the question of why such a boundary layer does not evolve from Titan's interaction with the Saturnian magnetospheric plasma is one of the major purposes of this work.

Finally, it should be noted that with respect to the nature of the obstacle itself, Titan possesses an even stronger analogy to a comet than to Mars or Venus. At Titan, the extension of the obstacle's atmosphere is comparable to the size of the planetary body itself, for the satellite's exobase is located in an altitude of 0.6 Titan radii above the surface. In contrast to this, at Venus or Mars, characteristic height scales for the extension of the atmosphere are of the order of only 200 km. Hence, Titan represents a significantly larger obstacle for the ambient plasma than the solid body of the satellite itself, while the spatial extensions of Mars and Venus also determine the size of the obstacle that is embedded into the solar wind. This aspect of Titan's plasma interaction points out at least a distant analogy to the characteristics of a comet, since the diameter of the cometary atmosphere (the coma) is typically one order of magnitude larger than the spatial extension of the nucleus. Nevertheless, the mechanism that gives rise to a cometary atmosphere is significantly different from the situation at Titan, Venus and Mars. Typically, more than 75% of a cometary nucleus consist of water ice and frozen volatiles like CO, H_2CO, CH_3OH and NH_3CO, whereas dust particles make up the rest. When the comet approaches the Sun, solar radiation causes the ice to sublimate, which leads to the formation of a neutral atmosphere around the nucleus. The cometary ionosphere evolves from ionization of this neutral cloud by solar ultraviolet radiation. Furthermore, as demonstrated by nearly every available simulation model, the relatively small gas velocity inside a planetary atmosphere can safely be neglected when analyzing the interaction with the ambient plasma flow. In contrast to this, Bagdonat [7] has demonstrated that the finite speed of the radially streaming cometary atmosphere particles plays a crucial role for the structure of the interaction region.

Of course, if Titan leaves the Saturnian magnetosphere in times of high solar wind dynamic pressure and therefore, the characteristics of the impinging plasma undergo significant modifications, the satellite's plasma interaction should exhibit an even stronger analogy to the effects near Venus and Mars than it already does in the situation inside the magnetosphere. Especially, a shock front and an Ion Composition Boundary should be formed. However, the case of Titan actually being located outside Saturn's magnetosphere has neither been observed by Voyager 1 nor by Cassini.

In this section, it has been tried to construct a picture of the key processes that determine the topology of Titan's plasma environment. Figure 2.4 provides an overview of the major results.

3 Summary

Titan is the only moon in the solar system that possesses an extended, nitrogen-rich atmosphere. Titan encircles Saturn in a distance of 20.3 Saturn radii and with an orbital period of 15.95 days. For average solar wind conditions, Titan is located within the outer regions of Saturn's magnetosphere. Due to Titan's orbital period being considerably larger than Saturn's rotational period of 10.7 hours, the satellite is permanently embedded into a flow of

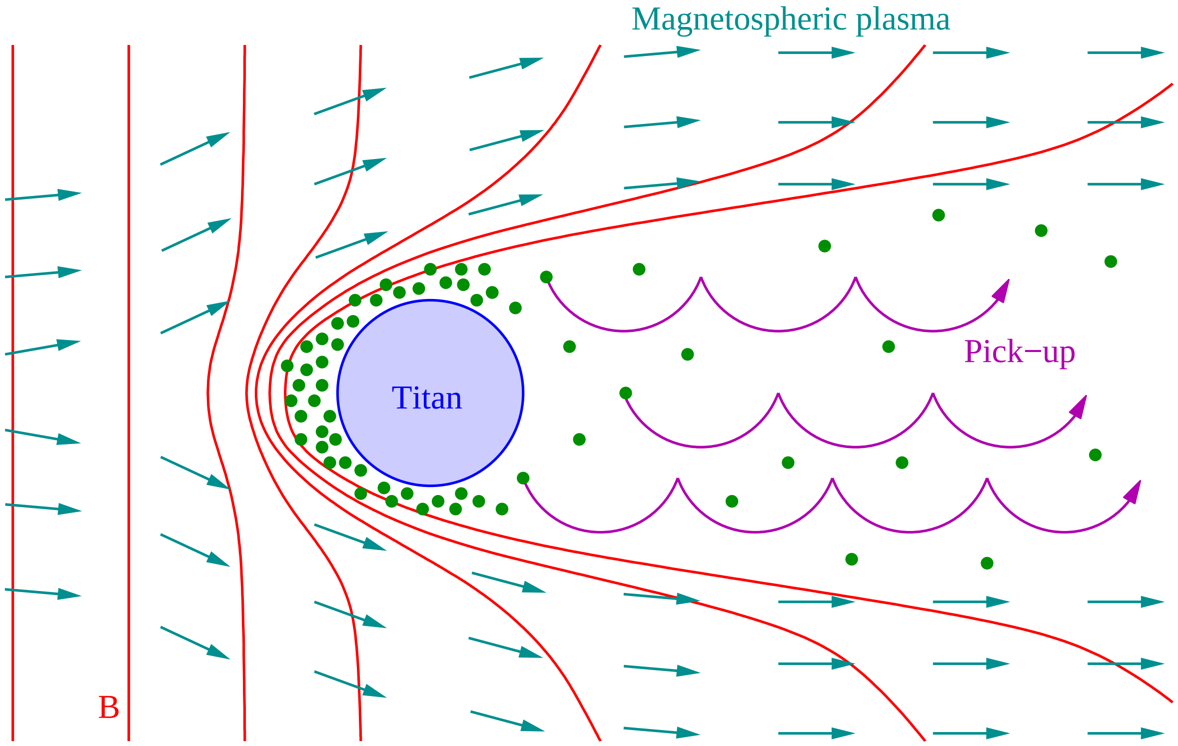

Figure 2.4: Schematic sketch of Titan's interaction with the Saturnian magnetospheric plasma flow. Due to the submagnetosonic nature of the impinging plasma (cyan arrows), no bow shock is formed at Titan's ramside. Instead, the magnetic field lines develop a strong draping pattern, featuring a magnetic pile-up region at Titan's ramside and two magnetic lobes in the tail region (red lines). In the wake region, newly generated ionospheric ions (green dots) are transported away from the satellite by means of the pick-up process. These particles are moving on cycloidal trajectories, the characteristic lengths of the cycloidal arcs being comparable to the size of the obstacle. As denoted by the schematic illustration of the flow pattern, the ambient magnetospheric plasma is deflected around the central tail region. The pattern indicated by the cyan arrows can rather be identified with the direction of the mean plasma velocity than with the trajectories of individual particles. In any case, it is important to notice that the sketch includes several massive simplifications: In reality, the magnetic lobes are mainly located in Titan's polar plane, whereas particles moving on cycloidal pick-up trajectories can primarily be found close to the satellite's orbital plane. According to Voyager 1 data, the ambient Saturnian magnetic field near Titan is directed perpendicular to the orbital plane. Therefore, in order to avoid any misinterpretation of the figure, no vector arrows have been attached to the magnetic field lines. Thus, this introductory figure provides only a rough illustration of the real situation. Dwelling on the details of the interaction process is left to the discussion of the simulation results in subsequent chapters.

at least partially corotating magnetospheric plasma with a relative velocity around 120 km/s. As Titan does not possess a significant intrinsic magnetic field, the impinging magnetospheric plasma interacts directly with the satellite's ionosphere, similar to the interaction between the ionospheres of Venus and Mars with the solar wind. Although the contribution of particle impact ionization is larger than at Venus or at Mars, Titan's ionosphere is mainly generated by solar extreme ultraviolet radiation. However, Titan's plasma interaction possesses several unique features. On the one hand, depending on the orbital position, Titan's dayside ionosphere is not necessarily located in the ramside hemisphere of the satellite. On the other hand, the properties of the impinging magnetospheric plasma have shown to be highly variable along Titan's orbit. In the outer regions of Saturn's magnetosphere, the satellite typically faces a plasma flow that is super-alfvénic, but subsonic and submagnetosonic, assigning Titan's plasma environment a unique character among the non-magnetized bodies in the solar system. In contrast to this, in Saturn's magnetotail, all three Mach numbers of the impinging plasma are smaller than 1. When Saturn's magnetosphere is compressed due to high solar wind dynamic pressure, Titan's plasma environment is likely to undergo a most remarkable transition, as the satellite may be able to leave the Saturnian magnetosphere and interact directly with the solar wind.

Currently, most of the studies that deal with Titan's plasma interaction are based on the data obtained during the Voyager 1 flyby on 12 November 1980, while only very few results from the Cassini mission have already been published. When Titan is located inside Saturn's magnetosphere, no bow shock is formed in front of the satellite. Instead, both Voyager and Cassini measurements indicate the presence of a strong magnetic draping pattern, giving rise to a set of magnetic lobes in the downstream region. Newly generated ionospheric ions are being picked up by the magnetospheric plasma flow, which leads to an erosion of Titan's ionosphere. As the gyroradius of the newly generated ions is comparable to the size of the obstacle, ion kinetic effects are likely to impose a significant asymmetry on the structure of Titan's plasma wake.

CHAPTER 3

Simulation model

This chapter deals with the major features of the simulation code that has been applied to Titan's plasma interaction. After giving an overview of foregoing simulation studies, the basic concepts of the hybrid plasma description are presented. Furthermore, the discussion focuses on the representation of Titan's ionosphere in the framework of the simulation model. Finally, a brief overview of the basic numerical techniques is given, including an analysis of several specific problems associated with the Titan scenario.

1 Simulation studies of Titan's plasma environment

Various simulation studies on the subject of Titan's plasma interaction have already been carried out, most of them being based on the fluid plasma description. Cravens *et al.* [39] studied the global characteristics of Titan's plasma environment by using a two-dimensional multi-fluid model. The numerical approach allowed to maintain a high spatial resolution in Titan's ionosphere by means of a grid that possesses a cylindrical geometry and a non-uniform radial grid spacing. Three different ion species had been incorporated into these simulations. In agreement with data from the Voyager 1 flyby, the model confirmed that no bow shock arises in front of the obstacle. Besides, the authors suggest that in the wake region, the presence of Titan leads to noticeable distortions of Saturn's magnetospheric plasma flow only for radial distances below 10 Titan radii. However, since this 2D model cannot reproduce the draping of the ambient magnetic field around the obstacle, the formation of a magnetotail in the downstream region does not occur in the simulation results.

In order to obtain a more realistic description of Titan's plasma environment, the model has been extended to three spatial dimensions by Ledvina and Cravens [87], who analyzed the characteristics of the interaction region for two different cases: On the one hand, the simulation parameters have been chosen in accordance to data from the Voyager 1 flyby. On the other hand, the upstream plasma flow was assumed to be both supersonic and super-alfvénic. This scenario might be of importance for those times when Titan is located in the solar wind or in Saturn's magnetosheath. The model results indicate that for upstream plasma conditions similar to those observed during the Voyager 1 flyby, Titan possesses a narrow magnetotail with a diameter of only 2–3 Titan radii. In agreement with the results of Ness *et al.* [116], the authors show that – as long as Titan is located inside the Saturnian magnetosphere – the interaction does not only result in the formation of a strong magnetic draping pattern, but it gives also rise to a set of Alfvén wings. When the upstream plasma flow is assumed to be supersonic, the simulation results show the formation of a bow shock, denoting a sharp decrease of plasma velocity.

In order to analyze the data collected during the Voyager 1 flyby, Kabin *et al.* [67] have applied a 3D magnetohydrodynamic model to Titan's plasma interaction. The effects of a conducting ionosphere, exospheric mass loading and ion-neutral charge exchange processes are taken into account. Although the current state of knowledge is that Titan does not possess a noticeable intrinsic magnetic field [6, 116, 119], the authors succeeded in explaining several details of the observed density and magnetic field signatures by assuming the existence of a small intrinsic magnetic dipole moment. In a companion paper, Kabin *et al.* [68] use the results of a numerical MHD model to compare the magnetic field topology in Titan's wake to an idealized picture of field line draping around a conductive, non-magnetic obstacle. The correspondence of the magnetic field topology in the Titan wake to such a simplifying scenario is also emphasized by Israelevich *et al.* [65]. However, this study is again based on the assumption of a small intrinsic magnetic dipole field which would cause strong magnetic field rotations in the wake region.

A three-dimensional resistive MHD study that emphasizes the importance of mass loading effects for the structure of Titan's plasma environment has been carried out by Kopp and Ip [84]. In contrast to all three-dimensional simulation studies mentioned above, the model of Kopp and Ip [84] assumes a non-uniform ion production profile, i.e. the ion production rate depends on the solar zenith angle. The model results suggest the existence of a significant asymmetry in the structure of the mass-loading patterns between the Saturn-facing hemisphere and the anti-Saturn-facing hemisphere of Titan. The results of this study are in general agreement with Voyager 1 measurements.

A similar three-dimensional MHD simulation model has been developed by Nagy *et al.* [115] who take into consideration the effects of exospheric mass-loading as well as major chemical reactions and ion-neutral collisions. Three different ion species are incorporated into the model calculations. In preparation of the first close flybys of Titan by Cassini, Ma *et al.* [100] applied a modified version of this model to the specific geometry of the TA flyby. By using a spherically structured simulation grid, the authors were able to achieve an extremely good altitude resolution of about 36 km in the ionospheric region of Titan. In this approach, Titan's atmosphere and ionosphere have been approximated by 10 neutral and 7 ion species, each of them being represented by a continuity equation. In a subsequent study (cf. Ma [98] as well as Ma *et al.* [99]), the authors demonstrate that the simulation model does not only allow a reproduction of the magnetic field signature detected during TA, but they also present a successful application to the second Titan flyby of the Cassini mission. In terms of a 3D resistive MHD model, the magnetic field signature detected during TA has also been interpreted by Backes *et al.* [5, 6]. Based on the same approach, Neubauer *et al.* [118] have recently accomplished a comparative analysis of the magnetic field signatures measured during the Cassini TA, TB and T3 flybys. These flybys did not only take place at nearly the same orbital position of Titan, but the spacecraft trajectories with respect to Titan were also quite similar. The authors are able to identify a sharply pronounced outer boundary of the magnetic draping pattern in the vicinity of Titan, as it has been detected by Voyager 1 as well. It is demonstrated that this boundary corresponds to an MHD wing arising from fast mode and Alfvén waves. Moreover, Neubauer *et al.* [118] are able to confirm the results of several earlier studies, such as the lack of an intrinsic magnetic field and a shock front at the obstacle's ramside.

The results of the fluid simulations reproduce the overall features of the interaction region quite well. However, because the gyroradii of magnetospheric and ionospheric ions are comparable to the size of Titan, it is clear that ion kinetic effects also play a decisive role for the structure of the interaction region and that the MHD approximation is not strictly applicable. Besides, most of the fluid codes include only one ion species and do not carry the Hall term. Since such a model is not capable of displaying diamagnetic effects, it must return a symmetric solution. Anyway, due to the fluid description of the plasma, these codes have proven adequate to accommodate the complex chemical processes occurring in Titan's ionosphere. Moreover, since fluid models require by far not as much computing capacity as semi-kinetic or full-particle codes, they can cover larger spatial regions in a reasonable computing time.

Nonetheless, the need for a self-consistent model that takes finite gyroradius effects into account – such as the hybrid approach – has for instance been emphasized by Ledvina *et al.* [91] who calculated the trajectories of several thousand ions in the vicinity of Titan by using the electromagnetic field parameters obtained from a three-dimensional, self-consistent MHD model. A similar combination of magnetohydrodynamic and test particle simulations has been realized by Ledvina *et al.* [89] to make predictions for the Cassini orbiter particle experiments. In an analogous way, i.e. by incorporating test particles into the results of self-consistent MHD modelling, the velocity space distributions of several ion species in the vicinity of Titan have been studied [88]. The strong connection between the diameter of Titan's plasma wake and the gyroradii of the involved ion species has been pointed out by Luhmann [96] who analyzed the motion of individual ions downstream of Titan in terms of a test particle model. Nevertheless, none of these approaches is capable of offering a self-consistent description of the influence of ion kinetic effects.

Within the framework of a one-dimensional electromagnetic hybrid simulation, Dobé and Szegö [43] have recently analyzed the characteristics of the turbulent interaction region above Titan's ionosphere where both cold ionospheric and hot magnetospheric plasma are present at comparable densities. The authors suggest that the velocity difference between the two plasma populations may excite modified two-stream instabilities which, on the other hand, give rise to significant wave activity in Titan's upper ionosphere and in adjacent regions. The first who applied a self-consistent, *three*-dimensional hybrid model to the Titan scenario were Brecht *et al.* [30], referring to the case of the satellite encountering a *super*sonic corotating Saturnian magnetospheric plasma. The results show that Titan's magnetotail exhibits an asymmetry with respect to the direction of the convective electric field and hence, they underline the importance of ion kinetic effects. Nevertheless, due to the finite magnetospheric ion temperature being completely neglected, this model is not capable of covering the real (subsonic) nature of the impinging plasma flow. Based on the same simplifying assumptions, further hybrid simulations have been carried out by Ledvina *et al.* [90]. Kallio *et al.* [74] were the first who applied the hybrid approximation to the case of Titan facing an actually super-alfvénic, yet subsonic and submagnetosonic magnetospheric plasma flow. However, this model does not take into consideration the plasma's finite electron pressure, i.e. the electron temperature is set to zero in the momentum equation describing the dynamics of the electron fluid. Because earlier hybrid simulations of weak comets [7] and Mars [26, 27, 110] have demonstrated that both the location and the sharpness of the evolving plasma boundaries are strongly affected by the assumption of a finite electron temperature, the Titan model presented in this work will be the first one to consider this aspect.

Another 3D hybrid simulation study of Titan's plasma environment has been carried out by Modolo [106]. Even though this model had been successfully applied to the interaction between the Martian ionosphere and the solar wind (cf. [107, 108]), it offered only a rough description of both the ion pick-up process and the magnetic field topology in the vicinity of Titan. Specifically, the hemispherical asymmetries in Titan's plasma environment that should arise from the finite ion gyroradii do not manifest in the results. A similar model has been presented by Sillanpää *et al.* [135]. However, as for the asymmetric orientation of Titan's plasma wake, the results obtained from the latter approach do not only deviate from the test particle results presented by Luhmann [96] and Ledvina *et al.* [88, 89, 91], but they have also proven to be in direct opposition to data from spacecraft measurements [151]. Therefore, the results of these simulations will not be included in the comparative studies presented in subsequent chapters.

2 The hybrid model: Limits of validity

In general, the electrodynamics of a collision-free plasma are described by the complete set of Maxwell's equations:

$$\nabla \cdot \underline{B} = 0 \quad ; \tag{3.1}$$

$$\nabla \times \underline{E} = -\frac{\partial \underline{B}}{\partial t} \quad ; \tag{3.2}$$

$$\nabla \cdot \underline{E} = \frac{\rho_c}{\epsilon_0} \quad ; \tag{3.3}$$

$$\nabla \times \underline{B} = \mu_0 \underline{j} + \frac{1}{c^2}\frac{\partial \underline{E}}{\partial t} \quad . \tag{3.4}$$

Besides, the Vlasov equation has to be solved for each ion species:

$$\frac{\partial f_j}{\partial t} + \underline{v} \cdot \frac{\partial f_j}{\partial \underline{x}} + \frac{q_j}{m_j}\left(\underline{E} + \underline{v} \times \underline{B}\right) \cdot \frac{\partial f_j}{\partial \underline{v}} = 0 \quad . \tag{3.5}$$

The subscript j has been introduced to distinguish between different constituents of the plasma; m_j and q_j are the mass and charge of the particles, respectively. However, depending on the characteristics of the specific problem, a self-consistent description can often be achieved by means of a less complex approach.

Particle dynamics in a magnetized plasma allow to define characteristic scales for each ion component. On the one hand, typical time scales, determined by the inverse plasma frequency,

$$\omega_{p,j} = \sqrt{\frac{n_j q_j^2}{\epsilon_0 m_j}} \quad , \tag{3.6}$$

and the inverse gyration frequency of an ion in the magnetic field B,

$$\Omega_{g,j} = \frac{q_j B}{m_j} \quad , \tag{3.7}$$

can be introduced. In eq. (3.6), n_j denotes the number density of species j.

On the other hand, the particle trajectories in the plasma's electromagnetic fields can be characterized by means of typical length scales. The mean gyroradius of an ion of species j in the magnetic field B is given by

$$r_{g,j} = \frac{v_j}{\Omega_{g,j}} = \frac{m_j v_j}{q_j B} \quad , \tag{3.8}$$

where v_j denotes the velocity component perpendicular to the magnetic field. Another typical scale of ion motion is defined by the "inertia length",

$$l_{0,j} = \frac{c}{\omega_{p,j}} \quad , \tag{3.9}$$

which is nothing else but the gyroradius of a particle moving with the Alfvén speed

$$v_j = v_A = \frac{B}{\sqrt{\mu_0 n_j m_j}} \tag{3.10}$$

in a plane perpendicular to the magnetic field.

A kinetic modelling of the plasma component j, i.e. covering the dynamics of each individual particle, is required, if the characteristic length and time scales of this species are comparable to or even larger than the characteristic scales of the plasma processes under consideration. In the case of Titan's interaction with the Saturnian magnetospheric plasma, such a typical scale is defined by the size of the obstacle that is embedded into the flow. However, if the scales that are relevant for the specific interaction process are significantly larger than the scales associated with species j, this plasma component can be described by a fluid approach. In such a model, the dynamics of the plasma component j are covered by macroscopic quantities, e.g. the mean particle density and the mean flow velocity. The interactions between the Terrestrial and the Saturnian internal magnetic fields with the solar wind can be considered typical examples, for the scales of the magnetized obstacles are about several orders of magnitude larger than ion gyroradii.

In the framework of this work, an electromagnetic hybrid model has been used to study Titan's plasma environment. As already stated, such a "semi-kinetic" approach treats the electrons as a fluid, whereas a completely kinetic description is applied to magnetospheric and ionospheric ion dynamics. Since all details of ion kinetics are covered by this kind of model, the hybrid approximation is capable of describing those processes in Titan's plasma environment whose characteristic time scales are comparable to the inverse ion gyration frequency $\Omega_{g,i}$. Besides, the characteristic length scales have to be of the order of the ion inertia length $c/\omega_{p,i}$ and the mean ion gyroradius $r_{g,i}$, respectively. Even though multiple ion species are involved in determining the key features of Titan's plasma environment, it should be kept in mind that on the one hand, their characteristic length and time scales are of the same order of magnitude. On the other hand, they are about several orders of magnitude larger than the corresponding electron quantities.

Several ancillary simplifications have been incorporated into the simulation model:

- The mean number densities of electrons and ions are assumed to be equal:

$$n_e = n_i \qquad \text{(quasi-neutrality)} \quad . \tag{3.11}$$

In general, the approximation of quasi-neutrality is appropriate for frequencies below the electron plasma frequency $\omega_{p,e}$ and for characteristic length scales above the Debye length

$$\lambda_D = \sqrt{\left(\sum_j \frac{q_j^2 n_j}{\epsilon_0 k T_j} \right)^{-1}} \quad . \tag{3.12}$$

On scales larger than the Debye length, plasma dynamics are dominated by collective effects.

- As discussed above, the hybrid approximation is able to describe processes whose characteristic scales are comparable to the mean ion gyration radii and frequencies. Since on these scales, the electrons are able to adapt to ion dynamics without any noticeable delay, their inertia can be neglected. Thus, the approximation

$$m_e \approx 0 \tag{3.13}$$

is justified, leading to a description of the electron component as a massless fluid. However, although yielding certain simplifications of the set of hybrid equations, this step is not absolutely mandatory. The basic principles of a hybrid code considering the *finite* electron inertia are discussed by Lipatov [93].

- The wave modes involved in the interaction between a flowing plasma and a planetary obstacle are typically characterized by both particle motion and electromagnetic field distortions. A decoupling of the fields from particle dynamics, as it is realized in vacuum light waves, does not occur. For the low frequency phenomena under consideration, the displacement current $\frac{1}{c^2}\partial_t \underline{E}$ in Ampère's law can be neglected. This simplification is referred to as the *Darwin Model* by Hewett [63]. Bagdonat [7] proved the consistency of this approximation with the assumed quasi-neutrality of the plasma.

Of course, a hybrid model is not capable of describing effects whose characteristic length scales are comparable to the mean electron gyroradius. These phenomena can only be covered by means of a *full particle code* which solves the individual equations of motion for the ions as well as for the electrons. However, since ion gyration periods are about three orders of magnitude larger than the corresponding electron scales, the intervals of real time that are accessible to such a simulation are significantly smaller than the intervals that can be covered by a hybrid code in the same computing time. Moreover, using a full particle code instead of a hybrid model goes along with a strong increase of the storage capacity that is required for the simulations.

3 The hybrid model: Basic equations

The hybrid model treats the electrons as a massless, charge-neutralizing fluid. In contrast to this, a statistical representation is applied to the ions, i.e. their dynamics are described by the distribution function f_i which can be obtained from the Vlasov equation (3.5). In a quasi-neutral plasma, the mean number densities of electrons and single-charged ions fulfill the condition

$$n_e = n_i = \frac{\rho_c}{e} \quad , \tag{3.14}$$

where ρ_c is the ion charge density. In the following sections, the dynamic equations of this model will be discussed.

3.1 Electrons

In the framework of the hybrid model, electron dynamics are described by the expression

$$n_e m_e \frac{\mathrm{d}\underline{u}_e}{\mathrm{d}t} = -en_e\left(\underline{E} + \underline{u}_e \times \underline{B}\right) - \nabla P_e + n_e R \underline{j} \quad , \tag{3.15}$$

which represents a conservation equation for the momentum density of the electron fluid [142, 156]. The mean velocity and the pressure of the electrons are denoted by $\underline{u}_e$ and P_e, respectively. The microscopic exchange of momentum between electrons and ions is covered by the third term on the r.h.s. of eq. (3.15) and depends linearly on the resistivity R. This coupling between electrons and ions is determined by the current density

$$\underline{j} = \underline{j}_e + \underline{j}_i = -en_e\underline{u}_e + en_i\underline{u}_i \overset{(3.14)}{=} -\rho_c\left(\underline{u}_e - \underline{u}_i\right) \tag{3.16}$$

and therefore by the difference between the mean velocities $\underline{u}_e$ and $\underline{u}_i$ of electrons and ions.

By setting

$$m_e \overset{!}{=} 0 \tag{3.17}$$

on the r.h.s. of eq. (3.15), electron kinetic effects are eliminated from the model. This approximation yields an explicit expression for the electric field:

$$\underline{E} = -\underline{u}_e \times \underline{B} - \frac{1}{\rho_c}\nabla P_e + R\underline{j} \quad . \tag{3.18}$$

By incorporating eq. (3.16) and using Ampère's law,

$$\nabla \times \underline{B} = \mu_0 \underline{j} \quad , \tag{3.19}$$

eq. (3.18) finally takes the form

$$\underline{E} = -\underline{u}_i \times \underline{B} + \frac{(\nabla \times \underline{B}) \times \underline{B}}{\mu_0 \rho_c} - \frac{\nabla P_e}{\rho_c} + \frac{R}{\mu_0} \nabla \times \underline{B} \quad . \tag{3.20}$$

This expression for the electric field will be referred to as *generalized Ohm's law* [17, 21, 52, 79]. Apparently, the electron velocity $\underline{u}_e$ does no longer occur in this equation.

Furthermore, an equation of state that correlates the electron pressure P_e with the number density n_e is required in order to obtain a complete set of equations. In the model employed in this work, this functional dependence is given by an adiabatic law,

$$P_e = P_{e,0}\left(\frac{n_e}{n_{e,0}}\right)^{\kappa} \overset{(3.14)}{=} P_{e,0}\left(\frac{\rho_c}{\rho_{c,0}}\right)^{\kappa} \quad , \tag{3.21}$$

where κ is the adiabatic exponent. The quantities $n_{e,0}$ and $P_{e,0}$ are background values that describe the undisturbed, homogeneous magnetospheric plasma upstream of Titan. In order to choose an appropriate value for the adiabatic exponent κ, it has to be kept in mind that the thermodynamic coupling in a collision-free plasma is realized exclusively by the electromagnetic fields. Hence, an adequate approximation is given by $\kappa = 2$, which, due to

$$\kappa = \frac{f+2}{f} \quad , \tag{3.22}$$

corresponds to $f = 2$ degrees of freedom for each electron. Choosing the adiabatic exponent in this manner takes account for the fact that, unlike the situation in an *un*magnetized plasma, the electrons cannot move freely in three spatial dimensions, but they are "more or less" confined to planes perpendicular to the magnetic field. Further details are discussed by Bagdonat [7] and Kuehs [85] as well as by Winske and Omidi [155].

The curl of the pressure term in eq. (3.20) vanishes, i.e.

$$\nabla \times \left(\frac{\nabla P_e}{\rho_c} \right) = 0 \quad . \tag{3.23}$$

It is important to notice that the adiabatic description of the electron fluid is a major condition for the validity of eq. (3.23), since

$$\begin{aligned} \nabla \times \left(\frac{\nabla n_e^\kappa}{n_e} \right) &= \frac{1}{n_e} \nabla \times [\nabla (n_e^\kappa)] + \left[\nabla \frac{1}{n_e} \right] \times [\nabla (n_e^\kappa)] \\ &= \left[\nabla \frac{1}{n_e} \right] \times [\nabla (n_e^\kappa)] \\ &= -\frac{1}{n_e^2} [\nabla n_e] \times \kappa n_e^{\kappa-1} [\nabla n_e] \\ &= 0 \quad . \end{aligned} \tag{3.24}$$

By using Faraday's law and eq. (3.23), a differential equation describing the time evolution of the magnetic field can be derived from the generalized form of Ohm's law:

$$\frac{\partial \underline{B}}{\partial t} = \nabla \times (\underline{u}_i \times \underline{B}) - \nabla \times \left(\frac{(\nabla \times \underline{B}) \times \underline{B}}{\mu_0 \rho_c} \right) - R \, \nabla \times \left(\frac{\nabla \times \underline{B}}{\mu_0} \right) \quad . \tag{3.25}$$

In space plasmas, momentum transfer due to collisions between the individual particles is only of minor importance. For this reason, setting

$$R \approx 0 \tag{3.26}$$

in eqs. (3.20) and (3.25) is a justified assumption [17]. In subsequent sections, the resistive term will be consequently neglected.

3.2 Ions

In the hybrid model, ion dynamics are covered by the distribution function f_i which can be obtained from the Vlasov equation (3.5). Any partial differential equation of first order can be represented by means of its characteristics, which – in this case – are nothing else but the equations of motion known from classical electrodynamics:

$$\frac{\mathrm{d}\underline{x}_\nu}{\mathrm{d}t} = \underline{v}_\nu \qquad \text{and} \qquad \frac{\mathrm{d}\underline{v}_\nu}{\mathrm{d}t} = \frac{e}{m_i}\left(\underline{E} + \underline{v}_\nu \times \underline{B}\right) \quad . \tag{3.27}$$

The subscript "ν" has been introduced to discriminate between individual ions. The particle positions $\underline{x}_\nu$ and velocities $\underline{v}_\nu$ include the entire information that are needed to compute the distribution function $f_i(\underline{x}, \underline{v})$. Consequently, the mean values of the charge density and ion velocity occurring in eqs. (3.20) and (3.25) can be obtained by integrating over the distribution function:

$$\rho_c(\underline{x}) = e \int f_i(\underline{x}, \underline{v})\,\mathrm{d}^3v \quad ; \tag{3.28}$$

$$\underline{j}_i(\underline{x}) = e \int \underline{v}\, f_i(\underline{x}, \underline{v})\,\mathrm{d}^3v \quad ; \tag{3.29}$$

$$\underline{u}_i = \frac{\underline{j}_i}{\rho_c} \quad . \tag{3.30}$$

Together with eqs. (3.20), (3.21) and (3.25), these expressions form a complete set of equations, describing the plasma within the scope of the hybrid model. Nevertheless, the situation at Titan enforces an additional modification of the description of electron dynamics.

3.3 Hybrid model with two electron fluids

So far, the dynamics of the electron population are governed by the fluid equation (3.18) and the adiabatic law (3.21). However, theoretical models developed by Gan *et al.* [49] and Roboz *et al.* [126] indicate the electron temperature in Titan's ionosphere to differ significantly from the electron temperature in the surrounding magnetospheric plasma. Hence, an adequate model should include two distinct electron populations with different temperatures, i.e. a *two-fluid description* should be applied to the electrons in the vicinity of Titan. Each of these populations has to be described by a momentum conservation law according to eq. (3.15), i.e.

$$0 = -en_{e,1}\left(\underline{E} + \underline{u}_{e,1} \times \underline{B}\right) - \nabla P_{e,1} \tag{3.31}$$

$$\text{and} \quad 0 = -en_{e,2}\left(\underline{E} + \underline{u}_{e,2} \times \underline{B}\right) - \nabla P_{e,2} \quad . \tag{3.32}$$

The subscripts 1 and 2 denote the magnetospheric and ionospheric electron populations, respectively. However, incorporating the additional momentum equation (3.32) into the model would go along with an increase of the number of free parameters, i.e. additional coupling equations would have to be introduced. In order to restrict the numerical complexity of the electric field solver, this problem has been circumvented by means of a less elaborate strategy.

Adding eqs. (3.31) and (3.32) yields

$$0 = -e\left(n_{e,1} + n_{e,2}\right)\underline{E} - e\left(n_{e,1}\underline{u}_{e,1} + n_{e,2}\underline{u}_{e,2}\right) \times \underline{B} - \nabla P_{e,1} - \nabla P_{e,2} \quad . \tag{3.33}$$

By incorporating the cumulative electron density

$$n_e \equiv n_{e,1} + n_{e,2} \qquad \left(= n_i = \frac{\rho_c}{e}\right) \quad , \tag{3.34}$$

the above expression yields

$$\underline{E} = -\left(\frac{n_{e,1}}{n_e}\underline{u}_{e,1} + \frac{n_{e,2}}{n_e}\underline{u}_{e,2}\right) \times \underline{B} - \frac{\nabla P_{e,1} + \nabla P_{e,2}}{en_e} \quad . \tag{3.35}$$

In the next step, a *mean electron velocity* $\underline{u}_e$ as well as a *mean electron current density* $\underline{j}_e$ are introduced by means of

$$\underline{u}_e = \frac{n_{e,1}}{n_e}\underline{u}_{e,1} + \frac{n_{e,2}}{n_e}\underline{u}_{e,2} \tag{3.36}$$

and

$$\underline{j}_e = -e\left(n_{e,1}\underline{u}_{e,1} + n_{e,2}\underline{u}_{e,2}\right) = -en_e\underline{u}_e \quad , \tag{3.37}$$

respectively. By using these definitions, the expression describing the electric field becomes

$$\underline{E} = -\underline{u}_e \times \underline{B} - \frac{\nabla P_{e,1} + \nabla P_{e,2}}{\rho_c} \quad . \tag{3.38}$$

In analogy to eq. (3.20), the mean electron velocity $\underline{u}_e$ can be eliminated by using Ampère's law,

$$\nabla \times \underline{B} = \mu_0\left(\underline{j}_i + \underline{j}_e\right) \quad \rightsquigarrow \quad \underline{u}_e = \frac{1}{\rho_c}\underline{j}_i - \frac{1}{\mu_0\rho_c}\nabla \times \underline{B} = \underline{u}_i - \frac{1}{\mu_0\rho_c}\nabla \times \underline{B} \quad , \tag{3.39}$$

yielding

$$\underline{E} = -\underline{u}_i \times \underline{B} + \frac{(\nabla \times \underline{B}) \times \underline{B}}{\mu_0\rho_c} - \frac{\nabla P_{e,1} + \nabla P_{e,2}}{\rho_c} \quad . \tag{3.40}$$

Based on this expression, the magnetic field can again be computed by means of Faraday's law. Both electron populations are assumed to be adiabatic, i.e.

$$P_{e,1} \propto (n_{e,1})^\kappa \tag{3.41}$$

$$\text{and} \qquad P_{e,2} \propto (n_{e,2})^\kappa \quad . \tag{3.42}$$

The constants of proportionality in eqs. (3.41) and (3.42) can be chosen independently of each other, therefore allowing to introduce an initial temperature for each of the two electron populations. If not stated otherwise, a value of $kT_{e,1} = 210\,\mathrm{eV}$ has been chosen for the magnetospheric electrons [119]. The ionospheric electron parameters will be discussed in section 6.

However, it is important to notice that the simulation model is able to distinguish between the densities *and* velocities of different ion species, whereas it takes into account both densities $n_{e,1}$ and $n_{e,2}$, but only the average velocity $\underline{u}_e$. Therefore, the convective term in eq. (3.38) includes an averaged quantity, while the discrimination between the two electron fluids is realized only by means of an additional pressure gradient in the numerator of the second term. Due to the quasi-neutrality, $n_{e,1}$ and $n_{e,2}$ are identical to the number densities of the corresponding ion populations.

Finally, the validity of this approximation has to be discussed. In general, the assumptions made above describe the real situation quite well in regions where the magnetospheric and the ionospheric plasma do not mix, i.e. inside the central plasma wake downstream of Titan and in a certain distance to the obstacle. Of course, in all intermediate regions, this approach can be considered only a rough approximation to the real situation. Furthermore, assuming the densities $n_{e,1}$ and $n_{e,2}$ to equal the respective ion densities implies that the electrons should mix in exactly the same way as magnetospheric and ionospheric ions do. This hypothesis may not be true in reality.

Nonetheless, the approach presented above is still more sophisticated than the assumptions included in other hybrid models. Brecht *et al.* [30] and Ledvina *et al.* [90] tried to analyze Titan's plasma environment by means of a hybrid model which assumes the magnetospheric as well as the ionospheric plasma to be cold. In a similar way, Kallio *et al.* [74] have developed a hybrid model of Titan's plasma environment that neglects the finite electron temperature. To the author's knowledge, a hybrid model including the electron pressure term has not yet been used to study Titan's plasma interaction. The hybrid codes applied by Bagdonat [7] to the plasma environment of weak comets and by Bößwetter *et al.* [26, 27] to the Martian plasma interaction are based on the same simplifying assumptions as described above.

4 Basic principles of ion and field dynamics

This section gives a short overview of the different forces acting on the particles and field lines in the framework of the hybrid model. The discussion refers to a plasma that consists of two different single-charged ion species, denoted by the subscripts 1 and 2. It is also assumed that the mean velocity $\underline{u}_2$ of species 2 is small compared to the velocity $\underline{u}_1$ of species 1. For instance, the first species may be the solar wind or the corotating plasma in Saturn's magnetosphere, whereas the second ion population may originate from Titan's ionosphere. For simplicity, the velocities of the individual particles are considered to be comparable to the mean flow speeds $\underline{u}_1$ and $\underline{u}_2$, i.e. both plasma constituents are assumed to be sufficiently cold.

Due to the kinetic description of the ions, their dynamics are governed by the Lorentz force $\underline{F}_L$, i.e.

$$\frac{\underline{F}_{L,1}}{m_1} = \frac{\mathrm{d}\underline{v}_1}{\mathrm{d}t} = \frac{e}{m_1}\left(\underline{E} + \underline{v}_1 \times \underline{B}\right) \tag{3.43}$$

$$\text{and} \quad \frac{\underline{F}_{L,2}}{m_2} = \frac{\mathrm{d}\underline{v}_2}{\mathrm{d}t} = \frac{e}{m_2}\left(\underline{E} + \underline{v}_2 \times \underline{B}\right) \quad , \tag{3.44}$$

$$\tag{3.45}$$

where an additional subscript that discriminates between different particles of the same species has been suppressed. The electric field is given by the generalized form of Ohm's law that can be written as

$$\underline{E} = -\left(\frac{n_1}{n_1+n_2}\underline{u}_1 + \frac{n_2}{n_1+n_2}\underline{u}_2\right) \times \underline{B} + \frac{(\nabla \times \underline{B}) \times \underline{B}}{\mu_0 e\,(n_1+n_2)} - \frac{\nabla P_{e,1} + \nabla P_{e,2}}{e\,(n_1+n_2)} \quad . \tag{3.46}$$

In this expression, n_j $(j = 1, 2)$ are the mean densities of the two ion species. In the following, the contribution of the three summands to the Lorentz force will be discussed. All quantities without an additional subscript "e" refer to the ion components. As discussed in the previous section, the electron density of each constituent equals the corresponding mean ion density, i.e.

$$n_1 = n_{e,1} \qquad \text{and} \qquad n_2 = n_{e,2} \quad , \tag{3.47}$$

respectively.

The first term in eq. (3.46) is the convective electric field $\underline{E}_c$,

$$\underline{E}_c = -\left(\frac{n_1}{n_1+n_2}\underline{u}_1 + \frac{n_2}{n_1+n_2}\underline{u}_2\right) \times \underline{B} \tag{3.48}$$

and corresponds to an ideal coupling of the magnetic field lines to the plasma flow (*Frozen-In Theorem*). In regions where species 1 is the predominant one, i.e.

$$n_1 \gg n_2 \quad , \tag{3.49}$$

the convective electric field is approximatively given by

$$\underline{E}_c = -\underline{u}_1 \times \underline{B} \quad . \tag{3.50}$$

In order to analyze the influence of this field on particle dynamics, it is assumed that $\underline{E}_c$ dominates the two other terms in eq. (3.46). Consequently, the Lorentz force acting on an ion of species 1 is given by

$$\underline{F}_{L,1} = e\,(\underline{v}_1 - \underline{u}_1) \times \underline{B} \quad . \tag{3.51}$$

Hence, the Lorentz force experienced by a particle of species 1 almost vanishes because the individual particle velocity $\underline{v}_1$ does not differ significantly from the mean plasma velocity $\underline{u}_1$. On the other hand, the Lorentz force on a particle of the second species is given by

$$\underline{F}_{L,2} = e\,(\underline{v}_2 - \underline{u}_1) \times \underline{B} \quad . \tag{3.52}$$

As the individual particle velocity $\underline{v}_2$ is assumed to be significantly smaller than the mean velocity $\underline{u}_1$, the Lorentz force can be written as

$$\underline{F}_{L,2} = -e\underline{u}_1 \times \underline{B} \quad . \tag{3.53}$$

For instance, this situation occurs when slow ions of ionospheric origin (species 2) try to gain access to an area where the ambient magnetospheric or solar wind ions are the predominant species. Arising from the convective electric field, species 2 particles experience a force that is directed perpendicular to both the flow direction of species 1 and the magnetic field.

The case of the slow species 2 being the predominant one can be discussed in an analogous manner. Such a situation can occur in the wake region downstream of a planetary obstacle, which is scarcely accessible to the ambient plasma species 1. Hence, an approximation for the convective electric field is given by

$$\underline{E}_c = -\underline{u}_2 \times \underline{B} \quad . \tag{3.54}$$

Again, it is assumed that the velocity of species 2 is negligible compared to $\underline{u}_1$ and $\underline{v}_1$. Consequently, the Lorentz force that is experienced by an ion of species 1 reads

$$\underline{F}_{L,1} = e\,(\underline{v}_1 - \underline{u}_2) \times \underline{B} \approx e\underline{v}_1 \times \underline{B} \quad . \tag{3.55}$$

On the other hand, an ion of species 2 is practically not accelerated, since

$$\underline{F}_{L,2} = e\,(\underline{v}_2 - \underline{u}_2) \times \underline{B} \approx 0 \quad . \tag{3.56}$$

In general, it is important to notice that the force arising from the convective electric field term $\underline{E}_c$ depends only on the magnetic field strength itself, but it is independent of magnetic field gradients.

Another contribution to the Lorentz force arises from the electron pressure terms:

$$\underline{E}_\nabla = -\frac{\nabla P_{e,1} + \nabla P_{e,2}}{e\,(n_1+n_2)} \quad . \tag{3.57}$$

For the simulations discussed in this work, the charge-neutralizing electron fluid of any ion species is assumed to be adiabatic, i.e.

$$P_{e,j} = (n_{e,j})^\kappa = (n_j)^\kappa \quad ; \quad j = 1,2 \quad , \tag{3.58}$$

where a constant proportionality factor is not mentioned explicitly. As a value of $\kappa = 2$ has been chosen for the adiabatic exponent, the electron pressure gradient can be written as

$$\nabla P_{e,j} = \kappa\,(n_j)^{\kappa-1}\,\nabla n_j = 2 n_j \nabla n_j \quad ; \quad j = 1,2 \quad . \tag{3.59}$$

In regions where the contribution of one of the two ion species, e.g. species 2, can be neglected, eq. (3.57) yields

$$\underline{E}_\nabla = -\frac{\nabla P_{e,1}}{e n_1} = -\frac{2}{e}\,\nabla n_1 \quad . \tag{3.60}$$

Due to the adiabatic description of the electron fluid, the force arising from the electron pressure term would depend only on the density gradient ∇n_1, but not on the absolute density value n_1 itself.

The Hall term

$$\underline{E}_H = \frac{(\nabla\times\underline{B})\times\underline{B}}{\mu_0 e\,(n_1+n_2)} = \frac{1}{\mu_0 e\,(n_1+n_2)}\left[-\frac{1}{2}\nabla\left(\underline{B}^2\right) + \left(\underline{B}\cdot\nabla\right)\underline{B}\right] \tag{3.61}$$

makes up the third contribution to the electric field. The first summand in brackets depends on the magnetic pressure gradient,

$$\nabla P_{\mathrm{magn}} = \nabla \frac{\underline{B}^2}{2\mu_0} \quad . \tag{3.62}$$

The electric field arising from this term is directed antiparallel to the magnetic pressure gradient, i.e. it points away from regions with high magnetic field strength. This term tends to accelerate the plasma in regions where the magnetic field lines are compressed, e.g. in the magnetic pile-up region that is formed at the ramside of a planetary obstacle. The second term describes the force arising from the magnetic tension. This term is responsible for accelerating the plasma in regions of high magnetic field curvature.

In the framework of the hybrid model, the magnetic field can be obtained from the partial differential equation

$$\frac{\partial\underline{B}}{\partial t} = \nabla\times\left[\left(\frac{n_1}{n_1+n_2}\underline{u}_1 + \frac{n_2}{n_1+n_2}\underline{u}_2\right)\times\underline{B}\right] - \nabla\times\left[\frac{(\nabla\times\underline{B})\times\underline{B}}{\mu_0 e\,(n_1+n_2)}\right] \quad . \tag{3.63}$$

The first term in this expression is equivalent to the Frozen-in Theorem, i.e. it describes the synchronous transport of the magnetic field by the plasma flow. In regions where the slow ionospheric species 2 becomes predominant, e.g. in the dayside ionospheres of Venus, Mars or Titan, the change of magnetic field strength arising from this term almost vanishes. Therefore, the magnetic field lines cannot be transported through these regions by means of convection and drape around the obstacle. However, a magnetic field transport through these regions can also arise from magnetic diffusion. Although a diffusion term has not been incorporated into the field equations used in this work, a certain amount of numerical diffusion is present in any simulation model, allowing the magnetic field to penetrate into the immediate vicinity of the planetary obstacle. The second term in eq. (3.63) is again correlated to the magnetic tension and the magnetic pressure. The occurrence of this term in the magnetic field equation demonstrates that the pressure and tension forces do not only act on the particles, but they also exert an influence on the field lines themselves: The pressure term tends to extend the distance between the field lines in regions of high field strength, whereas the magnetic tension term is responsible for reducing the curvature of the field lines. Consequentially, both terms are completely negligible in a perfectly homogeneous solar wind plasma.

5 Magnetospheric plasma parameters: The Voyager 1 scenario

This section deals with the simulation parameters that have been used to represent the undisturbed magnetospheric plasma impinging on Titan. Currently, the MHD models presented by Backes *et al.* [6] and by Ma *et al.* [99] are the only approaches that are *not* based on the plasma and magnetic field parameters derived from Voyager 1 data. Of course, before the first Cassini flybys in 2004, this material provided the only sophisticated characterization of Titan's plasma environment. Nonetheless, even most of the models that have been designed *after* the first Cassini encounters are based on the Voyager 1 data set as well. The major reason for this is the extremely simple geometry of the Voyager 1 scenario. As discussed by Neubauer *et al.* [119], the ambient magnetic field during the Voyager 1 encounter was directed nearly perpendicular to Titan's orbital plane and therefore to the corotating plasma flow, i.e. its components tangential to the orbital plane could safely be neglected. Thus, the undisturbed convective electric field vector is tangential to Titan's orbital plane, i.e. the Voyager 1 geometry allows to gain relatively clear and straightforward access to the involved physical processes. To date, such a simple situation has not been found during any of the Cassini flybys. In order to interprete the data collected during the Cassini mission, taking into account effects like deviations from the corotational flow direction and tilts of the magnetic field orientation has proven mandatory.

Therefore, the simulations carried out for the present study are categorized as follows:

- In order to investigate the basic physical mechanisms that are involved in the interaction process, the simulation parameters have been chosen in accordance to Voyager 1 data. On the one hand, this strategy allows an extensive comparative discussion of the simulation results, for a huge number of models with nearly the same input parameters are available. On the other hand, a foregoing analysis of the major physical processes in the framework of a simplifying geometry has proven to be extremely helpful for interpreting the rather complex data sets collected during the Cassini mission.

- The results obtained from the simple Voyager 1 geometry allow an application of the model to the more complex situations observed during the first Cassini encounters. The input parameters of these simulations have been chosen in accordance to specific flyby data.

An overview of the magnetospheric plasma and field parameters derived from Voyager 1 data is given in table 3.1. According to Neubauer *et al.* [119], the plasma mainly consisted of nitrogen (N^+) and hydrogen (H^+) ions.

The following sections dwell on some of the details. At first, since needed on many occasions throughout this work, the formal definitions of the alfvénic, sonic and magnetosonic Mach numbers are briefly summarized. Furthermore, the application of a simplifying representation to the magnetospheric plasma flow is discussed. In table 3.1, the corresponding parameters are denoted by the abbreviation "(N^+/H^+)". An explanation will be given in section 5.2.

5.1 Alfvénic, sonic and magnetosonic Mach number

In a magnetized plasma that consists of electrons and one ion species, the Alfvén velocity is given by

$$v_A = \frac{B_0}{\sqrt{\mu_0 \left(n_i m_i + n_e m_e\right)}} = \frac{B_0}{\sqrt{\mu_0 n_i \left(m_i + m_e\right)}} \approx \frac{B_0}{\sqrt{\mu_0 n_i m_i}} \quad , \tag{3.64}$$

where m_i and n_i are the ion mass and number density, respectively. The corresponding parameters for the electron component are denoted by m_e and n_e. The plasma flow is assumed to be homogeneous with a spatially constant magnetic field strength B_0. Given the bulk velocity u_0 of the plasma, the alfvénic Mach number can be obtained from

$$M_A = \frac{u_0}{v_A} \quad . \tag{3.65}$$

The sound velocity c_s in the undisturbed plasma flow is defined as

$$c_s = \sqrt{\kappa \frac{P}{n_i m_i}} \quad , \tag{3.66}$$

with both the electron and the ion component contributing to the pressure P:

$$P = P_i + P_e \quad . \tag{3.67}$$

Incorporating the plasma betas

$$\beta_i = \frac{P_i}{\frac{B_0^2}{2\mu_0}} = \frac{n_i k T_i}{\frac{B_0^2}{2\mu_0}} \quad \text{and} \quad \beta_e = \frac{P_e}{\frac{B_0^2}{2\mu_0}} = \frac{n_e k T_e}{\frac{B_0^2}{2\mu_0}} \quad , \tag{3.68}$$

defined as the ratio of the respective component's thermal pressure $P = nkT$ and the magnetic pressure $B_0^2/2\mu_0$, yields

$$c_S = \sqrt{\kappa \frac{B_0^2 \left(\beta_i + \beta_e\right)}{2\mu_0 n_i m_i}} = v_A \sqrt{\kappa \frac{\left(\beta_i + \beta_e\right)}{2}} \quad . \tag{3.69}$$

Quantity	Symbol	Numerical value
Magnetic field strength	B_0	$5\,\mathrm{nT}$
Number density	n_0	$n_0\,(H^+) = 0.1 \cdot 10^6\,\mathrm{m}^{-3}$
		$n_0\,(N^+) = 0.2 \cdot 10^6\,\mathrm{m}^{-3}$
		$n_0\,(N^+/H^+) = 0.3 \cdot 10^6\,\mathrm{m}^{-3}$
Bulk velocity	u_0	$120\,\mathrm{km/s}$
Electron temperature	T_e	$2.32 \cdot 10^6\,\mathrm{K}\,(200\,\mathrm{eV})$
Ion temperature	T_i	$T\,(H^+) = 2.44 \cdot 10^6\,\mathrm{K}\,(210\,\mathrm{eV})$
		$T\,(N^+) = 3.37 \cdot 10^7\,\mathrm{K}\,(2900\,\mathrm{eV})$
		$T\,(N^+/H^+) = 2.32 \cdot 10^7\,\mathrm{K}\,(2003\,\mathrm{eV})$
		Derived value
Electron gyrofrequency	$\Omega_{g,e}$	$879\,\mathrm{s}^{-1}$
Electron gyroradius	$r_{g,e}$	$136\,\mathrm{m}\,(5.3 \cdot 10^{-5} R_T)$
Electron plasma frequency	$\omega_{p,e}$	$30.9 \cdot 10^3\,\mathrm{s}^{-1}$
Electron inertia length	$l_{0,e} = c/\omega_{p,e}$	$10\,\mathrm{km}\,(3.9 \cdot 10^{-3} R_T)$
Debye length	λ_D	$164\,\mathrm{m}\,(6.4 \cdot 10^{-5} R_T)$
Ion gyrofrequency	$\Omega_{g,i}$	$\Omega_g\,(H^+) = 0.48\,\mathrm{s}^{-1}$
		$\Omega_g\,(N^+) = 0.03\,\mathrm{s}^{-1}$
		$\Omega_g\,(N^+/H^+) = 0.05\,\mathrm{s}^{-1}$
Ion gyroradius	$r_{g,i}$	$r_g\,(H^+) = 250\,\mathrm{km}\,(0.1 R_T)$
		$r_g\,(N^+) = 3507\,\mathrm{km}\,(1.4 R_T)$
		$r_g\,(N^+/H^+) = 2405\,\mathrm{km}\,(0.9 R_T)$
Ion plasma frequency	$\omega_{p,i}$	$\omega_p\,(H^+) = 416\,\mathrm{s}^{-1}$
		$\omega_p\,(N^+) = 157\,\mathrm{s}^{-1}$
		$\omega_p\,(N^+/H^+) = 232\,\mathrm{s}^{-1}$
Ion inertia length	$l_{0,i} = c/\omega_{p,i}$	$l_0\,(H^+) = 720\,\mathrm{km}\,(0.3 R_T)$
		$l_0\,(N^+) = 1905\,\mathrm{km}\,(0.7 R_T)$
		$l_0\,(N^+/H^+) = 1288\,\mathrm{km}\,(0.5 R_T)$
Alfvén velocity	v_A	$64.26\,\mathrm{km/s}$
Alfvénic Mach number	M_A	1.87
Electron plasma beta	β_e	0.97
Ion plasma beta	β_i	$\beta\,(H^+) = 0.34$
		$\beta\,(N^+) = 9.34$
		$\beta\,(N^+/H^+) = 9.68$
Sound velocity	c_S	$209.69\,\mathrm{km/s}$
Sonic Mach number	M_S	0.57
Magnetosound velocity	c_{MS}	$219.32\,\mathrm{km/s}$
Magnetosonic Mach number	M_{MS}	0.55

Table 3.1: Characteristic parameters of Titan's plasma environment according to Voyager 1 data, as given by Neubauer *et al.* [119]. The ambient magnetic field vector $\underline{B}_0$ is oriented perpendicular to Titan's orbital plane. The values denoted by the abbreviation (N^+/H^+) refer to a *single-species plasma* whose mean ion mass and mean particle density are given by $m(N^+/H^+) = (2 \cdot m(N^+) + 1 \cdot m(H^+))/3 = 9.67\,\mathrm{amu}$ and $n_0(N^+/H^+) = n_0\,(N^+) + n_0\,(H^+) = 0.3 \cdot 10^6\,\mathrm{m}^{-3}$, respectively. In the first simulation attempts, such a plasma has been used to approximate the composition of the magnetospheric flow near Titan.

Hence, the sonic Mach number of the plasma flow can be introduced by means of

$$M_S = \frac{u_0}{c_S} = \frac{M_A}{\sqrt{\frac{\kappa}{2}\left(\beta_i + \beta_e\right)}} \quad . \tag{3.70}$$

However, the characteristic velocity of compressional waves in a magnetized plasma is not the sound velocity c_S, but the magnetosound velocity c_{MS}. This quantity denotes the maximum velocity that can be achieved by fast magnetosonic waves and is given by

$$c_{MS} = \sqrt{c_S^2 + v_A^2} = v_A \sqrt{\frac{\kappa}{2}\left(\beta_i + \beta_e\right) + 1} \quad . \tag{3.71}$$

Consequently, the magnetosonic Mach number of the plasma flow can be introduced according to

$$M_{MS} = \frac{u_0}{c_{MS}} = \frac{M_A}{\sqrt{\frac{\kappa}{2}\left(\beta_i + \beta_e\right) + 1}} \quad . \tag{3.72}$$

The analysis of Titan's interaction with the Saturnian magnetospheric plasma requires a generalization of the equations derived above, for the ambient plasma consists of two ion species of masses m_1 and m_2, their densities being referred to as n_1 and n_2. According to Cap [32], the generalized Alfvén velocity can be expressed as

$$v_A = \frac{B_0}{\sqrt{\mu_0\left(n_1 m_1 + n_2 m_2 + n_e m_e\right)}} \approx \frac{B_0}{\sqrt{\mu_0\left(n_1 m_1 + n_2 m_2\right)}} \quad . \tag{3.73}$$

In the case of a multi-ion plasma, this velocity must be incorporated into eq. (3.65) in order to obtain the alfvénic Mach number M_A. In the framework of the simple gasdynamic picture that has already been used above, the total pressure P is the sum of the partial pressures of ions (P_1, P_2) and electrons:

$$P = P_1 + P_2 + P_e \quad . \tag{3.74}$$

In analogy to eqs. (3.70) and (3.72), the sonic and magnetosonic Mach numbers read

$$M_S = \frac{M_A}{\sqrt{\frac{\kappa}{2}\left(\beta_1 + \beta_2 + \beta_e\right)}} \tag{3.75}$$

and

$$M_{MS} = \frac{M_A}{\sqrt{\frac{\kappa}{2}\left(\beta_1 + \beta_2 + \beta_e\right) + 1}} \quad , \tag{3.76}$$

respectively [32]. The plasma betas β_1 and β_2 of the ion components are defined in analogy to eq. (3.68). As can easily be verified, these generalizations are consistent in such way that they fulfill the relation

$$M_{MS} = \frac{u_0}{\sqrt{c_S^2 + v_A^2}} = \frac{1}{\sqrt{\left(\frac{1}{M_S}\right)^2 + \left(\frac{1}{M_A}\right)^2}} = \frac{M_S M_A}{\sqrt{M_S^2 + M_A^2}} \quad . \tag{3.77}$$

5.2 Single-species representation of a multi-species flow

As stated above, the magnetospheric plasma that interacts with Titan's ionosphere consists of two different species, atomic nitrogen (N^+) and atomic hydrogen (H^+) ions. In most of the simulation models that have been applied to Titan's plasma interaction, this two-component plasma[1] is represented by a single species, featuring "intermediate" properties in the way that the alfvénic, sonic and magnetosonic Mach numbers of the model plasma and the (real) two-component flow are identical. Such a single-species representation has been successfully applied to the magnetospheric plasma near Titan in the MHD models designed by Kabin *et al.* [67, 68] and by Ma *et al.* [99] as well as in the hybrid approach presented by Kallio *et al.* [74]. Because for the first simulation attempts presented in this work, such a simplifying approach has been employed as well, the major parameters will be briefly discussed in the following. The single-species representation of the magnetospheric plasma used in the model is referred to as the (N^+/H^+) flow.

The first component of the two-species magnetospheric plasma impinging on Titan is denoted by the subscript 1, i.e. these ions possess the mass m_1, the number density n_1 and the temperature T_1, respectively. The corresponding parameters of the second component are m_2, T_2 and n_2. Both components are characterized by the same upstream velocity u_0. Thus, the Mach numbers of this two-component flow read

$$M_A = \frac{u_0}{B_0}\sqrt{\mu_0\left(n_1 m_1 + n_2 m_2\right)} \quad , \tag{3.78}$$

$$M_S = \frac{M_A}{\sqrt{\frac{\kappa}{2}\left(\beta_1+\beta_2+\beta_e\right)}} \tag{3.79}$$

$$\text{and} \quad M_{MS} = \frac{M_A}{\sqrt{\frac{\kappa}{2}\left(\beta_1+\beta_2+\beta_e\right)+1}} \quad , \tag{3.80}$$

where β_1 and β_2 are the ion plasma betas,

$$\beta_j = \frac{n_j k T_j}{\frac{B_0^2}{2\mu_0}} \quad ; \quad j = 1, 2 \quad . \tag{3.81}$$

A single-species representation of this two-species flow can be realized by introducing the total density

$$n = n_1 + n_2 \quad , \tag{3.82}$$

as well as the mean ion mass

$$m = \frac{n_1 m_1 + n_2 m_2}{n} \tag{3.83}$$

and the mean temperature

$$T = \frac{n_1 T_1 + n_2 T_2}{n} \quad . \tag{3.84}$$

Hence, the ion plasma beta of the single-species flow is given by

$$\beta = \frac{nkT}{\frac{B_0^2}{2\mu_0}} = \frac{nk\frac{n_1 T_1 + n_2 T_2}{n}}{\frac{B_0^2}{2\mu_0}} = \beta_1 + \beta_2 \quad . \tag{3.85}$$

---

[1] Within the framework of this work, the term "component" always refers to the number of ion species.

Let $\tilde{M}_A$, $\tilde{M}_S$ and $\tilde{M}_{MS}$ be the Mach numbers of the single-species flow used in the simulation model. Obviously, these parameters are identical to the Mach numbers of the real two-species flow, as given by eqs. (3.78)-(3.80):

$$\begin{aligned}
\tilde{M}_A &= \frac{u_0}{B_0}\sqrt{\mu_0 n m} = \frac{u_0}{B_0}\sqrt{\mu_0 n \frac{n_1 m_1 + n_2 m_2}{n}} = M_A \quad ; && (3.86)\\
\tilde{M}_S &= \frac{M_A}{\sqrt{\frac{\kappa}{2}\left(\beta + \beta_e\right)}} = \frac{M_A}{\sqrt{\frac{\kappa}{2}\left(\beta_1 + \beta_2 + \beta_e\right)}} = M_S \quad ; && (3.87)\\
\tilde{M}_{MS} &= \frac{M_A}{\sqrt{\frac{\kappa}{2}\left(\beta + \beta_e\right) + 1}} = \frac{M_A}{\sqrt{\frac{\kappa}{2}\left(\beta_1 + \beta_2 + \beta_e\right) + 1}} = M_{MS} \quad . && (3.88)
\end{aligned}$$

The parameters of the (N^+/H^+) plasma that have been used in this work can be found in table 3.1.

6 Modelling Titan's ionosphere

This section focuses on the representation of Titan's ionosphere in the framework of the simulation model. However, before dwelling on the details, a brief overview of the physics of planetary ionospheres will be given. A more extensive discussion is provided by Bauer [12], Bauer and Lammer [13] as well as Baumjohann and Treumann [17].

6.1 General properties

The ionosphere is located above a planet's or moon's neutral atmosphere and consists of neutral atoms as well as of plasma. A planet that possesses a neutral atmosphere is surrounded by an ionosphere, if an ionization source for the neutral atoms is present. On the one hand, the neutral atoms can be ionized by solar ultraviolet radiation (*photoionization*), but on the other hand, energetic particles penetrating into the atmosphere are also capable of acting as an ionization source. At Titan, the energetic particles originate primarily from Saturn's magnetospheric plasma and from the solar wind. In order to be capable of participating in the ionization process, the kinetic energy of the impinging particles must exceed the ionization potential of the atmospheric atoms. Two different ionization processes are associated with impinging particles:

- *Charge exchange reactions:*
  An electron is transferred from an impinging ion $\mathcal{I}^+$ to an atmospheric neutral atom $\mathcal{N}$:

  $$\mathcal{I}^+ + \mathcal{N} \longrightarrow \mathcal{I} + \mathcal{N}^+ \quad . \qquad (3.89)$$

  A process that has been observed in Titan's plasma environment is the generation of energetic neutral atoms (ENAs) due to charge exchange reactions between energetic, singly ionized magnetospheric ions and neutral atoms in the outer atmosphere or exosphere of the satellite [50, 105]. The transfer of an electron from a fast, magnetically trapped magnetospheric ion to a cold neutral exospheric or atmospheric atom results in the generation of an energetic, newly born neutral atom. This particle is able to escape from its previous magnetic confinement because it is no longer affected by the Lorentz force. Besides, the process leads to the generation of a cold ion which is picked up by the ambient electromagnetic fields.

- *Electron impact ionization:*
  The ionization of neutral atoms by electrons that impinge on the upper atmosphere is described by the reaction
  $$e^- + \mathcal{N} \longrightarrow \mathcal{N}^+ + 2e^- \quad . \tag{3.90}$$
  Since the collisions between electrons and atmospheric neutral atoms yield a strong deceleration of the electrons, they can produce additional ionizing radiation inside the atmosphere.

Nevertheless, as discussed in chapter 2, photoionization makes up the major contribution to Titan's ionosphere. In the simulation model, Titan's dayside ionosphere is assumed to originate completely from solar radiation, while particle impact processes have not been included yet. However, the model presented here is clearly more sophisticated than the assumptions made in other semi-kinetic approaches. For instance, Kallio *et al.* [74] approximate the ionosphere by means of an uniformly ion production at the surface of the obstacle, i.e. the dependence of the production rate on the solar zenith angle is completely neglected.

The next sections deal with a quantitative description of the solar UV ionization process, followed by a specialization to the Titan scenario.

6.2 Ionosphere formation

In order to simplify the description of the ionosphere and therefore, to reduce the computational effort, most simulation models take only account for the photoionization process. Of course, photoionization cannot occur in the nightside hemisphere of Titan. The photoionization of a neutral atom $\mathcal{N}$ is described by the reaction

$$h\nu + \mathcal{N} \longrightarrow \mathcal{N}^+ + e^- \quad . \tag{3.91}$$

Only those solar photons whose energies exceed the ionization potential of the atmospheric neutral atoms are able to contribute to the formation of an ionosphere. Thus, the ionizing photons originate from the ultraviolet (UV) or the extreme ultraviolet (EUV) spectral range ($\lambda = 10 \ldots 100\,\mathrm{nm}$). At higher energies, the solar radiation becomes very weak and sporadic, making this spectral regime nearly irrelevant for the ionization process. In the following, the neutral atmosphere is assumed to be horizontally structured, i.e. the variation of the neutral density n_n depends only on the altitude r above the surface. For a one-component, isothermal atmosphere, the neutral density profile is given by the barometric law

$$n_n(r) = n_0 \exp\left(-\frac{r}{H}\right) \quad . \tag{3.92}$$

The scale height H, defined as

$$H = \frac{kT_n}{m_n g} \quad , \tag{3.93}$$

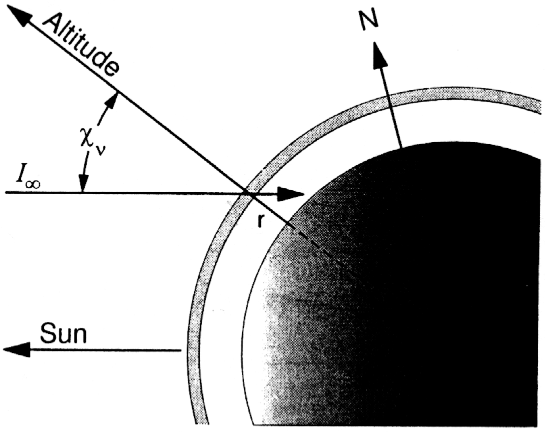

(a) Solar UV absorption in the ionosphere

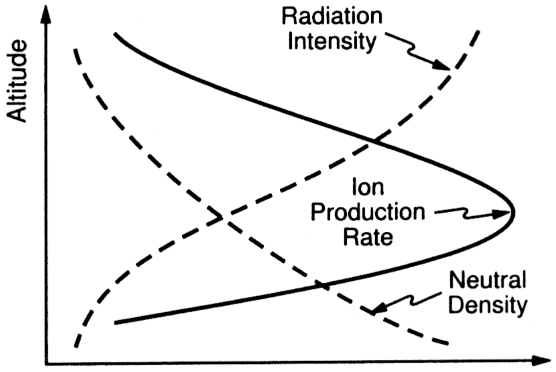

(b) Formation of an ionized layer

Figure 3.1: Formation of an ionosphere due to the solar UV photoionization process. As shown in fig. (a), the solar radiation impinges on a planetary atmosphere at an altitude r and under the solar zenith angle χ_ν. It is partially absorbed by the neutral atoms. The neutral gas profile of the atmosphere is described by an exponential function (barometric law). The absorption process results in a decrease of the radiation intensity. However, only a certain fraction of the absorbed radiation actually leads to ionization. The resulting ion production profile is shown in fig. (b). The radiation intensity decreases when approaching the surface, whereas the neutral gas density increases. Therefore, the ion production function possesses a maximum at a certain altitude above the surface. For the sketches of the intensity as well as of the ionization profile, the solar zenith angle was assumed to be constant. Both figures have been obtained from Baumjohann and Treumann [17].

can be considered a characteristic length scale for the extension of the neutral atmosphere. The temperature and the mass of the neutral atoms are given by T_n and m_n, respectively. The parameter n_0 denotes the neutral density at the planetary surface ($r = 0$). The gravitational acceleration g is assumed to be constant for the range of altitudes under consideration. As shown in fig. 3.1(a), solar UV radiation penetrates into the atmosphere at the altitude r and under a solar zenith χ_ν with respect to a radially directed unit vector. The radiation loses energy due to absorption by neutral particles. This process takes place along the oblique ray path $\mathcal{R}$, which can be expressed as

$$\mathcal{R} = \frac{r}{\cos \chi_\nu} \quad . \tag{3.94}$$

For a constant solar zenith angle, the differential ray path element is given by

$$\mathrm{d}\mathcal{R} = \frac{\mathrm{d}r}{\cos \chi_\nu} \quad . \tag{3.95}$$

The differential reduction of intensity $\mathrm{d}I$ that originates from the absorption process depends linearly on the local intensity I, the density of the neutral gas particles in the respective region and the path length of the radiation in the atmosphere:

$$\mathrm{d}I = \sigma_\nu n_n I \, \mathrm{d}R = \sigma_\nu n_n I \frac{\mathrm{d}r}{\cos \chi_\nu} \quad . \tag{3.96}$$

The *radiation absorption cross-section* σ_ν determines the absorption efficiency of the neutral species for the radiation wavelength under consideration. Introducing the solar flux I_∞ outside the absorbing atmosphere and integrating eq. (3.96) yields

$$\int_{I_\infty}^{I(r)} \frac{\mathrm{d}I}{I} = \int_\infty^r \mathrm{d}r \, \frac{\sigma_\nu n_0}{\cos \chi_\nu} \exp\left(-\frac{r}{H}\right) \quad . \tag{3.97}$$

Thus, the radiation intensity depends on the altitude r and the solar zenith angle χ_ν according to

$$I(r) = I_\infty \exp\left[-\frac{\sigma_\nu n_0 H}{\cos \chi_\nu} \exp\left(-\frac{r}{H}\right)\right] \quad . \tag{3.98}$$

As expected, the radiation intensity decreases when approaching the planetary surface.

The number of electron-ion-pairs that is locally produced by the solar UV radiation at a specific height is described by the *photoionization rate per unit volume* $q_\nu(r)$. On the one hand, this quantity depends on the fraction of the impinging radiation that is absorbed along the path element $\mathrm{d}\mathcal{R}$. On the other hand, only a certain fraction of the absorbed energy actually leads to ionization processes. The percentage of the absorbed radiation that finally acts as an ionization source is determined by the *photoionization efficiency* $\kappa_\nu \in [0, \ldots, 1]$. Hence, the photoionization rate can be written as

$$q_\nu(r) = \kappa_\nu \frac{\mathrm{d}I}{\mathrm{d}\mathcal{R}} = \kappa_\nu \cos \chi_\nu \frac{\mathrm{d}I}{\mathrm{d}r} \quad . \tag{3.99}$$

By using eq. (3.96) for the differential decrease of the intensity, the above expression becomes

$$q_\nu(r) = \kappa_\nu \sigma_\nu n_n(r) I(r) \quad . \tag{3.100}$$

Hence, the ion production due to photoionization is described by the profile

$$q_\nu(r) = \kappa_\nu \sigma_\nu n_0 I_\infty \exp\left[-\frac{r}{H} - \frac{\sigma_\nu n_0 H}{\cos \chi_\nu} \exp\left(-\frac{r}{H}\right)\right] \quad , \tag{3.101}$$

which is known as the *Chapman function*.

Since the density $n_n(r)$ decreases with altitude, whereas the solar radiation intensity increases, it is apparent that the production function (3.101) possesses a maximum at a certain altitude r_m. Setting the first derivative of eq. (3.101) to zero leads to

$$r_m = H \ln (\sigma_\nu n_0 H) + H \ln \left(\frac{1}{\cos \chi_\nu} \right) \quad . \tag{3.102}$$

The first term on the r.h.s. of eq. (3.102) denotes the hight of maximum ion production at the subsolar point ($\chi_\nu = 0$). For a given neutral profile, the quantity $H \ln (\sigma_\nu n_0 H)$ is a constant. Incorporating r_m into the Chapman function yields the maximum production rate

$$q_\nu (r_m) = \frac{\kappa_\nu I_\infty}{\exp(1) H} \cos \chi_\nu \quad , \tag{3.103}$$

where the first factor represents again the value for vertical incidence of the solar radiation.

As can be seen from eq. (3.102), the altitude of maximum ion production depends on the solar zenith angle in such way that for smaller χ_ν, the maximum is located at lower altitudes. Besides, the respective maximum value of the production function decreases with increasing χ_ν. Moreover, it should be noted that the altitude of maximum ion production depends on the scale height H and the absorption cross-section σ_ν, but not on the photon flux. In contrast to this, the maximum value of the ion production rate is a function of the scale height H and the efficiency κ_ν as well as the radiation intensity outside the atmosphere. A schematic sketch of the exponential neutral profile and the ion production function is displayed in fig. 3.1(b).

As briefly mentioned above, this general discussion of the photoionization process is based on several simplifying assumptions:

- The impinging solar radiation is assumed to be monochromatic, i.e. only a small wavelength interval is considered. In this interval, the absorption cross-section and the photoionization efficiency can be taken as constants.
- The atmosphere is assumed to be isothermal. For this reason, the scale height H does not vary with altitude.
- The curvature of the planetary surface is neglected. Thus, the atmosphere and the ionosphere are assumed to be horizontally structured.

However, the ion production profile given by eq. (3.101) can be extended to more general situations. On the one hand, incorporating a constant, finite scale height gradient

$$\frac{\mathrm{d}H}{\mathrm{d}r} = \mathrm{const} \tag{3.104}$$

requires only minor modifications. The resulting ionospheric profiles have been discussed in detail by Bauer and Lammer [13]. On the other hand, near sunrise and sunset ($\chi_\nu \approx 90°$), eq. (3.101) is not valid since the $1/\cos \chi_\nu$ term in the argument of the exponential function is a result of the plane atmosphere approximation. In order to take account for the atmosphere's curvature, the $1/\cos \chi_\nu$ term has to be replaced by the modified Chapman function

$$\mathrm{Ch}\,(\chi_\nu) \equiv \frac{\int_{\mathcal{R}}^{\infty} n_n(\mathcal{R})\, \mathrm{d}\mathcal{R}}{\int_r^{\infty} n_n(r)\, \mathrm{d}r} \quad , \tag{3.105}$$

if the solar zenith angle is larger than 75°. This expression describes the ratio of the total content of the atmosphere along the oblique ray path $\mathcal{R}$ to the vertical content [12, 13]. Because the above expression is not easy to compute, a number of analytical approximations to the function $\mathrm{Ch}\,(\chi_\nu)$ have been developed. For instance, in the case of an isothermal atmosphere, a useful approximation can be obtained by means of the *Error Function* $E(x)$,

$$E(x) \equiv \frac{1}{\sqrt{2\pi}} \int_0^x \exp\left(-\frac{t^2}{2}\right) \mathrm{d}t \quad . \tag{3.106}$$

Based on this function, the modified Chapman function for the angle interval of interest $(75^\circ \leq \chi_\nu \leq 90^\circ)$ takes the form

$$\mathrm{Ch}\,(h, \chi_\nu) = \sqrt{\frac{\pi h}{2}} \left[1 - E\left(\frac{\sqrt{h}\cos\chi_\nu}{\sqrt{2}}\right)\right] \exp\left(\frac{h\cos^2\chi_\nu}{2}\right) \quad , \tag{3.107}$$

where

$$h = \frac{r + R_P}{H} \quad . \tag{3.108}$$

Again, r denotes the height above the planetary surface, whereas R_P and H are the planetary radius and the scale height (3.93), respectively.

6.3 Numerical modelling

At the beginning of each simulation run, Titan does not possess an ionosphere. Ions of ionospheric origin are continuously produced while the simulation proceeds, i.e. a certain number of these particles per time interval is permanently inserted into the simulation domain. This situation evolves until a quasi-stationary state is reached.

Titan's atmosphere is modeled as a spherically symmetric gas cloud surrounding the satellite. The atmosphere is assumed to consist of molecular nitrogen[2]. For the simulations described in this work, a neutral density profile according to

$$n_n(r) = n_1 \exp\left(\frac{r_1 - r}{H_1}\right) + n_2 \exp\left(\frac{r_2 - r}{H_2}\right) + n_3 \frac{r_3}{r} \quad . \tag{3.109}$$

has been used. This function contains three reference densities (n_1, n_2 and n_3) as well as three reference heights (r_1, r_2 and r_3), allowing to adjust the profile to model calculations (cf. for instance Keller *et al.* [77]). Therfore, despite the rather low grid resolution achieved by semi-kinetic codes, the large number of free parameters allows a satisfactory adjustment to the density profiles provided by atmosphere models. In principle, the scale heights H_1 and H_2 allow the inclusion of data from temperature measurements in different altitude regimes.

Again, the decrease of solar UV intensity that emerges from absorption processes can be obtained from

$$\frac{\mathrm{d}I}{I} = \sigma_\nu n_n(r) \frac{\mathrm{d}r}{\cos\chi_\nu} \quad . \tag{3.110}$$

---

[2] An extension of the atmosphere to multi-species conditions will be presented in chapter 7.

Integrating this expression yields

$$I(r) = I_\infty \exp\left[-\frac{\sigma_\nu}{\cos\chi_\nu}\int_r^{r_{\max}} n_n(\tilde{r})\,\mathrm{d}\tilde{r}\right] \quad , \tag{3.111}$$

where $r_{\max}$ is the radius of a shell denoting the upper boundary of the atmosphere. For the simulations discussed in this work, a value of $r_{\max} = 3R_T$ has been chosen. Of course, such an artificial upper boundary, where the atmosphere is sharply cut off, does not exist in reality, but its inclusion is enforced by the finite size of the simulation box. In any case, the value of $r_{\max}$ should be comparable to the extension of the real atmosphere.

The remaining integral can be solved analytically:

$$\begin{aligned}\int_r^{r_{\max}} n_n(\tilde{r})\,\mathrm{d}\tilde{r} \quad = \quad & n_1 H_1 \exp\left(\frac{r_1 - r}{H_1}\right) + n_2 H_2 \exp\left(\frac{r_2 - r}{H_2}\right) + n_3 r_3 \ln\left(\frac{r_{\max}}{r}\right) - \\ & - \underbrace{\left[n_1 H_1 \exp\left(\frac{r_1 - r_{\max}}{H_1}\right) + n_2 H_2 \exp\left(\frac{r_2 - r_{\max}}{H_2}\right)\right]}_{\equiv \mathcal{T}} \quad .\end{aligned} \tag{3.112}$$

As the outer radius $r_{\max}$ has to be chosen significantly larger than the reference heights r_1 and r_2, the term $\mathcal{T}$ in eq. (3.112) can be neglected:

$$\mathcal{T} \approx 0 \quad . \tag{3.113}$$

Parameter	Symbol	Numerical value
Neutral profile (first term)	n_1	$1.0 \cdot 10^{18}\,\mathrm{m}^{-3}$
	r_1	700 km
	H_1	90 km
Neutral profile (second term)	n_2	$1.0 \cdot 10^{12}\,\mathrm{m}^{-3}$
	r_2	1700 km
	H_2	120 km
Neutral profile (third term)	n_3	$1.0 \cdot 10^{10}\,\mathrm{m}^{-3}$
	r_3	2700 km
Absorption cross-section	σ_ν	$8.37 \cdot 10^{-22}\,\mathrm{m}^2$
Photoionization efficiency	κ_ν	1
Photoionization frequency	$\omega = \sigma_\nu I_\infty$	$0.2 \cdot 10^{-9}\,\mathrm{s}^{-1}$
Lower boundary of atmosphere	$r_{\min}$	$R_T + 1000\,\mathrm{km}$
Upper boundary of atmosphere	$r_{\max}$	$3R_T$
Total ion production	Q	$1.26 \cdot 10^{25}\,\mathrm{s}^{-1}$

Table 3.2: Input parameters for the ion production profile according to eq. (3.114). The radius of Titan is $R_T = 2575\,\mathrm{km}$.

Hence, the ion production function q_ν takes the form

$$\begin{aligned} q_\nu\left(r,\chi_\nu\right) &= \kappa_\nu\sigma_\nu n_n(r) I_\infty \cdot \exp\left\{ -\frac{\sigma_\nu}{\cos\chi_\nu}\left[n_1 H_1 \exp\left(\frac{r_1-r}{H_1}\right) + \right.\right. \\ &\left.\left. + n_2 H_2 \exp\left(\frac{r_2-r}{H_2}\right) + n_3 r_3 \ln\left(\frac{r_{\max}}{r}\right)\right]\right\} \quad . \end{aligned} \tag{3.114}$$

Like the atmosphere, the ionosphere is assumed to be a spherical shell with the upper radius $r_{\max}$ and a lower boundary located at $r_{\min}$. In other words, the ionosphere is assumed to begin at an altitude of $r_{\min}$ above the surface and is cut off at the height $r_{\max}$. As will be explained in subsequent sections, the introduction of an artificial inner boundary arises from numerical needs. Of course, the inner shell of radius $r_{\min}$ is located below the ionospheric production maximum at an altitude of 1100 km. Depending on the specific simulation geometry, values in the range between $r_{\min} = R_T + 100\,\mathrm{km}$ and $r_{\min} = R_T + 1000\,\mathrm{km}$ have been chosen.

Since the argument of the exponential term in eq. (3.114) depends on $(\cos\chi_\nu)^{-1}$, this expression is not adequate for modelling the production rate near the terminator line. Furthermore, photoionization does not occur at the nightside of Titan. In the nightside hemisphere, Titan's ionosphere originates completely from particle impact processes. For the simulations described in this work, the production for $\chi \approx 90°$ as well as the production at the nightside have been approximated in a quite simple way by using eq. (3.114): For both solar zenith angles $\chi_\nu > 87°$ and the nightside of the obstacle, the production is assumed to be independent of the solar zenith angle. The production function in these regions has been set to

$$q_\nu\left(r,\chi_\nu\right) = q_\nu\left(r,\chi_\nu = 87° = \mathrm{const}\right) \quad . \tag{3.115}$$

A value of $\chi_\nu = 87°$ instead of $\chi_\nu = 90°$ has been chosen since the $1/\cos\chi_\nu$ term in the argument of the exponential function in eq. (3.114) diverges at the terminator line. Evidently, this treatment yields only a rough approximation to the ionization processes occurring at the nightside. The total ion production Q in the shell, i.e. the number of ions globally produced per second, can be obtained from

$$Q = \int_{\text{shell}} q_\nu(r,\chi_\nu)\,\mathrm{d}V \quad . \tag{3.116}$$

The values of the free parameters in eq. (3.114) are listed in tab. 3.2 and have been chosen to match the profiles for nitrogen discussed by Keller *et al.* [77] as well as by Nagy and Cravens [114]. The resulting neutral profile and the ionospheric production functions for different solar zenith angles are displayed in figs. 3.2, 3.3 and 3.4, respectively. In agreement with the model of Keller *et al.* [77], the region of maximum ion production is located at an altitude of $r = 1100\,\mathrm{km}$ $(0.4 R_T)$. However, it should also be noted that none of the available ionosphere models considered the functional dependence on the solar zenith angle. The total ion production rate is of the order of $Q = 10^{25}\,\mathrm{s}^{-1}$ and therefore matches the value suggested by Kallio *et al.* [74]. When being injected into the simulation box, the ionospheric ions are assumed to be cold, whereas a value of $\beta_e = 0.083$ has usually been chosen for the ionospheric electron plasma beta (cf. Nagy and Cravens [114]).

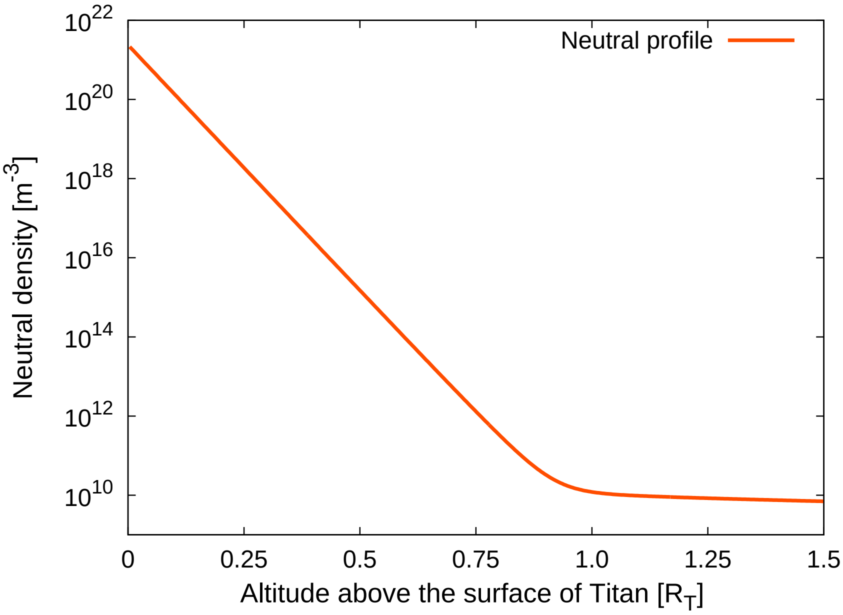

Figure 3.2: Neutral density profile – Density of molecular nitrogen as a function of altitude above the surface. Titan's atmospheric profile is approximated by using a neutral density according to eq. (3.109). The numerical values that have been incorporated into the model can be found in tab. 3.2.

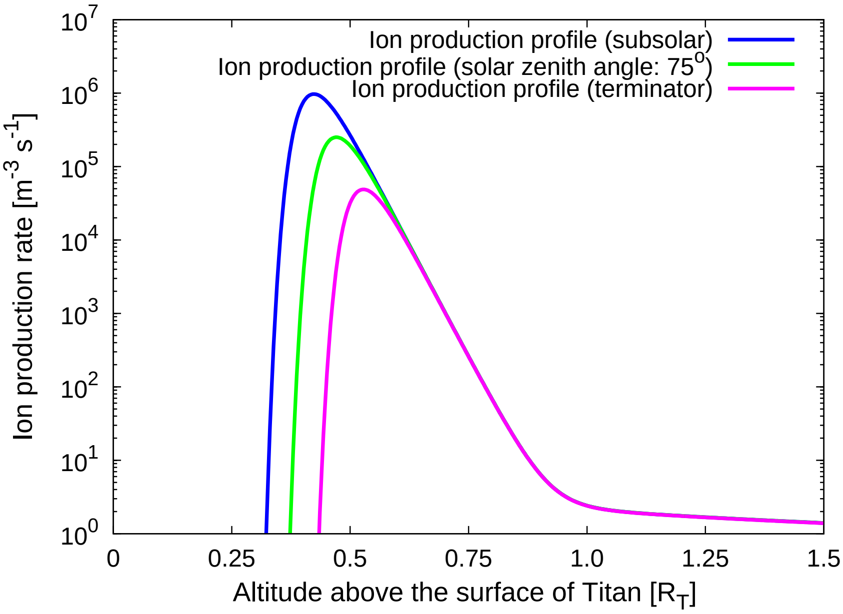

Figure 3.3: Production of molecular nitrogen as a function of the altitude above the surface. The figure displays the production rate q_ν at the subsolar point (blue line), at a solar zenith angle of $\chi_\nu = 75°$ (green line) and at the terminator (magenta line). As can also be seen in fig. 3.4, the altitude of the production maximum increases when moving from the subsolar point to the terminator. In contrast to this, the maximum production value diminishes for large solar zenith angles.

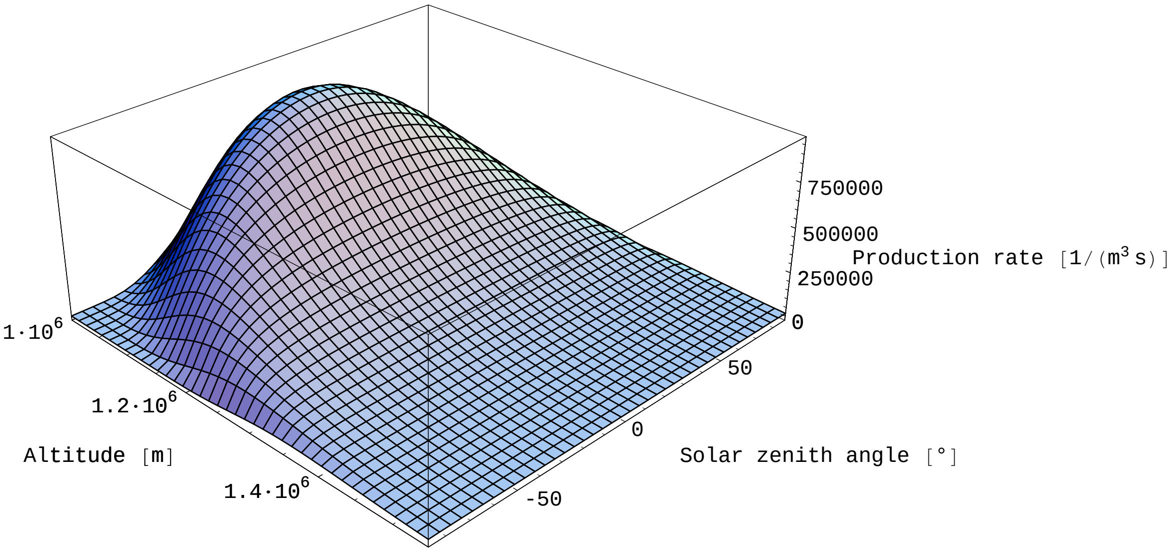

Figure 3.4: Three-dimensional illustration of the nitrogen production function. The profile is given by eq. (3.114), whereas the numerical values that have been used to generate the profile can be found in tab. 3.2.

7 Simulation code: Numerical details

This section deals with the numerical techniques that are used to solve the set of hybrid equations. However, only a brief discussion of the major ideas will be given. An extensive discussion can be found in the thesis of Bagdonat [7].

7.1 Basic principles of a Particle-in-Cell code

The set of hybrid equations is solved numerically by using the *Particle-in-Cell* method described by Birdsall and Langdon [20]. At first, a fixed grid is introduced in coordinate space. The electromagnetic field quantities as well as the particle densities and currents are defined only at the nodes of this grid, whereas the individual particles can be located anywhere in between (cf. fig. 3.5). In order to solve the equations of motion (3.27) for each particle, the electromagnetic fields at the individual particle positions are required. These quantities are obtained by interpolating the fields from the grid points to the particle positions by means of the *Cloud-in-Cell* technique presented by Othmer [122]. Some important details of this method are summarized in sections 7.2 and 7.3.

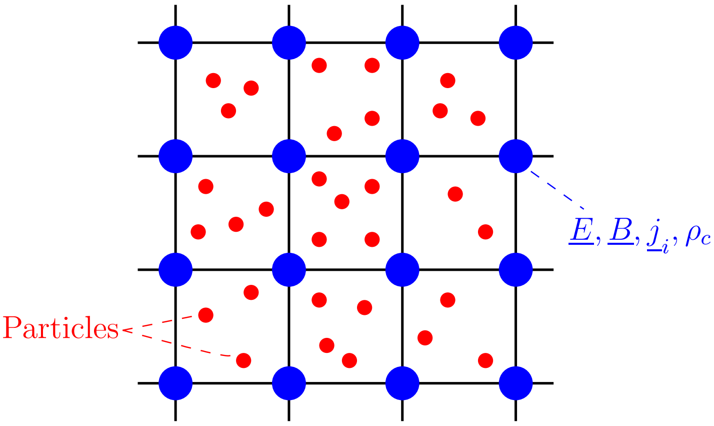

Figure 3.5: Basic idea of a Particle-in-Cell code. In order to solve the set of hybrid equations, a fixed grid is defined in coordinate space. On the one hand, the individual particles (red) can be located anywhere inside the grid cells. On the other hand, the electromagnetic fields as well as the moments of the distribution function are computed only at the grid nodes (blue). The fields $\underline{E}$ and $\underline{B}$ at each individual particle position are obtained from the values at the grid nodes by means of an interpolation technique.

Every single computational cycle consists of four basic steps. A complete cycle is called a *time step* and represents a certain interval of real time Δt. The parameter Δt is passed to the code as a pre-defined simulation parameter, During each computational cycle, the following basic operations are carried out in sequence (see fig. 3.6):

1. *Gather moments:*
   By using the positions and velocities of the individual particles, the charge density ρ_c and the current density $\underline{j}_i$ are computed for each node of the simulation grid.

2. *Solve field equations:*
   The particle and charge densities obtained in the first step are incorporated into the field equations (3.20) and (3.25). This allows to calculate an updated electric and magnetic field vector for each grid point.

3. *Interpolate forces:*
   For the position of each particle, the electromagnetic field quantities are obtained from the vectors $\underline{E}$ and $\underline{B}$ at the grid nodes by means of an interpolation technique.

4. *Move particles*:
   Finally, the electromagnetic field quantities at the individual particle positions allow to update the positions $\underline{x}_\nu$ and velocities $\underline{v}_\nu$. The algorithm computes the displacement and the velocity change that are imposed by the Lorentz force in the time interval Δt.

The hybrid code developed by Bagdonat [7] computes the electric as well as the magnetic field vector for every single grid point. In contrast to this, Winske and Omidi [154] suggest a simulation geometry that is based on two staggered grids. At the nodes of the first grid, only the magnetic field is calculated, whereas the electric field and the moments of the distribution

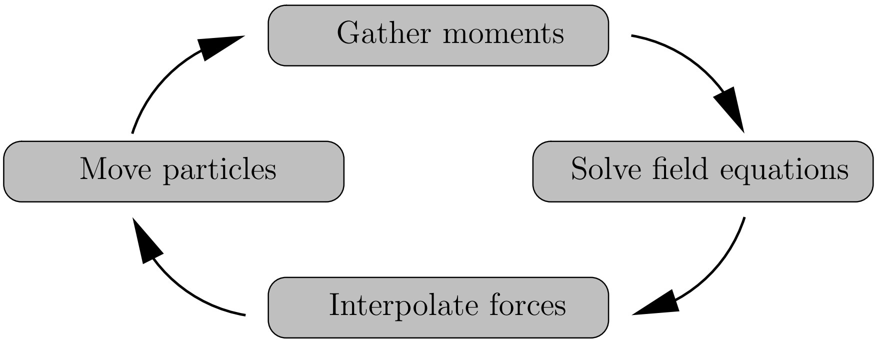

Figure 3.6: Each computational cycle carried out by a Particle-in-Cell code consists of four basic steps.

function are defined only at the nodes of the second grid. A detailed comparative discussion of both methods is given by Bagdonat [7].

7.2 Moments of the distribution function

In the first step of each computational cycle, the known particle positions and velocities are used to obtain the mean charge and current densities at the nodes of the simulation grid. This method is mainly based on the *Particle-in-Cell weighting function* $\mathcal{W}$, which determines the contribution of a particle at the position $\underline{x}_\nu$ to the moments ρ_c and $\underline{j}_i$ at a grid node $\underline{r}$. In a three-dimensional, equidistant Cartesian simulation grid whose step size in each spatial direction may be given by Δ_g, the grid nodes are located at the positions

$$\underline{r}_{q,r,s} = \Delta_g \begin{pmatrix} q \\ r \\ s \end{pmatrix} \quad ; \quad q, r, s \in \mathbb{Z} \quad . \tag{3.117}$$

The total charge $Q_{q,r,s}$, the charge density $\rho_{c|q,r,s}$ and the current density $\underline{j}_{i|q,r,s}$ that are assigned to the grid node $\underline{r}_{q,r,s}$ can then be expressed as

$$Q_{q,r,s} = e \sum_\nu \mathcal{W}\left(\underline{x}_\nu, \underline{r}_{q,r,s}\right) \quad \rightsquigarrow \quad \rho_{c|q,r,s} = \frac{e}{\Delta_g^3} \sum_\nu \mathcal{W}\left(\underline{x}_\nu, \underline{r}_{q,r,s}\right) \tag{3.118}$$

and

$$\underline{j}_{i|q,r,s} = \frac{e}{\Delta_g^3} \sum_\nu \underline{v}_\nu \mathcal{W}\left(\underline{x}_\nu, \underline{r}_{q,r,s}\right) \quad , \tag{3.119}$$

respectively. Of course, each ion has to fulfill the condition that the sum of its charge contributions at different grid points equals its total charge, i.e.

$$\sum_{q,r,s} \mathcal{W}\left(\underline{x}_\nu, \underline{r}_{q,r,s}\right) \overset{!}{=} 1 \quad . \tag{3.120}$$

Choosing an appropriate weighting function $\mathcal{W}$ is essential for the entire procedure. The procedure used in most hybrid codes is discussed in detail by Bagdonat [7]. In the following, only a brief illustration of the basic principle will be given for a two-dimensional Cartesian grid with equidistant reference points.

At first, only *one* single ion of mass m_i and charge e is considered. The ion is assumed to be located inside the grid cell whose corners are given by

$$\begin{aligned}
\underline{\tilde{r}}_1 &\equiv \underline{r}_{q,r} = \Delta_g \begin{pmatrix} q \\ r \end{pmatrix} \quad , \\
\underline{\tilde{r}}_2 &\equiv \underline{r}_{q+1,r} = \Delta_g \begin{pmatrix} q+1 \\ r \end{pmatrix} \quad , \\
\underline{\tilde{r}}_3 &\equiv \underline{r}_{q+1,r+1} = \Delta_g \begin{pmatrix} q+1 \\ r+1 \end{pmatrix} \quad \text{and} \\
\underline{\tilde{r}}_4 &\equiv \underline{r}_{q,r+1} = \Delta_g \begin{pmatrix} q \\ r+1 \end{pmatrix} \quad .
\end{aligned} \tag{3.121}$$

A non-vanishing value of the charge and current density is assigned only to the four corners $\underline{\tilde{r}}_k$, $k \in \{1, 2, 3, 4\}$ of the cell in which the particle is located. Grid points in neighbour cells are not considered. The specific contributions can be calculated from the particle's relative position inside the cell. The procedure requires the introduction of two straight lines parallel to the coordinate frame whose intersection point coincides with the position of the particle. As can be seen from fig. 3.7, the cell is divided into four rectangular areas by this construction. The fraction of the particle's charge e that is assigned to each of the four corners is proportional to the area of the *opposite* rectangle. To formalize this idea, the particle position can be written as

$$\underline{x} = \Delta_g \begin{pmatrix} q+\xi_1 \\ r+\xi_2 \end{pmatrix} \quad \text{, where} \quad 0 \leq \xi_1, \xi_2 \leq 1 \quad . \tag{3.122}$$

The fraction Q_k of the particle's charge that is assigned to the grid node $\underline{\tilde{r}}_k$ is then given by

$$\begin{aligned}
Q_1 &= e\,(1-\xi_1)\,(1-\xi_2) \quad , \\
Q_2 &= e\,\xi_1\,(1-\xi_2) \quad , \\
Q_3 &= e\,\xi_1\xi_2 \quad , \\
Q_4 &= e\,(1-\xi_1)\,\xi_2 \quad .
\end{aligned} \tag{3.123}$$

Obviously, charge conservation is guaranteed by this scheme: $\sum_{k=1}^{4} Q_k = e$. This procedure can be associated with the idea of the particle's charge being distributed homogeneously over the entire grid cell. The contributions at the corners can then be found by dividing this charge cloud into rectangles. Consequentially, the technique is referred to as *Cloud-in-Cell* scheme [7, 154].

In the way described above, the procedure is carried out for every particle in the simulation domain and hence, it allows to compute the total charge that is assigned to each grid point. Dividing through the area Δ_g^2 of a cell finally leads to the charge density ρ_c. The mean ion current density $\underline{j}_i$ and in consequence, the mean velocity

$$\underline{u}_i = \frac{\underline{j}_i}{\rho_c} \tag{3.124}$$

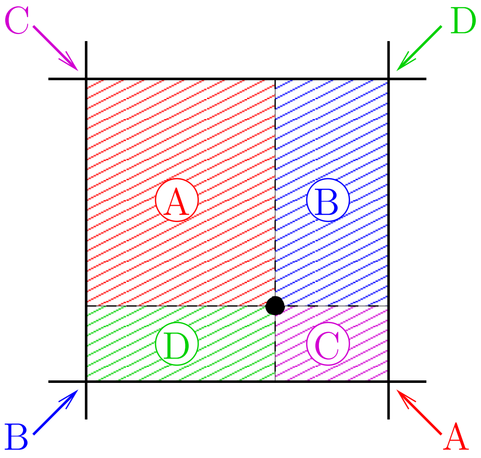

Figure 3.7: The charge density that is assigned to each corner of a grid cell is computed by means of the Cloud-in-Cell technique. The figure illustrates this procedure for a two-dimensional Cartesian grid. A non-vanishing contribution is assigned only to the corners of the cell in which the particle under consideration is currently located. In order to obtain these contributions, the cell is divided into four rectangles by the two straight lines intersecting at the particle position. The fraction of the particle's charge that is assigned to each corner is proportional to the area of the opposite rectangle.

at each reference point can be obtained in an analogous manner.

7.3 Force interpolation

Initially, the fields $\underline{E}$ and $\underline{B}$ are defined only at the nodes of the simulation grid. However, in order to solve the equations of motion (3.27) and thus, to obtain the updated particle positions and velocities, the electromagnetic field quantities have to be defined at the individual particle positions. The numerical technique that allows to compute these fields can be considered a formal inversion of the moment gathering algorithm described in the preceding section. A detailed description is given by Bagdonat [7].

7.4 Equations of motion and field equations

This section summarizes the major features of the algorithms that are used to solve the equations of motion for the individual particles as well as to the electromagnetic field equations (3.20) and (3.25).

In order to obtain the updated particle positions and velocities, the equations of motion (3.27) for each single ion have to be solved. In the code employed for the study described here, this is done by means of a *Leap Frog* algorithm. The basic idea of this scheme is to define the electromagnetic fields $\underline{E}$ and $\underline{B}$ as well as the particle positions $\underline{x}_\nu$ at the beginning of each time step, i.e.

$$\underline{E}^N \equiv \underline{E}\,(N\Delta t) \quad , \quad \underline{B}^N \equiv \underline{B}\,(N\Delta t) \quad \text{and} \quad \underline{x}_\nu^N \equiv \underline{x}_\nu\,(N\Delta t) \quad , \tag{3.125}$$

where $N \in \mathbb{N}$. The particle velocities, on the other hand, are defined only at intermediate points in time, i.e. at $\frac{2N+1}{2}\Delta t$.

The partial differential equation (3.25), which determines the time evolution of the magnetic field, is of the form

$$\frac{\partial \underline{B}}{\partial t} = \nabla \times \underline{f}\,(\underline{B}, \underline{u}_i, \rho_c) \quad , \tag{3.126}$$

whereas the discretized form of this equation is given by

$$\frac{\underline{B}^{N+1} - \underline{B}^{N}}{\Delta t} = \nabla \times \underline{f}\left(\underline{B}^{N+1/2}, \underline{u}_i^{N+1/2}, \rho_c^{N+1/2}\right) \quad . \tag{3.127}$$

This equation is solved by means of a combination of Leap Frog algorithm and a *Predictor-Corrector* scheme. The basic idea of the Predictor-Corrector technique is to obtain an estimate of the magnetic field $\underline{B}^{N+1/2}$ at first. This approximative value can then be used to compute $\underline{B}^{N+1}$ according to eq. (3.127).

The generalized form of Ohm's law (3.20) represents an explicit expression for the electric field:

$$\underline{E} = f\,(\underline{B}, \underline{u}_i, \rho_c) \quad . \tag{3.128}$$

This equation is solved by means of the so-called *Current Advancement Method* which has been discussed in detail by Matthews [103].

7.5 Curvilinear simulation grid

With respect to the grid resolution, the capabilities of magnetohydrodynamic simulation codes are clearly superior to any available (semi)kinetic model. Since in the framework of a fluid description, spatial resolutions below $0.01R_T$ can be achieved (cf. for instance Ma *et al.* [99]), these codes allow the incorporation of extremely sophisticated ionosphere models. When using an equidistant Cartesian grid, the hybrid simulation code used for this work is able to handle a number of about 100 grid nodes in each spatial direction, whereas the extension of the box in each direction ranges typically between $15R_T$ and $30R_T$. As will be discussed in section 9.1, placing the outer boundaries of the simulation domain closer to the obstacle is not possible.

The spatial resolution in the vicinity of Titan can be improved by introducing a curvilinear simulation grid, featuring an increased number of grid cells in the satellite's ionosphere region. When the diameter of the simulation box with respect to the size of Titan is relatively small, replacing the Cartesian grid by a curvilinear grid has even proven mandatory, for these geometries are quite susceptible to the formation of numerical artifacts. These difficulties are illustrated in fig. 3.8, displaying the results of a test simulation with a Cartesian grid. For simplicity, an isotropic production profile has been applied to Titan's ionosphere. The ambient magnetospheric plasma velocity is set to zero. Although the obstacle and its ionosphere possess a spherical structure[3], the imprint of the Cartesian simulation grid on the internal structure of the ionospheric ion cloud as well as on its global shape is clearly visible, i.e. the particles exhibit a certain tendency to move along the grid lines. However, this kind of

---

[3] To be precise, the ionospheric production profile exhibits only a cylindrical symmetry.

artifact did not occur in low resolution runs that do not resolve the spherical structure of Titan. The problem of artifact formation, and to a certain degree even the disadvantage of a low spatial resolution near Titan, can be circumvented by introducing a simulation grid that takes account for the curved structure of the obstacle and its ionosphere.

The non-orthogonal *fisheye grid* is derived from an equidistant Cartesian grid by modifying the radial distance of the grid points from the center of the coordinate frame. The following discussion refers to a cubic simulation domain of volume L^3, possessing the same number of grid points in each spatial direction. The grid points of the Cartesian reference grid will be referred to as

$$\underline{r}^C_{i,j,k} = \left(x^C_i, y^C_j, z^C_k\right) \quad , \tag{3.129}$$

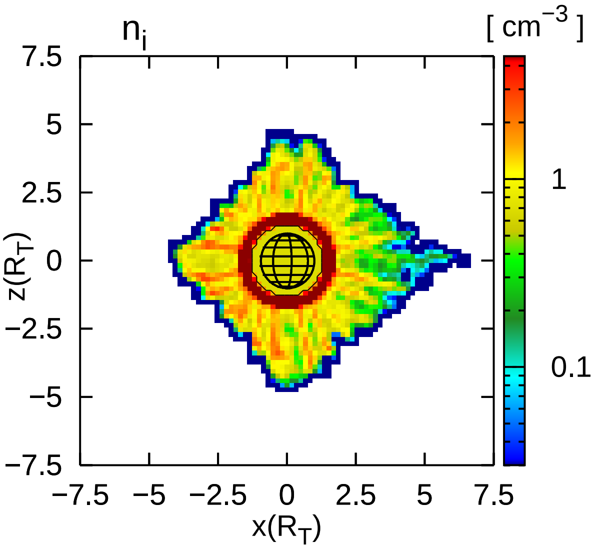

Figure 3.8: Cartesian simulation grid – Illustration of numerical artifacts. The figure displays the ionospheric nitrogen density in the vicinity of Titan. For this demonstration of the disadvantages of a Cartesian grid, an isotropic production profile has been applied, i.e. the production function q_ν depends on the altitude above the surface, but not on the solar zenith angle. The figure shows the mean ionospheric density in a cut through the (x, z) plane of the three-dimensional simulation domain, coinciding with Titan's polar plane. The rectangular structure of the Cartesian simulation grid gives rise to numerical artifacts: The ionospheric particles are accelerated away from Titan along the grid lines, resulting in the formation of ray-like structures. The outer boundaries of the heavy ion cloud clearly exhibit a rectangular structure. In fact, even the global shape of the heavy ion cloud surrounding the obstacle seems to be rhombic. The formation of these artificial structures can be avoided by using a curvilinear simulation grid which possesses a spherical symmetry. Such a grid can be adapted to the spherical structure of the obstacle. However, this kind of numerical artifact did not occur in large-scale simulations. In such a geometry, the obstacle possesses a spatial extension of only 2-3 grid cells, i.e. its spherical shape is not resolved.
Simulation parameters for the test run: Cubic simulation domain, spatial extensions: $(15R_T, 15R_T, 15R_T)$, equidistant Cartesian simulation gird with 90 cells in each spatial direction, isotropic ion production function, total ion production: $Q = 1.26 \cdot 10^{25}\,\mathrm{s}^{-1}$. The center of Titan coincides with the center of the simulation box. The upstream magnetospheric plasma flow is assumed to be at rest.

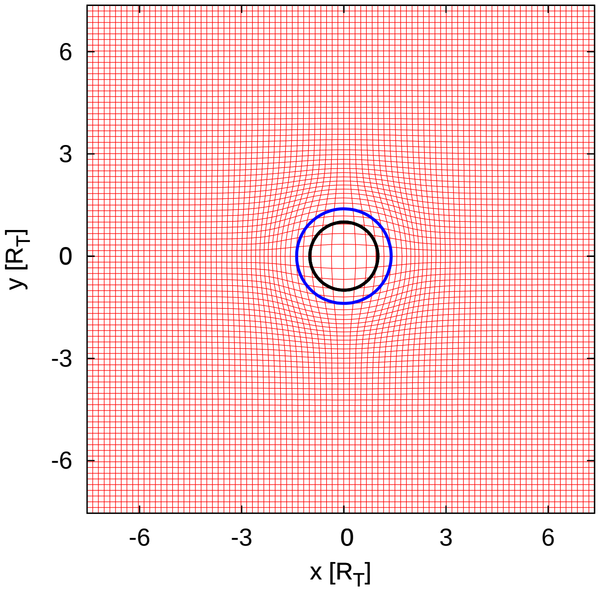

(a) Grid parameters: $\lambda = 19.0(R_T)^2$, $\mu = 0.7/R_T$ and $\nu = 0.5R_T$.

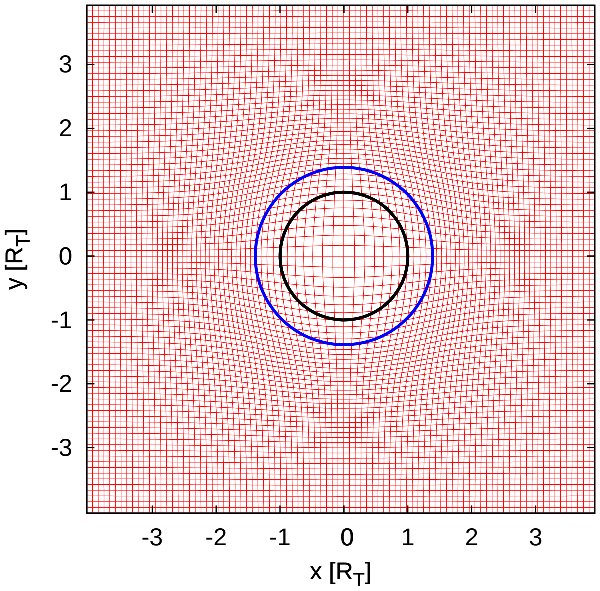

(b) Grid parameters: $\lambda = 15.0(R_T)^2$, $\mu = 0.7/R_T$ and $\nu = 0.35R_T$.

Figure 3.9: Curvilinear fisheye simulation grid. In order to avoid the formation of numerical artifacts in the structure of the heavy ion cloud, a curvilinear simulation grid has been introduced. The inner (black) circle in the sketch denotes the position of Titan's surface, whereas the outer (blue) one marks the lower boundary of the satellite's ionosphere at an altitude of about 1000 km. The fisheye grid is obtained from an equidistant Cartesian grid by means of a coordinate transformation according to eq. (3.135). The basic idea is to modify the radial distance of the Cartesian grid points from the center by using a scaling function $f(r)$. The function $f(r)$ that allows to generate the fisheye grid resembles the Fermi-Dirac distribution function. As can be seen from the figure, the major characteristic of this grid is a region of curved grid lines in the vicinity of the obstacle. With increasing distance to the center of the simulation domain, the grid slightly transforms into a rectangular one. The scaling function $f(r)$ includes three free parameters (λ, μ and ν) that determine both the curvature of the gird and the location of the region with maximum curvature. To generate the grids that are shown in the figure, these parameters have been set to (a) $\lambda = 19.0(R_T)^2$, $\mu = 0.7/R_T$, $\nu = 0.5R_T$ and (b) $\lambda = 15.0(R_T)^2$, $\mu = 0.7/R_T$, $\nu = 0.35R_T$, respectively. A similar approach has been employed by Bößwetter *et al.* [26, 27] for a 3D hybrid simulation study of the Martian plasma environment.

where the three components are given by

$$\begin{aligned} x_i^C &= \left(\frac{i}{N}-\frac{1}{2}\right)L \quad , \quad i=0,1,2,\dots,N \quad ; & (3.130)\\ y_j^C &= \left(\frac{j}{N}-\frac{1}{2}\right)L \quad , \quad j=0,1,2,\dots,N \quad ; & (3.131)\\ z_k^C &= \left(\frac{k}{N}-\frac{1}{2}\right)L \quad , \quad k=0,1,2,\dots,N \quad . & (3.132)\end{aligned}$$

Thus, the radial distance of the grid node (i,j,k) from the center can be expressed as

$$r^C_{i,j,k} = \left|\underline{r}^C_{i,j,k}\right| = \sqrt{\left(x_i^C\right)^2 + \left(y_j^C\right)^2 + \left(z_k^C\right)^2} \quad , \tag{3.133}$$

so that the position vector takes the form

$$\underline{r}^C_{i,j,k} = \underbrace{\frac{\underline{r}^C_{i,j,k}}{r^C_{i,j,k}}}_{=\underline{e}} r^C_{i,j,k} = r^C_{i,j,k}\,\underline{e} \quad . \tag{3.134}$$

The vector $\underline{e}$ is a unit vector, pointing from the origin of the Cartesian system to the point $\underline{r}^C_{i,j,k}$. In order to generate the curvilinear fisheye grid, the radial distance is modified according to the transformation

$$r^C_{i,j,k} \rightarrow \tilde{r}_{i,j,k} = r^C_{i,j,k} + f\left(r^C_{i,j,k}\right)\cdot\xi(i,j,k) \quad , \tag{3.135}$$

where

$$\xi(i,j,k) = \frac{2i(i-N)}{L}\frac{2j(j-N)}{L}\frac{2k(k-N)}{L} \quad . \tag{3.136}$$

The function f is given by

$$f\left(r^C_{i,j,k}\right) = \frac{\lambda}{1+\exp\left(\mu\left(r^C_{i,j,k}-\nu\right)\right)} \quad . \tag{3.137}$$

This function resembles the Fermi-Dirac distribution known from statistical mechanics. The free parameters λ, μ and ν allow to control the curvature of the modified grid. Hence, the positions of the modified grid points are given by

$$\underline{\tilde{r}}_{i,j,k} = \tilde{r}_{i,j,k}\,\underline{e} = \tilde{r}_{i,j,k}\frac{\underline{r}^C_{i,j,k}}{r^C_{i,j,k}} \quad . \tag{3.138}$$

As can be seen from eq. (3.136), the modified grid is asymptotically Cartesian at the outer boundaries of the simulation box, i.e.

$$\xi(i=0,j,k) = \xi(i,j=0,k) = \xi(i,j,k=0) = 0 \tag{3.139}$$

and

$$\xi(i=N,j,k) = \xi(i,j=N,k) = \xi(i,j,k=N) = 0 \quad . \tag{3.140}$$

The resulting curvilinear grid is shown in fig. 3.9. As can be seen, the grid possesses a spherically symmetric structure in the vicinity of the obstacle, whereas with increasing distance to the center, it slightly transforms into a Cartesian grid. This type of grid has already been used to study the interaction of the solar wind with the Martian ionosphere [26, 27, 110].

8 Numerical stability

This section deals with some numerical techniques that are required for insuring the stability of the simulations. On the one hand, a smoothing procedure is applied to the electromagnetic field quantities computed at the nodes of the simulation grid. On the other hand, since the electric and magnetic fields depend on the inverse charge density, a lower limit for ρ_c has to be defined. Besides, it is discussed how the time step Δt has to be chosen in order to maintain numerical stability.

8.1 Smoothing

In order to suppress strong local gradients in the electromagnetic fields that could compromise numerical stability, the electric and magnetic fields calculated at the grid points have to be modified by a smoothing procedure in each time step. Let P be an arbitrary node of the simulation grid and $\mathcal{A}$ a scalar physical quantity defined at this point[4]. Before the subsequent simulation cycle is carried out, $\mathcal{A}$ is replaced by a modified value $\tilde{\mathcal{A}}$ according to

$$\tilde{\mathcal{A}} = (1-\alpha_{\mathcal{S}})\,\mathcal{A} + \alpha_{\mathcal{S}}\mathcal{A}_{\mathcal{S}} \quad . \tag{3.141}$$

The *smoothing parameter* $\alpha_{\mathcal{S}} \in [0,1]$ determines the fraction of the initially calculated value $\mathcal{A}$ that is incorporated into the final value $\tilde{\mathcal{A}}$ used during the following computational cycle. The smoothed quantity $\mathcal{A}_{\mathcal{S}}$ is obtained by means of an averaging procedure that takes into account the reference point P as well as its 26 nearest neighbours. Considering P as the origin of the Cartesian coordinate system, the grid nodes included in the averaging procedure are located at

$$\underline{r}_{q,r,s} = \Delta_g \begin{pmatrix} q \\ r \\ s \end{pmatrix} \quad ; \quad q,r,s \in \{-1,0,1\} \quad , \tag{3.142}$$

where Δ_g is the step size of the equidistant Cartesian grid. The average value can then be written as

$$\mathcal{A}_{\mathcal{S}} = \sum_{q\in\{0,\pm1\}} \sum_{r\in\{0,\pm1\}} \sum_{s\in\{0,\pm1\}} \mathcal{A}\left(\underline{r}_{q,r,s}\right) \cdot \underbrace{2^{-\left(q^2+r^2+s^2+3\right)}}_{\equiv \mathcal{G}_{q,r,s}} \quad , \tag{3.143}$$

with the weighting factors $\mathcal{G}_{q,r,s}$ depending on the distance to the reference point (see fig. 3.10). A generalization to curvilinear coordinates requires only minor modifications. The condition

$$\sum_{q\in\{0,\pm1\}} \sum_{r\in\{0,\pm1\}} \sum_{s\in\{0,\pm1\}} \mathcal{G}_{q,r,s} \overset{!}{=} 1 \tag{3.144}$$

that has to be fulfilled by the weighting factors $\mathcal{G}_{q,r,s}$ can easily be verified. For the simulations described in this thesis, values in the range of $\alpha_{\mathcal{S}} = 0.05\ldots0.20$ have proven suitable to guarantee numerical stability without causing significant modifications in the sharpness of the evolving plasma signatures.

---

[4] Hence, $\mathcal{A}$ denotes a single component of the electric or the magnetic field.

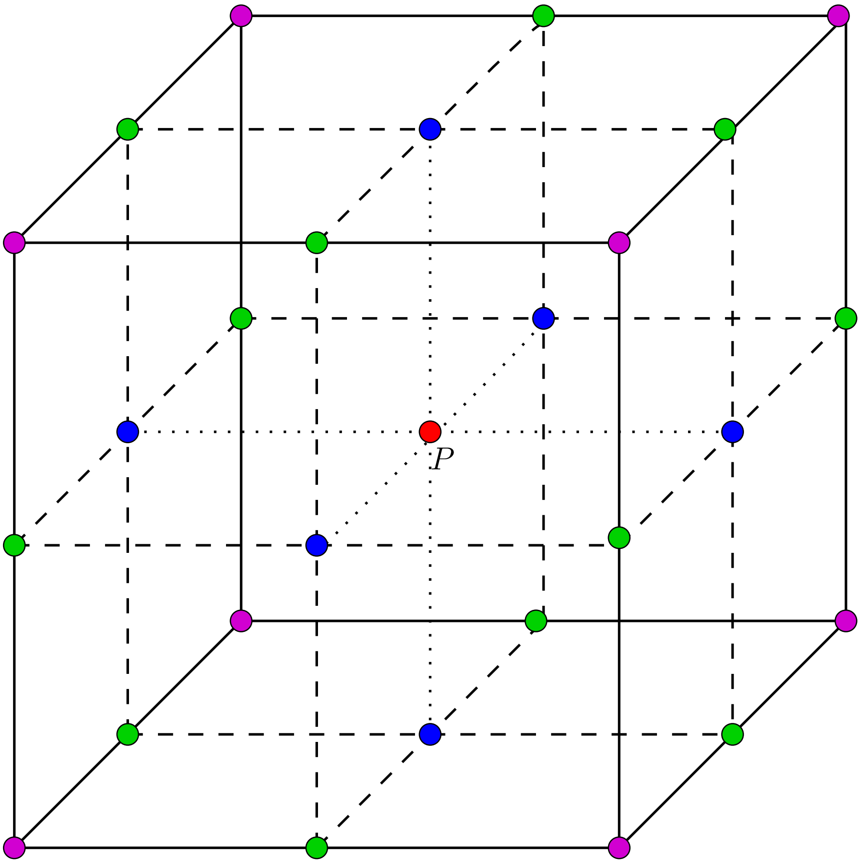

Figure 3.10: Illustration of the smoothing procedure that has been applied to the electromagnetic field quantities. Let $\mathcal{A}$ be a scalar quantity that has been calculated at an arbitrary grid point P. Before the following computational cycle is carried out, $\mathcal{A}$ is replaced by a modified value that is given by $\tilde{\mathcal{A}} = (1-\alpha_{\mathcal{S}})\,\mathcal{A} + \alpha_{\mathcal{S}} \sum_{q,r,s} \mathcal{A}\left(\underline{r}_{q,r,s}\right) \mathcal{G}_{q,r,s}$. The grid point P as well as its 26 nearest neighbours find consideration in the summation. The fraction of $\mathcal{A}$ that contributes to the final value is defined by the smoothing parameter $\alpha_{\mathcal{S}}$. The weighting factor $\mathcal{G}_{q,r,s}$ is 1/8 (red) for the reference point P itself. The values of $\mathcal{G}_{q,r,s}$ assigned to the neighbour points are given by 1/16 (blue), 1/32 (green) and 1/64 (violet), respectively.

8.2 Minimum charge density

Due to the mean charge density $\rho_c = n_{\mathrm{i}} e$ appearing in the denominators of eqs. (3.20) and (3.25), the limit $n_i \to 0$ cannot be described adequately in the framework of the hybrid approximation. In fact, a value of $n_i > 0$ has to be permanently insured at any node of the simulation gird, since otherwise, the numerical stability of the simulation is compromised. A lower limit for the mean particle density that cannot be undershot is defined by the simulation parameter $n_{\mathrm{i,min}}$. If the moment gathering procedure yields a value $n_i < n_{\mathrm{i,min}}$ for a certain grid point, this value is replaced by the fixed quantity $n_{\mathrm{i,min}}$. An important consequence is that an upper limit is imposed on the propagation velocity of Alfvén waves which depends linearly on $1/\sqrt{n_i}$. For the simulation results presented in this work, a value of $n_{\mathrm{i,min}} = 0.2 n_0$ has proven to be appropriate, where n_0 denotes the background density of the undisturbed magnetospheric plasma.

8.3 Courant-Friedrichs-Lewy condition

With respect to the time step Δt, the numerical stability of the simulation code is determined by the criterion of Courant *et al.* [37]. For an equidistant Cartesian grid whose step size in each spatial direction is given by Δ_g, the *Courant parameter* $\mathcal{C}$ can be introduced by means of

$$\mathcal{C} \equiv \frac{V_{\max}\Delta t}{\Delta_g} \quad , \tag{3.145}$$

where $V_{\max}$ is the largest physical velocity occurring in the problem under consideration. In order to insure numerical stability, the condition

$$\mathcal{C} \overset{!}{\ll} 1 \quad \rightsquigarrow \quad \Delta t \ll \frac{\Delta_g}{V_{\max}} \tag{3.146}$$

has to be fulfilled. For the high Mach number flows interacting with the ionospheres of Mars or comets, the average velocity u_0 of the undisturbed solar wind in the upstream region provides a good estimate of $V_{\max}$, whereas the finite thermal velocity of the particles can relatively safely be neglected.

In general, the velocity $\underline{v}_p$ of a newly generated particle is computed according to a Maxwellian distribution function,

$$f\left(\underline{v}_p\right) \propto \exp\left(-\frac{m\left(\underline{v}_p - \underline{u}_0\right)^2}{2kT}\right) \quad , \tag{3.147}$$

where $\underline{u}_0$ denotes the mean velocity of the upstream flow. Consequently, the "worst case scenario" for $V_{\max}$ is defined by those particles whose velocity is significantly larger than $u_0 = |\underline{u}_0|$. Of course, in the framework of the simulation code, the Maxwellian distribution function of the ions is cut off at a certain maximum velocity [7]. In general, this maximum velocity value has to be incorporated into the Courant condition. As stated above, if the model is applied to interaction processes with the solar wind, the approximation

$$V_{\max} \approx u_0 \tag{3.148}$$

has proven to be a suitable estimate for calculating the upper limit of the time step. However, as will be discussed in more detail in subsequent chapters, the thermal velocity of the plasma in Saturn's magnetosphere is by far not negligible. The magnetospheric plasma temperatures derived from Voyager 1 data by Neubauer *et al.* [119] even indicate the thermal velocity

$$v_{\text{th}} = \sqrt{\frac{3kT}{m}} \tag{3.149}$$

of the magnetospheric particles[5] to exceed the average flow speed by more than a factor of 2. This effect has to be taken into account when dealing with plasma processes inside Saturn's magnetosphere. Only a single particle whose velocity is significantly larger than u_0 can compromise the stability of the simulation.

---

[5] The thermal velocity v_{th} is a measure of the width of the Maxwellian distribution function.

The simulations carried out for this work have shown that a reasonable estimate of the upper limit for Δt can be obtained by using the thermal velocity (3.149) and setting

$$\Delta t \approx \mathcal{P} \cdot \frac{\Delta_g}{u_0 + \sqrt{\frac{3kT}{m}}} \quad , \tag{3.150}$$

where values of $\mathcal{P} = 0.2 \ldots 0.5$ have proven adequate.

9 Boundary conditions

Before initiating a simulation run, the electromagnetic fields as well as the mean ion velocity $\underline{u}_i$ and the charge density ρ_c have to be defined at the different kinds of boundary layers in the simulation geometry. On the one hand, adequate values have to be chosen at the outer boundaries of the cubic simulation domain. On the other hand, modelling the obstacle's surface and interior has proven to be a critical issue.

9.1 Outer boundaries of the simulation box

This section deals with the different kinds of boundary conditions that can be defined at the outer faces of the simulation box. Two basic concepts of treating the outer boundaries of the simulation domain are presented: inflow and outflow boundary conditions. Furthermore, the question of how to apply these conditions to a simulation of Titan's plasma environment is discussed.

Each of the six outer "walls" of the simulation domain can be treated either as inflow or as outflow boundary. These basic types of boundary conditions impose different values on the electromagnetic fields, the plasma density and the mean flow speed:

- *Inflow boundary:*
  At the grid points located at an inflow boundary layer, the electromagnetic field quantities as well as the plasma density and its mean velocity are set to constant values for the entire duration of the simulation. These values represent the undisturbed, homogeneous plasma entering the simulation box. The plasma parameters $\underline{u}_i$ and ρ_c are pre-defined simulation parameters; the direction and strength of the undisturbed magnetic field are treated in the same way. According to eq. (3.20), the electric field for a homogeneous plasma is given by $\underline{E} = -\underline{u}_i \times \underline{B}$. At an inflow boundary, newly generated particles are continuously injected into the simulation domain. In each time step, all particles which are located in the boundary cells are deleted, and the cells are filled with newly generated, homogeneous plasma.
- *Outflow boundary:*
  For the grid points located at an outflow boundary, the electromagnetic fields as well as the plasma parameters $\underline{u}_i$ and ρ_c are obtained by means of zero order extrapolation form the values at the nodes directly in front of the boundary, i.e. the quantities defined at neighbour grid points of both planes are assumed to be equal. Particles hitting an outflow boundary layer are removed from the simulation scenario.

A "standard" simulation geometry is illustrated in fig. 3.11. In each direction, the simulation box possesses an extension of $15R_T$. The center of Titan is identical to the center of the cubic simulation domain. The undisturbed magnetospheric plasma velocity $\underline{u}_0$ is oriented in positive x direction. The (x, y) plane coincides with Titan's orbital plane. In agreement with the Voyager 1 configuration, the undisturbed Saturnian magnetic field $\underline{B}_0$ is directed antiparallel to the z axis. As suggested by Bagdonat [7, 8, 9, 10, 11], inflow boundary conditions have been applied to those walls of the simulation domain which are parallel to the undisturbed flow direction. In the figure, these boundaries are located at $y = \pm 7.5R_T$ and $z = \pm 7.5R_T$, respectively. Of course, the left face of the simulation domain ($x = -7.5R_T$) is treated as an inflow boundary as well. However, the wall which is located in the wake region downstream of Titan at $x = +7.5R_T$ should evidently be treated as an outflow boundary. Although the assignment of outflow boundary conditions to the wake face of the simulation box has proven successful in simulations of the interaction between the solar wind and comets, Mars or asteroids, such a strategy has shown to be inadequate when studying the interaction between Saturn's magnetospheric plasma and Titan's ionosphere. Indeed, in the Titan scenario, inflow conditions have to be assigned to all six outer faces of the simulation domain. At first glance, treating the wake face as an inflow boundary may appear unphysical. Therefore, the following discussion will not only dwell on the problems that arise from the application of outflow boundary conditions to the wake face, but it will also be revealed why treating this wall as an inflow boundary does not create significant unphysical errors.

At an inflow boundary, the electromagnetic fields as well as the plasma density are set to the homogeneous upstream values throughout the entire duration of the simulation. Thus, such a boundary layer mimics an area of undisturbed, homogeneous magnetospheric plasma that has been attached to the simulation domain at the respective side. In contrast to this, an outflow boundary acts in the same way as a vacuum that has been connected to the respective wall of the simulation box, for all particles crossing such a boundary layer are deleted, while the electromagnetic fields are simply extrapolated. In principle, at such a boundary layer, the plasma is "drawn" out of the simulation domain into the vacuum. Therefore, in the vicinity of an outflow boundary layer, even the slightest density gradient experiences a strong enhancement due to the plasma being accelerated out of the simulation domain. This effect can be observed when attempting to simulate the interaction between Titan and the Saturnian magnetospheric plasma. The results of a test run are displayed in fig 3.12. The upstream magnetospheric plasma composition and velocity have been chosen in accordance to the Voyager 1 configuration (cf. tab. 3.1), i.e. the flow is slightly super-alfvénic, whereas its sonic and magnetosonic Mach numbers are smaller than 1. The simplifying single-species representation discussed in section 5.2 has been applied to the two-component magnetospheric plasma.

The time step Δt has been chosen in such way that 8000 time steps correspond to the duration in which the undisturbed magnetospheric plasma would pass through the entire simulation domain from $x = -7.5R_T$ to $x = +7.5R_T$ one time. However, because of the relatively slow motion of the ionospheric particles downstream of the obstacle, a total number of 80000 time steps would be required to achieve a quasi-stationary state. In order to illustrate the effects occurring near the outflow boundary layer, the figure compares the mean magnetospheric plasma velocity at the beginning of the simulation to the situation after 2000 and after 4000 time steps, respectively. In other words, the simulation is far from being stationary and the

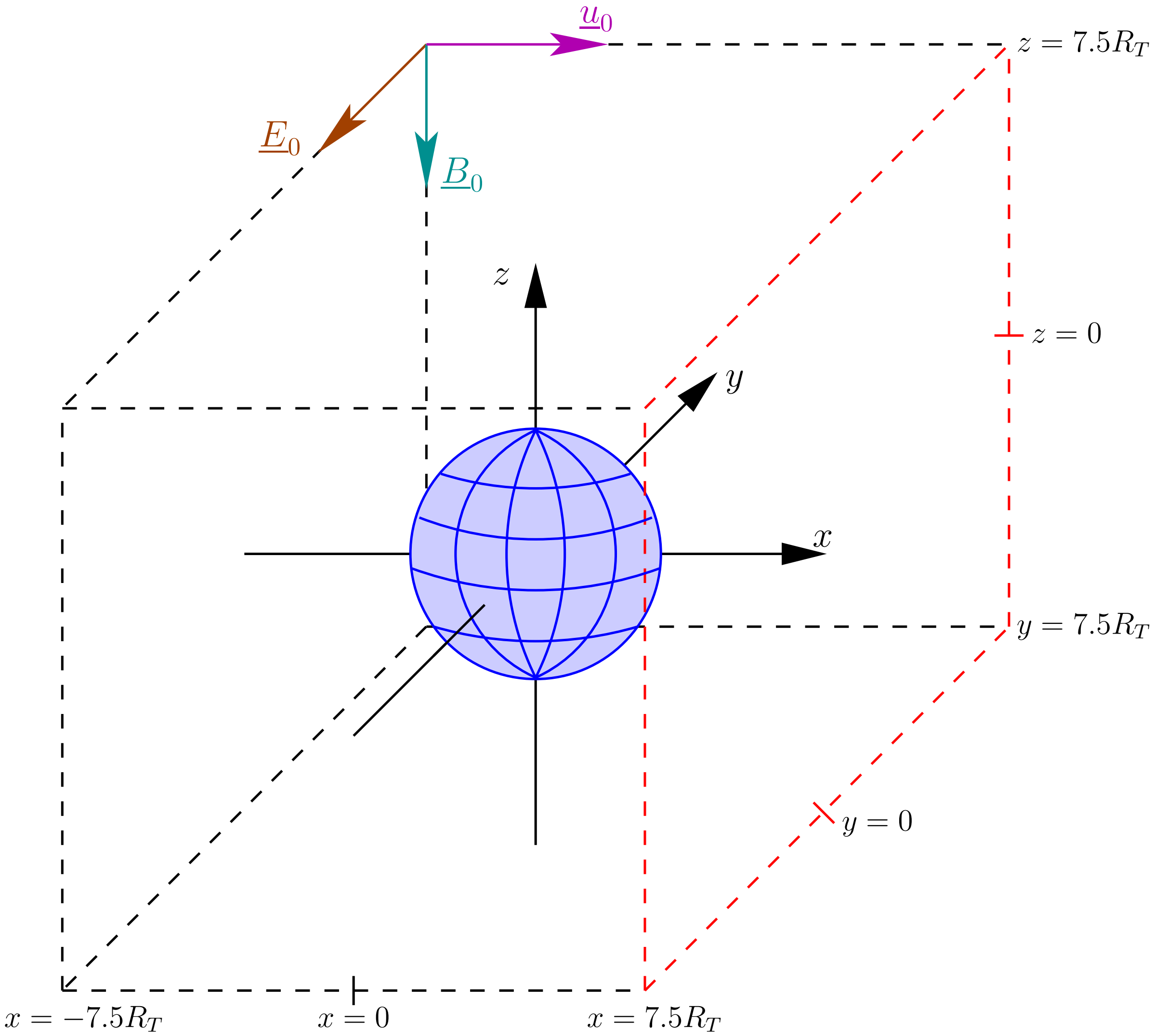

Figure 3.11: Schematic illustration of the three-dimensional cubic simulation geometry that has been used to study the influence of outflow boundary conditions on the simulated structure of Titan's plasma environment. The center of Titan coincides with the origin of the coordinate system. The undisturbed Saturnian magnetic field $\underline{B}_0$ points in negative z direction, whereas the mean velocity of the undisturbed magnetospheric plasma $\underline{u}_0$ is parallel to the $(+x)$ axis. Inflow boundary conditions have been chosen at all faces of the simulation box except for the plane at $x = +7.5R_T$ (denoted in red). According to a Maxwellian distribution function, particles are continuously generated at an inflow boundary. Therefore, an inflow boundary acts like an area of homogeneous, undisturbed plasma which has been connected to the simulation box at the respective face. In contrast to this, outflow boundary conditions have been applied to the right face of the simulation box at $x = +7.5R_T$. At such a boundary layer, the electromagnetic field quantities as well as the moments of the distribution function are obtained from the grid points that are located directly in front of the boundary by means of an extrapolation procedure. Besides, any particle hitting an outflow boundary is removed from the simulation domain. Thus, an outflow boundary mimics a vacuum that has been attached to the simulation domain at the respective side. When the undisturbed plasma velocity u_0 is in the sub-magnetosonic regime, the plasma is strongly drawn out of the simulation domain into the vacuum at an outflow boundary.

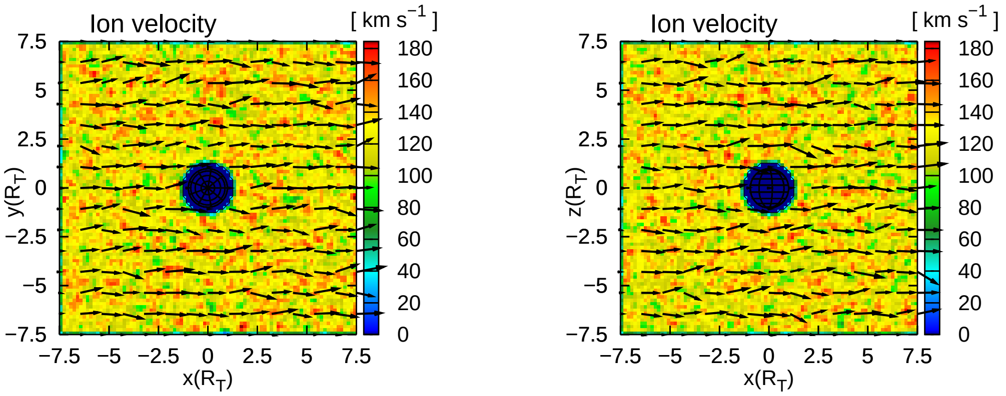

(a) Situation after 0 time steps (initial state)

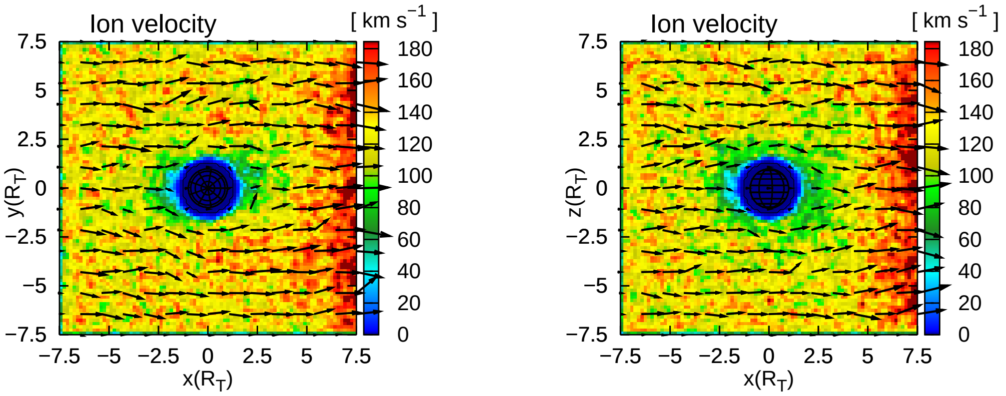

(b) Situation after 2000 time steps

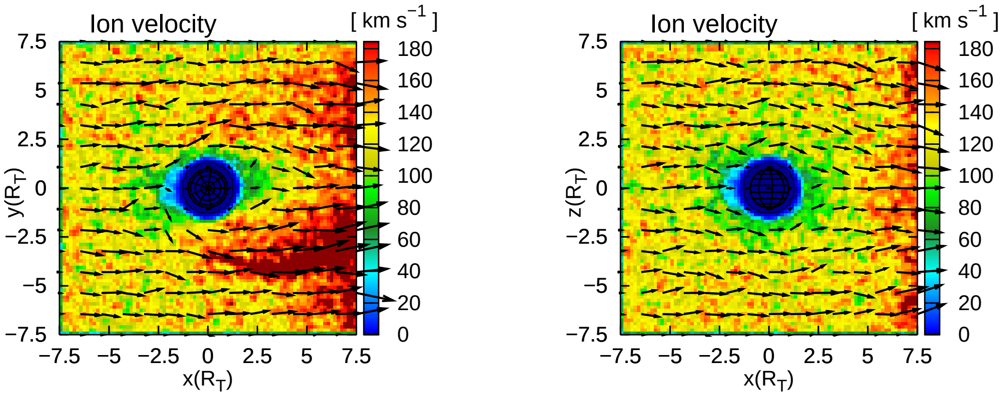

(c) Situation after 4000 time steps

Figure 3.12: The effect of outflow boundary conditions on the global structure of the interaction region has been examined in a test simulation. The overall geometry of the simulation domain is shown in fig. 3.11. The figure shows the mean magnetospheric ion velocity in the (x, y) and (x, z) planes of the simulation box (a) at the beginning of the simulation, (b) after 2000 time steps and (c) after 4000 time steps. The color scales denote the absolute flow speed, whereas the arrows represent the projection of the flow vectors on the cutting planes. Because the outflow boundary at the right face $(x = 7.5R_T)$ of the box mimics an attached vacuum, the plasma is accelerated out of the simulation domain. As can be seen from the figure, the structure of the near-Titan plasma environment is significantly falsified by this effect even in early states of the simulation. One passage of the plasma through the entire simulation domain corresponds to a total number of 8000 time steps, but in the scenario under consideration, more than 80000 time steps would be required to reach a quasi-stationary state. For this reason, the application of outflow boundary conditions has proven inadequate for the simulation of Titan's plasma environment.

build-up of the model ionosphere is still in a very early state. As can be seen in the two-dimensional cuts through the simulation domain, strong distortions of the magnetospheric plasma emerge near the wake face of the simulation box. Even after a rather small number of time steps, these distortions have already reached the immediate vicinity of Titan, where they take significant influence on the plasma flow pattern as well as on the electromagnetic field topology. Thus, the effect of the plasma being drawn out of the simulation box at the outflow boundary would make an application of the hybrid model to Titan's plasma interaction impossible. Due to the characteristic time scale for the formation of these boundary-induced distortions being about one order of magnitude smaller than the total duration of a simulation, a moderate increase of the distance between the satellite and the wakeside boundary layer is definitely not an option to circumvent this problem. Furthermore, since even an up-to-date personal computer would not be able to perform a simulation run with more than 100 cells in a certain direction, placing the boundary in a larger distance to the satellite would go along with a significant reduction of the spatial resolution. Nevertheless, it should be noted that the distortions manifesting near the $(x = +7.5R_T)$ boundary are far from being unphysical, but the contrary is the case. The plasma inside the simulation domain behaves in exactly the way that has to be expected when a vacuum is connected to one face of the simulation box.

The problem described above occurred neither in the simulations of the interaction between Mars or comets with the solar wind presented by Bagdonat *et al.* [7, 8, 9, 10, 11] and Bößwetter *et al.* [26, 27], nor in the study of an asteroid's plasma environment conducted by Simon *et al.* [138]. In fact, this effect originates from the specific features of the plasma in Saturn's magnetosphere. As stated above, the distortions manifesting near the outflow boundary arise from even minor statistical density perturbations, in the way that the build-up of such structures is increased. Therefore, the velocity of the compressional magnetosound waves in the magnetized plasma can be considered a characteristic scale for the propagation of these distortions into the simulation domain. In the case of comets, Mars and asteroids, the impinging solar wind is clearly supermagnetosonic, i.e. the dynamical processes in the solar wind take place on significantly shorter time scales than the propagation of the boundary-induced distortions into the simulation domain. Hence, these distortions are simply "overwritten" by the superfast solar wind and are therefore unable to cause any kind of noticeable distortion in the impinging plasma flow. Of course, when the simulation approaches its quasi-stationary state and the shock front at the obstacle's ramside starts to develop, the plasma is also decelerated to subfast velocities. However, in the case of comets, Mars and asteroids, the interaction gives rise to a "physical" evacuation of the region downstream of the obstacle, i.e. the solar wind is unable to gain access to the planetary wake. The effects arising from the application of inflow boundary conditions to the wakeside wall may accelerate this evacuation of the wake region, but they cannot cause unphysical perturbations downstream of the obstacle.

The numerical problems described above do not originate form the specific features of the simulation code employed for the present study, but they should occur in any simulation model of a realistic Titan scenario. Hence, as for the wakeside boundary conditions, an adequate compromise has to be found. Brecht *et al.* [30] "circumvent" the difficulties described above by simply setting the finite magnetospheric ion temperature to zero and hence, by generating a hypothetical supermagnetosonic upstream situation $(M_{MS} = M_A = 1.9)$. The applicability of this approach to the physics of the real problem has to be put into question. On the other hand, Kallio *et al.* [74] have successfully developed a Titan simulation model that treats all six faces of the simulation domain as inflow boundaries. Even though this may not be the most sophisticated way, this approach has been successfully incorporated into the simulation code used for the present study as well. Neither the plasma density and velocity nor the electromagnetic fields show any kind of noticeable distortion near the wakeside boundary. Nonetheless, in order to avoid any influence on the structure of the interaction region near Titan, all six outer faces of the simulation domain have consequently been placed in a distance of more than $7R_T$ to the satellite.

To dwell on the specific details that are associated with the assignment of inflow conditions to the wakeside boundary, it is helpful to understand *how* particles are being generated at such a boundary layer. As discussed by Bagdonat [7], the velocity $\underline{v}_p$ of a newly generated particle is determined by a Maxwellian distribution function, i.e.

$$f\left(\underline{v}_p\right) \propto \exp\left(-\frac{m\left(\underline{v}_p-\underline{u}_0\right)^2}{2kT}\right) \quad . \tag{3.151}$$

The vector $\underline{u}_0$ points in positive x direction, i.e. out of the simulation domain. In other words, most of the particles that are generated at the wakeside inflow boundary do not enter the simulation domain "from behind", for their velocity possesses a positive x component and is therefore directed away from Titan. However, the number of particles that are able to gain access to the simulation domain from the wakeside inflow boundary by moving antiparallel to the mean flow direction is definitely not negligible. Using the parameters for the (N^+/H^+) plasma from table 3.1 and $\underline{v}_p = -\underline{u}_0$ yields a value of

$$f\left(\underline{v}_p=-\underline{u}_0\right) \propto \exp\left(-\frac{2m\underline{u}_0^2}{kT}\right) = \exp\left(-1.45\right) = 0.23 \quad . \tag{3.152}$$

Before the inflow boundary cells are refilled with homogeneous plasma, the particles inside these cells are deleted in each time step. Therefore, the plasma that impinges on the wakeside boundary layer is automatically removed from the simulation box. In other words, the flow that “attempts” to leave the simulation domain at the wakeside does *not* accumulate near the boundary layer. This treatment of the wakeside boundary is referred to as *back-face emission* by Kallio *et al.* [74]. Of course, the less sophisticated approach presented by Brecht *et al.* [30] did not require a special treatment of the wakeside boundary, for the upstream plasma was supermagnetosonic. Thus, outflow boundary conditions could be assigned to the wakeside boundary, i.e. the same boundary conditions as in a simulation of the Martian plasma environment were used.

At an inflow boundary layer, the electromagnetic field components are set to the constant values of the undisturbed magnetospheric upstream plasma. Thus, when Titan's magnetotail is formed and the magnetic field lines drape around the satellite, the direction of $\underline{E}$ and $\underline{B}$ near the wakeside of the simulation box differs significantly from the orientation of these fields in the boundary layer. Although in the simulations presented in this work, this effect did not cause any kind of visible distortion in the electromagnetic fields near the boundary layer, an alternative treatment of $\underline{E}$ and $\underline{B}$ has also been tested. These modified wakeside boundary conditions do not set the electromagnetic fields to their background values, but the fields are instead obtained from the grid nodes in front of the boundary layer by means of extrapolation. In other words, the electromagnetic fields at the wakeside face of the simulation box are treated in the same way as at an *outflow* boundary layer. In such a configuration, the magnetic draping pattern is not artificially interrupted by the presence of the wakeside wall of the box. These modified wakeside boundary conditions can be considered a combination of inflow and outflow conditions. In order to prevent the plasma from being drawn out of the simulation box, the particles are treated in the same way as at an inflow boundary. The treatment of $\underline{E}$ and $\underline{B}$, on the other hand, corresponds to the situation at an outflow boundary layer. Only in distances below two grid cells to the wakeside, these modified boundary conditions yielded significantly different results than the simple application of inflow boundary conditions. Within the framework of this simulation study, both types of wakeside boundary conditions have been used.

An overview of specific problems associated with fluid simulations of Titan's plasma interaction is given by Bogdanov *et al.* [25].

9.2 Inner boundary – Surface of the obstacle

This section deals with the boundary conditions that have been chosen to represent the Titan obstacle in the simulations. At first, it should be noted that the spherically shaped *inner boundary* does not coincide with the surface of Titan, but it is instead located at the lower boundary of the satellite's ionosphere in an altitude range of 800 . . . 1000 km above the surface. The situation is illustrated in fig. 3.13. The necessity of such a treatment arises from the strong gradient along the Titan-facing flank of the ionospheric production profiles which cannot be resolved by the simulation grid in an adequate manner (cf. fig. 3.3). This technique has already been successfully integrated into the models of Ma *et al.* [99] as well as Kallio *et al.* [74]. The lower boundary of Titan's ionosphere is represented by an absorptive sphere, i.e. any particle hitting this surface is removed from the simulation scenario. Consequentially, the mean ion density at the grid nodes inside the obstacle should be set to a value of

$$n_i = 0 \quad . \tag{3.153}$$

However, assuming the plasma density to vanish inside the obstacle has shown to be critical for the stability of the simulation model. In fact, simply assigning a constant, finite density to the gird nodes below the boundary surface is not sufficient either, but the inner density must include a functional dependence on both time and the location of the respective grid point. The details of this problem will be discussed in the following.

While the simulation proceeds, the ionospheric plasma density in the immediate vicinity of the obstacle boundary is continuously increased, for newly generated ionospheric particles are injected into the simulation domain during each time step. Since the ionospheric particle density near Titan clearly exceeds the magnetospheric flow density, the electric field arising from the two electron pressure terms in eq. (3.46) is mainly governed by the ionospheric electron population, i.e.

$$\underline{E}_{\nabla} \propto \nabla n_{e,2} = \nabla n_2 \quad . \tag{3.154}$$

Thus, if a value of zero is chosen for the (ionospheric) ion density below the obstacle boundary, a massive density gradient and therefore, a strong electric field will locally emerge near the surface. Because the electric field strength would increase by more than an order of magnitude in a spatial distance of only one or two grid cells, the resulting field gradient would compromise

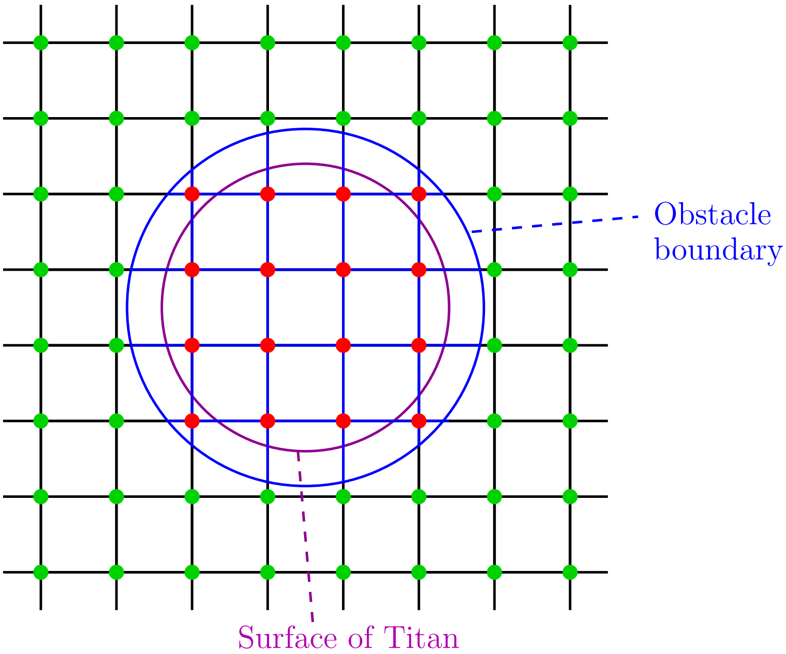

Figure 3.13: In the simulation scenario, Titan's interior is modelled by means of boundary conditions that have been imposed on the particle densities and currents. The artificial obstacle boundary is located at an altitude of about 1000 km above the surface of the satellite. Particles hitting this artificial inner boundary (blue circle) are removed from the simulation, representing absorption by the obstacle. Moreover, the mean ion current $\underline{j}_i$ at the grid points inside the obstacle (red) is set to zero. Nevertheless, the mean particle density at the grid points below the boundary layer has to be kept at a non-vanishing value in order to avoid numerical instabilities that emerge from a strong ionospheric ion density gradient near the surface. While the simulation proceeds, this artificial inner density is increased in time to match the ionospheric density increase that arises from the continuous generation of new particles directly above the boundary layer. On the other hand, the spatial variations of the ion production described by the Chapman function are taken into account by introducing a spatially inhomogeneity of the inner density profile. In contrast to the technique applied to the density, the model does not include a boundary condition determining the electromagnetic field quantities in the inner region, i.e. $\underline{E}$ and $\underline{B}$ are calculated according to eqs. (3.20) and (3.25) at all grid points in the simulation box.

numerical stability. The ionospheric density gradient near the obstacle can be reduced by introducing a finite value for the ion density below the boundary layer. This inner density has to be a function of time, for the ionosphere is not present at the beginning of a simulation run, but it is built up while the simulation proceeds towards a quasi-stationary state. Thus, the time variation of the ionospheric density near Titan can – for instance – be matched by an inner density profile according to

$$n_i(t) = \frac{t}{t+t_0} n_{\max} \quad , \tag{3.155}$$

where $t = 0$ refers to the beginning of a simulation run. The parameters t_0 and $n_{\max}$ are constants, with $n_{\max}$ denoting the quasi-stationary, final inner density value that is achieved after a sufficiently long simulation time t:

$$\lim_{t\to\infty} \frac{t}{t+t_0} n_{\max} = n_{\max} \quad . \tag{3.156}$$

However, while this technique is capable of countering any kind of density gradient that evolves from the increase of the ionospheric particle density in *time*, it does not take account for the *spatially* inhomogeneous production profile that is used to generate the ionosphere. For this reason, an additional term which is able to compensate for spatial variations of the ionospheric density near the surface must be incorporated into eq. (3.155).

The local ion production rate directly above the obstacle boundary is a function of the solar zenith angle χ_ν. The ion production achieves its maximum at the subsolar point and steadily diminishes when increasing χ_ν, i.e. when approaching the terminator line. If the x axis is assumed to be parallel to the direction of the impinging solar radiation, all surface points that are located in the same plane perpendicular to the x axis can be characterized by the same production rate, since their locations possess the same solar zenith angle. In other words, the production rate is spatially constant along circles on the obstacle boundary that are oriented perpendicular to the impinging solar radiation. Of course, for all points with $\chi_\nu > 87^\circ$ as well as at the nightside of Titan, the production rate is independent of the solar zenith angle.

Consequentially, the inner density profile should include a spatial dependence on the x coordinate of the grid nodes that are located directly below the surface, i.e.

$$n_i(x,t) = \frac{t}{t+t_0} n_{\max} \cdot f(x) \quad . \tag{3.157}$$

In the simulation runs carried out for the present work, the spatial variation of the inner density is represented by a Fermi profile according to

$$f(x) = \frac{1}{1+\exp\left(\frac{\alpha x-\beta}{\gamma}\right)} \quad , \tag{3.158}$$

where the free parameters α, β and γ allow an adaption to a specific ionospheric production profile. Without losing generality, the x coordinate of the grid nodes inside the obstacle is assumed to be positive, with the x axis pointing from the subsolar point to the nightside. The "jump" of the Fermi function $f(x)$ is located near $x_j = \beta/\alpha$, with the high values of $f(x)$ being located in Titan's dayside hemisphere and the low values being assigned to grid nodes in the nightside hemisphere. This construction provides at least a rough approximation to the dependence of the near-surface production profile on the solar zenith angle. The simulations have shown that in order to guarantee numerical stability, the parameters α, β and γ can be chosen in such way that the "Fermi block" is already significantly deformed, i.e. the density variations inside the obstacle are only moderate.

While the ion currents inside the obstacle are set to zero, no boundary conditions are imposed on $\underline{E}$ and $\underline{B}$, i.e. the electromagnetic field equations are solved at the grid points outside as well as inside the obstacle. As in such a geometry, the magnetic field can penetrate into the interior of the obstacle by means of numerical diffusion effects, this is of course only a rather rough approximation to the real situation. However, treating the fields in this way has proven to be uncritical in earlier simulation studies, for most of the magnetic field lines are prevented from gaining access to the immediate vicinity of the obstacle by ionospheric shielding currents.

Defining boundary conditions for the interior of the obstacle is typically one of the most critical issues in simulation studies of space plasma phenomena. For this reason, a variety of different boundary conditions has already been tested. For instance, in a number of test simulations of the Martian plasma environment, the electromagnetic fields inside the obstacle have simply been set to zero [26]. However, "cutting of" the field lines at the surface of the obstacle introduces a significant energy sink into the simulation geometry and has proven to yield strong deformations of the ramside magnetic pile-up region as well as the lobe structure.

In contrast to the technique described above, Shimazu [134] has applied a *reflective* boundary condition to particles hitting the surface in a three-dimensional hybrid model of the Martian plasma interaction. These boundary conditions have shown to lead to the formation of artifact-like ion clouds in the vicinity of the obstacle and therefore, they falsify the global structure of the interaction region. A quite promising approach has recently been presented by Müller [113] who has studied the characteristics of the lunar wake in the framework of the hybrid approximation. Unlike any other simulation model that is currently available, this code treats the electromagnetic fields in the obstacle's insulating interior by solving the appropriate Maxwellian field equations and by realizing a self-consistent coupling to the fields in the exterior region. If the problem of the ionospheric density gradients near the surface can be solved by such an approach as well, this technique will possibly be incorporated into future extensions of the Titan model.

10 Summary

Although a large number of simulation studies on the subject of Titan's plasma interaction have been carried out during the past 15 years, most of them are based on fluid plasma models and are therefore unable to account for the asymmetries that arise from finite gyroradius effects. Currently, most of the available kinetic models are either not self-consistent, i.e. test particles are simply injected into a pre-defined electromagnetic field configuration, or they include intolerable simplifications of the real Titan situation.

For the present study, a three-dimensional electromagnetic hybrid model has been applied to Titan's plasma interaction. This approach treats the electrons of the plasma as a fluid, whereas it allows to cover the dynamics of individual ions. Therefore, ion motion in the plasma's electromagnetic fields is described by Newton's equation of motion, with the Lorentz force providing the inhomogeneity. The electrons are described by a momentum conservation law obtained from the fluid plasma description. By using Ampère's law and by incorporating the approximation of vanishing electron inertia ($m_e = 0$), an explicit expression for the electric field can be obtained. The time evolution of the magnetic field is covered by Faraday's law. In order to obtain a closed set of equations, an adiabatic equation of state for the electrons is introduced. The model is capable of "partially" distinguishing between electrons of magnetospheric and of ionospheric origin. The validity of the hybrid approximation is restricted to processes whose characteristic time scales are of the order of the inverse ion gyrofrequencies. Typical length scales should be larger than or comparable to the ion gyroradii. The additional assumption of quasi-neutrality is fulfilled on scales above the Debye length.

In the model, Titan's dayside ionosphere is assumed to be generated by solar ultraviolet radiation. In consequence, the dayside ion production profile is given by a Chapman-like function, i.e. the local ion production rates depend on both the altitude above the surface and the solar zenith angle. The particle impact processes that give rise to the satellite's nightside ionosphere are represented in a simplifying way by means of a production rate that includes a functional dependence on the altitude, but not on the solar zenith angle. In order to counter any kind of numerical instability that arises from this specific ionosphere configuration, an artificial plasma density has to be defined in the obstacle's interior. In contrast to this, the model does not include a boundary condition for the electromagnetic fields.

Chapter 4

Titan in subsonic and supersonic flow: General characteristics

The simulation results presented in this chapter illustrate the key features of Titan's plasma environment as a function of the Mach numbers in the upstream flow. The single-species representation discussed in section 5.2 of chapter 3 has been applied to the impinging magnetospheric plasma. In the following, all physical quantities referring to the magnetospheric ions are denoted by the subscript m, whereas any parameter that has been assigned the subscript i refers to the ionospheric N_2^+ ion population.

A more extensive discussion of the results presented in this chapter, especially of the Lorentz forces acting on particles of magnetospheric and ionospheric origin, has been published in Annales Geophysicae by Simon *et al.* [139, 140].

1 Simulation geometry and parameters

The purpose of the simulations presented in this chapter is to identify the general characteristics of Titan's plasma interaction as a function of the Mach numbers in the upstream plasma flow. Three different scenarios have been taken into consideration. On the one hand, the case of Titan being located inside the Saturnian magnetosphere at 18:00 local time (LT) is analyzed. Since in this situation, the dayside ionosphere of the satellite is exposed to the upstream flow, the situation bears a strong resemblance to the interaction of Mars or Venus with the solar wind. The simulation parameters have been chosen in accordance to the configuration obtained from Voyager 1 data (cf. chapter 3). Thus, Titan is exposed to a super-alfénic, yet subsonic and submagnetosonic plasma flow.

However, in order to understand the interaction between Titan's ionosphere and the magnetospheric plasma, it has proven helpful to analyze the case of a superfast upstream flow at first. Because of the high thermal velocity of the particles inside Saturn's magnetosphere, the plasma signatures emerging in the vicinity of Titan are by far not as sharply pronounced as in the case of a relatively cold and superfast upstream flow. Therefore, in the first situation that will be discussed, Titan faces a super-alfénic and also slightly supersonic and supermagnetosonic plasma flow. As discussed in chapter 2, this situation may be realized, if the stand-off distance of Saturn's bow shock is reduced due to an enhanced level of solar wind dynamic pressure and hence, Titan can interact directly with the solar wind. Although such a scenario is theoretically possible, it has so far not been observed by any of the spacecraft missions to the Saturnian system, i.e. spacecraft data for a quantitative comparison to the simulation results are not available. Since the only purpose of the simulation is to obtain a qualitative reference for the interpretation of the situation inside the magnetosphere, the input parameters have been chosen in accordance to the model of Ledvina *et al.* [90]: Most of the simulation parameters from the Voyager 1 data set are retained. Especially, the upstream flow is still assumed to consist of a single ion species of mass $m(N^+/H^+) = 9.67\,\mathrm{amu}$. The only parameters that have actually been modified are the plasma betas of the upstream plasma. A value of $\beta_m = 0.38$ has been chosen for the ion beta[1] in the impinging flow, while the electron beta has been set to $\beta_{e,m} = 0.04$. This combination yields the Mach numbers

$$M_S = 2.90 \qquad \text{and} \qquad M_{MS} = 1.60 \tag{4.1}$$

for the upstream flow. Since neither the background magnetic field strength ($B_0 = 5\,\mathrm{nT}$) nor the undisturbed number density ($n_m = 0.3 \cdot 10^6\,\mathrm{m}^{-3}$) has been altered, the alfvénic Mach number is still given by $M_A = 1.87$. The parameters of the resulting super-alfvénic, supersonic and supermagnetosonic plasma regime are in consistency with the input configuration used in the MHD model of Ledvina *et al.* [90]. Of course, especially the choice of $m(N^+/H^+) = 9.67\,\mathrm{amu}$ for the upstream particle mass reduces the quantitative applicability of the simulation to the real situation when Titan is located in the solar wind. However, since only very few modifications of the simulation scenario are required in order to "generate" the situation inside the magnetosphere, the simplifying assumptions discussed above allow a straightforward comparison between the results of both runs.

The third geometry that has been considered allows to gain deep insight into the transition that Titan's plasma environment undergoes when the Mach numbers of the upstream flow are "switched" from solar wind to magnetospheric conditions. In this geometry, the upstream flow is assumed to be super-alfvénic, *super*sonic and submagnetosonic. Specifically, values of $M_A = 1.87$, $M_S = 1.08$ and $M_{MS} = 0.94$ have been chosen for the Mach numbers of the impinging flow, corresponding to values of $\beta_{e,m} = 0.97$ and $\beta_m = 2.00$ for the (N^+/H^+) plasma's electron and ion betas, respectively. All other simulation parameters, including the upstream plasma composition and density as well as the background magnetic field are the same as in the other simulation runs presented in this chapter.

The simulation geometry for all three scenarios is displayed in fig. 4.1. The simulation box is cubic with an extension of $15R_T$ in each spatial direction. The center of Titan coincides with the origin of the coordinate system. The undisturbed plasma flow velocity $\underline{u}_0$ points in $(+x)$ direction, whereas the background magnetic field $\underline{B}_0$ is oriented antiparallel to the z axis. Hence, the convective electric field $\underline{E}_0 = -\underline{u}_0 \times \underline{B}_0$ is antiparallel to the y axis and, inside the magnetosphere at 18:00 LT, to a unit vector pointing towards Saturn. The dayside of the satellite is located in the $(x < 0)$ hemisphere, i.e. the (y, z) plane of the coordinate frame is identical to the terminator plane. In the following sections, the (x, y) plane will be referred to as the equatorial plane, whereas the (x, z) plane will be called the polar plane. The spatial discretization is realized by means of a fisheye grid with $90 \times 90 \times 90$ cells in each direction. The maximum resolution as well as the maximum curvature of the coordinate lines are achieved in the immediate vicinity of the ionospheric production maximum, i.e. at an altitude of about 1100 km above Titan's surface. The specific grid parameters are given

---

[1] In order for the notation to be consistent with the other results presented in this chapter, the upstream (N^+/H^+) ion component is again denoted by the subscript m, although supermagnetosonic flow conditions do – of course – not occur inside the Saturnian magnetosphere.

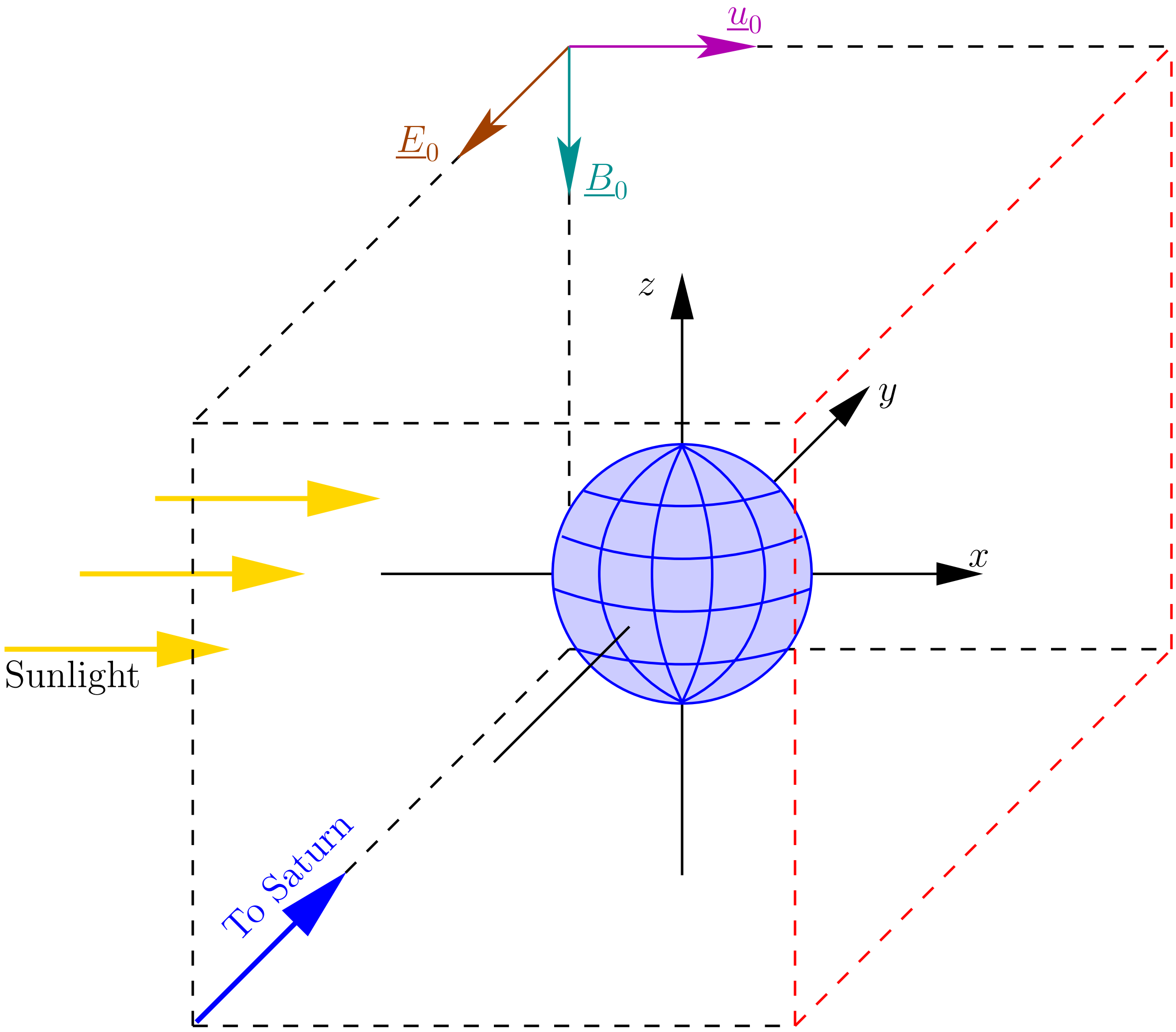

Figure 4.1: The key features of Titan's plasma environment have been studied by using a cubic simulation domain with a length of $15R_T$ in each direction. The center of the obstacle coincides with the origin of the Cartesian coordinate system shown in the sketch. The undisturbed plasma velocity $\underline{u}_0$ points in $(+x)$ direction; the homogeneous background magnetic field $\underline{B}_0$ is oriented in $(-z)$ direction. Thus, the convective electric field $\underline{E}_0$ is antiparallel to the $(+y)$ axis. In the 18:00 LT geometry, $\underline{E}_0$ points away from Saturn. The dayside of Titan is located in the $(x < 0)$ half space, i.e. the satellite's terminator plane is identical to the (y, z) plane. The boundary layer denoted by the red dashed lines is located in the wake region downstream of Titan.

by $\lambda = 0.5(R_T)^2$, $\mu = 0.7/R_T$ and $\nu = 19.0R_T$, respectively. The quasi-stationary state of the simulations was achieved after a duration in which the undisturbed plasma would have passed through the entire simulation box 15 times. Therefore, the total simulation time is given by

$$T_{\text{total}} = \frac{15 \cdot 15R_T}{120\,\text{km/s}} = 4828\,\text{s} = 1.3\,\text{h} \quad . \tag{4.2}$$

Since this value is about a factor of 300 smaller than Titan's orbital period of 15.95 days, the

Simulation run	M_A	M_S	M_{MS}
#1	1.87	2.90	1.60
#2	1.87	0.57	0.55
#3	1.87	1.08	0.94

Table 4.1: Simulation of Titan's plasma environment as a function of the Mach numbers in the upstream flow. Three different situations have been considered. On the one hand, the case of all three Mach numbers in the upstream flow being larger than 1 has been examined (run #1). This scenario may occur when Titan is able to leave Saturn's magnetosphere in the subsolar region of its orbit, so that the satellite's ionosphere is directly exposed to the solar wind. The parameters of the second simulation have been chosen in accordance to the Voyager 1 configuration, i.e. only the alfvénic Mach number of the upstream flow is larger than 1. The third geometry is meant to illustrate the transition between the two foregoing cases.

change of the satellite's orbital position during the simulation can safely be neglected.

Table 4.1 provides an overview of the three different sets of Mach numbers. The discussion will start with the case of all three Mach numbers being larger than 1, since it provides a reference for the interpretation of the other two scenarios.

2 Titan in supermagnetosonic flow

The results for the quasi-stationary state of the simulation are displayed in figs. 4.2, 4.3 and 4.4, respectively. The mean density n_m of the (N^+/H^+) plasma as well as the mean ionospheric ion density n_i and the magnetic field for the terminator plane are shown in fig. 4.2. In all vector plots, the color scale denotes the field strength, whereas the arrows indicate the projections of the respective vector field on the cutting plane. The results for the polar plane are shown in fig. 4.3. Specifically, the color plots display the mean density as well as the mean velocity of both the (N^+/H^+) plasma and the ionospheric plasma in the vicinity of the obstacle. Besides, the magnetic and electric field configurations are shown. In an analogous manner, the simulation results for the equatorial plane are shown in fig. 4.4.

Due to the supermagnetosonic speed of the impinging plasma flow, a bow shock is formed in front of the obstacle. As can be seen from fig. 4.2, in the terminator plane, the bow shock does not possess a spherical, but an elliptical shape. This asymmetry emerges from the anisotropic propagation velocity of the involved wave mode: The phase speed of the fast magnetosonic mode depends on the angle between the directions of wave propagation and the magnetic field vector. Furthermore, as can be seen from fig. 4.4, the structure of the bow shock is asymmetric with respect to the polar plane. This asymmetry results from a reduction of the downstream fast mode velocity due to the incorporation of the escaping ionospheric ions into the plasma flow (mass loading).

As can be seen from fig. 4.3(c), the magnetic field exhibits a strong draping pattern. An extended magnetic pile-up region is formed at the dayside of the obstacle, whereas the draping results in the formation of two magnetic lobes in the downstream region. Between these lobes, the magnetic field strength lies significantly below the upstream value. A wake region denoting

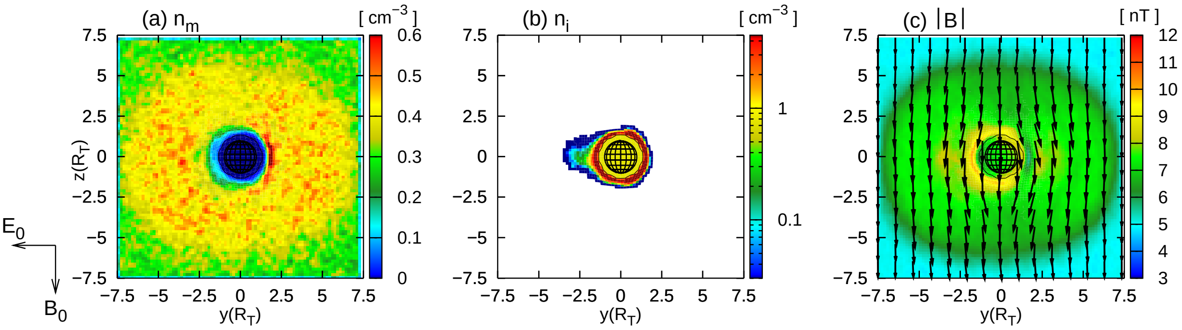

Figure 4.2: Interaction of Titan's ionosphere with a supermagnetosonic plasma flow – Results of a 3D hybrid simulation. The figure displays the simulation results for a cut through the (y, z) plane of the simulation domain, coinciding with the terminator plane of the obstacle. The undisturbed plasma velocity $\underline{u}_0$ points in positive x direction, i.e. out of the paper plane. The undisturbed magnetic field $\underline{B}_0$ is oriented in negative z direction. The figure shows (a) the mean (N^+/H^+) plasma density, (b) the ionospheric plasma density and (c) the magnetic field. The color scale denotes the field strength, whereas the arrows indicate the projection of the magnetic field vectors on the cutting plane. Due to the upstream plasma flow being supermagnetosonic, a bow shock arises in front of the obstacle. Since the phase velocity of the fast magnetosonic mode is not isotropic, but it depends on the angle between wave propagation and the magnetic field, the shock structure in the terminator plane is not circular. The elliptic structure of the bow shock is clearly identifiable in the magnetic field signature (cf. fig. (c)).
Mach numbers of the upstream plasma flow: $M_A = 1.87$ (alfvénic), $M_S = 2.90$ (sonic) and $M_{MS} = 1.60$ (magnetosonic).

a strongly reduced (N^+/H^+) density is formed downstream of the obstacle. As can be seen from fig. 4.3, the (N^+/H^+) plasma and the ionospheric plasma scarcely mix. In the wakeside vicinity of Titan, the (N^+/H^+) density is high in regions where the density of ionospheric ions is low and vice versa. The boundary layer between both plasma species is often called the *Ion Composition Boundary* (ICB). A similar separation of both plasma populations has also shown to be characteristic of the interaction between the Martian ionosphere and the solar wind [27, 110].

As can clearly be seen from figs. 4.3 and 4.4, the (N^+/H^+) ion density is significantly reduced in regions where the N_2^+ ions are the predominant species. However, the structure of the interaction region is highly symmetric in the polar plane, whereas an asymmetry with respect to the direction of the undisturbed convective electric field $\underline{E}_0 = -\underline{u}_0 \times \underline{B}_0$ occurs in the equatorial plane. In the following, the hemisphere where $\underline{E}_0$ points towards Titan will be referred to as the E^- hemisphere. The hemisphere in which the electric field $\underline{E}_0$ is directed away from Titan will be called the E^+ hemisphere. In the situation inside the magnetosphere, as discussed in chapters 4 to 6, the E^- hemisphere always coincides with Titan's Saturn-facing hemisphere. The E^+ hemisphere contains the anti-Saturn-facing side of the satellite[2]. In the equatorial plane, a sharp boundary layer between the ionospheric ion tail and the (N^+/H^+) plasma manifests in the E^- hemisphere. Besides, the N_2^+ tail does not expand significantly into this hemisphere. As displayed in fig. 4.4(d), the (N^+/H^+) plasma in the E^-

---

[2] In consistency with most publications, the $(y > 0)$ and the $(y < 0)$ *half space of the coordinate frame* are also referred to as the E^- and the E^+ *hemisphere of Titan*. Of course, this sloppy terminology is not completely correct.

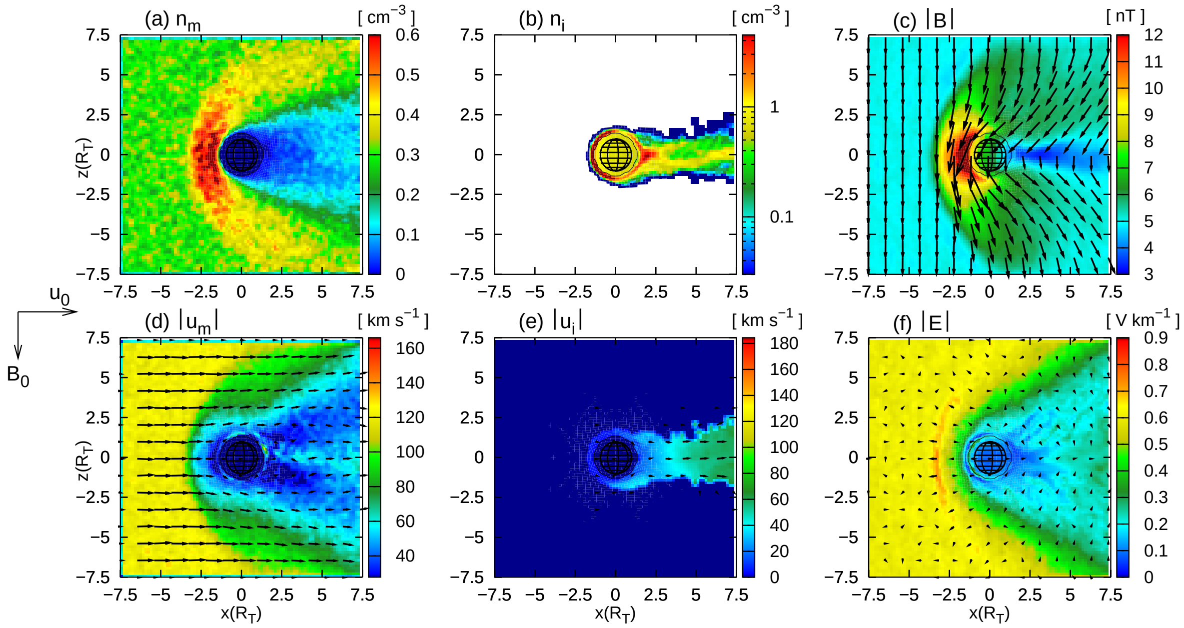

Figure 4.3: Interaction of Titan's ionosphere with a supermagnetosonic plasma flow – Cut through the (x, z) plane of the simulation box which coincides with Titan's polar plane. The undisturbed plasma velocity vector $\underline{u}_0$ is parallel to the positive x axis, while the background magnetic field $\underline{B}_0$ points in $(-z)$ direction. The figure shows (a) the mean (N^+/H^+) plasma density, (b) the ionospheric plasma density, (c) the magnetic field, (d) the mean (N^+/H^+) velocity, (e) the mean ionospheric ion velocity and (f) the electric field in the cutting plane. The magnetic field clearly drapes around the obstacle. On the one hand, this process results in the formation of an extended magnetic pile-up region at Titan's dayside; on the other hand, two pronounced magnetic lobes are formed in the downstream region. As displayed in the density plots, the (N^+/H^+) plasma and the ionospheric ion population scarcely mix in the tail region. The separating boundary is called Ion Composition Boundary. In the tail region, the ionospheric ions become the predominant species. Due to the deceleration of the (N^+/H^+) ions in the shock front and the small velocity of the ionospheric ions in the wake, an extended region of reduced (convective) electric field strength is formed downstream of the obstacle. In general, the structure of the interaction region is symmetric in the polar plane, whereas a strong asymmetry with respect to the direction of the convective electric field occurs in the equatorial plane of the obstacle.
Mach numbers of the upstream plasma flow: $M_A = 1.87$ (alfvénic), $M_S = 2.90$ (sonic) and $M_{MS} = 1.60$ (magnetosonic).

hemisphere flows almost tangential to the boundary layer between both populations. On the other hand, in the E^+ hemisphere, the ionospheric ion tail possesses a diameter of about five Titan radii. Furthermore, the boundary between both plasma populations is less pronounced in this hemisphere. The ionospheric density decreases in a slight way in regions where the (N^+/H^+) ions become predominant and their density similarly increases in a slight manner.

As will be discussed in the following, the convective electric field $\underline{E}_c = -\underline{u} \times \underline{B}$ is a major factor for this asymmetry to arise. In the tail region, the electric field has clearly diminished, compared to the background field in the undisturbed, homogeneous plasma outside the interaction region. As can be seen in figs. 4.3(f) and 4.4(f), the region characterized by a reduced electric field strength is symmetric in the polar plane, whereas an asymmetry occurs in the

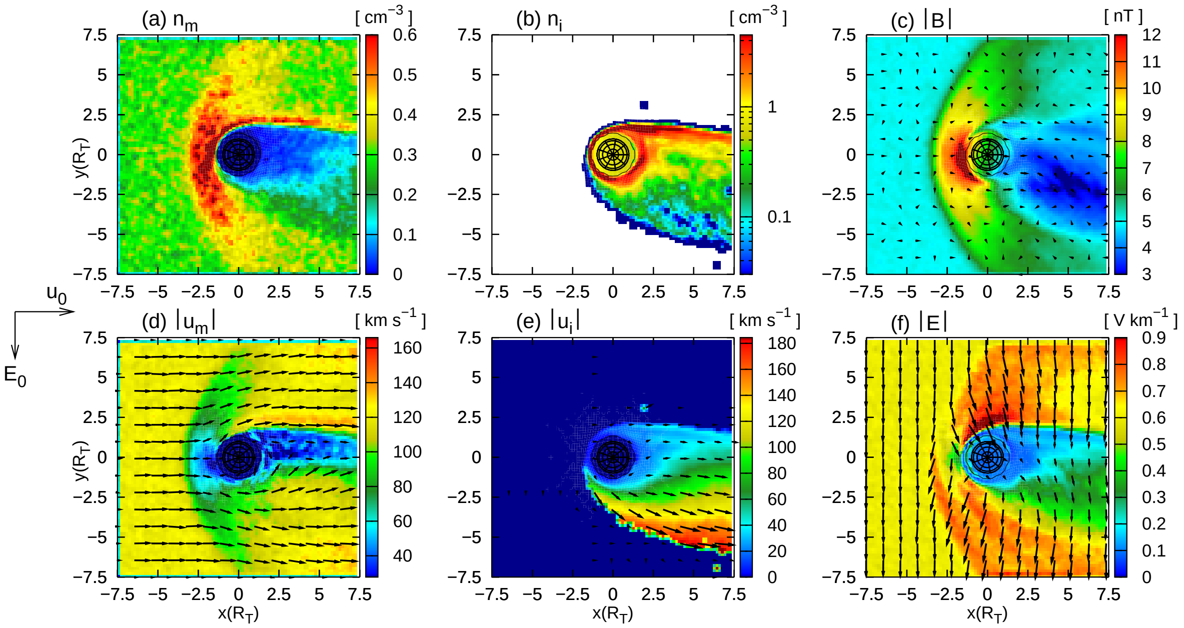

Figure 4.4: Interaction of Titan's ionosphere with a supermagnetosonic plasma flow – Cut through the (x, y) plane of the simulation box which coincides with Titan's equatorial plane. The undisturbed plasma flow is directed in $(+x)$ direction, whereas the background convective electric field $\underline{E}_0$ is antiparallel to the y axis. The figure shows (a) the mean (N^+/H^+) plasma density, (b) the ionospheric plasma density, (c) the magnetic field, (d) the mean (N^+/H^+) velocity, (e) the mean ionospheric ion velocity and (f) the electric field in the cutting plane. The simulation results exhibit an asymmetry between both hemispheres. The ionospheric tail and thus, the region of reduced electric field strength, cover a large area in the E^+ hemisphere, while they are prevented from gaining access to the E^- hemisphere by a sharply pronounced boundary layer. In the E^+ hemisphere, an extended pick-up region is formed where ionospheric ions are incorporated into the ambient plasma flow. Since their velocity is comparable to the ambient plasma velocity, the pick-up ions make a significant contribution to the convective electric field. In the E^- hemisphere, the convective electric field points into the ionospheric tail, preventing these ions from crossing the ICB from inward to outward and from mixing with the ambient (N^+/H^+) plasma. In this half space, the sharp decrease of ionospheric ion density at the ICB gives rise to a strong electron pressure gradient, pointing into the tail region. Hence, the ambient plasma is forbidden to cross the ICB from outward to inward by the electric field arising from the negative electron pressure gradient. As can be seen from fig. (d), the (N^+/H^+) plasma flow in the E^- hemisphere is almost tangential to the boundary layer. In contrast to the situation in the E^- hemisphere, the convective electric field points away from the ionospheric tail in the E^+ hemisphere. Hence, the focusing effect that is responsible for the sharp separation of both plasma populations in the E^- hemisphere does not occur and the boundary layer cannot be formed. The electric force acting on the ionospheric ions makes them mix with the ambient plasma flow. They are being picked up and begin to perform a cycloidal motion in $(+x)$ direction. Both the convective electric field and the field resulting from the electron pressure gradient are essential for the occurrence of asymmetries in the structure of the ICB.
Mach numbers of the upstream plasma flow: $M_A = 1.87$ (alfvénic), $M_S = 2.90$ (sonic) and $M_{MS} = 1.60$ (magnetosonic).

equatorial plane. These structures result primarily from the convective electric field term which can be written as

$$\underline{E}_c = -\left\{ \frac{n_m}{n_m + n_i} \underline{u}_m + \frac{n_i}{n_m + n_i} \underline{u}_i \right\} \times \underline{B} \quad . \tag{4.3}$$

In the polar plane, only a small fraction of the (N^+/H^+) ions are able to gain access to the central wake region downstream of Titan. Besides, these ions have undergone a strong deceleration in the shock front. The convective electric field directly behind Titan is therefore mainly governed by the motion of the predominant ionospheric ions. The almost complete lack of (N^+/H^+) ions and the small velocity of the ionospheric particles lead to the formation of a cavity in the electric field strength downstream of Titan (cf. figs. 4.3(a), (e) and (f)). A similar process occurs in the equatorial plane. However, in this plane, an extended pick-up region where ionospheric ions are incorporated into the ambient plasma flow arises in the E^+ hemisphere. In this area, the pick-up ion velocity becomes comparable to the ambient plasma velocity and hence, the accelerated pick-up ions are able to make a significant contribution to the convective electric field. For this reason, a strong reduction of electric field strength occurs only in the immediate vicinity of the E^- hemisphere's Ion Composition Boundary where the pick-up ion velocity is negligible. In contrast to this, the slight decrease of (N^+/H^+) density in the E^+ hemisphere is compensated by the presence of fast pick-up ions.

In order to understand the occurrence of the asymmetric structures in the equatorial plane, the electric field signatures in the vicinity of the Ion Composition Boundary, i.e. near the outer flanks of the ionospheric tail, are of major importance. In the E^- hemisphere, the convective electric field in the adjacent (N^+/H^+) flow is directed perpendicular to the ICB, pointing inside the tail. Hence, the ionospheric ions are forbidden to cross the ICB from inward to outward. This results in the formation of a sharp boundary layer, denoting a strong density jump at the flank of the tail. The resulting ionospheric electron pressure gradient is directed into the tail. Hence, the ambient (N^+/H^+) plasma is forbidden to cross the ICB from outward to inward by the electric field that emerges from the $-\nabla P_e$ term. A more extensive discussion of this mechanism is given by Simon *et al.* [139] who analyze the Lorentz forces acting on individual ions in detail. A quite different situation occurs in the E^+ hemisphere. Again, the convective electric field is directed perpendicular to the flank of the ionospheric tail, but in this half space, it points away from Titan. Thus, the N_2^+ ions are dragged away from the ionosphere and are picked up by the ambient (N^+/H^+) plasma. They can mix with the surrounding flow and form a cycloidal tail. This is the major reason for the ICB not to be sharply developed in the E^+ hemisphere. To sum up the major result, the convective electric field as well as the $-\nabla P_e$ term have to be considered essential for the ICB to be formed.

It should be noted that the Hall term in the electric field equation,

$$\underline{E}_H \equiv \frac{(\nabla \times \underline{B}) \times \underline{B}}{\mu_0 e \left(n_m + n_i\right)} \quad , \tag{4.4}$$

is only of minor importance for the discussion of the asymmetries occurring in Titan's equatorial plane. As discussed in section 4 of chapter 3, this contribution to the electric field arises mainly from the magnetic pressure gradient and the magnetic tension of the curved field lines. The influence of this term does not only manifest in an electric field acting on the ions, but it also yields a force on the magnetic field lines themselves. The magnetic pressure gradient plays a major role for particle dynamics in the magnetic pile-up region at Titan's ramside. The magnetic tension becomes important near the poles of the satellite, where the highly curved field lines can unwind. As discussed by Bößwetter *et al.* [26, 27], in the case of Mars, the resulting tension force yields a strong acceleration of the cold ionospheric plasma near the obstacle. However, for an analysis of the asymmetric tail structure in Titan's equatorial plane, forces on the particles that emerge from the Hall term $\underline{E}_H$ can safely be neglected. First of all, the asymmetries arise in the wake region of a plane that cuts through the neutral region between the two lobes. Thus, the magnetic pressure gradient in the wake should be directed almost perpendicular to the cutting plane. The only region in the equatorial plane where particle acceleration due to magnetic pressure forces may become important is the ramside magnetic pile-up region. The effects occurring in this region should have no influence on the large-scale characteristics of the wake structure. The magnetic tension term does not only depend on the curvature of the field lines, but also on the magnetic field magnitude itself. Therefore, the strongest tension forces arise at Titan's ramside. The contribution of the magnetic tension to $\underline{E}_H$ may not take significant influence on particle dynamics in the equatorial wake region either. This is consistent with the analysis of cometary plasma environments conducted by Bagdonat [7]. By comparing the results of a two-dimensional simulation approach – that completely neglects the finite curvature of the magnetic field lines – to the results of a more sophisticated three-dimensional model, the author demonstrates that the tail structure in the $(\underline{u}_0, \underline{E}_0)$ plane is nearly the same in both geometries. In general, $\underline{E}_H \propto (n_m + n_i)^{-1}$ should nearly vanish in regions of high ionospheric plasma density, such as the central wake directly behind the obstacle.

Finally, the results shall be compared to another hybrid simulation study carried out by Kallio *et al.* [74]. The authors have used a three-dimensional hybrid code to examine the interaction of Titan's ionosphere with a super-alfvénic, supersonic and supermagnetosonic plasma flow. However, this model neglects the electron pressure term in the generalized form of Ohm's law and consequently, the electron temperature is set to zero. Nevertheless, the results of this study are at least in qualitative agreement with the simulation presented above. The formation of a bow shock as well as a magnetic pile-up region in front of the obstacle and an induced magnetotail at the wakeside are reproduced by both simulation codes. Moreover, Kallio *et al.* [74] also demonstrate that the density of the ambient plasma is low in the center of the tail where the ionospheric ions become predominant. Besides, the simulation model developed by Kallio *et al.* [74] shows at least slight asymmetries in the density of the escaping ions.

3 Titan in submagnetosonic flow at 18:00 local time

The simulation results for a submagnetosonic upstream plasma flow are displayed in figs. 4.5, 4.6 and 4.7, respectively. The magnetic field strength as well as the mean magnetospheric and ionospheric plasma densities in the terminator plane are shown in fig. 4.5. The characteristic plasma and field parameters for the polar plane are displayed in fig. 4.6, whereas fig. 4.7 shows the simulation's quasi-stationary state for Titan's equatorial plane. In accordance with the results for a supermagnetosonic upstream flow, the structure of the interaction region

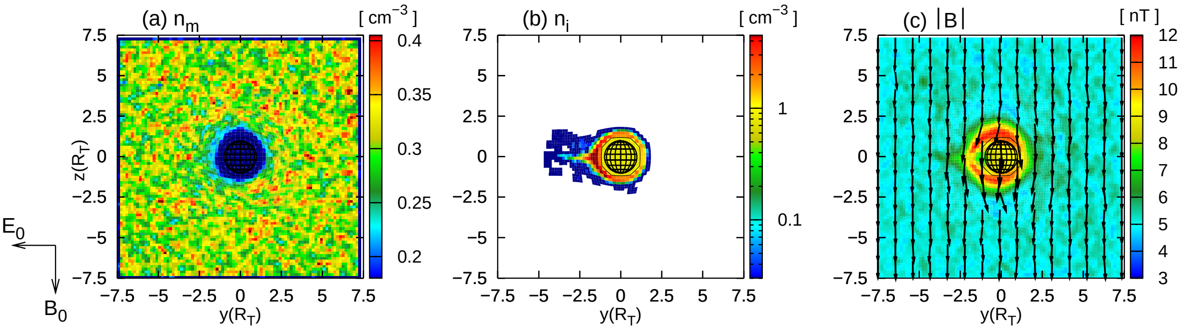

Figure 4.5: Interaction of Titan's ionosphere with the submagnetosonic Saturnian magnetospheric plasma at 18:00 local time. The figure displays the results for a cut through the (y, z) plane of the simulation box which coincides with Titan's terminator plane. The undisturbed magnetospheric plasma flow is directed in $(+x)$ direction, i.e. out of the paper plane. The background magnetic field $\underline{B}_0$ is oriented antiparallel to the z axis and thus, the convective electric field $\underline{E}_0$ points in $(-y)$ direction. The figure displays (a) the magnetospheric ion density n_m, (b) the ionospheric ion density n_i and (c) the magnetic field. Again, the arrows denote the projection of the field vectors in the cutting plane. Since the upstream plasma flow is submagnetosonic, no bow shock is formed in front of the obstacle. Like in the case of a supermagnetosonic flow, the obstacle's ionospheric tail is more extended in the E^+ hemisphere than in the E^- hemisphere. Due to Saturn's intrinsic magnetic field being draped around the obstacle, a magnetic pile-up region which is characterized by an increased field strength arises in the immediate vicinity of Titan.
Mach numbers of the upstream plasma flow: $M_A = 1.87$ (alfvénic), $M_S = 0.57$ (sonic) and $M_{MS} = 0.55$ (magnetosonic). The upstream flow parameters have been chosen in agreement with Voyager 1 data.

is symmetric in the polar plane. In both the submagnetosonic and the supermagnetosonic scenario, asymmetries between the E^- and the E^+ hemisphere occur in Titan's equatorial plane (cf. figs. 4.5 and 4.7).

Because the upstream plasma flow is submagnetosonic, no bow shock is formed in front of the obstacle. Saturn's intrinsic magnetic field clearly drapes around the obstacle, resulting in the formation of two pronounced magnetic lobes in the wake region and a magnetic pile-up region at Titan's dayside, denoting an increased field strength. The pile-up is clearly shifted in E^+ direction. Between the two lobes, a central field reversal region of reduced field magnitude is formed. The magnetotail possesses a spatial extension of about $3R_T$ in $\pm z$ direction and still affects the magnetic field structure at a distance of $7R_T$ to the $(z = 0)$ line (cf. fig. 4.6(c)). Thus, even when the upstream flow is submagnetosonic, the presence of Titan has a noticeable influence on the ambient plasma. However, in contrast to the case of a supermagnetosonic plasma flow, only a slight decrease of the (N^+/H^+) plasma density and velocity occur in the downstream region. Besides, the interaction region is no longer characterized by a clear separation of the magnetospheric (N^+/H^+) and the ionospheric N_2^+ plasma component. The interaction region does not exhibit a pronounced outer boundary.

Only a slight reduction of the electric field strength manifests in the tail region. On the one hand, the decrease of E is not as strong as in the case of a supermagnetosonic flow because the (N^+/H^+) density downstream of the obstacle does no longer vanish and hence, these ions can make a significant contribution to the convective electric field. On the other hand,

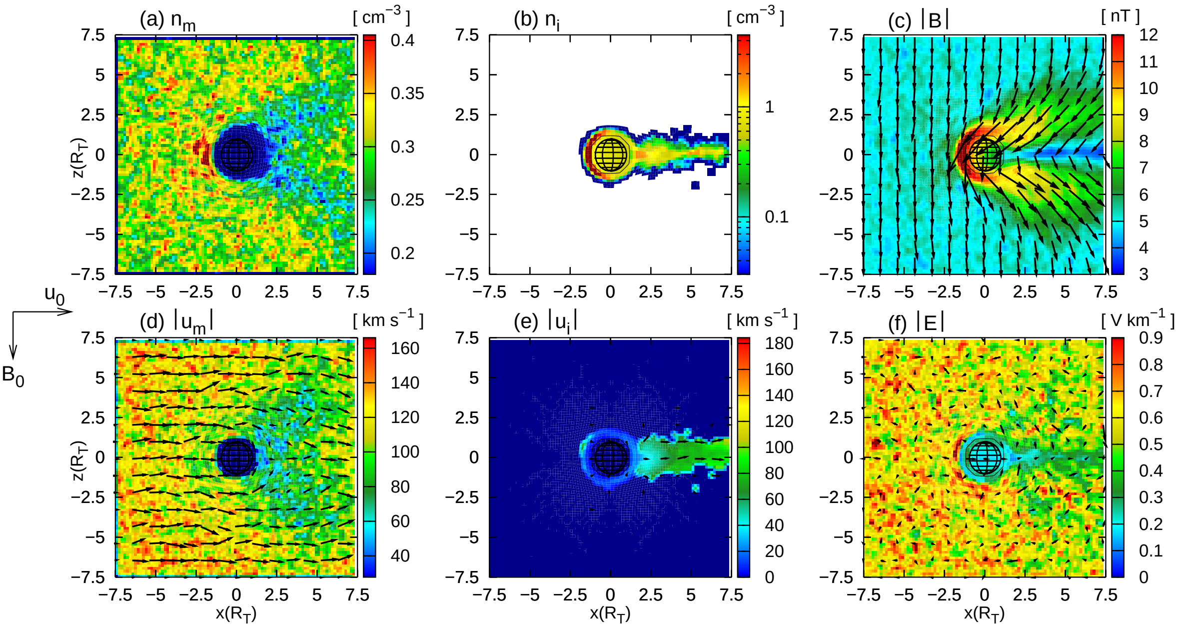

Figure 4.6: Interaction of Titan's ionosphere with the submagnetosonic Saturnian magnetospheric plasma at 18:00 local time. The figure shows a cut through the (x, z) plane which coincides with Titan's polar plane. The undisturbed plasma velocity points in $(+x)$ direction; the background magnetic field is antiparallel to the z axis. The figure displays (a) the magnetospheric ion density, (b) the heavy ion density, (c) the magnetic field, (d) the magnetospheric ion velocity, (e) the ionospheric ion velocity and (f) the electric field. In the polar plane, the interaction region features a symmetric structure. Like in the case of a supermagnetosonic plasma flow, the magnetic field exhibits a strong draping pattern, giving rise to a magnetic pile-up region at Titan's dayside and two magnetic lobes in the wake region. The region between these lobes is characterized by a significant decrease of magnetic field strength. In contrast to the results for supermagnetosonic upstream conditions, the magnetospheric plasma is no longer separated from the ionospheric tail by an Ion Composition Boundary. Because both plasma components contribute to the convective electric field, only a slight reduction of electric field strength occurs in the downstream region.
Mach numbers of the upstream plasma flow: $M_A = 1.87$ (alfvénic), $M_S = 0.57$ (sonic) and $M_{MS} = 0.55$ (magnetosonic). The upstream flow parameters have been chosen in agreement with Voyager 1 data.

an extended pick-up region arises in the E^+ hemisphere of the equatorial plane, as shown in figs. 4.7(b) and (e). In this area, the ionospheric ions are accelerated in the direction of $\underline{E} \times \underline{B}$, their velocity even exceeding that of the magnetospheric plasma. Because of the resulting contribution to the convective electric field, only a minor decrease of E occurs in the E^+ hemisphere. By comparing the structure of the ionospheric tail in fig. 4.7(e) with the shape of the area denoting a reduced electric field strength in fig. 4.7(f), it can clearly be seen that the reduction of electric field strength diminishes in exactly those regions where the N_2^+ velocity increases due to the pick-up process. In contrast to this, only an insignificant acceleration of the ionospheric ions occurs directly behind Titan. The decrease of electric field strength manifesting in the polar plane has to be explained in an analogous manner since the N_2^+ ions directly behind the obstacle are practically not accelerated. In the polar plane, the N_2^+ ions form a narrow tail whose diameter is of the order of only two Titan radii, as can be

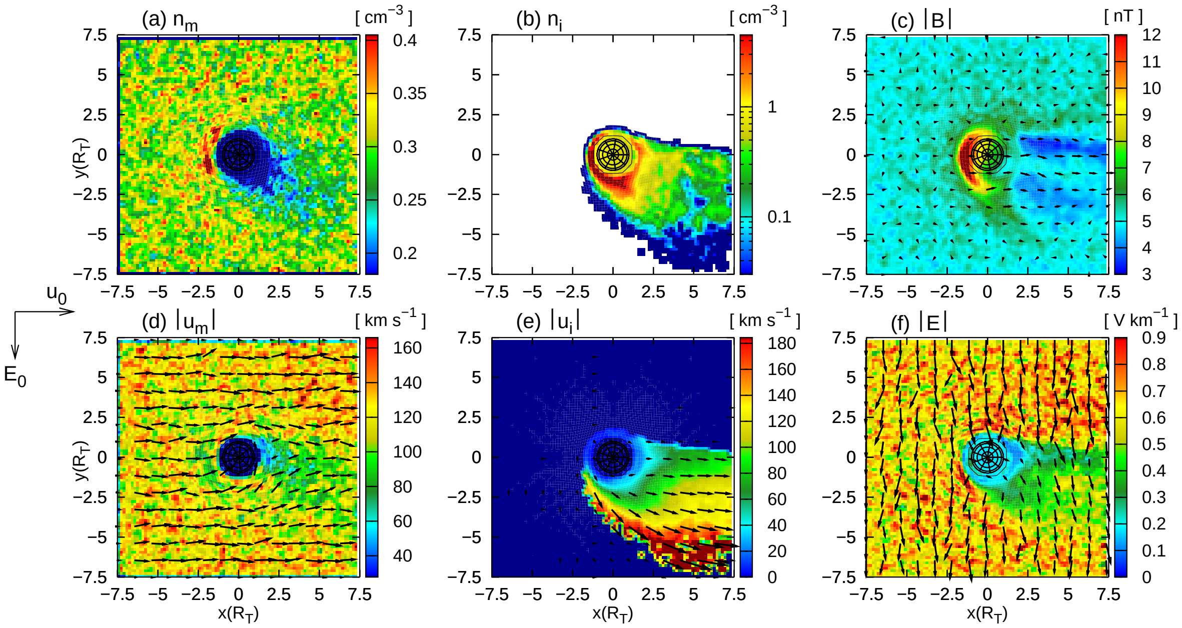

Figure 4.7: Interaction between Titan's ionosphere and the submagnetosonic Saturnian magnetospheric plasma flow at 18:00 local time. The figure displays a cut through Titan's equatorial plane. The undisturbed plasma flow is directed in $(+x)$ direction, whereas the convective electric field $\underline{E}_0$ is oriented antiparallel to the y axis. In analogy to the case of a supermagnetosonic flow, the structure of the interaction region exhibits a strong asymmetry between both hemispheres. The convective electric field in the adjacent magnetospheric plasma forbids the ionospheric tail to expand into the E^- hemisphere. On the other hand, the electric force drags the ions away from the obstacle in the E^+ hemisphere, resulting in the formation of an extended pick-up region. However, in the E^- hemisphere, the decrease of ionospheric density at the outer flank of the tail is not as sharp as in the case of supermagnetosonic flow. Due to the resulting electron pressure gradient being significantly weaker than in the supermagnetosonic scenario, the magnetospheric ions are no longer prevented from entering the tail region and from mixing with the ionospheric plasma. For this reason, only a slight, but still asymmetric, decrease of magnetospheric plasma density occurs downstream of the obstacle. In regions where the ionospheric ion velocity is low, the electric field strength is reduced as well. However, in those regions of the E^+ hemisphere where the ionospheric ion velocity is comparable to the ambient plasma velocity or even exceeds it, these ions are able to make a significant contribution to the convective electric field. For this reason, the reduction of electric field strength diminishes in regions where the ionospheric particles are accelerated because of the pick-up process.
Mach numbers of the upstream plasma flow: $M_A = 1.87$ (alfvénic), $M_S = 0.57$ (sonic) and $M_{MS} = 0.55$ (magnetosonic). The upstream flow parameters have been chosen in agreement with Voyager 1 data.

seen in figs. 4.6(b) and (e).

Comparing the magnetic field signature in the polar plane, as displayed in fig. 4.6(c), with the ionospheric ion density signature in this plane clearly illustrates that the curved magnetic field lines in the lobes provide a force that confines the ionospheric ions to a narrow region downstream of Titan. Particle dynamics in the tail region of the polar plane can be understood as follows: Since the ionospheric ions are not only affected by the magnetic, but also by the

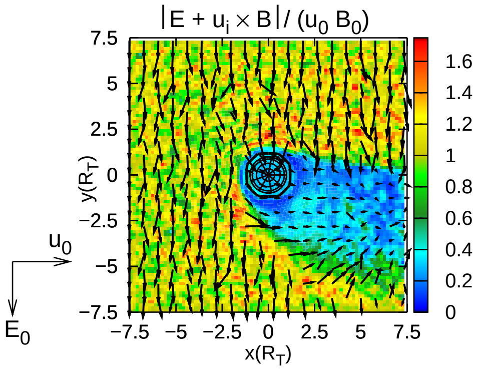

Figure 4.8: Lorentz force acting on ionospheric ions (18:00 Saturnian local time). For a cut through the equatorial plane, the figure displays the quantity $\underline{\tilde{F}}_L = \underline{E} + \underline{u}_i \times \underline{B}$ in normalized units. The normalization values are given by $u_0 = 120\,\mathrm{km/s}$ and $B_0 = 5\,\mathrm{nT}$, respectively. In regions where the ionospheric density does not vanish, this quantity represents the average Lorentz force that acts on the ionospheric ions. In regions with $n_i = 0$, the quantity displayed in the figure is identical to the electric field. Since the Lorentz force is oriented perpendicular to the Saturn-facing flank of the ionospheric tail and points inwards, it is responsible for preventing the tail from expanding into the Saturn-facing hemisphere. The figure also illustrates the acceleration of the ionospheric nitrogen ions parallel to the direction of $\underline{E} \times \underline{B} \uparrow\uparrow \underline{u}_0$ at the tail's outer flank in the E^+ hemisphere.
Mach numbers of the upstream plasma flow: $M_A = 1.87$ (alfvénic), $M_S = 0.57$ (sonic) and $M_{MS} = 0.55$ (magnetosonic). The upstream flow parameters have been chosen in agreement with Voyager 1 data.

electric field, a translation parallel to

$$\underline{\xi} = \underline{E} \times \underline{B} \tag{4.5}$$

is superimposed on their gyration around the magnetic field lines. For simplicity, the following discussion assumes the electromagnetic fields inside the neutral region to be spatially constant. Spatial field variations inside the lobes are neglected as well. On the one hand, in the neutral region between the two lobes (cf. fig. 4.6(c)), the magnetic field strength is about a factor of $1.5 - 2$ smaller than the background value of $B_0 = 5\,\mathrm{nT}$. On the other hand, in this region, the major component of the magnetic field is directed antiparallel to the z axis. The weakened electric field in this region is directed in $(-y)$ direction, i.e. perpendicular to the polar plane. Hence, exactly in the neutral region, the vector $\underline{\xi}$, which denotes the direction of the superimposed translation, can be written as

$$\underline{\xi} \propto \left(-\underline{e}_y\right) \times \left(-\underline{e}_z\right) = \underline{e}_x \quad . \tag{4.6}$$

In this expression, $\underline{e}_x$, $\underline{e}_y$ and $\underline{e}_z$ represent the unit vectors of the Cartesian coordinate system. Thus, in the neutral region between the two lobes, the newly generated ionospheric particles experience a force that draws them in $(+x)$ direction, i.e. away from the obstacle. Due to the reduced magnetic field strength between the two lobes, the acceleration of these ions is not as strong as in the anti-Saturn-facing pick-up region of the equatorial plane.

Now consider an ionospheric ion that is injected into the northern magnetic lobe, i.e. into the lobe that is located in the $(z > 0)$ hemisphere. Due to the curvature of the fields lines, the magnetic field vector in this region possesses a strong component in $(-x)$ direction. As the electric field is again perpendicular to the cutting plane, the direction of the vector $\underline{\xi}$ is approximatively given by

$$\underline{\xi} \propto \left(-\underline{e}_y\right) \times \left(-\underline{e}_x\right) = -\underline{e}_z \quad . \tag{4.7}$$

Because the translation vector points in $(-z)$ direction, the ionospheric ion is accelerated "downwards". In strong analogy, in the southern magnetic lobe, the predominant magnetic field component points in $(+x)$ direction, yielding

$$\underline{\xi} \propto \left(-\underline{e}_y\right) \times \left(+\underline{e}_x\right) = \underline{e}_z \quad . \tag{4.8}$$

Thus, the same deflection mechanism as in the northern hemisphere prevents the ionospheric tail from expanding into the region below Titan. Of course, this rather rough interpretation includes no information about the *transition* from the (spatially homogeneous) lobes to the neutral region.

To sum up, the highly draped magnetic field lines in the lobes exert some kind of *focusing effect* on the newly generated ionospheric ions in the polar plane. Due to the magnetic field enhancement in the lobes, this effect is significantly more prominent than the transport of the ionospheric particles away from Titan in the magnetic neutral region. Although the neutral region is the only area in the wake where $\underline{\xi}$ is mainly directed parallel to the $(+x)$ axis, the field magnitude in this region is too weak to provide an appreciable pick-up force. This is the reason why the ionospheric ion velocity in the polar plane cannot match the peak velocity value achieved in the E^+ pick-up region of the equatorial plane (cf. figs. 4.6(e) and 4.7(e)). The strong dependence of the ionospheric tail diameter in the polar plane on the magnetic field configuration in the lobes will again become of interest in section 3 of chapter 5, referring to the situation at 00:00 Saturnian local time.

The mechanism giving rise to the asymmetric structure of the interaction region in the equatorial plane can be explained in analogy to the previous discussion of the supermagnetosonic scenario. Again, the convective electric field at the outer flanks of the ionospheric tail has to be considered of major importance. On the one hand, in the E^- hemisphere, this field is directed perpendicular to the ionospheric tail, pointing inwards. In exactly the same manner as in the case of a supermagnetosonic upstream flow, the focusing effect arising from the electric force on the ions forbids the ionospheric N_2^+ tail to expand into the E^- hemisphere. On the other hand, the convective electric field in the E^+ hemisphere points away from the ionosphere and thus, it drags the ionospheric ions away from the obstacle. These ions are incorporated into the magnetospheric plasma flow, resulting in the formation of an extended pick-up region in the E^+ hemisphere.

The crucial question is why both plasma components are no longer clearly separated from each other. As discussed in the previous section, the electric force emerging from the negative electron pressure gradient is most important for the formation of a sharply pronounced Ion Composition Boundary in the E^- hemisphere. Due to a sharp decrease of ionospheric ion density near the outer flank of the tail in the E^- hemisphere, the resulting force is capable of preventing the ambient (N^+/H^+) plasma from entering the ionospheric tail in the case of a supermagnetosonic flow. However, the ionospheric density in the E^- hemisphere decreases only in a slight manner when the upstream flow is submagnetosonic (cf. fig. 4.7(b)). Hence, the resulting electron pressure gradient at the outer flank of the tail is significantly weaker than in the supersonic simulation and can no longer forbid the magnetospheric plasma to cross the outer boundary of the ionospheric tail from outward to inward. Nevertheless, as can be seen from fig. 4.7(a), at least a slight – but still asymmetric – decrease of magnetospheric plasma density occurs in the equatorial plane. This structure indicates that the electron pressure gradient at the outer flank of the ionospheric tail in the E^- hemisphere still affects the magnetospheric ions, preventing at least some of them from entering the ionospheric tail region. In general, the effect that leads to the asymmetries in the equatorial plane seems to be the same inside and outside the magnetosphere. However, the resulting boundaries are extremely sharp in the supermagnetosonic case. In contrast to this, no significant separation of magnetospheric and ionospheric plasma – and consequently no Ion Composition Boundary – is formed when the plasma flow is submagnetosonic. In any case, as the plasma flow achieves a submagnetosonic speed behind a bow shock, a qualitative resemblance of the interaction mechanisms in the two scenarios is absolutely expectable.

The asymmetric tail structure is also illustrated in fig. 4.8, displaying the Lorentz force that acts on ions of ionospheric origin. To be more specific, the figure shows the *average Lorentz force* $\underline{\tilde{F}}_L$, which can be calculated form the simulation data by means of

$$\underline{\tilde{F}}_L = m_i \left(\underline{E} + \underline{u}_i \times \underline{B} \right) \quad . \tag{4.9}$$

In this expression, m_i is the ionospheric ion mass (i.e. the mass of molecular nitrogen), whereas $\underline{u}_i$ represents the mean ionospheric plasma velocity at a certain position. Thus, for an ionospheric ion whose individual velocity $\underline{v}_i$ exactly matches the mean flow speed $\underline{u}_i$, the quantity $\underline{\tilde{F}}_L$ is identical to the Lorentz force $\underline{F}_L$ experienced by the ion,

$$\underline{\tilde{F}}_L \approx m_i \left(\underline{E} + \underline{v}_i \times \underline{B} \right) = \underline{F}_L \quad . \tag{4.10}$$

Even though for most of the particles, the individual velocity differs more or less from $\underline{u}_i$, the quantity $\underline{\tilde{F}}_L$ allows at least a rough illustration of how ionospheric ion dynamics are affected by the electromagnetic fields. Of course, the interpretation is also supported by the vanishing initial thermal velocity of the newly generated ionospheric plasma. For the plot shown in fig. 4.8, the unimportant factor m_i in eq. (4.9) has been omitted. At the ionospheric tail's outer flank in the E^- hemisphere, the force is directed inwards and thus, it forbids the tail to expand into the E^- hemisphere. On the other hand, in the outer regions of the tail in the E^+ hemisphere, the Lorentz force possesses a strong component parallel to the $(+x)$ axis, illustrating the pick-up force acting in the direction of $\underline{E} \times \underline{B}$. Inside the tail region itself, where particles of ionospheric origin become the predominant species, the Lorentz force almost vanishes due to both the mean ion velocity and the electric field strength being significantly smaller than the undisturbed upstream values. This phenomenon will play a decisive role for the results of the multi-species ionosphere model presented in chapter 6.

In agreement with the results presented above, the hybrid simulations carried out by Brecht *et al.* [30] indicate the structure of the interaction region to be asymmetric with respect to the direction of the electric field. On the one hand, this study confirmed that the global picture of the interaction region resembles the results obtained from MHD simulations (cf. [39, 87, 115]). On the other hand, the magnetic pile-up region has shown to be more prominent in the direction of the convective electric field. Brecht *et al.* [30] also demonstrate that the ionospheric tail region is not aligned with the undisturbed plasma flow, but it is offset towards the E^+ hemisphere of Titan. The hybrid simulation results presented by Kallio *et al.* [74] also imply that the tail structure in the equatorial plane is not symmetric.

The simulation results presented in this section are also in qualitative agreement with Cassini measurements of cold plasma in the vicinity of Titan, as discussed by Wahlund *et al.* [151]. During the Voyager 1 encounter as well as during Cassini's TB passage through Titan's wake on 13 December 2004, a large asymmetry in the structure of the mass-loading region has been detected (see also Gurnett *et al.* [57]). In the E^+ hemisphere, plasma of ionospheric origin has been detected as far as $9R_T$ away from Titan. The data obtained during these flybys also confirm the existence of an extended pick-up region in the E^+ hemisphere, as it is proposed by the theoretical models. In contrast to this, the outer boundary of the tail region in the E^- hemisphere has shown to be located much closer to Titan than the tail's outer flank in the E^+ hemisphere. Nevertheless, the data collected during the first Cassini flyby (TA) on 26 October 2004 revealed no large asymmetry in the structure of the mass-loading region [151]. Based on the simulation results discussed above, the lack of an asymmetry in Titan's equatorial tail structure cannot be explained. A possible interpretation can be provided by the incorporation of a multi-species ionosphere into the model. Further details shall be discussed in chapter 6.

4 Transition from supermagnetosonic to submagnetosonic flow

In the preceding sections, two different scenarios have been analyzed. On the one hand, the case of Titan being located outside of Saturn's magnetosphere in times of high solar wind dynamic pressure has been considered. In this situation, the alfvénic as well as the sonic and the magnetosonic Mach number of the upstream plasma are larger than 1. As discussed above, the interaction gives rise to a pronounced shock front at Titan's dayside and a prominent boundary layer, separating the ionospheric ion population from the ambient plasma. In general, this situation is characterized by a set of sharply pronounced plasma boundaries that manifest in the vicinity of the obstacle. On the other hand, the case of Titan being located in the outer regions of Saturn's magnetosphere has been analyzed. In this scenario, the plasma impinging on the obstacle's ionosphere is characterized by super-alfvénic, yet subsonic and submagnetosonic Mach numbers. In contrast to the first simulation, the Ion Composition Boundary that prevented the two different plasmas from mixing, has vanished. Sharply pronounced boundary layers, i.e. a bow shock separating the upstream flow from the obstacle-dominated region or an ICB, are no longer existent.

In this section, the transition between the two described scenarios shall be investigated in more detail. For this reason, another simulation run has been conducted. In order to gain access to the transition between the supermagnetosonic and the submagnetosonic situation, the upstream plasma flow is assumed to be super-alfvénic ($M_A > 1$) and supersonic ($M_S > 1$), yet submagnetosonic ($M_{MS} < 1$). The specific values of the Mach numbers are listed in section 1. Even though this situation may not be representative of a real stationary situation in Titan's plasma environment, the results have shown to be extremely valuable for understanding the transition that the satellite's plasma environment undergoes. In the framework of a three-dimensional MHD model, an analogous situation has recently been studied by Ma *et al.* [99].

The simulation geometry is displayed in fig. 4.1, i.e. the situation refers again to the 18:00 local time. The simulation results are shown in fig. 4.9 for the polar plane and in fig. 4.10 for the equatorial plane, respectively. Figure 4.11 displays a three-dimensional illustration of the ambient plasma density that has been obtained by merging the simulation results for terminator, polar and equatorial plane. For comparison, an analogous plot is shown for the supermagnetosonic case.

Figure 4.9 displays the characteristic plasma parameters and the electromagnetic fields for a cut through the polar plane, coinciding with the (x, z) plane of the coordinate system. It should be noted that, since the magnetosonic Mach number is smaller than 1, the fast mode velocity in the plasma can become larger than the plasma flow velocity itself. As can be seen in fig. 4.9(a), the clearly developed shock front at the obstacle's dayside has vanished. Nevertheless, a diffuse region of enhanced (N^+/H^+) plasma density is still present, denoting an increase from $n_m = 0.3\,\mathrm{cm}^{-3}$ in the undisturbed flow to $n_m = 0.4\,\mathrm{cm}^{-3}$ in the near-Titan upstream region. However, this structure is not as sharply confined as in the case of Titan being located outside the magnetosphere.

Moreover, when Titan is exposed to a supermagnetosonic plasma flow, a pronounced cavity of reduced plasma velocity is formed in the satellite's wakeside hemisphere. Such a decrease is still present in the scenario under consideration, as can be seen from fig. 4.9(d). Although the plasma is still decelerated, the region of reduced u_m in the polar plane is no longer clearly

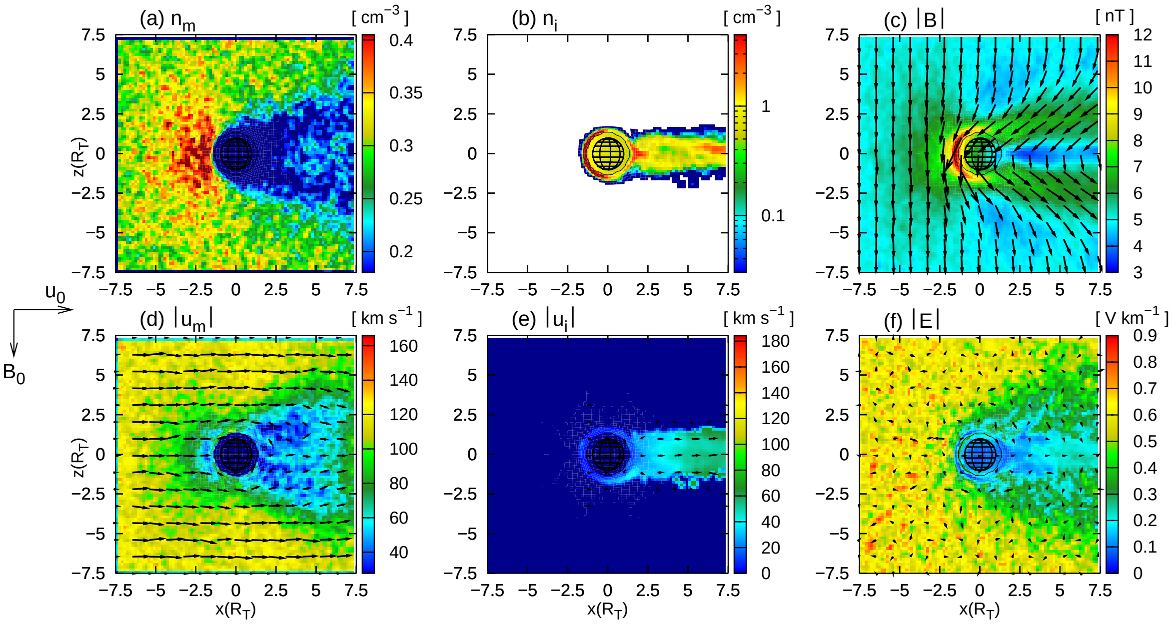

Figure 4.9: Transition from supermagnetosonic to submagnetosonic flow – Cut through the (x, z) plane of the coordinate system which coincides with Titan's polar plane. The figure displays the (N^+/H^+) plasma density and velocity (figs. (a) and (d)), the ionospheric ion density and velocity (figs. (b) and (e)) and the electromagnetic fields (figs. (c) and (f)). The figure illustrates the transition from the case of Titan being located outside the magnetosphere, where all three Mach numbers are larger than 1, to the interaction with the Saturnian magnetospheric plasma at 18:00 local time. Although magnetospheric and ionospheric plasma are no longer separated from each other, the former position of the cone-shaped Ion Composition Boundary is still identifiable. The bow shock has vanished, but nevertheless, a diffuse region of increased plasma density is still present at Titan's dayside.
Mach numbers of the upstream plasma flow: $M_A = 1.87$ (alfvénic), $M_S = 1.08$ (sonic) and $M_{MS} = 0.94$ (magnetosonic).

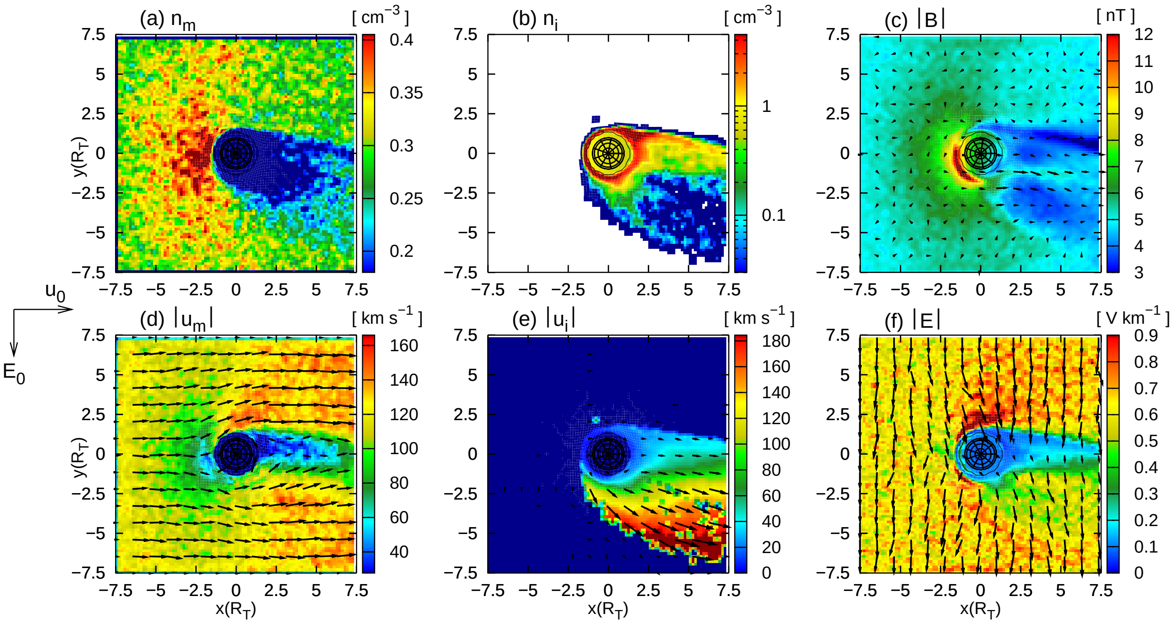

Figure 4.10: Transition from supermagnetosonic to submagnetosonic flow – Cut through Titan's equatorial plane which is parallel to the undisturbed convective electric field. The physical quantities shown in the figure are the same as in fig. 4.9. A region of increased ionospheric density can be identified near the outer flank of the tail in the E^- hemisphere. Since the steepness of the ionospheric density increase is not as pronounced as in the case of Titan being exposed to a super-alfvénic, supersonic and supermagnetosonic plasma, the sharp boundary between both plasma populations is no longer existent. However, a region of slightly reduced (N^+/H^+) plasma density is still present in the downstream region, its shape coinciding with the structure that can be seen in fig. 4.4(a).
Mach numbers of the upstream plasma flow: $M_A = 1.87$ (alfvénic), $M_S = 1.08$ (sonic) and $M_{MS} = 0.94$ (magnetosonic).

separated from the ambient plasma flow. When Titan is located outside the magnetosphere, the interaction gives rise to a cone-shaped region of reduced (N^+/H^+) density in the polar plane, its outer flanks denoting the position of the Ion Composition Boundary. This is displayed in fig. 4.3(a). An analogous cone-like structure can be identified in figs. 4.9(a) and 4.11(b) as well, even though the decrease of (N^+/H^+) density has significantly diminished. Besides, the outer regions of this structure denote no longer a sharp, but a smooth transition from the plasma inside the cone-shaped wake cavity to the ambient plasma flow. The position of the former Ion Composition Boundary is still identifiable, but the impinging plasma is no longer forbidden to cross this boundary layer and to mix with the ionospheric pick-up ions. These signatures clearly illustrate the transition to the situation inside the magnetosphere, where the boundary layer has vanished completely.

The same effect is illustrated by the magnetic field signature in the polar plane, as can be seen in fig. 4.9(c). In the case of Titan being located outside the magnetosphere, $\underline{B}$ exhibits a parabolically curved shock structure (cf. figs. 4.3(c) and 4.4(c)). When Titan is located inside the magnetosphere, the situation in the polar plane is dominated by a pronounced magnetic draping pattern, being confined to a narrow region with a diameter of $\pm 3R_T$ perpendicular to the undisturbed flow direction (cf. fig. 4.6(c)). Moreover, inside the magnetosphere,

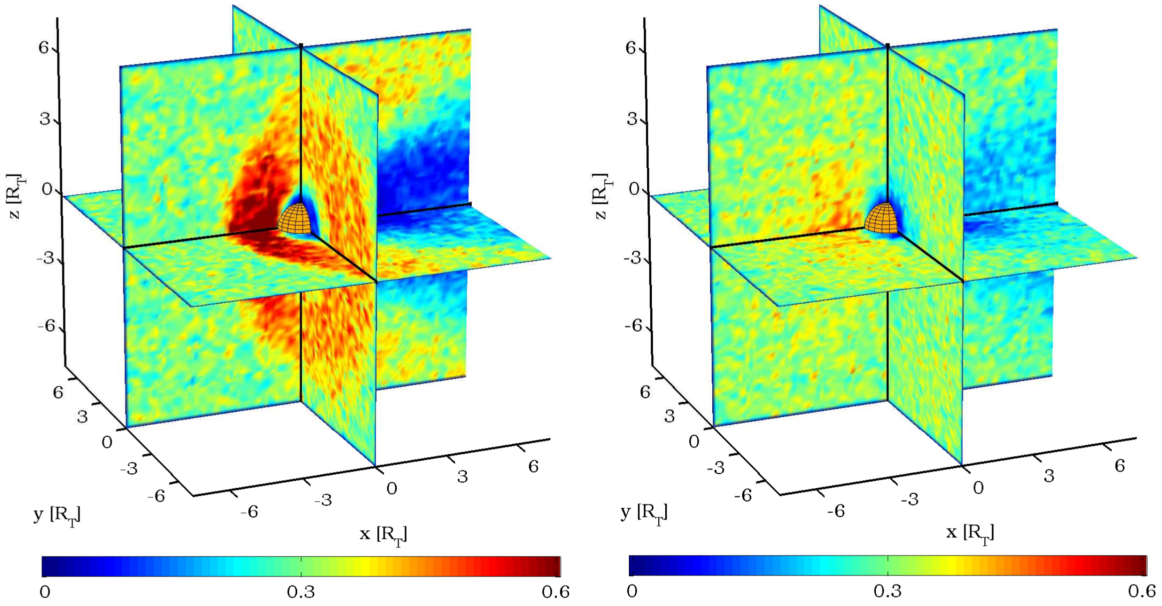

(a) Supermagnetosonic flow

(b) Submagnetosonic flow

Figure 4.11: Supermagnetosonic flow versus transition scenario. The figure displays three-dimensional illustrations of the ambient (N^+/H^+) plasma density $n_m[\mathrm{cm}^{-3}]$ in the vicinity of Titan (a) for the case of Titan being exposed to a super-alfvénic ($M_A = 1.87$), supersonic ($M_S = 2.90$) and supermagnetosonic ($M_{MS} = 1.60$) flow and (b) for the transition scenario, assuming the upstream flow to be super-alfvénic ($M_A = 1.87$), supersonic ($M_S = 1.08$) and submagnetosonic ($M_{MS} = 0.94$). Note that the color scale differs from the one used in figs. 4.9 and 4.10. In the supermagnetosonic scenario, a cone-shaped wake cavity is formed, denoting a significant decrease of plasma density. The outer flanks of this cone mark the position of the ICB. Although this structure is still identifiable in the submagnetosonic case, the boundary to the ambient (N^+/H^+) plasma is not as pronounced as in the situation displayed in plot (a).

the magnetic pile-up region at Titan's dayside possesses an extension of only about $1R_T$ in subsolar direction. In contrast to this, when the satellite is located outside the magnetosphere, the magnetic pile-up in the shock front becomes noticeable at a subsolar distance around $3R_T$. The transition between both cases is illustrated in fig. 4.9(c). On the one hand, the interaction leads to the formation of a magnetic draping pattern, being similar to the situation inside the magnetosphere at 18:00 LT. On the other hand, a slight increase of magnetic field strength can be noticed at a subsolar distance of around $2 - 3R_T$, denoting the position of the bow shock in the supermagnetosonic scenario. Furthermore, the magnetic enhancement in the two lobes achieves a maximum value of about $7\,\mathrm{nT}$, whereas a value of $9 - 10\,\mathrm{nT}$ is reached when Titan is located inside the magnetosphere at 18:00 LT. This implies that in the transition scenario under consideration, the field lines are incapable of draping completely around the obstacle, but they develop an intermediate structure between a parabolic, barely confined shock front and a strongly confined draping pattern. To summarize the major results for the polar plane, the boundary structures that have shown to be typical of the interaction region when Titan is located outside the magnetosphere are still identifiable in the transition scenario. However, the sharpness of the boundaries, especially of the Ion

Composition Boundary, has clearly diminished.

Nevertheless, the most important aspect of the transition scenario is the transformation that the ICB undergoes in the plane parallel to the undisturbed convective electric field $\underline{E}_0$. The situation in this plane, being highly asymmetric, is displayed in fig. 4.10. When Titan is located outside the magnetosphere, the interaction gives rise to a sharply developed Ion Composition Boundary in the E^- hemisphere. As can be seen in fig. 4.4(d), a sharp increase of ionospheric density manifests near the E^- flank of the tail. The ambient (N^+/H^+) plasma concentrates along the outer flank of the ionospheric tail as well. However, due to the electric field arising from the ionospheric electron pressure gradient, the (N^+/H^+) ions are incapable of crossing the boundary from outward to inward. Inside the magnetosphere, the region of sharply increased ionospheric density in the E^- hemisphere has vanished. Therefore, the two plasma populations are allowed to mix. The density plots in figs. 4.10(a) and (b) illustrate the transition between both cases: As the decrease of ionospheric density at the tail's flank in the E^- hemisphere is weaker than in the situation displayed in fig. 4.4(b), the ionospheric electron pressure gradient has diminished. Hence, the ambient (N^+/H^+) plasma is capable of gaining access to the ionospheric tail region. Nonetheless, the former position of the boundary is still identifiable.

5 Summary

In this chapter, the key features of Titan's plasma interaction have been analyzed as a function of the Mach numbers in the upstream plasma flow. The dependence of the near-Titan plasma signatures on the orientation of the dayside ionosphere with respect to the upstream flow direction has not yet been discussed, i.e. in analogy to the situation at Venus or at Mars, Titan's dayside ionosphere has always been exposed to the impinging plasma. When Titan is located inside the magnetosphere, this configuration corresponds to 18:00 clock angle position on the satellite's orbit around Saturn.

At first, the case of Titan being located outside the magnetosphere ($M_A > 1$, $M_S > 1$, $M_{MS} > 1$) has been compared to the situation inside the magnetosphere at 18:00 LT. The plasma parameters of the latter simulation run have been chosen in correspondence to the Voyager 1 configuration, i.e. only the alfvénic Mach number of the upstream flow was assumed to be larger than 1. In both simulation runs, the magnetic field lines exhibit a pronounced draping pattern, giving rise to a pile-up region at the ramside and a bipolar magnetotail at the wakeside of the satellite. In the polar plane, the confining effect of the highly curved magnetic field lines restricts the ionospheric tail to a narrow region downstream of the obstacle. Besides, the structure of the interaction region has shown to be highly symmetric in Titan's polar plane, whereas the convective electric field imposes a strong asymmetry on the plasma and magnetic field signatures in the equatorial plane.

When the upstream flow is supermagnetosonic, the global structure of the interaction region is characterized by the formation of a bow shock as well as a sharp separation of the ambient (N^+/H^+) flow from the ionospheric N_2^+ ion population. In analogy to the situation at Mars, an Ion Composition Boundary (ICB) is formed. In the wake region, where the ionospheric N_2^+ ions become the predominant species, the (N^+/H^+) density lies significantly below the background value of the undisturbed flow. The electric field almost vanishes inside the ionospheric tail region. In the E^- hemisphere of the equatorial plane, the convective electric field of the magnetospheric plasma is directed perpendicular to the outer flank of the ionospheric tail, pointing inwards. Therefore, it forbids the ionospheric ions to cross the ICB from inward to outward. The resulting ionospheric electron pressure gradient at the tail's flank leads to the formation of a potential barrier that cannot be crossed by the adjacent (N^+/H^+) ion population. On the other hand, in the E^+ hemisphere, the N_2^+ ions are dragged away from the ionosphere by the convective electric field and are being picked up by the ambient plasma flow. The convective electric field has proven to be essential for the asymmetries occurring in the global structure of the interaction region and especially, for the absence of an ICB in the E^+ hemisphere.

In general, the asymmetric structure of the interaction region has to be explained in an analogous way when Titan is located inside the Saturnian magnetosphere and hence, the upstream plasma flow is submagnetosonic. In the E^+ hemisphere, the convective electric field drags the ionospheric ions away from the obstacle, giving rise to an extended pick-up region. The tail possesses an extension of more than $7R_T$ in E^+ direction. In analogy to the case of a supermagnetosonic flow, the convective field forbids the ionospheric tail to expand into the E^- hemisphere. However, the decrease of ion density at the outer flank of the tail is not as sharp as in the supermagnetosonic scenario. Hence, the resulting electron pressure gradient is not strong enough to prevent the magnetospheric plasma from entering the tail region.

The transition between both situations has been illustrated by means of a third simulation scenario, assuming the upstream flow to be super-alfvénic and supersonic, yet submagnetosonic. In this case, the positions of the boundary layers, being characteristic of the supermagnetosonic situation, are still identifiable. However, these structures are no longer sharply pronounced, and therefore, the magnetospheric and ionospheric plasma populations are allowed to mix with each other. Instead of a bow shock, a diffuse region of increased magnetospheric plasma density arises upstream of the obstacle.

When Titan is located inside the magnetosphere, the high thermal velocity of the impinging (N^+/H^+) ions may also counter the formation of an ICB. However, as will be discussed in chapter 6, these effects can only be fully understood by applying a two-species representation to the magnetospheric plasma. Therefore, the interpretation given in this chapter does not yet consider the impact of the large (N^+/H^+) temperature in the magnetosphere.

Chapter 5

Simulation results for different orbital positions

In the preceding chapter, the dependence of Titan's plasma environment on the Mach numbers of the upstream flow has been analyzed. However, variations in the location of Titan's dayside ionosphere with respect to the direction of the impinging magnetospheric plasma have not been taken into consideration yet. Consequentially, the next step of the study shall focus on the question of how the density and electromagnetic field topology in the vicinity of Titan are modified when the dayside hemisphere is turned away from the ramside of the obstacle. Again, the impinging magnetospheric plasma is represented by a single ion species that features "intermediate" properties.

At first, the situation at 06:00 LT will be discussed. In this scenario, the upstream plasma impinges on Titan's nightside ionosphere. Furthermore, the case of the impinging solar UV radiation being perpendicular to the upstream flow direction at 12:00 LT is of interest. In order to gain straightforward access to the effects arising from such a change in the location of the dayside ionosphere, the magnetospheric plasma parameters in these two geometries have again been chosen in accordance to the Voyager 1 configuration. However, since subsequent modifications of the simulation model have shown that in these two situations, a number of important effects are not covered by the application of single-species representations to the ionospheric and magnetospheric plasmas, the results will be subject to only a brief discussion. The simulation results for 06:00 LT and 12:00 LT mainly provide a reference for the interpretation of the more sophisticated multi-species simulations presented in the next chapter.

An extensive analysis will be provided for the case of Titan being located in Saturn's magnetotail at 00:00 LT. In order to cover the key features of this situation within the framework of the simulation model, two modifications have to be incorporated into the 12:00 LT simulation run. On the one hand, as inferred by Wolf and Neubauer [157], the upstream flow velocity in the tail region of Saturn's magnetosphere is significantly smaller than 120 km/s. This yields an upstream flow configuration in which all three Mach numbers are smaller than 1. On the other hand, when being located in Saturn's magnetotail, Titan may experience at least a partial shielding from the ionizing solar radiation by Saturn. At the equinoxes of Saturn's orbit around the Sun, a total solar eclipse may occur at Titan. Such a scenario will probably be encountered by the Cassini spacecraft during the extended mission[1] that commences in the year 2008. Since the degree to which Titan is shielded from the solar radiation depends on Saturn's orbital position, two different scenarios will be analyzed, representing a lower and

---

[1] M. K. Dougherty, private correspondence.

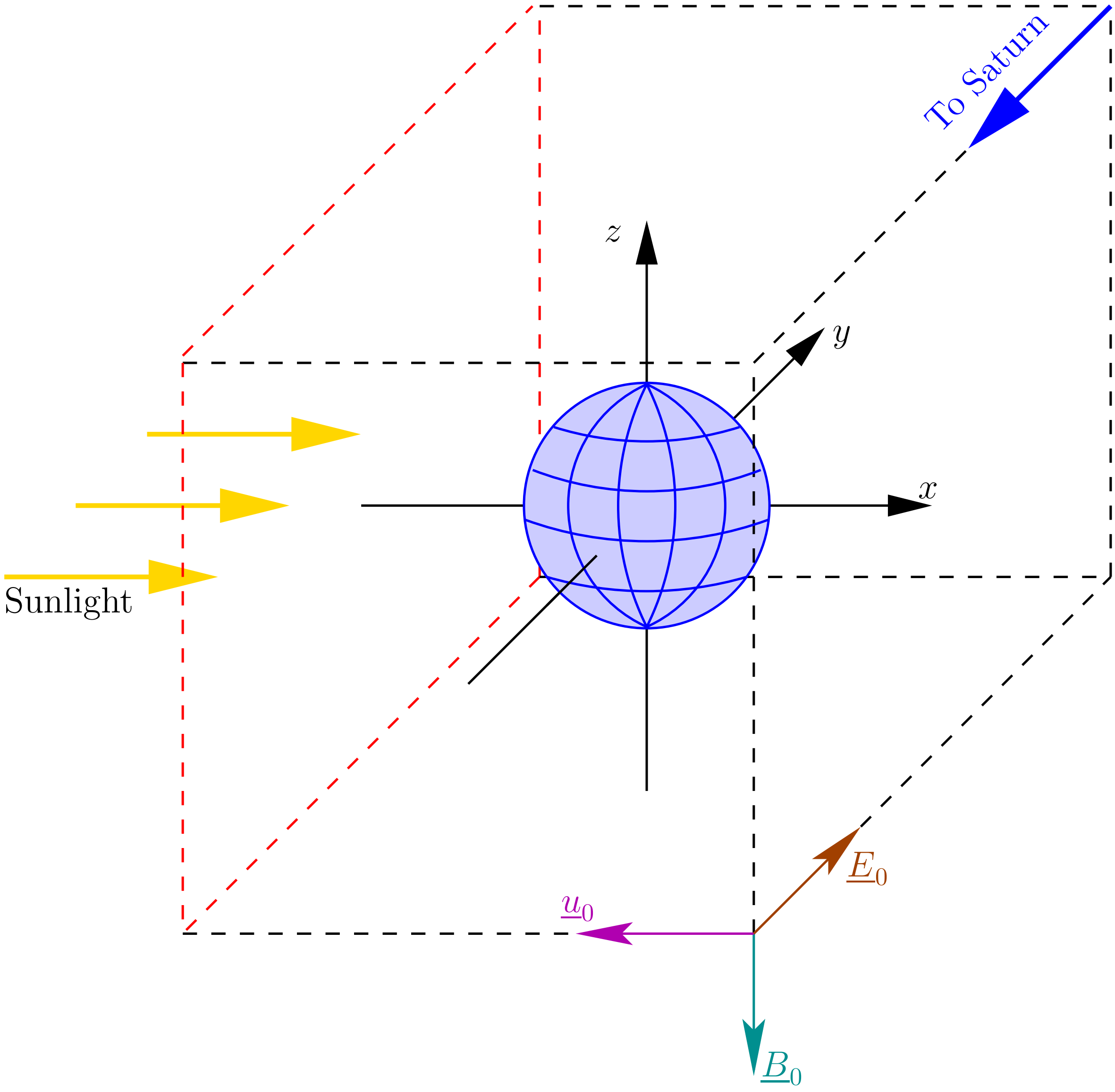

Figure 5.1: Titan's plasma environment at 06:00 Saturnian local time – Simulation geometry. The center of Titan coincides with the center of the cubic simulation domain. Again, the positive x axis is parallel to the direction of the solar UV radiation, whereas the undisturbed Saturnian magnetic field is oriented antiparallel to the z axis. Hence, the velocity vector of the undisturbed corotating plasma flow is directed antiparallel to the x axis. The convective electric field points in $(+y)$ direction, i.e. away from Saturn. The (x, y) plane of the coordinate system coincides with Titan's equatorial plane; the terminator line is located in the (y, z) plane. The wakeside boundary of the simulation box is denoted in red.

an upper "boundary" to the real situation. The case of Titan being completely protected from the solar radiation is compared to a geometry in which the dayside of the satellite is fully exposed to solar radiation, i.e. the dayside production profile is identical to the one included in the 18:00 LT, the 12:00 LT and the 06:00 LT simulations, respectively. Except for the reduced Mach numbers, all other upstream plasma parameters in the 00:00 LT run have again been set to the values obtained from Voyager 1 data. The simulation results for the 00:00 LT scenario will hopefully provide valuable information for the analysis of future Cassini flybys.

A systematic discussion of different Mach number regimes in the vicinity of planetary obstacles that does not only give an overview of the situation at Titan, but also emphasizes the parallels and differences to the Martian plasma interaction, has recently been published in Annales Geophysicae by Simon *et al.* [139].

1 Titan's plasma environment at 06:00 clock angle position

The simulation geometry is shown in fig. 5.1. The orientations of the x and z axes have been chosen in analogy to the 18:00 LT scenario, i.e. the x axis is parallel to the direction of the ionizing solar radiation, whereas the z axis is directed antiparallel to the homogeneous background magnetic field. Consequently, the undisturbed magnetospheric plasma velocity is now parallel to the *negative* x axis. The simulation results are displayed in fig. 5.2 for the terminator plane, while figs. 5.3 and 5.4 illustrate the situation in Titan's polar and orbital plane, respectively.

In general, the global features of the interaction region are the same as in the 18:00 LT situation. The magnetic field drapes around the obstacle, giving rise to a magnetic pile-up region at the ramside and two magnetic lobes in the wake region. It is interesting to notice that, compared to the situation at 18:00 LT, the change in the orientation of the dayside ionosphere has neither left a significant imprint on the magnetic field enhancement in the ramside pile-up region nor on the diameter and the peak field values of the lobes (cf. figs. 5.2(c), 5.3(c) and

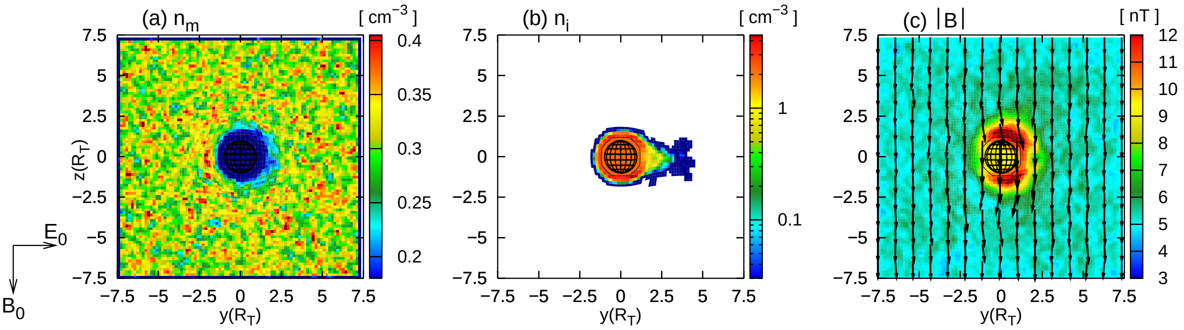

Figure 5.2: Titan's plasma environment at 06:00 Saturnian local time – Cut through the (y, z) plane of the coordinate system, coinciding with Titan's terminator plane. The figure displays (a) the magnetospheric ion density, (b) the ionospheric nitrogen density and (c) the magnetic field. The global characteristics of the interaction region, especially the asymmetry of the nitrogen tail with respect to the direction of the convective electric field, are in complete correspondence to the situation at 18:00 local time.
Mach numbers of the upstream plasma flow: $M_A = 1.87$ (alfvénic), $M_S = 0.57$ (sonic) and $M_{MS} = 0.55$ (magnetosonic). The upstream flow parameters have been chosen in agreement with Voyager 1 data.

5.4(c)). As inferred in the discussion of the magnetic field equation (3.25) in chapter 3, the draping of the magnetic field lines around the obstacle mainly originates from the incapability of the field lines to penetrate into regions where slow particles of ionospheric origin make up the major contribution to the ion population. Figures 5.3(b) and (e) show that such a situation still occurs at the ramside of Titan, despite the nightside production rate being clearly smaller than the values achieved in the wakeside (dayside) hemisphere. The ionospheric density in the ($x > 0$) hemisphere still exceeds the ambient magnetospheric plasma density by a factor of 5. The velocity of these particles in the ramside region is practically negligible. Consequently, the structure of the ramside magnetic pile-up region even exhibits a strong quantitative resemblance to the situation at 18:00 LT, i.e. in both cases, the maximum field value achieved by the ramside pile-up process is clearly larger than 12 nT. The structure of the magnetic lobes in the polar plane remains practically unaffected by the modified orientation of the dayside ionosphere, since the lobes are mainly located outside the ionospheric plasma population. The weak dependence of the magnetic field topology on the orientation of the dayside ionosphere is in consistency with the simulation results presented by Brecht *et al.* [30]. Indeed, as will be discussed below, the magnetic field topology in the vicinity of Titan is primarily determined by the characteristics of the upstream flow.

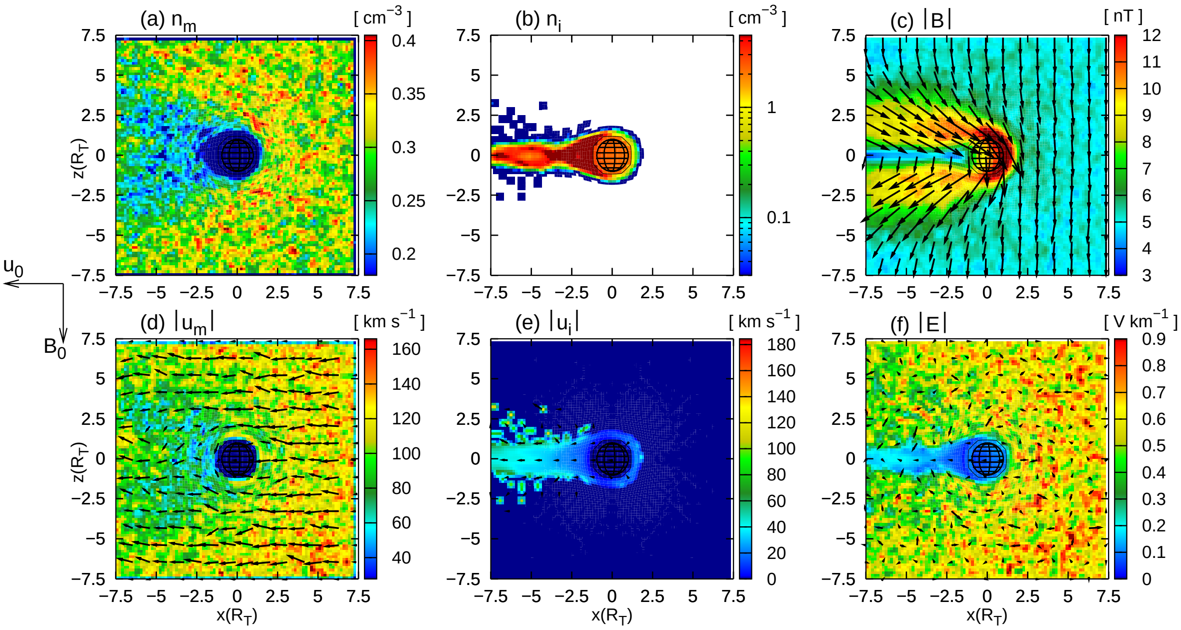

Figure 5.3: Titan's plasma environment at 06:00 Saturnian local time. The figure displays the magnetospheric and ionospheric ion densities (figs. (a) and (b)) and velocities (figs. (d) and (e)) as well as the electromagnetic field quantities (figs. (c) and (f)) for a cut through the (x, z) plane of the coordinate system. The simulation results show the formation of a strong magnetic draping pattern and a slight reduction of both magnetospheric ion density and velocity in the downstream region. Because the dayside of the obstacle is located in the wake region, the ionospheric nitrogen density in the tail is about one order of magnitude higher than in the 18:00 LT scenario. Again, the interaction region exhibits a symmetric structure in the plane perpendicular to the convective electric field.
Mach numbers of the upstream plasma flow: $M_A = 1.87$ (alfvénic), $M_S = 0.57$ (sonic) and $M_{MS} = 0.55$ (magnetosonic). The upstream flow parameters have been chosen in agreement with Voyager 1 data.

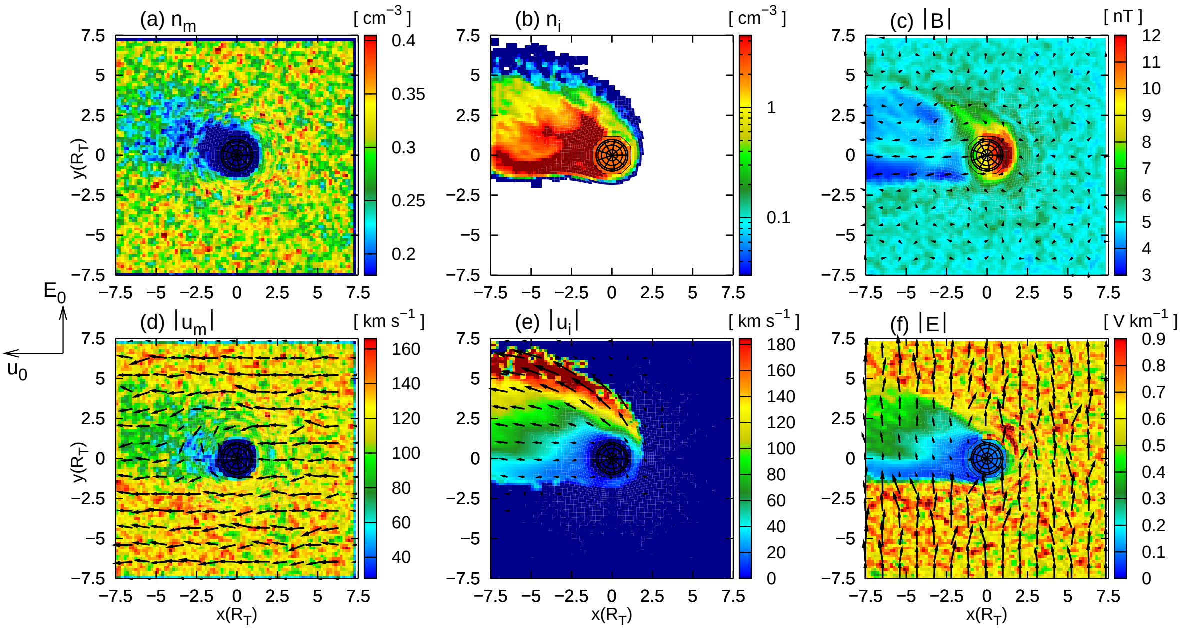

Figure 5.4: Titan's plasma environment at 06:00 Saturnian local time – Cut through the equatorial plane. In contrast to the (x, z) plane, the structure of the interaction region is highly asymmetric in Titan's equatorial plane. The nitrogen density in Titan's wake region is significantly higher than in the 18:00 LT situation, whereas the mechanism generating the asymmetries is the same in both scenarios. **Mach numbers of the upstream plasma flow:** $M_A = 1.87$ (alfvénic), $M_S = 0.57$ (sonic) and $M_{MS} = 0.55$ (magnetosonic). The upstream flow parameters have been chosen in agreement with Voyager 1 data.

Since the region of major ion production is now located in Titan's wake, the ion densities downstream of the satellite exceed the values achieved in the 18:00 LT simulation by an order of magnitude. However, it should be noted that in the polar plane, the ionospheric tail again exhibits a highly symmetric structure, whereas it is clearly turned away from Saturn in the equatorial plane. As shown in fig. 5.4(b), the Saturn-facing flank of the tail is nearly aligned with the direction of the undisturbed magnetospheric plasma. In strong analogy to the 18:00 LT situation, this asymmetry emerges from the electric field barrier that the adjacent (N^+/H^+) flow builds up at the tail's Saturn-facing flank, as can be seen from fig. 5.4(f). Since the density of slow ionospheric ions in the wake region is larger than at 18:00 LT, the (convective) electric field cavity downstream of Titan is sharper pronounced than in the 18:00 LT simulation. Nonetheless, as will be discussed in the subsequent chapter, within the framework of a *multi*-species ionosphere model, this interpretation of the 06:00 LT scenario will have to be subject to a careful reconsideration.

2 Titan's plasma environment at 12:00 clock angle position

Compared to the foregoing simulation scenarios, the situation at 12:00 clock angle position is special in such way that the direction of the impinging solar radiation is not collinear to the magnetospheric upstream flow velocity, but the flow speed is oriented perpendicular to

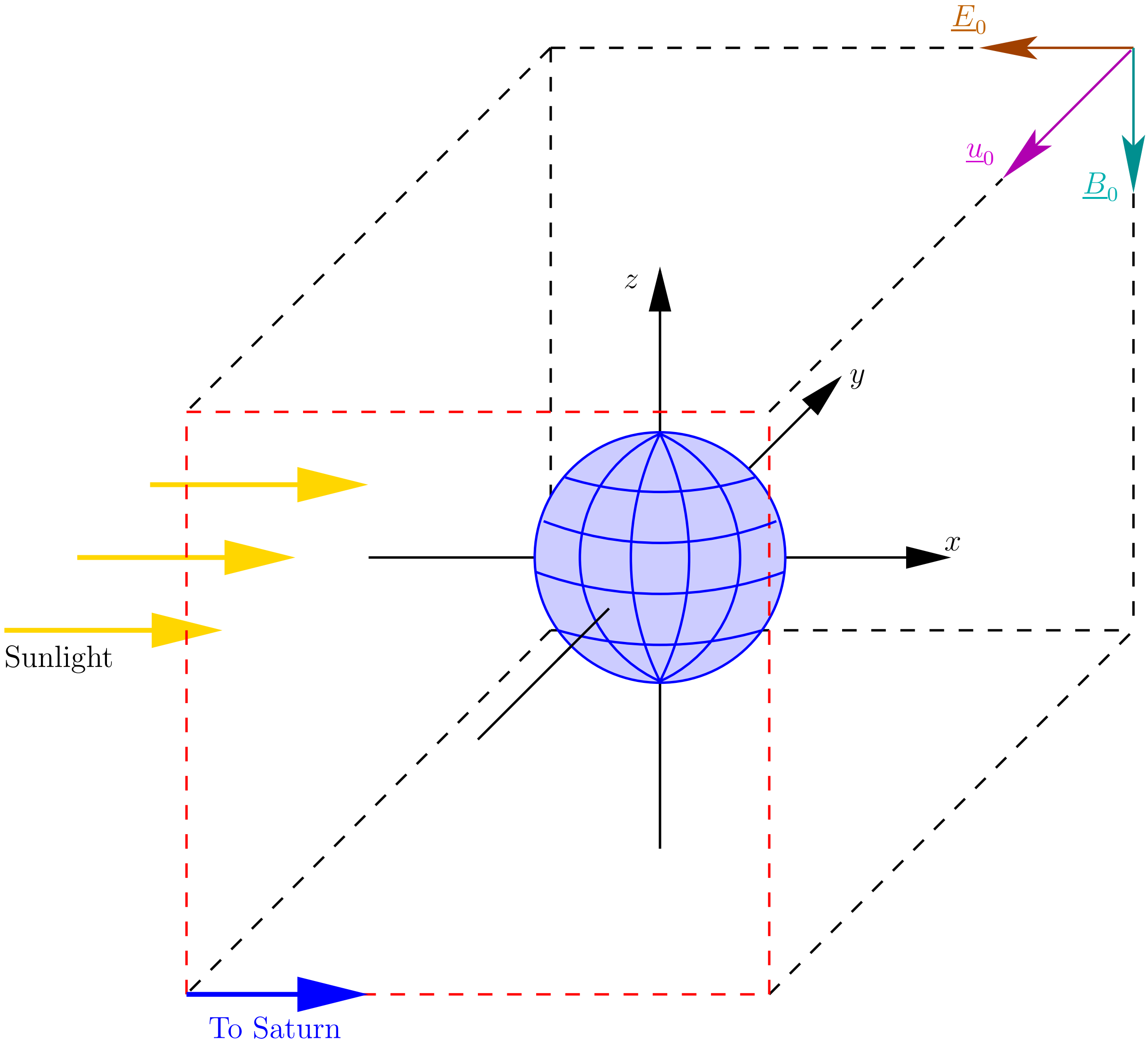

Figure 5.5: Simulation of Titan's plasma interaction at 12:00 clock angle position. The dayside of the satellite is again located in the $(x < 0)$ hemisphere. Consequently, the upstream magnetospheric plasma flow is aligned with the $(-y)$ direction. The convective electric field is directed towards the Sun, i.e. it points away from Saturn. The dashed red lines denote the wakeside wall of the simulation domain.

the path of the radiation. The simulation geometry is shown in fig. 5.5, illustrating that the magnetospheric plasma is now streaming in $(-y)$ direction, while the location of the dayside ionosphere in the $(x < 0)$ half space has been maintained. The simulation results for Titan's polar and equatorial plane are shown in figs. 5.6 and 5.7, respectively. Following the nomenclature introduced in chapter 4, the polar plane always contains the vectors $\underline{u}_0$ and $\underline{B}_0$. Therefore, in the 12:00 LT scenario, the (y, z) plane represents the polar as well as the terminator plane. In the text, it will consequently be referred to as the polar plane. This remark is valid for the 00:00 LT simulation geometry as well.

Because the global structure of the interaction region features a strong similarity to the

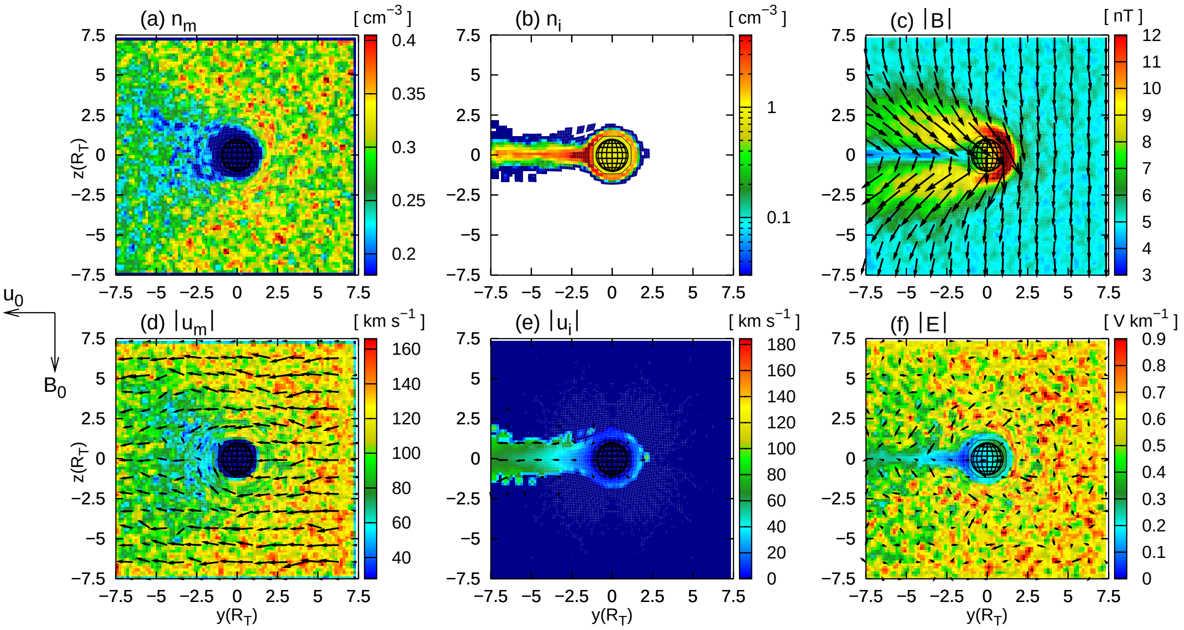

Figure 5.6: Simulation of Titan's plasma environment at 12:00 local time. The figure displays the simulation results in the satellite's polar/terminator plane, coinciding with the (y, z) plane of the coordinate system. The reduced magnetic field strength in between the two lobes gives rise to a ray-like region of enhanced ionospheric plasma density. This feature is well known from the Martian plasma interaction. In that case, the existence of such a density enhancement in the central field reversal region has been confirmed by both simulations and measurements [27]. The 12:00 LT scenario should be quite similar to the situation during the Voyager 1 flyby that took place at about 13:30 clock angle position. In correspondence to Voyager 1 data, the magnetic lobes exhibit a narrow structure with a sharply pronounced outer boundary. It is interesting to notice that in a distance of more than $\pm 2.5 R_T$ to the central wake region, the magnetospheric plasma flow direction remains practically unaffected. **Mach numbers of the upstream plasma flow:** $M_A = 1.87$ (alfvénic), $M_S = 0.57$ (sonic) and $M_{MS} = 0.55$ (magnetosonic). The upstream flow parameters have been chosen in agreement with Voyager 1 data.

situation at 18:00 LT and 06:00 LT, the discussion will focus on only a few key features. As can be seen from fig. 5.6(b), the ionospheric tail in the polar plane is not only confined by the magnetic lobes, but it also shows a ray-like enhancement of the number density along the central field reversal region in between the lobes. Due to the diminished magnetic pressure in the neutral region, an enhancement of the ionospheric density is required in order to ensure pressure balance and hence, the stability of the lobe structure. In a similar prominent manner, this structure has been found only in the results of the 00:00 LT simulations. In the equatorial plane, the ionospheric tail as well as the ramside magnetic pile-up region are clearly shifted away from Saturn. In the E^+ pick-up region, the high ion velocity makes the electric field strength return to its undisturbed background value, as shown in fig. 5.7(f).

A quite remarkable result is that neither in the polar nor in the equatorial plane, a significant reduction of the magnetospheric plasma density arises downstream of the obstacle. Of course, as displayed in figs. 5.6 (a) and (d), the flow is decelerated in the wake region and the mean density also experiences a slight reduction, but the effects are by far not as pronounced as indicated by the Voyager 1 measurements [119]. Although downstream of Titan, some minor distortions seem to be imposed on the *direction* of the magnetospheric plasma, the effect is clearly not as pronounced as in the situation outside the magnetosphere, where the deflection of the decelerated flow around the central wake region gave rise to an almost complete evacuation. As can be seen from fig. 5.6(d), in a vertical distance of more than $z = \pm 2.5 R_T$ to the $(z = 0)$ line, the flow direction remains nearly unaffected. In the E^- hemisphere of the equatorial plane, the flow velocity vectors are not turned away from their initial direction either. This rather weak reaction of the magnetospheric plasma points out one of the limitations that go along with the application of a single-species representation to the impinging flow. Further details shall be discussed in chapter 6.

In contrast to the hybrid simulation results presented by Brecht *et al.* [30], the overall topology of the interaction region exhibits only a weak dependence on the location of the dayside ionosphere. The dynamics of the magnetospheric plasma are, to a significant degree, controlled by the high thermal velocity of the particles, so that the formation of any kind of sharply pronounced structure is countered by a certain "smearing" effect. Strong changes in the magnetospheric flow pattern that arise from the modified location of the dayside ionosphere are therefore practically not existent. Due to the simplifying assumption of a vanishing plasma temperature, the influence of changes in the location of the dayside ionosphere is strongly overestimated by the model of Brecht *et al.* [30]. Thus, the results presented in this chapter place emphasis on the necessity of including the magnetospheric ion temperature into the

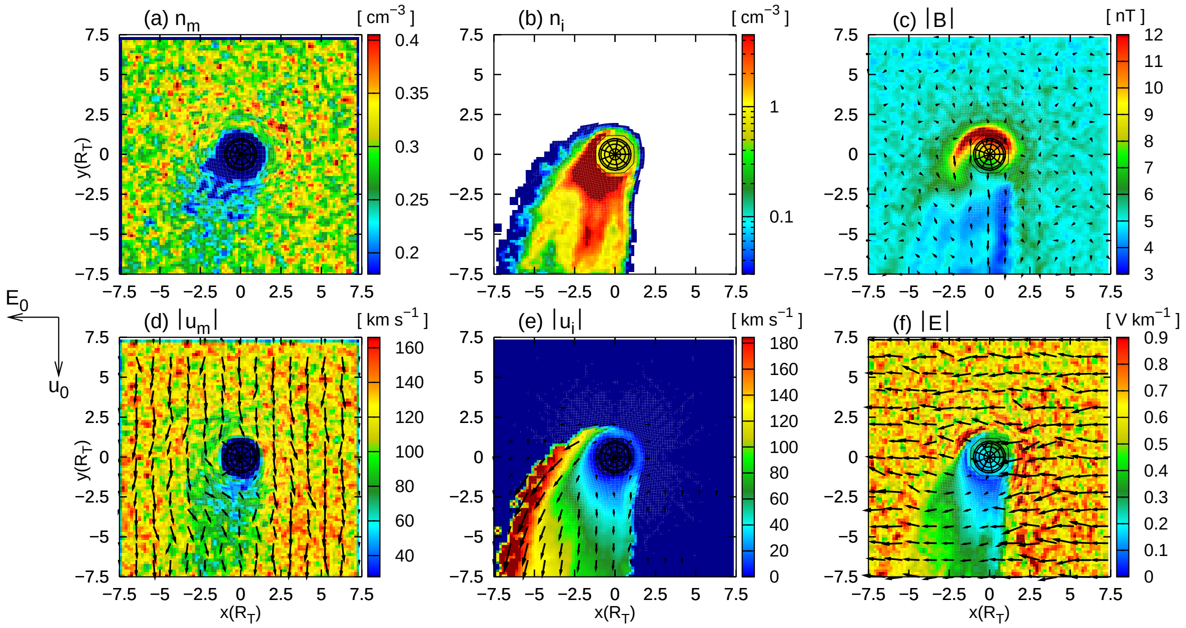

Figure 5.7: Simulation of Titan's plasma environment at 12:00 local time – Simulation results for the equatorial plane. In the (anti-Saturn-facing) E^+ hemisphere, the magnetospheric flow pattern remains nearly unaffected. The ionospheric tail is shifted away from Saturn, its extension perpendicular to the x axis being determined by the gyroradii of the newly generated N_2^+ ions.
Mach numbers of the upstream plasma flow: $M_A = 1.87$ (alfvénic), $M_S = 0.57$ (sonic) and $M_{MS} = 0.55$ (magnetosonic). The upstream flow parameters have been chosen in agreement with Voyager 1 data.

model. In the case of Titan being exposed to a superfast and rather cold flow, the simulation model used for the present study also shows strong changes in the electromagnetic field topology as well as in the near-Titan flow pattern, if the orientation of the dayside ionosphere is changed.

3 Titan's plasma environment at 00:00 clock angle position

In the simulation runs discussed in this section, Titan is assumed to be located in the Saturnian wake. Wolf and Neubauer [157] have stated that under these circumstances, the impinging plasma flow is sub-alfvénic as well as subsonic and submagnetosonic. Due to lack of concrete data for this situation, the Mach numbers of the upstream plasma have been chosen in accordance to the magnetohydrodynamic model of Ledvina *et al.* [90]. The values of the three Mach numbers are $M_A = 0.77$ (alfvénic), $M_S = 0.29$ (sonic) and $M_{MS} = 0.27$ (magnetosonic). The absolute value of the ambient magnetospheric flow speed is therefore given by

$$u_0 = \frac{0.77}{1.87} \cdot 120\,\mathrm{km/s} \approx 50\,\mathrm{km/s} \quad . \tag{5.1}$$

The simulation geometry refers to the case of Titan being located in Saturn's wake at 00:00 Saturnian local time. At first, the situation at the equinoxes of Saturn's orbit around the Sun is analyzed. In this situation, solar UV radiation cannot be considered an ionization source. Therefore, an approximative approach has been chosen to mimic the ionosphere at 00:00 LT. The model is based on the assumption that the ionosphere at 00:00 LT is significantly less pronounced than at any other orbital position. For simplicity, the ionosphere has been modeled by a weak and isotropic ion production profile, i.e. the production function q_ν depends only on the altitude above the surface, but not on the solar zenith angle. The total production in the model ionosphere has been set to a value that is one order of magnitude smaller than in the 18:00 LT situation, i.e. $Q = 1.25 \cdot 10^{24}\,\mathrm{s}^{-1}$.

The simulation geometry is displayed in fig. 5.8. The x axis still points from the Sun to Titan, but however, the satellite is now protected from the solar ultraviolet radiation by Saturn. The undisturbed upstream plasma flow is directed in $(+y)$ direction, yielding a convective electric field that is parallel to the positive x axis. The simulation results for a cut through the (x, z) plane are shown in fig. 5.9. The plasma and field parameters for the polar plane[2] are shown in fig. 5.10, whereas fig. 5.11 displays the results for Titan's orbital plane.

As can be seen in figs. 5.9(c) and 5.10(c), the magnetic draping pattern in the vicinity of Titan is significantly less pronounced than in the simulation results for 06:00 LT, 12:00 LT and 18:00 LT, where the upstream plasma flow was assumed to be super-alfvénic. In the 00:00 LT scenario, the magnetic lobes possess an extension of about $\pm 6 R_T$ in the direction of the z axis, i.e. the diameter of the magnetotail is about a factor of 2 larger than in the case of a super-alfvénic upstream flow. Moreover, the simulation results for 06:00 LT, 12:00 LT and 18:00 LT show the formation of a pronounced field reversal region between the two lobes in which the magnetic field strength almost vanishes. As displayed in figs. 5.10(c) and 5.11(c), such a structure is not formed when Titan is located in Saturn's wake. The magnetic

---

[2] The meaning of this term has been explained in the preceding section.

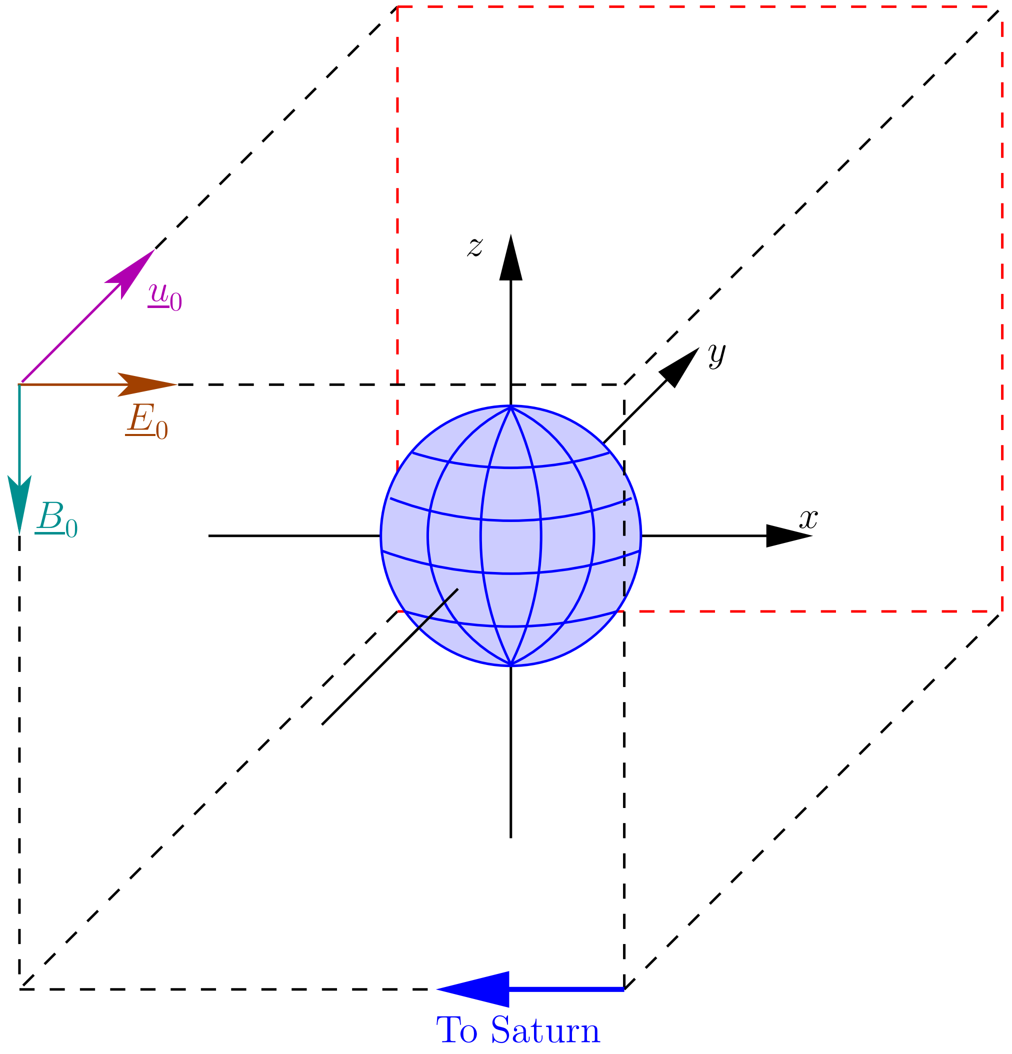

Figure 5.8: Titan's plasma environment at 00:00 Saturnian local time – Simulation geometry. Again, the x axis points from the Sun to Titan. The undisturbed magnetic field is oriented antiparallel to the z axis. The undisturbed plasma flow is directed in positive y direction. This yields a convective electric field that is parallel to the x axis, pointing away from Saturn. Two scenarios have been considered: The case of Titan being completely shielded from the solar UV radiation has been compared to a geometry in which the satellite's ($x < 0$) hemisphere is exposed to solar ultraviolet radiation. The former geometry refers to the situation at the equinoxes of Saturn's orbit around the Sun, whereas the latter one provides a simplified approximation to the general case of Titan being not completely shielded from the ionizing solar radiation.

field strength in between the lobes is nearly identical to the undisturbed background value of $B_0 = 5\,\mathrm{nT}$, for the curvature of the field lines is too weak to cause a noteworthy decrease of B. Besides, in the 00:00 LT scenario, only a minor increase of magnetic field strength occurs in front of the obstacle. Figs. 5.9(c), 5.10(c) and 5.11(c) illustrate that a peak field strength of about $9\,\mathrm{nT}$ is achieved at Titan's ramside, i.e. the magnetic field in the pile-up region is only around a factor 2 stronger than in the undisturbed upstream plasma flow. In contrast to this, when Titan is exposed to a super-alfvénic plasma, the magnetic pile-up yields a field

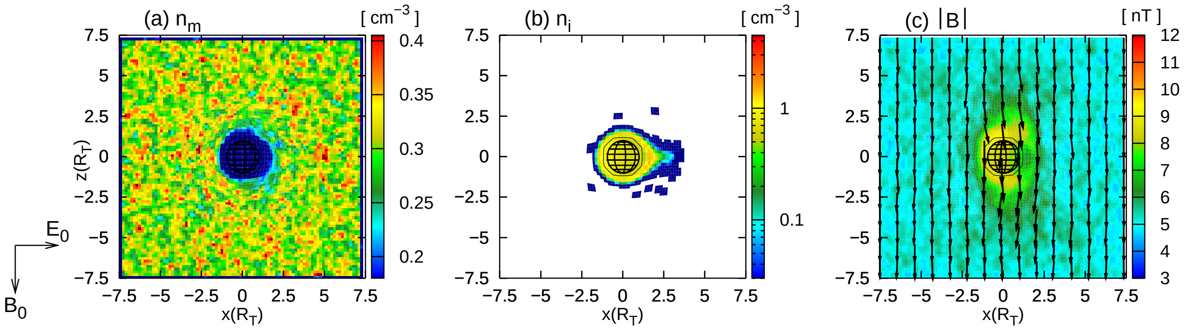

Figure 5.9: Titan's plasma environment at 00:00 Saturnian local time – Cut through the (x, z) plane of the coordinate system. Titan is completely shielded from the ionizing solar radiation. The figure displays (a) the magnetospheric ion density, (b) the ionospheric nitrogen density and (c) the magnetic field strength. Although the magnetic field still drapes around the obstacle, the peak field strength reached in the ramside pile-up region is significantly smaller than in the case of Titan being exposed to a super-alfvénic plasma flow. Again, the ionospheric tail exhibits a definite preference to expand in the direction of the convective electric field. The magnetospheric ion density in the (x, z) plane is almost homogeneous.
Mach numbers of the upstream plasma flow: $M_A = 0.77$ (alfvénic), $M_S = 0.27$ (sonic) and $M_{MS} = 0.22$ (magnetosonic). All other magnetospheric plasma parameters correspond to the Voyager 1 configuration.

strength of more than 12 nT at the ramside of the satellite.

In general, due to the upstream plasma velocity in the 00:00 LT run being about $1 - 0.77/1.87 = 60\%$ smaller than in the other situations under consideration, the transport of the magnetic field lines towards Titan is slowed down as well. The pressing of the field lines against the obstacle is by far not as strong as in the case of a super-alfvénic upstream flow. Thus, the imprint that the satellite leaves on the field lines is less pronounced. In the numerical scenario, the characteristic time scale for the formation of the magnetic lobes is significantly larger than at the other three orbital positions under consideration. Thus, when a field line "attempts" to reach the downstream region by evading Titan in the direction perpendicular to the (y, z) plane, only a minor curvature is imposed on its initially straight structure.

A more formal interpretation of the modified magnetic draping pattern can be given by means of eq. (3.63), describing the time evolution of $\underline{B}$ in a two-species plasma flow:

$$\frac{\partial \underline{B}}{\partial t} = \nabla \times \left[\left(\frac{n_m}{n_m + n_i} \underline{u}_m + \frac{n_i}{n_m + n_i} \underline{u}_i \right) \times \underline{B} \right] - \nabla \times \frac{(\nabla \times \underline{B}) \times \underline{B}}{\mu_0 e \, (n_m + n_i)} \quad . \tag{5.2}$$

As stated in chapter 3, the first term emerges from the convective electric field and is responsible for the draping process, whereas the second one arises from the Hall effect and contains the contributions of magnetic tension and pressure. Of course, in the immediate vicinity of Titan, the contribution of the ionospheric ions to the convective term is still predominant and at least partially forbids the field lines to gain access to the weakened ionosphere. However, in the regions covered by the lobes as well as outside the major ionospheric concentrations at the ramside, the convective term arises exclusively from the magnetospheric (N^+/H^+) ions. Due to the reduced magnetospheric plasma velocity in the scenario under consideration,

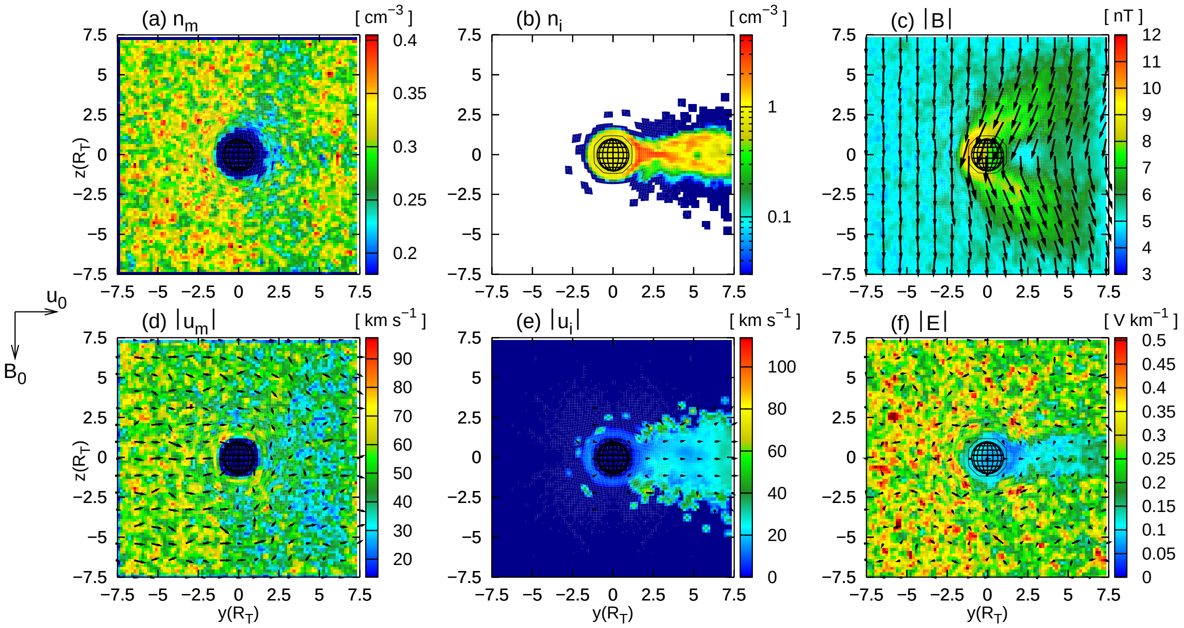

Figure 5.10: Titan's plasma environment at 00:00 Saturnian local time – Cut through the obstacle's polar plane which coincides with the (y, z) plane of the coordinate system. Titan is completely shielded from the ionizing solar radiation. The figure displays (a) the magnetospheric ion density, (b) the ionospheric nitrogen density, (c) the magnetic field strength, (d) the magnetospheric ion velocity, (e) the ionospheric ion velocity and (f) the electric field. The magnetic draping pattern is not as pronounced as in the 06:00 LT, the 12:00 LT and the 18:00 LT scenario. On the one hand, the magnetic lobes are widened and cover a larger area in the polar plane; on the other hand, the peak magnetic field strength in the lobe regions as well as in the pile-up region at Titan's ramside has clearly diminished. Moreover, the area of reduced magnetic field strength between the two lobes has almost vanished. Compared to the case of a super-alfvénic upstream flow, the characteristic time scale for the formation of the magnetic draping pattern is significantly larger, allowing the field lines to pass the obstacle in the direction perpendicular to the cutting plane without being significantly deformed. The modification of the lobe structure also leaves an imprint on the ionospheric tail in the polar plane. The tail's extension perpendicular to the flow direction is larger than in the 06:00 LT, the 12:00 LT and the 18:00 LT simulation, since the confining effect exerted by the lobes is weaker. In the downstream region, the electric field strength and the magnetospheric plasma parameters exhibit only a minor reduction.
Mach numbers of the upstream plasma flow: $M_A = 0.77$ (alfvénic), $M_S = 0.27$ (sonic) and $M_{MS} = 0.22$ (magnetosonic). All other magnetospheric plasma parameters correspond to the Voyager 1 configuration.

the Hall term is able to take a more predominant role than in the case of a super-alfvénic magnetospheric plasma. Thus, compared to the situation at 06:00 LT, at 12:00 LT or at 18:00 LT, the enhanced influence of the magnetic tension term yields a reduced curvature of the field lines and therefore a widening of the draping pattern. The contribution of the magnetic pressure expands the compressed magnetic field lines at Titan's ramside and hence, the sharpness and the magnitude of the pile-up are reduced.

The only other simulation study referring to the situation at 00:00 LT has been conducted by Ledvina *et al.* [90]. As the Mach numbers of the upstream plasma flow have been obtained

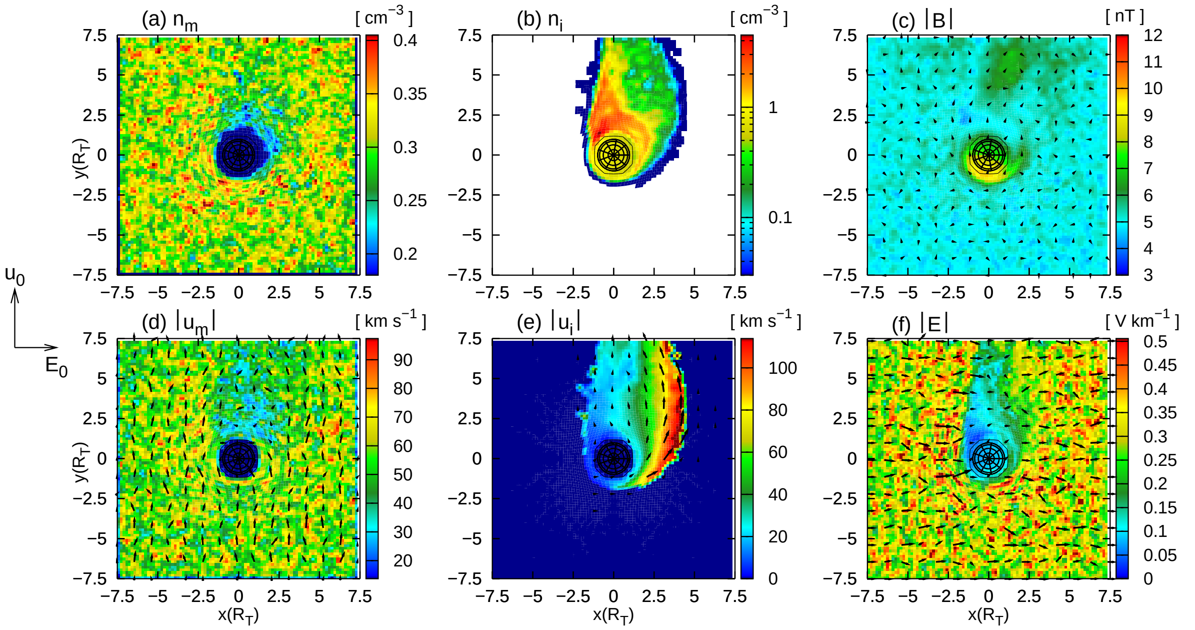

Figure 5.11: Titan's plasma environment at 00:00 Saturnian local time – Cut through Titan's equatorial plane which is perpendicular to the undisturbed magnetic field. Titan is completely shielded from the ionizing solar radiation. The figure displays (a) the magnetospheric ion density, (b) the ionospheric nitrogen density, (c) the magnetic field strength, (d) the magnetospheric ion velocity, (e) the ionospheric ion velocity and (f) the electric field. Like in the 06:00 LT, the 12:00 LT and the 18:00 LT scenario, the ionospheric tail exhibits a strong preference to expand into the E^+ hemisphere. However, the value of the upstream plasma velocity is about 60% smaller than in the other simulation runs. Therefore, the convective electric field and hence, the Lorentz force that drags the ionospheric ions into the E^+ hemisphere, are significantly weaker, yielding a tail diameter of only $5R_T$ in E^+ direction. In contrast to this, when the upstream flow is super-alfvénic, particles of ionospheric origin can be found in a distance of more than $7R_T$ perpendicular to the flow direction. Because the ionospheric ion velocity in the tail is comparable to the ambient plasma velocity, only an insignificant decrease of (convective) electric field strength occurs downstream of the obstacle.
Mach numbers of the upstream plasma flow: $M_A = 0.77$ (alfvénic), $M_S = 0.27$ (sonic) and $M_{MS} = 0.22$ (magnetosonic). All other magnetospheric plasma parameters correspond to the Voyager 1 configuration.

from this magnetohydrodynamic study, a direct comparison between the results is possible. In complete qualitative agreement with the results discussed in this section, Ledvina *et al.* [90] demonstrate that for the case of Titan being located in Saturn's wake, the magnetic draping pattern is significantly less confined to the immediate vicinity of the satellite than at 18:00 LT. The MHD simulations also indicate the field strength between the two lobes to be comparable to the background value of $B_0 = 5\,\mathrm{nT}$. Nevertheless, a complete quantitative agreement with the results of the magnetohydrodynamic model cannot be achieved. The simulations presented by Ledvina *et al.* [90] show practically no difference between the structure of the magnetic pile-up region in the 00:00 LT and the 18:00 LT scenario. In both simulations, the peak magnetic field strength at Titan's ramside is about a factor of 3 to 4 higher than the undisturbed upstream magnetic field. Furthermore, the results of the MHD model suggest the peak field strength in the magnetic lobes to be almost the same in both situations. As the

MHD model of Ledvina *et al.* [90] does not include the Hall term, the relaxation of the field lines cannot be described adequately. For this reason, quantitative differences to the results of the hybrid approach are absolutely expectable.

As can be seen in fig. 5.10(b), which displays the ionospheric ion density in the polar plane, the ionospheric tail possesses a larger extension perpendicular to the obstacle than at the other three orbital positions. Such a modification of the tail structure is expectable since the diameter of the tail in $\pm z$ direction is mainly controlled by the magnetic field in the lobes. In the 18:00 LT scenario (cf. section 3 of chapter 4), the focusing effect arising from the curved magnetic field lines in the polar plane has shown to be responsible for confining the ionospheric tail to a narrow region directly behind the obstacle. It has also been pointed out that the region of reduced magnetic field strength between the two lobes is the only area in the polar plane where the pick-up force is directed away from Titan. The modified magnetic lobe structure in the 00:00 LT geometry is the major reason for the transition that the ionospheric tail in the polar plane has undergone. Compared to the 18:00 LT scenario, the magnetic lobes are widened to a certain degree. Therefore, in the northern lobe, the magnetic field component antiparallel to the upstream flow direction $\underline{u}_0$ is clearly weaker than in the situation at 18:00 LT. Thus, the focusing effect that arises from the curved field lines in the northern lobe is not as strong as in the situation at 18:00 LT. An analogous argumentation is valid for the southern magnetic lobe. The component of the draped magnetic field parallel to the undisturbed magnetospheric flow direction $\underline{u}_0$ is weaker than in the 18:00 LT scenario, so that the magnetic confinement of the ionospheric particles is untightened. Besides, the magnetic field enhancement in the lobes, determining the magnitude of the focusing Lorentz force, has also diminished.

As can be seen from fig. 5.10(c), the major magnetic field component in the lobes is now oriented in $(-z)$ direction. The contact with the obstacle imposes only a minor deformation on the field lines. Thus, the pick-up vector $\underline{\xi} = \underline{E} \times \underline{B}$ in the lobes is aligned with the $(+y)$ axis,

$$\underline{\xi} \propto \underline{e}_x \times (-\underline{e}_z) = \underline{e}_y \quad , \tag{5.3}$$

i.e. it points in the same direction as in the weakly pronounced neutral region. Hence, in the entire downstream region of the polar plane, $\underline{\xi}$ is oriented parallel to the undisturbed magnetospheric flow direction[3]. In this region, newly generated ionospheric particles experience a force that drags them away from Titan. However, as displayed in fig. 5.10(e), the velocity of the ionospheric ions is even smaller than in the 18:00 LT simulation. The reason for this is the reduced magnitude of the Lorentz force. The convective electric field strength $\underline{E}_c = -\underline{u}_m \times \underline{B}$ is weaker than in the 18:00 LT scenario, for $\underline{u}_m$ has been reduced by a factor of $0.77/1.87 \approx 0.4$. Thus, the acceleration of the newly generated ionospheric particles is smaller, i.e. the pick-up process is less efficient.

However, the tail is still symmetric in the polar plane, whereas it exhibits a strong asymmetry with respect to the direction of the convective electric field, as displayed in fig. 5.11(b). Nevertheless, when Titan is located in Saturn's wake, the tail possesses an extension of only $5R_T$ perpendicular to the direction of $\underline{u}_0$, while tail diameters of more than $7R_T$ have shown to be characteristic of the situation at 06:00 LT, 12:00 LT and 18:00 LT. As will be discussed

---

[3] Of course, this qualitative discussion neglects any kind of spatial inhomogeneity in the wakeside field strength.

in more detail in chapter 6, the gyroradius of the newly generated ionospheric ions depends linearly on the *magnetospheric* flow speed. Since the value of $|\underline{u}_0|$ in the 00:00 LT scenario is smaller than at the other three orbital positions, the ion gyroradii and therefore, the extension of the tail in E^+ direction, are also reduced. As can be seen from figs. 5.11(b) and (e), the tail's outer flank in the E^+ hemisphere exhibits a cycloidal shape. The ion velocities achieved in the anti-Saturn-facing pick-up region are smaller than in the case of a super-alfvénic upstream flow, illustrating again the impact of the weaker pick-up force.

When Titan is located in Saturn's wake at 00:00 LT, only a small cavity of reduced electric field strength arises downstream of the obstacle, as can be seen in fig. 5.11(f). Besides, the decrease of electric field strength is less significant than at the other three orbital positions. On the one hand, the slight reduction of magnetospheric plasma velocity in the downstream region causes only a minor decrease of the convective electric field strength. On the other hand, this reduction is almost entirely compensated by the ionospheric pick-up ions, whose velocity in the E^+ hemisphere is comparable to or even significantly higher than the undisturbed upstream plasma velocity. This situation is illustrated in figs. 5.11(d) and 5.11(e), respectively.

Finally, the simulation results shall be compared to an alternative scenario. On the one

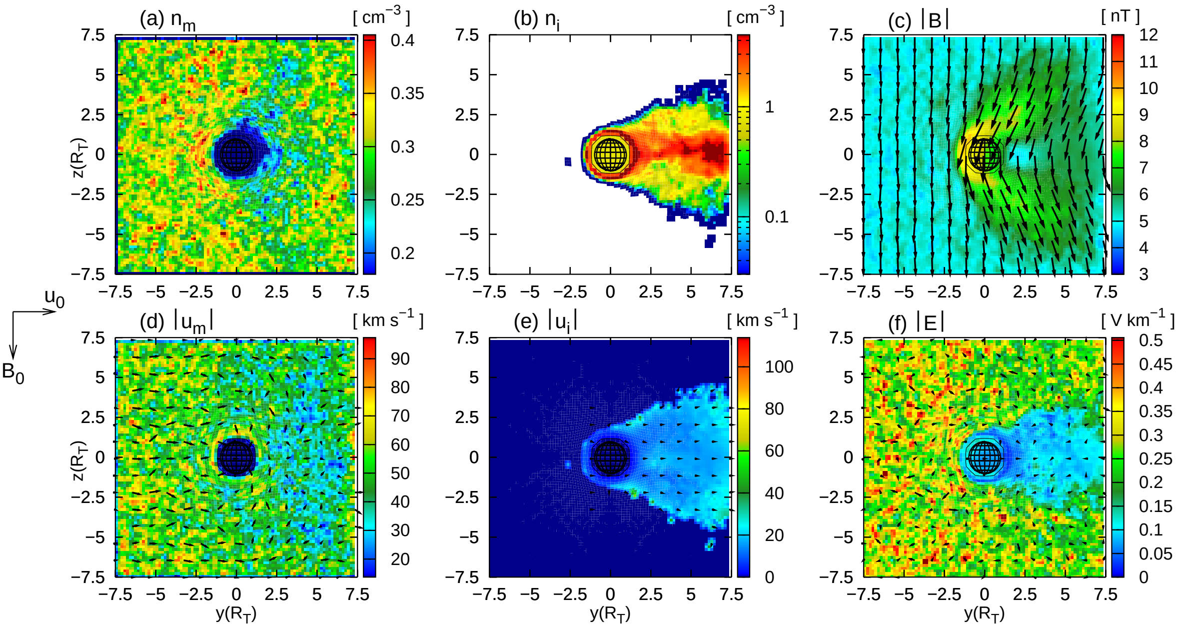

Figure 5.12: Titan's interaction with the sub-alfvénic, subsonic and submagnetosonic plasma flow in Saturn's magnetotail region – Cut through the polar plane. In contrast to the first simulation run, Titan's ($x < 0$) hemisphere is exposed to solar UV radiation. In the polar plane, the structure of the interaction region is still highly symmetric. The ionospheric tail exhibits a broad, cone-like structure with a pronounced region of increased plasma density in its center. The widened structure of the magnetic lobes allows the ionospheric tail to cover a larger area than in the case of a super-alfvénic flow. The magnetic draping pattern itself is not affected by the increased production rate.
Mach numbers of the upstream plasma flow: $M_A = 0.77$ (alfvénic), $M_S = 0.27$ (sonic) and $M_{MS} = 0.22$ (magnetosonic). All other magnetospheric plasma parameters correspond to the Voyager 1 configuration.

hand, Titan is still assumed to be located in the Saturnian magnetotail, but on the other hand, the satellite is no longer assumed to be completely shielded from the ionizing solar radiation. This modification takes account for the fact that most of the Cassini flybys do not take place at the equinoxes of Saturn's orbit, but in late southern summer, i.e. the south pole of Saturn (and Titan) is illuminated while the north pole is dark. However, in order to gain straightforward insight into the transition that the interaction region undergoes when the sunlight is "switched on", the simulation geometry has again been kept as simple as possible. While all other simulation parameters, including the directions of the upstream flow and the ambient magnetic field, have been retained, the isotropic ion production profile has been replaced by the original Chapman-like profile. The dayside ionosphere is located in the $(x < 0)$ half space, i.e. the shielding effect of Saturn has simply been removed from the model. Of course, the real geometry of a flyby that does not take place at the equinoxes is significantly more complex. Using the original Chapman profile in the $(x < 0)$ hemisphere also allows a more direct comparison to the results for 12:00 LT. The plasma and electromagnetic field configuration in the polar plane is displayed in fig. 5.12. In the modified geometry, this plane is also identical to Titan's terminator plane, as it has been in the 12:00 LT scenario.

As can be seen in fig. 5.12(c), the magnetic field topology in the polar plane is nearly identical to the results for a reduced production rate, implying that the formation of the magnetic lobes is at least to a certain degree decoupled from the ionospheric tail formation. However, a comparison between figs. 5.10(b) and 5.12(b) points out that the ionospheric tail structure has undergone a noticeable transition. In the case of a weak and isotropic production rate, the major concentrations of newly generated N_2^+ ions in the polar plane could be found along the y axis. Besides, the tail's outer flanks in the polar plane featured a rather diffuse structure. In contrast to this, if the original Chapman-like production profile is incorporated into the 00:00 LT scenario, the tail exhibits an almost cone-like structure. It possesses a strong resemblance to the shape of the nearly evacuated (N^+/H^+) wake cavity that is formed when the upstream flow is supermagnetosonic. This result clearly illustrates that the "flat" structure of the tail that manifested in the simulation results for 06:00 LT, 12:00 LT and 18:00 LT can definitely be ascribed to the confining effect of the magnetic lobes. Albeit being more diffuse than in the 12:00 LT scenario, a region of increased ionospheric density is clearly identifiable in the central tail region (cf. fig. 5.10(b)). The resulting enhanced pressure balances the slightly reduction of the magnetic pressure between the two lobes.

The two geometries discussed in this section provide a general impression of how Titan's plasma environment is modified when the satellite enters the Saturnian wake region. In any case, if a solar eclipse at Titan will really be observed during the extended Cassini mission, it will be interesting to determine a characteristic time scale for the transition from an UV-induced ionosphere to an ionosphere that emerges exclusively from particle impact processes. A more detailed discussion of the results for 00:00 LT is given by Simon *et al.* [139].

4 Summary

In this chapter, the dependence of the structures in Titan's plasma environment on the satellite's position inside the Saturnian magnetosphere has been investigated. Three different cases have been considered. On the one hand, Titan's plasma interaction at 06:00 LT and 12:00 LT clock angle position has been investigated. The upstream magnetospheric plasma parameters in these geometries have been chosen in correspondence to the Voyager 1 data set. On the other hand, the 00:00 LT scenario did not only allow to study the influence of a reduced ionospheric production rate, but it also illustrated the transition that Titan's plasma environment undergoes when all three Mach numbers of the upstream flow are reduced to values below 1. Single-species representations have been applied to the impinging magnetospheric plasma as well as to the ionosphere.

The simulation results for 06:00 LT and 12:00 LT have shown that Titan's plasma environment is only slightly affected by changes in the orientation of the dayside ionosphere. Although some modifications of the wakeside ionospheric densities could be identified, the electromagnetic field topology in these geometries exhibits a strong qualitative and quantitative resemblance to the situation at 18:00 LT. Only in the immediate vicinity of the satellite, noticeable distortions are imposed on the magnetospheric flow pattern.

The situation results for the 00:00 LT scenario finally illustrated that the magnetic field topology in the vicinity of Titan is indeed nearly independent of the ionospheric production rates, but a decisive character must be ascribed to the velocity of the upstream flow instead. A reduction of the ambient magnetospheric plasma velocity has shown to go along with a significant widening of the magnetic lobes as well as a reduction of the peak magnetic field strength achieved in the ramside pile-up region. Compared to the situation at 12:00 LT, the sharpness of the central field reversal region has clearly diminished. Due to the reduced curvature of the field lines in the polar plane, the ionospheric tail covers a larger area than in the case of a super-alfvénic upstream flow. In the lobes as well as in the neutral region, the pick-up force is directed downstream. The 00:00 LT simulation results also illustrated that the gyroradii of the newly generated ionospheric ions and therefore, the extension of the tail in the E^+ hemisphere of the equatorial plane, are affected by changes of the upstream magnetospheric flow speed.

Chapter 6

Multi-species hybrid simulation of Titan's plasma environment

In the preceding chapters, Titan's plasma environment has been studied in terms of a two-species hybrid model. The results allowed to obtain a general picture of how the major characteristics of the satellite's plasma environment change as a function of orbital position. Nonetheless, the real Titan situation is significantly more complex.

On the one hand, Titan's ionosphere has been represented in a rather rough manner by incorporating only a single ionospheric species into the simulation model. Numerous ionospheric models, especially those designed by Keller *et al.* [75, 76, 77, 78], clearly illustrate that Titan's ionosphere exhibits a complex ion chemistry and that interaction processes between different species make up a major characteristic of this region. These aspects can be taken into account by magnetohydrodynamic models of Titan's plasma environment. However, covering these features in the framework of hybrid simulations is presently impossible. Even a parallel computer would be incapable of storing the data of a sufficiently high number of particles. Of course, one could design a simulation scenario that allows an extremely high spatial resolution in the immediate vicinity of the obstacle. It is presently difficult to create a simulation scenario that allows more than 100 grid nodes in each spatial direction. Therefore, in such a geometry, Titan itself would fill almost the entire simulation domain, i.e. the outer boundaries of the simulation box would be located quite close to the interaction region and would therefore possibly affect the plasma flow in the vicinity of Titan. For this reason, enhancing the spatial resolution of the ionosphere region by reducing the total size of the simulation box can definitely not be considered an option. Using the curvilinear fisheye grid is a step towards achieving a sufficient resolution in Titan's ionosphere region, but even by means of this grid, it is impossible to gain access to spatial scales below $0.1R_T$. Furthermore, when increasing the curvature of the fisheye grid, it becomes more likely that numerical stability is compromised. For this reason, a hybrid simulation including a detailed multi-species model of Titan's ionosphere is beyond the scope of any existing code. Nevertheless, the first question that such a multi-species ionosphere model should address is how the presence of several species of different masses would affect the global structure of the ionospheric tail. For this reason, the first stage of expansion for the model presented in the preceding chapters is the incorporation of a simple production profile for several different ionospheric species.

On the other hand, according to Voyager 1 measurements, the upstream plasma in the vicinity of Titan consists of two major species, hydrogen and nitrogen (cf. Neubauer *et al.* [119]). For the simulations that have been presented in the preceding chapters, these upstream plasma conditions have been approximated by using a singe ion species with an average particle mass and number density. The simulation results have shown that when Titan is located inside Saturn's magnetosphere, the magnetospheric flow pattern is not significantly affected by the presence of the obstacle. Of course, a region of reduced plasma density and velocity manifests downstream of Titan, but nevertheless, the effect on the upstream flow is definitely not as strong as in the case of Titan being exposed to a supermagnetosonic plasma flow. Since the two species that make up the upstream flow inside Saturn's magnetosphere have significantly different masses, it must be expected that their densities and velocities are modified on different scales. In general, the smaller the ion mass of an upstream species, the more significant should be the acceleration of the particles by the Lorentz force. For this reason, splitting up the upstream plasma flow in two different species must be considered a necessary extension of the simulation model presented in the preceding chapters.

The extension of the hybrid code to the case of multi-species conditions has been realized in two steps:

- In the first step, two additional ionospheric species have been incorporated into the model. In agreement with the approach presented by Modolo [106], Titan's ionosphere is assumed to consist of molecular nitrogen (N_2^+), methane (CH_4^+) and molecular hydrogen (H_2^+). Considering these three species as the major constituents of the pick-up tail is also in agreement with the work of Hartle *et al.* [60] who provide a preliminary interpretation of Titan's plasma interaction by analyzing data from the Cassini Plasma Spectrometer. The authors emphasize the strong analogy between the features observed during the Voyager 1 and the first Cassini flyby. For instance, the data collected during both flybys indicate H^+, H_2^+, N^+, CH_4^+ and N_2^+ to be the major pick-up species. Based on these measurements, Hartle *et al.* [60] also point out the important role that molecular nitrogen and methane play for the mass loading process, yielding a deceleration of the ambient magnetospheric plasma on the anti-Saturn-facing side of Titan. Although the modified hybrid model described in the present chapter does not include the ionospheric H^+ and N^+ ions, it should be capable of offering an adequate description of Titan's ionospheric tail structure: The dynamics of the ionospheric N^+ ions should be quite similar to that of methane, while the incorporation of H_2^+ ions into the model allows to gain access to the behaviour of very light ionospheric species. The three ionospheric species included in the modified simulation code should therefore rather be considered *representatives of certain ionospheric mass regimes* of the variety of chemical compounds in Titan's ionosphere. For instance, the dynamics of molecular nitrogen also resemble those of H_2CN^+, being one of the major products of the "chemical factory" in Titan's upper ionosphere. The upstream plasma, on the other hand, is still assumed to consist of a single species of mass $m = 9.67\,\text{amu}$ and density $n = 0.3 \cdot 10^6\,\text{m}^{-3}$. Hence, the model will include one species (N_2^+) which is significantly heavier than the upstream plasma species, another species (CH_4^+) whose mass is comparable to the ion mass in the upstream plasma flow, and finally a third species (H_2^+) whose mass is around a factor of 5 smaller than the ion mass in the upstream flow. Such an extension of the model should allow to identify major features of the ionospheric tail structure as a function of the relative ion mass as well as changes in the overall magnetic field topology that arise from the multi-species description of the ionosphere.

- In the second step, the multi-species description of the ionosphere has been maintained.

> In addition, the upstream plasma flow has been split up in the two species that have been measured during the Voyager 1 flyby. Hence, the simulation scenario will include five different ion species. Due to the high number of particles, this kind of simulation requires a huge amount of storage capacity and can barely be performed on a serial computer. These simulations are expected to allow a more sophisticated analysis of Titan's effect on the upstream plasma flow.

In the following sections, the results for the two different stages of extension of the existing hybrid model are presented. A simplifying analytical model of the pick-up process will allow to validate the simulation results. Besides, the applicability of the different approaches to the plasma environment of Titan will be analyzed in an extensive comparative discussion. The magnetospheric plasma parameters have been chosen in accordance to the Voyager 1 configuration. However, at first it will be shown that the electric field equation (3.38), taking into account two different electron populations, can easily be generalized to the case of multi-species conditions. In this and the following chapters, the term *multi-species* hybrid model refers to any scenario that takes into account a total number of more than two ion species.

Most of the results presented in the following sections have also been published in Annales Geophysicae [141].

1 Electric field equation

In section 3.3 of chapter 3, the basic concept of a hybrid model that contains two different ion components and consequently, two electron fluids, has been presented. This discussion can easily be generalized to the case of a hybrid code that takes into account an arbitrary number of N ion species. In principle, N different electron species (with different temperatures) have to be incorporated into the model as well. In this section, the electric field equation for such a scenario will be briefly discussed.

In the following it is assumed that the simulation contains N different ion species whose charge-neutralizing electron populations possess, in general, significantly different properties. The subscript j ($j = 1, \dots, N$) is introduced to distinguish between different electron populations. However, at this point, it is not relevant whether the ions and electrons are of magnetospheric or of ionospheric origin. The dynamics of each electron population are described by the momentum equation

$$0 = -en_{e,j}\left(\underline{E} + \underline{u}_{e,j} \times \underline{B}\right) - \nabla P_{e,j} \quad ; \quad j = 1, \dots, N \quad . \tag{6.1}$$

The quantities $n_{e,j}$, $\underline{u}_{e,j}$ and $P_{e,j}$ denote the mean density, velocity and pressure of electron species j, respectively. In order to obtain a single equation for the electric field, the N momentum equations (6.1) are added, yielding

$$0 = -e\underline{E}\sum_{j=1}^{N} n_{e,j} - e\left(\sum_{j=1}^{N} n_{e,j}\underline{u}_{e,j}\right) \times \underline{B} - \sum_{j=1}^{N} \nabla P_{e,j} \quad . \tag{6.2}$$

In analogy to eq. (3.34), a total electron density n_e is introduced by means of

$$n_e \equiv \sum_{j=1}^{N} n_{e,j} \quad . \tag{6.3}$$

In exactly the same manner, expression (3.36) can be generalized:

$$\underline{u}_e \equiv \frac{1}{n_e} \sum_{j=1}^{N} n_{e,j} \underline{u}_{e,j} \quad . \tag{6.4}$$

Hence, the electric field equation reads

$$\underline{E} = -\underline{u}_e \times \underline{B} - \frac{\sum_{j=1}^{N} \nabla P_{e,j}}{e n_e} \quad . \tag{6.5}$$

Incorporating Ampère's law and the charge density $\rho_c = en_e = en_i$ yields

$$\underline{E} = -\underline{u}_i \times \underline{B} + \frac{(\nabla \times \underline{B}) \times \underline{B}}{\mu_0 \rho_c} - \frac{\sum_{j=1}^{N} \nabla P_{e,j}}{\rho_c} \tag{6.6}$$

for the electric field. In this expression, $\underline{u}_i$ denotes the mean ion velocity at the respective position. However, again it is important to notice that the simulation model is able to distinguish between different ion densities *and* velocities, whereas it takes into account only a single electron velocity $\underline{u}_e$. The distinction between the electron populations that correspond to different ion species is realized only by means of the electron pressure terms. For the simulations discussed in this chapter, the electrons are assumed to be adiabatic, i.e.

$$P_e \propto \beta_{e,j} \, (n_{e,j})^{\kappa} \quad ; \quad j = 1, \ldots, N \quad . \tag{6.7}$$

The constant quantities $\beta_{e,j}$ are the plasma betas of the different electron populations, allowing to introduce an independent initial temperature for each of them. Again, a value of $\kappa = 2$ has been chosen for the adiabatic exponent. By including this set of N coupling expressions, a closed system of equations has been obtained. For the simulations presented in this work, the same value of $\beta_e = 0.083$ has been chosen for all involved ionospheric electron populations.

2 Ion pick-up at Titan

In order to understand the simulation results presented in the following sections, it is useful to at first discuss the ion pick-up process at Titan from a quantitative point of view. Specifically, the analysis refers to a single ionospheric particle of mass m and charge e which is inserted into the ambient magnetospheric plasma flow. The ion is treated as a *test particle*, i.e. its dynamics in a pre-defined electromagnetic field topology are considered. The particle's equation of motion reads

$$\ddot{\underline{x}} = \dot{\underline{v}} = \frac{e}{m} \left(\underline{E} + \underline{v} \times \underline{B} \right) \quad , \tag{6.8}$$

where $\underline{x}$ and $\underline{v}$ denote its position and velocity, respectively. Assuming the electric field to be governed by the convective term $\underline{E}_c = -\underline{u}_m \times \underline{B}$ yields

$$\dot{\underline{v}} = \frac{e}{m} \left(-\underline{u}_m + \underline{v} \right) \times \underline{B} \quad . \tag{6.9}$$

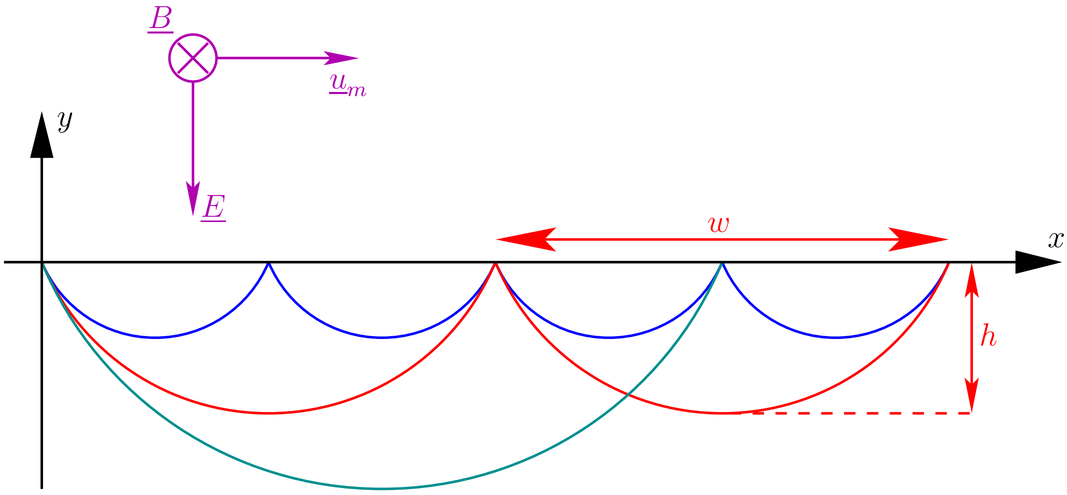

Figure 6.1: Schematic illustration of the pick-up process in Titan's equatorial plane. The homogeneous ambient plasma flow $\underline{u}_m$ is directed parallel to the x axis, whereas the background magnetic field $\underline{B}$ is oriented antiparallel to the z axis. The sketch shows the cycloidal motion of three ions with different masses which have been inserted into the magnetospheric plasma flow at $\underline{x}(t=0)=0$, their initial velocity being $\underline{v}(t=0)=0$. Both the height h and the width w of the cycloidal trajectories depend linearly on the ion mass. This is illustrated for three pick-up ions of mass m (blue), $2m$ (red) and $3m$ (cyan). Due to these differences in the height of the cycloids, the spatial extension of the ionospheric tail in the direction of the convective electric field is a measure of the particle mass.

In this expression, $\underline{u}_m$ denotes the mean magnetospheric plasma velocity. In the following, the discussion focuses on the situation in Titan's equatorial plane where, according to the simulation results presented in the preceding chapters, the magnetospheric plasma velocity is not significantly distorted by the presence of the obstacle. Therefore, without losing generality, $\underline{u}_m$ is assumed to be directed parallel to the positive x axis,

$$\underline{u}_m = \begin{pmatrix} u_m \\ 0 \\ 0 \end{pmatrix} \quad . \tag{6.10}$$

For simplicity, u_m is set to a spatially constant and positive value. In other words, the discussion refers again to the situation at 18:00 Saturnian local time. The geometry of this scenario is illustrated in fig. 6.1. Even in the case of highly draped field lines, the magnetic field is oriented almost perpendicular to the equatorial plane, i.e.

$$\underline{B} = \begin{pmatrix} 0 \\ 0 \\ B \end{pmatrix} \quad , \tag{6.11}$$

where B is negative and, for simplicity, considered to be spatially constant. Now, eq. (6.9) is transformed into the rest frame of the plasma by means of the Galilei transformation:

$$\underline{\mathcal{V}} = \underline{v} - \underline{u}_m \quad . \tag{6.12}$$

The transformed equation of motion is

$$\underline{\dot{\mathcal{V}}} = \frac{e}{m}\underline{\mathcal{V}} \times \underline{B} \qquad \text{or equivalently} \qquad \underline{\dot{\mathcal{V}}} = \underline{\underline{M}} \cdot \underline{\mathcal{V}} \tag{6.13}$$

with the 3 × 3 matrix

$$\underline{\underline{M}} = \begin{pmatrix} 0 & \Omega & 0 \\ -\Omega & 0 & 0 \\ 0 & 0 & 0 \end{pmatrix} \quad . \tag{6.14}$$

The ion gyrofrequency is given by

$$\Omega = \frac{eB}{m} \quad . \tag{6.15}$$

The solution of eq. (6.13) is obtained by diagonalizing the matrix $\underline{\underline{M}}$ and can be written as

$$\underline{\mathcal{V}}(t) = \xi_1 \begin{pmatrix} 0 \\ 0 \\ 1 \end{pmatrix} + \xi_2 \exp(i\Omega t) \begin{pmatrix} 1 \\ i \\ 0 \end{pmatrix} + \xi_3 \exp(-i\Omega t) \begin{pmatrix} 1 \\ -i \\ 0 \end{pmatrix} \quad , \tag{6.16}$$

where ξ_1, ξ_2 and ξ_3 are integration constants. Transforming $\underline{\mathcal{V}}$ in the rest frame of Titan by means of eq. (6.12) and assuming the ionospheric particle's initial velocity at $t = 0$ to be negligible (i.e. $\underline{v}(t = 0) = 0$) yields

$$v_x(t) = u_m (1 - \cos \Omega t) \quad ; \tag{6.17}$$

$$v_y(t) = u_m \sin \Omega t \quad ; \tag{6.18}$$

$$v_z(t) = 0 \quad . \tag{6.19}$$

The cosine and sine terms in eqs. (6.17) and (6.18) represent the particle's gyration in the plasma rest frame. Because of the constant term in eq. (6.17), a uniform motion in x direction is superimposed on this circular trajectory. Assuming that the particle is inserted into the ambient plasma flow at point $\underline{x}(t = 0) = (0, 0, 0)$ leads to the following expressions for the particle trajectory:

$$x(t) = \frac{u_m}{\Omega} (\Omega t - \sin \Omega t) \quad ; \tag{6.20}$$

$$y(t) = \frac{u_m}{\Omega} (1 - \cos \Omega t) \quad ; \tag{6.21}$$

$$z(t) = 0 \quad . \tag{6.22}$$

Hence, the pick-up ion moves in a plane perpendicular to the magnetic field, i.e. it remains confined to Titan's equatorial plane in the simplified case discussed here. It is important to notice that, due to $B < 0$, the ion gyrofrequency Ω is negative. By introducing

$$|\Omega| = -\frac{eB}{m} = \frac{e|B|}{m} \tag{6.23}$$

and the ion gyroradius

$$R_g = \frac{u_m}{|\Omega|} \quad , \tag{6.24}$$

Ion species	Molecular weight	Height h	Width w
H_2^+	2 amu	$0.4R_T$	$1.2R_T$
CH_4^+	16 amu	$3.1R_T$	$9.8R_T$
N_2^+	28 amu	$5.4R_T$	$17.1R_T$

Table 6.1: Due to the pick-up process, ionospheric ions are moving on cycloidal trajectories in the direction of $\underline{E} \times \underline{B}$. For three representative ion species, the table shows the width w and the height h of the cycloidal trajectories, as given by eqs. (6.28) and (6.29). The extensions of the cycloids are comparable to or even significantly larger than the diameter of Titan. It can also be seen that, perpendicular to the undisturbed flow direction, the cycloids are well located inside the simulation boxes, which possess an extension of $7.5R_T$ in E^+ direction. The magnetospheric plasma velocity u_m and the magnetic field magnitude $|B|$ in eqs. (6.28) and (6.29) have been set to $u_m = 120\,\mathrm{km/s}$ and $|B| = 5\,\mathrm{nT}$, respectively.

the particle trajectory takes the form

$$x(t) = R_g\left(|\Omega|\,t - \sin|\Omega|\,t\right) \quad ; \tag{6.25}$$

$$y(t) = R_g\left(\cos|\Omega|\,t - 1\right) \quad ; \tag{6.26}$$

$$z(t) = 0 \quad . \tag{6.27}$$

According to eqs. (6.25)-(6.27), the ionospheric ion performs a cycloidal motion in the plane perpendicular to the magnetic field, as displayed in fig. 6.1. The height h of one arc of the cycloid is given by

$$h = \left| y\left(t = \frac{\pi}{|\Omega|}\right)\right| = 2R_g = 2\frac{u_m m}{e|B|} \quad , \tag{6.28}$$

whereas its width w can be written as

$$w = x\left(t = \frac{2\pi}{|\Omega|}\right) - x(t=0) = 2\pi R_g = 2\pi\frac{u_m m}{e|B|} = \pi h \quad . \tag{6.29}$$

As can be seen from eqs. (6.28) and (6.29), both h and w depend linearly on the mass m of the pick-up ion. Therefore, it is important to notice that in Titan's equatorial plane, the parameter h determines the extension of the particle trajectory in the direction of the convective electric field. Consequentially, the extension of the ionospheric tail in the direction of the convective electric field is a measure of the mass of the respective ion species. For three representative species, the parameters w and h are listed in tab. 6.1.

Finally, it should be emphasized that the following simplifying assumptions have been incorporated into the approach presented in this section:

- The magnetospheric plasma in the vicinity of Titan is assumed to be spatially homogeneous. Therefore, the Hall term and the pressure term have not been included in the electric field equation.
- The effect of the newly generated pick-up ions on the electromagnetic field topology is neglected.
- The finite radius of the obstacle is not considered.

3 First step: Single-species upstream flow and multi-species ionosphere

In the first step, two additional ionospheric species have been incorporated into the simulation model. The heaviest of the three ionospheric species is molecular nitrogen ($m\left(N_2^+\right) =$ 28 amu), the corresponding production parameters are listed in table 3.2. Methane particles ($m\left(CH_4^+\right) = 16\,\text{amu}$) have been chosen as the second ionospheric species. The dynamics of these ions are also representative for the behaviour of atomic nitrogen (N^+), which is another important ionospheric constituent [77]. In agreement with the model developed by Modolo [106], molecular hydrogen ($m\left(H_2^+\right) = 2\,\text{amu}$) is assumed to be the third component of the model ionosphere. The model does not include interaction processes between ions of different species, such as collisions or charge exchange reactions. Moreover, due to the large size of the simulation box, the spatial resolution in the ionosphere region is limited, i.e. the diameter of a single cell of the simulation grid is of the order of 400 km. For this reason, a distinction between the specific features of different ionospheric production profiles cannot be realized by means of the existing model. Since resolving minor differences in the production profiles of the three species is not the objective of the present simulation study, the same production function has been used for nitrogen, methane and hydrogen.

Of course, this approach is also quite useful for restricting the numerical complexity of the ionosphere model. This configuration is in correspondence to the MHD study presented by Ma *et al.* [99], who assume the ion production rates in the three ionospheric mass regimes under consideration to be of nearly the same magnitude. As the discussion shall again focus on the global characteristics of Titan's induced magnetotail instead of covering the complex chemical properties of the ionosphere in detail, such an approach is absolutely justified. Besides, any difference between the flow patterns of the three species can definitely be ascribed to the different particle masses. Of course, for a direct comparison with ionosphere data from the Huygens descent [4] and from close-in Titan flybys, both the resolution near the surface and the quality of the ionosphere model would have to be improved.

By means of the modified simulation code, it is possible to gain access to the problem of how the flow pattern in the vicinity of Titan is affected by the multi-component nature of the satellite's ionosphere. Since the two-species composition of the magnetospheric plasma is not yet taken into consideration, any kind of modification in the electromagnetic field topology can be ascribed to the application of a more sophisticated model to the ionosphere. A comparison with a study of Titan's ionospheric tail conducted by Luhmann [96] will allow to validate the simulation results. In the following discussion, the three ionospheric species are denoted by the subscripts 1 (nitrogen), 2 (methane) and 3 (hydrogen).

3.1 18:00 Saturnian local time

The simulation discussed in this section refers to the case of Titan being located inside Saturn's magnetosphere at 18:00 Saturnian local time, i.e. the dayside of the obstacle faces the corotating magnetospheric plasma flow. The simulation geometry is displayed in fig. 4.1. For a cut through Titan's polar plane, fig. 6.2 displays the magnetospheric plasma density and velocity as well as the electromagnetic fields. The ionospheric densities and velocities for the

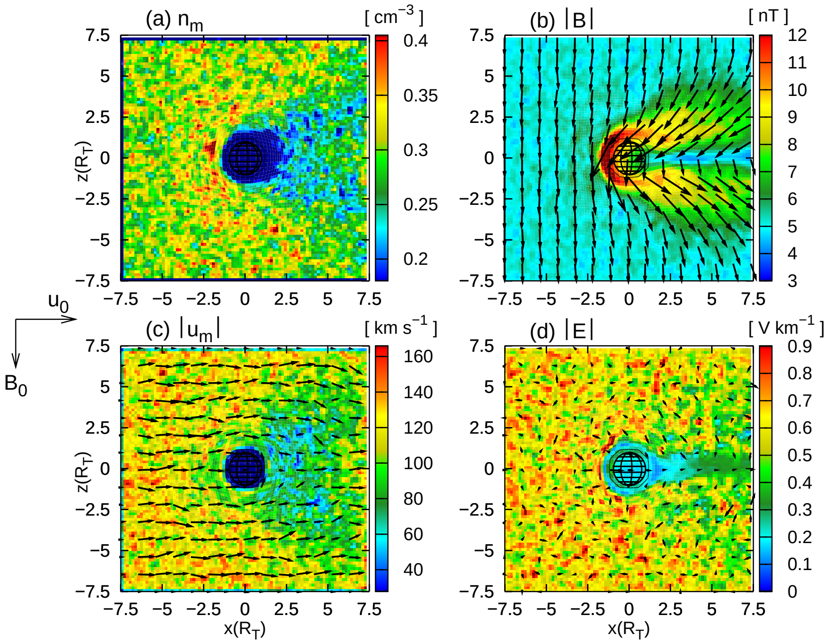

Figure 6.2: Titan's plasma environment at 18:00 Saturnian local time. In contrast to the simulations presented in the preceding chapters, the ionosphere is assumed to consist of three different species. The figure displays (a) the magnetospheric plasma density, (b) the magnetic field strength, (c) the magnetospheric plasma velocity and (d) the electric field strength for a cut through the polar plane, coinciding with the (x, z) plane of the coordinate system. Both the magnetospheric plasma parameters and the electromagnetic field configuration are quite similar to the results presented in the preceding chapters, i.e. these quantities are not significantly affected by the incorporation of CH_4^+ and H_2^+ into the simulation model.

same cutting plane are shown in fig. 6.3. Figures 6.4 and 6.5 illustrate the plasma parameters and the electromagnetic field quantities for a cut through the (x, y) plane of the coordinate system, being identical to Titan's equatorial plane.

As can be seen from fig. 6.2, the situation in the polar plane is quite similar to the results obtained by using a single-species ionosphere model (cf. fig. 4.6). Neither the magnetospheric plasma density nor the velocity is dramatically affected by the interaction with Titan's ionosphere[1], i.e. only a slightly pronounced wake cavity manifests in the downstream region. Besides, the magnetic draping pattern remains nearly unaffected by extending the complexity of the ionosphere model. The magnetic lobes are still confined to a region with a diameter of around $\pm 3R_T$ perpendicular to the direction of the undisturbed flow. The peak field strength achieved at Titan's dayside as well as the magnetic field enhancement in the lobes have almost the same values as in the two-species results displayed in fig. 4.6. The magnetic field topology in the vicinity of Titan arises mainly from the transport of the field lines by the plasma flow. Due to the ionospheric ion density in the magnetic lobe regions being negligible, the convection of the field lines along the flow is primarily governed by the magnetospheric

---

[1] The reason for this phenomenon will be revealed when the upstream plasma flow is split up in two species with different masses.

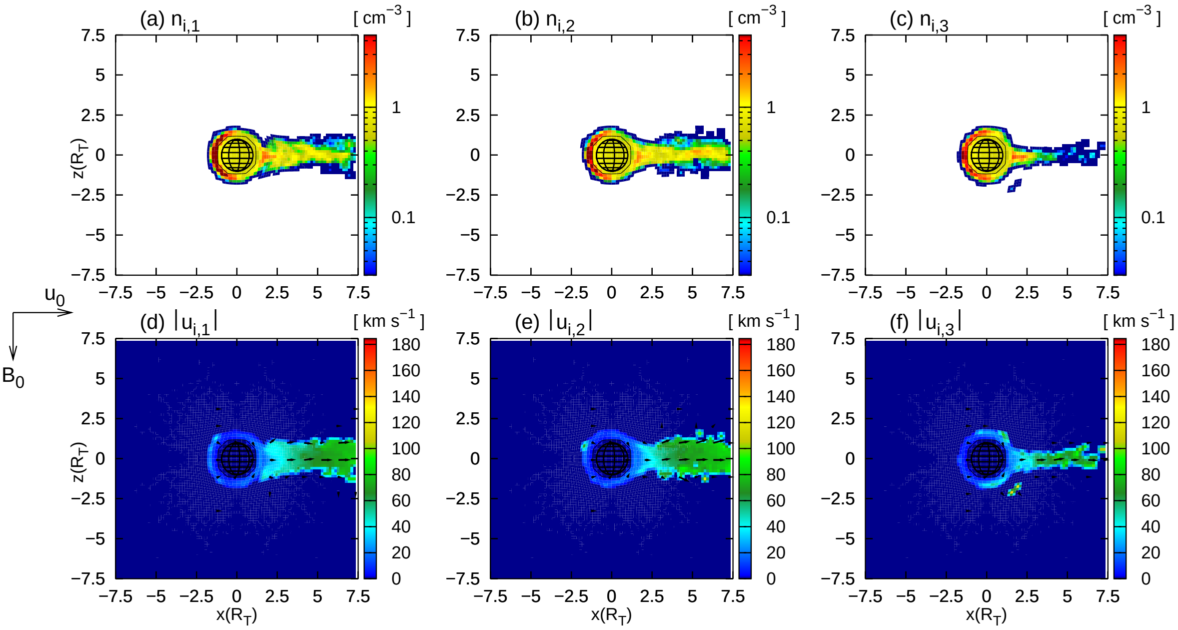

Figure 6.3: Titan's plasma environment at 18:00 Saturnian local time. The figure shows the ionospheric plasma parameters for a cut through Titan's polar plane. Figures (a) and (d) display the mean density $n_{i,1}$ and velocity $u_{i,1}$ of molecular nitrogen (N_2^+) ions, whereas figures (b) and (e) show the same parameters for the methane (CH_4^+) component of the ionosphere. The density and velocity of the lightest ionospheric species, molecular hydrogen (H_2^+), are displayed in figs. (c) and (f). Each of these species forms a narrow tail downstream of the obstacle. At least in the polar plane, no significant difference manifests in the tail structures of ions of different masses.

plasma, i.e. the convective electric field can be expressed as

$$\underline{E}_c = -\left(\frac{n_m}{n_m + \sum_{j=1}^{3} n_{i,j}} \underline{u}_m + \sum_{j=1}^{3} \frac{n_{i,j}}{n_m + \sum_{k=1}^{3} n_{i,k}} \underline{u}_{i,j} \right) \times \underline{B} \approx -\underline{u}_m \times \underline{B} \quad . \tag{6.30}$$

The change $\partial_t \underline{B}$ of magnetic field strength arising from this term can therefore be written as

$$\frac{\partial \underline{B}}{\partial t} = \nabla \times (\underline{u}_m \times \underline{B}) \quad , \tag{6.31}$$

i.e. magnetic field dynamics in the lobe regions are almost entirely controlled by the magnetospheric plasma. As the magnetospheric flow remains practically unaffected by the modification of the ionosphere model, the magnetotail structures obtained from the different simulation approaches are almost identical. As shown in fig. 6.3, in the downstream region, each of the three ionospheric species forms a narrow tail. Except for the particle density $n_{i,3}$ in the H_2^+ tail being around a factor of 5 smaller than in the other two tails, the overall wake structure of the three species in the polar plane is nearly identical.

In strong analogy to the results shown in fig. 4.7(c), a pronounced magnetic pile-up region is formed at Titan's dayside. As can be seen from fig. 6.4(b), the region of enhanced magnetic field strength is asymmetric with respect to the direction of the electric field. The major reason for the formation of this structure is the incapability of the frozen-in magnetic field

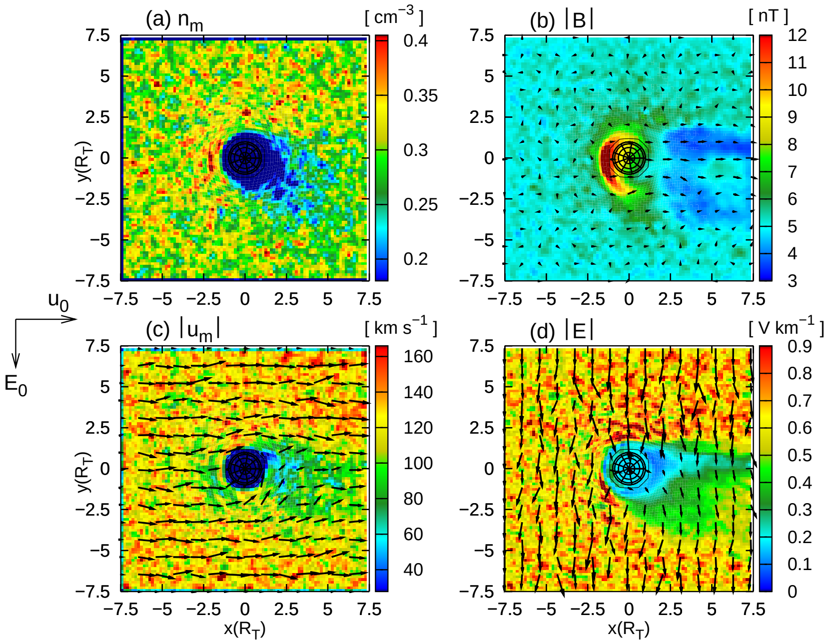

Figure 6.4: Titan's plasma environment at 18:00 Saturnian local time. In analogy to fig. 6.2, the figure displays the magnetospheric plasma parameters and the electromagnetic fields for a cut through the (x, y) plane which is identical to Titan's orbital plane. As the formation of the magnetic pile-up region at Titan's dayside is mainly governed by the field convection along the magnetospheric plasma flow, the magnetic field signature in the vicinity of Titan is quite similar to the results obtained by using a single-species ionosphere model. The magnetic field lines are incapable of penetrating into regions where the slow ionospheric plasma becomes predominant. Since even in the case of a single-species ionosphere model, the ionospheric density near Titan's dayside has shown to be around a factor of 17 higher than the ambient magnetospheric density, the process that leads to the formation of a magnetic pile-up region is not significantly affected by extending the ionosphere model to multi-species conditions.

to penetrate the dayside ionosphere region. As can be seen from figs. 4.7(b) and 6.5, in the dayside ionosphere region, even the density of a single ionospheric species is around a factor of $5/0.3 = 16.7$ higher than the ambient magnetospheric plasma density. Thus, the presence of a single ionospheric species seems to be absolutely "sufficient" to prevent the magnetic field lines from penetrating into the ionosphere. Consequently, the structure of the magnetic pile-up region at Titan's dayside is not significantly affected by the incorporation of two additional lighter ionospheric species into the model. The magnetic signatures displayed in figs. 4.7(c) and 6.4(b) are almost identical.

As shown in fig. 6.5, each of the three ionospheric tails exhibits a strong asymmetry with respect to the direction of the convective electric field. However, it is also obvious that the tail extension in the E^+ hemisphere differs significantly for the three species. This effect depends on the mass of the respective ion species and is in complete agreement with the analytical discussion given in the previous section. On the one hand, according to eq. (6.28), the height h of the cycloidal particle trajectories for molecular nitrogen ions is approximatively

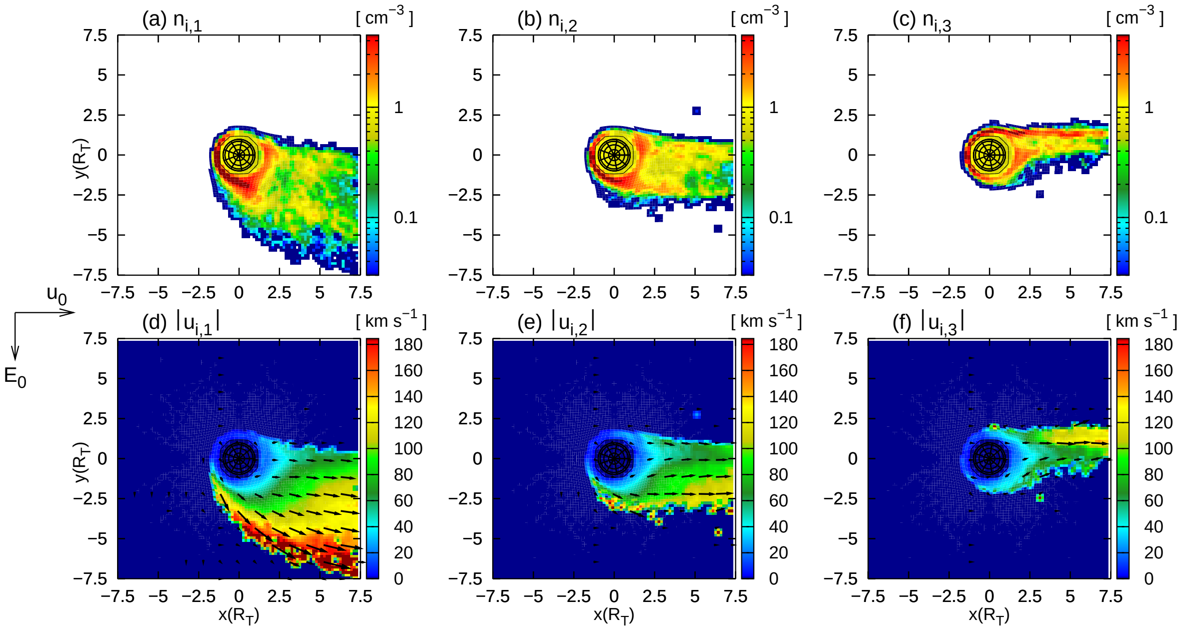

Figure 6.5: Titan's plasma environment at 18:00 Saturnian local time. The figure displays the ionospheric plasma parameters for a cut through Titan's equatorial plane. Specifically, the figure shows the densities (a) of molecular nitrogen ions, (b) of methane ions and (c) of molecular hydrogen ions. The corresponding plasma velocities are shown in figs. (d) to (f). Since at the Saturn-facing flank, the convective electric field is directed perpendicular to the tail and points inwards, each of the three ionospheric species is confined to the anti-Saturn facing hemisphere. The particles are moving on cycloidal trajectories, their extension h in the direction of the convective electric field depending linearly on the ion mass. For this reason, the nitrogen tail possesses the largest extension, whereas the hydrogen ions form only a narrow tail directly behind the obstacle. The tail structures are in good qualitative agreement with the results obtained from the simplifying analytical model. The spatial dispersion of ionospheric species of different masses is referred to as the *mass spectrometer effect* by Luhmann [96] who has also found evidence for the formation of such a structure in the Voyager 1 data. However, sufficiently homogeneous ambient magnetospheric plasma conditions are mandatory for the formation of such a natural ion mass spectrometer.

given by

$$h_{N_2^+} = 2\frac{u_m m}{e|B|} \approx 2\frac{120\,\mathrm{km/s}\cdot 28 m_p}{e \cdot 5\,\mathrm{nT}} = 5.4R_T \quad , \tag{6.32}$$

where u_m and $|B|$ have been set to the values of the undisturbed magnetospheric plasma. Although the finite size of the ion source is completely neglected, this estimate of the N_2^+ tail diameter yields a quite appropriate result: As displayed in fig. 6.5(a), in distances of $0 > y > -6R_T$ perpendicular to the undisturbed flow direction, the nitrogen density in the tail is comparable to or even larger than the ambient magnetospheric plasma density. On the other hand, the orientation of the tail with respect to the direction of $\underline{E}$ is also in complete correspondence to the theoretical discussion (cf. fig. 6.1).

The mass of methane ions is about a factor of 1.75 smaller than the molecular weight of N_2^+. Therefore, the ionospheric tail of this species should possess an extension of about

$$h_{CH_4^+} \approx \frac{5.4R_T}{1.75} = 3.1R_T \tag{6.33}$$

in the direction of the electric field. As can be seen from fig. 6.5(b), ionospheric methane ions can be found in distances below $2.7R_T$ perpendicular to the x direction. As the electromagnetic field topology in the vicinity of Titan is far from being spatially homogeneous, the simulation results are in reasonable agreement with the theoretical prediction of the simplifying test particle model.

Finally, the tail developed by the molecular hydrogen ions shall be investigated. As can be seen from fig. 6.5(c), the particles of this species are definitely forbidden to enter the Saturn-facing hemisphere of Titan. Furthermore, it is important to notice that significant hydrogen densities can be found only in a narrow tail region between $y \geq 0$ and $y \leq 1.5R_T$. Setting both the magnetic field strength and the magnetospheric plasma velocity to the undisturbed upstream values yields a height of

$$h_{H_2^+} \approx \frac{3.1R_T}{8} = 0.4R_T \tag{6.34}$$

for the cycloidal particle trajectories. Thus, the tail developed by the hydrogen ions is practically not shifted in the direction of the convective electric field. Since the plasma velocity directly behind Titan is around a factor 1.5 smaller than the upstream value of $u_0 = 120\,\mathrm{km/s}$ (cf. fig. 6.4(c)) and the magnetic field strength also differs from the homogeneous background value, the deviation of the theoretical value from the simulation result is absolutely expectable. However, assuming a field strength of $B \approx 4\,\mathrm{nT}$ and a mean plasma velocity of around $u_m = 80\,\mathrm{km/s}$ in the tail region (cf. figs. 6.4(b) and (c)) yields a modified height $\tilde{h}$ of

$$\tilde{h}_{H_2^+} \approx \frac{5}{6} h_{H_2^+} \quad , \tag{6.35}$$

which is almost identical to the original value. Therefore, one should keep in mind that the theoretical estimation of the tail extensions presented in the previous section is based on the simplifying assumption of a point-like ion source. Moreover, the analytical model does not account for any kind of spatial variation in $\underline{E}$ and $\underline{B}$, such as the reduction of the electric field strength due to the massive presence of slow ionospheric ions.

Reasonably good agreement between test particle calculations and simulation results could be achieved for the nitrogen and the methane ions. For the light H_2^+ ions, the finite extension of the obstacle and the distorted electromagnetic fields near Titan give rise to noticeable quantitative deviations from the test particle approach. In other words, the larger is the mass of an ionospheric ion species, the better is the extension of the corresponding tail in E^+ direction reproduced by the simplifying assumption of a point-like source that is embedded into a perfectly homogeneous flow.

However, this statement will have to be reconsidered after the application of a two-species representation to the magnetospheric plasma. Besides, although not being very prominent, the three tails shown in fig. 6.5 exhibit a quite interesting tendency: The smaller the mass of an ionospheric species, the more significant is the shift of the corresponding tail in E^- direction. This is at least roughly illustrated by comparing the locations of the Saturn-facing tail flanks.

3.2 Titan's ionospheric tail: A natural ion mass spectrometer

The spatial dispersion of the pick-up ion trajectories in Titan's ionospheric tail has also been investigated by Luhmann [96] who has applied a simple numerical test particle model to the situation during the Voyager 1 flyby. In complete agreement with the simulation results presented in the previous section, Luhmann [96] predicts the formation of a broad and highly asymmetric wake in which ion species of different masses become spatially dispersed. Therefore, Luhmann [96] suggests that Titan's ionospheric tail may be considered a *natural ion mass spectrometer*. In agreement with the hybrid simulation results presented above, it is illustrated that light hydrogen ions are confined to the plasma flow wake directly behind Titan, whereas the heavier ions move on cycloidal trajectories in Titan's equatorial plane, the extension of the cycloids in the direction of the convective electric field depending on their masses. Thus, a spacecraft that passes through Titan's ionospheric wake should be able to detect a sequence of ion beams of different masses. The ion flux in each of these beams should be a direct measure of the ion production rate as well as of the corresponding neutral density of the respective species. The results of the study conducted by Luhmann [96] have shown to be fully reproducible in the framework of the hybrid model. As Luhmann [96] has also found evidence for the occurrence of such a mass spectrometer effect in the data obtained by Voyager 1, it is reasonable to expect the formation of such a spatially dispersive tail structure, at least in the case of sufficiently homogeneous ambient magnetospheric conditions. If Titan's plasma environment is highly perturbed by local magnetospheric variations, the formation of the "mass spectrometer" is most likely suppressed and therefore, a clear distinction between species of different masses is no longer possible.

4 Multi-species versus single-species ionosphere model

Due to the height of the molecular nitrogen component's cycloidal trajectories being largest, the extension of the ionospheric N_2^+ tail in the direction of the electric field exceeds the tail diameters of the two lighter species. Therefore, the N_2^+ ions also determine the extension of the cavity in the electric field strength, being characteristic of the field topology in the equatorial plane. The trajectories of newly generated CH_4^+ and H_2^+ ions are almost completely located inside this electric field cavity and therefore, the pick-up force acting on these ions is significantly weaker than the force on the nitrogen ions. As displayed in figs. 6.5(d)-(f), the velocity of the nitrogen ions at the tail's anti-Saturn-facing flank exceeds the maximum velocity of both other species by almost a factor of 2 and is even significantly larger than the upstream magnetospheric flow velocity. Although the CH_4^+ and H_2^+ ions are lighter than the molecular nitrogen particles and hence, even a reduced Lorentz force should be able to provide an acceleration that is comparable to the effect on the N_2^+ ions, the CH_4^+ and H_2^+ velocity near the tail's flank in the E^+ hemisphere does not match the N_2^+ velocity. In other words, the pick-up process of the light ionospheric species is slowed down by the heaviest one. This process emerges from the impact of the heaviest ionospheric species on the electric field topology.

In any case, the major features of the electric field topology in the equatorial plane seem to be determined by the heaviest ionospheric species, for their gyration trajectories possess the

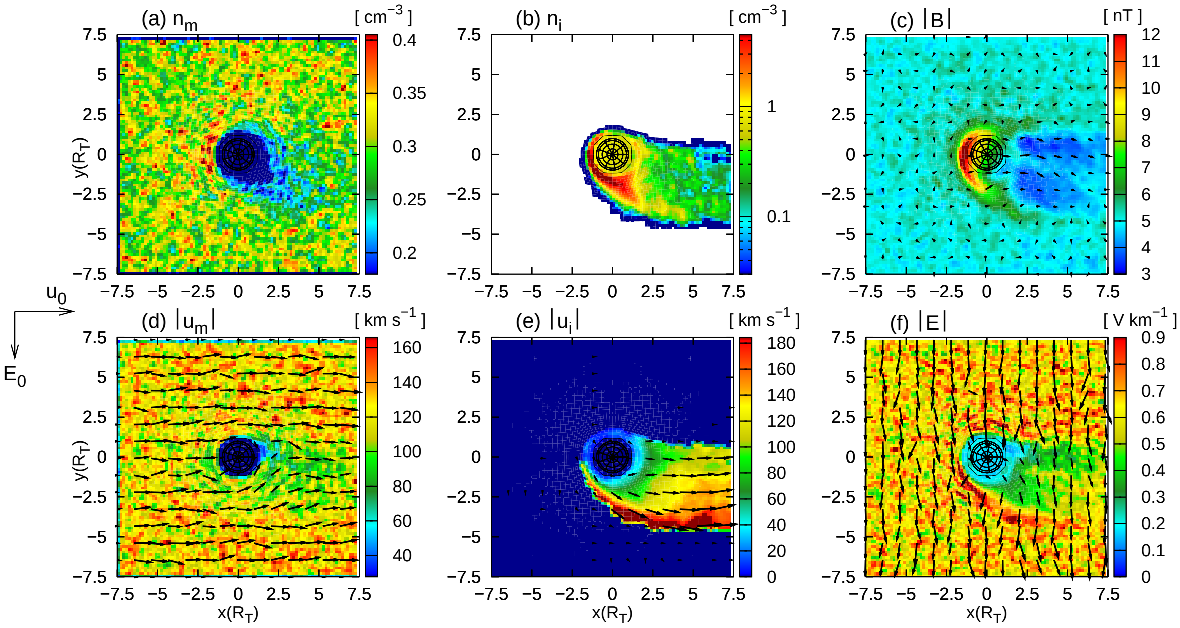

Figure 6.6: Titan's plasma environment at 18:00 local time. The figure displays a cut through the equatorial plane for the case of methane being the only species of ionospheric origin. Compared to the results for a three-species ionosphere, the peak ionospheric velocity u_i that is achieved by the CH_4^+ ions in the E^+ hemisphere is about a factor of 1.5 higher. The extension of the electric field cavity in E^+ direction is determined by the shape of the methane tail.

largest extension. Since the tails of the lighter species, CH_4^+ and H_2^+, are almost completely located inside the area covered by the N_2^+ tail, they are unable to alter the extension of the electric field cavity. Of course, if the two-species hybrid simulations presented in chapters 3 and 4 had contained molecular hydrogen or methane instead of molecular nitrogen as the only ionospheric species, an additional incorporation of the heavy N_2^+ ions would have gone along with a widening of the cavity in the electric field strength. Therefore, if a simulation model is meant to provide a global picture of the electric field structure in the vicinity of Titan, it is sufficient to include the heavy ionospheric species, such as molecular nitrogen. The incorporation of relatively light ions like methane or hydrogen is mandatory for covering the ionospheric mass spectrometer effect, but it cannot significantly alter the electric field topology. Besides, the major features of the magnetic draping pattern have also proven to be completely covered by the two-species model. In the E^+ hemisphere, the magnetic pile-up region is nearly aligned with the outer flank of the N_2^+ tail. Since the flank of the CH_4^+ tail is less steep, the magnetic field does not "notice" the additional incorporation of these ions into the model. As the H_2^+ tail does not expand into the E^+ hemisphere, it cannot take influence on the asymmetric structure of the pile-up region either.

These aspects are also illustrated in fig. 6.6. For the case of Titan's dayside being exposed to the upstream plasma flow, the figure displays the situation in the equatorial plane when methane ions (CH_4^+) are the *only* species of ionospheric origin. Compared to the multi-species run that includes both the methane and the molecular nitrogen component of the ionosphere, the diameter of the electric field cavity is clearly reduced, since the gyroradii of methane ions are smaller than those of molecular nitrogen. In addition, the peak velocity that the methane ions achieve in the E^+ pick-up region matches the value achieved by the N_2^+ ions in the multi-species simulation (cf. fig. 6.5(d)). The mean velocity of the pick-up flow is about a factor of 1.5 higher than in the methane tail that is developed when the ionosphere also consists of molecular nitrogen (cf. figs. 6.5 and 6.6). This clearly illustrates that the pick-up process of the lighter species is *enslaved* by the heaviest one. Of course, a major condition for such a behaviour is that the production rate and therefore, the number density of the heaviest species in the wake, is sufficiently large. Otherwise, the heavy N_2^+ ions would neither affect the electromagnetic field topology nor the pick-up process of the lighter ions. In section 6, these aspects will be discussed in more detail.

To sum up the major result, in the case of a multi-species ionosphere, the heavy nitrogen ions form an extended tail in the E^+ hemisphere and, at the outer flank of this tail, achieve a velocity that even exceeds the magnetospheric flow velocity by a factor of 2. However, directly behind Titan, the formation of the N_2^+ tail goes along with the development of a cavity in the electric field strength. Due to their smaller masses, the newly generated methane and molecular hydrogen ions are developing a tail structure that is almost completely located inside the electric field cavity. Therefore, they experience a reduced pick-up force and are unable to match the high velocities at the outer flank of the N_2^+ tail.

5 Second step: Multi-species upstream flow and multi-species ionosphere

The most critical simplification that has remained in the model is the approximation of the ambient magnetospheric plasma conditions by using a single ion species. According to Voyager 1 data, the plasma flow that impinges on Titan's ionosphere consists of two major species: atomic nitrogen (N^+) and hydrogen (H^+) ions. This aspect of Titan's plasma interaction will be addressed in the following sections. Of course, the simulations will also maintain the multi-species nature of Titan's ionosphere.

It is interesting to notice that, even though the temperature of the hydrogen component, $kT_{H^+} = 210\,\text{eV}$, is around a factor of $2900\,\text{eV}/210\,\text{eV} \approx 14$ smaller than the temperature of the nitrogen ions (cf. Neubauer *et al.* [119]), the thermal velocities

$$v_{\text{th}} = \sqrt{\frac{3kT}{m}} \tag{6.36}$$

of both species are almost identical. Due to the mass of the hydrogen ions being about a factor of 14 smaller than the mass of atomic nitrogen, the thermal velocity of H^+ reads

$$v_{\text{th,H}^+} = \underbrace{\sqrt{\frac{210}{2900} \cdot 14}}_{\approx 1} v_{\text{th,N}^+} \approx v_{\text{th,N}^+} \quad . \tag{6.37}$$

Since the mean velocity value

$$v_{\text{th,H}^+} \approx v_{\text{th,N}^+} = 244\,\text{km/s} \tag{6.38}$$

is around a factor of 2 higher than the upstream velocity of $u_0 = 120\,\mathrm{km/s}$, the dynamics of both the hydrogen and the nitrogen ions are mainly governed by their thermal motion. The hypothetical (N^+/H^+) ions feature the same property.

In the following sections, the simulation results obtained with the five-species code will be presented. Four geometries shall be considered: At first, the case of Titan's dayside being exposed to the upstream plasma at 18:00 local time will be revisited. This situation will be directly compared to the case of the upstream flow interacting with Titan's nightside ionosphere at 06:00 local time. Moreover, a comparative analysis of the results for 00:00 LT and 12:00 LT will show that the influence of the magnetospheric flow velocity on the structure of Titan's plasma environment is significantly stronger than suggested by the original simulation runs.

In all figures presented in the following sections, the magnetospheric ion species will be denoted by the subscripts $m, 1$ (nitrogen) and $m, 2$ (hydrogen). The three ionospheric components are again denoted by the subscripts $i, 1$ (nitrogen), $i, 2$ (methane) and $i, 3$ (hydrogen), respectively.

5.1 18:00 Saturnian local time

The simulation results for the case of Titan's dayside being exposed to the upstream plasma flow are presented in figs. 6.7-6.10. Figure 6.7 displays the magnetospheric plasma parameters and the electromagnetic fields for a cut through the polar plane, coinciding with the (x, z) plane of the coordinate system. The ionospheric plasma densities and velocities for the polar plane are shown in fig. 6.8. For a cut through Titan's orbital plane, the magnetospheric and ionospheric parameters as well as the field quantities are displayed in figs. 6.9 and 6.10, respectively. Due to the high thermal velocity, the magnetospheric plasma parameters exhibit a rather blurred and diffuse structure. Therefore, the interpretation given in this section will be supported by an additional simulation run, assuming the thermal velocity of the H^+ component to be about a factor of 5 smaller than in the Voyager 1 scenario. In this modified geometry, some of the structures will be sharper and therefore, better identifiable. The results are presented in the next section.

As can be seen from figs. 6.7(a) and (d), the signatures developed by the heavier magnetospheric species N^+ exhibit a strong similarity to the results that have been obtained by assuming the upstream plasma to consist only of a single species. Obviously, a slightly pronounced cavity of reduced N^+ plasma density arises downstream of the obstacle, the particle density being around a factor of 0.7 smaller than in the undisturbed upstream flow. In the same region, the velocity $u_{m,1}$ decreases from values around $120\,\mathrm{km/s}$ to a value of only $80-90\,\mathrm{km/s}$. The weak reaction of the nitrogen component on the presence of the obstacle is in complete correspondence to the interaction of a single-species flow with Titan's ionosphere. This analogy is absolutely expectable, for the mass of nitrogen ions differs only by a factor of 1.5 from the mass of the hypothetical (N^+/H^+) species that had represented the impinging magnetospheric plasma. In other words, at a certain position in the simulation box, a nitrogen ion and a hypothetical (N^+/H^+) ion would experience the same Lorentz force as well as – because their masses are of the same order of magnitude – the same acceleration

$$\underline{\ddot{x}} = \frac{e}{m}\left(\underline{E} + \underline{v} \times \underline{B}\right) \quad . \tag{6.39}$$

Hence, the global topology of the plasma parameters should exhibit a quite similar structure.

However, the mass of the second upstream species H^+ is one order of magnitude smaller than the mass of the hypothetical (N^+/H^+) particles. Moreover, in the scenario under consideration, the mass of the hydrogen ions is about a factor 14 smaller than the mass of the other upstream species N^+. At a certain position, a hydrogen particle experiences the same electromagnetic fields as a nitrogen particle and hence, the Lorentz force acting on both ions is of the same strength. Nevertheless, as expressed by eq. (6.39), the acceleration of the hydrogen ion is around a factor 14 larger. Therefore, as can be seen in figs. 6.7(b) and (e), in the vicinity of Titan, the plasma parameters of this species undergo a noticeable

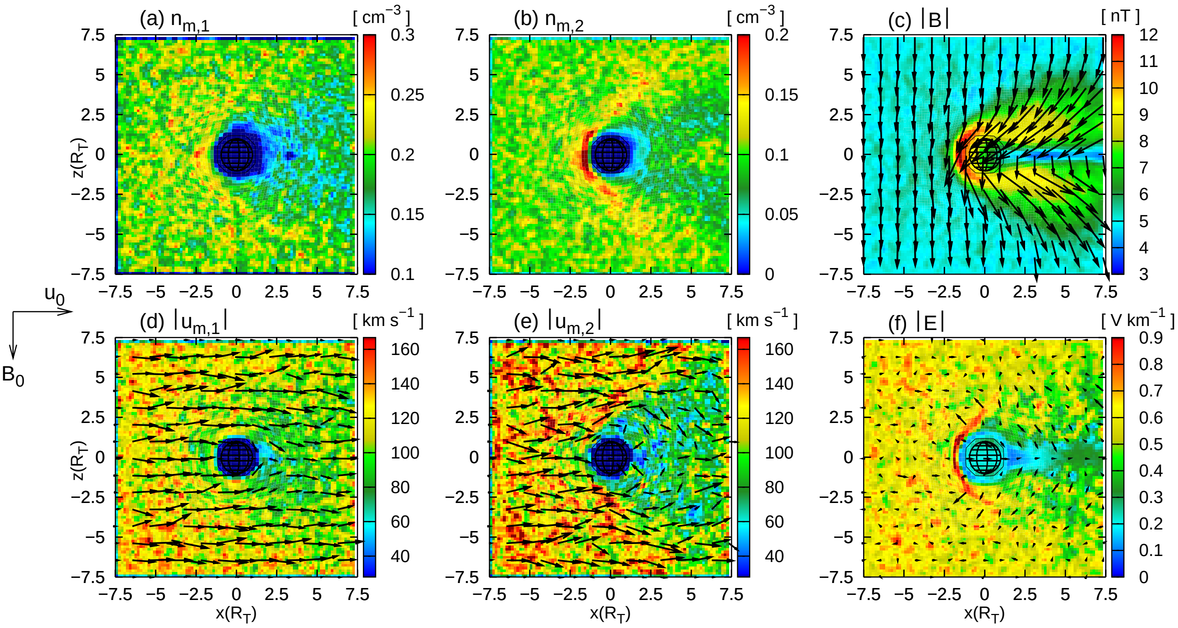

Figure 6.7: Titan's plasma environment at 18:00 local time. On the one hand, the multi-species nature of the ionosphere has been maintained, but on the other hand, the magnetospheric plasma flow is now represented by two distinct ion species. For a cut through the polar plane, the figure displays (a) the magnetospheric N^+ density $n_{m,1}$, (b) the magnetospheric H^+ density $n_{m,2}$, (c) the magnetic field, (d) the mean N^+ velocity $u_{m,1}$, (e) the mean H^+ velocity $u_{m,2}$ and (f) the electric field strength. The heavy nitrogen ions behave similar to the hypothetical (N^+/H^+) ions that have represented the magnetospheric plasma flow in foregoing simulations, since the masses of these two species differ only by a factor of 1.5. Only a slight reduction of N^+ density occurs downstream of the obstacle; the mean velocity vectors of this species are nearly parallel to the $(+x)$ direction in the entire interaction region. Even though both magnetospheric species experience the same electromagnetic fields, determining the Lorentz force, the acceleration of the light H^+ ions is about a factor of 14 larger than the effect on the N^+ particles. Therefore, the H^+ ions are clearly deflected around the obstacle. As can be seen in fig. (e), near the outer flanks of the magnetic draping pattern, the mean H^+ velocity vectors form an angle of $\pm 45°$ with the $(+x)$ direction. A slight cavity of reduced H^+ density arises downstream of the obstacle, its cone-like structure resembling the plasma wake in the case of Titan being exposed to a supersonic flow. Although, due to their high thermal velocity, the separation of the two magnetospheric species is definitely not as sharp as the effect that manifests in the equatorial ionospheric tail structure, the flow patterns displayed in figs. (b) and (e) may indicate that the magnetospheric flow also exhibits some kind of mass spectrometer effect.

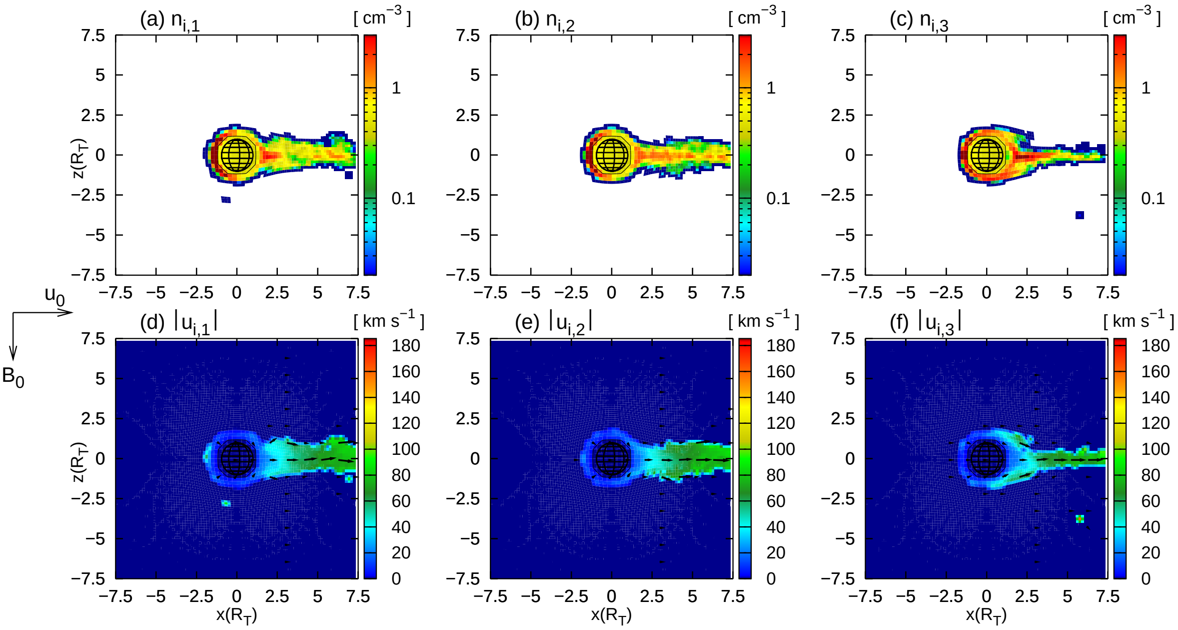

Figure 6.8: Five-species simulation of Titan's plasma environment at 18:00 local time – Ionospheric plasma parameters. For a cut through the polar plane, the figure displays the densities of (a) molecular nitrogen, (b) methane and (c) molecular hydrogen. The corresponding velocities are shown in figs. (d)-(f), respectively. Each of the three species forms a narrow tail downstream of the obstacle. The tail structure corresponds to the results obtained from the more simplifying single-species ionosphere model. Due to the small velocity of the ionospheric ions, a narrow cavity of reduced electric field strength is formed directly behind the obstacle.

modification. The hydrogen particles are clearly deflected around the obstacle, giving rise to a cone-shaped region of slightly reduced hydrogen density in the downstream region. As displayed in fig. 6.7(b), the structure of the H^+ wake exhibits at least a distant similarity to the cavity of reduced magnetospheric density that was formed in the case of Titan being exposed to a supersonic upstream plasma flow (see also Simon *et al.* [140]). In contrast to the flow pattern of the nitrogen component, the velocity vectors of the hydrogen component are noticeably distorted near the flanks of the tail, i.e. the flow is guided along the flanks of the cone-like cavity and is at least partially forbidden to penetrate this structure. The interaction leads to the formation of a diffuse, parabolically shaped area of slightly enhanced hydrogen density that is surrounding the H^+ wake. This structure is clearly identifiable near the dayside of the obstacle (cf. fig. 6.7(b)). Due to the electron pressure terms, this slight density enhancement goes along with the formation of electric fields that are directed radially away from the obstacle, as can be seen near the ramside of Titan in fig. 6.7(f). Since the velocity of the ionospheric ions in the tail region (cf. fig. 6.8(d)-(f)) almost vanishes, their contribution to the convective electric field is practically negligible. Consequently, the electric field strength in the polar plane achieves its minimum value along the x axis where the ionospheric ions are predominant.

The velocity plots of nitrogen and hydrogen for the polar plane (cf. fig. 6.7) clearly illustrate that the smaller is the mass of an impinging ion species, the more significant is the deflection that the particles experience in the vicinity of the obstacle. Thus, in analogy to the ionospheric

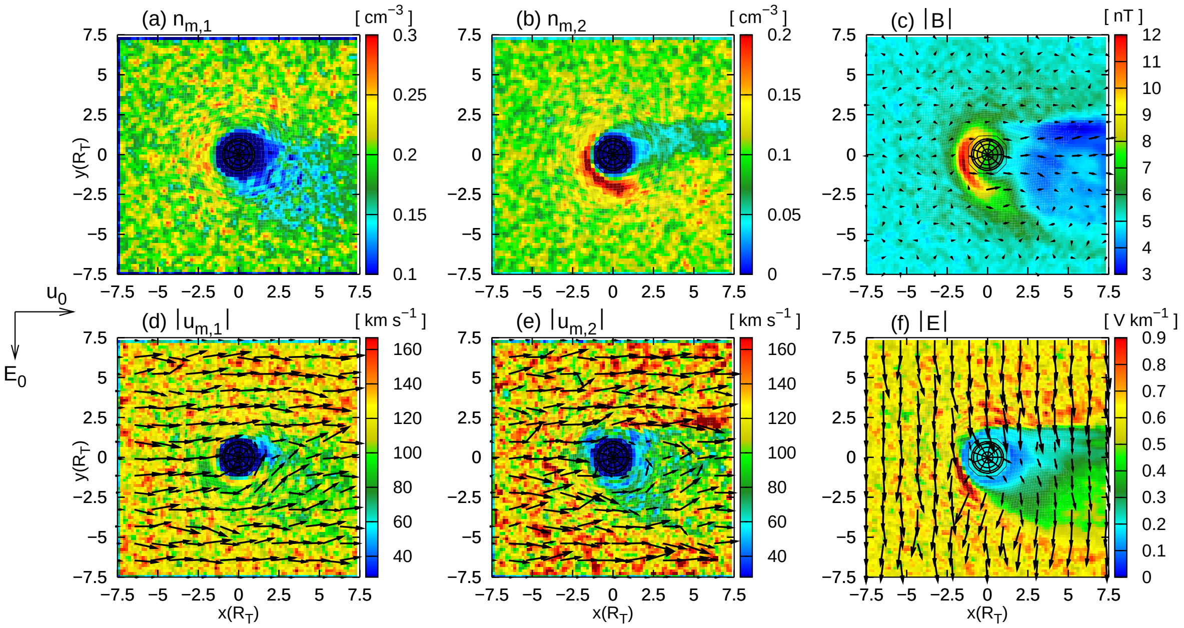

Figure 6.9: Five-species simulation of Titan's plasma environment at 18:00 local time – Magnetospheric plasma parameters and electromagnetic fields in the equatorial plane. The figure displays the N^+ density and velocity (figs. (a) and (d)), the H^+ density and velocity (figs. (b) and (e)) and the electromagnetic fields (figs. (c) and (f)). In the E^+ hemisphere, a certain fraction of the light hydrogen ions are incapable of gaining access to the central tain region, i.e. these particles are moving along the outer flank of the nitrogen tail. Due to this effect, the extension of the magnetic pile-up region in the E^+ hemisphere is enlarged. In the simulations that applied a single-species representation to the upstream flow, the pile-up region possessed an extension of less than $3.5R_T$ in the direction of $\underline{E}$, while in fig. (c), a sharp magnetic field enhancement is clearly identifiable in a distance of about $5R_T$. In the central tail region downstream of Titan, the magnetospheric ions tend to move antiparallel to the weakened electric field.

tail, the magnetospheric plasma flow in the vicinity of Titan exhibits some kind of *mass spectrometer effect*. The light upstream species is at least partially incapable of gaining access to the central tail region, whereas only a slight deflection of the nitrogen flow occurs. This *magnetospheric ion mass spectrometer* should at least allow a rough distinction between heavy and light upstream ions, for the latter ones should not be predominant in the central wake downstream of the obstacle. In contrast to the ionospheric ion mass spectrometer, this effect should be observable in the polar plane which is directed perpendicular to the convective electric field. Besides, the mechanism that leads to the partial separation of nitrogen and hydrogen ions is quite different from the distinction between ionospheric species, the width of their cycloidal pick-up trajectories depending on the particle masses. Future investigations that use a parallel computer and a noticeably higher number of macroparticles[2] could possibly examine the degree to which the upstream mass spectrometer allows to distinguish between ion species with comparable masses. As demonstrated in the preceding section, although the masses of the molecular nitrogen and the methane pick-up ions differs only by a factor of 1.75, a clear separation of both species manifests in the ionospheric tail structure. It would be interesting to know whether the upstream mass spectrometer possesses a similarly high

---

[2] Details are discussed in appendix B.

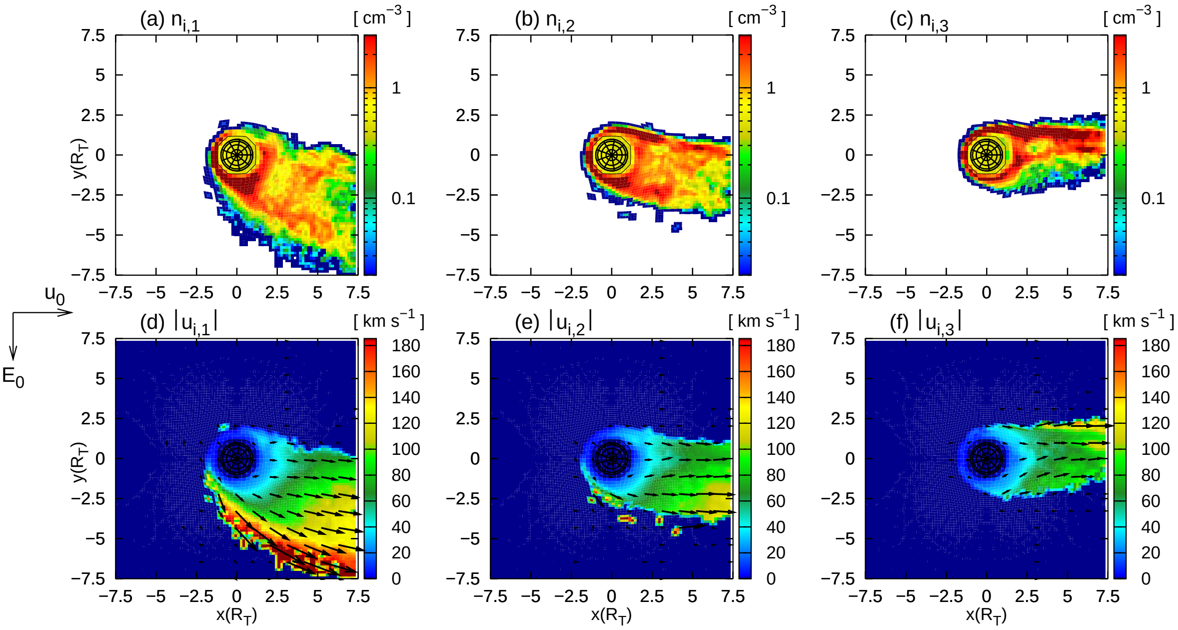

Figure 6.10: Five-species simulation of Titan's plasma environment at 18:00 local time – Ionospheric densities and velocities in the equatorial plane. The figure displays the density and velocity of molecular nitrogen (figs. (a) and (d)), methane (figs. (b) and (e)) and molecular hydrogen (figs. (c) and (f)). The mass spectrometer effect in the ionospheric tail structure is clearly identifiable. Again, the nitrogen tail possesses an extension of more than $5R_T$ in the flow direction, whereas the major concentration of light H_2^+ ions is confined to a narrow region directly behind the obstacle. The ionospheric densities in the central tail are about a factor of $1.5-2$ higher than in the simulation using a single-species model for the upstream flow. Since, compared to the results presented in section 3.1, the electromagnetic fields inside the tail are at least slightly reduced, the Lorentz force dragging the newly generated ionospheric particles away from Titan is also weaker, allowing the ionospheric particles to accumulate near the obstacle to a higher degree. However, the strong resemblance to the results presented in the preceding sections indicates that the overall topology of the tail is well covered by applying a single-species representation to the magnetospheric plasma.

sensitivity, or if it only allows a rough discrimination between light and heavy species, whose masses differ by an entire order of magnitude. In any case, a critical aspect is the extremely high thermal velocity of the magnetospheric ions. The extent to which the ion temperature takes influence on the hydrogen and nitrogen tail structures and the spectrometer phenomenon will be investigated in the following section.

The magnetic draping pattern in the polar plane (cf. fig. 6.7(c)) resembles the field topology obtained from the simulation runs with a single upstream species, except for a minor reduction of the maximum value that is reached in the dayside pile-up region. The extension of the magnetic lobes perpendicular to the undisturbed upstream flow direction is not significantly affected. The convection of the field lines along the flow is described by the expression

$$\frac{\partial \underline{B}}{\partial t} = \nabla \times \left[\left(\frac{n_{m,1}}{n_{m,1}+n_{m,2}} \underline{u}_{m,1} + \frac{n_{m,2}}{n_{m,1}+n_{m,2}} \underline{u}_{m,2} \right) \times \underline{B} \right] \quad , \tag{6.40}$$

i.e. in general, the formation of the magnetic lobes is governed by the dynamics of both upstream species. The nitrogen component behaves similar to the hypothetical (N^+/H^+)

ions. In the entire interaction region, their mean velocity is almost parallel to the positive x axis. In contrast to this, the H^+ flow pattern is strongly modified by the deflection of this species around the central tail region. Due to the upstream N^+ density being around a factor 2 higher than the density of H^+, the formation of the draping pattern is still mainly governed by the heavier nitrogen ions, behaving quite similar to the single-species (N^+/H^+) upstream plasma. Only in regions of increased H^+ density – for instance, near the outer flanks of the cone-like wake region at Titan's ramside –, the influence of the term that depends on $\underline{u}_{m,2}$ may be enhanced (cf. eq. (6.40)). Nevertheless, comparing the magnetic field pattern in fig. 6.7(c) with the results presented in the preceding sections clearly indicates that this effect may only be of minor relevance. As will be discussed below, the modification of the magnetic field topology is significantly more prominent in the equatorial plane.

In strong analogy to the simulation presented in section 3, in the polar plane, each of the three ionospheric species forms a narrow tail between the lobes, being confined to an area with a diameter of less than $\pm 2R_T$ perpendicular to the flow direction. The ionospheric mass spectrometer effect does not manifest in this cutting plane. Thus, even though the flow characteristics of the magnetospheric N^+ and H^+ ions are modified on different scales, the tail structure in the polar plane may not be adequate for a discrimination between different ionospheric populations.

The simulation results for Titan's equatorial plane are shown in figs. 6.9 and 6.10, respectively. Again, the ionospheric tail exhibits a pronounced mass spectrometer effect. The structure of the tail is not significantly affected by splitting up the upstream flow in two components. In analogy to the behaviour of the hypothetical (N^+/H^+) ions, a slightly pronounced, but nevertheless asymmetric cavity occurs in the nitrogen density downstream of the obstacle. Furthermore, in complete correspondence to the results obtained by using a single upstream species, a cavity of reduced electric field strength is formed in the wake region. In the E^- hemisphere, this cavity is sharply confined. In contrast to this, it possesses an extension of more than $5R_T$ in the direction of the undisturbed convective electric field, its flank in the E^+ hemisphere forming an angle of about 40° with the direction of the undisturbed plasma flow. A slight cavity of reduced hydrogen density arises downstream of the obstacle (cf. fig. 6.9(b)), its flank in the E^- hemisphere being located at nearly the same position as the flank of the ionospheric tails and the outer boundary of the electric field cavity. This feature will become significantly more prominent in the ancillary simulation run presented in the subsequent section. As can be seen from figs. 6.9(d) and (e), in the E^- hemisphere, the flow velocities of both magnetospheric species are directed almost parallel to the outer flank of the electric field cavity, illustrating that these ions seem to be at least partially incapable to cross the tail's boundary in the Saturn-facing hemisphere from outward to inward. The electron pressure gradient near the tail's flank in the E^- hemisphere has proven to be the major reason for this deflection process.

In the anti-Saturn facing hemisphere, the hydrogen flow is also deflected around the tail region which is denoted by an increased density of ionospheric ions. As displayed in fig. 6.9(e), in the E^+ hemisphere, the H^+ ion velocity is directed nearly parallel to the flank of the ionospheric tail, the velocity vectors forming an angle of about 30° with the $(+x)$ direction. As H^+ ions are at least partially incapable of gaining access to the tail region downstream of Titan, they are pressed against the anti-Saturn-facing flank of the ionospheric tail and are guided along this boundary layer. This gives rise to a pronounced, highly asymmetric region of enhanced hydrogen density near the ramside of Titan.

However, the flow pattern of the magnetospheric nitrogen ions is practically not affected when these particles encounter the tail's flank in the E^+ hemisphere. As can be seen in fig. 6.9(f), at the tail's flank in the E^+ hemisphere, the convective electric field arising from the fast pick-up ions is directed perpendicular to the tail and points outwards. Therefore, it poses a potential barrier to any positive ion that attempts to enter the tail region from outward to inward. Even though both magnetospheric species experience the same electric field barrier, the acceleration of the heavy N^+ ions is about a factor 14 smaller than the effect on the light H^+ particles. Thus, the velocity of the N^+ ions is practically not altered. In contrast to this, a larger fraction of the H^+ ions, which attempt to gain access to the central tail region, is decelerated, making them partially incapable of passing into the ionospheric tail. As can be seen from fig. 6.9(f), the region of maximum electric field strength near the tail's flank coincides with the location of the H^+ density enhancement near the ramside of Titan. The component of the H^+ velocity tangential to the boundary layer partially cancels with the deceleration arising from the electric field in the pick-up region. This yields the deflection of the H^+ flow along the flank of the ionospheric N_2^+ tail. However, in addition to this deflection phenomenon, the flow pattern of the magnetospheric ions is also affected by a second process. Due to the reduced electric field strength inside the central tail region, the magnetospheric ions inside the tail are to a certain degree able to move antiparallel to the direction of the convective electric field and therefore, to gain access to the region directly behind the obstacle. This effect is illustrated in fig. 6.9(d).

The high temperature of the magnetospheric H^+ ions takes major influence on their flow pattern. Due to their low mass, they are stronger affected by the potential barrier at the ionospheric tail's flank in the E^+ hemisphere than the heavy N^+ ions. As stated above, the H^+ component possesses a thermal velocity that exceeds the velocity u_0 of the upstream flow by more than a factor of 2. Therefore, the velocity of a huge number of H^+ ions that try to cross the tail's flank is significantly larger than the mean flow speed. The relative change $\delta v_{m,2}/v_{m,2}$ that the velocity of such a fast particle undergoes when attempting to cross the potential barrier is significantly smaller than the effect on a particle whose velocity is comparable to or even exceeded by u_0. Thus, it is justified to expect that especially those H^+ ions whose individual velocity $v_{m,2}$ (where $\underline{v}_{m,2} \uparrow\uparrow \underline{u}_0$) is significantly larger than u_0 are able to cross the oblique tail flank from outward to inward. In any case, the fraction of H^+ ions that possess a sufficiently high velocity to cross the potential barrier at the E^+ flank of the ionospheric nitrogen tail should depend on the ion temperature. In the following section, this aspect will be investigated in more detail by comparing the simulation results to a situation in which the thermal velocity of the H^+ component has been reduced by a factor of 5. This investigation will also yield new insights into the question of why the Ion Composition Boundary vanishes when Titan is located inside the Saturnian magnetosphere.

A comparison to the results shown in fig. 6.4 illustrates that the magnetic pile-up region in the equatorial plane has undergone a noticeable transition. In the foregoing simulation run that used a single-species representation for the ambient magnetospheric plasma flow, the pile-up region in the equatorial plane possessed an extension of only about $3 - 3.5R_T$ in the direction of the convective electric field. In contrast to this, in fig. 6.9(c), a sharply developed enhancement of magnetic field strength is identifiable in a distance of more than $5R_T$ in E^+ direction, the structure of this pile-up signature coinciding with the outer flank of the tail developed by the heaviest ionospheric species and the cavity in the electric field strength. This modification clearly emerges from splitting up the magnetospheric plasma in two distinct components. As expressed by eq. (6.40), the expansion of the pile-up region is mainly based on the convection of the field lines along the magnetospheric plasma flow. Since the lighter species experiences a significant deflection, i.e. the H^+ velocity vectors a noticeably altered in the vicinity of Titan, the magnetic field topology is also slightly affected. The extension of the pile-up region in the E^+ hemisphere is stretched, following the motion of the H^+ ions along the oblique outer flank of the ionospheric tail. This effect will play an even more important role in the 06:00 LT and the 12:00 LT scenarios.

5.2 Influence of the proton temperature

A major result of the two-species simulations presented in chapter 4 has been that in the case of a supermagnetosonic upstream flow, the ambient plasma is clearly separated from the ionospheric particles by means of an Ion Composition Boundary. When Titan is exposed to the slow and hot magnetospheric plasma, this boundary layer is no longer present. Only a weakly pronounced, asymmetric cavity is formed in the magnetospheric plasma density downstream of the satellite. One major effect that leads to the disappearance of the Ion Composition Boundary could be attributed to the changes in the ionospheric tail structure when Titan reenters Saturn's magnetosphere: Since inside the magnetosphere, the density gradient near the tail's Saturn-facing flank is weaker than outside the magnetosphere, the electric force arising from the electron pressure term is not strong enough to forbid the magnetospheric plasma to gain access to the central tail region. However, the results presented in the preceding section also suggest that the high thermal velocity of the ambient magnetospheric plasma is of consequence for Titan's wake structure. In fact, for the simulations presented in chapter 4, the supermagnetosonic scenario has not been obtained from the Voyager 1 parameters by altering the alfvénic, but by increasing the sonic and magnetosonic Mach numbers of the magnetospheric flow. The temperatures of both magnetospheric ions and electrons have been reduced to generate a hypothetical scenario with a super-alfvénic, supersonic and supermagnetosonic upstream plasma.

The extent to which the high thermal velocity of the magnetospheric plasma takes influence on the wake structure, especially on the sharpness of the boundaries evolving from the interaction, can be studied by analyzing the dynamics of the magnetospheric H^+ ions in the five-species simulation model. Due to their low mass, their flow pattern is – in contrast to that of the heavy N^+ or (N^+/H^+) ions – clearly modified by the distorted electromagnetic environment of Titan. Therefore, another simulation run for 18:00 LT has been conducted, assuming the thermal velocity of the H^+ component to be about a factor of 5 smaller than in the run presented in the preceding section.

The results of this simulation scenario are displayed in figs. 6.11-6.13. The magnetospheric plasma parameters and the electromagnetic fields in the polar plane are shown in fig. 6.11. Figures 6.12 and 6.13 show the situation in the equatorial plane. Both the N^+ and the H^+ ions are again injected into the simulation box with a bulk velocity of $\underline{u}_0 = (120\,\mathrm{km/s}, 0, 0)$.

However, while the thermal velocity of the nitrogen component has been set to a value of

$$v_{\mathrm{th}} = \sqrt{\frac{3kT}{m}} = \sqrt{\frac{3 \cdot 2900\,\mathrm{eV}}{14\,\mathrm{amu}}} \approx 244\,\mathrm{km/s} \tag{6.41}$$

and therefore exceeds the mean plasma velocity by a factor of two, the thermal velocity of the H^+ ions is about a factor 5 smaller. The initial temperature of the H^+ ions is given by $kT = 210\,\mathrm{eV}/25$. Thus, the dynamics of the N^+ ions are mainly governed by their thermal motion, whereas most of the H^+ ions possess a velocity vector that is almost parallel to the $(+x)$ direction. The influence of the reduced H^+ temperature on the plasma flow in the polar plane is displayed in figs. 6.11(b) and (e). The proton flow is now clearly deflected around the obstacle, giving rise to a cone-shaped region in which the magnetospheric H^+ density almost vanishes. Practically no protons are present in the central tail region. As displayed in fig. 6.11(b), the structure of the H^+ wake exhibits a strong resemblance to the cavity of

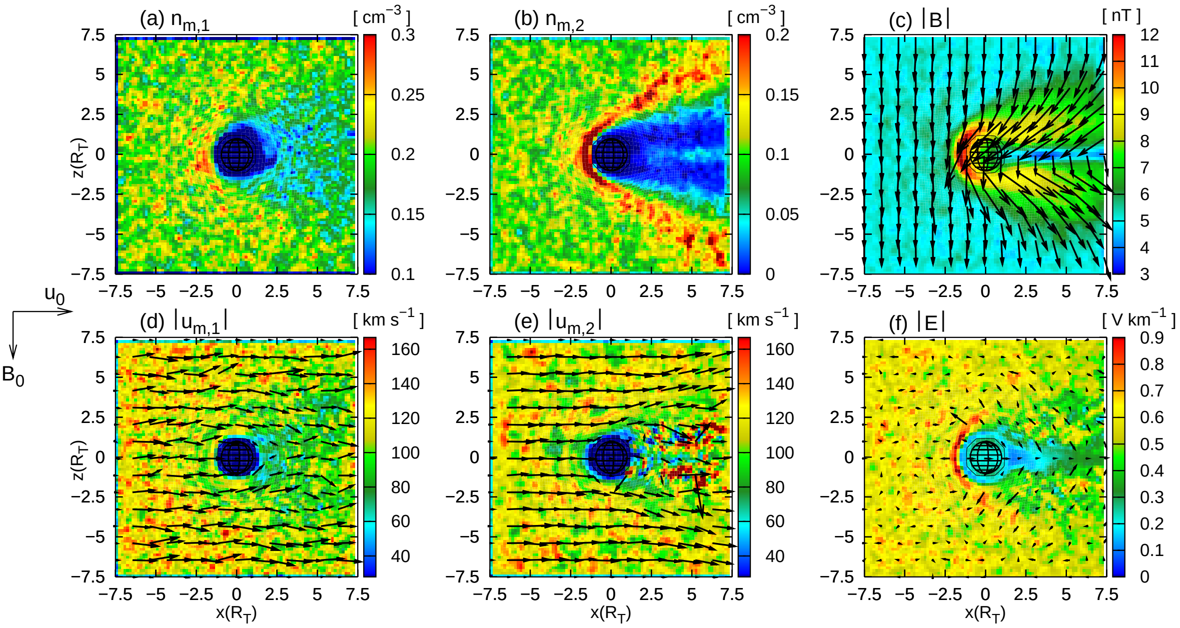

Figure 6.11: Five-species simulation of Titan's plasma environment at 18:00 local time – Influence of the proton temperature. In the real Titan situation, the thermal velocities of magnetospheric protons and nitrogen ions are almost equal and exceed the average velocity of the impinging magnetospheric plasma flow by a factor of 2. In order to investigate the influence of the proton temperature on the sharpness of the plasma boundaries in the vicinity of Titan, the thermal velocity of the protons has been reduced by a factor of 5. For this situation, the figure displays the magnetospheric plasma parameters and the electromagnetic fields in the polar plane: (a) nitrogen density, (b) hydrogen density, (c) magnetic field, (d) nitrogen velocity, (e) hydrogen velocity and (f) electric field. As can be seen from fig. (b), a cone-shaped cavity of nearly vanishing hydrogen density is formed in the downstream region, its outer flanks being clearly identifiable. At the outer flanks of this structure, the H^+ density exceeds the background value by more than a factor of two. In the case of a hot hydrogen plasma, the fastest particles are capable of gaining access to the wake region downstream of Titan. By reducing the H^+ temperature and therefore, the number of extremely fast protons, this process is more and more suppressed. Hence, the sensitivity of the magnetospheric mass spectrometer increases when the proton temperature is reduced.

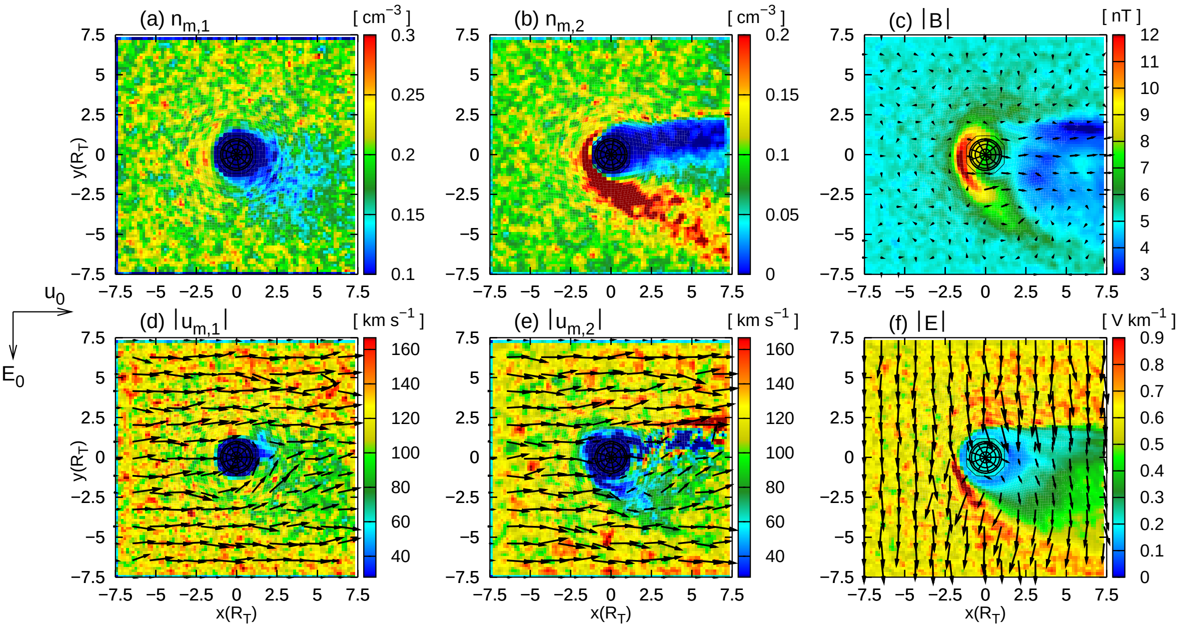

Figure 6.12: Five-species simulation of Titan's plasma environment at 18:00 local time – Influence of the proton temperature. For the case of a reduced H^+ temperature, the figure displays the magnetospheric plasma parameters as well as the electromagnetic fields in the equatorial plane. Directly behind Titan, a pronounced cavity of reduced hydrogen density is formed. Thus, the smaller is the thermal velocity of this species, the more pronounced is the tendency to form an Ion Composition Boundary. In the E^+ hemisphere, the electric field in the pick-up region is oriented nearly perpendicular to the oblique outer boundary of the tail. Hence, a proton that tries to pass the boundary layer, must possess a sufficiently high velocity in order for the deceleration in the potential barrier to be negligible. As in the case of a cold proton component, the number of extremely fast particles is reduced compared to the real Titan situation, the fraction of particles being able to penetrate the tail structure has diminished. This is the reason for the massive increase of H^+ density along the tail's flank in the E^+ hemisphere. Hence, two factors must be considered of major importance for the question of whether an Ion Composition Boundary is formed: On the one hand, a decisive character must be attributed to the potential barriers at the outer flanks of the ionospheric tail. The sharper is the density gradient at the tail's flank in the E^- hemisphere, and the more pronounced is the electric field barrier in the pick-up region of the E^+ hemisphere, the steeper is the potential barrier surrounding the tail. It is important to notice that this factor is determined only by ionospheric parameters, i.e. by the density reduction near the tail's Saturn-facing flank and by the electric field in the anti-Saturn-facing pick-up region. On the other hand, the temperature of the ambient plasma flow plays an important role. The larger is the temperature, the more particles possess a sufficient energy to penetrate into the ionospheric tail region.

reduced (N^+/H^+) number density that was formed in the case of Titan being exposed to a supermagnetosonic upstream plasma flow. Again, the H^+ ions are pressed against the outer flanks of the central tail, but now, the density in these regions exceeds the upstream value by more than a factor of 2. Thus, the colder the H^+ ions are, the more pronounced is the mass spectrometer effect exhibited by the magnetospheric plasma in the polar plane. An analogous effect occurs in the equatorial plane. The proton density is now increased along the entire tail flank in the E^+ hemisphere, the peak density in this region being more than a factor of 3 larger than the background value. However, because an analogous change manifests neither

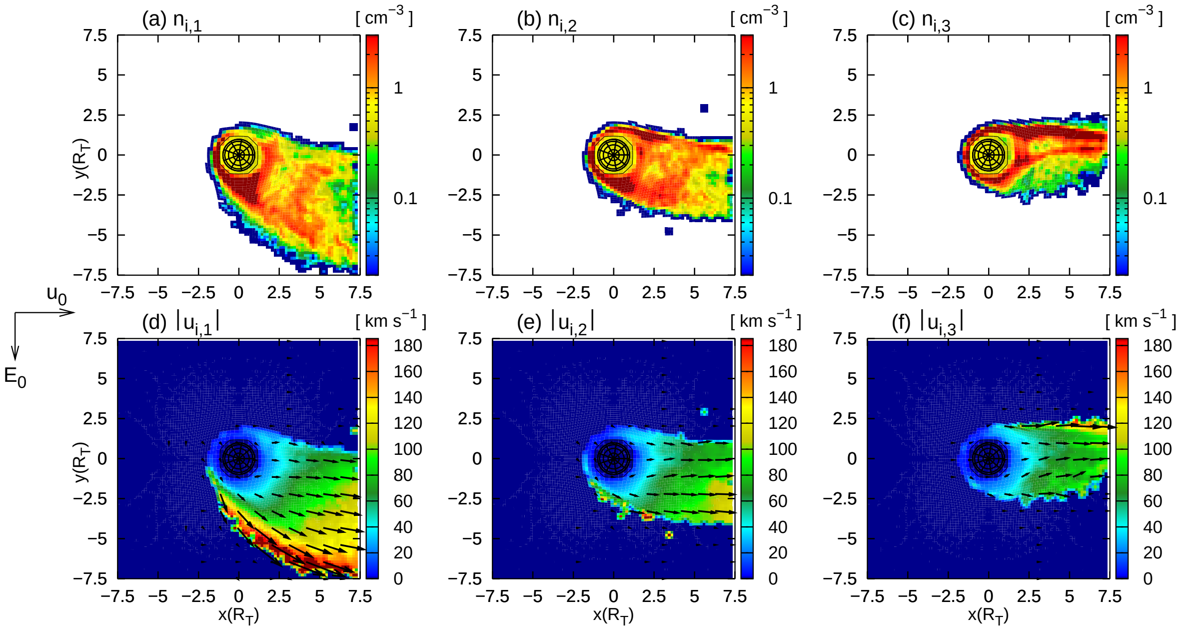

Figure 6.13: Five-species simulation of Titan's plasma environment at 18:00 local time – Influence of the proton temperature. For a cut through the equatorial plane, the figure displays the ionospheric plasma densities and velocities. The characteristic features of the ionospheric tail are almost identical to the case of a warm ambient H^+ plasma flow, as displayed in fig. 6.10. Therefore, the electric field barrier that the H^+ ions must pass when attempting to access the tail region is nearly the same in both scenarios. This is why the simulation results clearly illustrate the importance of the plasma temperature for the question of whether an Ion Composition Boundary is formed. A reduction of the H^+ temperature goes along with a decrease of the number of extremely fast particles that are capable of penetrating the outer flanks of the ionospheric tail. Thus, the sharpness of the boundary between H^+ ions and particles of ionospheric origin is increased. The selectivity of the magnetospheric mass spectrometer effect diminishes when increasing the H^+ temperature. In the same way, the high sensitivity of the ionospheric mass spectrometer is not only based on the differences in the ion masses, but also on the vanishing temperature of the newly generated ions.

in the velocity nor in the electromagnetic fields, it is obvious that the enhancement of the H^+ density does not indicate the formation of some kind of shock-like structure, as it is developed when Titan is located outside of Saturn's magnetosphere.

Besides, a definite tendency to form an Ion Composition Boundary manifests in the proton density downstream of Titan (cf. fig. 6.12). A narrow region of almost vanishing H^+ density has evolved at the wakeside of Titan, being clearly confined to the E^+ hemisphere. Since the proton temperature is the only simulation parameter that has been altered, it is obvious that the ion temperature definitely plays a decisive role for the sharpness of the plasma boundaries near Titan. The ionospheric tail region is surrounded by potential barriers: In the E^- hemisphere, the relatively sharp decrease of the ionospheric density gives rise to an electric field that is directed outward the tail. Therefore, it prevents magnetospheric particles from entering the ionospheric tail region from outward to inward. On the other hand, at the tail's oblique flank in the E^+ hemisphere, it is the convective electric field inside the pick-up region that acts as a barrier to the impinging magnetospheric plasma flow.

The ionospheric tail structure itself is not affected by altering the temperature of the magnetospheric hydrogen component. This is clearly illustrated by a comparison of the ionospheric densities and velocities in fig. 6.13 with the situation when the magnetospheric hydrogen component is assumed to be hot (cf. fig. 6.10). The density and velocity distribution inside the tail, but the electromagnetic fields as well, are almost identical in both simulations. Thus, both the warm and the cold protons are facing the same obstacle when encountering Titan's ionospheric tail. Therefore, the thermal velocity is the relevant parameter for the penetration problem.

Whether a particle is able to cross the potential barriers at the tail's outer flanks is determined by two factors: First of all, the larger is the mass of an ion, the smaller is the deceleration that it experiences when encountering the potential barrier surrounding the ionospheric tail. Therefore, the effect on the nitrogen ions, i.e. their tendency to form an Ion Composition Boundary, is by far not as pronounced as the deflection of the light protons around the tail region. Besides, the larger is the temperature of the protons, the more of them are able to pass the potential barrier surrounding the ionospheric tail, i.e. the Ion Composition Boundary becomes more and more penetrable. If the velocity of an ion is sufficiently large, the relative velocity change $\delta v/v$ that it undergoes when attempting to access the ionospheric tail region is negligible, to a certain degree even for the light H^+ ions. Thus, the selectivity of the magnetospheric mass spectrometer can be considered a function of the temperatures of the involved ion species. In any case, if the hydrogen plasma is sufficiently cold, the magnetospheric mass spectrometer effect occurs in both the polar and the equatorial plane. In the polar plane, the cavity of reduced H^+ density is cone-like and symmetric, whereas in the equatorial plane, it is confined to the region directly behind Titan. The proton density in the equatorial plane exhibits an asymmetric structure.

Another important conclusion that can be drawn from this numerical experiment concerns the *ionospheric* mass spectrometer effect. In general, the simulation discussed in this section indicates that only if a certain plasma component is sufficiently cold, the interaction gives rise to sharply pronounced boundary layers in the corresponding density signature. The warmer is the H^+ component, the less sharp is its separation from the ionospheric plasma flow. This also means that a major condition for the formation of the *ionospheric* mass spectrometer is the low initial temperature of the ionospheric plasma. In fact, in all simulations presented here, the initial ionospheric ion temperature is set to zero. Compared to the high magnetospheric ion temperature, the thermal velocity of the ionospheric components is assumed to be negligible. The ionospheric ions are placed in the simulation box at rest, i.e. $\underline{v} = \underline{0}$. A similar assumption has also proven to be adequate for the simulation of the interaction between the ionosphere of Mars and the solar wind (cf. Bößwetter *et al.* [27]). If a sufficiently high ionospheric ion temperature was incorporated into the model[3], this would most likely interfere with the ionospheric mass spectrometer effect. It should be noted that the analytical test particle model also assumed the initial velocity of the ionospheric ions to vanish.

---

[3] Of course, this would only be a hypothetical simulation scenario.

5.3 06:00 Saturnian local time

In the preceding sections, Titan's plasma environment at 18:00 local time has been discussed in the framework of a five-species hybrid model. It has been shown that the global features of the interaction region are well covered by a two-species approach, whereas several slight modifications of both the electromagnetic field topology and the flow pattern have to be attributed to the multi-species nature of the ambient magnetospheric plasma. In the following, the situation at 18:00 local time shall be compared to the case of Titan being located inside the magnetosphere at 06:00 local time, i.e. the obstacle's dayside ionosphere is assumed to be located in the wake region. As discussed in chapter 5, the results obtained from the two-species model indicate that the situation at 06:00 local time differs only insignificantly from the case of Titan's dayside ionosphere being exposed to the upstream plasma flow.

The simulation results for the polar plane are displayed in figs. 6.14 and 6.15, while figs. 6.16 and 6.17 illustrate the electromagnetic field signatures and plasma parameters for a cut through the equatorial plane. As can be seen from fig. 6.14(c), the draping pattern in the polar plane clearly resembles the magnetic signatures obtained by using a two-species hybrid model. However, in analogy to the situation at 18:00 local time, the magnetic pile-up value achieved at Titan's ramside has slightly diminished. While the two-species simulation presented in chapter 5 shows only a minor reduction of the magnetic field strength in the equatorial plane, the results obtained from the five-species model indicate that the field strength between the

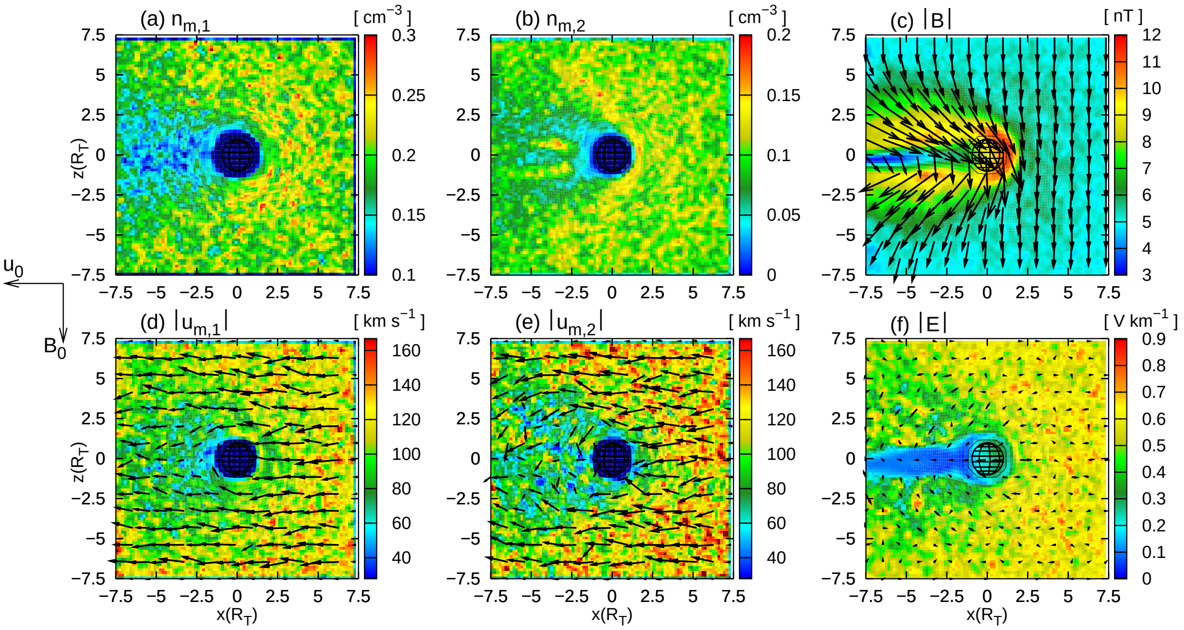

Figure 6.14: Five-species hybrid simulation of Titan's plasma environment at 06:00 local time – Magnetospheric plasma parameters and electromagnetic fields in the polar plane. In correspondence to the 18:00 LT scenario, the hydrogen ions are clearly deflected around the obstacle, whereas the magnetospheric nitrogen component is decelerated, but does not undergo a significant modification of its flow direction. The region of reduced magnetic field strength between the two lobes is sharper pronounced than in the results of the two-species model. The field magnitude diminishes to values well below 3 nT.

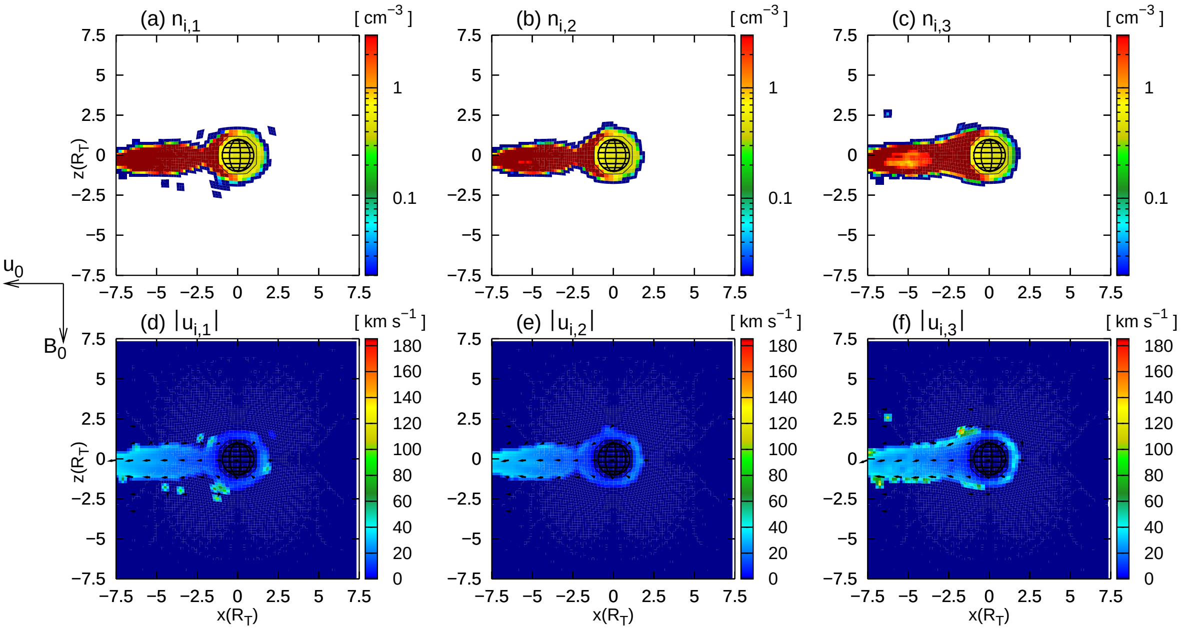

Figure 6.15: Five-species hybrid simulation of Titan's plasma environment at 06:00 local time – Ionospheric densities and velocities in the polar plane. Again, the molecular nitrogen component is denoted by the subscript 1, whereas the subscripts 2 and 3 refer to the methane and the molecular hydrogen component, respectively. Each of the three species forms a narrow tail directly behind the obstacle. Because the magnetic field strength in the tail region almost vanishes, a newly generated ionospheric particle experiences practically no acceleration. Furthermore, the dayside ionosphere is now located in the wake region. Because of these two factors, the ionospheric densities in the tail are about an order of magnitude larger than in the 18:00 LT scenario.

lobes nearly vanishes (cf. fig. 6.16(c)). In the wake region of the equatorial plane, the electric field magnitude also drops to values below 0.1 V/km. As the dayside of Titan is located in the wake region, the density of slow ionospheric ions in the tail exceeds the magnetospheric ion density by several orders of magnitude, yielding this strong reduction of electric field strength (cf. fig. 6.16(f)). Because in the tail region directly behind the obstacle, neither the magnetic nor the electric field makes a significant contribution to the Lorentz force, a newly generated ionospheric particle that is entering the wake is practically not accelerated. Especially the CH_4^+ and the H_2^+ ions do not experience a noticeable pick-up force, since – due to their small gyroradii – their tails are almost completely located inside this cavity of reduced electromagnetic field strength. Because these particles are not transported away from the obstacle in an efficient manner, they accumulate in the vicinity of Titan, as can be seen in fig. 6.17. The density of slow ionospheric ions in the tail clearly exceeds the densities in the 18:00 local time scenario. An accumulation of the slow ionospheric ions downstream of the obstacle also occurs in the polar plane, as displayed in fig. 6.15.

In other words, the accumulation of slow ionospheric particles in the wake can be understood by means of a *positive feedback mechanism*. The high density of slow ionospheric ions reduces the magnetospheric convective electric field strength and thus, the efficiency of the pick-up process. As the transport of the ionospheric ions away from Titan is slowed down, their density can increase even further. As discussed by Bagdonat [7], a similar process occurs in

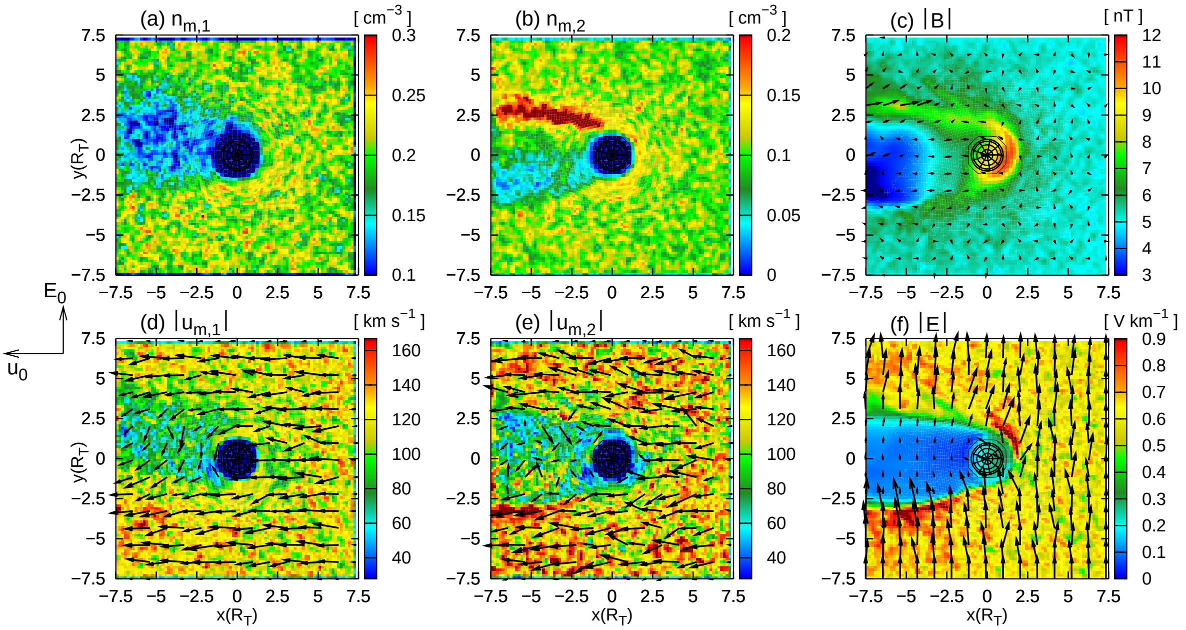

Figure 6.16: Five-species hybrid simulation of Titan's plasma environment at 06:00 local time – Magnetospheric plasma parameters and electromagnetic fields in the equatorial plane. At the ionospheric tail's flank in the E^+ hemisphere, the convective electric field inside the N_2^+ pick-up region poses a barrier to magnetospheric ions that try to gain access to the ionospheric tail region. Due to their smaller mass, a significant fraction of the protons are forbidden to pass this barrier. This yields a pronounced region of enhanced H^+ density along the tail's flank. The magnetic pile-up region is stretched along the entire area of increased H^+ density.

the plasma wake of weakly outgassing comets.

In Titan's equatorial plane, the massive concentration of slow ionospheric particles, especially of methane and hydrogen, yields a certain deformation of the ionospheric tail structure. In correspondence to the situation at 18:00 LT, the nitrogen tail is clearly shifted in the direction of the convective electric field, its extension exceeding the diameters of the CH_4^+ and the H_2^+ tails perpendicular to the flow direction. Again, the mass spectrometer effect should allow to discriminate between the heavier N_2^+ ions and the two lighter species. However, as their ionospheric tails are almost completely located inside the N_2^+-induced electromagnetic field cavity downstream of Titan, the pick-up of both H_2^+ and CH_4^+ ions is massively suppressed, i.e. the Lorentz forces are too weak to transport the ions away from Titan sufficiently fast and therefore, to compensate for the ongoing production of new ionospheric particles. As a result of this, the flanks of the H_2^+ and the CH_4^+ tail in the E^+ hemisphere are located nearly at the same position, making it impossible to distinguish between these two species by means of the ionospheric mass spectrometer effect. In other words, a substantial pick-up process, determined by a sufficiently high electromagnetic field strength in the tail region, must be considered a major condition for the mass spectrometer to be clearly identifiable. Besides, the tail's flank in the E^- hemisphere has undergone a deformation: Compared to the two-species simulations, the ionospheric tail exhibits a widening antiparallel to the electric field. Due to their small gyroradii, this effect yields an almost symmetric tail structure for the H_2^+ ions. As can be seen from figs. 6.16(b) and (e), the widening of the tail in the E^- hemisphere also

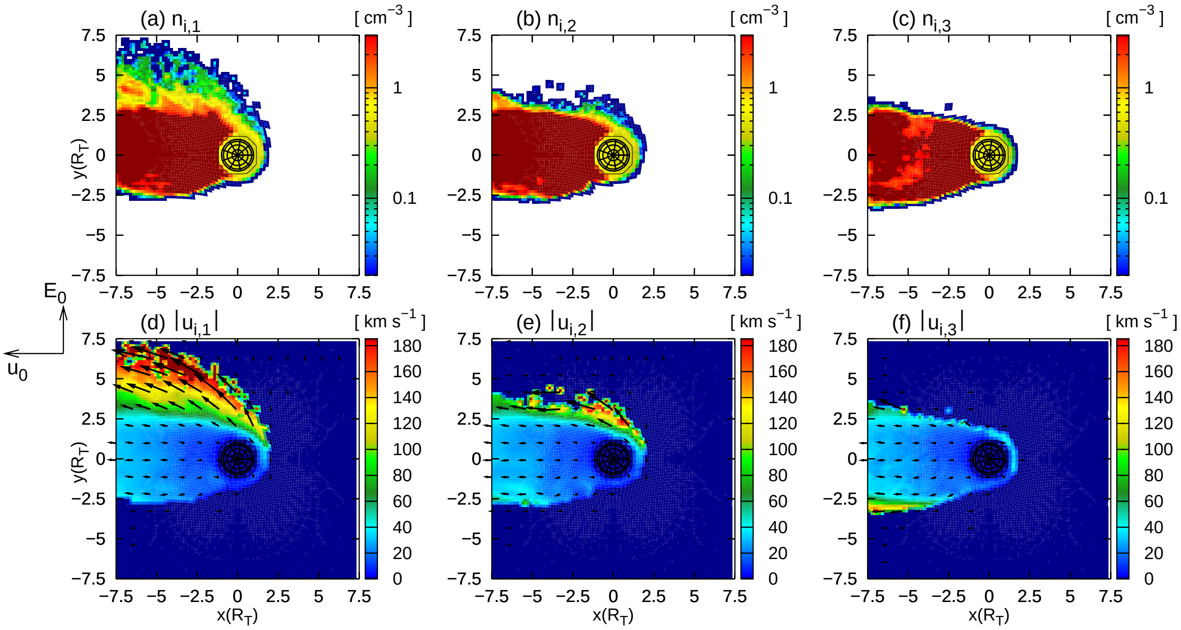

Figure 6.17: Five-species hybrid simulation of Titan's plasma environment at 06:00 local time – Ionospheric densities and velocities in the equatorial plane. Since the dayside ionosphere is located in the wake region, a massive concentration of slow ionospheric particles can be found in the immediate vicinity of Titan. Especially the trajectories of newly generated CH_4^+ and H_2^+ ions are almost entirely located in the cavity of reduced electromagnetic field strength downstream of the obstacle. Therefore, the transport of these particles away from Titan cannot compensate for the continuous production of new ions. This effect also yields a deformation of the tail structure. As can be seen from fig. (c), the hydrogen tail exhibits an almost symmetric structure.

affects the flow pattern of the light magnetospheric ions. Especially, the slightly pronounced cavity in the wakeside H^+ density is clearly shifted in the E^- hemisphere.

In the polar plane, the density signature of the magnetospheric H^+ ions qualitatively resembles the situation in the 18:00 LT scenario, showing a slight reduction of the number density behind the obstacle. However, in the equatorial plane, a massive increase of H^+ density manifests near the entire flank of the ionospheric tail, as can be seen from fig. 6.16(b). The influence of the light H^+ ions on the extension of the magnetic pile-up region in the E^+ hemisphere is clearly visible in fig. 6.16(c). Along the entire region of increased H^+ density, the magnetic field is enhanced. In contrast to the original 06:00 LT simulation, the region of enhanced magnetic field even reaches the wakeside wall of the simulation domain.

5.4 00:00 Saturnian local time

As discussed in the preceding section, the simulation results for the case of Titan's dayside being located in the wake region indicate that only the heaviest ionospheric species experiences a pick-up force that is sufficiently strong to drag these particles away from the satellite. Since, due to their smaller masses, the methane and molecular hydrogen populations are located completely inside the electric field cavity generated by the heavy N_2^+ ions, they are practically not accelerated, yielding an accumulation of these ions in the vicinity of the moon. To a certain degree, the concentration of slow ionospheric ions is even able to penetrate the electric field barrier at the tail's Saturn-facing flank.

The transition from the highly asymmetric tail structure obtained by using a single-species representation for the ionosphere to a nearly symmetric signature in the case of a multi-species description is also illustrated by the simulation results for 00:00 local time. As stated in chapter 5, in this situation, all three Mach numbers of the impinging plasma are smaller than 1. Based on recent Cassini results, Ma *et al.* [99] suggest that under certain magnetospheric conditions, such a combination of Mach numbers may also be representative of the situation between 06:00 LT and 12:00 LT. Again, the discussion refers to the geometry displayed in fig. 5.8, i.e. the impinging magnetospheric plasma flow is directed parallel to the $(+y)$ axis, whereas the undisturbed Saturnian magnetic field is oriented along the $(-z)$ direction. In correspondence to the second scenario discussed in chapter 5, the $(x < 0)$ hemisphere of Titan is exposed to solar UV radiation. Of course, the real geometry, i.e. the orientation of the solar UV flux with respect to the magnetospheric plasma velocity and the undisturbed magnetic field, is significantly more complex. However, as will be discussed in the following, in the framework of the multi-species approach, even this simplifying geometry yields a quite complex tail structure. Hence, a further increase in the complexity of the simulation geometry

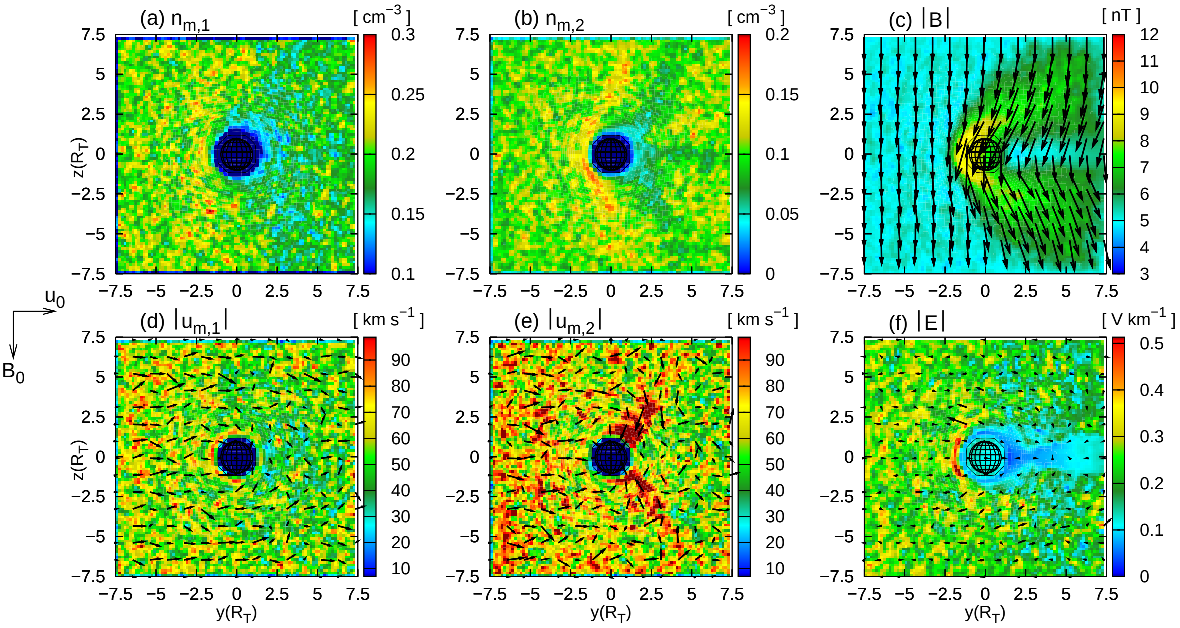

Figure 6.18: Five-species hybrid simulation of Titan's plasma environment at 00:00 local time. The upstream plasma is assumed to be sub-alfvénic ($M_A = 0.77$), subsonic ($M_S = 0.27$) and submagnetosonic ($M_{MS} = 0.22$). For a cut through the polar plane, the figure displays (a) the magnetospheric nitrogen density, (b) the magnetospheric hydrogen density, (c) the magnetic field, (d) the magnetospheric nitrogen velocity, (e) the magnetospheric hydrogen velocity and (f) the electric field strength. The magnetospheric N^+ plasma flow is only insignificantly affected by the presence of the obstacle. The maximum magnetic field value achieved at Titan's ramside lies only about a factor of 2 above the background value. The magnetic lobe structure is nearly identical to the field topology in the original simulation scenario.

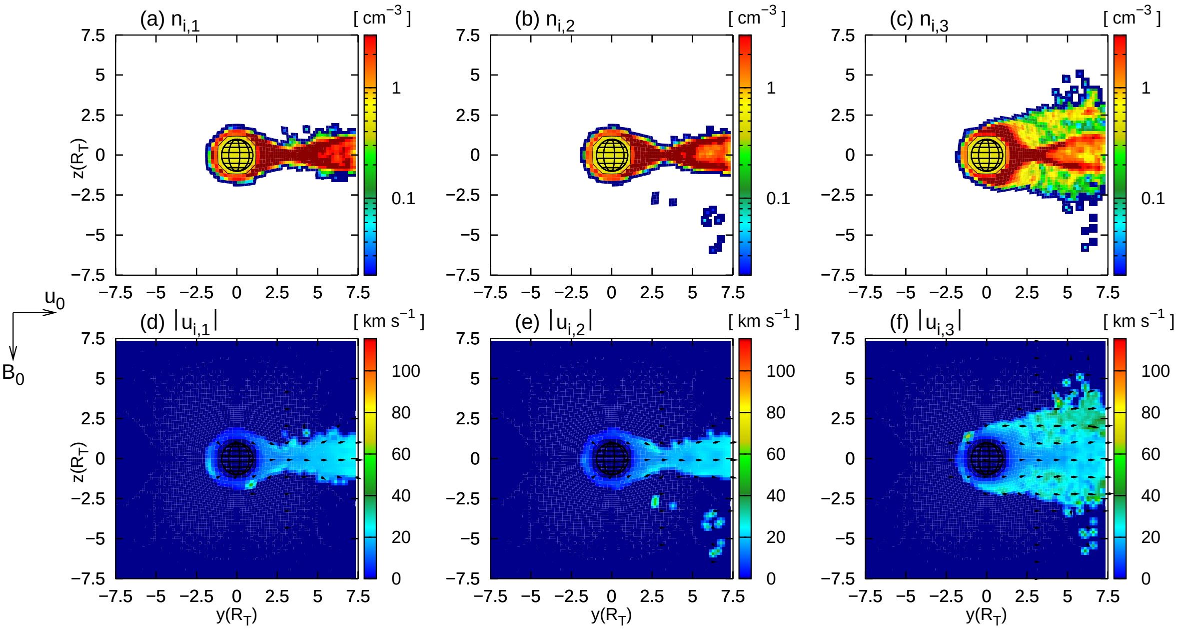

Figure 6.19: Five-species hybrid simulation of Titan's plasma environment at 00:00 local time. For a cut through the (y, z) plane, the figure displays the ionospheric N_2^+ density and velocity (figs. (a) and (d)), the methane density and velocity (figs. (b) and (e)) and the plasma parameters of molecular hydrogen ions (figs. (c) and (f)). In analogy to the results obtained from the single-species ionosphere model, the major concentrations of each ionospheric species are located directly behind the obstacle. In the polar plane, none of the three species experiences a noticeable acceleration. The reduced curvature of the field lines gives rise to a widening of the H_2^+ tail perpendicular to the flow direction.

will make it nearly impossible to reveal the underlying physical mechanism.

The simulation results for Titan's polar plane are displayed in figs. 6.18 and 6.19, while figs. 6.20 and 6.21 illustrate the situation in the satellite's orbital plane. As can be seen from figs. 6.21(a) and (d), in the E^+ hemisphere, the structure of the nitrogen tail clearly resembles the results obtained from the single-species ionosphere model. An extensive pick-up region is formed, the peak velocity of the ions achieving values well above 100 km/s. In the E^- hemisphere, the structure of the tail is modified due to the presence of two additional ionospheric species. This effect is significantly more pronounced than in the 06:00 LT scenario, where the nitrogen tail possessed an extension of less than $2.5R_T$ in E^- direction. As can be seen from fig. 6.21(a), in the E^- hemisphere, massive concentrations of molecular nitrogen can now be found in a distance of about $5R_T$ perpendicular to the magnetospheric flow direction. The nitrogen ions develop an almost symmetric tail structure. However, in correspondence to the Cassini data analysis conducted by Wahlund *et al.* [151], a substantial pick-up process occurs only in the anti-Saturn-facing hemisphere.

The tails developed by the two lighter species even exhibit a preference to expand into the Saturn-facing hemisphere, i.e. *antiparallel* to the direction of the convective electric field. As displayed in figs. 6.21(e) and (f), the methane and molecular hydrogen ions experience practically no acceleration, illustrating that the pick-up of these species is again slowed down by the heavy N_2^+ ions. As can be seen in figs. 6.20(f) and 6.21(a), the flank of the electric

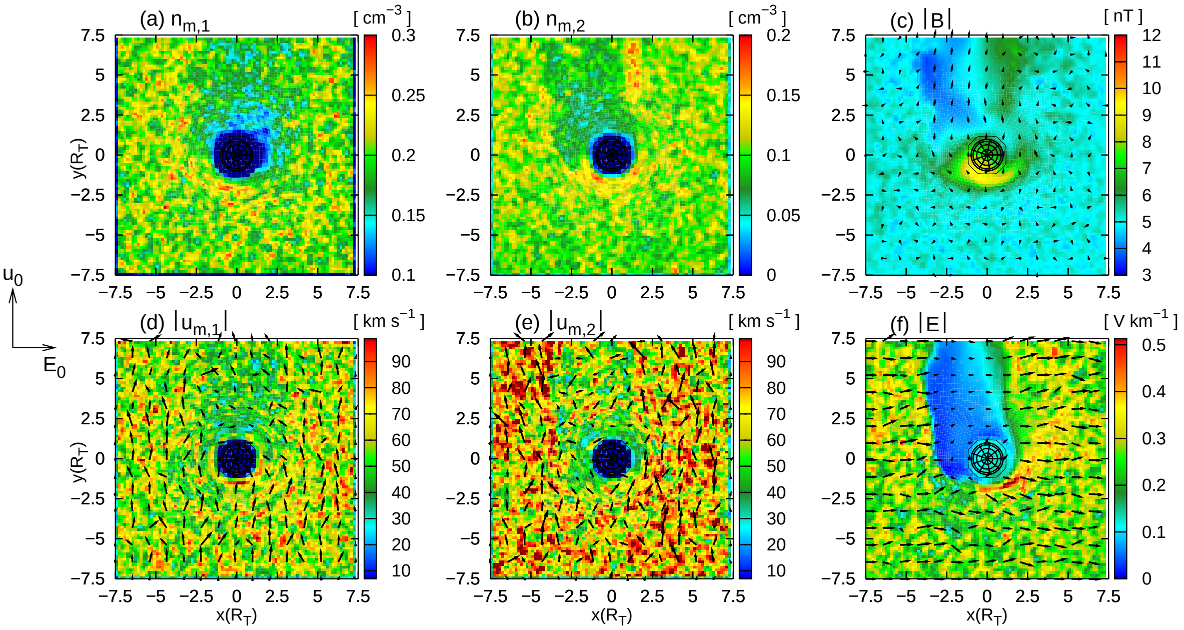

Figure 6.20: Five-species hybrid simulation of Titan's plasma environment at 00:00 local time – Magnetospheric plasma parameters and electromagnetic fields in the equatorial plane. In contrast to the two-species simulations of the 00:00 LT scenario presented in chapter 5, the electric field cavity downstream of the obstacle is no longer confined to the E^+ hemisphere. This modification can be ascribed to the accumulation of slow methane and hydrogen ions in the wake. The deformed electric field cavity leaves a clear imprint on the magnetospheric H^+ flow pattern.

field cavity in the E^- hemisphere coincides with the boundary of the region in which the N_2^+ density is highest. As the two light species are not dragged away from Titan, they concentrate in the vicinity of the satellite, their density exceeding the values achieved in the major N_2^+ pick-up region of the E^+ hemisphere by several orders of magnitude. To a certain degree, the convective electric field at the tail's Saturn-facing flank is able to prevent the ionospheric particles from entering the Saturn-facing hemisphere. However, compared to the situation at 06:00 LT, the impinging magnetospheric plasma is about more than a factor of 2 slower: In the 06:00 LT situation, a value of $M_A = 1.87$ has been chosen for the alfvénic Mach number, while in the situation at 00:00 LT, this parameter has again been set to a value of $M_A = 0.77$. The background magnetic field value has not been altered. Thus, the convective electric field barrier $\underline{E}_c = -\underline{u}_m \times \underline{B}$ at the tail's Saturn-facing flank is weaker than in the 06:00 LT scenario, allowing a larger fraction of the ionospheric ions to gain access to the Saturn-facing hemisphere. This tendency may also arise from the location of the dayside hemisphere, which – in the 00:00 LT geometry presented here – is identical to the E^- hemisphere of Titan. Anyway, the magnitude of the pick-up forces and therefore, the efficiency of the ion transport away from Titan, is smaller than at any other orbital position.

Since the interplay between different ionospheric species takes a predominant role in the 00:00 LT situation, the mass spectrometer discrimination between methane and hydrogen is no longer possible. Of course, this is expectable, as neither the simple pick-up calculations presented in section 2 nor the test particle simulations conducted by Luhmann [96] are able to consider any kind of interconnection process between different species. In these approaches,

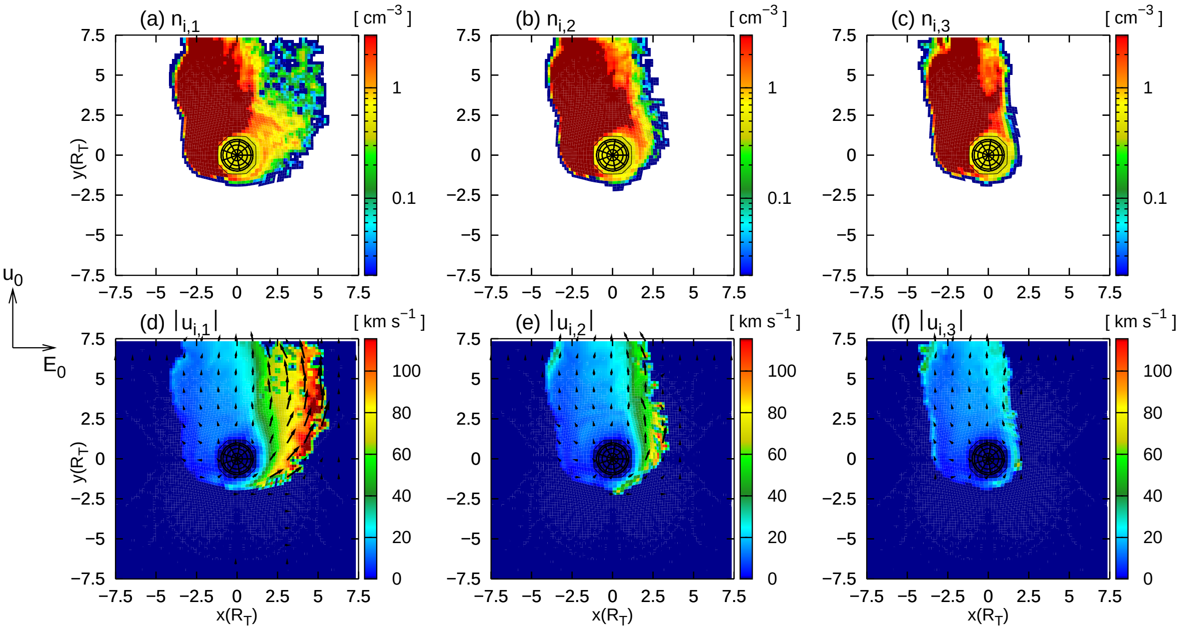

Figure 6.21: Five-species hybrid simulation of Titan's plasma environment at 00:00 local time. For a cut through Titan's orbital plane, the figure displays the ionospheric densities and velocities. Only in the E^+ hemisphere, the structure of the nitrogen tail exhibits a strong similarity to the results obtained from the two-species simulation model. An extensive pick-up region is formed; the velocity of the nitrogen ions increases to values well above the magnetospheric flow speed. In contrast to this, the lighter methane and hydrogen ions experience practically no acceleration, for their tails are almost entirely located inside the electric field cavity that arises from the concentration of slow nitrogen ions at the wakeside. The pick-up of the light species is suppressed by the heaviest one. As the hydrogen and methane ions are not transported away from the obstacle, they accumulate in Titan's wake region. To a certain degree, the accumulation of slow ionospheric particles in the downstream region even weakens the electric field barrier at the Saturn-facing flank of the tail, so that a region filled with slow ionospheric ions is formed in the E^- hemisphere. Thus, the simplifying explanation of the tail structures obtained from the two-species model is not valid in the case of a multi-species ionosphere. Even the tail developed by the N_2^+ ions exhibits a tendency to expand into the Saturn-facing hemisphere, so that ionospheric nitrogen ions can now be found in distances of about $5R_T$ perpendicular to the flow direction. The location of the dayside ionosphere in the E^- hemisphere may also play a role for this tail deformation.

none of the ion species "notices" the presence of the other ones, since the electromagnetic fields are kept at constant values that are not altered by particle dynamics. The inter-species connections investigated here are completely governed by the modification of the electromagnetic field topology in the wake. Furthermore, due to the reduced magnetospheric flow speed in the 00:00 LT scenario, the characteristic width w and height h of the cycloidal particle trajectories are also smaller than in the case of a super-alfvénic flow, for

$$w, h \propto u_m \quad . \tag{6.42}$$

Even the results of the 18:00 LT simulations have shown that the smaller is the gyroradius of an ionospheric species with respect to R_T, the stronger are the quantitative deviations from the tail extensions predicted by the test particle approach.

As displayed in fig. 6.19, in the polar plane, the nitrogen and methane ions form a narrow tail directly behind the obstacle. The confined nitrogen tail structure clearly deviates from the signatures obtained from the original two-species simulation model. Although the major concentrations of H_2^+ ions are also located along the y axis, the tail developed by this species possesses a diameter of about $\pm 2.5 R_T$ perpendicular to the undisturbed flow direction. As stated in chapter 5, the focusing effect exerted by the draped magnetic field lines in the lobes determines the tail diameter in Titan's polar plane. In the situation at 00:00 LT, this effect has proven to be weaker than in the case of Titan being exposed to a super-alfvénic, subsonic and submagnetosonic plasma flow. Therefore, in the simulations applying a single-species representation to the ionosphere, the reduction of the upstream flow's alfvénic Mach number (i.e. the transition from the 12:00 LT to the 00:00 LT scenario) goes along with a widening of the tail developed by the nitrogen ions. However, in the multi-species simulation of the 00:00 LT case, only the hydrogen (H_2^+) tail in the polar plane covers a larger area than in the situation at 18:00 LT or at 06:00 LT. The simulation results do not reveal an obvious explanation for this behaviour.

In contrast to the ionospheric plasma and electric field signatures, the magnetic field topology in the vicinity of Titan is completely covered by the two-species simulation model. Compared to any simulation that assumes the upstream flow to be super-alfvénic, the magnetic draping pattern is widened, while the magnetic pile-up value achieved at Titan's dayside lies less than a factor of 2 above the background magnetic field strength (cf. figs. 6.18(c) and 6.20(c)). The magnetospheric nitrogen flow pattern in the wake region is only slightly modified. The cavity in the H^+ density clearly coincides with the locations of the major ionospheric particle concentrations in the E^- hemisphere (cf. fig. 6.21(b)).

Especially the multi-species results of the 06:00 LT and the 00:00 LT runs illustrate that Titan's ionospheric tail exhibits an extremely complex structure. Both the tail orientation and the ion densities undergo significant transitions during a complete orbit of the satellite. A comparison between the 00:00 LT and the 12:00 LT scenarios will grant additional insights into the involved physics.

5.5 12:00 Saturnian local time

The situation at 12:00 clock angle position can be directly compared to the 00:00 LT scenario discussed in the previous section, because in both geometries, the undisturbed magnetospheric plasma velocity is parallel to the obstacle's terminator line. One of the major differences between the two simulation runs are the Mach numbers of the upstream plasma flow: In the 12:00 LT simulation, the impinging magnetospheric plasma is about a factor of $1.87/0.77 = 2.4$ faster than in the case of Titan being located inside Saturn's magnetotail. Since the magnetospheric plasma velocity determines the strength of the convective electric field barrier at the tail's Saturn-facing flank, the increase of M_A is expected to go along with a modification of the ionospheric tail structure in the E^- hemisphere. Such an effect may also be ascribed to the altered location of the dayside ionosphere: In the 12:00 LT scenario, the region of maximum ion production is located in the E^+ hemisphere, so that the bulk of newly generated ionospheric ions do not have to surround the entire obstacle "when trying to reach" the major pick-up region at the anti-Saturn-facing side of Titan.

The simulation results for 12:00 LT are displayed in figs. 6.22-6.24. For a cut through Titan's polar plane, the magnetospheric plasma parameters as well as the electromagnetic fields can be seen in fig. 6.22, whereas the situation in the equatorial plane is displayed in figs. 6.23 and 6.24. Compared to the results obtained from the two-species simulation model (cf. section 2 of chapter 5), the magnetic draping pattern in the polar plane has undergone a noticeable transition. On the one hand, the magnetic pile-up value achieved at Titan's ramside has diminished from well above 12 nT to a value of 9 nT; on the other hand, the magnetic enhancement in the lobes has also decreased. The two-species simulation predicts a peak value of 9 nT, while according to the multi-species simulation, the peak field value in the lobes does not exceed a value of 7 nT. According to the multi-species model, the magnetic field topology in the polar plane exhibits a stronger resemblance to the situation at 00:00 LT than suggested by the original two-species approach. Therefore, the simulation results for the polar plane clearly emphasize the necessity of treating the 12:00 LT scenario in the framework of a multi-species model.

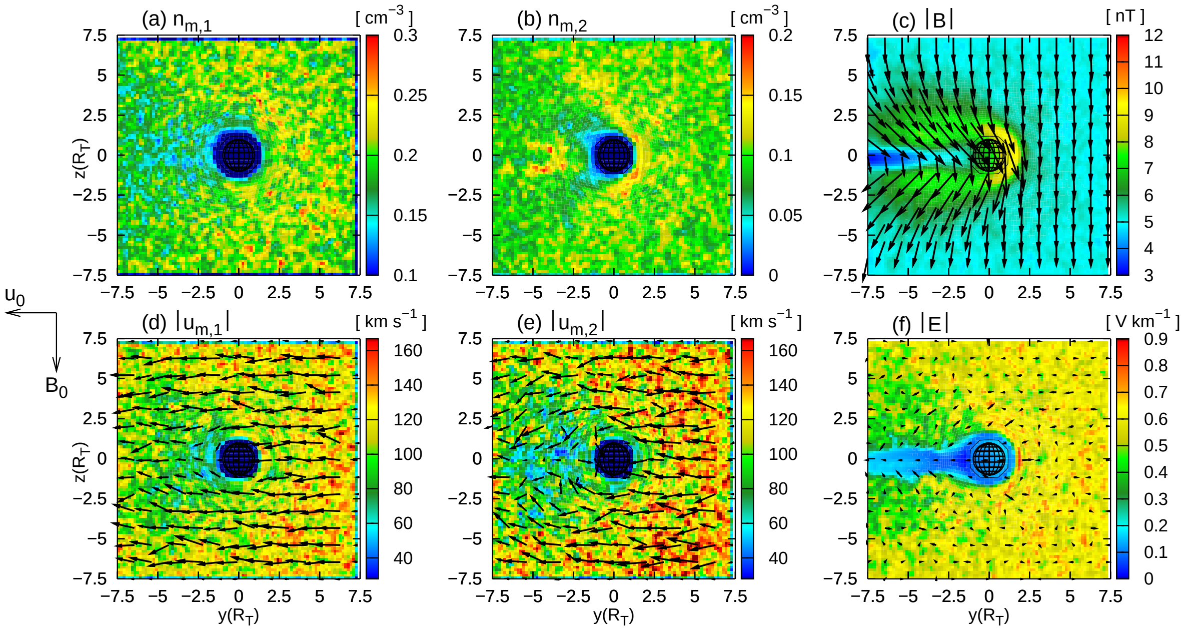

Figure 6.22: Five-species hybrid simulation of Titan's plasma environment at 12:00 Saturnian local time. The figure displays the magnetospheric plasma parameters and the electromagnetic fields in Titan's polar plane which is perpendicular to the undisturbed convective electric field. In both the 12:00 LT and the 00:00 LT scenario, the undisturbed impinging magnetospheric plasma flow is directed parallel to the obstacle's terminator line. At 12:00 LT, the region of major ion production is located in the E^+ hemisphere, whereas in the 00:00 LT geometry presented in the preceding section, it could be found in the E^- hemisphere. Even though several features of the interaction region, such as the formation of a confined electric field cavity directly behind Titan, resemble the situations at 06:00 LT and 18:00 LT, the structure of the magnetic draping pattern exhibits a certain similarity to the results of the 00:00 LT run. In the 00:00 LT as well as the 12:00 LT scenario, a peak pile-up value of only 9 nT is achieved at Titan's ramside. When Titan's dayside or nightside is exposed to the upstream flow, the maximum field value in the pile-up region is about a factor of 1.4 larger. However, the diameter of the magnetic lobes perpendicular to the flow direction does not differ appreciably from the situation at 06:00 LT or at 18:00 LT.

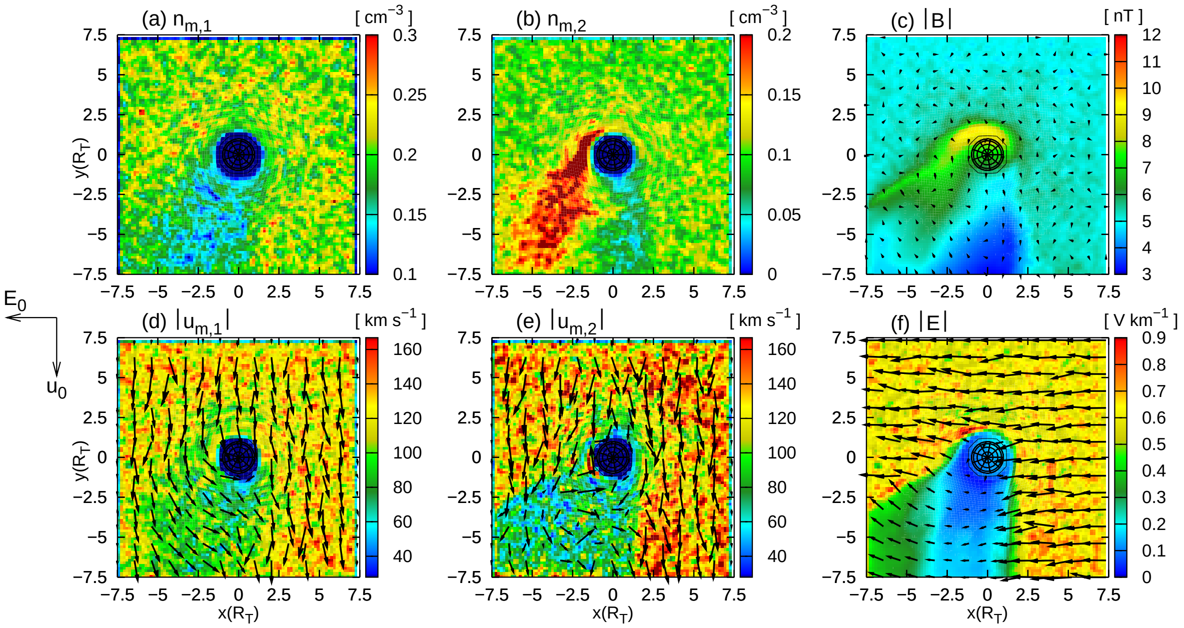

Figure 6.23: Five-species hybrid simulation of Titan's plasma environment at 12:00 Saturnian local time – Magnetospheric plasma parameters and electromagnetic fields in the equatorial plane. The magnetic pile-up region at Titan's ramside is clearly shifted in the E^+ hemisphere. However, in contrast to the situation at 18:00 LT and 06:00 LT, even in a distance of more than $7R_T$ perpendicular to the flow direction, a peak field strength of about 7 nT is achieved. As can be seen from fig. (c), the magnetic field cavity between the two lobes also exhibits a strong asymmetry, its Saturn-facing flank coinciding with the boundary of the ionospheric tail. In the E^- hemisphere, the magnetospheric plasma velocities as well as the electromagnetic fields remain nearly undistorted. The tendency of the magnetospheric plasma to refill the cavity directly behind the obstacle by streaming antiparallel to the direction of the weakened electric field clearly manifests in the nitrogen flow pattern, as displayed in fig. (d).

The situation in Titan's equatorial plane is illustrated in figs. 6.23 and 6.24, respectively. As can be seen from fig. 6.23(c), the reduction of the magnetic pile-up value also manifests in the equatorial plane. However, compared to the results of the two-species simulation, the extension of the magnetic pile-up region in E^+ direction has clearly increased: A noticeable magnetic field enhancement, characterized by a peak field value of about 7 nT, can be identified in a distance of more than $7R_T$ perpendicular to the y axis. In analogy to the 18:00 LT and the 06:00 LT scenario, the magnetospheric H^+ ions are deflected around the central tail region (cf. figs. 6.23(b) and (e)), yielding an increase of hydrogen density near the tail's flank in the E^+ hemisphere. As can be seen from fig. 6.23(d), the tendency of the magnetospheric plasma to refill the cavity directly behind the obstacle by streaming antiparallel to the reduced electric field in the central tail region clearly manifests in the N^+ flow downstream of Titan.

In contrast to the situation at 00:00 LT, the ionospheric tails are clearly shifted in the direction of the electric field. None of the three tails is capable of expanding significantly into the Saturn-facing hemisphere like in the 00:00 LT geometry (cf. fig. 6.24). The most important difference to any other scenario under consideration is that the tail extensions in E^+

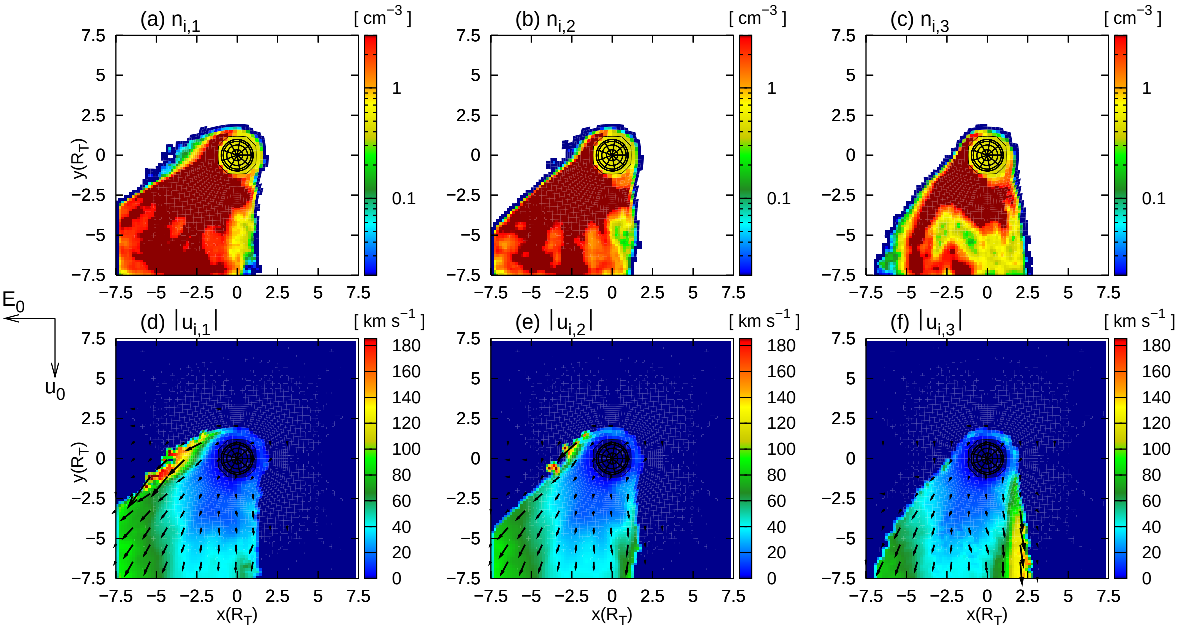

Figure 6.24: Five-species hybrid simulation of Titan's plasma environment at 12:00 Saturnian local time – Ionospheric plasma parameters in Titan's equatorial plane. In strong contrast to the situation at 00:00 LT, none of the three ionospheric tails is significantly expanded into the Saturn-facing hemisphere. In the 00:00 LT simulation, the nitrogen ions exhibited a broad and nearly symmetric tail structure, while the tails developed by the light methane and hydrogen ions have even shown to be slightly shifted in the E^- hemisphere. Due to the alfvénic Mach number of the magnetospheric plasma being about a factor of $1.84/0.77 = 2.4$ larger than in the 00:00 LT scenario, the electric field barrier $|E_c| = u_m B$ at the tail's Saturn-facing flank is also strengthened and is now capable of confining the ionospheric particles to the E^+ hemisphere. Thus, the modification of the ionospheric tail structure can, on the one hand, be ascribed to the increase of the upstream plasma velocity, going along with an enhancement of the convective electric field. Besides, in contrast to the situation at 00:00 LT, the region of major ion production is located in the E^+ hemisphere, allowing a direct injection of newly generated ionospheric ions into the major pick-up region at the anti-Saturn-facing side of Titan. In any case, the structure of the ionospheric tails is not covered by the test particle model, for their extensions perpendicular to the flow direction clearly exceed the heights of the cycloids given in table 6.1. The region in which the nitrogen ions are accelerated to velocities comparable to the magnetospheric flow speed is no longer located inside the simulation domain.

direction clearly exceed the values obtained from the simple test particle model presented in section 2. The major nitrogen pick-up region, in which the velocity becomes larger than the undisturbed magnetospheric flow speed, is no longer located inside the simulation domain. However, comparing the angles that the three tail flanks form with the x axis clearly illustrates that the extension of the nitrogen tail is still larger than the diameter of the methane tail, while the hydrogen tail is almost completely located inside the region covered by methane ions. Thus, in correspondence to the situation at 18:00 LT, ions of different masses become spatially dispersed in the tail. Nevertheless, the results clearly point out the limited validity of a pick-up model that assumes Titan to be a point-like ion source which is embedded into a perfectly homogeneous plasma flow. Since the results of the 18:00 LT simulation have shown to be in reasonable agreement with the simplified test particle approach, the widening of the ionospheric tails in the 12:00 LT geometry must be ascribed to the modified orientation of the dayside ionosphere with respect to the upstream plasma flow. In the 12:00 LT scenario, the magnetospheric flow pattern – especially that of the H^+ ion component – in the E^+ hemisphere shows more significant differences from the perfectly homogeneous ambient conditions of the test particle model than at 18:00 LT.

The major H_2^+ concentrations in the equatorial plane are located between $x = -5R_T$ and $x = +2.5R_T$. In a small region at the tail's Saturn-facing flank, ionospheric hydrogen ions are located outside the regions covered by the CH_4^+ and the N_2^+ tails (cf. fig. 6.24(c)). The hydrogen tail is at least slightly widened antiparallel to the undisturbed electric field. Since the anti-Saturn-facing boundary of the electric field cavity coincides with the flank of the methane tail, these H_2^+ ions are exposed to the undisturbed electric field in the adjacent magnetospheric plasma. For this reason, the maximum velocity of the H_2^+ ions in the equatorial plane is achieved at the tail's Saturn-facing flank.

6 Test particle regime

In the preceding sections, it has been demonstrated that the pick-up of the light methane and molecular hydrogen ions is slowed down by the heavy N_2^+ ions. However, the heaviest ionospheric species will only be able to affect the dynamics of the lighter ones, if its production rate is sufficiently high. In the simulations presented above, the numbers of N_2^+, CH_4^+ and H_2^+ ions generated per second were assumed to be equal. In the following, it will be analyzed how the structure of the interaction region, especially the pick-up process of the lighter ionospheric species, is affected when the production rate of the heavy ions is about several orders of magnitude smaller than the number of light ionospheric particles generated per time interval. Even though this is only a hypothetical scenario, it will provide additional insight into the complex mechanism giving rise to Titan's tail structure. The importance of such a study is also emphasized by first estimates of the ion escape flux during Cassini's TA and TB flyby. The results presented by Wahlund *et al.* [151] indicate that the production rates of different ionospheric species are indeed strongly dependent on the local magnetospheric conditions.

In a first step, the production rate of molecular nitrogen is assumed to be about two orders of magnitude smaller than the rates of methane and molecular hydrogen, i.e. a value of $Q(N_2^+) = 1.3 \cdot 10^{23}\,\mathrm{s}^{-1}$ has been chosen for the nitrogen production rate. In contrast to this, the total production of both methane and hydrogen is given by $Q(CH_4^+) = Q(H_2^+) = 1.3 \cdot 10^{25}\,\mathrm{s}^{-1}$. As a result, the molecular nitrogen density in the tail is practically negligible with respect to the ambient magnetospheric plasma density. In an additional step, the production rate of the "intermediate" ionospheric constituent, methane, is reduced in the same manner. In the following, the case of the number density of an ionospheric species being completely negligible is referred to as the *Test Particle Regime*. If the production rate of a certain ionospheric species is drastically reduced, the dynamics of these particles are controlled by the electromagnetic fields of the ambient plasma flow, while the field modification arising from the presence of these ions should not be of any importance. As demonstrated by Bagdonat [7], in the plasma environment of weak comets, the test particle trajectories are nearly identical to the cycloids described in section 2. In contrast to the results presented by Bagdonat [7], the following discussion will consider a multi-component ionosphere.

6.1 Simulation results: 18:00 local time

At first, the 18:00 LT scenario is analyzed again. However, in contrast to the previous discussion, the ionospheric nitrogen ions are now treated as test particles, i.e. a drastically reduced production rate has been assigned to this species. The simulation results for the equatorial plane can be seen in figs. 6.25 and 6.26, respectively. The diameter of the electric field cavity is now determined by the height of the CH_4^+ cycloids and is therefore clearly exceeded by the extension of the nitrogen tail. The sharp electric field enhancement in the E^+ hemisphere denotes the position of the major methane pick-up region. Neither in the electric nor in the magnetic field topology, the ionospheric nitrogen ions are capable of leaving a noticeable imprint, i.e. these ions behave indeed like test particles that are injected into a given, quasi-stationary field configuration. Thus, in the case of a sufficiently low production rate, the evolution of Titan's electromagnetic environment becomes decoupled from the dynamics of the heaviest pick-up species. However, as shown in fig. 6.25(c), the overall magnetic field topology in the equatorial plane is only slightly affected by the reduction of the nitrogen production rate. The reason for this will be discussed below.

Pick-up ion dynamics in the tail region are now mainly controlled by the methane component. As displayed in fig. 6.26(e), the bulk velocity achieved by the methane ions at the tail's E^+ flank has become comparable to the nitrogen velocity in the initial scenario, where the same value had been chosen for the production rates of all three species. In the inner part of the

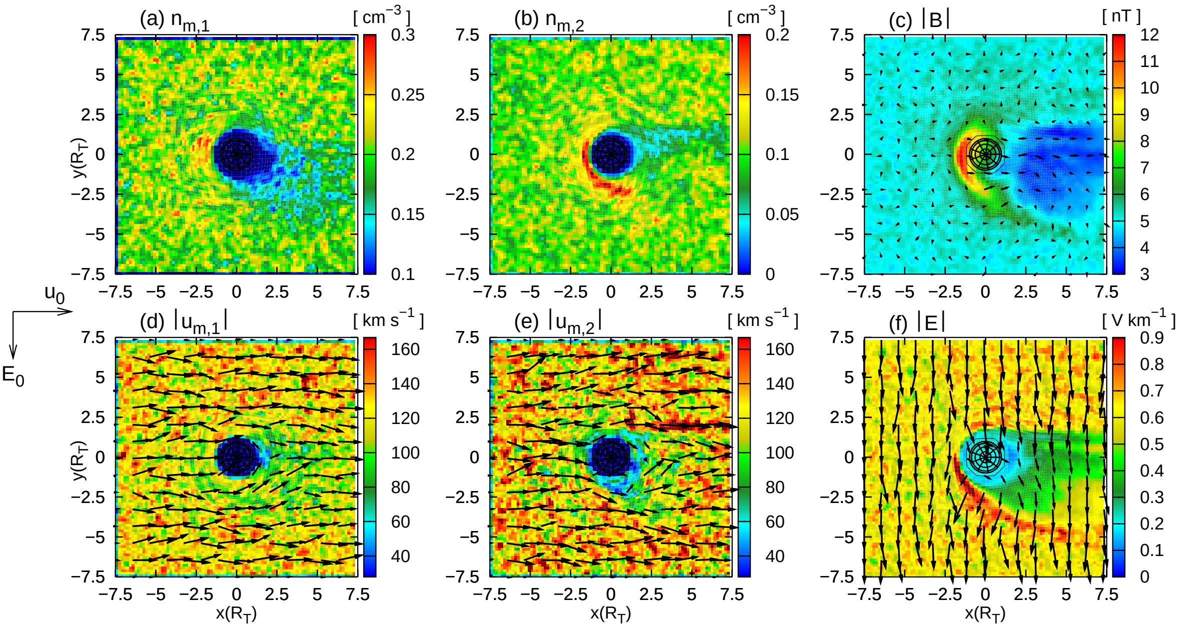

Figure 6.25: Test particle regime (molecular nitrogen) at 18:00 Saturnian local time – Magnetospheric plasma parameters and electromagnetic fields in the equatorial plane. Due to their reduced production rate, the N_2^+ ions are no longer able to cause noticeable distortions of the electromagnetic fields in the E^+ hemisphere. Instead, the shape of the electric field cavity is now mainly determined by the diameter of the methane tail. The electric field enhancement along the outer flank of the methane pick-up region is also clearly visible.

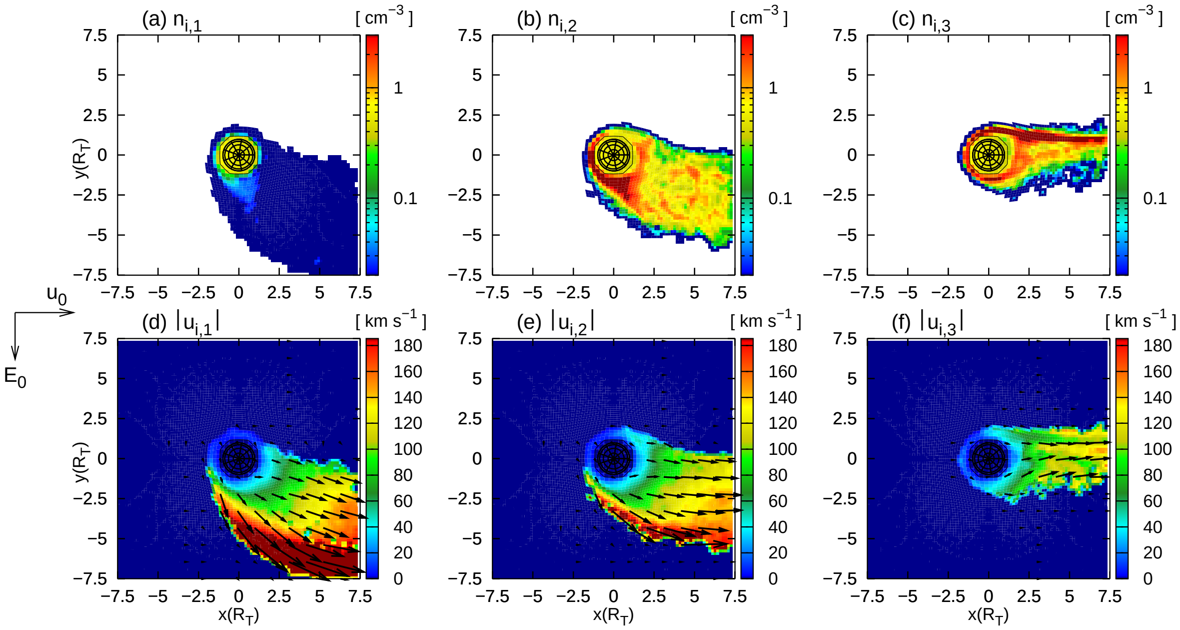

Figure 6.26: Test particle regime (molecular nitrogen) at 18:00 Saturnian local time – Ionospheric plasma parameters in the equatorial plane. In contrast to the initial simulation run, the pick-up of the methane ions is no longer suppressed by the presence of the heavier molecular nitrogen constituent. Therefore, the reduction of the N_2^+ production rate yields an increase of the methane bulk velocity in the anti-Saturn-facing pick-up region. Even though the wakeside velocity of the H_2^+ component is clearly larger than in the original simulation run, the transport of these particles away from Titan is still at least slightly suppressed by the heavier methane component.

methane-dominated region downstream of Titan, the mean N_2^+ velocity is unable to exceed the methane speed, since the N_2^+ component is affected by the electric field reduction arising from the relatively slow methane ions. In other words, the lighter methane component is able to exert a certain level of control on the dynamics of the heavier nitrogen particles. Due to the larger height of their cycloidal trajectories, the N_2^+ ions are capable of leaving the methane-dominated region in the E^+ hemisphere and are then exposed to the nearly undisturbed electromagnetic fields outside the CH_4^+ tail. Consequently, the nitrogen velocity in the E^+ hemisphere becomes comparable to the mean speed achieved by the CH_4^+ ions in the outer regions of their tail.

In the scenario under consideration, the dynamics of the light H_2^+ constituent are strongly affected by the presence of the methane tail. As can be seen in fig. 6.26(f), the maximum velocity reached in the H_2^+ tail is still smaller than the maximum nitrogen and methane velocities in the E^+ hemisphere, thus clearly illustrating the influence of the methane-induced electric field cavity downstream of Titan. Nevertheless, it should be noted that in the original 18:00 LT simulation scenario, the hydrogen ions featured a characteristic velocity of about $60 - 80\,\mathrm{km/s}$ in the downstream region, whereas in fig. 6.26(f), a typical value of about $100 - 120\,\mathrm{km/s}$ can be identified in the wakeside tail region near Titan. This clearly illustrates that in the case of identical production rates for the three species, the transport of the H_2^+ ions is not only suppressed by the nitrogen component, but a decelerating effect on the H_2^+ constituent must be ascribed to all ionospheric species that possess a larger mass. Since

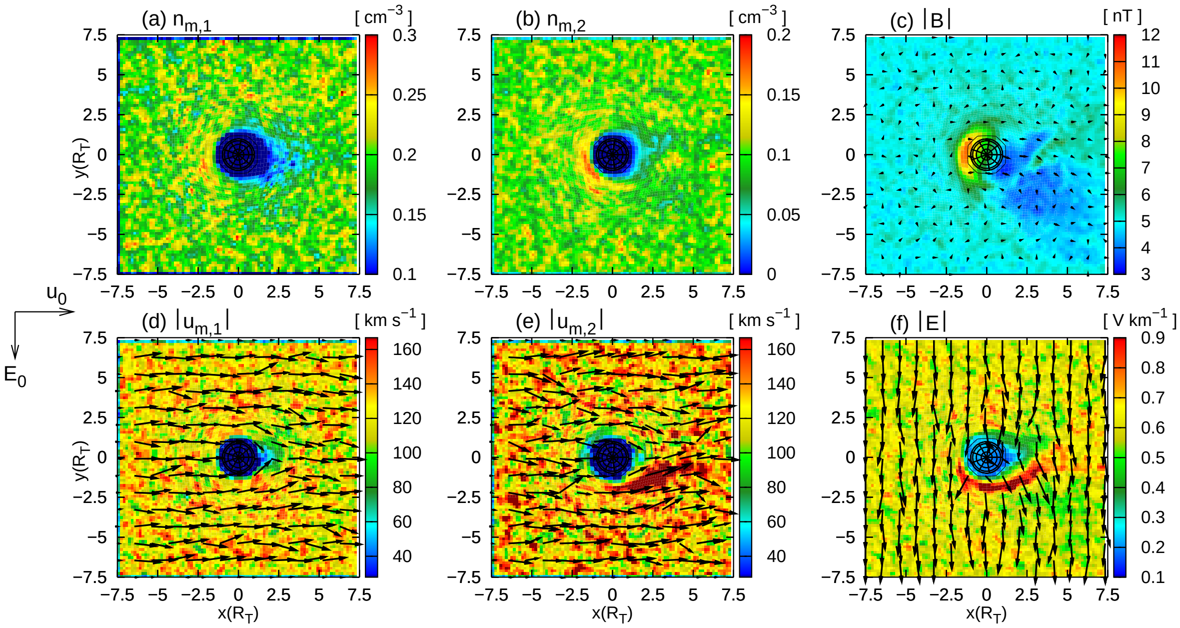

Figure 6.27: Test particle regime (molecular nitrogen and methane) at 18:00 Saturnian local time – Magnetospheric plasma parameters and electromagnetic fields in the equatorial plane. In this hypothetical scenario, molecular hydrogen has become the only ionospheric constituent that appears in noteworthy concentrations. Since the gyroradius of these ions is comparable to the size of Titan, the major hydrogen concentrations can be found directly downstream of the satellite. Consequently, the electromagnetic fields in the E^+ hemisphere remain practically unaffected by the presence of newly generated ionospheric particles. Both the N_2^+ and CH_4^+ components experience the nearly undisturbed electromagnetic fields in the E^+ hemisphere, i.e. their dynamics are determined by the simplifying test particle approach presented in section 2.

directly behind the obstacle, neither the nitrogen nor the methane constituent experienced a strong pick-up force, both species made a contribution to the electric field reduction. Hence, the lack of noticeable concentrations of nitrogen in the wake region is the reason for the increased hydrogen speed in the central tail.

In a second step, the production parameters of the methane component have been reduced to test particle conditions as well, i.e. molecular hydrogen has become the only ionospheric species occurring in noteworthy concentrations. The results of the simulation run are displayed in figs. 6.27 and 6.28, again illustrating only the situation in the plane which contains the cycloidal pick-up tails. The reduction of the methane production rate leaves a significant imprint on the magnetic field topology in the equatorial plane. Compared to the situation shown in fig. 6.25(c), the magnetic field magnitude at Titan's dayside has not only clearly diminished, but the magnetic pile-up region is practically not shifted in the direction of the convective electric field. The region of reduced magnetic field strength downstream of Titan has clearly become smaller. In general, the additional reduction of the methane production rate left a stronger imprint on the magnetic field topology than the decrease of $Q(N_2^+)$ in the first step. As discussed above, the magnetic pile-up region in the E^+ hemisphere is nearly aligned with the tail flank of the heaviest ionospheric species that possesses a noteworthy production rate. In the first step, the replacement of nitrogen by methane as the new

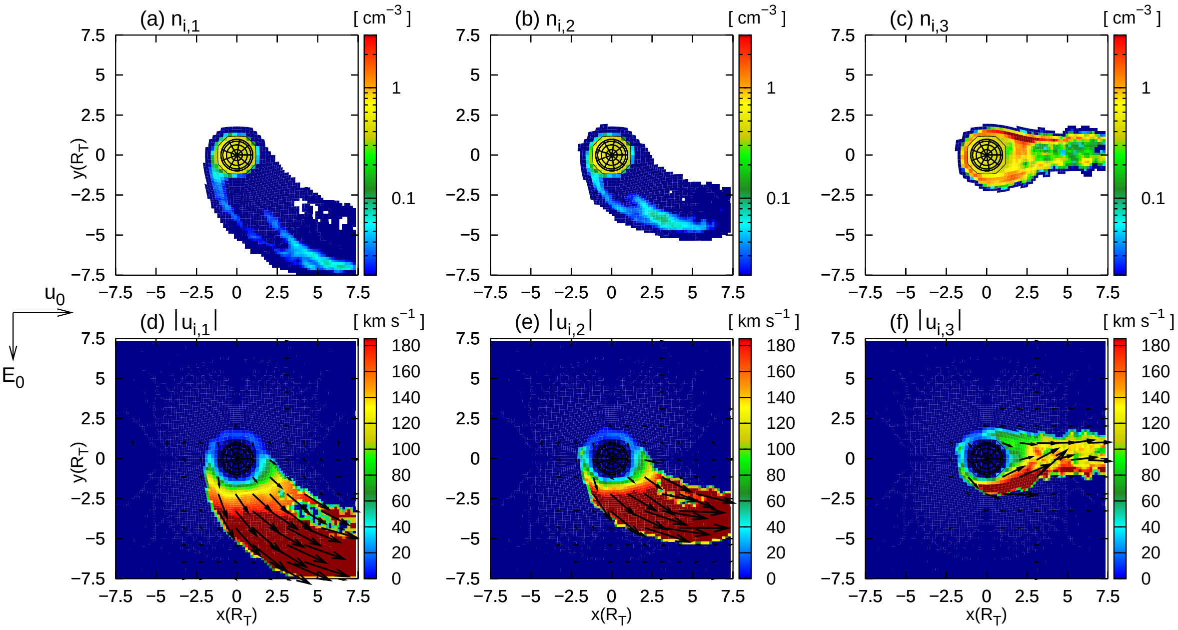

Figure 6.28: Test particle regime (molecular nitrogen and methane) at 18:00 Saturnian local time – Ionospheric plasma parameters in the equatorial plane. Because the H_2^+ dynamics are no longer affected by the presence of the heavier nitrogen and methane ions, the characteristic velocity achieved in the anti-Saturn-facing pick-up region has clearly increased (cf. plot (f)). The cycloidal shape of the methane and nitrogen tails is clearly visible. The reduction of the CH_4^+ production rate has also left an imprint on the structure of the N_2^+ tail: The velocity in the region covered by the methane tail has increased, the cycloidal shape of the tail has become more prominent.

predominant ionospheric species went along with a reduction of the major component's gyroradius by only a factor of 28 amu/16 amu = 1.75, whereas the height h of hydrogen cycloids is about a factor of 8 smaller than that of methane ion trajectories. Therefore, only in the second step, the "effective" size of the ionospheric tail was strongly reduced.

As can be seen from fig. 6.27(f), because of the small hydrogen gyroradii, an electric field cavity downstream of Titan is practically not existent. The presence of the hydrogen component gives rise to an electric field enhancement at the tail's anti-Saturn-facing flank, where the H_2^+ velocity has become comparable to that of the CH_4^+ and N_2^+ constituent in the preceding simulations. The more of the heavier ionospheric species are "switched off" in sequence, the larger becomes the pick-up efficiency of the light H_2^+ component and the stronger is the electromagnetic field topology near Titan determined by the spatial extensions of the H_2^+ trajectories. The cycloidal shape of the nitrogen and the methane tails is clearly visible in figs. 6.28(a) and (b), for these ions experience the nearly unchanged electromagnetic fields in the E^+ hemisphere. Their dynamics are therefore well covered by the test particle treatment. Again, neither the CH_4^+ nor the N_2^+ constituent is able to cause a noticeable distortion of the electromagnetic fields. As displayed in figs. 6.26(d) and 6.28(d), the additional reduction of the CH_4^+ production rate has gone along with a significant increase of the N_2^+ velocity in the immediate vicinity of Titan. Besides, the cycloidal shape of the tail is also much better identifiable. This confirms that the heaviest species that is produced in sufficiently high concentrations – i.e. the methane component in the first test particle run – exerts control on the dynamics of all other pick-up species, even on those with a larger mass. In fig. 6.28, the pick-up of the nitrogen and methane components is *not* significantly affected by the predominant hydrogen constituent, for the cycloidal N_2^+ and CH_4^+ trajectories apparently "evade" the major H_2^+ concentration behind Titan.

6.2 Simulation results: 06:00 and 00:00 local time

A final issue that can be resolved by means of the test particle approach is the tail deformation that could be observed in the 06:00 LT and 00:00 LT runs. For the case of reduced N_2^+ and CH_4^+ production rates, figs. 6.29 and 6.30 display ancillary simulation results for the 06:00 LT and the 00:00 LT scenario, respectively. As shown in figs. 6.29(b) and (e), when the N_2^+ and CH_4^+ production rates are reduced, the E^+ flanks of the corresponding tails clearly exhibit a cycloidal shape, whereas their Saturn-facing flanks do no longer penetrate the E^- hemisphere. The expansion of the H_2^+ tail in E^- direction has diminished as well. In the region outside the major H_2^+ concentration, the nitrogen and methane particles experience a strong acceleration in the undisturbed electromagnetic fields. The imprint that the region of slow H_2^+ ions leaves on the velocity patterns of the two other species is clearly identifiable in figs. 6.29. In the wake region directly behind Titan, the pick-up of the N_2^+ and the CH_4^+ ions is now suppressed by the predominant H_2^+ ions.

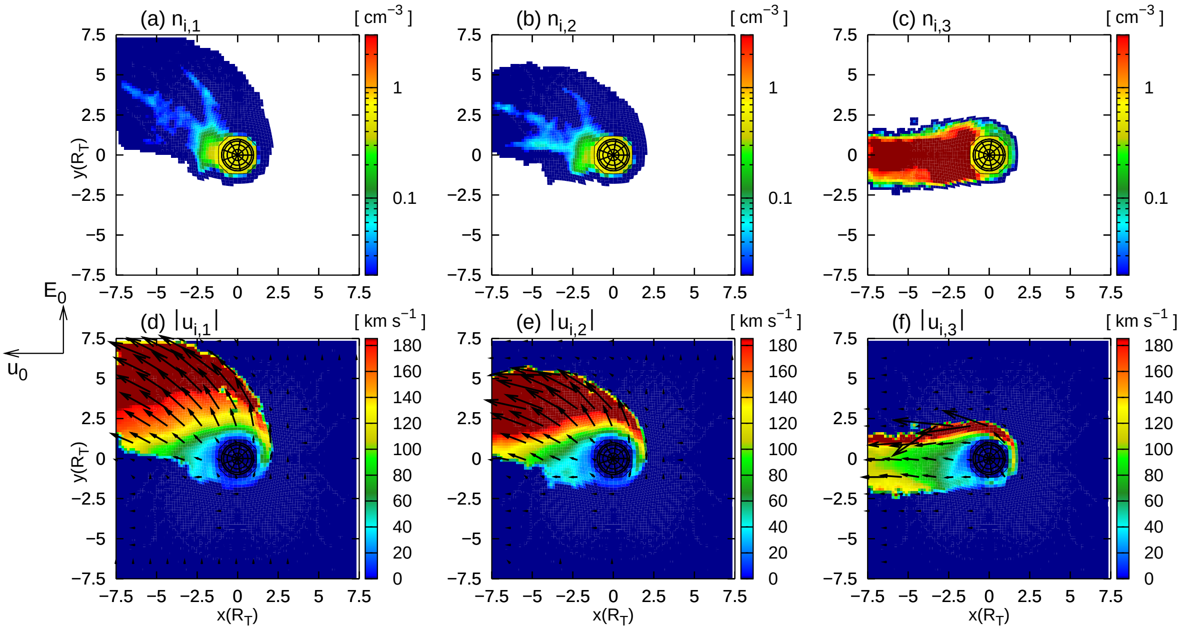

Figure 6.29: Test particle regime (molecular nitrogen and methane) at 06:00 Saturnian local time – Ionospheric plasma parameters in the equatorial plane. The production rates of nitrogen and methane are about a factor of 100 smaller than that of the molecular hydrogen component, so that the latter one has become the predominant species of ionospheric origin. Compared to the original 06:00 LT multi-species scenario, the shape of the nitrogen and the methane tail has undergone significant modifications. Instead of being shifted into the Saturn-facing hemisphere, the tails exhibit a rather cycloidal shape. The accumulation of H_2^+ ions in the E^- hemisphere is also clearly reduced.

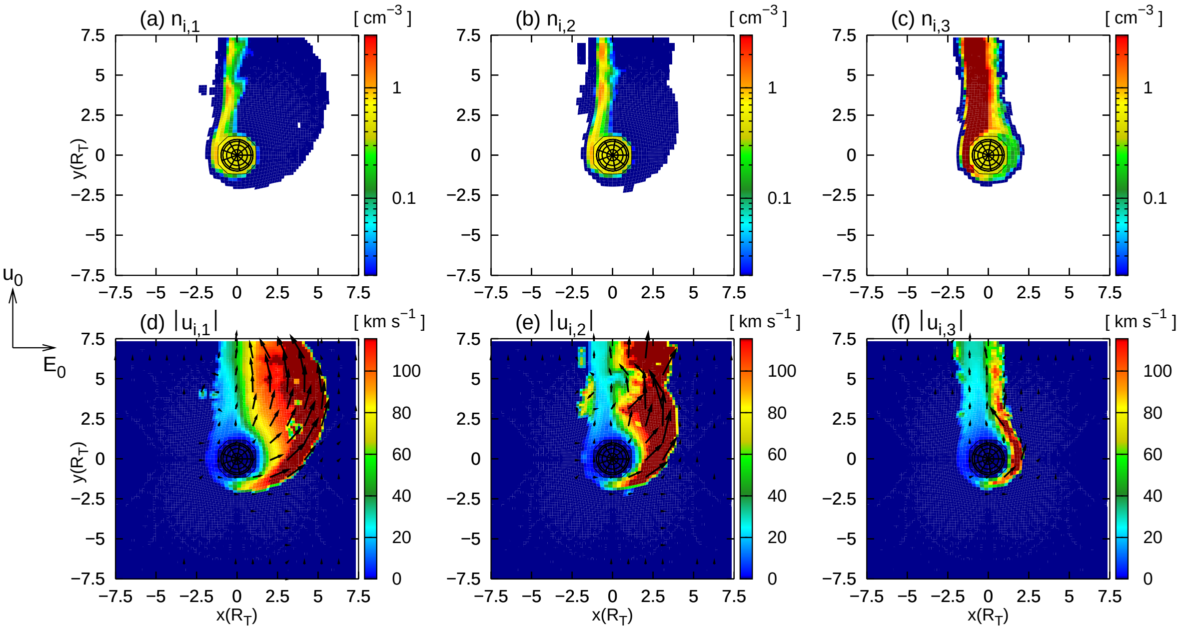

Figure 6.30: Test particle regime (molecular nitrogen and methane) at 00:00 Saturnian local time – Ionospheric plasma parameters in the equatorial plane. In the original 00:00 LT multi-species scenario, identical production rates had been chosen in all three ionospheric mass regimes. As a result of this, the three tails clearly expanded into the Saturn-facing hemisphere, the extension of the H_2^+ tail in E^- direction being of the order of several Titan radii. However, if the two heavier ionospheric species are generated only in test particle concentrations, the deformation of the H_2^+ tail vanishes completely. Thus, a sufficiently high production rate of the heavy species is mandatory for generating a noticeable effect on the tail shape of the light ionospheric constituents. The tails of the N_2^+ and the CH_4^+ ions are confined to the E^+ hemisphere as well.

In the initial 00:00 LT simulation run, the tail developed by the light H_2^+ ions was clearly deformed, i.e. it exhibited a strong tendency to penetrate into the E^- hemisphere. However, as displayed in fig. 6.29, in the test particle simulation, the H_2^+ tail does no longer expand into the Saturn-facing hemisphere. Due to the small ambient magnetospheric plasma velocity in the 00:00 LT scenario, the parameters w and h of the cycloidal trajectories are reduced as well. Consequently, as can be seen in fig. 6.29(e), the simulation domain now contains several complete arcs of the cycloidal methane trajectories. In any case, the test particle run illustrates that both the nitrogen and the methane component played a role in the modification of the hydrogen tail structure.

In another "extreme" scenario for 00:00 LT and 06:00 LT, the production rates of CH_4^+ and H_2^+ have been reduced to test particle conditions. The high production rate of molecular nitrogen has been maintained. The simulations have shown that the N_2^+ tail resumes its original asymmetric shape known from the two-species hybrid approach (cf. chapter 5). The two light species, on the other hand, accumulate in the wake region, but the electric field barrier forbids them to expand into the E^- hemisphere. Thus, a sufficiently high production rate of the two lighter species is required in order to cause a noticeable deformation of the N_2^+ tail in E^- direction.

7 Summary and concluding remarks

The main objective of the simulations presented in this chapter was to improve the simplifying models of the magnetospheric as well as of the ionospheric plasma that have been used in the first simulation attempts. In the simulations discussed in chapters 4 and 5, Titan's complex ionosphere had been represented by only a single ion species (N_2^+). Therefore, in a first step, the ionosphere model has been extended to multi-species conditions by introducing methane and molecular hydrogen as additional species. The three selected ion species are assumed to be representative of the mass regimes occurring in Titan's ionosphere. The mass of N_2^+ ions is about a factor 2 larger than the mean magnetospheric ion mass, whereas the mass of CH_4^+ is comparable to the mass of the hypothetical (N^+/H^+) ions. Finally, the tail structure developed by the H_2^+ ions should illustrate the interaction of a relatively light ionospheric species with the Saturnian magnetospheric plasma. This four-species model has been applied to the 18:00 LT scenario.

Compared to simulations that employed a single-species representation of Titan's ionosphere, neither the magnetic field topology nor the magnetospheric flow pattern in the vicinity of the satellite is noticeably affected by improving the ionosphere model. Especially, the topology of the magnetic draping pattern remains practically unaffected. These features have shown to be mainly determined by the heavy ionospheric nitrogen ions, so that the incorporation of two additional lighter species causes only minor changes. In the equatorial plane, each of the three ionospheric species develops a tail that is shifted in the direction of the convective electric field. However, due to the height and the width of the cycloidal pick-up trajectories depending linearly on the respective particle mass, the tail extension in the direction of the electric field is significantly different for the three species. This phenomenon may be called a *natural ion mass spectrometer* and should allow to distinguish between ions of different masses by means of spacecraft measurements. The quantitative properties of this mass spectrometer have shown to be in good agreement with both a simplified analytical model of the pick-up process and earlier test particle simulations conducted by Luhmann [96].

The modified ionosphere model also revealed that the pick-up processes of different ionospheric species cannot be understand independently of each other, but the heavier ionospheric species exert a decelerating influence on the lighter ones. The shape and diameter of the electric field cavity downstream of Titan are mainly controlled by the heaviest ionospheric species. Because of their smaller gyroradii, the tails of the lighter species are completely located inside this electric field cavity. On the one hand, the light ionospheric components are therefore unable to leave a noticeable imprint on the electromagnetic field topology near Titan, especially on the extension of the electric field cavity in E^+ direction. However, a test particle approach confirmed that they make at least a minor contribution to the reduction of $|\underline{E}|$ inside the central tail region. On the other hand, their transport away from the obstacle is at least partially suppressed by the reduced electric field strength in the wake. As has been demonstrated by means of a test particle model, the degree to which the heaviest ionospheric species is able to exert this kind of control on the dynamics of the lighter ones is strongly dependent on its production rate.

In a second step, the multi-species ionosphere conditions have been maintained and the magnetospheric plasma has been split up in a nitrogen (N^+) and a hydrogen (H^+) component.

Within the framework of this five-species approach, the four basic interaction scenarios at 00:00 LT, 06:00 LT, 12:00 LT and 18:00 LT have been revisited. At first, the case of Titan's dayside being exposed to the upstream flow has been investigated. The dynamics of the nitrogen ions have proven to be quite similar to the behaviour of the hypothetical (N^+/H^+) ions, as the masses of these two species differ only by a factor of 1.5. The characteristics of the nitrogen flow experience only a minor modification, i.e. only a weakly pronounced cavity of reduced N^+ density arises downstream of the obstacle. The direction of the N^+ flow does not undergo significant changes. Since the mass of the H^+ ions is about a factor of 14 smaller than the mass of nitrogen, the acceleration of these particles due to the Lorentz force is more than one order of magnitude larger. Therefore, the H^+ ions are clearly deflected around the obstacle, making a certain fraction of them incapable of gaining access to the region directly behind Titan. Hence, the magnetospheric plasma also exhibits some kind of *mass spectrometer effect*. The modification of the H^+ velocities also manifests in the magnetic field topology, for the field lines are synchronously transported by the magnetospheric plasma flow. While merely a minor widening of the draping pattern manifests in the polar plane, the extension of the magnetic pile-up region in the direction of the convective electric field is increased from a diameter of $3 - 3.5R_T$ to $5R_T$. As to be expected, the ionospheric mass spectrometer effect is also clearly identifiable in the results of this five-species model of Titan's plasma environment. The degree to which the H^+ ions are forbidden to enter the ionospheric tail region has proven to be strongly dependent on the temperature of these particles. The smaller is the thermal velocity of the protons, the less of them are able to pass the potential barriers at the outer flanks of the ionospheric tail and consequently, the more pronounced is the boundary separating the protons from the ionospheric plasma population.

It is of major importance to notice that these additional 18:00 LT simulations clearly illustrate the necessity to extend the simplifying model used in chapters 4 and 5 in two distinct steps. The results obtained in the first step, i.e. by including two additional ionospheric species while maintaining the single-species representation of the magnetospheric flow, have shown that in the 18:00 LT scenario, upgrading the ionosphere model does neither have a remarkable effect on the electromagnetic field topology nor on the magnetospheric plasma flow pattern obtained from the single-species model. The second step, i.e. splitting up the magnetospheric plasma flow, illustrated that in the 18:00 LT geometry, even the more complex three-species ionospheric tail structure is only slightly affected by the application of a more realistic model to the impinging magnetospheric plasma.

The second scenario that has been investigated by means of the five-species hybrid model is the case of Titan's nightside being exposed to the magnetospheric plasma at 06:00 local time. The ionospheric N_2^+ ions develop an extended, highly asymmetric tail. The ionospheric tails of methane and molecular hydrogen are again completely located in the region of reduced electromagnetic field strength downstream of the obstacle. On the one hand because of the weak Lorentz forces acting on these ions, on the other hand because the region of major ion production is located in the wake, the ionospheric densities in the tail are about an order of magnitude larger than in the 18:00 LT scenario. The massive accumulation of slow ionospheric particles in the vicinity of Titan also yields a certain deformation of the tail structures, i.e. a discrimination between CH_4^+ and H_2^+ by means of the ionospheric mass spectrometer is no longer possible. Besides, in contrast to the simulation results presented in chapter 5, the tail even exhibits a slight tendency to expand into the E^- hemisphere. In combination with their small gyroradii, this effect yields an almost symmetric tail structure for methane and hydrogen ions.

The five-species simulation of the 00:00 LT scenario clearly points out the restrictions of the original two-species simulation approach. In this situation, the wake structure is clearly affected by the presence of three ionospheric components, leading to a significant shift of the ionospheric tail into the E^- hemisphere. A similar effect does not occur in the multi-species analysis of the situation at 12:00 LT. The remarkable differences between both cases do not only emerge from the reduced magnetospheric electric field strength at 00:00 LT, but the expansion of the tail into the E^- hemisphere can also be ascribed to the location of the dayside ionosphere in the 00:00 LT geometry.

The simulations presented in this chapter provide a general impression of the physical processes that determine the large-scale features of Titan's ionospheric tail. However, in reality, the production rates in different ionospheric mass regimes, especially the "output" of the complex reaction chains in Titan's upper ionosphere, have shown to depend strongly on the satellite's orbital position and the ambient magnetospheric conditions. Therefore, the real physics of Titan's ionospheric tail should be considered an intermediate scenario between the two extreme cases discussed in this chapter: on the one hand, high production rates in all ionospheric mass regimes; on the other hand, test particle conditions in all ionospheric mass regimes.

CHAPTER 7

Hybrid simulations versus Cassini magnetometer data

While the preceding simulation results provided a qualitative overview of Titan's plasma interaction, this chapter deals with an application of the simulation model to the situation during specific Cassini flybys. Specifically, the simulation results shall be compared to data from the Cassini Magnetometer Instrument (MAG), consisting of a Fluxgate Magnetometer and a Vector Helium Magnetometer. A detailed description of the instrument is given by Dougherty *et al.* [44]. The data used for the study presented in this chapter have been collected by the Fluxgate Magnetometer.

In the years 2004–2006, more than 20 Cassini flybys of Titan have been accomplished. An overview of the major flyby parameters is given in table 7.1. The magnetic field data collected during these flybys indicate that the Voyager 1 flyby provided indeed only a snapshot of the magnetospheric plasma near Titan: During *none* of the Cassini flybys, the magnetic field was directed strictly perpendicular to the satellite's orbital plane. Furthermore, even during those flybys of Titan that took place at nearly identical orbital positions of the satellite, significant differences in the background magnetic field were detected (cf. Ma *et al.* [99] and Neubauer *et al.* [118]). For the study presented here, the magnetic field data collected during a series of five flybys have been analyzed. On the one hand, the flybys T9, T11 and T15 provide an impression of the structure of Titan's induced magnetotail. The T8 flyby, on the other hand, was a passage through the magnetic pile-up region at Titan's ramside. These four flybys feature a rather simple geometry, for the spacecraft trajectory was completely located in Titan's equatorial plane. Thus, they allow a straightforward interpretation of the measured magnetic field signatures. However, the simulation model has also been applied to the geometry of the T6 flyby. During this passage, Cassini crossed Titan's orbital plane on an "oblique" trajectory from "above" to "below". Titan's orbital position during the five flybys under consideration can be seen in fig. 7.1. During each of these five flybys, the major component of the ambient Saturnian magnetic field was directed parallel to Titan's orbital plane. This is the reason why – in contrast to the geometries discussed in the preceding chapters – a pronounced magnetic lobe structure was formed in Titan's orbital plane.

At the time of this writing, only data from the MAG instrument were available, whereas the analysis of the material collected by the Cassini plasma instruments was still in a very early stage. Therefore, following the strategy chosen in the simulation studies of Ma *et al.* [99] and Neubauer *et al.* [118], parameters like the upstream magnetospheric plasma velocity and flow direction as well as the composition had to be "guessed" in such way that optimum agreement between the simulated and measured magnetic field signatures was achieved. Moreover, this

Flyby	Closest approach time	Closest approach altitude
TA	26 October 2004, 15:30 UT	1174 km
TB	13 December 2004, 11:38 UT	1200 km
T3	15 February 2005, 06:58 UT	1577 km
T4	31 March 2005, 20:05 UT	2402 km
T5	16 April 2005, 19:05 UT	950 km
T6	22 August 2005, 08:54 UT	3669 km
T7	7 September 2005, 08:12 UT	1075 km
T8	28 October 2005, 04:16 UT	1353 km
T9	26 December 2005, 18:59 UT	10409 km
T10	15 January 2006, 11:41 UT	2043 km
T11	27 February 2006, 08:25 UT	1813 km
T12	18 March 2006, 23:12 UT	1951 km
T13	30 April 2006, 20:58 UT	1855 km
T14	20 May 2006, 12:18 UT	1879 km
T15	2 July 2006, 09:21 UT	1906 km
T16	22 July 2006, 00:25 UT	950 km
T17	7 September 2006, 20:16 UT	1000 km
T18	23 September 2006, 18:59 UT	960 km
T19	9 October 2006, 00:23 UT	980 km
T20	25 October 2006, 15:58 UT	1030 km
T21	12 December 2006, 11:41 UT	1000 km
T22	28 December 2006, 10:05 UT	1300 km

Table 7.1: Cassini flybys of Titan in the years 2004–2006.

method also provides some hints towards the characteristics of the impinging plasma, since a reduced magnetospheric flow speed has already proven to leave a strong "fingerprint" on the structure of Titan's magnetic lobes. Hence, the simulation results can also be considered an additional source of information for the interpretation of the Cassini plasma data. For the simulation runs presented in this chapter, the input parameter sets are modified versions of the Voyager 1 configuration. Choosing the parameters in this way is supported by the study that has recently been published by Neubauer *et al.* [118].

All simulation results for specific Cassini flyby geometries are presented with respect to the *Titan interaction coordinate system* that has been introduced by the Cassini magnetometer team [6]. In contrast to the other coordinate systems used in this work, the axes of the Titan interaction system are denoted by capital letters (X, Y, Z). The system is suitable for an illustration of effects like deviation from ideal corotation, since its X axis is assumed to be parallel to Titan's orbital motion, i.e. to the direction of an ideally corotating flow. The positive Y axis points from Titan towards Saturn, whereas the Z axis completes the right-

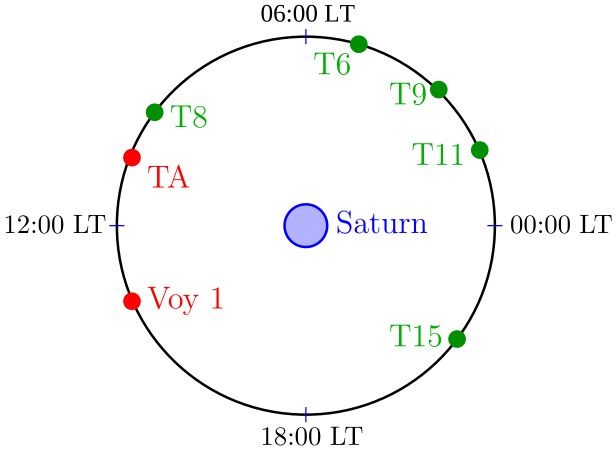

Figure 7.1: Locations of Titan during the Cassini flybys that have been selected for a comparison of the simulation results with data from the MAG instrument. During T9, the spacecraft passed through Titan's wake at 03:00 Saturnian local time. In the same way, the scientific objective of T11 and T15 was an analysis of Titan's wake structure; these flybys took place at 01:30 LT and 21:30 LT, respectively. Cassini's trajectory during the T8 flyby crossed the magnetic pile-up region at Titan's ramside while the satellite was located in the dayside region of Saturn's magnetosphere at about 09:30 LT. The T6 flyby took place at 05:00 LT. The location of Titan during the Voyager 1 flyby (Voy 1) on 12 November 1980 as well as the position of the Cassini TA encounter on 26 October 2004 are denoted by red circles.

handed coordinate system, pointing "upwards". For the T9 flyby of Titan that took place at about 03:00 clock angle position, this coordinate frame is illustrated in fig. 7.2.

The flybys are not discussed in a chronological sequence, but with respect to the specific features of the flyby trajectory. At first, the discussion will focus on the equatorial wake flybys T9, T11 and T15, followed by an analysis of the data collected during the ramside T8 encounter. Finally, the discussion will focus on the T6 flyby. The analysis of specific flyby geometries will also allow to quantify the degree to which the magnetic field topology is controlled by the properties of Titan's ionosphere. Of course, the location of the dayside ionosphere has been adjusted to the specific flyby geometries, including Titan's orbital position and the tilt of the satellite's orbital plane with respect to the direction of the solar radiation. However, the latter factor has shown to take practically no influence on the structure of the magnetotail.

The simulation results for the T9 flyby will be revisited in the subsequent chapter, where a modified simulation scenario is presented, trying to include at least preliminary material from the Cassini Plasma Spectrometer.

1 Titan's magnetic lobes during Cassini's T9 flyby

This section deals with the magnetic field signature detected during the T9 flyby of Titan. The discussion of the major flyby and simulation parameters is followed by an extensive comparative analysis of Titan's magnetic field signature.

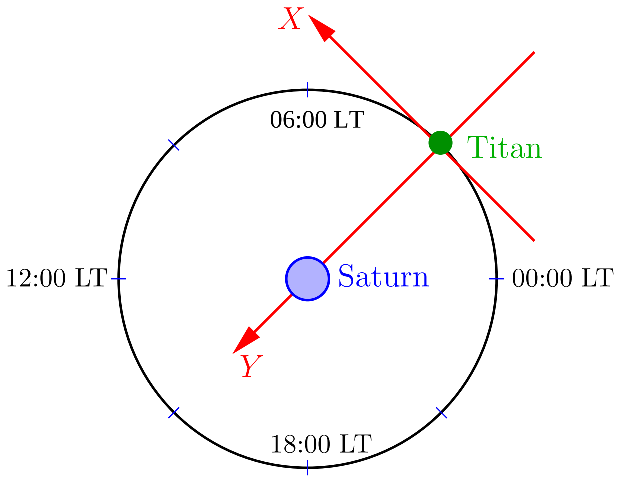

Figure 7.2: Cassini's T9 flyby of Titan took place at about 03:00 Saturnian local time, i.e. the Saturn-Titan-line formed an angle of about 45° with the 12:00 LT-Saturn-00:00 LT line. The simulation results presented in this chapter refer to the Titan interaction system, i.e. the X axis is aligned with the direction of ideal corotation, whereas the Y axis points from Titan to Saturn. The Z axis (not shown here) completes the right-handed coordinate system and points upwards.

1.1 Flyby and simulation parameters

During T9, Cassini passed through Titan's magnetotail in the equatorial plane while the satellite was located at about 03:00 clock angle position on its orbit around Saturn. Cassini achieved its closest approach altitude of $4R_T$ at 18:59 UT on 26 December 2005. As Cassini passed through Titan's wake in a relatively large distance to the surface of the satellite, the T9 flyby provides a unique chance to study the structure of Titan's induced magnetotail. Because during the entire Cassini mission, no flyby with a similar trajectory will take place, the analysis of the data collected during T9 is currently in the focus of scientific interest. The flyby trajectory is illustrated in fig. 7.3. As can be seen from fig. 7.3(b), displaying the projection of the spacecraft trajectory on the (X, Z) plane, Cassini's passage was completely located in Titan's orbital plane. Therefore, the discussion of the magnetic field signature detected during T9 will be based on two-dimensional plots of the plasma and electromagnetic field parameters in the (X, Y) plane of the Titan interaction system.

The simulation parameters for the T9 scenario are listed in tab. 7.2. Since the flyby occurred at 03:00 Saturnian local time, the Y axis of the Titan interaction system formed an angle of about 45° with the (12:00 LT)-Saturn-(00:00 LT) line. Best agreement between simulation and MAG measurements could be achieved by choosing the upstream plasma composition similar to the Voyager 1 parameters, i.e. the upstream flow consists of atomic nitrogen and hydrogen, the ratio of the number densities being $2:1$. One the one hand, the upstream plasma velocity is again given by $u_0 = 120\,\mathrm{km/s}$. On the other hand, in the first T9 simulation scenario, the vector $\underline{u}_0$ is assumed to form an angle of $\Psi = -34°$ with the $(+X)$ axis that points in the direction of ideal corotation. In other words, $\underline{u}_0$ is parallel to Titan's orbital plane, but it points away from Saturn. In order to investigate the degree to which deviations from ideal corotation affect the magnetotail structure, a second simulation geometry in which the impinging flow is aligned with the positive X axis has been considered.

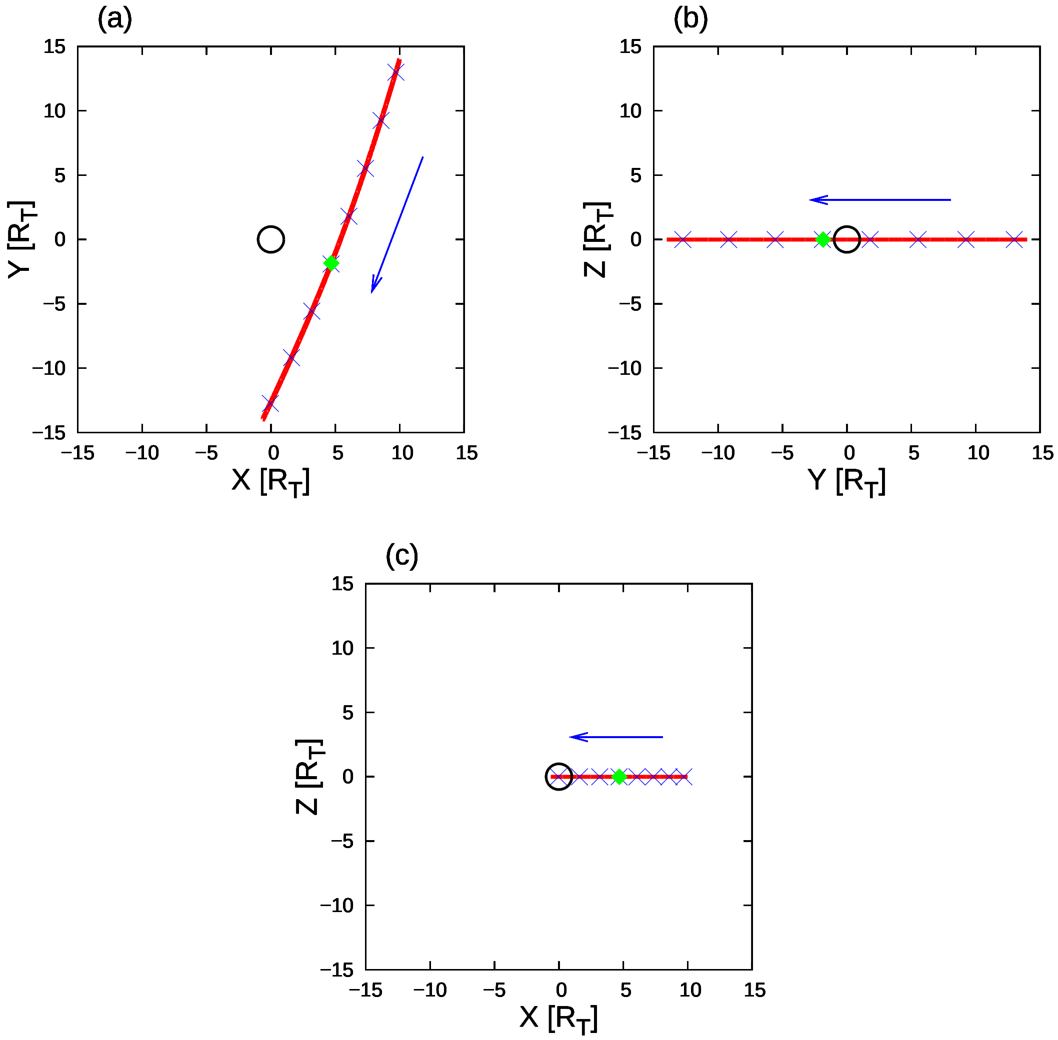

Figure 7.3: Cassini's trajectory during the T9 flyby of Titan. The figure displays the projection of the spacecraft trajectory (a) on the (X, Y) plane, (b) on the (Y, Z) plane and (c) on the (X, Z) plane of the Titan interaction system. The X axis is aligned with the direction of ideal corotation. The Y axis points from Titan to Saturn. The blue arrows indicate the direction of the passage, whereas the green diamond marks the position of the closest approach at a distance of $4R_T$ to the surface of the obstacle. The blue crosses along the trajectory are 30 minutes apart, starting at 17:00 UT. The figures display the part of the trajectory which is located inside a cubic box with $-15R_T < X, Y, Z < +15R_T$. For a region with $-14R_T < X, Y, Z < +14R_T$, the magnitude and orientation of the magnetic field vector detected by the MAG instrument have been compared to the results of several hybrid simulations with different input parameters. As can be seen from fig. (a), during the T9 flyby, the spacecraft passed through the wake region downstream of Titan. Fig. (b) illustrates that Cassini's trajectory was completely located in Titan's equatorial plane, coinciding with the (X, Y) plane of the Titan interaction system. Therefore, the T9 flyby provides an optimal opportunity to study the structure of Titan's magnetotail.

Quantity	Symbol	Numerical value
Magnetic field	$\underline{B}_0$	$(3.73, 4.70, -2.15)$ nT
	$\lvert\underline{B}_0\rvert$	$6.37\,\mathrm{nT}$
Plasma flow velocity (run 1)	$\underline{u}_0$	$(120\ \cos 34°, -120 \sin 34°, 0)$ km/s
	$\lvert\underline{u}_0\rvert$	$120\,\mathrm{km/s}$
Plasma flow velocity (run 2)	$\underline{u}_0$	$(120\ \cos 0°, -120 \sin 0°, 0)$ km/s
	$\lvert\underline{u}_0\rvert$	$120\,\mathrm{km/s}$
Nitrogen (N^+) density	$n_{m,1}$	$0.2 \cdot 10^6\,\mathrm{m}^{-3}$
Hydrogen (H^+) density	$n_{m,2}$	$0.1 \cdot 10^6\,\mathrm{m}^{-3}$
Nitrogen temperature	$kT_{m,1}$	$1578.48\,\mathrm{eV}$
Hydrogen temperature	$kT_{m,2}$	$112.75\,\mathrm{eV}$
Thermal velocity	$v_{th,N^+} = v_{th,H^+}$	$180\,\mathrm{km/s}$
Nitrogen plasma beta	$\beta_{m,1}$	3.13
Hydrogen plasma beta	$\beta_{m,2}$	0.11
Alfvén velocity	v_A	$81.64\,\mathrm{km/s}$
Alfvénic Mach number	M_A	1.47
Sound velocity	c_S	$146.34\,\mathrm{km/s}$
Sonic Mach number	M_S	0.82
Magnetosound velocity	c_{MS}	$169.01\,\mathrm{km/s}$
Magnetosonic Mach number	M_{MS}	0.71
N_2^+ production rate (high emission)	$Q_{i,1}$	$2.18 \cdot 10^{25}\,\mathrm{s}^{-1}$
CH_4^+ production rate (high emission)	$Q_{i,2}$	$2.18 \cdot 10^{25}\,\mathrm{s}^{-1}$
H_2^+ production rate (high emission)	$Q_{i,3}$	$2.18 \cdot 10^{25}\,\mathrm{s}^{-1}$
N_2^+ production rate (low emission)	$Q_{i,1}$	$6.54 \cdot 10^{24}\,\mathrm{s}^{-1}$
CH_4^+ production rate (low emission)	$Q_{i,2}$	$6.54 \cdot 10^{24}\,\mathrm{s}^{-1}$
H_2^+ production rate (low emission)	$Q_{i,3}$	$6.54 \cdot 10^{24}\,\mathrm{s}^{-1}$
Box size	X	$-15R_T \leq X \leq +15R_T$
	Y	$-15R_T \leq Y \leq +15R_T$
	Z	$-15R_T \leq Z \leq +15R_T$
Number of grid cells	(N_X, N_Y, N_Z)	$(100, 100, 100)$
Time step	Δt	$0.48\,\mathrm{s}$
Total number of time steps	$N_{\Delta t}$	20000
Smoothing parameter	α_S	0.12

Table 7.2: Simulation parameters for Cassini's T9 flyby of Titan on 26 December 2005. The parameters refer to the Titan interaction system (X, Y, Z). In the first geometry, the impinging magnetospheric plasma flow forms an angle of 34° with the direction of ideal corotation, while in a companion simulation, the flow is assumed to be aligned with the $(+X)$ axis. In contrast to the situation during the Voyager 1 flyby, the major component of the Saturnian magnetic field $\underline{B}_0$ does not point in $(-Z)$ direction, but it is directed parallel to Titan's orbital plane. However, in analogy to the Voyager 1 scenario, the upstream plasma is super-alfvénic, yet subsonic and submagnetosonic. For the simulation, the curvilinear fisheye grid has been replaced by an equidistant Cartesian grid with 100 cells in each spatial direction.

An estimate of the undisturbed Saturnian magnetic field B_0 at Titan's position during T9 has been provided by the Cassini magnetometer team:

$$\underline{B}_0 = (3.73, 5.70, -2.15)\ \mathrm{nT} \quad . \tag{7.1}$$

Transforming the B_X and the B_Y component into a coordinate system whose $\tilde{X}$ axis forms an angle of $\Psi = -34^\circ$ with the X axis of the Titan interaction system yields

$$\begin{aligned} B_{\tilde{X}} &= B_X \cos(-34^\circ) + B_Y \sin(-34^\circ) \approx -0.10\,\mathrm{nT} \quad ; & (7.2)\\ B_{\tilde{Y}} &= -B_X \sin(-34^\circ) + B_Y \cos(-34^\circ) \approx 6.81\,\mathrm{nT} \quad . & (7.3) \end{aligned}$$

Hence, the projection of the background magnetic field on Titan's equatorial plane is oriented nearly perpendicular to the direction of the impinging magnetospheric plasma in the first simulation run. However, best agreement between simulation results and measurements could be achieved by using a slightly modified upstream value: The values of B_X and B_Z suggested by the Cassini Magnetometer team have been maintained, while the second component has been reduced from $B_Y = 5.7\,\mathrm{nT}$ to $B_Y = 4.7\,\mathrm{nT}$. Thus, in a coordinate system whose X axis is aligned with the undisturbed flow direction, the upstream magnetic field is given by

$$\begin{aligned} B_{\tilde{X}} &\approx 0.46\,\mathrm{nT} \quad ; & (7.4)\\ B_{\tilde{Y}} &\approx 5.98\,\mathrm{nT} \quad ; & (7.5)\\ \arctan\frac{B_{\tilde{Y}}}{B_{\tilde{X}}} &\approx 85.6^\circ \quad , & (7.6) \end{aligned}$$

i.e. the projection of $\underline{B}_0$ on the equatorial plane is still nearly perpendicular to the undisturbed flow direction.

In analogy to the situation during the Voyager 1 flyby, the thermal speed of the magnetospheric ions still exceeds the mean plasma velocity u_0. The values of the plasma betas of nitrogen and hydrogen (cf. tab. 7.2) have been chosen in such way that the thermal velocities of H^+ and N^+ ions possess equal values, i.e. the temperatures of these ion species differ by a factor of 14, whereas the plasma beta of the dominant nitrogen component is about a factor of 28 larger than the hydrogen beta. The upstream plasma flow is again super-alfvénic ($M_A > 1$), yet subsonic ($M_S < 1$) and submagnetosonic ($M_{MS} < 1$).

The simulations presented in the preceding chapters have indicated that the magnetic field topology in the vicinity of Titan is mainly controlled by the characteristics of the impinging magnetospheric plasma. The production rates in the ionosphere play only a minor role. The T9 scenario provides an opportunity to quantify the influence of the ionospheric production rates on the large-scale magnetic field topology. Therefore, for both directions of the upstream plasma flow, two simulation runs have been carried out, each of them being based on the assumption of equal production rates for the three ionospheric species included in the model. In the first simulation run, the production rate of each species is set to a value of $Q = 2.18 \cdot 10^{25}\,\mathrm{s}^{-1}$. In the companion simulation, the production value is about a factor of 3.3 smaller.

In order to circumvent even slight modifications of the tail structure due to the presence of the outer boundaries of the simulation box, a large computational domain with an extension of $\pm 15 R_T$ in each direction has been chosen. The number of grid cells in each spatial direction is $N_X = N_Y = N_Z = 100$, yielding a spatial resolution of $0.3R_T = 772.5\,\mathrm{km}$. In such a geometry, the obstacle itself possesses a radius of only three cells. The simulation will neither be able to resolve the detailed features of the magnetic pile-up region nor the region of major ionospheric production. Because in such a geometry, the fisheye grid is not able to provide a noticeable enhancement of the spatial resolution and is also, according to several test runs, no longer required to avoid the formation of numerical artifacts, the curvilinear grid has been replaced by an equidistant Cartesian grid.

1.2 Comparison between simulation results and MAG measurements

The simulation results for the T9 flyby are displayed in figs. 7.4 to 7.7. For the case of an upstream flow that deviates from ideal corotation, the simulated magnetic field along the Cassini trajectory is displayed in the panels on the left-hand side of fig. 7.4. The green line denotes the magnetic field signature obtained from the high emission run, whereas the red line refers to the case of a weakly emitting obstacle. For comparison, the data from the Cassini magnetometer are shown in the right-hand panels. In the same way, the magnetic field signature for an ideally corotating upstream flow is displayed in fig. 7.5. Two-dimensional illustrations of the magnetic field components in Titan's equatorial plane are displayed in figs. 7.6 and 7.7, respectively. In the following, the runs assuming the plasma flow to form an angle of $\Psi = -34^\circ$ with the X axis will be referred to as the 34° simulations.

As can be seen from the left-hand panels in figs. 7.4 and 7.5, the key features developed by the magnetic field are nearly independent of the total ion production, i.e. a reduction of the production rate by a factor of 3.3 goes along with only a slight modification of the magnetic field along Cassini's trajectory. Thus, it is evident that the structure of the magnetic lobes is primarily controlled by the magnetospheric upstream conditions. The newly generated ionospheric particles, on the other hand, affect the electric field and therefore the pick-up process, whereas they have only minor influence on the magnetic field structure in the lobes. This is consistent with the simulation results presented in the preceding sections.

As displayed in fig. 7.4(b), Cassini measurements show that the B_X component remained nearly undisturbed until closest approach at about 19:00 UT. Right after closest approach, a dip was detected in the B_X component, indicating a decrease from $B_X \approx 4\,\mathrm{nT}$ to values below $B_X \approx -3\,\mathrm{nT}$, i.e. the B_X component reversed its direction. The notch is relatively sharp: Only 40 minutes after the beginning of the break-in, B_X returned to the original value of $B_X \approx 4\,\mathrm{nT}$. As can be seen from fig. 7.4(a), the position of the notch in B_X is well reproduced by the 34° simulations. The model predicts a minimum value of $B_X = -1\,\mathrm{nT}$ for the case of a weakly emitting obstacle, whereas a value of $B_X = -2\,\mathrm{nT}$ can be obtained from the simulation using a high production rate. However, in both 34° simulations, the dip is broader than the structure detected by the Cassini magnetometer; especially the steepness of the dip's outbound flank around 19:40 UT is underestimated by the simulation model.

Directly before closest approach at about 19:00 UT, the 34° simulations predict the existence of an enhancement in the B_X component which is not consistent with the measurements. As can be seen from fig. 7.4(a), according to the simulations, B_X reaches a maximum, followed by a strong decrease to the minimum value achieved in the notch after 19:00 UT. In the case of a high ion production rate, B_X reaches a peak value of about $8.8\,\mathrm{nT}$, which is about a factor of

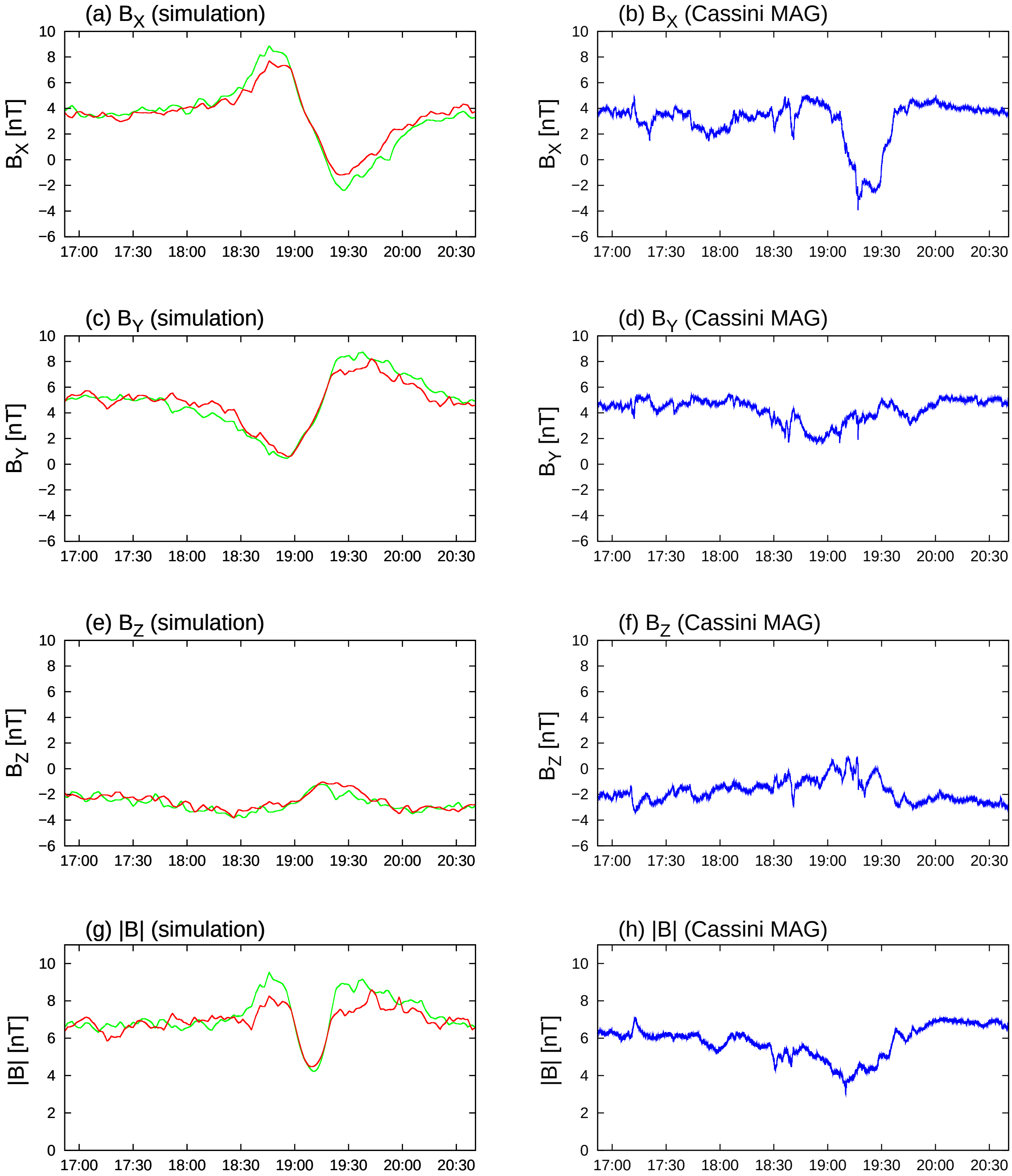

Figure 7.4: Titan's magnetic field signature during Cassini's T9 flyby. The figure displays the simulation results for the case of an upstream flow that forms an angle of 34° with the direction of ideal corotation. The flow is directed away from Saturn. The panels on the left-hand side show the magnetic field signatures obtained from the simulations. Two different cases have been considered: On the one hand, the total ion production rate for each species has been set to a value of $Q = 6.54 \cdot 10^{24}\,\mathrm{s}^{-1}$ (red line). On the other hand, a second scenario in which Q is about a factor of 3.3 larger has been analyzed (green line). The panels on the right-hand side display the magnetic field signature detected by the Cassini magnetometer. The closest approach occurred at 19:00 UT. In the geometry under consideration, the projection of the undisturbed magnetic field on the equatorial plane is nearly perpendicular to the impinging plasma flow. This yields a nearly symmetric structure for the magnetic lobes, as can be seen from figs. (a) and (c). However, even though the positions of the peaks and minima are in good agreement with magnetometer data, the magnetic field distortions are clearly overestimated by this simulation approach.
Simulation parameters: see table 7.2.

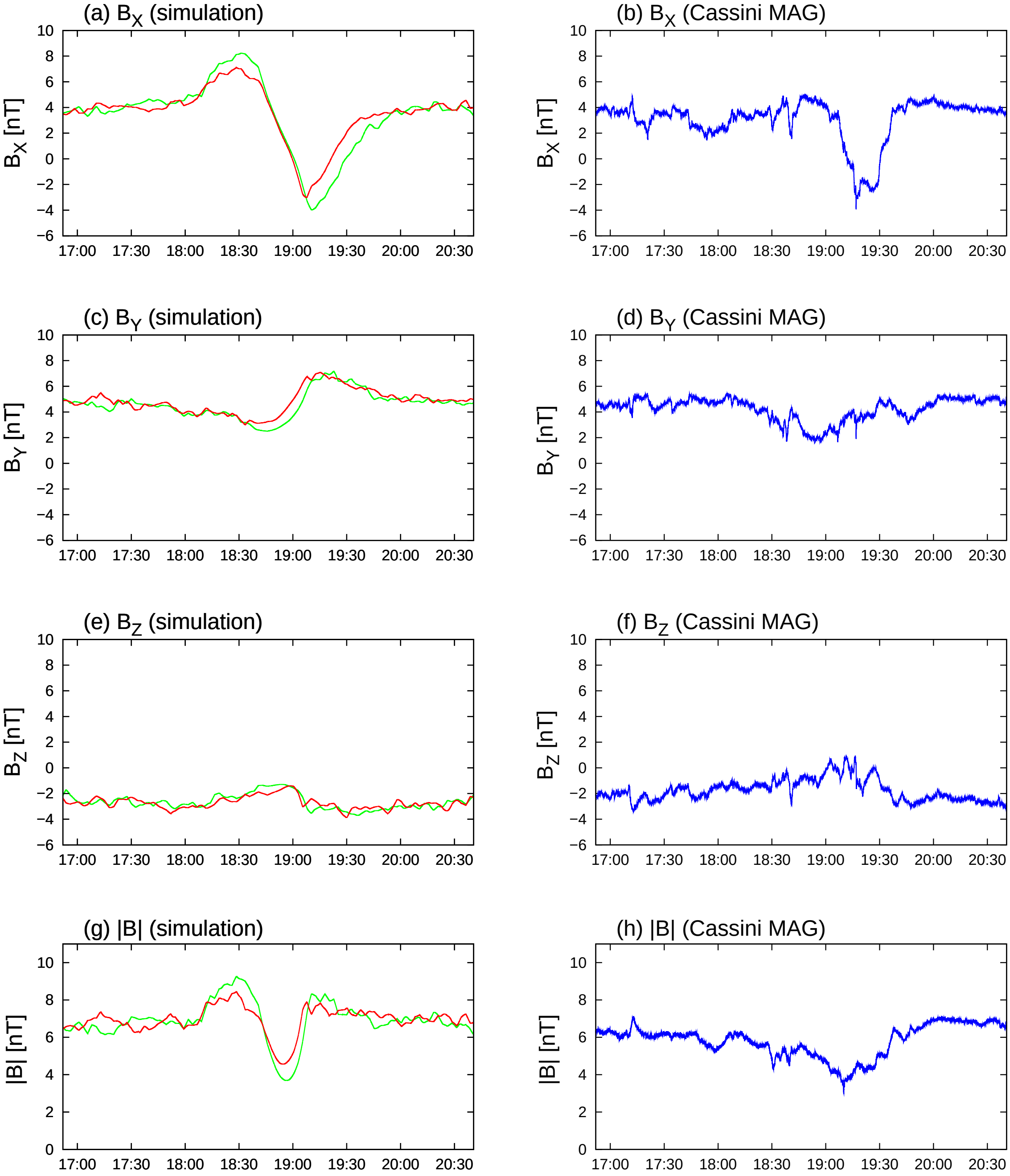

Figure 7.5: Titan's magnetic field signature during Cassini's T9 flyby. The figure displays the simulation results for the assumption of an ideally corotating plasma flow. Again, the case of a low ion production rate (red line) is compared to a scenario with an increased ion production (green line). The corresponding magnetic field signatures from the Cassini magnetometer are displayed on the right-hand side. Due to the projection of the upstream magnetic field vector on the (X, Y) plane being no longer perpendicular to the impinging plasma flow, the equatorial magnetic lobe structure in this geometry exhibits a pronounced asymmetry. The simulation model predicts the formation of a relatively sharp notch in the B_X component directly after closest approach at 19:00 UT, which is in complete correspondence to Cassini magnetometer data. Even though the occurrence of an overshoot in B_X before closest approach is not consistent with magnetometer data, this structure is clearly not as pronounced as in the case of the impinging velocity vector not being collinear to the X axis. During the flyby, the magnetometer detected nearly homogeneous B_Y and B_Z components. These features are well reproduced by the simulation model.
Simulation parameters: see table 7.2.

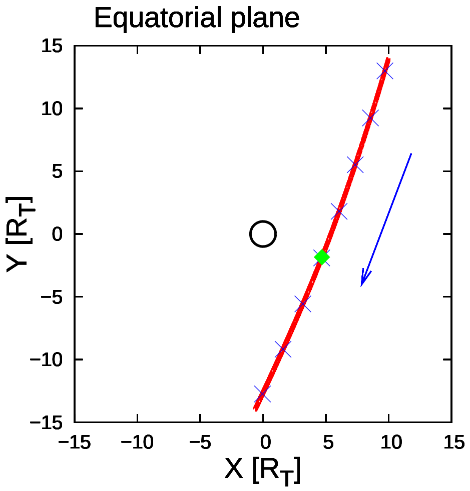

(a) Cassini flyby trajectory in the equatorial plane

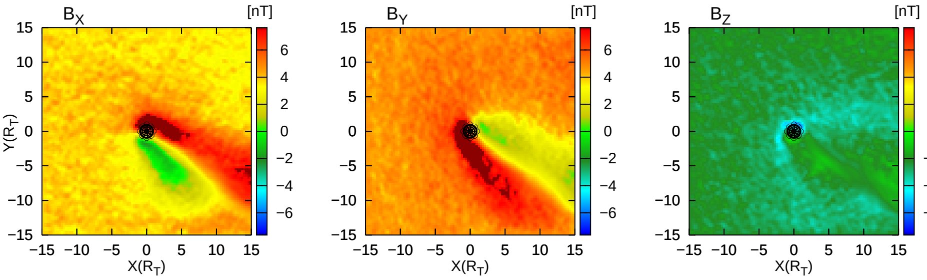

(b) Low emission: Magnetic field components

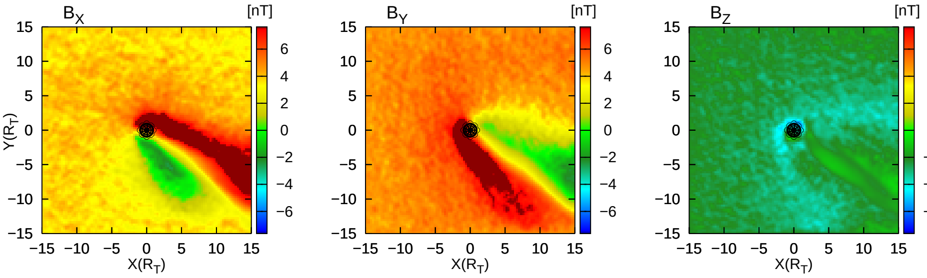

(c) High emission: Magnetic field components

Figure 7.6: Simulation of Titan's magnetic field signature during Cassini's T9 flyby. For the case of Titan being exposed to a flow that forms an angle of 34° with the direction of ideal corotation, the figure provides a two-dimensional illustration of the magnetic field components in the satellite's equatorial plane. For the low emission scenario, the components of $\underline{B}$ are displayed in panel (b), whereas panel (c) illustrates the situation for the case of an increased ion production rate. For a better orientation, the spacecraft trajectory in the equatorial plane is again displayed in fig. (a). The plots illustrate that the global magnetic field topology in the vicinity of Titan does not undergo significant modifications when the obstacle's ion production is enhanced. Due to the projection of the undisturbed magnetic field vector on the equatorial plane being nearly perpendicular to the impinging flow, the magnetic lobes exhibit a nearly symmetric structure with respect to the direction of the undisturbed magnetospheric plasma. While the B_Z component remains nearly undisturbed, the magnetic lobes clearly manifest in the B_X and the B_Y component. Perpendicular to the flow direction, the lobe region possesses an extension of about $10R_T$. Downstream of Titan, magnetic distortions should be identifiable in distances of more than $15R_T$ to the center of the obstacle. However, such a highly symmetric lobe structure is not in best agreement with the magnetometer data collected during T9.
Simulation parameters: see table 7.2.

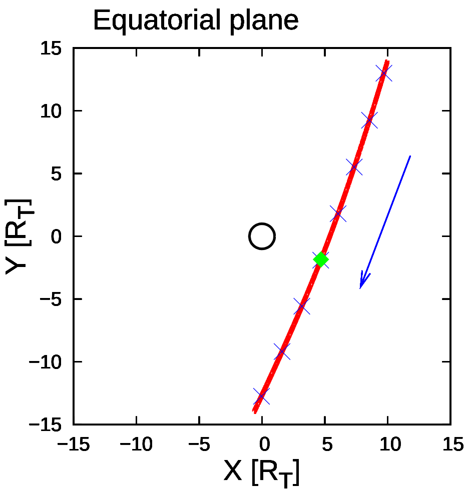

(a) Cassini flyby trajectory in the equatorial plane

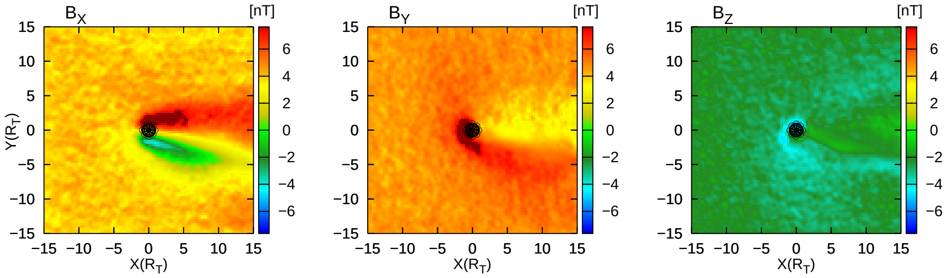

(b) Low emission: Magnetic field components

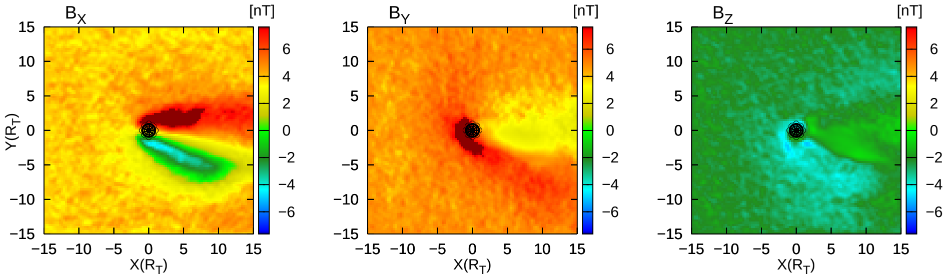

(c) High emission: Magnetic field components

Figure 7.7: Simulation of Titan's magnetic field signature during Cassini's T9 flyby. For the assumption of an ideally corotating magnetospheric flow, the figure displays the magnetic field components in the equatorial plane: (b) low emission and (c) high emission. Aligning the direction of the impinging flow with the X axis of the Titan interaction system goes along with an asymmetrization of the magnetic lobe structure as well as a reduction of the magnetic field enhancements in the wake region. The lobe structure obtained from this simulation scenario is in better agreement with the data obtained during T9 than the results of the 34° geometry. However, the existence of an enhanced B_X component in the Saturn-facing lobe is not consistent with Cassini measurements.
Simulation parameters: see table 7.2.

2.4 larger than the background value of $B_{X,0} = 3.73\,\mathrm{nT}$. In contrast to this, the assumption of a weakly emitting obstacle leads to a peak value of only 7.5 nT, i.e. the background value is exceeded by a factor of 2.0. The mechanism that gives rise to this overshoot is illustrated in fig. 7.6, displaying the components of the magnetic field in the equatorial plane. Both 34° simulation runs indicate the formation of two lobes in the B_X component which are aligned with the direction of the undisturbed magnetospheric plasma. Because in the 34° simulations, the projection of the undisturbed magnetic field vector on the equatorial plane is oriented nearly perpendicular to the direction of the impinging flow, the situation features a strong similarity to the simplified scenarios discussed in the preceding chapters. The draping of the magnetic field lines around the obstacle yields a strong magnetic field component tangential to the flow direction (cf. figs. 7.6 and 7.8). Thus, the formation of the Saturn-facing lobe goes along with an increase of the B_X component, while in the anti-Saturn-facing lobe, the B_X component is reduced and even reverses its direction.

According to the simulation model, when approaching Titan, Cassini should first have entered the Saturn-facing magnetic lobe from a region with relatively homogeneous magnetic field. Then, the spacecraft should have crossed the neutral region where B_X decreases to its background value. During the outbound pass, the spacecraft should have passed through the anti-Saturn-facing lobe in which B_X reverses its direction. The position of the notch in B_X that indicates the pass through the anti-Saturn-facing lobe is extremely well reproduced by the simulation model, although the simulated B_X lobe is not as sharply confined as the structure detected by Cassini. Nevertheless, the enhancement of B_X in the Saturn-facing lobe obtained from the 34° simulations has not been detected by the spacecraft. As can be seen from fig. 7.4(a), according to both 34° simulations, the lobe structure features only a slight asymmetry, i.e. the overshoot of B_X in the Saturn-facing lobe possesses almost the same magnitude with respect to the background value $B_{X,0} = 3.73\,\mathrm{nT}$ as the decrease of B_X in the anti-Saturn-facing lobe. However, this highly symmetric B_X structure suggested by the 34° simulations is not consistent with the Cassini measurements.

In the following, the agreement between simulation and measurements is discussed for the magnitude of the B_X notch on the one hand and for its position on the other hand. Concerning the structure of the break-in, the results of the simulation scenario that uses an ideally corotating flow are in better agreement with Cassini measurements. As can be seen from the red lines in fig. 7.5, referring to the results for a weakly emitting obstacle that is exposed to an ideally corotating flow, only a slight magnetic enhancement occurs in the Saturn-facing lobe, followed by a sharp dip that denotes a decrease of B_X to values below $B_X = -3\,\mathrm{nT}$. The structure of this dip, especially the steepness of its outbound flank, is in better correspondence to the magnetometer measurements than the results obtained from the 34° simulations. Even though the position of this dip is closer to 19:00 UT than in the results obtained from the 34° simulations, the agreement between simulated and measured dip position is reasonably good. Indeed, several test runs have shown that the larger is the angle between the plasma flow direction and the direction of ideal corotation[1], the better is the agreement between the position of the B_X notch detected by Cassini and the position of the break-in predicted by the simulations, i.e. the later should this structure have been detected by the spacecraft. However, an increase of the angle goes also along with a symmetrization of the magnetic lobe

---

[1] For this interpretation, the velocity vector is given by $\underline{u}_0 = u_0 \left(\cos\tilde{\Psi}, -\sin\tilde{\Psi}, 0\right)$, $\tilde{\Psi} > 0$.

structure. While in the simulations using an ideally corotating plasma, the increase of B_X in the Saturn-facing lobe is clearly exceeded by the decrease in the anti-Saturn-facing lobe, the magnitudes of the overshoot and the break-in become nearly identical when the angle between u_0 and the X axis is increased and consequently, the projection of $\underline{B}_0$ on the equatorial plane approaches perpendicularity to the undisturbed flow direction (cf. figs. 7.6 and 7.7).

On the other hand, when the upstream velocity is rotated from the direction of ideal corotation towards Saturn, i.e. when the vector $\underline{u}_0$ is assigned a non-vanishing component in $(+Y)$ direction, the asymmetry of the magnetic lobe structure is increased, compared to the case of an ideally corotating flow: The break-in of B_X in the anti-Saturn-facing lobe becomes sharper, whereas the minimum field value is reduced and becomes clearly smaller than the minimum value detected by Cassini. Simultaneously, the overshoot of B_X in the Saturn-facing lobe diminishes. Nevertheless, this process goes along with an additional rotation of the lobe structure towards Saturn, so that the position of the minimum detected by Cassini clearly differs from the location of the notch obtained from the simulations. For instance, although it is possible to develop a scenario in which the overshoot in the Saturn-facing lobe is about a factor of 10 smaller than the minimum achieved in the anti-Saturn-facing lobe, such a geometry predicts the lobe structure to be crossed around 18:00 UT. According to the simulation model, it is not possible to create a situation in which the overshoot of B_X in the Saturn-facing lobe vanishes completely.

Nevertheless, in the Cassini magnetometer data for T9, an enhancement in the B_X component, denoting the passage through the Saturn-facing lobe, is missing completely. Based on the data from a single flyby, it is impossible to determine whether the lack of the B_X peak arises from a systematic problem concerning the basic assumptions of the simulation model. For instance, the inflow boundary conditions assigned to the outer faces of the simulation box are based on the idea that the magnetospheric plasma flow in the vicinity of Titan is homogeneous on a characteristic length scale of about $30R_T$. Given the highly dynamic structure of Saturn's magnetosphere, this assumption may not always be justified. In any case, a complete series of flybys through the tail at nearly the same position as T9 would be necessary to investigate the magnetotail structure, particularly the enhancement of B_X in the lobes, in more detail. As discussed by Neubauer *et al.* [118], such a series has already been accomplished to investigate the magnetic field topology in the immediate vicinity of Titan, i.e. in altitudes below $1R_T$. However, to the author's knowledge, there are no additional magnetotail crossings with a similar trajectory like T9 planned for the near future.

As can be seen in fig. 7.4(d), only a slight distortion of the B_Y component was detected during the T9 flyby. The B_Y component exhibits a quite homogeneous structure and achieves a slightly pronounced minimum around closest approach at 19:00 UT, the minimum value being $B_Y = 1.8\,\mathrm{nT}$. While both simulation geometries show only slight differences between the high and low emission cases, the assumption of an ideally corotating flow yields significantly better agreement with the Cassini data than the 34° simulations. Even though the position of the minimum in the B_Y component at 19:00 UT is correctly reproduced by both simulation geometries, the 34° simulations predict the outbound flank of the notch to be significantly sharper than the structure detected by Cassini. As can be seen from fig. 7.4(c), a sharp decrease from the background value of $B_{Y,0} = 4.7\,\mathrm{nT}$ to values below $B_Y = 1\,\mathrm{nT}$ is followed by a steep increase of the B_Y component, yielding an overshoot with a peak value of about $B_Y = 8\,\mathrm{nT}$. According to the 34° simulations, after 19:30 UT, B_Y slightly decreases from the maximum to the undisturbed background field. In strong contrast to Cassini magnetometer data, the 34° simulations predict B_Y to clearly exceed $B_{Y,0}$ until 20:00 UT. However, as displayed in fig. 7.5(c), the simulations assuming the upstream flow to be aligned with the X axis show only a slight decrease of the Y component to values of about $3\,\mathrm{nT}$. The minimum is followed by a slight increase, before B_Y steadily returns to its background value well before 20:00 UT. The key features of the signature shown in fig. 7.5(c) are in good correspondence to magnetometer data, especially the positions of the regions with nearly undisturbed B_Y are well reproduced by the simulation model. Only the weakly pronounced minimum detected by Cassini right before 20:00 UT (cf. fig. 7.5(d)) does not occur in the simulation results. Besides, it should be noted that in the region near Titan, $B_{Y,0} = 4.7\,\mathrm{nT}$ seems to be an adequate background value for the B_Y component, indicating that the value of $B_{Y,0} = 5.7\,\mathrm{nT}$ suggested by the Cassini magnetometer team may indeed be a little to high.

In order to understand the mechanism giving rise to the structures in the B_Y component, it is helpful to consider the two-dimensional plots, as displayed in figs. 7.6 and 7.7. According to figs. 7.6(b) and (c), referring to an upstream flow that forms an angle of 34° with the X axis, the Y component clearly exhibits a lobe structure. However, unlike the B_X lobes, the Saturn-facing B_Y lobe is characterized by a decrease of B_Y to values of about $1-2\,\mathrm{nT}$, whereas the anti-Saturn-facing lobe indicates an increase of B_Y to values well above $8\,\mathrm{nT}$. In complete analogy to the B_X component, the 34° simulations indicate the B_Y lobes to be quite symmetric, i.e. the magnitude of the decrease in the Saturn-facing lobe is nearly identical to the overshoot in the anti-Saturn-facing lobe. On the one hand, changing the plasma flow direction from $\Psi = -34°$ to ideal corotation yields an alignment of the B_Y lobes with the flow direction, i.e. by altering the direction of $\underline{u}_0$, the B_Y lobes are rotated towards Saturn (cf. fig. 7.7). Of course, the same effect occurs in the B_X component. On the other hand, reducing the angle between the X axis and the flow direction does not only go along with a reduction of the peak field values in the B_Y component, but gives also rise to a certain asymmetrization of the lobe structure. As can be seen from figs. 7.6 and 7.7, in the case of an ideally corotating flow, the Saturn-facing B_Y lobe is clearly not as sharply confined as in the 34° scenario, while the diameter of the anti-Saturn-facing B_Y lobe perpendicular to the undisturbed flow direction remains nearly unchanged.

To sum up the major idea, the signatures exhibited by the B_X as well as the B_Y component can be understood by rotating the symmetric lobe structure that is formed when $(B_{X,0}, B_{Y,0})$ is nearly perpendicular to the undisturbed flow direction. The rotation of the lobe structure in the way that it becomes aligned with the direction of ideal corotation goes along with an asymmetrization, i.e. the anti-Saturn-facing lobe becomes more prominent than the Saturn-facing lobe structure.

In analogy to the B_Y component, the Cassini magnetometer detected only a weak distortion of the B_Z component. As can be seen from fig. 7.4(f), this component remains nearly constant at $B_Z = -2\,\mathrm{nT}$, before exhibiting a weakly pronounced peak around closest approach at 19:00 UT. A maximum field strength of about $B_Z = 1\,\mathrm{nT}$ is achieved by the Z component. The simulation results for B_Z are shown in figs. 7.4(e) and 7.5(e), respectively. Again, the magnetic field signatures obtained from the two different emission scenarios possess nearly identical key features. However, while the 34° simulation predicts the maximum to be achieved directly after closest approach at 19:00 UT, the assumption of ideal corotation leads to the formation of a weakly pronounced maximum right before closest approach. Even though the peak position predicted by the 34° run is a little closer to the location obtained from the Cassini magnetometer data, for the B_Z component, both simulation runs are in good agreement with the observed signatures. The peak value of $B_Z = 1\,\mathrm{nT}$ that has been detected by Cassini is achieved in neither of the two simulations, i.e. according to the model, B_Z does not reverse its direction in the region of the maximum. In any case, the overall homogeneous structure of the B_Z component is well confirmed by the simulation model.

The magnetic field magnitude observed by Cassini is displayed in fig. 7.4(h). Before closest approach, $|\underline{B}|$ exhibits a steady decrease from the background value of $6.4\,\mathrm{nT}$ to a minimum of about $3\,\mathrm{nT}$. This minimum is followed by a steep increase, before $|\underline{B}|$ again achieves the nearly homogeneous background value. Of course, in order to understand the simulation results for the magnetic field magnitude, one has to notice that the simulation results for $|\underline{B}|$ are affected by a number of slight deviations between simulated and measured magnetic field signature. The 34° simulations indicate the formation of a magnetic field minimum directly after closest approach. In the case of an ideally corotating flow, $|\underline{B}|$ achieves its minimum short before 19:00 UT. In the case of a strongly emitting obstacle, both simulation geometries indicate the minimum of $|\underline{B}|$ to be embedded into an overshoot at the inbound as well as at the outbound flank. In contrast to this, in the scenarios using a reduced ion production rate, the overshoot at the inbound flank is significantly less pronounced, whereas the additional peak at the outbound flank is missing completely (cf. figs. 7.4(g) and 7.5(g)). In each of the four simulation runs, the dip in the magnetic field magnitude is significantly sharper than the structure observed by Cassini. In general, the overshoot at the dip's inbound flank arises from the maximum in the B_X component before closest approach, which is predicted by all simulation runs, but has not been detected by Cassini. As can clearly be seen from figs. 7.4 and 7.5, in both simulation geometries, the maximum of B_X is located at nearly the same position as the overshoot at the inbound flank of the $|\underline{B}|$ dip. The other differences between the $|\underline{B}|$ values obtained from the simulations and the measured values can be understood in an analogous manner. Although the sharpness of the predicted minimum is not in agreement with the steady, slight decrease of the magnetic field magnitude detected by Cassini, the low emission scenarios for both simulation geometries exhibit at least reasonable agreement with the data obtained by the spacecraft.

Finally, at least a brief discussion of the other plasma and field parameters shall be given. This analysis will mainly provide a reference for the interpretation of the modified T9 geometry that is presented in the next chapter. Since the case of an ideally corotating flow has been extensively discussed in the preceding chapters, the analysis will consider only the 34° simulation scenario. The discussion will be restricted to the results for a weakly emitting obstacle. For the 34° simulation, the magnetospheric plasma parameters and the electromagnetic fields in the (X, Y) plane of the Titan interaction system are displayed in fig. 7.8. The nomenclature is the same as in the preceding chapter, i.e. the subscript $m, 1$ refers to the magnetospheric nitrogen component, whereas $m, 2$ denotes atomic hydrogen ions. The ionospheric plasma densities and velocities in the equatorial plane are displayed in fig. 7.9, the molecular nitrogen component again being denoted by the subscript $m, 1$. The abbreviations $m, 2$ and $m, 3$ denote the methane and the hydrogen component, respectively.

Although the large size and therefore, the relatively rough resolution of the simulation grid, does not allow an analysis of the magnetic pile-up region at Titan's ramside, this scenario is suitable for determining the characteristic length scales on which the plasma in the vicinity

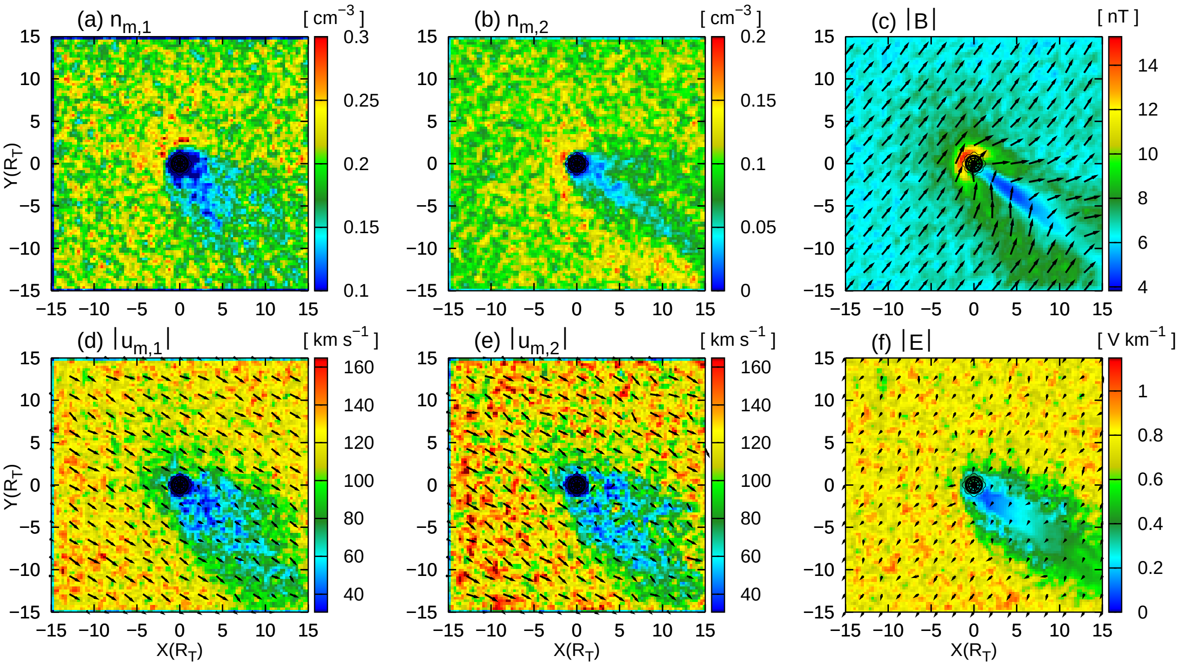

Figure 7.8: Simulation of Titan's plasma environment during the Cassini T9 flyby. For a cut through the equatorial plane, the figure shows the magnetospheric plasma parameters as well as the electromagnetic fields. The magnetospheric flow direction deviates from ideal corotation: The undisturbed flow velocity $\underline{u}_0$ forms an angle of $(-34°)$ with the $(+X)$ axis of the Titan interaction system, i.e. it is directed away from Saturn. In this configuration, the projection of the undisturbed magnetic field on the (X, Y) plane is nearly perpendicular to the direction of the impinging magnetospheric plasma. The figure illustrates that even in distances of more than $15R_T$, Titan leaves a noticeable imprint on the magnetospheric flow pattern. The plasma downstream of the satellite is slightly decelerated, but a noticeable wake cavity in the density is not formed. The magnetic lobes are clearly identifiable in plot (c), although they do not seem to be as sharply confined as in the Voyager-like simulation geometries. **Simulation parameters:** see table 7.2.

of Titan is affected by the presence of the obstacle. As can be seen from the velocity plots (d) and (e) in fig. 7.8, the region of decelerated plasma possesses an extension of well above $15R_T$ parallel to the flow direction. Moreover, the impinging magnetospheric plasma already experiences a gradual deceleration upstream of the obstacle. In the 34° simulation, the region characterized by a noticeable field enhancement due to the formation of the magnetic lobes possesses an extension of about $10R_T$ perpendicular to the flow direction, whereas the lobes possess a length of at least $15R_T$ in the downstream region, probably being restricted only by the outer boundaries of the simulation domain (cf. fig. 7.8(c)). In contrast to the simulations based on Voyager-like upstream conditions, the magnetic lobes exhibit a broader structure, making it difficult to define some kind of outer boundary for the draping pattern. As can be seen from fig. 7.9, the ionospheric tails are located in the $(Y < 0)$ hemisphere, i.e. they are again turned away from Saturn. It is interesting to notice that each of the three ionospheric species develops a rather narrow tail, the diameter perpendicular to the flow direction being smaller than $5R_T$. In this situation, the tail is not turned away from Saturn due to the cycloidal particle motion, but the ionospheric ions in the equatorial plane are confined to the region between the two lobes. Since the lobes are turned away from Saturn, the tail is

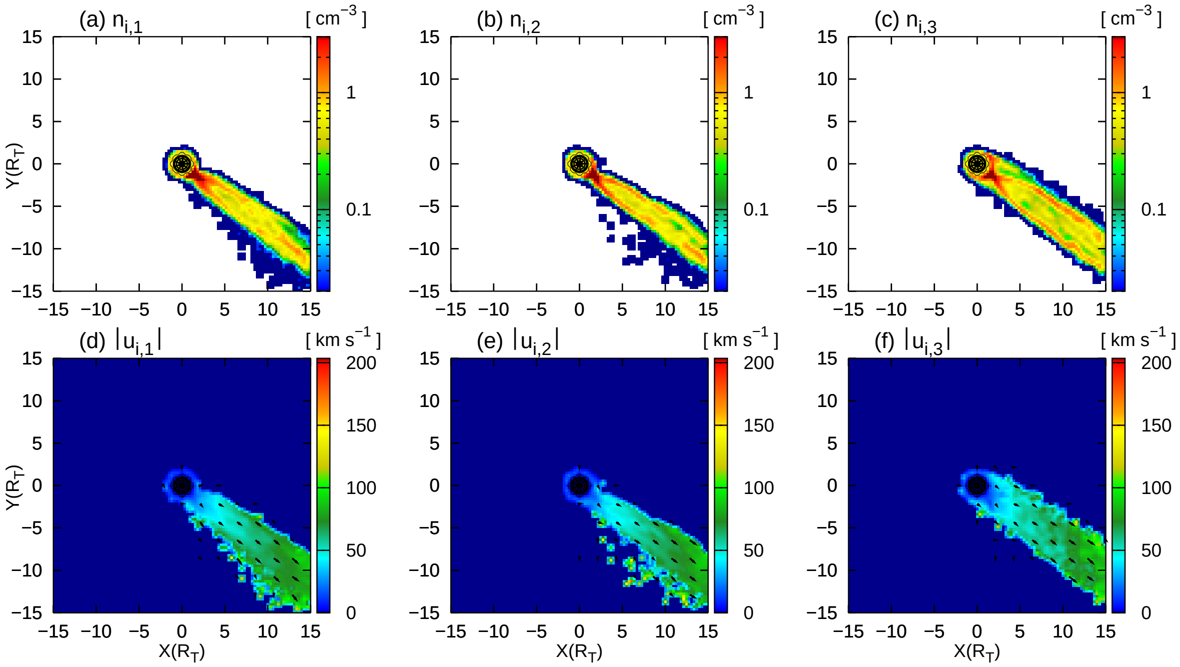

Figure 7.9: Simulation of Titan's plasma environment during the T9 flyby. The magnetospheric upstream flow is directed away from Saturn in an angle of 34°. The figure illustrates the ionospheric plasma densities and velocities in the equatorial plane. Each of the three tails is shifted in the anti-Saturn-facing hemisphere, the tail diameters ranging below $5R_T$. The tails are confined to the region between the magnetic lobes. In the Voyager-like simulations, such an effect has shown to be characteristic of the wake structure in the polar plane. The pick-up velocities achieved in the tail region are clearly exceeded by the values in the Voyager-based simulations.
Simulation parameters: see table 7.2.

shifted into the anti-Saturn-facing hemisphere as well. As will be discussed in the subsequent chapter, this characteristic of the tail is confirmed by a preliminary analysis of Cassini plasma data.

Since needed again in the context of the analysis presented in chapter 8, the major results for the T9 flyby shall be briefly summarized:

- During the T9 flyby, Cassini passed through Titan's induced magnetotail in the satellite's equatorial plane.
- In order to analyze the magnetic field signature detected during T9, four hybrid simulation runs have been carried out. On the one hand, the impinging plasma flow was assumed to be aligned with the X axis of the Titan interaction system, on the other hand, a second geometry in which $\underline{u}_0$ forms an angle of 34° with the X axis was investigated. For both geometries, the influence of the ion production rate has been analyzed by using two different values, the second one being about a factor of 3.3 larger than the first one.
- The simulations show that the magnetic field topology in the vicinity of Titan is only slightly modified by changes in the ion production rate.

- In the case of $\underline{u}_0$ forming an angle of 34° with the X axis, the projection of the upstream magnetic field on the (X, Y) plane is nearly perpendicular to the flow direction. Hence, in the equatorial plane, the structure of Titan's induced magnetotail is nearly symmetric. However, while the positions of the peaks and minima exhibited by the magnetic field are in good agreement with Cassini measurements, the magnitudes of the distortions are clearly overestimated by the 34° scenario.

- The assumption of an ideally corotating magnetospheric plasma has proven adequate for reproducing the magnetic field signature observed during T9. In such a geometry, $\underline{B}$ is no longer perpendicular to the flow direction. Although the positions of the peaks and minima show minor deviations from the T9 magnetometer data, the simulated structures have proven to be in good agreement with measurements. Especially the break-in observed in the B_X component, accompanied by a complete lack of a B_X enhancement, suggests that during T9, Titan's magnetotail structure was highly asymmetric. The nearly homogeneous structure of the B_Y and B_Z components detected by Cassini has also shown to be completely reproducible.

- Best agreement between simulations and magnetometer data could be achieved for the case of a weakly emitting obstacle (total ion production rate of each species: $Q = 6.54 \cdot 10^{24}\,\mathrm{s}^{-1}$) that is exposed to an ideally corotating plasma flow.

The next section deals with the magnetic field signature detected during the T11 flyby. In analogy to T9, the Cassini spacecraft passed through Titan's wake in the equatorial plane.

2 A closer look at Titan's magnetic lobes I: Cassini's T11 flyby

In this section, Titan's magnetic field signature during the T11 flyby of the Cassini spacecraft is discussed. In analogy to T9, Cassini passed through Titan's wake region in the equatorial plane. However, while T9 took place in a distance of about $4R_T$ to the surface of the satellite, the closest approach altitude of T11 was significantly smaller.

2.1 Flyby and simulation parameters

The T11 flyby took place on 27 February 2006 when Titan was located at 01:30 clock angle position on its orbit around Saturn. The Cassini spacecraft reached its closest approach altitude of 1813 km at 08:25 UT. As can be seen in fig. 7.10, the flyby trajectory of T11 is quite similar to that of T9, i.e. the passage of the spacecraft is completely located in the satellite's equatorial plane. Due to the relatively small distance to the surface, this flyby allows to gain insight into the near-Titan lobe structure. The results obtained for T11 will allow at least a rough comparison to the situation during T15, for the trajectories of both flybys with respect to Titan are nearly identical. Nevertheless, a direct comparison between these two flybys cannot be accomplished since they took place at different orbital positions.

Even though during the T13 flyby, Cassini also passed through Titan's wake in the equatorial plane, the closest approach altitude being comparable to the T11 value, this flyby will be

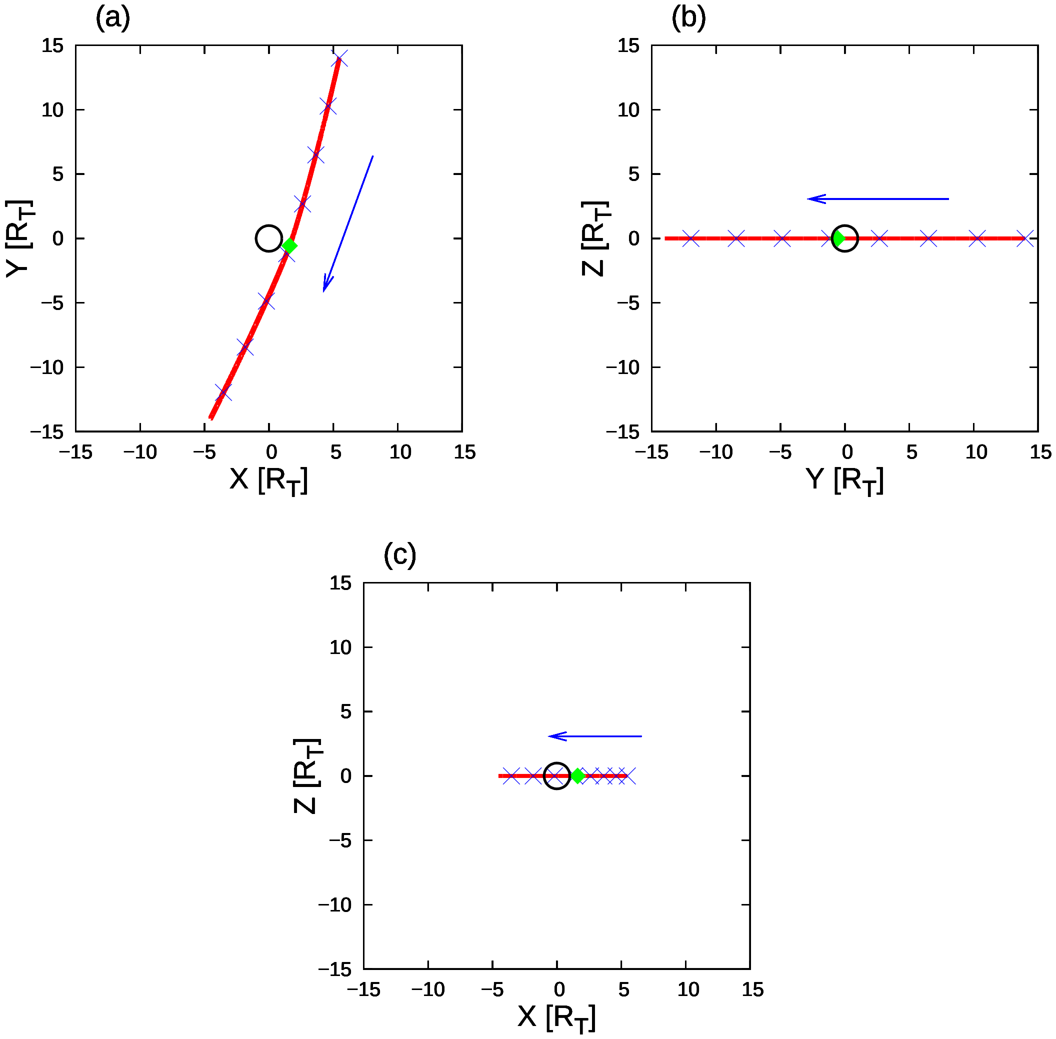

Figure 7.10: Cassini's trajectory during the T11 flyby of Titan. The figure displays the projection of the spacecraft trajectory on the planes of the Titan interaction system (X, Y, Z), the (X, Y) plane coinciding with Titan's orbital plane. In analogy to T9, the spacecraft passed through Titan's induced magnetotail in the equatorial plane. The spacecraft achieved its closest approach altitude of 1813 km on 27 February 2006 at 08:25 UT. The green diamond refers to the position of closest approach; the blue markers denote Cassini's position in intervals of 30 minutes, beginning at 06:30 UT.

excluded from the discussion. Due to a gap in the magnetometer data of T13 right before closest approach, this flyby does not provide substantially new material for the analysis of the lobe structure. A comparative analysis of the magnetic field signatures detected during a complete series of flybys has been presented by Neubauer *et al.* [118] for TA, TB and T3.

Table 7.3 gives an overview of the simulation parameters that yielded best agreement between model calculations and spacecraft measurements. Again, Titan is exposed to an ideally corotating flow. The combination of Mach numbers corresponds to the situation during the Voyager 1 flyby. In analogy to the discussion of the T9 scenario, the case of a high ion production rate has been compared to the results for a weakly emitting obstacle. In

Quantity	Symbol	Numerical value
Magnetic field	$\underline{B}_0$	$(1.5, 3.0, -2.0)$ nT
	$\lvert\underline{B}_0\rvert$	$3.9\,\mathrm{nT}$
Plasma flow velocity	$\underline{u}_0$	$(120, 0, 0)\,\mathrm{km/s}$
	$\lvert\underline{u}_0\rvert$	$120\,\mathrm{km/s}$
Nitrogen (N^+) density	$n_{m,1}$	$0.2 \cdot 10^6\,\mathrm{m}^{-3}$
Hydrogen (H^+) density	$n_{m,2}$	$0.1 \cdot 10^6\,\mathrm{m}^{-3}$
Nitrogen temperature	$kT_{m,1}$	$1578.48\,\mathrm{eV}$
Hydrogen temperature	$kT_{m,2}$	$112.75\,\mathrm{eV}$
Thermal velocity	$v_{th,N^+} = v_{th,H^+}$	$180\,\mathrm{km/s}$
Nitrogen plasma beta	$\beta_{m,1}$	8.34
Hydrogen plasma beta	$\beta_{m,2}$	0.30
Alfvén velocity	v_A	$50.02\,\mathrm{km/s}$
Alfvénic Mach number	M_A	2.40
Sound velocity	c_S	$146.34\,\mathrm{km/s}$
Sonic Mach number	M_S	0.82
Magnetosound velocity	c_{MS}	$155.84\,\mathrm{km/s}$
Magnetosonic Mach number	M_{MS}	0.77
Total N_2^+ production rate (high emission)	$Q_{i,1}$	$2.18 \cdot 10^{25}\,\mathrm{s}^{-1}$
Total CH_4^+ production rate (high emission)	$Q_{i,2}$	$2.18 \cdot 10^{25}\,\mathrm{s}^{-1}$
Total H_2^+ production rate (high emission)	$Q_{i,3}$	$2.18 \cdot 10^{25}\,\mathrm{s}^{-1}$
Total N_2^+ production rate (low emission)	$Q_{i,1}$	$6.54 \cdot 10^{24}\,\mathrm{s}^{-1}$
Total CH_4^+ production rate (low emission)	$Q_{i,2}$	$6.54 \cdot 10^{24}\,\mathrm{s}^{-1}$
Total H_2^+ production rate (low emission)	$Q_{i,3}$	$6.54 \cdot 10^{24}\,\mathrm{s}^{-1}$
Box size	X	$-15R_T \leq X \leq 15R_T$
	Y	$-15R_T \leq Y \leq 15R_T$
	Z	$-15R_T \leq Z \leq 15R_T$
Number of grid cells	(N_X, N_Y, N_Z)	$(100, 100, 100)$
Time step	Δt	$0.48\,\mathrm{s}$
Total number of time steps	$N_{\Delta t}$	20000
Smoothing parameter	α_S	0.15

Table 7.3: Simulation parameters for the Cassini T11 flyby. During T11, the spacecraft achieved a closest approach altitude of only 1813 km above the surface. Therefore, in order to minimize the influence of the artifical obstacle, the inner boundary has been placed at an altitude of 500 km above the surface, i.e. about 2 grid cells are located between the point of closest approach and the artificial boundary layer.

order to avoid any influence of the artificial inner obstacle boundary on the plasma and field parameters along the spacecraft trajectory, a value of $r_{\text{min}} = R_T + 500\,\text{km}$ has been chosen for the location of the artificial boundary layer. The computational domain possesses an extension of $-15R_T \leq X, Y, Z \leq +15R_T$, whereas the comparison between simulation and measurements has been performed in the interval $-14R_T \leq X, Y, Z \leq +14R_T$.

2.2 Comparison between simulation results and MAG measurements

The simulation results for the T11 encounter are displayed in figs. 7.11 and 7.12, respectively. The simulated magnetic field signature along the spacecraft trajectory can be seen in the left-hand panels of fig. 7.11. Again, the green line refers to a total production rate of $Q = 2.18 \cdot 10^{25}\,\text{s}^{-1}$ for each of the three ionospheric species. The red line illustrates the field signature when Q is assumed to be about a factor of 3 smaller. The plots on the right-hand side of fig. 7.11 show the magnetic field signature detected by the Cassini Fluxgate Magnetometer. A two-dimensional illustration of the magnetic field components in Titan's equatorial plane is given in fig. 7.12, showing the results of the high as well as the low emission run.

As can be seen from the left-hand panels in fig. 7.11, the simulated magnetic field signature along the spacecraft trajectory remains nearly unaffected by changes in the obstacle's ion production rate. The influence of the number of ions produced per second appears to be even less important for the magnetic field signature along the trajectory than in the T9 scenario. Nevertheless, as can be seen in figs. 7.12(b) and (c), the global topology of the B_X component is at least slightly modified when the obstacle's ion production is altered. On the one hand, both the maximum magnetic field value achieved in the Saturn-facing lobe and the minimum field value reached in the anti-Saturn-facing lobe show only minor differences between both emission cases. On the other hand, in the low emission simulation, the regions with strong magnetic field distortions possess a smaller extension *parallel* to the flow direction than in the high emission run. As displayed in fig. 7.12(b), which refers to the low emission run, at $X = 12.5R_T$, the X component reaches a value of $B_X = 4\,\text{nT}$ in the Saturn-facing lobe, whereas a value of about $B_X = -3\,\text{nT}$ is achieved in the anti-Saturn-facing lobe. These field values are clearly exceeded by the distortions that are formed when Q is increased. However, at least in the region where Cassini passed through the magnetotail, the structure of the B_X lobes exhibits only slight differences between both cases. Besides, the overall topology of the B_Y and the B_Z component seems to be nearly identical in both emission scenarios.

The B_X component detected by the Cassini magnetometer is displayed in fig. 7.11(b). Until about 07:45 UT, this component remained nearly homogeneous at a value of $B_X = 1.5\,\text{nT}$. This region is followed by a sharply pronounced peak around 08:00 UT, the maximum field value being $B_X \approx 7\,\text{nT}$. The outbound flank of this relatively narrow peak denotes a decrease of B_X well below the undisturbed background value of $1.5\,\text{nT}$. Around 08:30 UT, the magnetometer detected a broad notch in the B_X component, its outbound flank describing a steady return to the undisturbed background value. In the dip, a minimum field value of $B_X \approx -7\,\text{nT}$ is achieved. While the overshoot in the peak almost equals the decrease of B_X in the notch, the region characterized by a reduced B_X component is clearly not as sharply confined as the magnetic field enhancement around 08:00 UT. As can be seen from

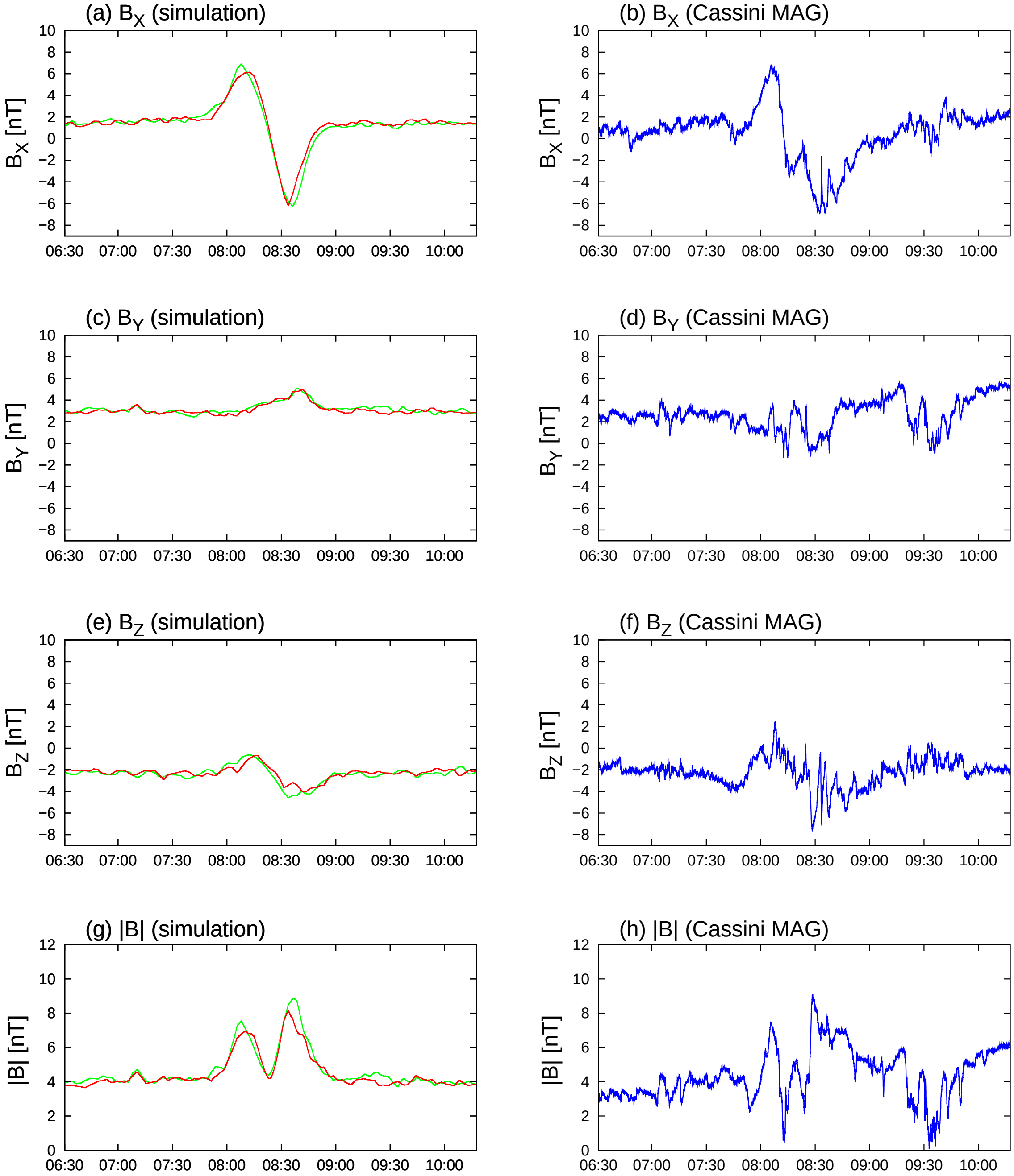

Figure 7.11: Simulation of Titan's magnetic field signature during Cassini's T11 flyby. The plots on the left-hand side display the simulated magnetic field signature along the spacecraft trajectory (green lines: high emission, red lines: low emission), whereas the measured field signatures are shown in the right-hand column. A comparison between plots (a) and (b) shows that the positions of Titan's magnetic lobes are well reproduced by the simulation model. The simulated and measured magnitudes of the distortions are also in good agreement. The rather inhomogeneous structure of the measured B_Y component is not reproduced in such a satisfactory manner, since the data do not show a homogeneous region providing an adequate background value. Although the magnitude of the overshoot in the B_Z component is underestimated by the simulation approach, its position has shown to be completely reproducible.
Simulation parameters: see table 7.3.

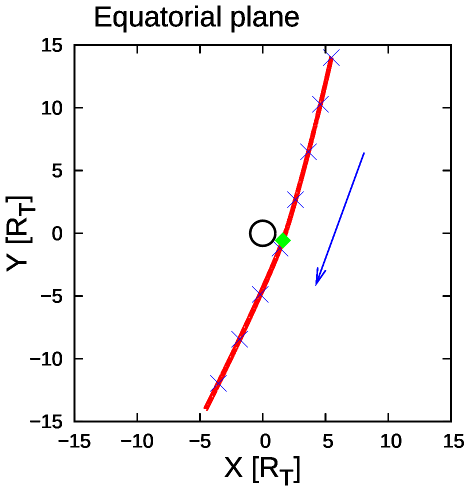

(a) Cassini flyby trajectory in the equatorial plane

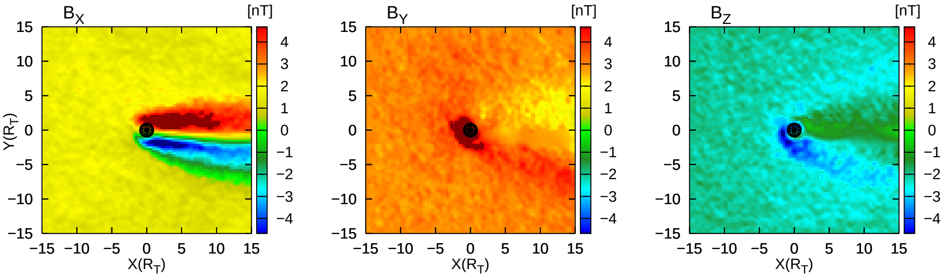

(b) Low emission: Magnetic field components

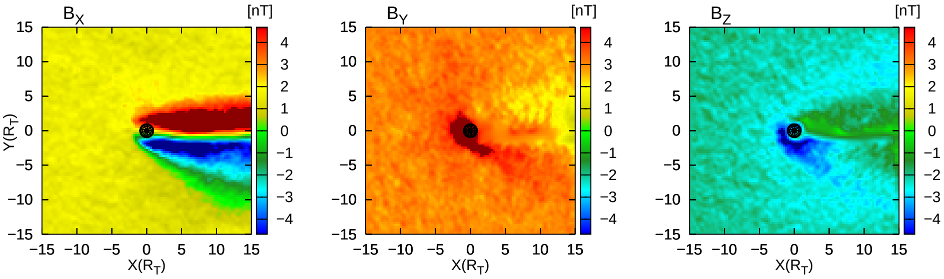

(c) High emission: Magnetic field components

Figure 7.12: Simulation of Titan's magnetic field signature during T11. The figure shows two-dimensional illustrations of Titan's magnetic environment in the orbital plane which also contains the spacecraft trajectory. In both emission scenarios, two sharply pronounced magnetic lobes can be identified in the B_X component. The Saturn-facing lobe denotes an increase of magnetic field strength, whereas in the anti-Saturn-facing lobe, B_X is reduced with respect to the background value. In contrast to this, the imprint left by the lobes on the B_Y and B_Z components is rather diffuse. While in the immediate vicinity of Titan, only insignificant differences between high and low emission run can be identified, the large-scale features of the lobes are at least slightly affected by an increase of the production rate. A comparison of the B_X signatures illustrates that in the high emission case, the width of the anti-Saturn-facing lobe as well as the magnitude of the B_X field distortions exceed the values of the low emission scenario.
Simulation parameters: see table 7.3.

fig. 7.11(a), the key features of the B_X signature are well reproduced by the simulation model. The simulated B_X component remains nearly constant before 08:00 UT. Between 08:00 UT and 08:30 UT, the passage through a peak with a maximum field value of about $B_X = 6.5\,\mathrm{nT}$ is predicted by the simulation model. The position as well as the maximum field value are in very good agreement with the structure detected by Cassini. The outbound flank of this peak is directly followed by a monotonous decrease to a minimum value of $B_X = -6.5\,\mathrm{nT}$. The steep outbound flank of this dip is connected to a region where B_X again returns to the undisturbed background value. Both the position of the dip and the minimum field value are confirmed by the Cassini magnetometer data. Nevertheless, the dip structure detected by the spacecraft is clearly not as sharply confined as the notch signature obtained from the simulation model. In any case, the positions and the magnitudes of both distortions in the B_X component have shown to be reproducible.

In order to reveal the mechanism that gives rise to the distortions in the B_X component, the contour plots shown in fig. 7.12 provide again a helpful source of information. As displayed in figs. 7.12(b) and (c), the overshoot in the B_X component corresponds to Cassini's passage through the Saturn-facing lobe, whereas the dip denotes the position of the anti-Saturn-facing lobe. In contrast to the T9 scenario, the field enhancement in the Saturn-facing B_X lobe occurs in both the simulation results and the spacecraft measurements. The data collected during T9 only allowed to identify the position of the anti-Saturn-facing lobe, while the signature corresponding to the Saturn-facing lobe was missing completely.

The simulation results for the B_Y component are shown in fig. 7.11(b). The hybrid model predicts B_Y to be nearly featureless along the T11 trajectory; only a slight peak is formed around 08:30 UT. However, the B_Y signature detected by Cassini is quite inhomogeneous, exhibiting a number of slightly pronounced maxima and minima which are not reproduced by the simulation model. In general, finding an explanation for the B_Y signature detected by Cassini has proven difficult due to the lack of an adequate background value for this component. In the inbound region of T11, the magnetometer detected values around $B_Y = 2.5\,\mathrm{nT}$, but when Cassini left Titan's magnetotail, a field magnitude of about $B_Y = 6\,\mathrm{nT}$ has been measured. Hence, the incapability of the simulation model to reproduce the B_Y signature shown in fig. 7.11(c) may arise from the necessity to choose a background value as input parameter, representing the B_Y component at any point outside the interaction region. The two-dimensional illustrations of B_Y in figs. 7.12(b) and (c) show that the formation of the magnetic pile-up region at Titan's ramside goes along with a noticeable enhancement of the B_Y component. Nevertheless, in the downstream region, the modifications of B_Y are clearly not as strong as the distortions that occur in the B_X component. In the lobe region, the deviations of B_Y from the background value $B_{Y,0} = 3\,\mathrm{nT}$ are not larger than $\delta B_Y = \pm 1\,\mathrm{nT}$.

The simulation results for the B_Z component are displayed in fig. 7.11(e), whereas the signature detected by the Fluxgate Magnetometer is shown in plot (f). The simulation model predicts the existence of a slight enhancement around 08:15 UT, which is followed by a minimum at 08:30 UT. The maximum field value achieved in the peak is only about 1.5 nT larger than the background value of $B_{Z,0} = -2\,\mathrm{nT}$. Since a minimum field value of $B_Z = -4\,\mathrm{nT}$ is achieved in the notch, the distortion of the B_Z component predicted by the simulation model is nearly symmetric. The positions of both signatures are in agreement with Cassini magnetometer data. As displayed in fig. 7.11(f), the B_Z component achieved its peak value around 08:10 UT. However, the magnetometer data indicate a maximum of about $B_Z = 2\,\mathrm{nT}$, i.e. B_Z reversed its direction. The minimum field value of $B_Z = -8\,\mathrm{nT}$ achieved in the notch is also clearly smaller than the value obtained from the simulation. As can be seen from figs. 7.12(b) and (c), even though the distortions are clearly not as strong as the effect on B_X, the B_Z component exhibits a lobe-like structure. An enhancement in the Saturn-facing lobe is followed by at least a slight decrease in the anti-Saturn-facing structure. At least the enhancement of B_Z in the Saturn-facing lobe is definitely confirmed by the simulation model. In the region where the simulation results indicate the passage through the anti-Saturn-facing B_Z lobe, the signature detected by Cassini is quite inhomogeneous. Therefore, it is not clear whether the dip can be ascribed to the existence of a well-defined anti-Saturn-facing B_Z lobe. Nevertheless, the regions of quite homogeneous B_Z passed by Cassini before 07:30 UT and after 09:00 UT are well reproduced by the simulation model.

The magnetic field magnitude along the Cassini trajectory is shown in plots 7.11(g) and (h). Both the simulation results and the field magnitude obtained from the Cassini measurements indicate the existence of two maxima in $|\underline{B}|$ at about 08:00 UT and 08:30 UT, the second enhancement being only a little stronger than the first one. By comparing plots (a) and (g) or (b) and (h), it becomes obvious that these peaks must be ascribed to the passage through the lobes developed by the B_X component. Since the fluctuations detected in the B_Y and the B_Z component do not occur in the simulated magnetic field topology, the field magnitude obtained from the model possesses a nearly constant value of $|\underline{B}| = 4\,\mathrm{nT}$ before and after the passage through the lobe region.

In general, the key features of the T11 magnetic field signature have proven to be reproducible by the simulation model. Especially the signatures detected in the B_X component confirm the existence of both a Saturn-facing and an anti-Saturn-facing lobe, as it is not only suggested by the hybrid model used for this work, but by numerous MHD models and the Voyager 1 observations as well (cf. for instance [5, 90, 99]). The fact that only one B_X peak was detected during T9 suggests that Titan's magnetic environment reacts highly sensitive to inhomogeneities in the ambient magnetospheric plasma. This hypothesis is also confirmed by the data collected during T15, as will be discussed in the following section.

During T11, Titan was located in Saturn's wake region. Therefore, following the suggestion of Ledvina *et al.* [90], the case of Titan being exposed to a sub-alfvénic, subsonic and sub-magnetosonic plasma has also been investigated. However, for the plasma composition and magnetic field strength given in table 7.3, a reduction of the upstream velocity by a factor of 3 would be required in order to realize a sub-alfvénic upstream situation. Under these conditions, the upstream flow velocity is of the order of only $40\ldots50\,\mathrm{km/s}$. As discussed in the preceding chapters, a reduction of the impinging magnetospheric flow speed goes along with a widening of the satellite's magnetic lobes and a reduction of the maximum magnetic field strength in the interaction region. Consequentially, a simulation scenario that assumes the value of u_0 to be significantly smaller than $100\,\mathrm{km/s}$ has proven inadequate for reproducing the relatively sharp enhancement of B_X that was detected during T11. The degree to which the magnetic field topology in the vicinity of Titan is affected by the upstream plasma composition itself will be investigated in the following chapter.

3 A closer look at Titan's magnetic lobes II: Cassini's T15 flyby

In analogy to T9, and T11, Cassini's T15 flyby of Titan was a passage through the moon's wake region in the orbital plane. The flyby trajectory is displayed in fig. 7.13. Similar to the other wake flybys, Cassini entered the near-Titan region from the Saturn-facing hemisphere, whereas the outbound part of the trajectory is located in the anti-Saturn-facing hemisphere. Cassini reached its closest approach altitude of 1906 km on 2 July 2006 at 09:21 UT, i.e. the spacecraft came again significantly closer to Titan than during T9. During the flyby, Titan was located at 21:30 clock angle position on its orbit around Saturn.

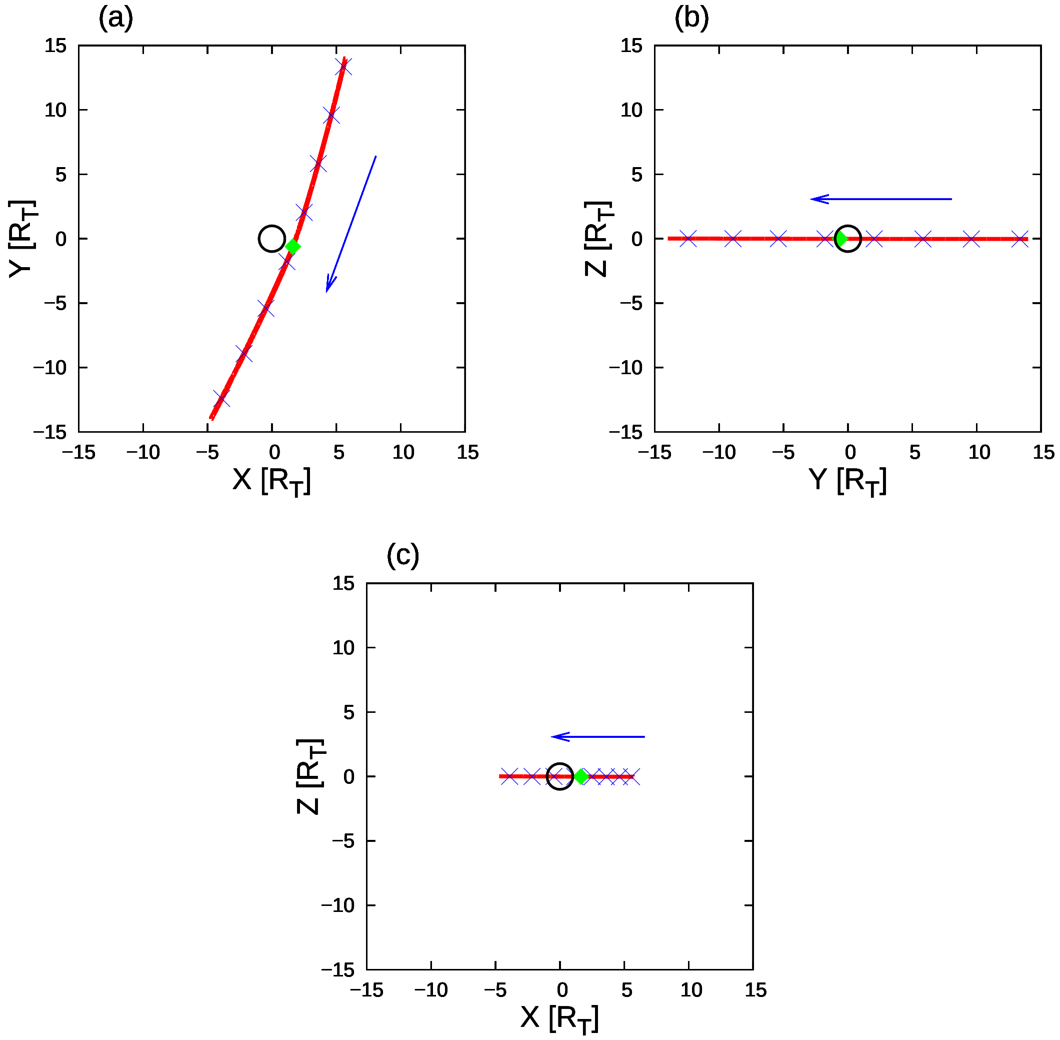

Figure 7.13: Cassini's trajectory during the T15 flyby of Titan. In correspondence to T9 and T11, the spacecraft passed through the satellite's wake in the equatorial plane. The closest approach distance of 1906 km was achieved on 2 July 2006 at 09:21 UT (green diamond). The markers along the trajectory are 30 minutes apart, beginning at 07:30 UT.

3.1 Simulation parameters

Again, the ambient magnetospheric plasma is represented by a Voyager-like configuration. The only difference between the parameters of T11 and the parameters for the T15 simulations

Quantity	Symbol	Numerical value
Magnetic field	$\underline{B}_0$	$(1.0, 4.0, -1.0)$ nT
	$\lvert\underline{B}_0\rvert$	$4.24\,\mathrm{nT}$
Plasma flow velocity	$\underline{u}_0$	$(120, 0, 0)\,\mathrm{km/s}$
	$\lvert\underline{u}_0\rvert$	$120\,\mathrm{km/s}$
Nitrogen (N^+) density	$n_{m,1}$	$0.2 \cdot 10^6\,\mathrm{m}^{-3}$
Hydrogen (H^+) density	$n_{m,2}$	$0.1 \cdot 10^6\,\mathrm{m}^{-3}$
Nitrogen temperature	$kT_{m,1}$	$1578.48\,\mathrm{eV}$
Hydrogen temperature	$kT_{m,2}$	$112.75\,\mathrm{eV}$
Thermal velocity	$v_{th,N^+} = v_{th,H^+}$	$180\,\mathrm{km/s}$
Nitrogen plasma beta	$\beta_{m,1}$	7.06
Hydrogen plasma beta	$\beta_{m,2}$	0.25
Alfvén velocity	v_A	$54.34\,\mathrm{km/s}$
Alfvénic Mach number	M_A	2.21
Sound velocity	c_S	$146.97\,\mathrm{km/s}$
Sonic Mach number	M_S	0.81
Magnetosound velocity	c_{MS}	$156.69\,\mathrm{km/s}$
Magnetosonic Mach number	M_{MS}	0.77
Total N_2^+ production rate (high emission)	$Q_{i,1}$	$2.18 \cdot 10^{25}\,\mathrm{s}^{-1}$
Total CH_4^+ production rate (high emission)	$Q_{i,2}$	$2.18 \cdot 10^{25}\,\mathrm{s}^{-1}$
Total H_2^+ production rate (high emission)	$Q_{i,3}$	$2.18 \cdot 10^{25}\,\mathrm{s}^{-1}$
Total N_2^+ production rate (low emission)	$Q_{i,1}$	$6.54 \cdot 10^{24}\,\mathrm{s}^{-1}$
Total CH_4^+ production rate (low emission)	$Q_{i,2}$	$6.54 \cdot 10^{24}\,\mathrm{s}^{-1}$
Total H_2^+ production rate (low emission)	$Q_{i,3}$	$6.54 \cdot 10^{24}\,\mathrm{s}^{-1}$
Box size	X	$-15R_T \leq X \leq 15R_T$
	Y	$-15R_T \leq Y \leq 15R_T$
	Z	$-15R_T \leq Z \leq 15R_T$
Number of grid cells	(N_X, N_Y, N_Z)	$(100, 100, 100)$
Time step	Δt	$0.48\,\mathrm{s}$
Total number of time steps	$N_{\Delta t}$	20000
Smoothing parameter	α_S	0.05

Table 7.4: Input parameters for the simulation of Titan's magnetic field signature during the T15 flyby. The table contains the parameters for the assumption of an ideally corotating flow. However, the case of $\underline{u}_0$ not being aligned with the $(+X)$ axis has also been investigated. The specific parameters are summarized in the subsequent table 7.5.

is the ambient magnetic field vector: For T15, the vector $\underline{B} = (1.0, 4.0, -1.0)\,\mathrm{nT}$ provides a reasonable approximation to the homogeneous regions in the Cassini magnetometer data. Since the ambient field magnitude of $|\underline{B}| = 4.24\,\mathrm{nT}$ is comparable to the background field during T11, neither the Mach numbers of the upstream flow nor its plasma betas differ significantly from the values used in the preceding section. The major input parameters are summarized in table 7.4. As will be discussed in the next section, the T15 flyby of Titan provided an opportunity to study the changes that a non-vanishing Z component of the upstream flow speed causes in the simulated magnetic field signature. Therefore, a total number of seven simulation runs has been carried out, each of them assuming the upstream flow speed to be given by $u_0 = 120\,\mathrm{km/s}$. However, the case of ideal corotation is compared to several scenarios in which the plasma velocity points in a significantly different direction.

With respect to the Titan interaction system, the flow direction is defined by two angles Ψ and Φ. The angle Ψ defines the rotation of the flow velocity's projection on the (X, Y) plane of the Titan interaction system. A positive value of Ψ corresponds to the flow being directed towards Saturn, while in the case of $\Psi < 0$, the ambient flow speed possesses a non-vanishing component in $(-Y)$ direction and is therefore oriented away from Saturn. The parameter Φ defines the angle between $\underline{u}_0$ and the (X, Y) plane of the Titan interaction system. A positive value of Φ corresponds to a flow component in $(+Z)$ direction, whereas for $\Phi < 0$, the flow is oriented "downwards". Hence, the initial magnetospheric plasma velocity can be expressed as

$$\underline{u}_0 = u_0 \begin{pmatrix} \cos\Phi\,\cos\Psi \\ \cos\Phi\,\sin\Psi \\ \sin\Phi \end{pmatrix} \quad . \tag{7.7}$$

For the seven scenarios under consideration, the simulation parameters are given in tables 7.4 and 7.5.

Run #	Ion production	Ψ	Φ
#1	high	0°	0°
#2	low	0°	0°
#3	low	−20°	0°
#4	low	+20°	0°
#5	low	+20°	+15°
#6	low	+20°	−15°
#7	low	+20°	−25°

Table 7.5: Simulation of Titan's magnetic field signature during the T15 flyby. In order to investigate the influence of deviations from ideal corotation on the simulated magnetic field signature, a total number of 7 different scenarios has been considered. The basic input parameters have been chosen in accordance to the Voyager 1 configuration, but the flow direction in runs #3 to #7 differs from ideal corotation. As defined by eq. (7.7), the flow velocity vector is given in spherical polar coordinates, with Φ denoting the angle between $\underline{u}_0$ and the (X, Y) plane of the Titan interaction system. In the case of $\Phi > 0$, the flow is directed upwards. For $\Phi < 0$, it possesses a non-vanishing component in $(-Z)$ direction. The angle Ψ characterizes the orientation of the flow in the (X, Y) plane. A positive value of Ψ corresponds to a velocity component in the direction of Saturn.

3.2 Comparison between simulation results and Cassini MAG data

The simulation results are shown in figs. 7.14 and 7.15, respectively. However, the discussion will at first focus on runs #1 to #4, in which the flow velocity is parallel to Titan's orbital plane. The simulated magnetic field signatures for these geometries are displayed in the left-hand panels of fig. 7.14. The case of an ideally corotating magnetospheric plasma (high emission versus low emission) is compared to the scenarios in which $\underline{u}_0$ is directed away from Saturn (run #3, violet line) and towards Saturn (run #4, grey line). The data obtained by the Cassini magnetometer are displayed in the panels on the right-hand side. As can be seen from fig. 7.14(a), each of the four simulations predicts the B_X component to exhibit a lobe structure in the equatorial plane, i.e. an overshoot in the Saturn-facing lobe should be followed by a break-in at the anti-Saturn-facing side of Titan. However, the B_X signature detected by Cassini features only a single break-in around closest approach at 09:21 UT, denoting a decrease of the field strength from $B_X = 1\,\mathrm{nT}$ to a minimum value of $B_X = -5\,\mathrm{nT}$. Overall, the structure of the B_X component bears at least a strong qualitative resemblance to the B_X data collected during T9. In both scenarios, a single, relatively sharp dip of the B_X component is embedded into two regions that feature a nearly homogeneous value of B_X. The purpose of the T15 simulations is to clarify whether a non-vanishing flow component in $(\pm Z)$ direction is able to provide an explanation for the lack of the Saturn-facing lobe, i.e. whether the spacecraft trajectory simply "missed" the Saturn-facing lobe.

The tendencies that can be identified in the simulated B_X lobe structure are highly analogous to the results for T9, i.e. turning the flow direction from outward to inward does not only yield a slight shift of the lobe positions towards Saturn, but it also goes along with a reduction of the enhancement in the Saturn-facing B_X lobe. Simultaneously, the magnitude of the break-in in the anti-Saturn-facing lobe is increased. Changing the ion production rate from high to low emission yields a reduction of the dip and peak magnitudes below 1 nT. When the flow is directed towards Saturn, the enhancement in the Saturn-facing lobe exceeds the background value by $\delta B_X = +4\,\mathrm{nT}$, while the relative magnitude of the break-in at the anti-Saturn-facing side is about a factor of 2 larger.

As displayed in fig. 7.14(d), the B_Y component measured by Cassini exhibits a rather inhomogeneous structure. Before 08:15 UT, the spacecraft detected a quite homogeneous B_Y component with a field value of $B_Y = +4\,\mathrm{nT}$. This region also provided the input value for the simulation model. The featureless part is followed by a steady decrease to a minimum of $B_Y = -3\,\mathrm{nT}$ and a subsequent steep enhancement. After 10:30 UT, a stable value of about $B_Y = 2.5\,\mathrm{nT}$ was observed. Even though the signature obtained from run #3 ($\Psi = -20°$, violet line) features the tendency of a break-in around 09:00 UT, none of the four geometries under consideration yields satisfactory agreement between simulated and measured B_Y signature. The discrepancy may mainly arise from the rather rough representation of the undisturbed regions by the homogeneous background value $B_{Y,0}$.

Before 09:00 UT, the B_Z component shows a nearly undisturbed structure with a field value of about $B_Z = -1\,\mathrm{nT}$ (cf. fig. 7.14(f)). Around closest approach at 09:21 UT, a peak has been detected, denoting a reversal of the B_Z direction and a maximum field value of $B_Z = 3\,\mathrm{nT}$. As shown in fig. 7.14(e), each of the four simulation runs predicts an enhancement of the B_Z component, but neither its position nor the magnitude of the overshoot are in optimum

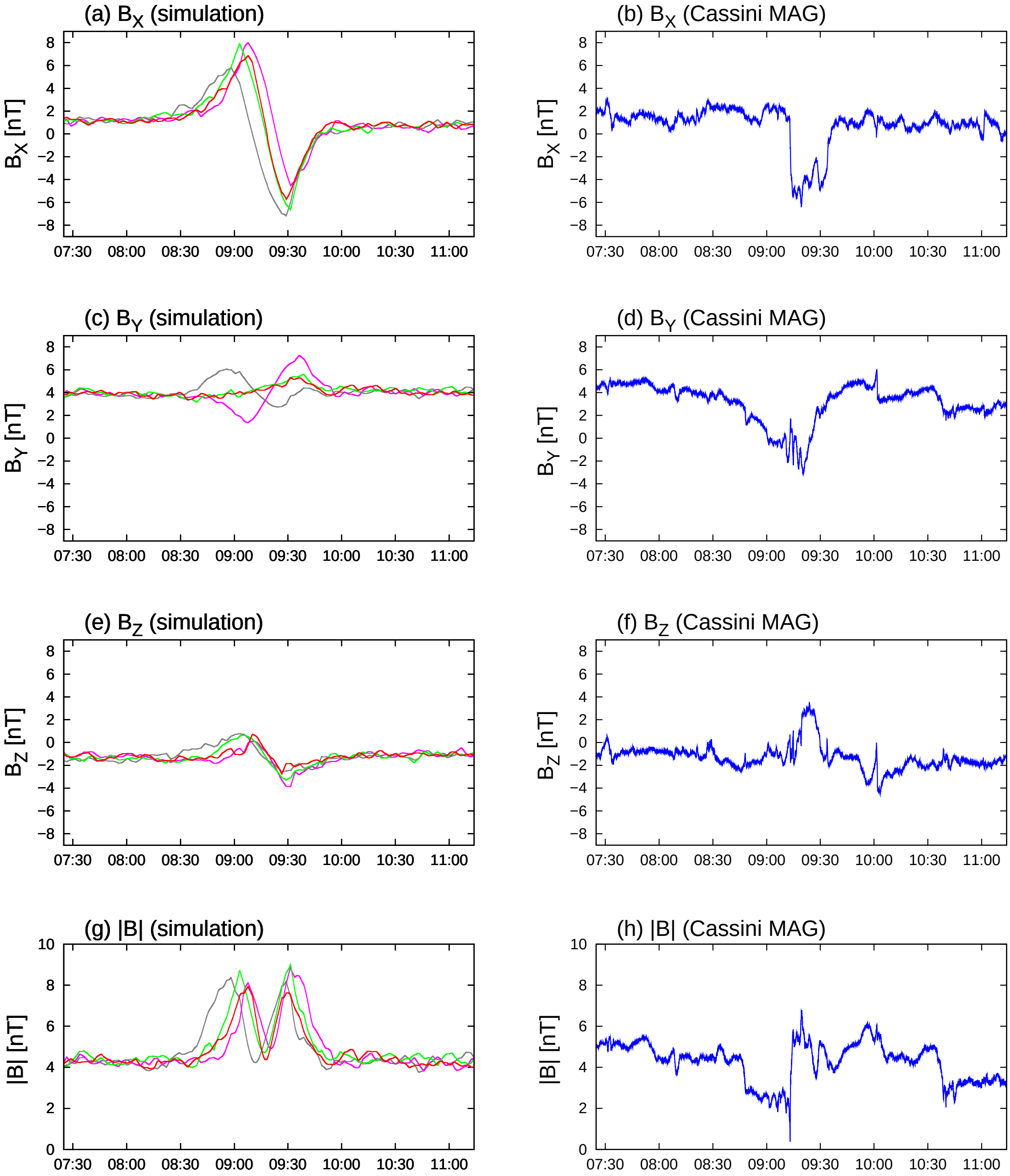

Figure 7.14: Simulation of Titan's magnetic field signature during the Cassini T15 flyby. The figure shows the results of runs #1 to #4 which assume the upstream velocity $\underline{u}_0$ to be parallel to the (X, Y) plane. For the case of an ideally corotating flow, the red and green lines represent the results of the low and high emission scenarios, respectively. These results are compared to a scenario where the flow velocity points away from the direction of ideal corotation (violet line, run #3) as well as to a geometry in which $\underline{u}_0$ points towards Saturn (grey line, run #4). In agreement with MAG measurements, all four simulation runs predict the existence of a break-in in the B_X component around closest approach at 09:21 UT, while the existence of an overshoot around 09:00 UT is not consistent with Cassini data. Although the results of run #4 show the correct tendency, the inhomogeneous structure of the B_Y component, especially the break-in between 09:00 UT and 09:30 UT, is reproduced by none of the simulation geometries. The simulations suggest the formation of a slightly pronounced peak in the B_Z component. As for this structure, agreement between simulation and measurements could be improved by assigning the flow velocity a non-vanishing component perpendicular to the (X, Y) plane.
Simulation parameters: see tables 7.4 and 7.5.

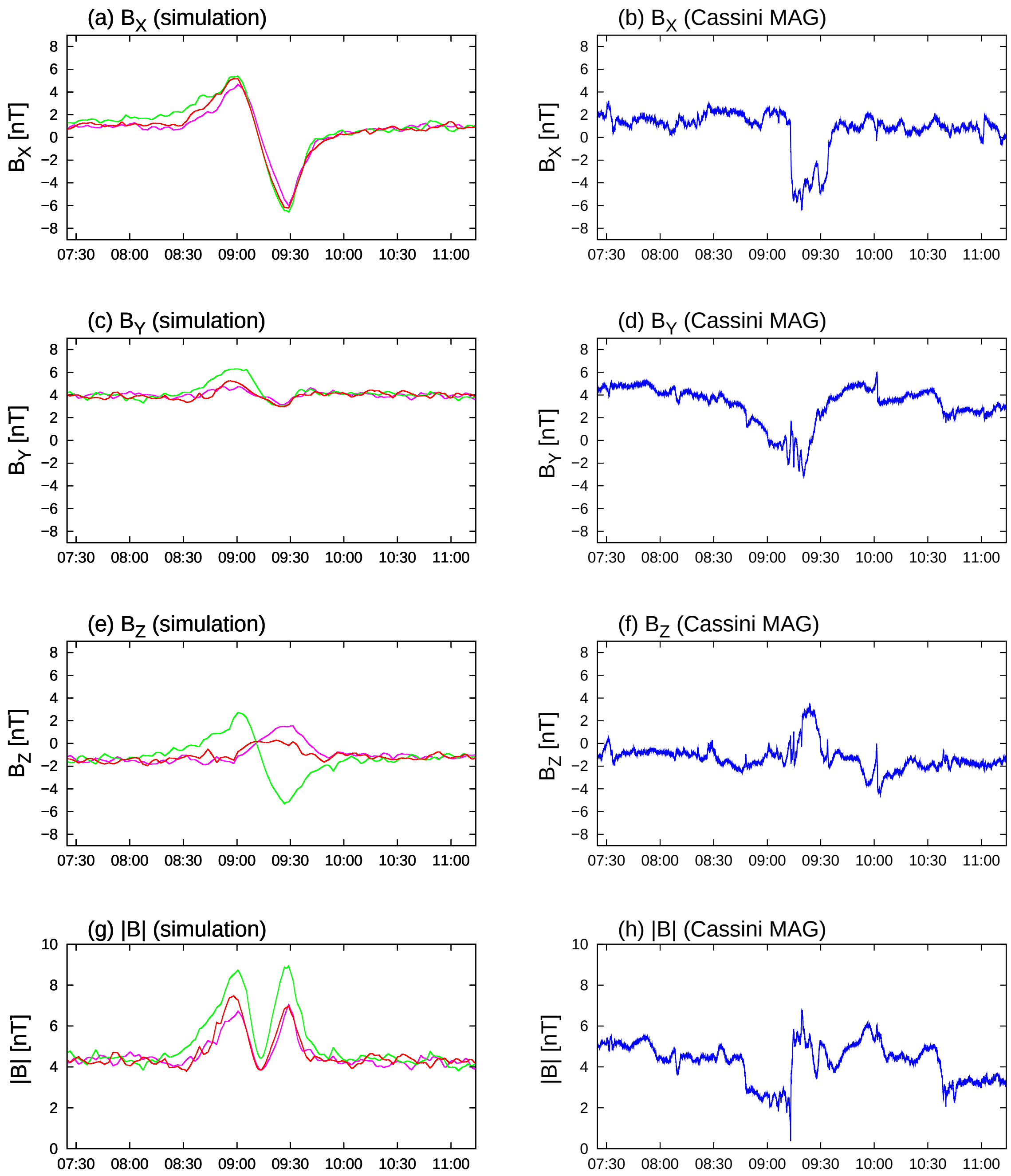

Figure 7.15: Simulation of Titan's magnetic field signature during the Cassini T15 flyby. Based on run #4 in which $\underline{u}_0$ was directed towards Saturn, a finite Z component for the plasma velocity has been introduced. The angle between Titan's orbital plane and $\underline{u}_0$ is given by $\Phi = +15°$ (green lines, run #5), by $\Phi = -15°$ (red lines, run #6) and by $\Phi = -25°$ (violet lines, run #7), respectively. In the cases of the flow being directed "downwards", the simulated B_Z component fits significantly better to MAG data than in the other simulations.
Simulation parameters: see tables 7.4 and 7.5.

agreement with Cassini magnetometer data. According to the simulation model, the slight B_Z enhancement around 09:00 UT ... 09:15 UT is even followed by a minor dip at the very position of the detected overshoot. However, at least for the B_Z component, agreement between simulation and measurements could be improved by introducing a non-vanishing flow component perpendicular to the (X, Y) plane. It is interesting to notice that, although the results of run #3 bear at least a distant resemblance to the measured B_Y component, the assumption of $\underline{u}_0$ being directed towards Saturn (run #4) has proven to be the best base for an improvement of the results. Therefore, a series of three additional simulations has been carried out (runs #5 to #7 in table 7.5), each of them using an upstream flow whose projection on the orbital plane forms an angle of $\Psi = 20°$ with the direction of ideal corotation. Several finite values for the angle between $\underline{u}_0$ and the (X, Y) plane have been tested. The results are shown in the left-hand panels of fig. 7.15 for an angle of $\Phi = +15°$ (green lines), $\Phi = -15°$ (red lines) and $\Phi = -25°$ (violet lines), respectively.

As can be seen from fig. 7.15(a), choosing a value of $\Phi = -25°$ still yields reasonably good agreement between simulated and measured B_X break-in. The behaviour of the measured B_Y component is reproduced by none of the three scenarios. Nonetheless, the $\Phi = -25°$ run does not only predict the peak in the B_Z component to be located at the correct position, the B_Z component clearly reverses its direction as well. The magnitude of the simulated peak is only about one 1 nT smaller than that of the overshoot detected by Cassini. Thus, assuming the flow to be directed "downwards" yields a significantly better agreement between simulated and measured B_Z component. It should also be noted that using a positive value for Φ leads to a stronger pronounced dip around 19:30 UT than the original simulation, while the simulated overshoot is located around 19:00 UT (cf. fig. 7.15(e)). At least the enhancement in the measured B_Z signature can be understood by assuming a strong deviation from ideal corotation. However, none of the simulation runs yields at least a partial elimination of the overshoot in the Saturn-facing lobe. Thus, based on the available material, the possibility that Cassini "missed" one of the two lobes can definitely be excluded. In general, the situation during T15 seems to exhibit a stronger resemblance to T9 than to the T11 dataset.

4 Titan's magnetic pile-up region during Cassini's T8 flyby

During the T8 flyby of Titan at 09:30 Saturnian local time, Cassini passed through the magnetic pile-up region at the moon's ramside. As shown in fig. 7.16, the spacecraft trajectory was again completely located in Titan's orbital plane. Currently, T8 is the only flyby of Titan whose trajectory possesses these properties, thus providing a unique chance to study the ramside magnetic field topology. Cassini achieved its closest approach altitude of 1333 km on 28 October 2005 at 04:16 UT.

4.1 Simulation parameters

An overview of the simulation parameters is given in table 7.6. The major input values have again been chosen in accordance to the Voyager 1 configuration, i.e. Titan is assumed to be exposed to an ideally corotating magnetospheric plasma that consists of atomic nitrogen

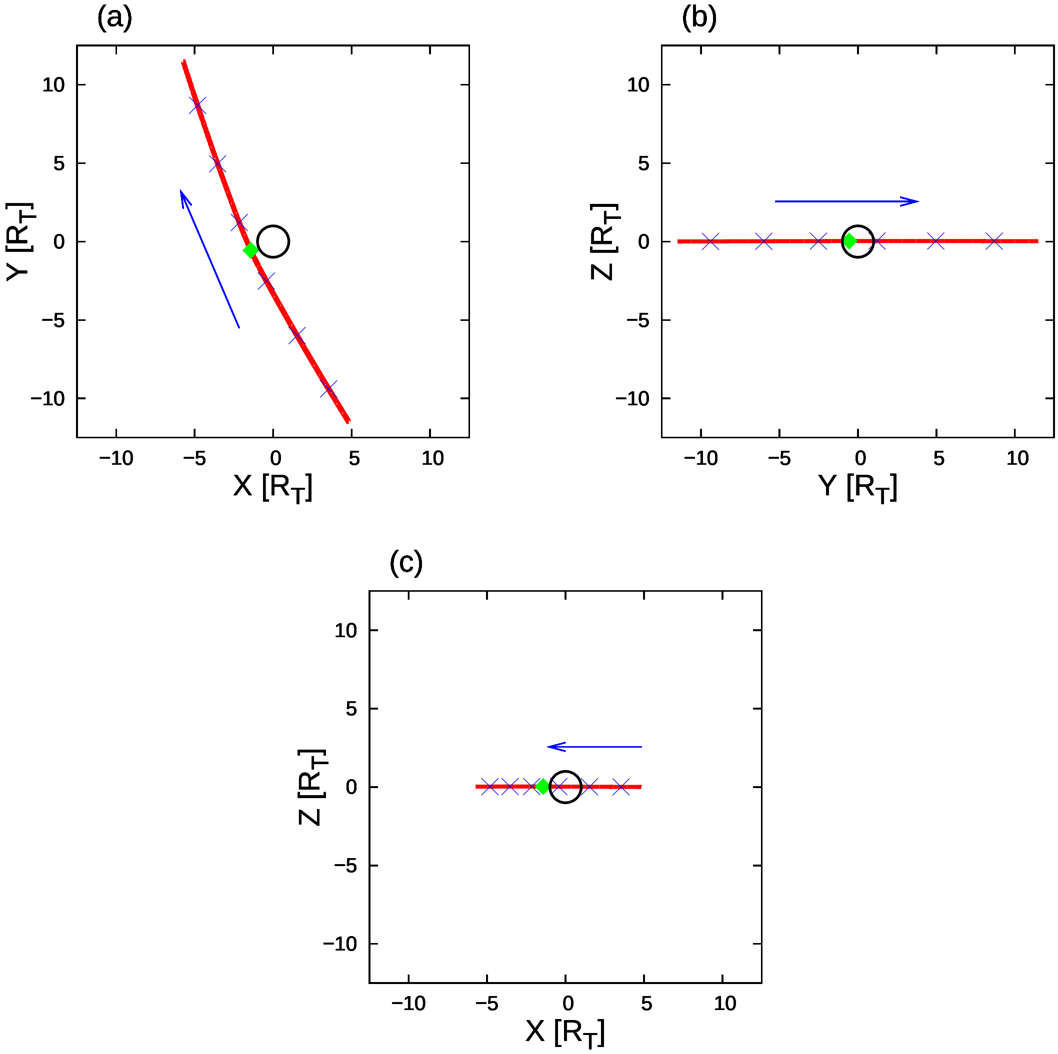

Figure 7.16: Cassini's trajectory during the T8 flyby of Titan. During this flyby, the spacecraft passed through the magnetic pile-up region at Titan's ramside when the satellite was located at about 09:30 clock angle position on its orbit around Saturn. On 28 October 2005 at 04:16 UT, i.e. about one year after the first Titan flyby, Cassini achieved its closest approach altitude of 1450 km. The position of closest approach is again denoted by a green diamond, whereas the markers along the trajectory are 30 minutes apart, beginning at 03:00 UT. The first Titan encounters TA, TB and T3 took place at nearly the same orbital position of Titan.

and hydrogen. In the case of T8, choosing the upstream parameters in this way is also motivated by the analysis of the magnetometer data collected during the Cassini TA, TB and T3 flybys. During each of these flybys, Titan was located at about 10:30 clock angle position on its orbit around Saturn, so that its position was nearly identical to the location during T8. Backes *et al.* [6] analyzed Titan's magnetic field signature during TA in terms of a three-dimensional resistive MHD model. By choosing Voyager-like upstream conditions, the authors achieved formidable agreement between the simulated magnetic fields and data from the MAG instrument. Neubauer *et al.* [118], who compared the TA results of Backes *et al.* [6]

to the magnetic field measurements conducted during TB and T3, suggest that Voyager-like upstream conditions may be appropriate for the situation during these two flybys as well. Of course, the preceding analyses of Titan's plasma environment during TA, TB and T3 do not include data from the Cassini plasma spectrometer and provide only snapshots of the situation. Nevertheless, following the assumption of Neubauer *et al.* [118], who consider Voyager-like flow conditions to be representative for the region of the magnetosphere where TA, TB and T3 took place, has proven suitable for T8 as well.

Of course, the background magnetic field vector of $\underline{B}_0 = (0, 0, -5)\,\mathrm{nT}$ is again replaced by an appropriate approximation to the homogeneous regions in the Cassini magnetic field signature (cf. figs. 7.17(b), (d) and (f)). The only "critical" input parameter is the background magnetic field value for the B_Y component. As can be seen from fig. 7.17(d), before closest approach at about 04:16 UT, B_Y possesses a nearly constant value of about $2.5 \ldots 3\,\mathrm{nT}$, whereas $B_Y \approx 4\,\mathrm{nT}$ is an adequate approximation to the magnetic field signature in the outbound region. Three simulation geometries have been considered, two of them using the nearly homogeneous inbound and outbound values for B_Y as input parameters. In the third run, the background value for B_Y has been set to an intermediate value of $B_Y = 3.5\,\mathrm{nT}$. Since the qualitative differences in the results obtained from these three geometries have proven to be practically negligible, the discussion will only dwell on the $B_Y = 3.5\,\mathrm{nT}$ case. Again, the results for a high ion production are compared to a scenario in which Q for each species is about a factor of 3 smaller.

4.2 Comparison between simulation results and MAG measurements

The simulated magnetic field signatures along the Cassini trajectory can be seen in the left-hand panels of fig. 7.17, whereas fig. 7.18 displays a two-dimensional illustration of the magnetic field topology in Titan's orbital plane. In the framework of the relatively simple ionosphere model used here, the magnetic field components along the flyby trajectory have again shown to be only slightly affected by a moderate reduction of the total production rate. As shown in fig. 7.17(a), the simulated B_X component exhibits a nearly homogeneous structure. Only in the region between 04:00 UT and 04:30 UT, the model predicts the existence of a notch where the B_X component reverses its direction. In the case of a weakly emitting obstacle (red line), a minimum field value of $B_X = -3\,\mathrm{nT}$ is achieved, while the high emission scenario (green line) suggests the minimum value to be about $1\,\mathrm{nT}$ smaller. A similar structure was not only detected by Cassini around closest approach at 04:16 UT, but the magnitude of the measured break-in is also in good agreement with the results of the low emission scenario. As can be seem from fig. 7.17(b), the B_X component detected by the MAG instrument exhibits a break-in from $B_X \approx 1.5\,\mathrm{nT}$ to a value of $B_X = -2.5\,\mathrm{nT}$ at the "bottom" of the dip.

The physical mechanism from which this structure evolves is illustrated by the two-dimensional plot of the B_X component in fig. 7.18(b). The field line draping gives rise to two magnetic lobes with an enhancement of B_X in the Saturn-facing one, whereas in the anti-Saturn-facing lobe, the B_X component reverses its direction. However, the model does not show an enhancement of B_X at Titan's ramside. The contour plot clearly illustrates that in between the two lobes at Titan's ramside, B_X nearly remains at its undisturbed background value. A comparison between figs. 7.18(a) and 7.18(b) illustrates that when approaching Titan, Cassini

Quantity	Symbol	Numerical value
Magnetic field	$\underline{B}_0$	$(1.5, 3.5, -2.0)$ nT
	$\lvert\underline{B}_0\rvert$	$4.30\,\mathrm{nT}$
Plasma flow velocity	$\underline{u}_0$	$(120, 0, 0)\,\mathrm{km/s}$
	$\lvert\underline{u}_0\rvert$	$120\,\mathrm{km/s}$
Nitrogen (N^+) density	$n_{m,1}$	$0.2 \cdot 10^6\,\mathrm{m}^{-3}$
Hydrogen (H^+) density	$n_{m,2}$	$0.1 \cdot 10^6\,\mathrm{m}^{-3}$
Nitrogen temperature	$kT_{m,1}$	$1578.48\,\mathrm{eV}$
Hydrogen temperature	$kT_{m,2}$	$112.75\,\mathrm{eV}$
Thermal velocity	$v_{th,N^+} = v_{th,H^+}$	$180\,\mathrm{km/s}$
Nitrogen plasma beta	$\beta_{m,1}$	6.87
Hydrogen plasma beta	$\beta_{m,2}$	0.25
Alfvén velocity	v_A	$55.08\,\mathrm{km/s}$
Alfvénic Mach number	M_A	2.18
Sound velocity	c_S	$146.34\,\mathrm{km/s}$
Sonic Mach number	M_S	0.82
Magnetosound velocity	c_{MS}	$157.89\,\mathrm{km/s}$
Magnetosonic Mach number	M_{MS}	0.76
Total N_2^+ production rate (low emission)	$Q_{i,1}$	$7.70 \cdot 10^{24}\,\mathrm{s}^{-1}$
Total CH_4^+ production rate (low emission)	$Q_{i,2}$	$7.70 \cdot 10^{24}\,\mathrm{s}^{-1}$
Total H_2^+ production rate (low emission)	$Q_{i,3}$	$7.70 \cdot 10^{24}\,\mathrm{s}^{-1}$
Total N_2^+ production rate (high emission)	$Q_{i,1}$	$2.47 \cdot 10^{2}\,\mathrm{s}^{-1}$
Total CH_4^+ production rate (high emission)	$Q_{i,2}$	$2.47 \cdot 10^{2}\,\mathrm{s}^{-1}$
Total H_2^+ production rate (high emission)	$Q_{i,3}$	$2.47 \cdot 10^{2}\,\mathrm{s}^{-1}$
Box size	X	$-12.5R_T \le X \le 12.5R_T$
	Y	$-12.5R_T \le Y \le 12.5R_T$
	Z	$-12.5R_T \le Z \le 12.5R_T$
Number of grid cells	(N_X, N_Y, N_Z)	$(100, 100, 100)$
Time step	Δt	$0.40\,\mathrm{s}$
Total number of time steps	$N_{\Delta t}$	20000
Smoothing parameter	α_S	0.05

Table 7.6: Simulation parameters for the Cassini T8 flyby. Motivated by the study presented by Neubauer *et al.* [118], the plasma composition and flow speed have been chosen in accordance to the Voyager 1 configuration. The upstream B_Y value is located in between the homogeneous values detected during the inbound and the outbound part of the flyby. While the number of 100 grid nodes in each direction is identical to the value selected for the other simulations in this chapter, a value of $25R_T$ instead of $30R_T$ has been chosen for the box length. On the one hand, this yields at least a slight increase of resolution near the obstacle, but on the other hand, the outer walls of the simulation domain are still sufficiently far away from Titan to circumvent any influence on the simulated field signature.

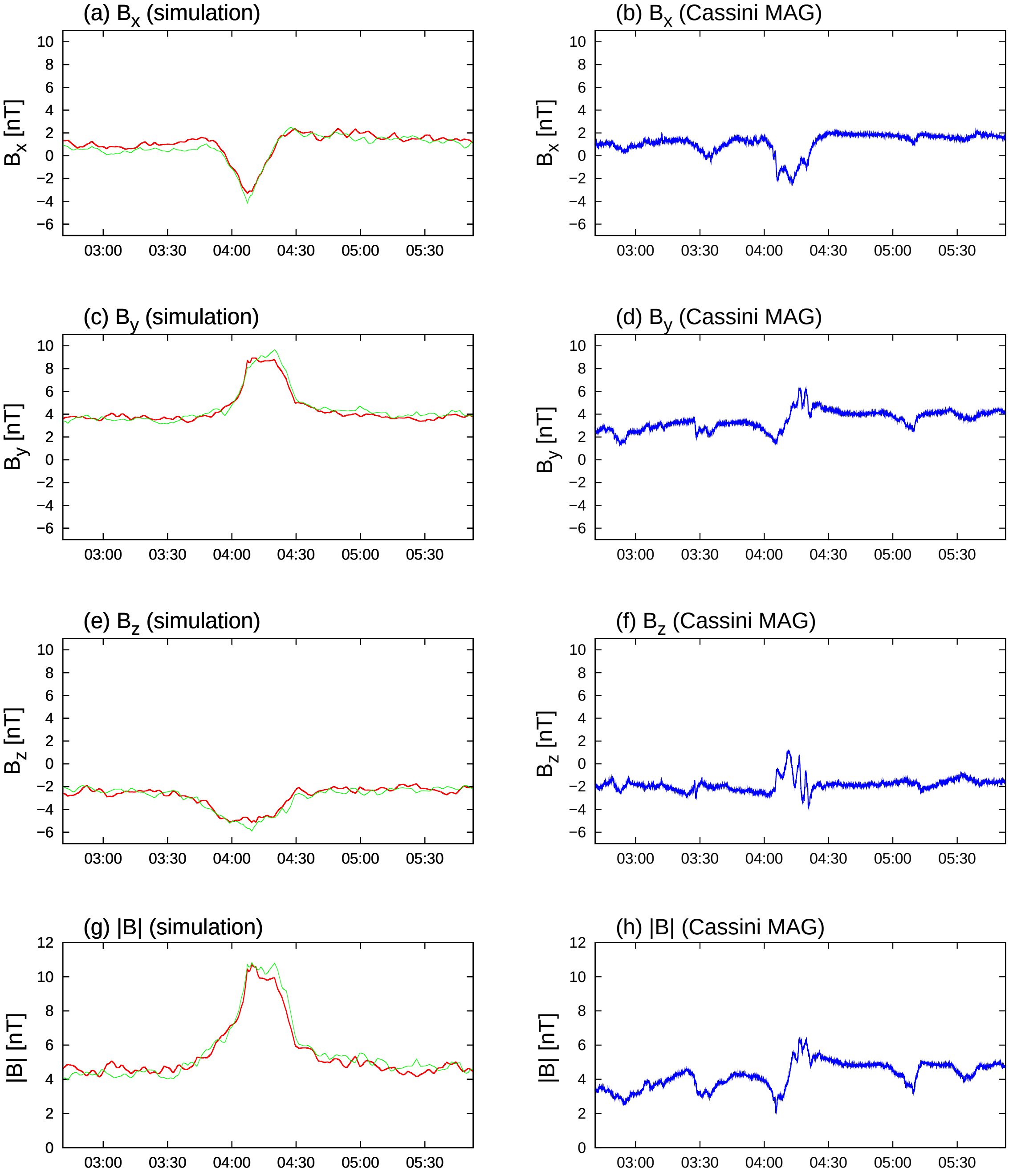

Figure 7.17: Hybrid simulation of Titan's magnetic field signature during Cassini's T8 flyby. The simulation results are shown in the left-hand plots (green: high emission, red: low emission), while the signatures detected by the MAG instrument can be seen in the figures on the right-hand side. Both the position and the magnitude of the dip in the B_X component have proven to be well reproducible by the simulation model. However, the magnetic enhancement predicted for the B_Y component does not manifest in the measured field signature. Instead, the data collected by the MAG instrument show the presence of a slightly pronounced step, indicating an increase from a homogeneous level of $B_Y = 2.5\,\mathrm{nT}$ to a different stable value of $B_Y = 4\,\mathrm{nT}$. For the B_Z component, the model suggests the presence of a broad break-in, whereas MAG measurements show an inhomogeneous region of enhanced B_Z at the corresponding position. The simulated field magnitude exhibits a quite homogeneous structure, with the plateau-like enhancement in the B_Y component being superimposed. In contrast to this, the field magnitude obtained from the MAG data shows various small maxima and minima. The imprint of the step in the B_Y component is also clearly identifiable.
Simulation parameters: see table 7.6.

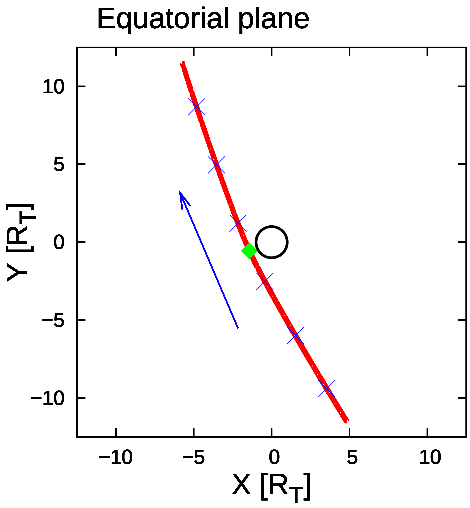

(a) Cassini flyby trajectory in the equatorial plane

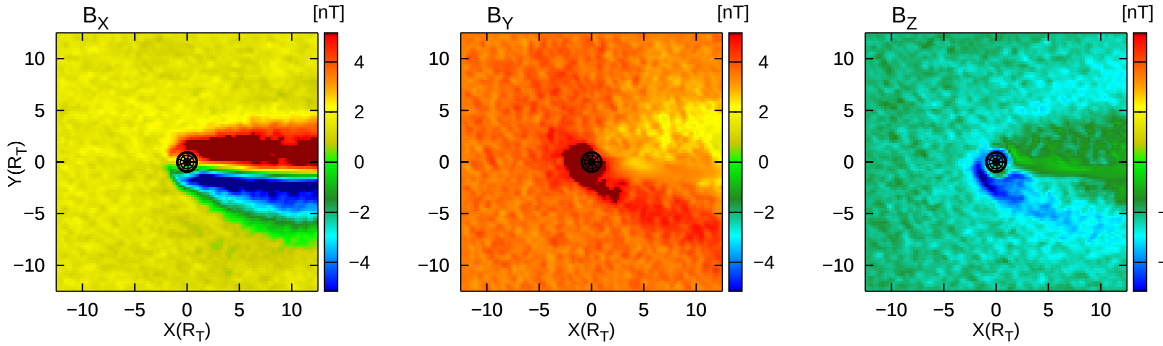

(b) Low emission: Magnetic field components

Figure 7.18: Titan's magnetic field signature during Cassini's T8 flyby. The figure shows a two-dimensional illustration of the magnetic field components in Titan's orbital plane which also contains the trajectory of the spacecraft. The B_X component features a pronounced lobe structure. In the anti-Saturn-facing lobe, B_X is reduced with respect to the background value and it even reverses its direction. The Saturn-facing lobe is characterized by a strong magnetic field enhancement. The dip observed in the B_X component denotes Cassini's passage through the forward part of the anti-Saturn-facing lobe. On the other hand, the tilted shape of the trajectory prevented a passage through the forward regions of the Saturn-facing lobe. The simulation results indicate a strong enhancement of B_Y at Titan's ramside, whereas the B_Y lobe structure is by far not as sharply confined as the B_X signature. In the anti-Saturn-facing hemisphere, B_Z is slightly reduced in the vicinity of Titan.
Simulation parameters: see table 7.6.

passed through a region of nearly homogeneous B_X at first. Near closest approach at Titan's ramside, the spacecraft came into contact with the outer flank of Titan's anti-Saturn-facing lobe that is characterized by a negative B_X component. However, in the $Y > 0$ hemisphere, the Cassini trajectory leads quite straight away from Titan. In this region, the spacecraft was already too far away from the moon to pass through the forward region of the Saturn-facing lobe, in which B_X is positive. As can be seen from 7.18(b), both lobes show only a small penetration into Titan's ramside hemisphere ($X < 0$). Cassini passed only through the anti-

Saturn-facing structure, while the trajectory's tilt in negative X direction avoided a detection of the Saturn-facing B_X lobe. Therefore, the B_X signature along the trajectory exhibits only a dip before closest approach, but it does not show an additional peak in the outbound region. Although in contrast to the simulation results, the observed B_X dip features rather a flat than a spiky structure, the behaviour of the B_X component is reproduced by the model in an excellent manner.

As can be seen from the two-dimensional illustration of the B_Y component in fig. 7.18(b), the model predicts the ramside magnetic pile-up to be mainly realized by an increase of the B_Y component. Neither the B_X nor the B_Z component exhibits a noticeable magnetic field enhancement at Titan's ramside; B_Z is even reduced with respect to the background value. On the other hand, the imprint of the magnetic lobe structure is primarily identifiable in the B_X signature. Although the B_Y component shows an increase in the anti-Saturn-facing wake region and a reduced value in the Saturn-facing hemisphere, compared to the sharply pronounced B_X lobes, these structures exhibit a rather diffuse character. Simply put, the model suggests the B_X component to be responsible for the wakeside lobe structure, whereas the B_Y component mainly governs the topology of the ramside magnetic pile-up region.

Nevertheless, a comparison between figs. 7.17(c) and (d) illustrates that this interpretation is not consistent with Cassini measurements. Between 04:00 UT and 04:30 UT, the simulated B_Y component exhibits a broad, plateau-like overshoot to values of $8 \ldots 10\,\mathrm{nT}$, thus exceeding the background value by more than a factor of 2.5. The manifestation of such a peak in the B_Y component should correspond to the passage through the ramside magnetic pile-up region, as implied by the contour plot of B_Y in fig. 7.18(b). However, as already stated above, the measured B_Y component exhibits a homogeneous structure before as well as after closest approach. The position of the slight step detected around 04:15 UT coincides with the location of the simulated peak, but the minor B_Y enhancement of about $1\,\mathrm{nT}$ around 04:30 UT is clearly exceeded by the magnitude of the simulated overshoot.

Indeed, none of the three magnetic field components measured by Cassini shows any sign of a strong magnetic field enhancement whose magnitude is comparable to the simulated increase of the B_Y component. Actually, there seems to be no pile-up at Titan's ramside. Only the B_Z component exhibits an increase from $B_Z = -2\,\mathrm{nT}$ to $B_Z = +1\,\mathrm{nT}$ between 04:00 UT and 04:30 UT (cf. fig. 7.17(f)). As can be seen from fig. 7.17(e), the position of the distortion in the B_Z component is again well predicted by the simulation model. But instead of an enhancement, the simulations suggest the formation of a broad, flat break-in that denotes a decrease from $B_Z = -2\,\mathrm{nT}$ to $B_Z = -5 \ldots -6\,\mathrm{nT}$. The B_Z enhancement detected by Cassini is not only narrower, but it also exhibits a quite inhomogeneous sub-structure of several small peaks and dips in close sequence. If this structure has to be ascribed to the magnetic enhancement that can be expected for the ramside pile-up region, Cassini measurements suggest the pile-up to be mainly realized by an increase of the B_Z component. The model, on the other hand, predicts the pile-up to manifest in the B_Y component. In any case, the measured pile-up would be clearly smaller than the increase of field magnitude detected by Cassini. However, based only on the magnetometer data, the interpretation of the pile-up structure observed during T8 cannot come to a final conclusion. Especially, the mechanism giving rise to different "background" values for B_Y in either hemisphere of Titan cannot be clarified in the framework of the simulation approach.

The absolute values of both the simulated and the measured magnetic field are shown in figs. 7.17(g) and (h), respectively. The imprint of the B_Y enhancement is clearly identifiable in the simulated field magnitude which exhibits a quite homogeneous structure before and after the encounter. In contrast to this, the measured magnetic field is rather inhomogeneous. If a background value should be defined for the ambient field magnitude, the inbound value before 04:16 UT would have to be about 2 nT smaller than the value for the outbound region. It is important to notice that this is not the first observation of such a step during a Titan flyby. Backes *et al.* [6] as well as Neubauer *et al.* [118] report on a quite remarkable observation during the Cassini TA, TB and T3 encounters[2]. During TA, the magnetospheric field seemed to jump from a relatively stable level of about $|\underline{B}| = 6.35\,\mathrm{nT}$ before the encounter to a different stable level of $|\underline{B}| = 5.74\,\mathrm{nT}$ after the encounter (see also Ma [98] and Ma *et al.* [99]). In contrast to this, the field signature detected during TB did not show such a behaviour on a similar length scale. The T3 flyby again showed a noteworthy difference between the inbound and outbound pass. Neubauer *et al.* [118] also point out that the ambient magnetospheric conditions for TA, TB and T3 were quiet, disturbed and slightly disturbed, respectively. This may indicate that in the relevant region of the magnetosphere, the ambient field undergoes strong changes on a characteristic length scale which is comparable to the size of the simulation box. Due to stability reasons, covering the effects that arise from inhomogeneous upstream conditions has so far not been realized by any global numerical approach.

Finally, it should be noted that in the case of T8, agreement between simulated and measured signatures could neither be significantly improved by altering the direction of the impinging flow nor by reducing its velocity. The position of the B_X notch has shown to be highly susceptible to changes in the upstream flow direction. This is absolutely understandable because for instance, turning the upstream velocity vector away from Saturn[3] would apparently increase the diameter of the intersection segment of the Cassini trajectory and the anti-Saturn-facing magnetic lobe. Thus, the length of the interval in which a negative B_X value was predicted would increase. On the other hand, assuming the upstream flow to possess a non-vanishing component in the direction of Saturn would finally cause an intersection between the forward region of the Saturn-facing lobe and the spacecraft trajectory. Hence, an additional region with increased B_X would occur along the trajectory. Even though a reduction of the magnetospheric plasma speed to values well below 120 km/s goes along with a decrease of the overshoot in the B_Y component, the magnitude and width of the B_X dip have shown to be affected as well: The smaller is the upstream value for the flow speed, the broader is the B_X dip and the smaller is its relative magnitude. Hence, the assumption of the ambient flow speed during TA, TB and T3 being comparable to the value obtained from Voyager 1 data (cf. Neubauer *et al.* [118]) may be considered an adequate approximation for the T8 scenario as well.

With respect to the Titan interaction system, all flybys that have been analyzed in the preceding sections were "two-dimensional", i.e. the flyby trajectory was completely located in one of the coordinate planes. However, only very few Cassini flybys of Titan feature this characteristic. Therefore, the final section of this chapter will deal with the analysis of a flyby

---

[2] The reader should keep in mind that during these flybys, the location of Titan was nearly identical to the satellite's position during T8.

[3] In this case, the vector $\underline{u}_0$ would still be parallel to the (X, Y) plane, but it would possess a component in $(Y < 0)$ direction.

whose trajectory was not located in Titan's equatorial plane.

5 The Cassini T6 flyby of Titan

The T6 flyby of Titan took place on 22 August 2005 when Titan was located at about 05:00 clock angle position. At 08:51 UT, the spacecraft achieved its closest approach altitude of 3669 km. The flyby trajectory is displayed in fig. 7.19. Again, the projection on the (X, Y) plane would indicate a lobe passage in the equatorial plane, but in the T6 situation, the Z component of the spacecraft position does not vanish. As can be seen from plots (b) and (c), the spacecraft approached the moon's orbital plane from "above" and intersected it at about 07:30 UT. By the time of closest approach (green diamond), the spacecraft was located well

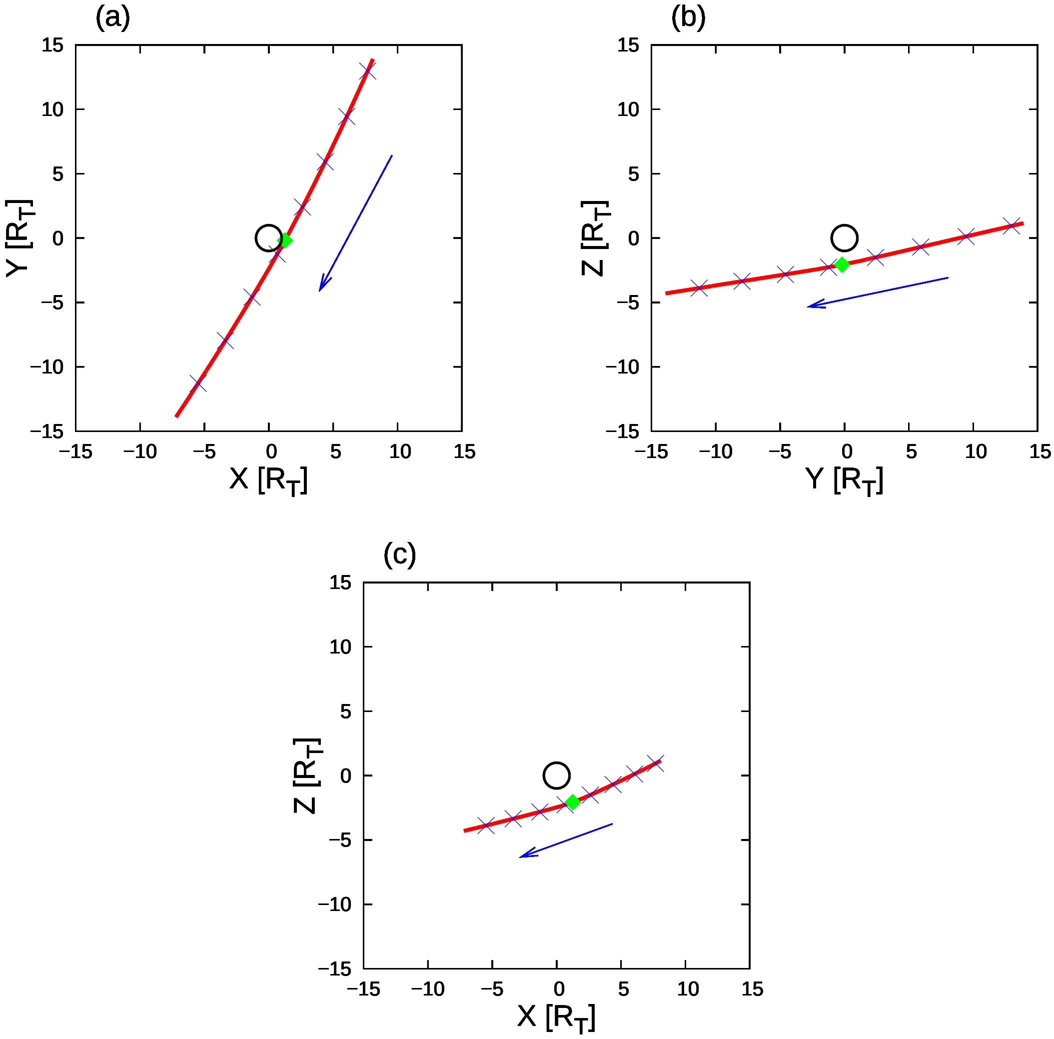

Figure 7.19: Cassini's trajectory during the T6 flyby. The blue markers along the trajectory are 30 minutes apart; the first one denotes the spacecraft position at 07:00 UT. Cassini approached Titan's orbital plane from "above" and intersected it at about 07:30 UT.

Quantity	Symbol	Numerical value
Magnetic field	$\underline{B}_0$	$(1.0, 3.0, -2.0)\,\mathrm{nT}$
	$\lvert\underline{B}_0\rvert$	$3.74\,\mathrm{nT}$
Plasma flow velocity	$\underline{u}_0$	$(120, 0, 0)\,\mathrm{km/s}$
	$\lvert\underline{u}_0\rvert$	$120\,\mathrm{km/s}$
Nitrogen (N^+) density	$n_{m,1}$	$0.2 \cdot 10^6\,\mathrm{m}^{-3}$
Hydrogen (H^+) density	$n_{m,2}$	$0.1 \cdot 10^6\,\mathrm{m}^{-3}$
Nitrogen temperature	$kT_{m,1}$	$1578.48\,\mathrm{eV}$
Hydrogen temperature	$kT_{m,2}$	$112.75\,\mathrm{eV}$
Thermal velocity	$v_{th,N^+} = v_{th,H^+}$	$180\,\mathrm{km/s}$
Nitrogen plasma beta	$\beta_{m,1}$	9.08
Hydrogen plasma beta	$\beta_{m,2}$	0.32
Alfvén velocity	v_A	$47.9\,\mathrm{km/s}$
Alfvénic Mach number	M_A	2.50
Sound velocity	c_S	$146.34\,\mathrm{km/s}$
Sonic Mach number	M_S	0.82
Magnetosound velocity	c_{MS}	$153.85\,\mathrm{km/s}$
Magnetosonic Mach number	M_{MS}	0.78
Total N_2^+ production rate (high emission)	$Q_{i,1}$	$2.18 \cdot 10^{25}\,\mathrm{s}^{-1}$
Total CH_4^+ production rate (high emission)	$Q_{i,2}$	$2.18 \cdot 10^{25}\,\mathrm{s}^{-1}$
Total H_2^+ production rate (high emission)	$Q_{i,3}$	$2.18 \cdot 10^{25}\,\mathrm{s}^{-1}$
Total N_2^+ production rate (low emission)	$Q_{i,1}$	$6.54 \cdot 10^{24}\,\mathrm{s}^{-1}$
Total CH_4^+ production rate (low emission)	$Q_{i,2}$	$6.54 \cdot 10^{24}\,\mathrm{s}^{-1}$
Total H_2^+ production rate (low emission)	$Q_{i,3}$	$6.54 \cdot 10^{24}\,\mathrm{s}^{-1}$
Box size	X	$-15R_T \leq X \leq 15R_T$
	Y	$-15R_T \leq Y \leq 15R_T$
	Z	$-15R_T \leq Z \leq 15R_T$
Number of grid cells	(N_X, N_Y, N_Z)	$(100, 100, 100)$
Time step	Δt	$0.48\,\mathrm{s}$
Total number of time steps	$N_{\Delta t}$	20000
Smoothing parameter	α_S	0.05

Table 7.7: Cassini's T6 flyby of Titan – Simulation parameters.

below Titan's orbital plane. Another difference to the other flybys discussed in this chapter concerns the magnetic field data collected during T6. For this flyby, only low resolution data have been available at the time of this writing. Specifically, for T8, T9, T11 and T15, the MAG field signature inside the $(-15R_T \leq X, Y, Z \leq +15R_T)$ box typically consisted of about 15000 data points. Thus, the number of data points clearly exceeds the number of grid nodes in each direction. Since in a Particle-in-Cell code, the electromagnetic field quantities are defined only at the nodes of the simulation grid, the specific magnetic field vector at each of the 15000 positions is computed by means of the Cloud-in-Cell interpolation technique. As for T6, only about 300 data points are available for the trajectory segment inside the simulation domain. Thus, it should be noted that in this case, the grid resolution is at least comparable to the resolution of the data set.

An overview of the major input parameters is given in table 7.7, whereas fig. 7.20 displays the comparison between simulated and measured magnetic field signature. Again, the red and green lines refer to the results for low and high emission, respectively. As shown in fig. 7.20(a), the simulation model predicts a nearly homogeneous structure of the B_X component before 08:00 UT. Between 08:00 UT and 09:00 UT, a broad peak is formed. The steepness of the overshoot's inbound flank is clearly exceeded by that of the outbound flank. Both the high and the low emission scenario indicate the peak field strength to be achieved around closest approach at 08:51 UT. In the case of a weakly emitting obstacle, a maximum field strength of about 5 nT is reached. In the high emission run, the maximum value is about 1 nT larger. At about 09:00 UT, the peak is followed by a slightly pronounced dip which denotes a reduction of B_X to minimum values of $B_X = -0.5\,\mathrm{nT}$ and $B_X = -1.5\,\mathrm{nT}$, respectively. Both of these distortions can be ascribed to the passage through Titan's magnetic lobes. As already demonstrated in the preceding sections, if the upstream flow is assumed to be in a state of ideal corotation, the formation of Titan's magnetotail gives rise to strong distortions of B_X in the equatorial plane. The overshoot that can be seen in fig. 7.20(a) would correspond to Cassini's passage through the Saturn-facing lobe. However, as implied by fig. 7.19, the spacecraft did not remain in the equatorial plane, but it moved downwards and was therefore expected to miss the central region of the anti-Saturn-facing lobe. Therefore, the dip is followed by only a minor reduction of the B_X component.

These key features of the simulated B_X signature have shown to be well confirmed by Cassini magnetometer data. As can be seen from fig. 7.20(b), the spacecraft passed through a region of quite homogeneous B_X before 08:00 UT, followed by the detection of an enhancement between 08:00 UT and 09:00 UT. In consistency with the results of the low emission run, the peak field strength of $B_X = 5\,\mathrm{nT}$ is achieved around 09:00 UT. After 09:30 UT, both model results and MAG measurements show a rather homogeneous structure of the B_X component. However, the magnetic field enhancement detected by Cassini exhibits a sub-structure which is not reproduced by the simulation model. As shown in fig. 7.20(b), a first enhancement to $B_X = 4\,\mathrm{nT}$ around 08:30 UT is followed by a slightly pronounced break-in, before the spacecraft detected the subsequent major peak at 09:00 UT. The measured field signature also lacks evidence of a passage through the anti-Saturn-facing lobe. Although the outbound flank of the major peak is followed by a slightly pronounced dip around 09:15 UT, the magnitude of this structure is comparable to that of the minor fluctuations detected after 09:30 UT and can therefore not be ascribed to a lobe passage.

As can be seen in fig. 7.20(d), the B_Y component measured by the Cassini magnetometer

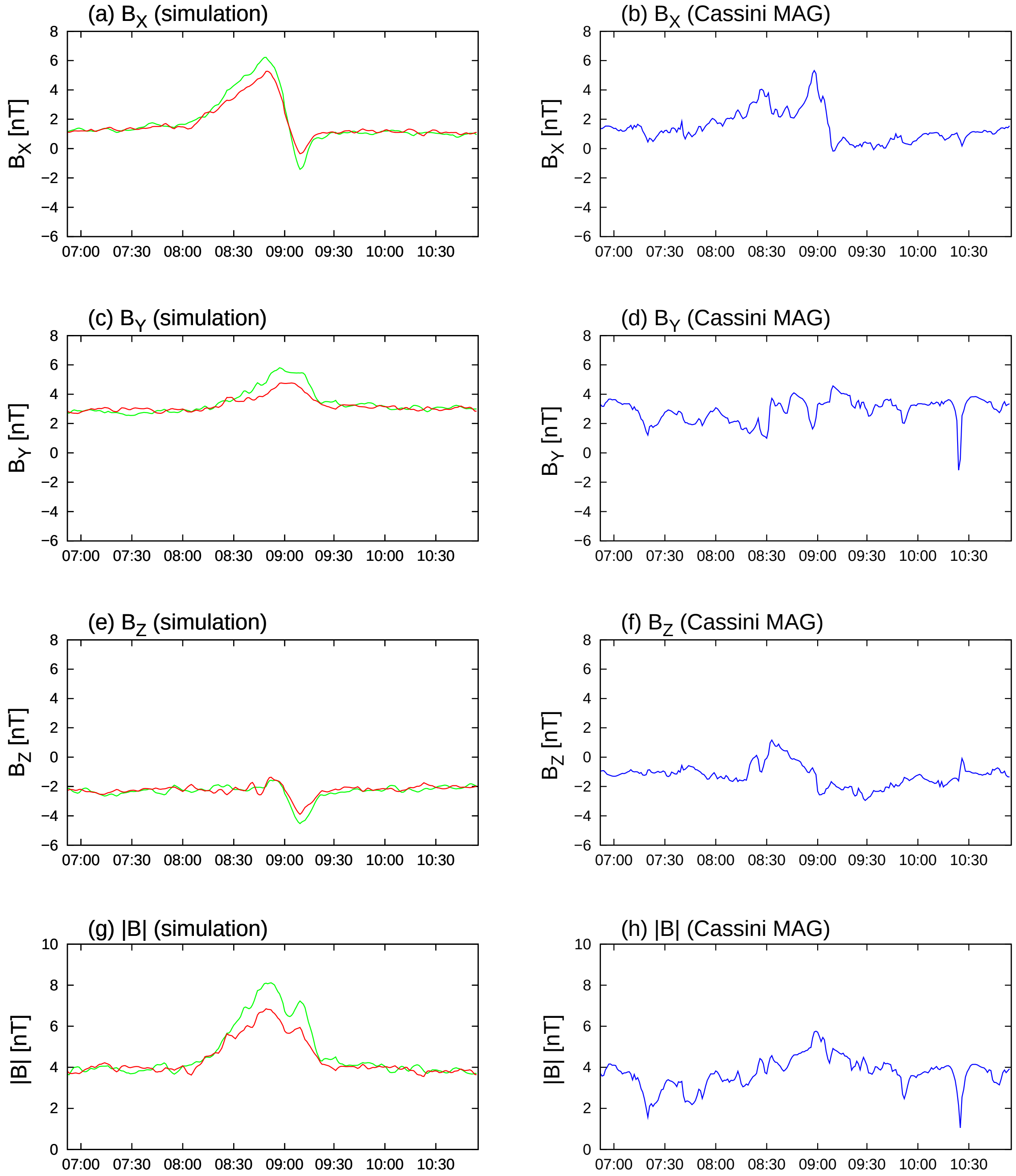

Figure 7.20: Simulation of Titan's magnetic field signature during Cassini's T6 flyby. The simulation results can be seen in the panels on the left-hand side (green lines: high emission, red lines: low emission). The simulation model predicts an enhancement in the B_X component that denotes the passage through Titan's Saturn-facing magnetic lobe. The subsequent minor break-in is likely to mark the outer regions of the anti-Saturn-facing lobe. Although the fine-structure of the peak differs from Cassini observations, both its magnitude and its position are well confirmed by the data from the MAG instrument. The simulated B_Y component shows only a slightly pronounced peak around 09:00 UT, whereas MAG measurements show the presence of multiple minor fluctuations between 1.5 nT and 4 nT. The definition of an adequate background value for B_Y is therefore quite problematic. Concerning the B_Z component, only the regions of rather homogeneous field strength before 08:15 UT and after 09:30 UT are reproduced by the simulation model.
Simulation parameters: see table 7.7.

exhibits a quite inhomogeneous structure and is characterized by fluctuations in the range of $B_Y = 1.5 \ldots 4\,\mathrm{nT}$. In contrast to the B_X signature, neither pronounced peaks nor minima have been detected. The B_Y signature obtained from the low emission scenario is confined to the interval of $1.5 \ldots 4\,\mathrm{nT}$ as well, except for a slightly pronounced peak of magnitude $B_Y = 4.8\,\mathrm{nT}$ around 09:00 UT. Thus, the results of the low emission run provide an adequate reproduction of the measured B_Y signature. Given the high variability in the B_Y measurements, the signature obtained from the high emission run can be considered to show at least satisfactory agreement.

A comparison of figs. 7.20(e) and (f) shows that the measured increase of B_Z between 08:30 UT and 09:00 UT is not reproduced by the simulation model. Instead, both simulation scenarios predict the formation of a slightly pronounced dip right after 09:00 UT. Test runs have shown that the larger is the background value chosen for B_Z, the larger is the relative magnitude of this dip. Therefore, the background value of $B_Z = -2\,\mathrm{nT}$ is a little smaller than the homogeneous value around $B_Z = -1\,\mathrm{nT}$ measured before 08:15 UT. The background value has been chosen to approximate the outbound B_Z signature between 09:15 UT and 10:45 UT. The data collected for the B_X component suggest that in this interval, Cassini had already left the region in which $\underline{B}$ is significantly distorted by the presence of Titan.

The inhomogeneous structure of the measured B_Y component leaves a clear imprint on the magnetic field magnitude obtained from MAG data (cf. fig. 7.20(h)). The overall tendency of $|\underline{B}|$ featuring a maximum around 09:00 UT is reproduced by the simulation approach, whereas its width and its magnitude are overestimated.

6 Summary

During the past two years, the Cassini spacecraft has accomplished more than 20 flybys of Titan and collected detailed information on the satellite's magnetic environment. For the study presented in this chapter, the simulation model has been applied to the geometries of specific Cassini flybys. The purpose was a reproduction and interpretation of the magnetic field signatures measured by the Cassini Magnetometer. A series of three wake flybys in the equatorial plane (T9, T11 and T15), a passage through the ramside magnetic pile-up region (T8) and another "oblique" passage through the lobes (T6) have been taken into consideration.

The simulations of Titan's magnetic lobe structure have shown to be in reasonable agreement with Cassini measurements. The positions of the detected wakeside magnetic field distortions have proven to be completely reproducible by the simulation model. For the T11 scenario, even the simulated magnitudes of the field enhancements were fully confirmed by the simulation model. For T9 and T15, the simulation model suggested the existence of additional enhancements in the B_X component that did not occur in the measured magnetic field signature. To a certain degree, the distortions in the B_Y and B_Z components detected during these flybys could be explained by assuming the upstream plasma flow to deviate from ideal corotation.

For the ramside flyby T8, formidable agreement between simulation and measurements could be achieved for the B_X component, whereas the model was able to predict only the positions, but not the magnitudes of the distortions in the B_Y and B_Z component. Curiously, no strong enhancement of $|\underline{B}|$ was detected at Titan's ramside. Cassini measurements showed an enhancement of B_X during the T6 flyby. By means of the simulation model, this structure could be ascribed to a passage through one of Titan's magnetic lobes. In general, the simulations have shown that the applicability of the model to the Titan scenario is restricted by the assumption of highly homogeneous conditions in the ambient magnetospheric plasma. As will also be discussed in more detail in the next chapter, this approximation is far from being perfectly fulfilled in reality.

Chapter 8

Multi-instrument analysis of the Cassini T9 flyby

The magnetic field signature detected during Cassini's T9 flyby of Titan has already been analyzed in the preceding chapter. The magnetospheric plasma composition and velocity had been "guessed" in such way that reasonable agreement between simulation results and Cassini Magnetometer data could be achieved. However, even though the data analysis for T9 is far from being complete, at least preliminary data from the Cassini Plasma Spectrometer are available for this flyby. The purpose of the study presented in this chapter is to incorporate the available information into the simulation model in order to create a more realistic approximation to the real situation during T9.

Unfortunately, successful plasma measurements are available for only one hemisphere of Titan. Based on this material, a modified simulation scenario has been designed. Since the upstream plasma is no longer assumed to consist mainly of atomic nitrogen, but only of the light species H^+ and H_2^+, the results will also allow to estimate the degree to which the near-Titan plasma environment is affected by the composition of the magnetospheric upstream flow.

The first section of this chapter gives an overview of the material that has been provided by the Cassini Plasma Spectrometer Team on a preliminary base. The discussion will also dwell on the problems and critical issues that are still associated with the interpretation of the data. The description of the modified simulation geometry is followed by a comparison to Cassini Magnetometer as well as to Plasma Spectrometer data. At the time of this writing, the plasma data for T9 have not been published in a refereed journal yet. Therefore, the reader should definitely keep in mind the preliminary character of the data description given in the first section.

1 Plasma parameters during Cassini's T9 flyby of Titan

In this section, an overview of the data obtained during T9 by the Cassini Plasma Spectrometer (CAPS) will be given. This instrument consists of three sensors: an electron spectrometer, an ion beam spectrometer and an ion mass spectrometer. The electron spectrometer measures the energy of the incoming electrons in an energy range between 0.7 and 30000 eV. Within an energy interval from 1 eV to 50 keV, the ion beam spectrometer measures the energy-to-charge ratio of the incoming ions. The ion mass spectrometer, which measures the local ion flux as a function of particle energy, mass and angle, operates in the same energy range. It is important to notice that the results obtained from this detector are sensitive to the orienta-

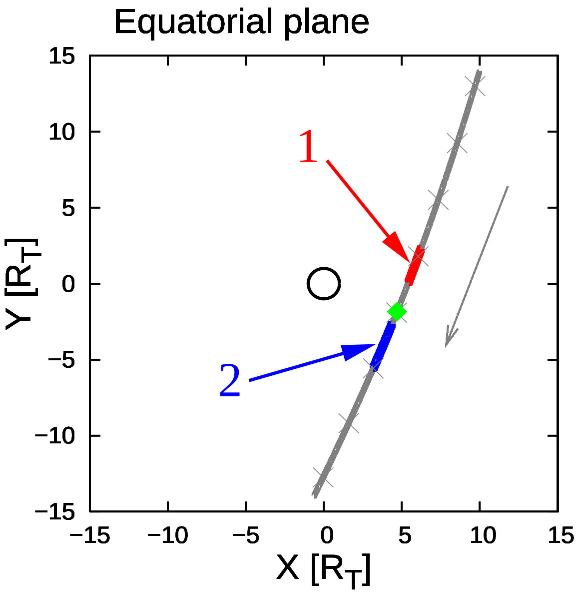

Figure 8.1: During Cassini's T9 flyby of Titan on 26 December 2006, the spacecraft passed through the satellite's wake in the equatorial plane. The position of closest approach at 18:59 UT is again denoted by a green diamond; the markers along the trajectory are 30 minutes apart. The figure illustrates the position of the *split signature* which was observed by the Cassini Plasma Spectrometer. Cold ions of possibly ionospheric origin were detected only in interval 1, denoting the time interval from 18:25 UT to 18:45 UT, and in interval 2 which begins about 6 minutes after closest approach and ends at 19:30 UT. However, heavy ions with masses above 14 amu were detected only in interval 1, whereas the plasma in interval 2 consisted mainly of 2 amu ions. The center of the wake, i.e. the region between these two intervals, was primarily populated by energetic protons and only very few heavier particles. As these features are neither symmetrically centered around nor located in the corotational wake region, the data collected by the CAPS instrument indicate that the ambient magnetospheric plasma flow was not aligned with the direction of ideal corotation. To date, a similar signature has not been detected during any other wake flyby of Titan.

tion of the spacecraft with respect to the plasma flow direction. A detailed description of the instrument as well as the scientific purposes of the Cassini plasma investigation is presented by Young *et al.* [158].

During the T9 flyby, Cassini passed through Titan's wake in the equatorial plane. Under ideal circumstances, i.e. under the assumptions of an ideally corotating upstream flow and the direction of the ambient magnetic field vector being perpendicular to Titan's orbital plane, the simulation results presented in the preceding chapters suggest that particles of ionospheric origin should have been forbidden to gain access to the Saturn-facing hemisphere. However, as stated in chapter 7, the major component of the ambient magnetic field vector detected by the MAG instrument was oriented in $(+Y)$ direction. Besides, measurements of the Cassini Plasma Spectrometer presented by Crary *et al.* [38] show that during T9, the ambient plasma velocity vector did not point in the direction of ideal corotation.

The flyby trajectory with respect to Titan is again displayed in fig. 8.1. At 17:50 UT, i.e. about one hour before closest approach, the CAPS ion analyzers sensed Titan's presence for the first time by detecting a deceleration of all ion components in the magnetospheric plasma flow (cf. Szegö [144]). After closest approach at about 19:00 UT, i.e. in the segment of the trajectory which is located in the $(Y < -3R_T)$ hemisphere, CAPS measurements indicated the upstream flow to be directed away from Saturn, forming an angle of about 65° with the $(+X)$ axis of the Titan interaction system. In this region, the flow velocity obtained from CAPS data is given by $u_0 \approx 100\,\mathrm{km/s}$. Since in the pre-encounter region of Cassini's trajectory, the impinging plasma was not in the field of view of the CAPS instrument, the available data do not allow a definite estimate of the magnetospheric plasma velocity in the $(Y > 0)$ hemisphere. Crary *et al.* [38] even suggest that the flow in the inbound region might have been deflected towards Saturn. Near closest approach, the instrument detected a strong deceleration of the plasma to velocities of about $10 - 40\,\mathrm{km/s}$. However, the data available from the CAPS instrument do neither allow to infer a definite value for the homogeneous upstream velocity vector $\underline{u}_0$, which is required as an input parameter for any numerical simulation model, nor do they completely clarify whether a global, homogeneous upstream velocity can actually be defined for the magnetospheric conditions during the T9 encounter. Determining the magnitude of the ambient flow speed is further complicated by the fact that the data collected by the CAPS instrument do not include a sufficiently long period of time in the region where the flow was not yet decelerated.

Based on an analysis of the energy-mass-spectra conducted by Crary *et al.* [38], atomic hydrogen $(m_1 = 1\,\mathrm{amu})$ and a species of mass $m_2 = 2\,\mathrm{amu}$ could be identified as the major constituents of the magnetospheric plasma in the outbound region of T9, their densities being highly variable between $0.04\,\mathrm{cm}^{-3}$ and $0.4\,\mathrm{cm}^{-3}$. Although heavier magnetospheric ion species, such as atomic nitrogen or oxygen, have been detected during other encounters of Titan, they did not occur in significant concentrations during T9. Nonetheless, it is not clear whether the heavy magnetospheric component was really absent, since in the inbound region, the CAPS instrument did not collect reliable data.

The data collected in the plasma wake downstream of Titan reveal the presence of a unique *split signature*, which has so far not been detected during any other flyby. Especially, an analogous structure did not occur during the later wake flyby T11, whose trajectory was also completely located in the equatorial plane (Coates *et al.* [35]). Based on the CAPS measurements, Crary *et al.* [38] were able to identify three distinct regions along the T9 trajectory, which possess significantly different plasma properties. The situation is illustrated in fig. 8.1. As denoted by the red bar along the Cassini trajectory, at 18:25 UT and in a distance of about $6.3R_T$ to the satellite, the spacecraft entered into a region which was characterized by a sudden increase of the electron density, jumping up by an order of magnitude. In this region, the ion sensors detected a cold, dense population of heavy ions, its major constituents being particles in the mass regime of $16 \ldots 19\,\mathrm{amu}$ and between $28 \ldots 40\,\mathrm{amu}$. Apparently, the position of this ion population crosses the edge of the wake which would be formed in the case of ideal corotation, but it is not located exactly behind the obstacle. The particle energies measured in this interval were relatively low and ranged between $10\,\mathrm{eV}$ and $50\,\mathrm{eV}$, suggesting that this ion population was of ionospheric origin. The Cassini spacecraft departed from this region of cold plasma at about 18:45 UT, as denoted by the anti-Saturn-facing edge of the red bar in fig. 8.1. In the following, the region denoted by the red bar will be referred to as interval 1.

A preliminary interpretation of the signature observed in interval 1 is given by Szegö [144] who proposes that these particles escaped from the ionosphere and were thermalized on a time scale that is an order of magnitude smaller than the characteristic time scale of ion gyration. A detailed discussion of such a thermalization mechanism is given by Dobé and Szegö [42]. Szegö [144] suggests that these cold particles reached the spacecraft by escaping along the magnetic field lines on corkscrew-like trajectories. Nevertheless, interpreting the signature detected in interval 1 is extremely complicated, because the spacecraft speed of 5.9 km/s has not been negligible relative to the bulk speed of the decelerated plasma. Moreover, the spacecraft potential of about $-2\,\mathrm{V}$ gave rise to an additional acceleration of the ions before they were detected by the spacecraft. In consequence, the interpretation and analysis of the signature observed in interval 1 is still pending.

After it had left the region populated by heavy ions, Cassini entered the center of Titan's wake which was located between the intervals 1 and 2 in fig. 8.1. Since the flow direction in this region was not aligned with the instrument's field of view, only very little is known about the plasma parameters in this segment of the trajectory [144]. Crary *et al.* [38] suggest that the plasma in this region consisted mainly of protons and a small amount of 2 amu ions. In strong contrast to the signatures observed in interval 1, practically no heavy ions were detected in this region. The proton energies observed in this interval were of the order of 1 keV, and therefore clearly exceeded the temperature of the adjacent plasma. Furthermore, the region between intervals 1 and 2 does not coincide with the wake position which would be expected for the case of an ideally corotating upstream flow. So far, the complete lack of heavy ions in the center of the wake has not been observed during any other Cassini flyby of Titan.

Between 19:06 UT and 19:30 UT and in a distance of about $5.0 - 6.4 R_T$ to Titan, Cassini passed through the region which is referred to as interval 2 in fig. 8.1. According to Crary *et al.* [38] and Szegö [144], the plasma spectrometer detected mostly light ions with masses of $m = 1\,\mathrm{amu}$ in this part of the trajectory. Since the detector measured particle energies in the range of $20 \ldots 100\,\mathrm{eV}$, the plasma in part 2 of the trajectory was significantly colder than in the region between the two intervals. As discussed by Coates *et al.* [35], the electron data obtained in interval 2 revealed a quite complex structure, indicating that the electron population in this region was a mixture of magnetospheric electrons with a low energy population of possibly ionospheric origin. In any case, it is important to notice the strong differences between the plasma compositions in intervals 1 and 2. Moreover, these regions are neither located in the wake region expected for ideal corotation, nor do they seem to be centered around the corotational wake.

2 Simulations

Based on the data that are available for the T9 encounter, a set of input parameters for the hybrid code has been derived. The following sections deal with an extensive discussion of the numerical results. An overview of the major input parameters is followed by a comparison between the numerical results and the data collected by the Cassini Magnetometer as well as by the Plasma Spectrometer.

Quantity	Symbol	Numerical value
Magnetic field	$\underline{B}_0$	$(3.73, 4.70, -2.15)$ nT
	$\lvert\underline{B}_0\rvert$	$6.37\,\mathrm{nT}$
Plasma flow velocity	u_0	$120\,\mathrm{km/s}$
Atomic hydrogen (H^+) density	$n_{m,1}$	$0.3 \cdot 10^6\,\mathrm{m}^{-3}$
Molecular hydrogen (H_2^+) density	$n_{m,2}$	$0.1 \cdot 10^6\,\mathrm{m}^{-3}$
H^+ temperature	$kT_{m,1}$	$112.75\,\mathrm{eV}$
H_2^+ temperature	$kT_{m,2}$	$225.50\,\mathrm{eV}$
Thermal velocity	$v_{th,H^+} = v_{th,H_2^+}$	$180\,\mathrm{km/s}$
H^+ plasma beta	$\beta_{m,1}$	0.33
H_2^+ plasma beta	$\beta_{m,2}$	0.22
Alfvén velocity	v_A	$196.61\,\mathrm{km/s}$
Alfvénic Mach number	M_A	0.61
Sound velocity	c_S	$146.97\,\mathrm{km/s}$
Sonic Mach number	M_S	0.82
Magnetosound velocity	c_{MS}	$245.47\,\mathrm{km/s}$
Magnetosonic Mach number	M_{MS}	0.49
Total N_2^+ production rate (high emission)	$Q_{i,1}$	$2.18 \cdot 10^{25}\,\mathrm{s}^{-1}$
Total CH_4^+ production rate (high emission)	$Q_{i,2}$	$2.18 \cdot 10^{25}\,\mathrm{s}^{-1}$
Total H_2^+ production rate (high emission)	$Q_{i,3}$	$2.18 \cdot 10^{25}\,\mathrm{s}^{-1}$
Total N_2^+ production rate (low emission)	$Q_{i,1}$	$6.54 \cdot 10^{24}\,\mathrm{s}^{-1}$
Total CH_4^+ production rate (low emission)	$Q_{i,2}$	$6.54 \cdot 10^{24}\,\mathrm{s}^{-1}$
Total H_2^+ production rate (low emission)	$Q_{i,3}$	$6.54 \cdot 10^{24}\,\mathrm{s}^{-1}$
Box size	X	$-15R_T \leq X \leq +15R_T$
	Y	$-15R_T \leq Y \leq +15R_T$
	Z	$-15R_T \leq Z \leq +15R_T$
Number of grid cells	(N_X, N_Y, N_Z)	$(100, 100, 100)$
Time step	Δt	$0.48\,\mathrm{s}$
Total number of time steps	$N_{\Delta t}$	20000
Smoothing parameter	α_S	0.165

Table 8.1: Comparison between hybrid modelling and Cassini data: Basic simulation parameters for the T9 flyby.

2.1 Simulation parameters

Considering both the high variability and the uncertainties of the plasma parameters measured during T9, it is quite difficult to determine a definite set of input parameters for the simulation model. In order to infer the influence of different upstream flow conditions on the plasma signatures in Titan's wake region, a complete series of six simulation runs has been carried out. The upstream magnetospheric plasma is assumed to consist of atomic (H^+) and molecular

Run #	Upstream flow speed u_0	Flow angle Ψ	Ion production
#1	120 km/s	0°	high emission
#2	120 km/s	0°	low emission
#3	120 km/s	34°	high emission
#4	60 km/s	34°	high emission
#5	120 km/s	65°	high emission
#6	60 km/s	65°	high emission

Table 8.2: Simulation of Titan's plasma environment during Cassini's T9 flyby. The results of six simulation runs are discussed in the following sections, the basic input parameters differing only in the magnitude and direction of the upstream flow speed as well as in the ionospheric production rates. The angle Ψ is defined with respect to the $(+X)$ axis of the Titan interaction system, i.e. the flow velocity can be expressed as $\underline{u}_0 = u_0\,(\cos\Psi, -\sin\Psi, 0)$. Thus, a positive value of Ψ corresponds to an upstream flow that is directed away from Saturn. In runs #1 and #2, the upstream flow is assumed to be aligned with the $(+X)$ axis of the Titan interaction system, whereas in the other four runs, it clearly deviates from the direction of ideal corotation. In the case of a high emission rate, the total production of each ionospheric species has been set to $Q = 2.18 \cdot 10^{25}\,\mathrm{s}^{-1}$, while in the low emission scenario, it is about a factor of 3 smaller.

Ion species	$r_g(u_0 = 120\,\mathrm{km/s})$	$r_g(u_0 = 60\,\mathrm{km/s})$	t_g
H^+	$0.08R_T$	$0.04R_T$	1.64 s
H_2^+	$0.15R_T$	$0.08R_T$	3.28 s
CH_4^+	$1.22R_T$	$0.61R_T$	26.21 s
N_2^+	$2.14R_T$	$1.07R_T$	45.86 s

Table 8.3: Simulation of Titan's plasma environment during the Cassini T9 flyby – Gyration radii and periods. For all four ion species included in the model, the table gives an overview of the characteristic length and time scales defined by r_g and t_g. The model includes two populations of molecular hydrogen: On the one hand, it is part of the magnetospheric upstream flow; on the other hand, it is a species of ionospheric origin. Although this may not be completely valid for the tail region downstream of Titan, the magnetic field in eqs. (8.2) and (8.3) has been set to the homogeneous background value of $B_0 = 6.37\,\mathrm{nT}$.

hydrogen (H_2^+), which is consistent with the mass spectrometer data collected in the outbound region of T9. While the upstream plasma composition is the same in all runs, some of the input parameters differ in up to three key aspects:

1. *Direction of the impinging magnetospheric flow*:
   In all simulation runs, the ambient flow velocity vector is parallel to Titan's orbital plane. However, the case of $\underline{u}_0$ being aligned with the $(+X)$ axis of the Titan interaction system has been compared to two scenarios in which the plasma is directed away from Saturn. On the one hand, the angle between $\underline{u}_0$ and the direction of ideal corotation has been set to 34°, for this value yielded at least satisfactory agreement between MAG data and the results obtained from the simulation model (cf. section 1.2 of chapter 7). On the other hand, the angle has been set to 65°, following the analysis of the CAPS data in the anti-Saturn-facing hemisphere presented by Crary *et al.* [38].

2. *Velocity of the ambient magnetospheric flow*:
   The case of Titan being exposed to a relatively slow plasma with $u_0 = 60\,\mathrm{km/s}$ has been compared to a scenario in which the flow velocity is given by $u_0 = 120\,\mathrm{km/s}$. The latter value refers to the CAPS data analysis conducted by Crary *et al.* [38], suggesting u_0 in the outbound region to be of the order of $100\,\mathrm{km/s}$.

3. *Ionospheric production rates:*
   In analogy to the simulations presented in the preceding chapter, Titan's ionosphere is modeled by three species of representative masses: molecular hydrogen (H_2^+), methane (CH_4^+) and molecular nitrogen (N_2^+). Again, the case of a weakly emitting obstacle ($Q = 6.54 \cdot 10^{24}\,\mathrm{s}^{-1}$) is compared to a scenario that is based on a three times higher production rate.

In all simulation runs, the densities of the ambient magnetospheric ions are set to $n(H^+) = n_{m,1} = 0.3 \cdot 10^6\,\mathrm{m}^{-3}$ and $n(H_2^+) = n_{m,2} = 0.1 \cdot 10^6\,\mathrm{m}^{-3}$. Although the atomic hydrogen ions make up the major contribution to the number density, the mass density ratio

$$\frac{M(H^+)n_{m,1}}{M(H_2^+)n_{m,2}} = \frac{3}{2} \tag{8.1}$$

is relatively close to 1, making the situation clearly different from the Voyager 1 input parameters used in previous simulations[1]. Even though it is not clear whether this upstream composition is suitable for the situation during T9, studying the influence of the composition on the tail structure is interesting anyway. Especially, the effects that arise from the lack of a heavy magnetospheric ion species have to be discussed. The thermal velocity of the magnetospheric particles is again set to $v_{th} = 180\,\mathrm{km/s}$, thus exceeding the average upstream flow speed by a factor of 1.5 or 3, respectively. The ambient magnetic field is again given by $\underline{B}_0 = (3.73, 4.70, -2.15)$ nT, which can be considered an adequate approximation to the homogeneous regions in the signatures obtained from the MAG instrument. These input parameters yield an ambient magnetospheric plasma which is clearly sub-alfvénic, subsonic and submagnetosonic. If a value of $u_0 = 120\,\mathrm{km/s}$ is used for the flow speed, the alfvénic and magnetosonic Mach numbers are given by $M_A = 0.61$ and $M_{MS} = 0.49$, respectively. In the case of a slow magnetospheric flow, these values have to be reduced by a factor of 2. In combination with the small particle masses, these Mach numbers also define a lower limit for the applicability of the simulation model: The smaller are the Mach numbers of the ambient flow, the more susceptible is the simulation to numerical instabilities. This must also be ascribed to the small particle masses, as both upstream species are strongly affected by even slight noise in the electromagnetic fields. Thus, in order to prevent the stability of the simulation from being compromised, relatively high values for the smoothing parameter α_S have to be chosen in the low Mach number regime. In some parts of the T9 trajectory, densities below $n_m = 0.04\,\mathrm{cm}^{-3}$ have been detected. However, a further reduction of the ambient plasma density to match these values cannot be realized. Another reduction of the ambient mass density would go along with a further increase of the Alfvén velocity. In the regime of extremely small Mach numbers that would result from maintaining the ambient magnetospheric flow speed, the simulation results would definitely be affected by the measures required to

---

[1] The particle mass is denoted by the capital letter M, whereas the subscript m refers to the magnetospheric ion components in general.

guarantee the numerical stability. This is not an intrinsic problem of the code used for the present study, but any (semi)kinetic approach will face the same restrictions.

For the case of an ideally corotating, fast magnetospheric plasma flow, the major simulation parameters are summarized in table 8.1. By varying the input parameters according to points (1.)-(3.) listed above, a total number of twelve different simulation scenarios can be realized. Six runs whose results have shown to be representative will be discussed in the following sections. An overview of the specific input parameters is given in table 8.2. In order to be able to verify Szegö's [144] interpretation of the split signature's first part (interval 1), the time step has been set to a value which is about two orders of magnitude smaller than the heavy ion gyration periods. An overview of the gyroradii

$$r_g = \frac{Mu_0}{eB} \tag{8.2}$$

as well as the gyration periods

$$t_g = \frac{M}{eB} \tag{8.3}$$

of all species included in the model is given in table 8.3. It is interesting to notice that in contrast to the Voyager 1 scenario, the gyroradii of all magnetospheric species are significantly smaller than the radius of Titan. Besides, as can be seen from table 8.1, the plasma betas of both magnetospheric species are clearly smaller than 1. Thus, in contrast to the Voyager 1 scenario, the characteristics of the upstream flow are not controlled by its thermal, but by its magnetic pressure.

2.2 Simulation results I: Cassini MAG data revisited

This section deals with the analysis of the magnetic field data collected along the Cassini trajectory. Especially, the discussion will address the question of how the magnetic field signature is modified when the "average" magnetospheric plasma composition used in earlier T9 simulations (cf. section 1.2 of chapter 7) is replaced by more specific parameters obtained from the Cassini plasma spectrometer. The simulation results for all six simulation runs are shown in figs. 8.2 and 8.3, respectively. The panels on the left-hand side of fig. 8.2 display the results for the scenarios assuming the upstream flow speed to be $u_0 = 120\,\mathrm{km/s}$. For the case of an ideally corotating plasma, the results for a high ion production rate (green line) are again compared to a situation in which the production rate is about a factor of 3 smaller (red line). The results of the 34° and 65° runs are represented by the magenta and grey lines, respectively. In order to infer the influence of the magnetospheric flow speed on the magnetic field topology, both the 34° and the 65° run have also been carried out with a reduced speed of $u_0 = 60\,\mathrm{km/s}$. The results of these simulations are shown in fig. 8.3; the magnetic field signatures are presented in the same color coding as in fig. 8.2. However, the following discussion will mainly focus on the runs that use a value of $u_0 = 120\,\mathrm{km/s}$ for the upstream flow speed.

The simulation results presented in the preceding chapters have indicated that for Voyager-like upstream conditions, the structure of Titan's magnetic lobes is mainly controlled by the ambient plasma velocity, whereas moderate changes in the ionospheric production rates lead only to minor modifications of the magnetic field topology. As can be seen from fig. 8.2, this

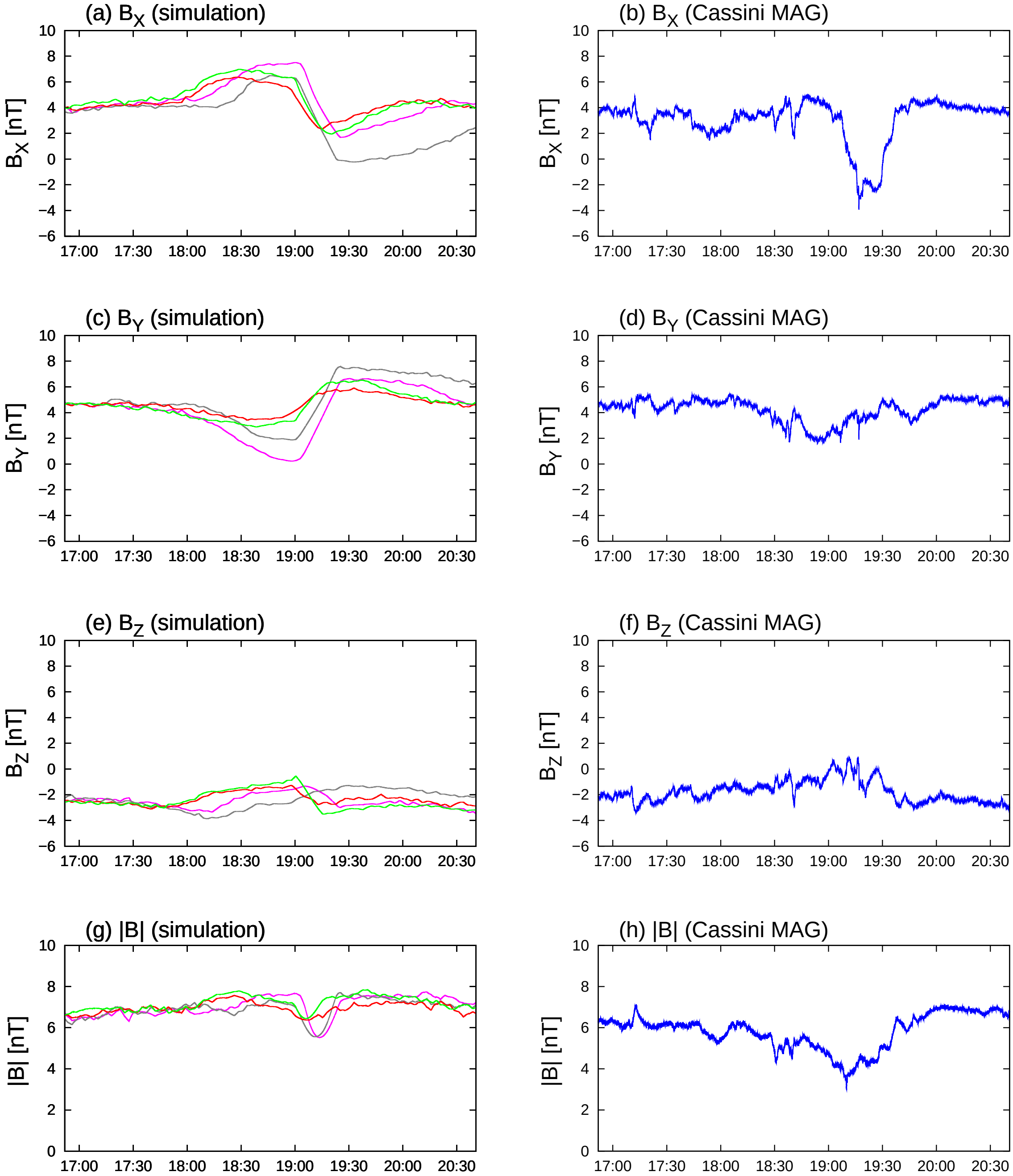

Figure 8.2: Titan's magnetic field signature during Cassini's T9 flyby. The plots in the left-hand column display the simulation results for the scenarios which assume Titan to be exposed to a magnetospheric plasma with $u_0 = 120\,\mathrm{km/s}$: run #1 (green), run #2 (red), run #3 (magenta) and run #5 (grey). An increase of the angle between the direction of corotation and the ambient flow velocity $\underline{u}_0$ from 34° to 65° goes along with a reduction of the field strength in the anti-Saturn-facing lobe, as denoted by the minimum of the B_X component around 19:30 UT. However, in contrast to the simulations using Voyager-like upstream conditions, the steep outbound flank of the B_X notch is reproduced by none of the scenarios under consideration. For the B_Y component, the assumption of an ideally corotating flow yields best agreement between modelling and measurements, whereas the nearly homogeneous structure of the measured B_Z component manifests in the results of all four simulation runs.
Simulation parameters: see tables 8.1 and 8.2.

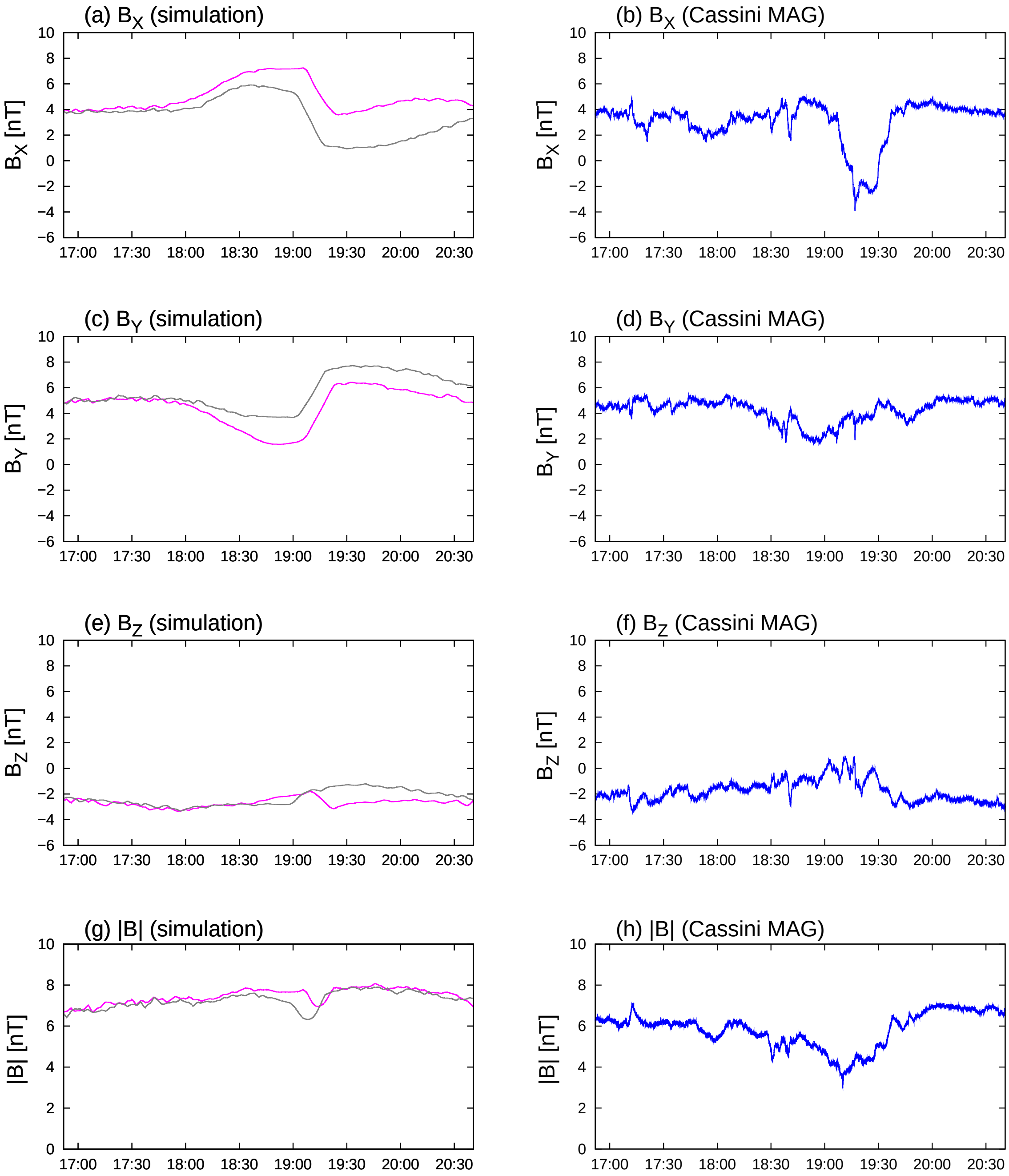

Figure 8.3: Simulation results for Titan's magnetic field signature during T9. The simulation results of runs #4 and #6 are shown in the plots on the left-hand side. In both simulations, the magnetospheric flow velocity is set to a value of $u_0 = 60\,\mathrm{km/s}$. However, in run #4 (magenta line), the vector $\underline{u}_0$ forms an angle of 34° with the direction of ideal corotation, whereas an angle of 65° has been chosen in run #6 (grey line). Compared to the 34° (magenta line) and 65° (grey line) scenarios presented in fig. 8.2, the distortions of the B_X and B_Y components are clearly reduced. According to the simulation model, an upstream velocity of about 100 km/s is required to achieve at least reasonable agreement between simulation and measurements.
Simulation parameters: see tables 8.1 and 8.2.

is valid for the modified upstream conditions as well. The magnetic signatures obtained from simulation scenarios #1 and #2 show that the field along the Cassini trajectory is again only slightly affected by a drastic reduction of the ionospheric production rate. The decrease of the ion production rate goes along with a minor reduction of the peak and dip magnitudes, the differences between both cases ranging below 1 nT in all three components. Besides, the peak positions of the magnetic field enhancements and break-ins remain practically unaffected.

As can be seen from figs. 8.2(a) and 8.3(a), the key features developed by the B_X component exhibit at least a strong qualitative resemblance to the results presented in section 1.2 of chapter 7. In all six simulation runs, the B_X component features a region of enhanced field strength, followed by a more or less sharply pronounced break-in, the position of the latter signature corresponding reasonably good to that of the dip detected by Cassini. As can be seen from the positions of the overshoot in fig. 8.2(a), the magnetic lobes are turned away from Saturn when the angle between $\underline{u}_0$ and the direction of ideal corotation is increased. In the case of an ideally corotating flow, the simulations show the formation of a relatively broad Saturn-facing lobe, denoted by a plateau-like magnetic field enhancement from 4 nT to a value of about $6 \ldots 7\,\mathrm{nT}$ between 18:00 UT and 19:00 UT. The larger is the angle between the flow speed and the direction of ideal corotation, the smaller becomes the diameter of the Saturn-facing lobe, while the magnitude of the break-in in the anti-Saturn-facing lobe is increased. In complete correspondence to the T9 simulations presented in chapter 7, the simulations always indicate the formation of two distinct lobes in the (X, Y) plane. Nevertheless, in the 34° simulation, the structure of the B_X lobes is no longer highly symmetric. Besides, in the results for an ideally corotating flow, the Saturn-facing lobe has become the more prominent one.

However, as can also be seen from fig. 8.2(a), in none of the four simulation runs, the formation of the anti-Saturn-facing lobe gives rise to a reversal of the B_X direction. The field perturbations in the B_X component are clearly exceeded by the magnitude of the distortions that occur when the upstream flow consists of hydrogen and a heavy nitrogen component (cf. figs. 7.4(a) and 7.5(a)). Even though the position of the B_X notch is reproduced by a simulation scenario using Voyager-like upstream conditions as well as by an approach based on the specific CAPS data for T9, the inclusion of an upstream flow that consists only of light ion species has shown to be inadequate for reproducing the sharply pronounced break-in of B_X detected by Cassini. Both the magnitude of the dip and the steepness of its outbound flank are underestimated when the heavy magnetospheric plasma component is completely absent. The simulations suggest that a magnetospheric plasma which predominantly consists of heavy ions is required in order for a strong and narrowly confined B_X break-in to be formed. Furthermore, a decisive role must be ascribed to both the mass density and the particle mass of the heavy magnetospheric plasma constituent. Increasing the relative number density of the H_2^+ ions in the scenarios presented in tables 8.1 and 8.2 has proven insufficient for improving the agreement between the simulated B_X dip structure and the signature detected by Cassini. A comparison between the multi-species approach presented in chapter 6 and the simplifying single-species approximation (cf. chapter 4) has shown that in the vicinity of Titan, light and heavy magnetospheric ion components exhibit a significantly different flow pattern: On the one hand, the flow direction of the heavy magnetospheric species is only slightly affected by the presence of Titan, thus allowing the magnetic field lines to form a strong draping pattern. This yields two narrowly confined magnetic lobes. On the other hand, adding a lighter species to the magnetospheric flow gives rise to a widening of the magnetic field pattern, due to the light particles being clearly deflected around the central wake region. Therefore, using the upstream plasma composition derived from the CAPS data yields a weaker pronounced notch in the B_X component than the inclusion of a plasma that mainly consists of heavy N^+ ions.

Any global numerical approach approximates the initial magnetospheric plasma conditions in the vicinity of Titan by a homogeneous magnetospheric plasma composition and a spatially constant magnetospheric flow speed. Especially the second assumption may not be valid for the situation during T9, since based on the limited information about the plasma velocity, Crary *et al.* [38] could not infer whether the flow in the inbound region was directed away from Saturn as well. However, in the six scenarios under investigation, choosing an upstream flow velocity of $u_0 = 120\,\mathrm{km/s}$ and a value of $\Psi = 65^\circ$ yielded best possible agreement with the B_X notch detected by Cassini. Especially, the break-in obtained from this scenario clearly exceeds the magnitude of the dip in the other cases shown in figs. 8.2(a) and 8.3(a). To sum up the major result for the B_X component, a simulation that is based on the upstream flow composition and direction suggested by CAPS data does not yield optimum quantitative agreement between simulation and MAG measurements, but the magnetic field signature obtained from run #5 definitely exhibits the same tendencies as the measured signature.

As shown in fig. 8.2(c), a reasonably good reproduction of the quite homogeneous B_Y structure is again only achieved when the upstream flow is aligned with the direction of ideal corotation. In both the 34° and the 65° scenario, the B_Y component exhibits a sharp step around 19:00 UT. This structure clearly exceeds the magnitude of the slightly pronounced dip detected by the MAG instrument. Since in the case of a non-corotating flow, the T9 hybrid simulations recently presented by Sillanpää *et al.* [136] also show the formation of strong distortions in the B_Y component, it must be assumed that the B_Y signature detected by Cassini cannot be explained by using the assumption of a homogeneous background magnetic field.

Although there are minor differences in the location and magnitude of the peaks, the results of all four simulation runs presented in fig. 8.2(e) show a relatively homogeneous B_Z component, the field values ranging from $B_Z = -4\,\mathrm{nT}$ to $B_Z = -1\,\mathrm{nT}$. Concerning the B_Z component, all four simulation runs shown in fig. 8.2 are in reasonably good agreement with the data collected by Cassini.

Finally, the magnetic field signatures for a slow magnetospheric plasma shall be briefly discussed (cf. fig. 8.3). As suggested in the preceding chapters, a reduction of the ambient magnetospheric flow speed yields a widening of the lobe structure as well as a reduction of the maximum magnetic field value achieved in the wake region. This tendency clearly manifests in the results of the 65° scenarios (runs #5 and #6). In the case of a fast magnetospheric plasma, the B_X component decreases to values of about $B_X = 0\,\mathrm{nT}$, whereas in the run using $u_0 = 60\,\mathrm{km/s}$, the minimum value is about $1.5\,\mathrm{nT}$ larger. The diameter of the Saturn-facing lobe has also increased by a factor of 1.5. Thus, reducing the magnetospheric flow speed further increases the discrepancy between numerical modelling and MAG measurements. On the other hand, choosing a value well above $u_0 = 120\,\mathrm{km/s}$ would increase both the magnitude of the notch in the B_X component and the steepness of its outbound flank. However, several test runs have shown that if the magnetospheric densities and the magnetic field are set to the values given in table 8.1, an unrealistically high value of $u_0 > 200\,\mathrm{km/s}$ would be required for achieving significantly better agreement between model results and MAG data.

2.3 Simulation results II: Comparison with CAPS data

This section deals with an analysis of the magnetospheric and ionospheric plasma parameters obtained from the simulation model. Since in the 34° and the 65° simulations, the structures developed in the interaction region bear at least a strong qualitative resemblance, the discussion will focus on the latter scenario. Besides, as the comparison between numerical results and MAG data presented in the preceding section suggests a value of $u_0 \approx 120\,\mathrm{km/s}$ to be more suitable for the situation during T9 than $u_0 \approx 60\,\mathrm{km/s}$, only the case of a fast magnetospheric plasma will be considered in the following. In fact, the comparison between simulation and MAG data indicated that if the upstream flow composition is known, the sharpness and magnitude of the magnetic field distortions in the vicinity of Titan provide at least a rough measure of the ambient magnetospheric flow speed. The more pronounced are these signatures, the larger is the value of the plasma velocity. The simulation results for the plane including both the center of the satellite and the Cassini trajectory are shown in figs. 8.4 and 8.5, respectively. Due to lack of data, the signatures developed in Titan's polar

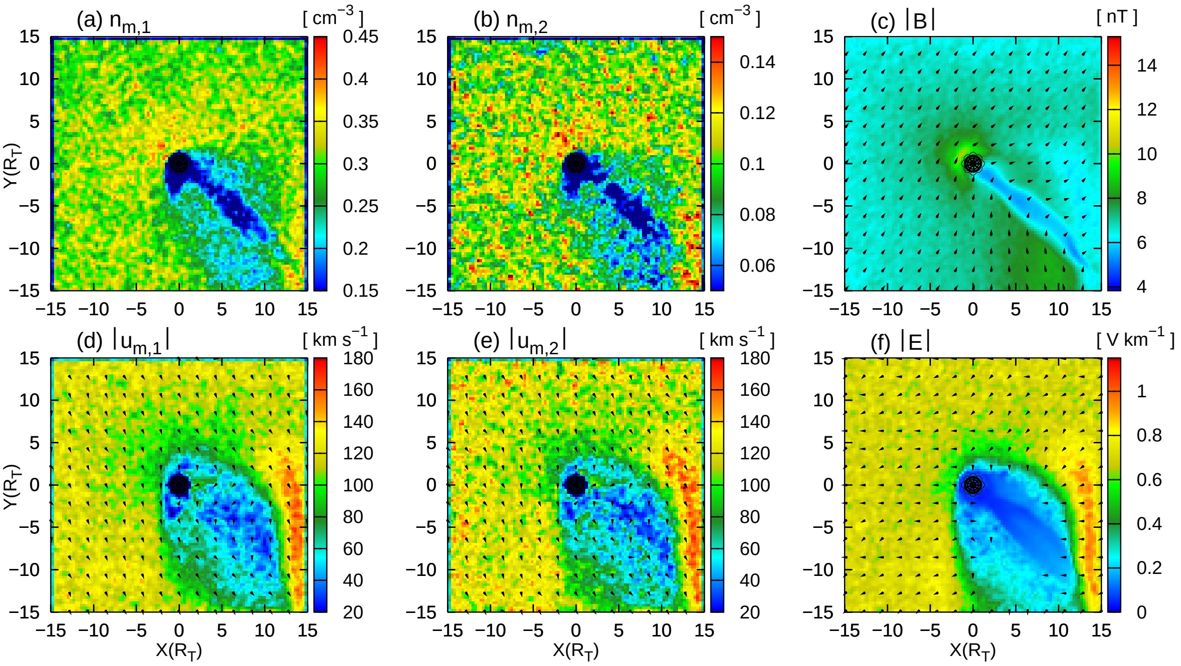

Figure 8.4: Titan's plasma environment during Cassini's T9 flyby − Magnetospheric plasma parameters and electromagnetic fields in Titan's orbital plane (results of run #5). The figure displays the magnetospheric H^+ density and velocity in plots (a) and (d), the magnetospheric H_2^+ density and velocity in plots (b) and (e) as well as the electromagnetic fields in plots (c) and (f). The ambient magnetospheric plasma velocity is assumed to form an angle of 65° with the X axis, i.e. it is oriented away from Saturn. Both magnetospheric species experience a strong deceleration downstream of the satellite, their velocity being reduced by more than a factor of 2. This effect gives rise to a cavity in which the electric field strength almost vanishes. In contrast to simulations that assume the upstream flow to include heavy N^+ ions as well, the size of this cavity clearly exceeds the diameter of the region where cold ionospheric particles can be found.

Simulation parameters: see tables 8.1 and 8.2.

plane are only of minor relevance and are therefore omitted from the discussion.

A two-dimensional illustration of the magnetospheric plasma parameters in the (X, Y) plane of the Titan interaction system is displayed in fig. 8.4, the subscripts $m,1$ and $m,2$ referring to the magnetospheric H^+ and H_2^+ components, respectively. The ionospheric plasma densities and velocities are displayed in fig. 8.5. Again, the magnetospheric nitrogen (N_2^+) component is denoted by the subscript $i,1$, while methane (CH_4^+) and molecular hydrogen (H_2^+) are referred to as species $i,2$ and $i,3$, respectively. The ambient magnetospheric plasma flow forms an angle of 25° with the negative Y axis of the Titan interaction system. The ambient magnetic field points in the $(X > 0, Y > 0, Z < 0)$ sector of the coordinate system.

As can be seen from figs. 8.4(d) and (e), in the downstream region, both magnetospheric plasma components experience a strong deceleration, as it has also been observed by the CAPS instrument [38]. In the wake region, the magnetospheric flow speed is about more than

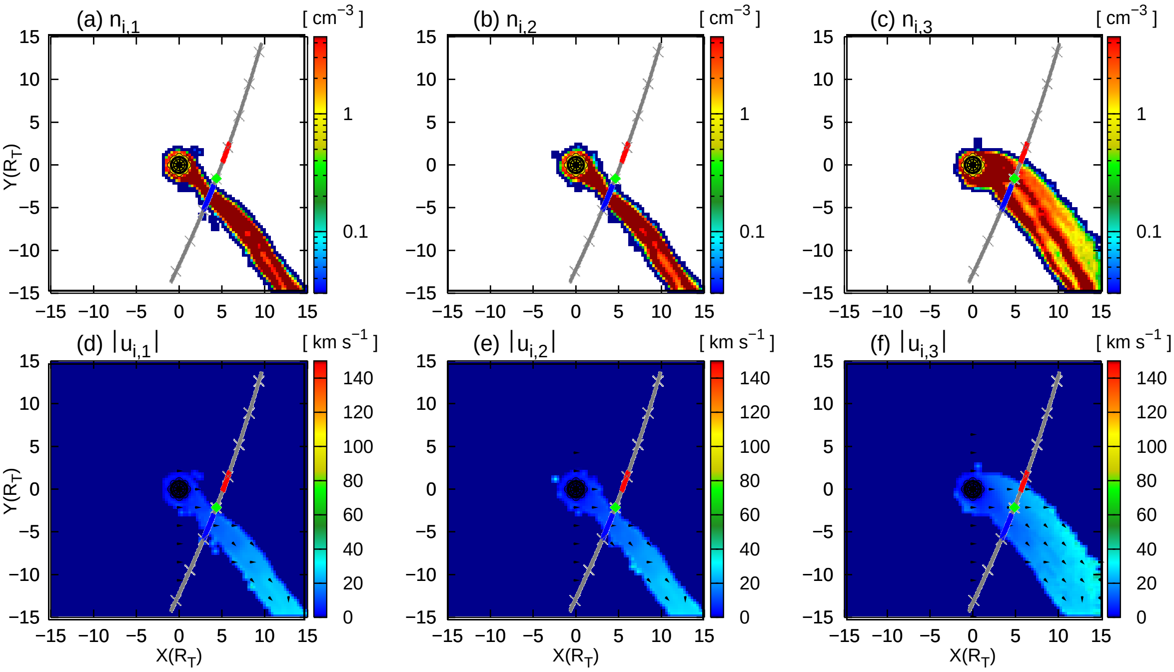

Figure 8.5: Titan's plasma environment during Cassini's T9 flyby – Ionospheric plasma parameters in Titan's equatorial plane and Cassini's flyby trajectory (results of run #5). The figure displays the density of (a) molecular nitrogen, (b) methane and (c) molecular hydrogen. The corresponding velocities are shown in plots (d) to (f). Again, the characteristic segments detected by the Cassini Plasma Spectrometer are denoted by a red (interval 1) and a blue bar (interval 2). The position of Cassini's closest approach at 18:59 UT is marked by a green diamond. In correspondence to the CAPS data, particles of ionospheric origin are confined to the region between the inbound point of interval 1 and the outbound point of interval 2. However, the sub-structure observed in this interval is not reproduced by the simulation model. The hybrid approach suggests the major concentrations of all three ionospheric species to be located in interval 2, whereas a significant number of heavy ions was measured only in interval 1. Nevertheless, the observation that no heavy ions were located between the two segments is confirmed by the simulation model.
Simulation parameters: see tables 8.1 and 8.2.

a factor of 2.5 smaller than the upstream value. In the simulations that assume the ambient plasma to consist of one light and one heavy constituent (cf. chapters 4 to 7), only the light hydrogen (H^+) ions experienced such a strong deceleration, whereas the heavy nitrogen ions seemed to be able to pass through the central tail region without strong modifications in their flow pattern. As displayed in fig. 8.4(f), the strong deceleration of both magnetospheric plasma components gives rise to an electric field cavity downstream of Titan whose diameter clearly exceeds that of the region populated by slow ionospheric particles. In all simulation runs that included the heavy nitrogen ions as well, the extension and shape of the electric field cavity were mainly determined by the diameter of the pick-up tail. The reduction of the magnetospheric hydrogen velocity downstream of Titan yielded only a slight influence on the electric field strength, because simultaneously, the predominant nitrogen component experienced only a moderate deceleration.

As can be seen from fig. 8.4(f), in Titan's wake region, the electric field strength is reduced by more than a factor of three compared to the background value of $E_c = 0.7\,\mathrm{V\,km^{-1}}$. Of course, this also takes noticeable influence on the $\underline{E} \times \underline{B}$ pick-up acceleration of the newly generated ionospheric ions. Even though a direct quantitative comparison between different geometries is of course impossible, it is interesting to notice that in the 34° simulation of T9 presented in chapter 7, the pick-up ions achieved a characteristic velocity of about $80-90\,\mathrm{km/s}$ (cf. figs. 7.9(d)-(f)). In contrast to this, a velocity of only about $20 - 30\,\mathrm{km/s}$ can be obtained from fig. 8.5. Since in both simulation runs, identical values have been chosen for the upstream flow speed as well as for the ionospheric production rates, the strong difference in the ionospheric ion velocities can definitely be ascribed to the modification of the upstream plasma composition[2]. Due to the reduced strength of the pick-up force, the efficiency of the ion transport away from Titan is smaller than in the case of Voyager-like upstream conditions. Consequentially, the ionospheric tail densities obtained from the H^+/H_2^+ scenario (cf. fig. 8.5) are about one order of magnitude larger than in the Voyager-like situation displayed in figs. 7.9(a)-(c). Hence, if the ambient magnetospheric plasma does not include a heavy constituent, but it is made up only of light species, the pick-up of newly generated ionospheric particles is strongly suppressed by the deceleration of the magnetospheric species in the downstream region.

Before proceeding with the analysis of the ionospheric tail, a comment on the rather strange structure on the right-hand side of figs. 8.4(d), (e) and (f) seems appropriate. The acceleration of the magnetospheric plasma near the $X = +15R_T$ face of the simulation box is a numerical artifact that arises from the application of inflow boundary conditions to this face of the simulation domain. In this region, the expansion of the wake cavity perpendicular to the flow direction is interrupted by the presence of the wall, i.e. the plasma flow is significantly distorted by the outer face of the simulation domain.

In order to allow a direct comparison between CAPS observations and the simulated tail structure, the characteristic intervals along the Cassini trajectory are overplotted in fig. 8.5. Again, the red bar denotes interval 1 in which cold heavy ions were detected. In interval 2, cold ions of masses 1 amu and 2 amu made up the major part of the plasma population. On the one hand, the simulation model shows that each of the three tails intersects Cassini's

---

[2] Of course, a direct quantitative comparison to the results shown in fig. 7.9 can only be performed by using the results of the 34° simulation run #3. However, this figure is not shown here, as it includes exactly the same physical effects that can be derived from fig. 8.5.

trajectory between the inbound edge of interval 1 and the outbound edge of interval 2. On the other hand, the sub-structure observed between these points by the CAPS instrument does not occur in the simulation results. In any case, it is stunning to see that the intersection line between the spacecraft trajectory and the nitrogen (N_2^+) and methane (CH_4^+) tails is almost identical to the region denoted as interval 2. As can be seen from figs. 8.5(c) and (f), the tail developed by the light molecular hydrogen ions is a little broader than the other ones, but major concentrations of H_2^+ ions can be found in interval 2 as well. Figure 8.5(c) illustrates that the hydrogen tail exhibits some kind of internal ray structure, with one ray intersecting the Cassini trajectory in interval 2 and the other one being located in between the two intervals where, according to Crary *et al.* [38], no heavy ions were detected. At least the complete lack of heavy ionospheric species between the two intervals is well confirmed by the simulation model.

According to the numerical model, interval 2 is the region where major concentrations of ionospheric particles should have been located, if the ambient plasma conditions had been homogeneous. This aspect is consistent with foregoing simulation results, since interval 2 is located in the neutral region between the two magnetic lobes that form a confinement along the ionospheric tail's flanks. The confined structure of the ionospheric tail is in complete qualitative agreement with the T9 results presented in the preceding chapter (cf. fig. 7.9). As can be seen from fig. 8.4(c), the magnetotail is asymmetric in such way that the Saturn-facing lobe is narrower and features a weaker field enhancement than the anti-Saturn-facing one. This might make it easier for the ionospheric particles to escape from the confinement into the Saturn-facing hemisphere. The Cassini MAG data even indicate a complete lack of the Saturn-facing lobe, so that the ionospheric tail might have been confined only at its anti-Saturn-facing flank. However, the question of why only the light species have been detected in interval 2, but the heavier ones were found only in the first interval, is not resolved by the simulation model. Since an analogous split signature has not been observed during any other Cassini flyby and the complete lack of a Saturn-facing magnetic lobe in the MAG data has also shown to be inconsistent with the modelling approach, these discrepancies can most likely be ascribed to extremely inhomogeneous ambient magnetospheric plasma conditions. The limited information available for T9, especially the uncertainties of the magnetospheric flow speed and direction in the inbound region, do not allow to chose a more sophisticated set of input parameters.

To give a review of the situation, the questions that remain unresolved by data interpretation as well as by the modelling approach will be summarized in the following:

- The simulation model suggests that during T9, major concentrations of all ionospheric species should have been detected in interval 2. Although the tail developed by the light ionospheric H_2^+ ions is a little broader than the nitrogen and methane tails, this observation should have been more or less independent of the particle mass. Interval 2 represents the location of the tail for homogeneous ambient conditions. What kind of mechanism could shift the heavy N_2^+ and CH_4^+ tails in the region of interval 1, while retaining the position of the light H_2^+ tail at the same time?
- To what degree is the assumption of homogeneous ambient plasma conditions valid for the T9 scenario? When using an upstream flow that consists of atomic and molecular hydrogen, best agreement between simulation results and MAG data was achieved by

turning the vector $\underline{u}_0$ away from the direction of ideal corotation in an angle of about 65°. This value corresponds to the CAPS observations in the outbound region of the T9 flyby. However, both data analysis and numerical studies of the situation during other Cassini flybys (see for instance Ma *et al.* [99], Neubauer *et al.* [118, 119] and chapter 7 of this work) suggest that such a strong deviation from ideal corotation is not typical of the situation near Titan's orbit.

- Was the heavy component of the upstream flow really absent during the T9 flyby? At least the simulation model suggests that the heavy N^+ ions are required in order to generate a strong notch in the B_X component, as it has been detected by the MAG instrument. When the N^+ component is included in the upstream flow, agreement between simulation and MAG data is significantly better than in the case of a plasma that consists only of hydrogen ions.

Further work will be required in order to clarify the origin of the plasma signatures observed during T9.

3 Summary

During Cassini's T9 flyby of Titan, the spacecraft passed through the wake region in the equatorial plane. Titan was located at about 03:00 clock angle position on its orbit around Saturn. Although the overall picture obtained from the CAPS data suggest that the ambient magnetospheric flow velocity was not aligned with the direction of ideal corotation, the measurements do not allow to determine definite values for the orientation or the magnitude of the magnetospheric flow speed. Because along Cassini's inbound pass, the incoming plasma was not in the instrument's field of view, the error bars for defining a global upstream flow speed can definitely not be neglected. The ion data collected during T9 reveal the presence of three regions with significantly different plasma parameters along the spacecraft trajectory, which are referred to as a *split signature* by Coates *et al.* [35] as well as Crary *et al.* [38]. Both the inbound and the outbound edge of Titan's wake contained cold ions, their energy ranging below 100 eV. The CAPS instrument detected cold heavy ions of masses $16-19$ amu and about 30 amu at the Saturn-facing edge of the wake, whereas the anti-Saturn-facing edge was populated by ions of mass 2 amu and some protons. However, no heavy ions were detected at the anti-Saturn-facing edge of the wake. According to the CAPS measurements, the center of the wake, i.e. the region in between these two segments of cold plasma, was mainly populated by protons with energy values of about 1 keV and relatively few ions of mass 2 amu, but no heavy ions could be found in the central tail region either.

Based on the available information, a modified simulation scenario has been designed for T9, assuming the upstream plasma to consist only of the light species H^+ and H_2^+. On the one hand, this geometry allowed to study the influence of the upstream plasma composition on the pick-up process. The relatively strong deceleration of the magnetospheric plasma in the wake region gives rise to an electric field cavity whose diameter clearly exceeds that of the rather narrow ionospheric tails. Therefore, the ionospheric ion velocities achieved in the tail have shown to be about a factor of 3 smaller than in an analogous scenario that uses a Voyager-like upstream plasma composition.

On the other hand, the simulation results have been compared to data from the MAG and CAPS instruments. As for the magnetic field data, agreement between simulation and measurements is by far not as good as in the case of Voyager-like upstream conditions. Especially the distortions in the B_X component are clearly underestimated by the model, if the upstream flow does not include a heavy N^+ component. Probably, during the T9 flyby, Titan was exposed to extremely inhomogeneous plasma conditions, making a reproduction of the measured data difficult. However, if the angle between the upstream velocity $\underline{u}_0$ and the direction of ideal corotation is set to a value of $\Psi = 65^\circ$, the simulated magnetic field signature features at least the same tendencies as the distortions in the measured magnetic field components.

In agreement with CAPS data, the simulation model shows that the ionospheric tail intersects the Cassini trajectory in a narrowly confined segment. The sub-structure observed in this segment could not be reproduced by the simulation model. Nonetheless, the simulation results may be considered of some value for the interpretation of the CAPS data, for they illustrate the situation in the case of homogeneous upstream conditions. The simulations suggest that if the upstream conditions had been homogeneous, the ionospheric tail should have been confined by a magnetic lobe at either side. The confining effect of the Saturn-facing lobe has possibly been weakened by disturbed upstream conditions that prevented the formation of a stable magnetotail structure. The analysis of the distortions that were superimposed on the homogeneous upstream situation during T9 has not yet been completed.

Chapter 9

Shock formation in a multi-ion plasma flow

In the preceding chapters, Titan's plasma interaction has been analyzed in the framework of a multi-species hybrid model. The simulations have revealed that the structure of Titan's induced wake can only be completely understood by considering the multi-component nature of the plasma. On the one hand, the efficiency of the ionospheric pick-up process has shown to be highly susceptible to the composition of the impinging magnetospheric plasma. The smaller is the average magnetospheric mass density, the more prominent is the electric field cavity evolving downstream of Titan and hence, the weaker is the pick-up force that transports the newly generated ionospheric particles away from the satellite. The different flow patterns of light and heavy magnetospheric species also leave an imprint on the structure of the satellite's magnetic pile-up region. On the other hand, the tail structures developed by different ionospheric species cannot be understood independently of each other, but the heaviest pick-up species exerts a strong control on the dynamics of the lighter ones. All these phenomena have been studied for the case of Titan being located inside Saturn's magnetosphere, i.e. because of the *sub*magnetosonic nature of the impinging plasma, no bow shock evolves in front of the obstacle. The purpose of this chapter is to give at least a brief overview of the basic effects that occur when a planetary obstacle is exposed to a *super*magnetosonic multi-ion plasma flow.

Motschmann [109] as well as Motschmann and Raeder [111] have analyzed the key features of shocks in a multi-component plasma by means of analytical calculations and one-dimensional hybrid simulations. Specifically, these works focus on the case of test particles (mass m_2) being admixed to a supermagnetosonic plasma (particle mass m_1) that is decelerated in a shock front. The test particle mass is assumed to be significantly different from the mass of the primary ion component. Motschmann [109] demonstrates that in the one-dimensional hybrid scenario, the predominant species is only capable of dictating the dynamics of the test particles, if $m_1 \gg m_2$. Otherwise, the test particles are capable of crossing the shock potential defined by the first species without experiencing a noticeable deceleration. Motschmann [109] as well as Motschmann *et al.* [112] also show that the single-fluid Rankine-Hugoniot conditions cannot be generalized to the physics of multi-ion flows without incorporating additional specializations: An increase of the number of particle species in the plasma flow goes along with the inclusion of additional free parameters into the model, since the conservation laws for momentum and energy can only be formulated globally for the entire multi-ion system, but not for each single species.

To the author's knowledge, the only three-dimensional hybrid model that considers the multi-component nature of the supermagnetosonic plasma flow interacting with a planetary obstacle is the approach described by Modolo *et al.* [107, 108]. For an analysis of the Martian interaction with the solar wind, the authors consider both the hydrogen and the helium component of the impinging superfast plasma. However, due to the rather bad statistical representation of the helium component, the model provides only a rough description of the dynamics of the light species. A systematic discussion of multi-ion shocks in the framework of the three-dimensional hybrid model has so far not been carried out by any simulation group.

For this reason, this final chapter deals with an application of the multi-ion model presented in chapter 6 to the physics of multi-ion shocks. In analogy to the study presented by Motschmann [109], the analysis will focus on a plasma flow that consists of a primary species of mass m_1 and test particles of mass m_2, the number density n_2 of the test particles being exceeded by the density n_1 of the primary species by a factor of 1000. Three different situations will be discussed: On the one hand, the case of nearly equal masses ($m_1 \approx m_2$) is compared to the case of heavy test particles being admixed to a light primary species ($m_2 \gg m_1$). On the other hand, the shock formation will be investigated for a plasma flow that consists of nitrogen ions and a significantly lighter test particle species ($m_2 \ll m_1$). An overview of the three simulation scenarios is given in table 9.1. Since the discussion will focus on discriminating between the qualitative differences in the simulation results, the model parameters have not been applied to any specific real situation. The scenario of test particles being admixed to a light primary species is based on the Titan scenario described in chapter 8, in which light hydrogen ions were assumed to make up the major contribution of the impinging plasma flow. The Voyager-like Titan situation where nitrogen ions are the major constituent of the impinging plasma has been used to generate a geometry in which a shock is formed in a flow that is dominated by heavy ions.

In analogy to simulations of the Martian interaction with the solar wind or to the case of Titan being located outside Saturn's magnetosphere, the shock formation is enforced by placing an ionospheric obstacle in the way of the flow. For simplicity, the obstacle is provided by a sphere of radius $R = R_T = 2575\,\mathrm{km}$ with a Titan-like ionosphere profile. The dayside of the obstacle is exposed to the impinging plasma flow. Since the deceleration in the shock wave yields a submagnetosonic flow in the downstream region, the effects of the ambient plasma on the obstacle's ionospheric tail structure are likely to exhibit a strong resemblance to the Titan scenarios discussed in the preceding chapters. Therefore, the discussion will focus only on the signatures evolving in the impinging multi-component flow. In order to prevent the interpretation of the simulation results from being complicated by the high temperature of the particles, a thermal speed of only $v_{th} = 25\,\mathrm{km/s}$ has been chosen for all upstream species. The electrons are assumed to be cold. Since the results are not affected by the "smearing" that arises from the high thermal velocity of the magnetospheric plasma near Titan, the simulations have also shown to provide some additional insights into the interaction between Titan and a subfast plasma. Even though the following sections provide only a general overview of the effects that can occur in such a multi-component flow, a specialization of the simulation geometry – e.g. for an analysis of the interaction between Mars or comets with the solar wind – requires only minor modifications of the existing model.

In the following sections, the subscript 1 always refers to the predominant ion component, while the test particle species is denoted by the subscript 2. The simulations are based on the "classical" Titan geometry, with the upstream plasma velocity being aligned with the positive x axis and the undisturbed magnetic field of magnitude $B_0 = 5\,\mathrm{nT}$ pointing in $(-z)$ direction. Hence, the convective electric field $\underline{E}_0$ is oriented parallel to the $(-y)$ axis. In analogy to the

Simulation run	m_2/m_1	$n_2/n_1 = \rho_{c,2}/\rho_{c,1}$	$\rho_{m,2}/\rho_{m,1}$
#1	2	1/1000	1/500
#2	20	1/1000	1/50
#3	1/14	1/1000	1/14000

Table 9.1: Simulation of shock formation in a multi-ion plasma flow. In the simulations, test particles of mass m_2 have been admixed to a superfast plasma that consists of particles of mass m_1. The number density of the test particles is assumed to be about a factor of 1000 smaller than that of the primary constituent. Three different situations have been investigated: At first, the case of m_1 and m_2 being of the same order of magnitude (run #1) has been compared to a scenario where the test particles are about a factor of 20 heavier than the primary component (run #2). Besides, the analysis focuses on a geometry in which test particles of mass $m_2 = 1\,\mathrm{amu}$ have been incorporated into an atomic nitrogen flow (run #3). The table gives an overview of the number density ratios n_2/n_1 as well as the mass density ratios $\rho_{m,2}/\rho_{m,1}$ for these geometries. Since all particles occurring in the model are assumed to be single-charged, the charge density ratio $\rho_{c,2}/\rho_{c,1}$ equals the ratio between the number densities.

discussion in previous chapters, the (x, y) plane that contains $\underline{u}_0$ and the undisturbed electric field will be referred to as the equatorial plane, whereas the (x, z) plane, including $\underline{u}_0$ and $\underline{B}_0$, is called the polar plane. In all scenarios under consideration, the mean upstream velocities of both species are set to equal values.

1 Major and minor component of nearly identical mass

The first scenario under consideration is based on the Titan geometry presented in chapter 8, with atomic hydrogen being the primary component of the impinging plasma. The mass of the second species is about a factor of 2 larger than the mass of H^+, while its mean number density is exceeded by the hydrogen density by a factor of 1000. The upstream velocity is set to a value of $u_0 = 500\,\mathrm{km/s}$. An overview of the simulation parameters is given in table 9.2. Using the definition of the Alfvén velocity in a multi-component flow provided by Motschmann [109],

$$v_A = \frac{B_0}{\sqrt{\mu_0\,(n_1 m_1 + n_2 m_2)}} \quad , \tag{9.1}$$

as well as the definitions of the sonic and magnetosonic Mach numbers,

$$M_S = \frac{M_A}{\sqrt{\frac{\kappa}{2}\,(\beta_1 + \beta_2)}} \qquad \text{and} \qquad M_{MS} = \frac{M_A}{\sqrt{\frac{\kappa}{2}\,(\beta_1 + \beta_2) + 1}} \quad , \tag{9.2}$$

shows that the upstream flow is clearly super-alfvénic, supersonic and supermagnetosonic. However, if the plasma flow consisted *only* of the test particle species, the alfvénic Mach number

$$M_A = \frac{u_0}{B_0}\sqrt{\mu_0 n_2 m_2} = 0.11 \quad , \tag{9.3}$$

and consequently the magnetosonic Mach number, would both be clearly smaller than 1. Thus, if the planet's ionosphere interacted with an extremely thin upstream flow that consisted only of the test particles, no shock would evolve in front of the obstacle.

Quantity	Symbol	Numerical value
Magnetic field	$\underline{B}_0$	$(0, 0, -5)$ nT
Plasma flow velocity	u_0	$500\,\mathrm{km/s}$
Atomic hydrogen (H^+) density	n_1	$0.3 \cdot 10^6\,\mathrm{m}^{-3}$
Molecular hydrogen (H_2^+) density	n_2	$0.3 \cdot 10^3\,\mathrm{m}^{-3}$
H^+ temperature	kT_1	$2.17\,\mathrm{eV}$
H_2^+ temperature	kT_2	$4.35\,\mathrm{eV}$
Thermal velocity	$v_{th,1} = v_{th,2}$	$25\,\mathrm{km/s}$
H^+ plasma beta	β_1	0.011
H_2^+ plasma beta	β_2	$2.10 \cdot 10^{-5}$
Alfvén velocity	v_A	$198.92\,\mathrm{km/s}$
Alfvénic Mach number	M_A	2.51
Sound velocity	c_S	$20.41\,\mathrm{km/s}$
Sonic Mach number	M_S	24.49
Magnetosound velocity	c_{MS}	$199.96\,\mathrm{km/s}$
Magnetosonic Mach number	M_{MS}	2.50
Box size	X	$-7.5R_T \leq X \leq +7.5R_T$
	Y	$-7.5R_T \leq Y \leq +7.5R_T$
	Z	$-7.5R_T \leq Z \leq +7.5R_T$
Number of grid cells	(N_X, N_Y, N_Z)	$(100, 100, 100)$
Time step	Δt	$0.24\,\mathrm{s}$
Total number of time steps	$N_{\Delta t}$	20000
Smoothing parameter	α_S	0.13

Table 9.2: Shock formation in a multi-ion plasma flow – Simulation parameters for run #1. In this run, the impinging plasma flow mainly consists of atomic hydrogen ions, whereas molecular hydrogen ions have been admixed as test particles. The thermal velocity of the particles is assumed to be about a factor of 20 smaller than the upstream speed u_0. All three Mach numbers of the upstream plasma are larger than 1. Since the purpose of the simulations is to give a qualitative overview of the effects that can occur in a multi-ion flow, most of the parameters have been obtained from the Titan scenario presented in chapter 8. However, the input parameters can easily be specialized to simulate the interaction between a planetary or cometary ionosphere and a solar wind consisting of hydrogen and helium.

The simulation results can be seen in fig. 9.1 for the polar plane and in fig. 9.2 for the equatorial plane. The sub-figures are arranged in the same way as in previous chapters. Both the primary species and the test particle component develop a sharply pronounced, parabolically shaped shock front which is denoted by a sudden increase of the plasma density as well as a strong deceleration of the impinging plasma. The characteristics of the interaction process are clearly defined by the supersonic nature of the primary flow, which gives also rise to the noticeable electric field enhancement near the ramside of the obstacle (cf. figs. 9.1(f) and 9.2(f)). In contrast to this, the test particles do not make a noticeable contribution to the electromagnetic field topology, but they are simply decelerated in the shock potential provided by the primary species. The situation can be interpreted in such way that at first, the shock front in the primary species is fully established, defining the location and strength of the decelerating electromagnetic fields. Then, the test particles are injected into the quasi-stationary scenario and experience the pre-defined electromagnetic field configuration, but they do not modify the field topology themselves. Because the mass-to-charge ratios of both species differ only by a factor of 2, the deceleration of the test particles is of the same order of magnitude as the effect on the primary flow component. Thus, the dynamics of the minor component are dictated by the primary species that sets up the field configuration almost independently of the test particles. Again, the shock structure is highly symmetric in the polar plane, while the situation in the equatorial plane exhibits a pronounced asymmetry. The ramside magnetic pile-up region is shifted in the E^+ hemisphere (cf. fig. 9.2(c)).

As can be seen in figs. 9.1(b) and (e) for the polar plane as well as in figs. 9.2(b) and (e) for the equatorial plane, the bow wave developed by the second species exhibits some kind

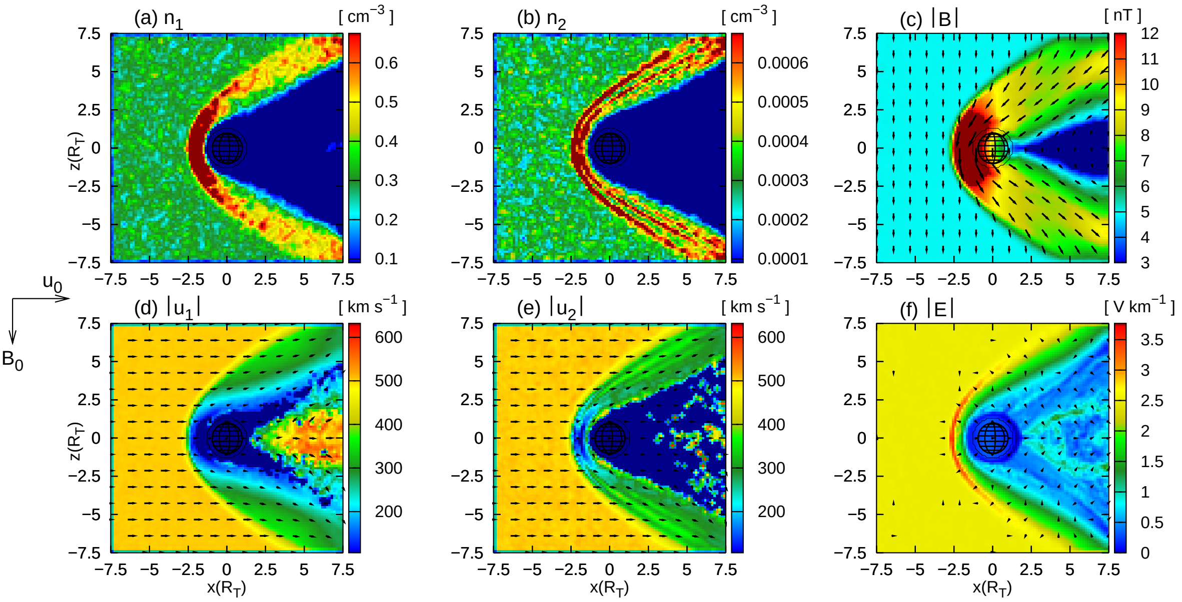

Figure 9.1: Shock formation in a multi-ion plasma flow – Primary species: atomic hydrogen, test particles: molecular hydrogen. For a cut through the obstacle's polar plane, the figure displays the number density and velocity of the primary species (plots (a) and (d)), the density and velocity of the test particles (plots (b) and (e)) and the electromagnetic fields. Even though the single-species magnetosonic Mach number of the test particles is smaller than 1, both constituents develop a pronounced shock front, denoting a sudden deceleration as well as a strong density enhancement. As their number density is extremely small, the molecular hydrogen ions are unable to take noticeable influence on the electromagnetic field topology. Instead, the H_2^+ ions are simply decelerated in the field configuration determined by the primary component, i.e. the formation of a shock front in the test particle component is enforced by the primary species. At first glance, it may seem that the density of both species vanishes in the wake, although the velocity in this region possesses a finite value. However, one should notice that a relatively large value has been chosen for the lower limit of the color scales in plots (a) and (b) in order to guarantee a good resolution of the density signatures in the shock. Since the specifications of the ion-producing obstacle do not match the parameters of any real situation, the structures developed in the wake region are only of minor relevance.
Simulation parameters: see table 9.2.

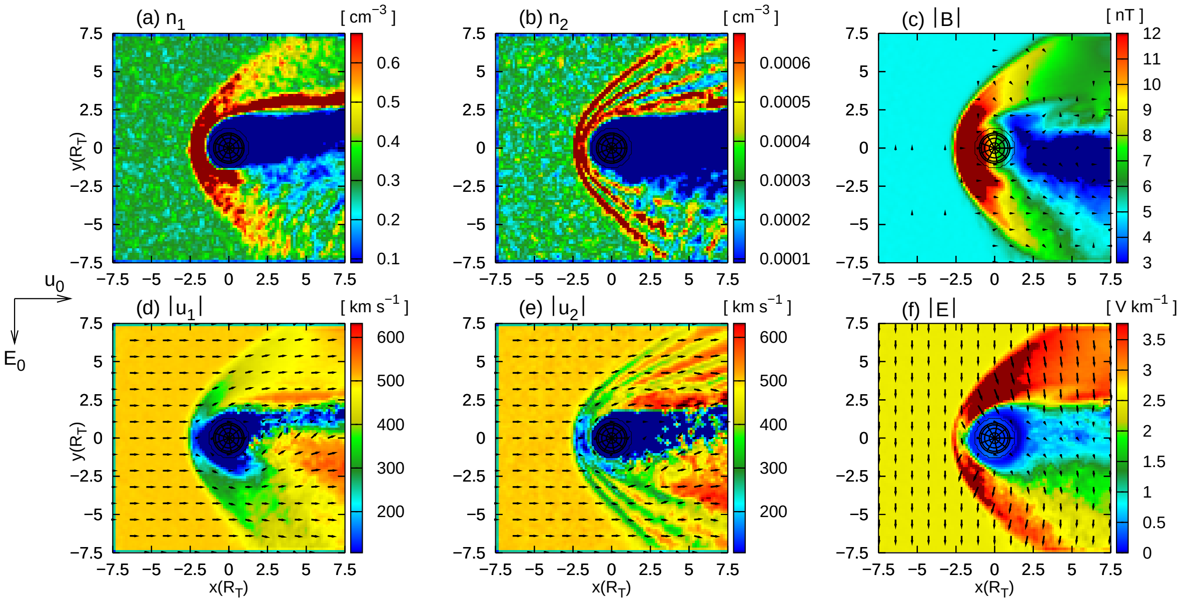

Figure 9.2: Shock formation in a multi-ion plasma flow – Primary species: atomic hydrogen, test particles: molecular hydrogen. The simulation results for the equatorial plane are shown in the figure. The shock front developed by the test particle component exhibits a so-called *shocklet* sub-structure. As can be seen from plot (b), the boundary layer consists of several distinct parabolically shaped regions, each of them denoting an increase of the mean plasma density. As shown in plot (e), in the regions of enhanced density, the mean plasma velocity is clearly reduced. These shocklets arise from the finite gyroradius of the particles and therefore emphasize the kinetic nature of the interaction process. A similar sub-structure emerges in the polar plane as well. However, while in the polar plane, the shocklet structure is highly symmetric, it features an asymmetry in the equatorial plane. The shocklets are more prominent in the E^- hemisphere, for in the E^+ hemisphere, the shock structure is modified due to the presence of slow ionospheric ions.
Simulation parameters: see table 9.2.

of periodic sub-structure. As displayed in fig. 9.1(b), the outer curve denoting an increase of plasma density is followed by a second one and finally by a third density enhancement. The same structure manifests in the particle velocity (cf. fig. 9.1(e)). Although being more prominent in the E^- hemisphere, the same sub-structure can clearly be identified in the equatorial plane as well. On the one hand, these structures look like shock waves, but on the other hand, Bagdonat [7] demonstrated for the case of weak comets that globally, such a signature shows nearly adiabatic behaviour. The particles are decelerated and experience a heating in a region of enhanced density, but they are again accelerated and cooled down before entering the next region of high density. Such an anti-correlation between density and velocity can formidably be identified by comparing plots 9.2(b) and 9.2(e). This so-called *shocklet structures* also appeared in numerical modelling (cf. Shimazu [134], Bagdonat [7] and Bößwetter *et al.* [26]) as well as in observations (cf. Omidi and Winske [121] and Sauer *et al.* [128]) of the plasma environments of Mars and weakly outgassing comets. A simulation study conduced by Simon *et al.* [138] also suggests the existence of such a structure in the plasma environment of magnetized asteroids. By analyzing the trajectories of individual particles, the authors have proven the kinetic character of the shocklets, i.e. these features arise from finite gyroradius effects and therefore, they do not occur in (multi)fluid plasma simulations. The regions of enhanced density can be considered tangents to the cycloidal particle trajectories (cf. Simon *et al.* [138]).

However, in the single-species simulations conducted by Bagdonat [7], the "fingerprint" of the shocklet structure did not only manifest in the densities and velocities, but it was clearly identifiable in the electromagnetic field topology as well. In strong contrast to this, in the situation displayed in figs. 9.1 and 9.2, the extremely small density of the minor species keeps the shocklet structure from imprinting its signature on the electromagnetic fields as well. Thus, in a multi-ion scenario where only one of the two constituents develops a shocklet structure, this signature can provide a measure of the degree to which the test particle species is capable of affecting the electromagnetic field topology. If the density of the second species is sufficiently high, the shocklets should be clearly visible in the electromagnetic fields.

Quantity	Symbol	Numerical value
Magnetic field	$\underline{B}_0$	$(0, 0, -5)$ nT
Plasma flow velocity	u_0	$500\,\mathrm{km/s}$
Atomic hydrogen (H^+) density	n_1	$0.3 \cdot 10^6\,\mathrm{m}^{-3}$
Test particle density ($m_2 = 20m_1$)	n_2	$0.3 \cdot 10^3\,\mathrm{m}^{-3}$
H^+ temperature	kT_1	$2.17\,\mathrm{eV}$
Test particle temperature	kT_2	$43.50\,\mathrm{eV}$
Thermal velocity	$v_{th,1} = v_{th,2}$	$25\,\mathrm{km/s}$
H^+ plasma beta	β_1	0.011
Test particle plasma beta	β_2	$2.10 \cdot 10^{-4}$
Alfvén velocity	v_A	$197.15\,\mathrm{km/s}$
Alfvénic Mach number	M_A	2.54
Sound velocity	c_S	$20.41\,\mathrm{km/s}$
Sonic Mach number	M_S	24.49
Magnetosound velocity	c_{MS}	$198.21\,\mathrm{km/s}$
Magnetosonic Mach number	M_{MS}	2.52
Box size	X	$-7.5R_T \le X \le +7.5R_T$
	Y	$-7.5R_T \le Y \le +7.5R_T$
	Z	$-7.5R_T \le Z \le +7.5R_T$
Number of grid cells	(N_X, N_Y, N_Z)	$(100, 100, 100)$
Time step	Δt	$0.24\,\mathrm{s}$
Total number of time steps	$N_{\Delta t}$	20000
Smoothing parameter	α_S	0.13

Table 9.3: Shock formation in a multi-ion plasma flow – Simulation parameters of run #2. In this scenario, test particles of mass $m_2 = 20\,\mathrm{amu}$ have been admixed to a flow that mainly consists of atomic hydrogen ions. Except for the particle mass of the second species, the configuration of the simulation scenario is identical to the situation presented in table 9.2. Increasing the mass of the second species while retaining its number density goes along with an increase of the test particle plasma beta. However, the Mach numbers of the upstream flow are only slightly modified.

2 Light major component, heavy test particles

The input parameters for the second scenario are equal to those of the situation discussed in section 1, except for the test particle mass being about a factor of 10 larger (i.e. $m_2 = 20m_1$). Although this modification increases the mass density of the second species by one order of magnitude, the single-species alfénic and magnetosonic Mach numbers ($M_{MS} \approx M_A = 0.36$) of the test particles are still clearly smaller than 1. Thus, if the obstacle was exposed only to the thin test particle component, again no shock front would evolve at its ramside. Table 9.3 gives an overview of the only slightly modified set of input parameters. The simulation results for the polar and equatorial plane can be seen in figs. 9.3 and 9.4, respectively. The results clearly indicate that it depends on the mass of the test particles whether the primary species is able to impose a shock-like behaviour on the minor component. As can for instance be seen from plots 9.3(a) and (d), a shock front is developed by the primary component, its parabolic shape also being clearly identifiable in the electromagnetic field topology. However, no shock is formed in the test particle component. As displayed in figs. 9.3(e) and 9.4(e), these particles do not experience a significant deceleration in the vicinity of the planet. In

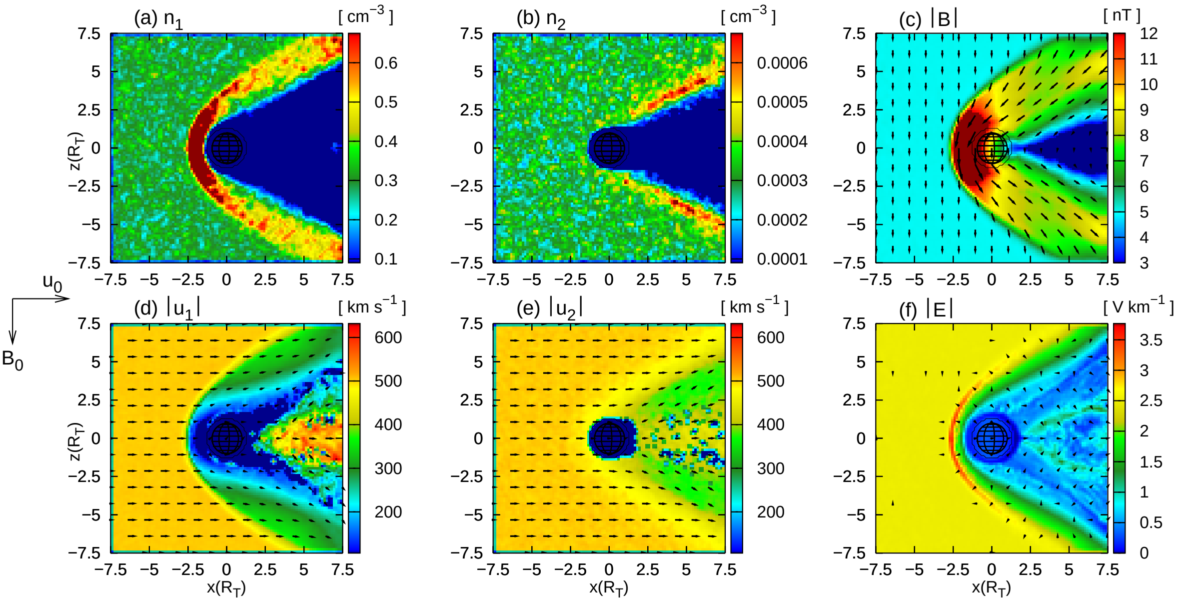

Figure 9.3: Shock formation in a multi-component plasma flow – Primary species: H^+, test particles: $m_2 = 20m(H^+)$. The figure displays the simulation results in the polar plane which is perpendicular to the undisturbed convective electric field. While the electromagnetic field configuration is again dictated by the shock formation in the primary component, the relatively heavy test particles experience only a minor deceleration and consequently, they do not exhibit a shock-like behaviour. The ratio between the mass of the primary species and that of the test particles plays a decisive role for the question of whether a shock is developed by the minor component. The larger is the mass of the test particles, the less are their dynamics affected by the field configuration set up by the primary species. Since in the scenario under consideration, the fields are not strong enough to enforce a shock-like behaviour of the second component, the test particles are simply deflected around the obstacle (cf. fig. (e)), giving rise to a cavity in the downstream region.
Simulation parameters: see table 9.3.

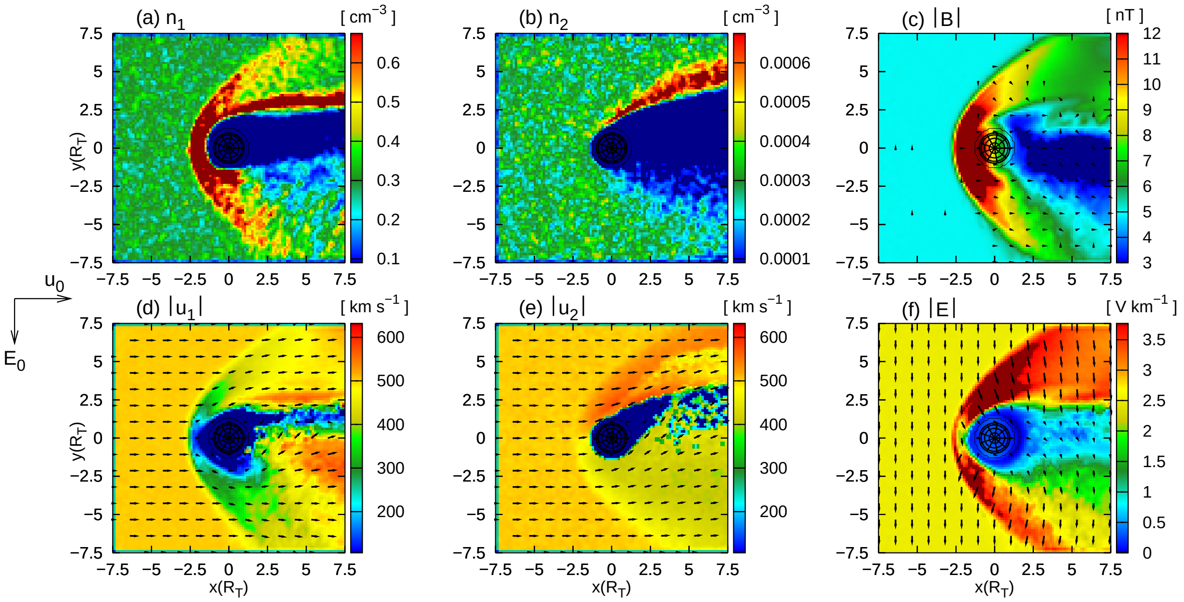

Figure 9.4: Shock formation in a multi-component plasma flow – Primary species: H^+, test particles: $m_2 = 20m(H^+)$. The simulation results for the equatorial plane are shown in the figure. A cone-like cavity of reduced plasma density is developed by the test particle component. If the thermal velocity of the magnetospheric N^+ plasma was not so high, a similar structure would emerge from Titan's interaction with Saturn's magnetospheric plasma as well. In the Titan scenario, any cavity in the magnetospheric flow is refilled almost instantaneously due to the predominant non-directional motion of the ions.
Simulation parameters: see table 9.3.

contrast to this, the velocity of the primary component is not only reduced by more than a factor of 2, but the decelerated flow also clearly deviates from its original direction. The primary component is deflected around the obstacle.

In this geometry, the electromagnetic field configuration is again set up by the main constituent. In contrast to the situation discussed in the previous section, the mass-to-charge ratio of the second species is one order of magnitude larger than the value of the first species. Therefore, a heavy test particle experiences only a minor deceleration and is able to nearly retain its initial velocity when crossing the shock layer, whereas a species 1 particle loses most of its velocity when passing the shock region. The heavier are the test particles, the less are their dynamics affected by the field configuration provided by the primary species. Thus, in this scenario, the test particles behave as expected for a subfast flow and do not form a shock front. In the equatorial plane, the test particles form a cone-shaped cavity downstream of the obstacle, its outer flanks denoting an increase of plasma density by a factor of 2 (cf. fig. 9.3(b)). A similar, albeit asymmetric, cavity occurs in the obstacle's equatorial plane, as can be seen in fig. 9.4(b). In principle, a similar wake cavity in the heavy N^+ component would be formed in the case of Titan's interaction with the subfast Saturnian magnetospheric plasma as well. However, in that situation, the cavity is refilled with plasma due to the high thermal velocity of the particles. In both the Titan scenario and in the situation shown in figs. 9.3 and 9.4, the major features of the electromagnetic field signature are determined by the species whose mass density is predominant. This tendency clearly manifested in the Titan situation as well, when the single-species representation of the ambient Saturnian magnetospheric flow was split up in two different components (cf. chapter 6).

3 Heavy major component, light test particles

Finally, the discussion will focus on the case of light test particles being admixed to a plasma that mainly consists of heavy ions. The simulation is based on the standard geometry for Titan, i.e. the impinging plasma flow is assumed to consist of nitrogen (N^+) and hydrogen (H^+) ions. However, in contrast to the Voyager-like simulation scenarios, the hydrogen density is about three orders of magnitude smaller than the number density of the nitrogen constituent. An overview of the simulation parameters is given in table 9.4. Again, if the upstream flow was made up only of the test particle component, no bow shock would form in front of the obstacle.

Quantity	Symbol	Numerical value
Magnetic field	$\underline{B}_0$	$(0, 0, -5)$ nT
Plasma flow velocity	u_0	$400\,\mathrm{km/s}$
Atomic nitrogen (N^+) density	n_1	$0.2 \cdot 10^6\,\mathrm{m}^{-3}$
Atomic hydrogen (H^+) density	n_2	$0.2 \cdot 10^3\,\mathrm{m}^{-3}$
N^+ temperature	kT_1	$30.45\,\mathrm{eV}$
H^+ temperature	kT_2	$2.17\,\mathrm{eV}$
Thermal velocity	$v_{th,1} = v_{th,2}$	$25\,\mathrm{km/s}$
N^+ plasma beta	β_1	0.10
H^+ plasma beta	β_2	$7.01 \cdot 10^{-6}$
Alfvén velocity	v_A	$65.17\,\mathrm{km/s}$
Alfvénic Mach number	M_A	6.14
Sound velocity	c_S	$20.41\,\mathrm{km/s}$
Sonic Mach number	M_S	19.60
Magnetosound velocity	c_{MS}	$68.30\,\mathrm{km/s}$
Magnetosonic Mach number	M_{MS}	5.86
Box size	X	$-7.5R_T \leq X \leq +7.5R_T$
	Y	$-7.5R_T \leq Y \leq +7.5R_T$
	Z	$-7.5R_T \leq Z \leq +7.5R_T$
Number of grid cells	(N_X, N_Y, N_Z)	$(100, 100, 100)$
Time step	Δt	$0.24\,\mathrm{s}$
Total number of time steps	$N_{\Delta t}$	20000
Smoothing parameter	α_S	0.13

Table 9.4: Shock formation in a multi-ion plasma flow – Simulation parameters for run #3. The simulation parameters are mainly based on the Voyager-like Titan situation and represent the case of light hydrogen test particles being incorporated into a flow that primarily consists of atomic nitrogen.

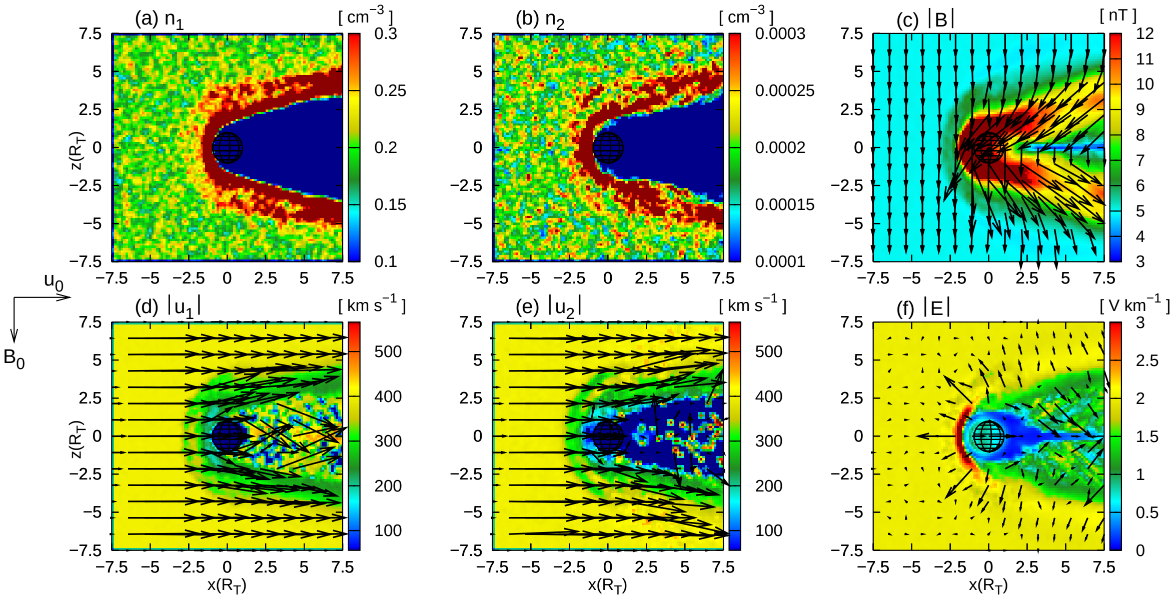

Figure 9.5: Shock formation in a multi-component plasma flow – Primary species: N^+, test particle species: H^+. The figure displays the simulation results in the polar plane. Again, the formation of a shock is imposed on the test particles by the primary component. As can be seen from plots (e) and (f), at the ramside, the test particles experience a strong deceleration in the electric field that is directed radially away from the obstacle. The shock structure is more diffuse than in the scenarios using H^+ as the primary plasma constituent.
Simulation parameters: see table 9.4.

The simulation results are shown in fig. 9.5 for the polar plane and in fig. 9.6 for the equatorial plane. As can be seen from figs. 9.5(a) and (b), both plasma components develop a shock front, i.e. the light test particles again experience a strong deceleration in the electromagnetic field configuration determined by the primary species. The decelerating electric field in the polar plane, which is directed radially away from the obstacle, is clearly identifiable in fig. 9.5(f). Due to the mass of the test particles being about a factor of 14 smaller than the mass of the predominant nitrogen component, the deceleration of the test particles is even larger than the effect on the nitrogen flow. This tendency clearly manifests in the wake region downstream of the obstacle where the H^+ velocity nearly vanishes. While the situation in the polar plane is highly symmetric, the shock structure in the equatorial plane features a strong asymmetry with respect to the direction of the electric field. Only in the E^- hemisphere, the shock front developed by the heavy nitrogen ions is characterized by a strong, sharply pronounced density enhancement. In the E^+ hemisphere, such a signature is practically not existent (cf. fig. 9.6(a)). In contrast to this, the light test particles do not only experience a strong deceleration in the E^+ hemisphere, but a broad region of enhanced H^+ density is formed as well. As can be seen from fig. 9.6(e), the H^+ ions are clearly deflected in E^+ direction, i.e. they are dragged away from the obstacle. At least in the E^+ hemisphere, the signatures developed by the light species bear a strong resemblance to the behaviour of the light magnetospheric component in the Titan scenario (cf. chapter 6). The light particles were pressed against the anti-Saturn-facing flank of the ionospheric tail, giving rise to a strong density enhancement along the tail's flank. In analogy, the rather complex structure occurring in the E^+ hemisphere

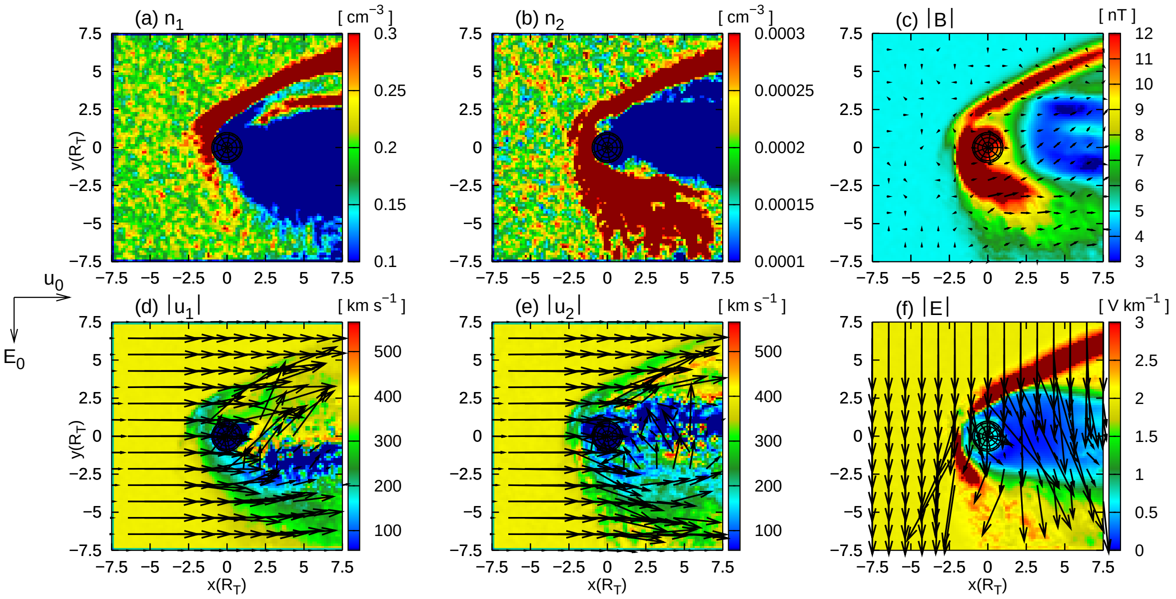

Figure 9.6: Shock formation in a multi-component plasma flow – Primary species: N^+, test particle species: H^+. The figure shows the simulation results in the equatorial plane. The shock front features a pronounced asymmetry with respect to the direction of the electric field. In the E^- hemisphere, the density enhancement of the primary component as well as the increases in the electromagnetic field magnitudes are sharply pronounced. In the E^+ hemisphere, these signatures exhibit a rather diffuse structure. In the E^+ hemisphere, the shock structure undergoes strong modifications due to the massive accumulation of newly generated ionospheric ions. Bearing a strong resemblance to the results of the multi-ion Titan simulations presented in chapter 6, the light H^+ ions are pressed against the outer flank of the ionospheric tail. As can be seen from fig. (b), this effect gives rise to a broad region of enhanced test particle density. In the E^+ hemisphere, the test particles are clearly decelerated and deflected away from the obstacle.
Simulation parameters: see table 9.4.

in figs. 9.6(b) and (e) must be ascribed to the massive presence of ionospheric pick-up ions in this region. However, since neither the input plasma parameters nor the details of the ionosphere model correspond to a specific real situation, the modification of the E^+ shock structure due to the accumulation of ionospheric particles in this region will not be discussed in more detail.

4 Summary

In this chapter, a first application of the multi-species simulation model to the physics of shock waves has been presented. Specifically, the analysis has focused on the admixture of test particles of mass m_2 to a supermagnetosonic flow, consisting of particles of mass m_1. Three different scenarios have been compared: $m_1 \approx m_2$, $m_1 \gg m_2$ and $m_1 \ll m_2$. In all three simulation runs, the electromagnetic field topology of the shock front is exclusively determined by the primary constituent. If the test particles are not significantly heavier than the primary constituent, their dynamics are completely controlled by this pre-defined electromagnetic field topology. Although the Mach numbers of the minor component flow are located in the subfast regime, a shock-like behaviour of this species is enforced by the predominant constituent. In the case of comparable particle masses, the shock front in the minor component exhibits a quasi-adiabatic sub-structure, arising from finite gyroradius effects. Only if the minor component is relatively heavy, these particles have shown to be able to cross the pre-defined shock potential without experiencing a noticeable deceleration. In this case, no shock front is developed by the test particles. Instead, a cone-like cavity is formed downstream of the planetary obstacle that has been placed in the plasma flow. This structure gives at least a rough impression of how Titan's wakeside plasma environment would be structured, if the emerging plasma signatures were not "smeared" by the high thermal velocity of the magnetospheric N^+ particles.

Chapter 10

Summary and outlook

Titan, the largest satellite of Saturn, possesses an extended atmosphere that consists mainly of molecular nitrogen. A variety of different ionization sources, with solar ultraviolet radiation being the predominant one, lead to the formation of an ionosphere around Titan. As the moon does not possess a significant intrinsic magnetic field, the interaction between Titan and the ambient plasma exhibits a strong resemblance to the plasma environments of Venus, Mars and comets. However, the Titan scenario possesses several unique features. For average solar wind conditions, Titan's orbit is located inside the Saturnian magnetosphere where the satellite faces a subsonic and submagnetosonic plasma flow. The alfvénic Mach number of the at least partially corotating magnetospheric plasma varies along Titan's orbit. In the outer regions of Saturn's magnetosphere, the satellite faces a super-alfénic plasma flow, whereas when being located in Saturn's magnetotail, Titan is exposed to a plasma with $M_A < 1$. In times of high solar wind dynamic pressure, Titan might even be able to leave the magnetosphere in the subsolar regions of its orbit and interact directly with the solar wind. Furthermore, Titan's dayside ionosphere is not necessarily located in the hemisphere that is exposed to the upstream plasma flow, yielding a diversity of different interaction scenarios.

In the framework of the present study, the interaction between Titan's ionosphere and the impinging plasma has been studied in terms of a three-dimensional electromagnetic hybrid model, treating the ions as individual particles, while the electrons are represented by a massless fluid. Such an approach is mandatory since the characteristic length scales of the interaction region are comparable to the mean ion gyroradii in the ambient plasma and hence, ion kinetic effects cannot be neglected. In the simulation model, Titan's dayside ionosphere is represented by a Chapman profile. A curvilinear simulation grid was introduced to achieve a high spatial resolution in the immediate vicinity of the obstacle.

1 Simulation results

In the following, a brief overview of the major simulation results will be given.

- Chapter 4 presented an analysis of Titan's plasma interaction as a function of the Mach numbers in the upstream flow. The model included two different ion species: The impinging plasma was represented by a heavy ion component of mass $m = 9.67\,\mathrm{amu}$, whereas molecular nitrogen was assumed to be the only species of ionospheric origin. In the case of a supermagnetosonic flow, the impinging plasma does not only develop a bow shock, but it is clearly separated from the ionospheric ion population by means of an Ion Composition Boundary. Such a boundary layer does not evolve from the interaction between Titan's ionosphere and the subfast magnetospheric plasma. The structure of the magnetic pile-up region at Titan's ramside as well as the orientation of the wakeside ionospheric tail have shown to exhibit a strong asymmetry with respect to the direction of the convective electric field. The simulations also illustrated the "flat" structure of Titan's ionospheric tail: In the polar plane, particles of ionospheric origin are confined to a narrow region directly behind the obstacle, the tail diameter being smaller than $3R_T$. In the equatorial plane, the tail possesses an extension of more than $7R_T$ perpendicular to the direction of the magnetospheric plasma flow.

- Chapter 5 dealt with the situation inside the magnetosphere. Specifically, the dependence of the structures in Titan's plasma environment on the satellite's orbital position was investigated. The simulation results showed that the orientation of Titan's dayside ionosphere with respect to the direction of the impinging plasma exerts only a minor influence on the flow pattern of the magnetospheric plasma as well as on the electromagnetic field topology. Instead, the sharpness and extension of Titan's magnetic lobes are mainly determined by the velocity of the impinging magnetospheric plasma. By means of the magnetic lobes, the upstream flow also controls the extension of the ionospheric tail in a plane perpendicular to the electric field. Along Titan's entire orbit, the ionospheric tail is shifted away from Saturn.

- Chapter 6 presented a major improvement of the simulation code. On the one hand, two additional ionospheric species have been incorporated into the model; on the other hand, a two-species representation has been applied to the impinging magnetospheric plasma. This approach allowed to gain deep insight into the interplay between different pick-up species. The heaviest ionospheric component does not only determine the key features of the electromagnetic field topology in the vicinity of Titan, but it also exerts control on the dynamics of the lighter ionospheric components. By means of the distortions that they impose on the electric field topology, the heavy ionospheric species slow down the pick-up process of the lighter ones. The simulations also illustrated that the finite gyroradii of the involved ions give rise to a spatial dispersion of different pick-up species in Titan's wake region. Besides, at certain orbital positions, Titan's tail may exhibit a rather symmetric structure. This characteristic is not covered by the single-species ionosphere model. As for the magnetospheric flow pattern, the light H^+ ions are strongly affected by the distorted electromagnetic fields near Titan. The degree to which these ions are forbidden to enter the central plasma wake downstream of Titan is mainly controlled by their temperature. In contrast to this, the heavy magnetospheric N^+ ions experience only a weak deflection.

- Currently, the Cassini mission to the Saturnian system provides a diversity of new information on Titan and its plasma environment. Chapter 7 presented a study of the field distortions detected near Titan by the Cassini Magnetometer instrument. The simulated magnetic field signatures have shown to be in reasonably good agreement with Cassini magnetometer data. Especially, the field enhancements in the wakeside magnetic lobes are well reproduced by the simulation model.

- In chapter 8, an analysis of the plasma and magnetic field signatures measured during Cassini's T9 flyby of Titan was presented. During this flyby, a unique split signature was detected in the structure of Titan's ionospheric tail. Although the simulation model was not able to reproduce this structure in detail, the results provided valuable information for the interpretation of the data collected by the Cassini Plasma Spectrometer. Moreover, the T9 geometry allowed to infer the degree to which Titan's ionospheric tail structure is affected by the composition of the magnetospheric upstream flow. If the impinging magnetospheric plasma consists only of light hydrogen ions, the flow experiences a strong deceleration in the downstream region. The resulting reduction of the convective electric field strength slows down the pick-up of newly generated ionospheric particles.

- Finally, the physics of multi-ion shock waves have been briefly discussed. Specifically, the analysis focused on the dynamics of light test particles that have been admixed to a superfast plasma flow. The results illustrated that, similar to the situation at Titan, the dynamics of the test particles are "enslaved" by the major component. The test particles are unable to take noticeable influence on the electromagnetic field topology of the shock wave developed by the major component. Furthermore, despite their velocity being subfast, the test particles can be forced to form a shock wave themselves, if their mass is sufficiently small.

This thesis has attempted to answer a number of questions on Titan and its plasma interaction. However, the simulations also pointed out some problems that have not yet been resolved. Therefore, the final section gives an overview of possible improvements and future applications of the multi-species simulation code.

2 Outlook

At the time of this writing, the most critical aspect that has remained in any available semi-kinetic plasma model is the rather rough description of the complex physical and chemical processes in Titan's ionosphere. The hybrid approach is currently incapable of considering the large number of particles that is required for describing at least the basic reaction chains in Titan's upper ionosphere. Thus, with respect to the near-ionosphere region, none of the available hybrid codes is able to achieve self-consistency. Although the semi-kinetic approach can provide an extremely sophisticated model of the large-scale asymmetries in Titan's tail structure, the limitations imposed on the simulation codes by the available computing capacities make the hybrid approximation fail in spatial regions where complex chemical processes play a decisive role. As for this aspect, most of the MHD models are currently one step ahead of the hybrid codes. However, the global picture of Titan's plasma environment offered by the fluid models is significantly falsified by the negligence of individual particle dynamics. Hence, at the current state of research, both MHD and hybrid models must be taken into consideration for an analysis of the data obtained by the Cassini plasma instruments. Joining the advantages of both approaches, i.e. designing a hybrid code that is able to reproduce the major processes of ionospheric chemistry as well, can be considered the next step of improvement.

The hybrid code that has been used for the present study is currently in the process of being parallelized. First test runs on a multi-processor machine have been accomplished.

Performing the simulations on a multi-processor computer does not only go along with a significant reduction of the computing times by more than a factor of 5 – currently, achieving stationarity requires a total simulation time of about 7-10 days –, but the number of particles included in each simulation run will also be increased by a factor of 3 to more than 25 million ions per simulation. Under these conditions, the incorporation of additional ionization sources and at least one or two major reaction chains into the ionosphere model should definitely be realizable. In recent years, the observation of large concentrations of energetic neutral clouds (ENAs) near Titan has drawn a lot of attention in the scientific community [3, 50, 105]. Thus, a first step towards improving the existing model could be the inclusion of a simple charge-exchange process as an ionization source.

Currently, particles entering the immediate vicinity of the obstacle are "artificially" removed from the simulations by means of an absorptive boundary condition. However, in reality, most of these ions are scattered by neutral atoms in Titan's dense atmosphere. This aspect could be taken into consideration by incorporating some kind of collision term into the equations of motion for the individual ions. Based on a modified equation of motion,

$$\frac{\mathrm{d}\underline{v}_\nu}{\mathrm{d}t} = \frac{q_\nu}{m_\nu}\left(\underline{E} + \underline{v}_\nu \times \underline{B}\right) - \mathcal{K} n_n(r)\underline{v}_\nu \quad , \tag{10.1}$$

where $\mathcal{K} = 1.0 \cdot 10^{-7}\,\mathrm{cm}^3\,\mathrm{s}^{-1}$ is a collision constant and $n_n(r)$ denotes the neutral density in the altitude r above the surface, a preliminary test run has already been carried out (cf. fig. 10.1). Apparently, the improved equations of motion do not only yield an accentuation of the ramside pile-up region, but the extension and the velocity pattern of the equatorial

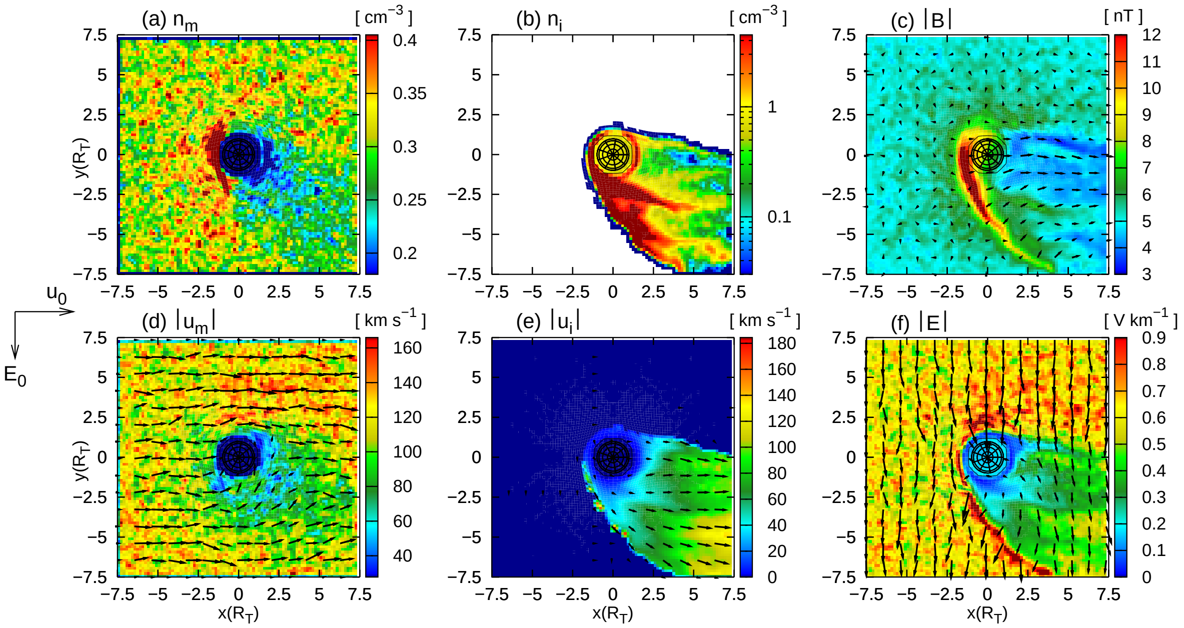

Figure 10.1: Test run: Influence of collisions between ions and neutral atoms in Titan's atmosphere. The magnetospheric plasma is represented by (N^+/H^+) ions, whereas molecular nitrogen is the only atmospheric/ionospheric species. The figure illustrates the situation in the equatorial plane at 18:00 clock angle position.

pick-up tail are modified as well. Unfortunately, due to the insufficient spatial resolution near the surface, the simulation did not achieve a stationary state. Furthermore, it is not clear whether the modifications of the pick-up tail and the ramside magnetic pile-up region have to be considered numerical artifacts, especially since the original code tended to *over*estimate the magnetic field distortions detected by Cassini.

Besides, it shall be investigated whether some of the deviations between simulation results and measurements can be explained by superimposing inhomogeneities on the magnetospheric upstream conditions, e.g. spatial or time variations in the direction of the ambient magnetic field. It is known that time variations in the solar wind magnetic field do not only yield strong modifications of the shock structure at the ramside of a weak comet, but they can even lead to a detachment of the plasma tail from the nucleus. However, in the case of planets or moons, the numerical investigation of these effects is still a nearly unexplored terrain, mainly because the inclusion of any kind of time variation into a simulation code increases the risk of numerical instabilities. Moreover, the involved particle dynamics have shown to be extremely complex. Consequentially, an analysis should start in the test particle regime where ion dynamics in pre-defined electromagnetic field configurations are studied. Currently, some of these aspects are investigated by a diploma student in our working group.

Apart from Titan's plasma environment, the multi-species model presented in this thesis should be able to provide new insights into the plasma interactions of other solar system bodies as well. For instance, recently published Cassini results reveal the existence of an atmosphere and ionosphere around the Saturnian moon Enceladus (cf. Dougherty *et al.* [45], Jones *et al.* [66], Tokar *et al.* [145]). To the author's knowledge, only preliminary applications of numerical simulation models to the plasma interaction of Enceladus are currently available. Besides, only very few three-dimensional hybrid studies of the interaction between a multi-component solar wind and planetary or cometary ionospheres have already been carried out. Although the multi-component shock simulations presented in chapter 9 have shown that the simulation code provides an appropriate description of the involved physics, the parameters have not yet been specialized to a real scenario. For instance, the Martian interaction with a two-component solar wind (protons and alpha particles) could be reanalyzed in this way. By using a 3D hybrid code, Modolo *et al.* [108] presented a first analysis of the dynamics of the helium component. This aspect of the Martian plasma interaction has not yet been addressed by any other simulation model.

In any case, the ongoing Cassini mission will place Titan and its plasma interaction in the focus of scientific interest for at least the next decade. Advantages in the development of new simulation techniques will provide invaluable support for the analysis of more than 20 Titan flybys that still lie ahead.

Appendix A

Simulation code: Basic input parameters

The initial parameters of a simulation run – e.g. the direction of the background magnetic field, grid parameters, time step, ionospheric parameters, boundary conditions – have to be defined in an additional data file that is attached to the simulation code. For the original simulation code that had been applied to the plasma environment of comets, the general structure of this parameter file has been discussed by Bagdonat [7].

The basic input parameters of the hybrid code used for this thesis do not differ significantly from those of the original code. However, the simulation code which has been applied to Titan's plasma environment includes several new parameters that did not occur in the original version, whereas other comet-specific parameters are no longer needed. In order to update the "user's manual" of the original version, at least a brief description of how to handle these newly introduced simulation parameters shall be given here. The following sections deal only with those parameters that had to be added to the original version. On the other hand, most input parameters that are required for defining the properties of a cometary ionosphere have been removed from the parameter file. The monolithic code itself is written in C++.

It is important to notice that the discussion given in this chapter refers to an upstream flow that consists of only a single ion species. This code has been used for the simulations presented in chapters 4 and 5. The basic principles as well as the input parameters of the multi-species code are presented in the following two chapters.

1 Plasma velocity

In the original version of the code, the undisturbed plasma velocity vector $\underline{u}_0$ is assumed to be oriented in positive x direction. In order to study the effect of different angles between $\underline{u}_0$ and the ionizing solar radiation, an arbitrary velocity vector that includes three non-vanishing components had to be introduced. The parameters `UX0`, `UY0` and `UZ0` in the new parameter file are used to determine the undisturbed flow velocity. The components of $\underline{u}_0$ are not given in SI units, but with respect to the Alfvén velocity of the undisturbed magnetospheric upstream plasma,

$$v_A = \frac{B_0}{\sqrt{\mu_0 n_0 m}} \quad . \tag{A.1}$$

In this expression, n_0 and m denote the number density and the mass of the magnetospheric upstream species. For the Voyager 1 scenario, these values are given by $n_0 = 0.3 \cdot 10^6\,\mathrm{m}^{-3}$ and $m = 9.67\,\mathrm{amu}$. The alfvénic Mach number M_A of the upstream flow is required as an input parameter.

In the parameter file, the alfvénic Mach number M_A as well as two angles θ and ϕ have to be defined:

```
#define    M_A     (1.87)
#define    theta   (PI/2)
#define    phi     (PI)
```

The angles θ and ϕ characterize the orientation of $\underline{u}_0$ with respect to the axes of the Cartesian coordinate system:

```
#define  UX0      M_A * sin(theta) * cos(phi)
#define  UY0      M_A * sin(theta) * sin(phi)
#define  UZ0      M_A * cos(theta)
```

For the parameter set given above, the flow velocity $\underline{u}_0$ is directed in $(-x)$ direction, whereas the absolute value is given by $u_0 = 120\,\mathrm{km/s}$.

2 Ionosphere model

This section deals with the parameters that allow to specify the properties of Titan's ionosphere. In order to generate an ionosphere around the obstacle, the switch `TITAN_3D` has to be uncommented:

```
#define TITAN_3D
```

The ionosphere emerges from the moon's neutral atmosphere due to solar UV ionization. Thus, the density profile $n_n(r)$ of the neutral atmosphere has to be defined at first. In the simulations discussed in this thesis, the radial distribution of the neutral gas is given by eq. (3.109),

$$n_n(r) = n_1 \exp\left(\frac{r_1 - r}{H_1}\right) + n_2 \exp\left(\frac{r_2 - r}{H_2}\right) + n_3 \frac{r_3}{r} \quad .$$

The required parameters have to be entered as follows:

```
#define RT           2575.0e+3

#define H1           90.0e+3
#define H2           120.0e+3

#define n1           1.0e+18
#define n2           1.0e+12
#define n3           1.0e+10

#define R1           (700.e+3 + RT)
#define R2           (1700.e+3 + RT)
#define R3           (2700.e+3 + RT)
```

All parameters are given in SI units. The first one, `RT`, denotes the radius of Titan ($R_T = 2575\,\mathrm{km}$). The scale heights `H1` and `H2` as well as the reference densities (`n1`, `n2`, `n3`) and altitudes (`R1`, `R2`, `R3`) are defined according to eq. (3.109). It is of importance that all position vectors refer to the origin of the coordinate grid which coincides with the center of Titan. For this reason, an additional `RT` has to be incorporated into the definitions of `R1`, `R2` and `R3`.

In the simulations, the ionosphere is modeled as a spherical shell surrounding the obstacle (cf. section 6 of chapter 3). The inner and outer radius of this shell are given by the parameters `TITAN_a` and `TITAN_b`, respectively:

```
#define TITAN_a        (RT+1000.0e+3)
#define TITAN_b         (4.0*RT)
```

For the numerical values given above, the neutral gas profile as well as Titan's ionosphere begin 1000 km above the surface. The upper boundary of the ionosphere is located at an altitude of *three* Titan radii above the surface of the satellite. The value of `TITAN_a` also defines the location of the artificial inner obstacle boundary.

According to eq. (3.114), three further parameters are required for determining the final structure of the ionosphere profile: the photoionization efficiency κ_ν, the absorption cross-section σ_ν and the radiation intensity I_∞ have to be defined. Instead of I_∞, the photoionization frequency

$$\omega_\nu = \sigma_\nu I_\infty \tag{A.2}$$

has been introduced. This parameter has to be defined in SI units:

```
#define TITAN_omega      (0.2e-9)
```

Due to lack of experimental values, the photoionization efficiency is usually set to a value of $\kappa_\nu = 1$ ($= 100\%$):

```
#define kappa          (1.0)
```

Thus, the entire energy of the impinging solar radiation is assumed to be available for the ionization process. The absorption cross-section σ_ν has to be defined in SI units (`sigma_SI`) as well as with respect to the inertia length c/ω_p of the undisturbed magnetospheric upstream plasma (`sigma`):

```
#define sigma_SI       (8.37411e-22)
#define sigma          (3.23607e-10)
```

Because numerical values for the absorption cross-section are often not available, an adequate approximation can be found as follows: At first, the neutral density profile (3.109) is approximated by a one-term profile according to eq. (3.92),

$$n_n(r) = n_0 \exp\left(-\frac{r}{H}\right) \quad . \tag{A.3}$$

For such a profile, the subsolar production maximum is located at an altitude of

$$r_m = H \ln\left(\sigma_\nu n_0 H\right) \tag{A.4}$$

above the surface of the obstacle. This expression yields

$$\sigma_\nu = \frac{1}{n_0 H} \exp\left(\frac{r_m}{H}\right) \tag{A.5}$$

for the absorption cross-section. The subsolar production maximum of the three-term-ionosphere (3.114) can be obtained numerically. The value of σ_ν is now chosen in such way that the subsolar production maximum of the one-term profile coincides with that of the three-term profile. For Titan and Mars, this technique has proven to provide an adequate approximation.

At the nightside of the obstacle, the ion production rate is kept at a value that does not depend on the solar zenith angle, i.e.

$$q_\nu = q_\nu\left(r, \chi = \chi_0\right) \quad ; \quad \chi_0 = \text{const} \quad . \tag{A.6}$$

The respective value of χ_0 is given by

$$\chi_0 = \frac{\pi}{2} - \epsilon \quad , \tag{A.7}$$

where ϵ has to be defined in the simulation parameter file. For all simulations described in this thesis, a value of $\epsilon = 0.05 = 2.86°$ has been chosen:

```
#define epsilon       (0.05)
```

Thus, the nightside ion production is characterized by

$$q_\nu = q_\nu\left(r, \chi_0 = 87.14°\right) \quad . \tag{A.8}$$

The total ion production Q in the ionosphere shell is given by

$$Q = \int_{\text{shell}} q_\nu(r, \chi_\nu)\, \mathrm{d}V \quad . \tag{A.9}$$

This parameter is required as a normalization value and has to be defined in SI units as well as with respect to the characteristic time scale Ω_g^{-1} of ion gyration in the magnetospheric upstream plasma:

```
#define Q_Photo_SI_INT   (1.25972e+25)
#define Q_Photo_INT      (19.6462)
```

The parameter `Q_Photo_SI_INT` is given in s^{-1}, while `Q_Photo_INT` is dimensionless. In general, the integral (A.9) has to be solved numerically by using a computer algebra system.

The number of heavy ion macroparticles[1] that are generated in each time step is defined by the parameter `TITAN_N`:

---

[1] This term will be explained in more detail in the next section.

```
#define  TITAN_N             300
```

The mass of the ionospheric ions has to be defined with respect to the mass of the magnetospheric ion component. In the simulations described in chapters 4 and 5, the magnetospheric ion mass is given by $m(N^+/H^+) = 9.67\,\mathrm{amu}$, whereas the mass of molecular nitrogen is $m(N_2^+) = 28.00\,\mathrm{amu}$. Hence, the normalized heavy ion mass is $28.00/9.67 = 2.90$:

```
#define  TITAN_ION_MASS      2.90
```

Finally, the location of the subsolar point with respect to Titan's orbital plane has to be defined by means of the subsolar latitude `SSL`:

```
#define SSL    0.38
```

The value given above corresponds to an angle of `SSL` = 22°.

3 Inner density

As discussed in section 9.2 of chapter 3, the artificial density values below the surface of the obstacle boundary are assumed to depend on both the simulation time and the position:

$$n_i(x,t) = \frac{t}{t+t_0} n_{\max} \cdot \frac{1}{1+\exp\left(\frac{\alpha x-\beta}{\gamma}\right)} \quad . \tag{A.10}$$

The parameters $n_{\max}$, t_0, α, β and γ have to be defined as input parameters, with t_0 being again normalized to the inverse ion gyrofrequency Ω_g^{-1} of the magnetospheric upstream flow. The reference density $n_{\max}$ is defined with respect to the magnetospheric upstream density $n_0 = 0.3\,\mathrm{cm}^{-3}$. While β and γ are dimensionless, α is given in units of the *inverse* (N^+/H^+) inertia length.

```
#define n_max    3.0
#define t_0      0.035
#define alpha    1.6
#define beta     3.3
#define gamma    2.0
```

The following chapters describe the basic concept of incorporating an additional upstream species into the simulation model. As for the upstream flow velocity and the representation of the ionosphere, it is important to notice that the normalization values used in the above discussion will *not* be defined with respect to the parameters of the multi-component upstream plasma. Only *one* of the two upstream species is taken into consideration for calculating the normalization values.

Appendix B

Multi-species simulation code: Numerical details

Of course, it is impossible to simulate the dynamics of all individual particles which are located in a simulation box of the size $15R_T \times 15R_T \times 15R_T$. Therefore, hybrid codes are based on the concept of merging large numbers of real particles to so-called macroparticles or superparticles. In the following, it will be discussed how the mass and the charge of these superparticles are derived from the physical properties of the individual ions. The hybrid code described in this work is based on the model developed by Bagdonat [7] to study the plasma environment of weak comets. However, in contrast to the Titan model presented in this work, the algorithms of the original code were designed for an upstream plasma that is composed of only a single ion species. The modifications that had to be incorporated into the code developed by Bagdonat [7] will be briefly summarized. Especially, the discussion will focus on the Current Advancement Method (cf. Matthews [103]) which is used to solve the electric field equation (3.20).

1 Particle administration in the multi-species code

This section deals with the basic principles of deriving the mass and charge of the superparticles that represent a given ion species. The treatment of the magnetospheric ions which are generated at the outer faces of the simulation domain is a little different from the method that is used to compute the superparticle parameters of an ionospheric species. The formalism that is applied to the ionospheric species is highly analogous to the numerical model of cometary ionospheres developed by Bagdonat [7]. For this reason, the following discussion will only describe how the magnetospheric upstream flow can be split up in two different components, i.e. how the mass and charge of the superparticles have to be chosen. For simplicity, the discussion refers to an equidistant Cartesian grid, the cell volume being V_g. However, the formalism can easily be generalized to the case of an arbitrary curvilinear grid. All ion species are assumed to consist of single-charged particles ($q = +e$).

Let n_1, $\rho_{m,1}$ and $\rho_{c,1}$ be the homogeneous upstream number density, mass density and charge density[1] of the first magnetospheric upstream species, consisting of particles with mass m_1. The box is not only filled with such a plasma at the beginning of each simulation run, but

---

[1] In other chapters of this thesis, the upstream quantities are denoted by an additional subscript 0. However, since all physical quantities in the appendix chapters refer to the homogeneous upstream plasma flow, this subscript can be consequently suppressed without causing any misunderstandings.

the continual generation of new species 1 particles at the inflow boundaries of the simulation domain is also controlled by these parameters. The mass $M_{SP,1}$ and charge $Q_{SP,1}$ of the corresponding superparticles are given by

$$M_{SP,1} = m_1 n_1 \frac{V_g}{N_{ppc,1}} \tag{B.1}$$

and

$$Q_{SP,1} = e n_1 \frac{V_g}{N_{ppc,1}} \quad , \tag{B.2}$$

where $N_{ppc,1}$ denotes the constant number of superparticles that is placed in each cell of the grid at the beginning of a simulation run. This parameter also defines the number of superparticles that are placed in an inflow boundary cell during each time step. Thus, the number $N_{SP,1}$ of real particles that have been merged to one superparticle can be written as

$$N_{SP,1} = \frac{Q_{SP,1}}{e} = n_1 \frac{V_g}{N_{ppc,1}} \quad . \tag{B.3}$$

It can easily be verified that choosing $M_{SP,1}$ and $Q_{SP,1}$ in this manner yields the correct values for the homogeneous upstream parameters:

- Number density:

$$\frac{N_{ppc,1} \cdot N_{SP,1}}{V_g} = n_1 \frac{V_g}{N_{ppc,1}} \frac{N_{ppc,1}}{V_g} = n_1 \quad , \tag{B.4}$$

- Mass density:

$$\rho_{m,1} = \frac{N_{ppc,1} \cdot M_{SP,1}}{V_g} = m_1 n_1 \quad , \tag{B.5}$$

- Charge density:

$$\rho_{c,1} = \frac{N_{ppc,1} \cdot Q_{SP,1}}{V_g} = e n_1 \quad . \tag{B.6}$$

The corresponding parameters for the second upstream species can now be derived in two different ways. On the one hand, the number $N_{SP,2}$ of real ions that are merged to one species 2 superparticle can be set to the same value as $N_{SP,1}$,

$$N_{SP,1} = N_{SP,2} \quad . \tag{B.7}$$

Since according to eq. (B.3), the total charge of a superparticle is a measure of the real number of ions it represents, the parameter $Q_{SP,2}$ can be written as

$$Q_{SP,2} = Q_{SP,1} = e n_1 \frac{V_g}{N_{ppc,1}} \quad . \tag{B.8}$$

By introducing the relative mass

$$\mu \equiv \frac{m_2}{m_1} \tag{B.9}$$

of a (real) species 2 ion, the mass $M_{SP,2}$ of a species 2 superparticle can be expressed as

$$M_{SP,2} = \mu M_{SP,1} \quad . \tag{B.10}$$

Apparently, these definitions yield the correct charge-to-mass-ratio for a species 2 superparticle:

$$\frac{Q_{SP,2}}{M_{SP,2}} = \frac{1}{\mu}\frac{Q_{SP,1}}{M_{SP,1}} \quad . \tag{B.11}$$

By introducing the number $N_{ppc,2}$ of species 2 superparticles per cell, the densities n_2, $\rho_{m,2}$ and $\rho_{c,2}$ can be expressed as follows:

- Number density:

$$n_2 = \frac{N_{ppc,2} \cdot N_{SP,2}}{V_g} = \frac{n_1 \frac{V_g}{N_{ppc,1}} \cdot N_{ppc,2}}{V_g} = \frac{N_{ppc,2}}{N_{ppc,1}} n_1 \quad , \tag{B.12}$$

- Mass density:

$$\rho_{m,2} = \frac{N_{ppc,2} \cdot M_{SP,2}}{V_g} = \frac{N_{ppc,2}}{N_{ppc,1}} m_1 n_1 \mu = \frac{N_{ppc,2}}{N_{ppc,1}} \mu \rho_{m,1} \quad , \tag{B.13}$$

- Charge density:

$$\rho_{c,2} = \frac{N_{ppc,2} \cdot Q_{SP,2}}{V_g} = \frac{N_{ppc,2}}{N_{ppc,1}} e n_1 = \frac{N_{ppc,2}}{N_{ppc,1}} \rho_{c,1} \quad . \tag{B.14}$$

Hence, in the numerical model, the difference in the number and charge densities of the two species is realized by choosing the ratio $N_{ppc,2}/N_{ppc,1}$ of the superparticle numbers in an adequate way. However, an upper limit for the particle numbers per cell is set by the available computing capacities. When using a grid with about 100 × 100 × 100 cells in each spatial direction, a personal computer of the latest generation is unable to handle more than 20 magnetospheric superparticles per cell. For most of the Titan simulations presented in this work, this restriction does not pose a significant problem. The $n(N^+)/n(H^+)$ density ratio of 2 : 1 can for instance be realized by setting $N_{ppc,1} = 12$ and $N_{ppc,2} = 6$. A number of six superparticles per cell guarantees at least a rough approximation to the Maxwellian distribution function of the H^+ component. Other codes, such as the model presented by Modolo *et al.* [108], currently use only two particles per cell for the N^+ component.

Nevertheless, the concept presented above is inappropriate for modelling a two-component upstream flow when the density ratio of the two species does not fulfill the condition

$$\frac{n_2}{n_1} \approx 1 \quad . \tag{B.15}$$

For instance, the solar wind consists to 95% of protons and to only 5% of helium particles [83, 132]. Realizing such a number density ratio requires a number of 19 superparticles for hydrogen, when only a single helium superparticle is placed in each cell of the simulation grid at the same time. Apart from the fact that currently, no computer memory is able to administrate such a huge number of particles, the statistical representation of the helium component would be rather bad: A lower limit for the number of helium macroparticles per cell arises from the necessity to include an adequate representation of the Maxwellian distribution function.

A possible solution of this problem will be presented in the following. Without losing generality, it is assumed that the number density of species 1 is significantly larger than that of the second species, i.e.

$$n_1 \gg n_2 \quad . \tag{B.16}$$

Since in the framework of this thesis, only the case of single-charged ions has been studied, the charge of a species 2 ion is again set to a value of $q_2 = e$. Applying the multi-species model to the He^{++} component of the solar wind necessitates only minor modifications of the procedure.

In the previous discussion, the parameters $N_{SP,1}$ and $N_{SP,2}$ were assumed to be identical. The basic idea for the modifications is to split up the superparticles of species 2 into smaller ones, i.e. the number of real ions represented by a type 2 superparticle is reduced. This process maintains the macroscopic densities of species 2, i.e. the same values of n_2, $\rho_{m,2}$ and $\rho_{c,2}$ are now realized by a *larger* number of species 2 superparticles per cell, each of them representing a *smaller* number of real ions than before. Since each superparticle is assigned a velocity vector independently of the others, this procedure guarantees an adequate reproduction of the distribution function for species 2.

It is assumed that the parameters for the second species have already been chosen according to eqs. (B.7) to (B.10), i.e. the difference in the plasma densities is modeled by choosing a relatively large value for $N_{ppc,1}$ and only a small value for the number $N_{ppc,2}$ of species 2 superparticles per cell. The parameters of the second species are now modified as follows:

$$\tilde{N}_{ppc,2} = \eta N_{ppc,2} \quad ; \tag{B.17}$$

$$\tilde{M}_{SP,2} = \frac{1}{\eta} M_{SP,2} \quad ; \tag{B.18}$$

$$\tilde{Q}_{SP,2} = \frac{1}{\eta} Q_{SP,2} \quad , \tag{B.19}$$

where $\eta \in \mathbb{Z}_{>0}$ is a scaling parameter. The last equation yields

$$\tilde{N}_{SP,2} = \frac{\tilde{Q}_{SP,2}}{e} = \frac{1}{\eta}\frac{Q_{SP,2}}{e} = \frac{1}{\eta} N_{SP,2} \tag{B.20}$$

for the number $\tilde{N}_{SP,2}$ of ions that are merged to one superparticle. Obviously, the charge-to-mass ratio of the second species is not affected by the modifications:

$$\frac{\tilde{Q}_{SP,2}}{\tilde{M}_{SP,2}} = \frac{Q_{SP,2}}{M_{SP,2}} \quad . \tag{B.21}$$

Moreover, the modified parameters for species 2 yield the same macroscopic plasma quantities as the original ones:

- Number density:

$$\tilde{n}_2 = \frac{\tilde{N}_{ppc,2} \cdot \tilde{N}_{SP,2}}{V_g} = \frac{N_{ppc,2} \cdot N_{SP,2}}{V_g} = n_2 \quad , \tag{B.22}$$

- Mass density:

$$\tilde{\rho}_{m,2} = \frac{\tilde{N}_{ppc,2} \cdot \tilde{M}_{SP,2}}{V_g} = \frac{N_{ppc,2} \cdot M_{SP,2}}{V_g} = \rho_{m,2} \quad , \tag{B.23}$$

- Charge density:

$$\tilde{\rho}_{c,2} = \frac{\tilde{N}_{ppc,2} \cdot \tilde{Q}_{SP,2}}{V_g} = \frac{N_{ppc,2} \cdot Q_{SP,2}}{V_g} = \rho_{c,2} \quad . \tag{B.24}$$

Thus, the two different ways of representing species 2 by macroparticles are completely equivalent.

In the following, a concrete example will be discussed. The mass of a species 2 ion is assumed to be about a factor of $\mu = m_2/m_1 = 2$ larger than the mass of a species 1 particle, whereas the number density of species 2 is given by

$$n_2 = \frac{1}{20} n_1 \quad . \tag{B.25}$$

The charge of both species is given by $q_1 = q_2 = +e$. Such a plasma flow could for instance be included in the model by setting $N_{ppc,1} = 20$ and $N_{ppc,2} = 1$ or, on the other hand, by setting $N_{ppc,1} = 8$ and choosing a (hypothetical) value of $N_{ppc,2} = 0.4$ for the second species. Referring to the latter set of parameters, a value of $\eta = 10$ is now chosen for the scaling factor. Hence, the parameters of the second species can be expressed as

$$\tilde{N}_{ppc,2} = 4 = \frac{1}{2} N_{ppc,1} \quad ; \tag{B.26}$$

$$\tilde{N}_{SP,2} = \frac{1}{10} N_{SP,2} = \frac{1}{10} N_{SP,1} \quad ; \tag{B.27}$$

$$\tilde{M}_{SP,2} = \frac{1}{10} M_{SP,2} = \frac{2}{10} M_{SP,1} \qquad (\mu = 2) \quad ; \tag{B.28}$$

$$\tilde{Q}_{SP,2} = \frac{1}{10} Q_{SP,2} = \frac{1}{10} Q_{SP,1} \quad . \tag{B.29}$$

This yields the correct macroscopic densities:

- Number density:

$$n_2 = \frac{\tilde{N}_{ppc,2} \cdot \tilde{N}_{SP,2}}{V_g} = \frac{1}{20} \frac{N_{ppc,1} \cdot N_{SP,1}}{V_g} = \frac{1}{20} n_1 \quad , \tag{B.30}$$

- Mass density:

$$\rho_{m,2} = \frac{\tilde{N}_{ppc,2} \cdot \tilde{M}_{SP,2}}{V_g} = \frac{1}{10} \frac{N_{ppc,1} \cdot M_{SP,1}}{V_g} = \frac{1}{10} \rho_{m,1} \quad , \tag{B.31}$$

- Charge density:

$$\rho_{c,2} = \frac{\tilde{N}_{ppc,2} \cdot \tilde{Q}_{SP,2}}{V_g} = \frac{1}{20} \frac{N_{ppc,1} \cdot Q_{SP,1}}{V_g} = \frac{1}{20} \rho_{c,1} \quad . \tag{B.32}$$

It is interesting to notice that in the initial parameter set $(N_{ppc,1}, N_{ppc,2})$, which is modified by the parameter η, the particle number of species 2 does not have to be integer. Of course, η has to be chosen in the way that the final values $(N_{ppc,1}, \tilde{N}_{ppc,2})$, which are used in the simulation code, are integers. For the simulation runs presented in chapter 9, the number density ratio was set to a value of $n_2/n_1 = 1/1000$. The corresponding parameters for the generation of the superparticles have been set to $N_{ppc,1} = 8$, $N_{ppc,2} = 0.008$ or, as used in the code, $N_{ppc,1} = 8$, $\tilde{N}_{ppc,2} = 4$ and $\eta = 500$. Evidently, the statistical representation of the minor component is still worse than that of the primary constituent. However, since the electromagnetic field topology is almost exclusively determined by the dynamics of the major component, a high number of species 1 superparticles – at least 6 to 8 particles per cell – is required in order to obtain a ”smooth” solution of the field equations. Currently, a personal computer cannot handle more than a total number of 18 to 20 particles per cell. With respect to these problems, the statistical representation of the minor component is only of subordinate priority. This is valid for the multi-species Titan simulations as well. Nonetheless, in view of recent advances in parallel computing technology, the author remains confident that this obstacle will be overcome in the near future.

A generalization of the concepts presented above to the case of three or more upstream species can be realized in an analogous manner. A possible improvement of the technique discussed in this section is suggested by Kallio *et al.* [70, 71, 72, 73]. Their studies of the Martian plasma environment have been carried out by means of a hybrid code that allows to locally enhance the spatial resolution by dividing the cells in a certain region into smaller ones. The particle administration in this code is based on a technique that allows a dynamical merging and splitting of superparticles into larger or smaller ones while the simulation proceeds. Incorporating such an algorithm into the Titan code presented in this work is planned for the near future.

2 Current Advancement Method

As stated in chapter 3, the hybrid code presented by Bagdonat [7] computes the electric field by means of the Current Advancement Method developed by Matthews [103]. As an extensive discussion of this technique can be found in both works, the following discussion will not dwell on the details of the algorithm. Instead, only a short overview of the modifications that were necessary for incorporating a second upstream species into the original code will be given. Again, the discussion refers to an equidistant Cartesian grid. The upstream plasma flow is assumed to consist of single-charged particles.

According to Bagdonat [7], the quantities

$$\Lambda_{q,r,s} = e^2 \sum_{\nu} \frac{1}{m_\nu} \mathcal{W}\left(\underline{x}_\nu, \underline{r}_{q,r,s}\right) \tag{B.33}$$

and

$$\underline{\Gamma}_{q,r,s} = e^2 \sum_{\nu} \frac{1}{m_\nu} \underline{v}_\nu \mathcal{W}\left(\underline{x}_\nu, \underline{r}_{q,r,s}\right) \tag{B.34}$$

play a key role in computing the updated electric field vector at each grid point. The notation, especially the meaning of the subscripts, has been introduced in section 7.2 of chapter 3. The weighting factors of the Cloud-in-Cell procedure are again denoted by $\mathcal{W}\left(\underline{x}_\nu, \underline{r}_{q,r,s}\right)$. In order to realize homogeneous plasma conditions at the inflow boundaries of the simulation box, adequate boundary values have to be chosen for these parameters. For simplicity, the subscripts q, r, s will be suppressed in the following.

For an upstream plasma flow that is made up of only a single species, the boundary values Λ_1 and $\underline{\Gamma}_1$ can be expressed by means of the homogeneous number density n_1 and the current density

$$\underline{j}_1 = n_1 e \underline{u}_1 \quad , \tag{B.35}$$

where $\underline{u}_1$ denotes the homogeneous macroscopic upstream flow velocity. Incorporating these quantities into eqs. (B.33) and (B.34) and using eqs. (3.118) and (3.119) yields

$$\Lambda_1 = \frac{e^2}{m_1} V_g n_1 \tag{B.36}$$

for the first parameter. The second one, $\underline{\Gamma}_1$, can be written as

$$\underline{\Gamma}_1 = \frac{e^2}{m_1} \frac{V_g}{e} \underline{j}_1 = \frac{e^2 V_g}{m_1} n_1 \underline{u}_1 \quad . \tag{B.37}$$

If a second upstream species is incorporated into the model, the boundary value Λ_1 has to be replaced by Λ_{1+2} in the following way:

$$\begin{aligned} \Lambda_{1+2} &= e^2 \sum_\nu \frac{1}{m_\nu} \mathcal{W}_\nu \\ &= e^2 \left\{ \frac{1}{m_1} \sum_1 \mathcal{W}_\nu + \frac{1}{m_2} \sum_2 \mathcal{W}_\nu \right\} \\ &= e^2 \left\{ \frac{1}{m_1} V_g n_1 + \frac{1}{m_2} V_g n_2 \right\} \\ &= \frac{e^2}{m_1} V_g n_1 \left\{ 1 + \frac{1}{\mu} \frac{n_2}{n_1} \right\} \\ &= \Lambda_1 \left\{ 1 + \frac{1}{\mu} \frac{n_2}{n_1} \right\} \quad , \end{aligned} \tag{B.38}$$

where $\mathcal{W}_\nu \equiv \mathcal{W}\left(\underline{x}_\nu, \underline{r}_{q,r,s}\right)$. The symbol $\sum_1$ denotes a sum over the weighting factors of all species 1 particles in the respective grid cell. In analogy, the sum over all species 2 particles is referred to as $\sum_2$. Thus, the original boundary value Λ_1 has to be modified by introducing a scaling parameter

$$\xi \equiv 1 + \frac{1}{\mu} \frac{n_2}{n_1} \quad , \tag{B.39}$$

including the relative particle mass μ and the ratio of the two upstream densities. The modified boundary parameter $\underline{\Gamma}_{1+2}$ can be derived in the same way:

$$\begin{aligned}
\underline{\Gamma}_{1+2} &= e^2 \sum_{\nu} \frac{1}{m_\nu} \underline{v}_\nu \mathcal{W}_\nu \\
&= e^2 \left\{ \frac{1}{m_1} \sum_{1} \underline{v}_\nu \mathcal{W}_\nu + \frac{1}{m_2} \sum_{2} \underline{v}_\nu \mathcal{W}_\nu \right\} \\
&= e^2 \left\{ \frac{1}{m_1} \frac{V_g}{e} \underline{j}_1 + \frac{1}{m_2} \frac{V_g}{e} \underline{j}_2 \right\} \\
&= \frac{eV_g}{m_1} n_1 e \underline{u}_1 + \frac{eV_g}{m_2} n_2 e \underline{u}_2 \\
&= \frac{eV_g}{m_1} n_1 e \underline{u}_1 + \frac{eV_g}{m_2} n_2 e \underline{u}_1 \\
&= \frac{e^2 V_g}{m_1} n_1 \underline{u}_1 \left\{ 1 + \frac{1}{\mu} \frac{n_2}{n_1} \right\} \\
&= \xi \underline{\Gamma}_1 \quad .
\end{aligned} \tag{B.40}$$

Hence, the background value for $\underline{\Gamma}$ has to be modified in the same way as Λ. Note that the discussion is based on the assumption of equal macroscopic upstream velocities for both species:

$$\underline{u}_1 = \underline{u}_2 \quad . \tag{B.41}$$

If the ions of the second species are not single-charged, but their charge is given by

$$q_2 = Ze \quad , \quad Z \in \{2, 3, \ldots\} \quad , \tag{B.42}$$

and if a difference between the absolute values of the two upstream velocities must be taken into consideration as well,

$$\underline{u}_1 \parallel \underline{u}_2 \qquad u_2 = U u_1 \quad , \quad U \in \mathbb{R}_{>0} \quad , \tag{B.43}$$

the scaling factor ξ in eq. (B.38) differs from that in eq. (B.40). In the first equation,

$$\xi_\Lambda \equiv 1 + \frac{Z^2}{\mu} \frac{n_2}{n_1} \quad . \tag{B.44}$$

has to be introduced, whereas

$$\xi_{\underline{\Gamma}} \equiv 1 + \frac{Z^2 U}{\mu} \frac{n_2}{n_1} \quad . \tag{B.45}$$

has to be incorporated into the expression for $\underline{\Gamma}_{1+2}$.

It should be noted that deriving an analogous set of boundary conditions for particles of ionospheric origin is not necessary, for these particles are neither present at the beginning of a simulation run, nor are they generated at the outer faces of the simulation domain according to certain homogeneous background values.

Appendix C

Multi-species simulation code: Input parameters

This section gives an overview of the basic input parameters that are required for performing simulations with a multi-species upstream flow and a multi-species ionosphere. In general, all quantities are normalized with respect to certain background values that are defined by one of the two upstream species. In the following, this upstream species will be called the *primary species* or the *reference species*. In the "standard" Titan simulations, atomic nitrogen has been used as the reference species, whereas the magnetospheric hydrogen component has been treated as the second species.

1 Two upstream species

As discussed in the previous chapter, the ion species included in the model are represented by superparticles. The number of superparticles initially placed in the smallest cell of the simulation gird has to be defined in the input parameter file. For the case of an equidistant Cartesian grid, the number of superparticles generated at the beginning of a simulation run is the same for each grid cell.

```
#define  N_PPC_1          8

#define  N_PPC_2          4

#define  ETA_SPLIT      500
```

The first parameter defines the number $N_{ppc,1}$ of superparticles for the primary species, while `N_PPC_2` represents the value $\tilde{N}_{ppc,2}$ for the second species. The scaling parameter η has been defined in the preceding chapter. For the set of parameters given above, the number density of the second species is about a factor of 1000 smaller than that of the primary component. This setting has been used for the analysis of multi-ion shocks presented in chapter 9. In most of the Titan simulations, the density ratio of $n(N^+)/n(H^+) = 2:1$ has simply been represented by the numbers of superparticles themselves, i.e. $N_{ppc,1} = 2N_{ppc,2}$ and $\eta = 1$. In such a configuration, superparticles of both upstream species represent the same number of real ions.

Besides, the following parameters have to be defined for the second upstream species:

```
#define  UPSTREAM_MASS_2   (1.0/14.0)

#define  REL_DENSITY        (1.0/2.0)

#define  LAMGAMFAK         (1.0+ REL_DENSITY/UPSTREAM_MASS_2)
```

The first parameter defines the mass of the secondary upstream component *with respect to the primary ion mass*. Thus, in the "standard" Titan scenario, a value of $m(H^+)/m(N^+) = 1/14$ has to be chosen. The second input parameter denotes the relative number density of the additional upstream species. The third parameter is the scaling factor ξ that has to be incorporated into the Current Advancement Method, as discussed in appendix B. This parameter can be globally defined in the input parameter file. However, it is important to notice that currently, the modifications of the Current Advancement Method are only valid for the case of single-charged ions.

In the internal notation of the simulation code, the upstream species are denoted by even subscripts $(0, 2, 4, \ldots)$, while odd subscripts $(1, 3, 5, \ldots)$ are used to discriminate between different species of ionospheric origin. According to the discussion in appendix B, the mass and the charge of a type 2 superparticle have to be derived from the values of the primary species (subscript 0) in the following manner:

```
SP_CHARGE[2]=(1.0/ETA_SPLIT)*SP_CHARGE[0];

SP_MASS[2]=(1.0/ETA_SPLIT)*UPSTREAM_MASS_2*SP_MASS[0];
```

The plasma betas of the two upstream species have to be defined in the parameter file as well:

```
#define  BETA         (9.00)   // primary species

#define  BETA_2       (0.50)   // secondary species
```

In the same way, the plasma betas of the corresponding electron populations have to be defined:

```
#define  BETA_E        (0.3)    // primary species

#define  BETA_E_2      (0.3)    // secondary species
```

While the electron betas occur only in the adiabatic laws, the plasma betas of the ion components also determine their thermal velocities,

$$v_{th} = \sqrt{\frac{3kT}{m}} \quad . \tag{C.1}$$

The ion betas are required in the code, because the thermal velocities are defined with respect to the Alfvén velocity of the primary upstream component. The *normalized* thermal velocity

$\tilde{v}_{th,1}$ of the primary component can be expressed as follows:

$$\tilde{v}_{th,1}^2 = \left(\frac{v_{th,1}}{v_A}\right)^2 = \frac{3kT_1}{m_1}\frac{\mu_0 n_1 m_1}{B_0^2} = \frac{3}{2}\beta_1 \quad . \tag{C.2}$$

However, for the second species, an additional scaling factor has to be introduced:

$$\tilde{v}_{th,2}^2 = \frac{3kT_2}{m_2}\frac{\mu_0 n_1 m_1}{B_0^2} = \frac{3kT_2}{m_2}\frac{\mu_0 n_1 m_1}{B_0^2}\frac{n_2 m_2}{n_2 m_2} = \frac{3}{2}\beta_2\,\frac{n_1 m_1}{n_2 m_2} \quad . \tag{C.3}$$

Thus, in the simulation code, the mass density ratio of the two upstream species,

$$\frac{\rho_{m,2}}{\rho_{m,1}} = \frac{n_1 m_1}{n_2 m_2} \tag{C.4}$$

must be included in the definition of the thermal velocity for the second species. In the parameter file, the quantities given in eqs. (C.2)-(C.4) are defined as follows:

```
#define  v2mean        (3./2.*BETA)

#define  CORR           (28.0)         //mass density ratio

#define  v2mean_2      (3./2.*BETA_2*CORR)
```

The following section deals with the boundary conditions that do not only have to be assigned to the outer faces of the simulation box, but also represent the homogeneous ambient plasma flow at the beginning of each simulation run.

2 Boundary conditions

The homogeneous background parameters are defined in the parameter file by using the density ratio n_2/n_1 introduced in the preceding section:

```
float  rhobound[3]={(1.0+REL_DENSITY),0.,0.};

float  rhobound_b[3]={1.0,0.,0.};

float  rhobound_c[3]={(REL_DENSITY),0.,0.};
```

The first parameter represents to total upstream number density with respect to the ambient density of the primary species. The parameter `rhobound_b` denotes the ambient density of the primary species, whereas `rhobound_c` is the normalized background density of the additional upstream species.

Applying the Current Advancement Method to a multi-species upstream flow requires the incorporation of the following parameters into the input file:

```
float  Jbound[3]=
       {(1.0+REL_DENSITY)*UX0,(1.0+REL_DENSITY)*UY0,(1.0+REL_DENSITY)*UZ0};

float  Lambound[3]={LAMGAMFAK,0.,0.};

float  Gambound[3]={LAMGAMFAK*UX0,LAMGAMFAK*UY0,LAMGAMFAK*UZ0};
```

The first parameter represents the total current density of the upstream flow. Note that the upstream flow speeds of both species are assumed to be equal. The parameters `UX0`, `UY0` and `UZ0` denote the three components of the upstream velocity $\underline{u}_0$, as introduced in appendix A. The last two parameters represent the boundary values for Λ and $\underline{\Gamma}$ in the Current Advancement Method.

3 Multi-species ionosphere

In most of the multi-species simulations carried out for this work, a rather simple approach has been applied to Titan's ionosphere, assuming the production rates of the three ionospheric species to be equal. Therefore, only very few new input parameters had to be introduced for realizing a multi-component ionosphere. On the one hand, the masses of the three ionospheric species have to be defined, again with respect to the mass of the primary upstream species (atomic nitrogen, $m(N^+) = 14\,\text{amu}$):

```
#define  TITAN_ION_MASS_1      (2.0)         // molecular nitrogen

#define  TITAN_ION_MASS_2      (16.0/14.0)   // methane

#define  TITAN_ION_MASS_3      (2.0/14.0)    // molecular hydrogen
```

On the other hand, the number of ionospheric superparticles *globally* generated in each time step has to be defined:

```
#define  TITAN_N_1            150          // molecular nitrogen

#define  TITAN_N_2            150          // methane

#define  TITAN_N_3            150          // molecular hydrogen
```

A more detailed discussion of the properties of the ionospheric superparticles is given by Bagdonat [7]. The author also explains how the number of real ions represented by an ionospheric superparticle can be inferred. As stated in chapter 3, the temperature of newly generated ionospheric ions is set to $kT = 0$.

List of Figures

List of Tables

Bibliography

[1] N. Achilleos, C. Bertucci, C. T. Russell, G. B. Hospodarsky, A. M. Rymer, C. S. Arridge, M. E. Burton, M. K. Dougherty, S. Hendricks, E. J. Smith, and B. T. Tsurutani. Orientation, location, and velocity of Saturn's bow shock: Initial results from the Cassini spacecraft. *J. of Geophysical Research*, 111:A03201 (doi:10.1029/2005JA011297), 2006.

[2] M. H. Acuna, P. Wasilewski, G. Kletetshka, C. T. Russell, B. J. Anderson, L. Zanetti, and N. Omidi. Near magnetic field observations at 433 Eros: First measurements from the surface of an asteroid. *Icarus*, 155:220–228, 2002.

[3] A. Amsif, J. Dandouras, and E. C. Roelof. Modelling the production and the imaging of energetic neutral atoms from Titan's exosphere. *J. of Geophysical Research*, 102(A10):22,169–22,181, 1997.

[4] D. H. Atkinson, B. Kazeminejad, V. Gaborit, F. Ferri, and J. P. Lebreton. Huygens probe entry and descent trajectory analysis and reconstruction techniques. *Planet. Space Sci.*, 53(5):586–593, 2005.

[5] H. Backes. *Titan's Interaction with the Saturnian Magnetospheric Plasma*. PhD thesis, Universität zu Köln, 2005.

[6] H. Backes, F. M. Neubauer, M. K. Dougherty, N. Achilleos, N. André, C. S. Arridge, C. Bertucci, G. H. Jones, K. K. Khurana, C. T. Russell, and A. Wennmacher. Titan's Magnetic Field Signature During the First Cassini Encounter. *Science*, 308(5724):992–995, 2005.

[7] T. Bagdonat. *Hybrid Simulation of Weak Comets*. PhD thesis, Technische Universität Braunschweig, 2005.

[8] T. Bagdonat and U. Motschmann. 3d hybrid simulation of solar wind interaction with comets. In J. Büchner, C.T. Dum, and M. Scholer, editors, *Space Plasma Simulation - Proceedings of the Sixth International School/ Symposium ISSS-6*, pages 80–83, 2001.

[9] T. Bagdonat and U. Motschmann. 3D Hybrid Simulation Code Using Curvilinear Coordinates. *J. of Computational Physics*, 183:470–485, 2002.

[10] T. Bagdonat and U. Motschmann. From a weak to a strong comet – 3D global hybrid simulation studies. *Earth, Moon and Planets*, 90:305–321, 2002.

[11] T. Bagdonat, U. Motschmann, K.-H. Glassmeier, and E. Kührt. Plasma environment of comet Churyumov-Gerasimenko – 3D hybrid code simulations. In L. Colangeli, E. Mazzotta Epifani, and P. Palumbo, editors, *ASSL Vol. 311: The New Rosetta Targets. Observations, Simulations and Instrument Performances*, pages 153–157, October 2004.

[12] S. J. Bauer. *Physics of Planetary Ionospheres*, volume 6 of *Physics and Chemistry in Space*. Springer-Verlag, Berlin, Heidelberg, New York, 1973.

[13] S. J. Bauer and H. Lammer. *Planetary Aeronomy: Atmosphere Environments in Planetary Systems*. Springer-Verlag, Berlin, Heidelberg, New York, 2004.

[14] K. Baumgärtel, K. Sauer, and A. Bogdanov. A Magnetohydrodynamic Model of Solar Wind Interaction with Asteroid Gaspra. *Science*, 263:653–655, 1994.

[15] K. Baumgärtel, K. Sauer, and T. R. Story. Comment on "the whistler-mode bow wave of an asteroid" by D. A. Gurnett. *J. of Geophysical Research*, 101(A11):24,495–24,498, 1996.

[16] K. Baumgärtel, K. Sauer, T. R. Story, and J. F. McKenzie. Solar wind response to a magnetized asteroid: Linear theory. *Icarus*, 129(1):94–105, 1997.

[17] W. Baumjohann and R. A. Treumann. *Basic space plasma physics*. Imperial College Press, London, 1999.

[18] C. Bertucci, C. Mazelle, D. H. Crider, D. Vignes, M. H. Acuña, D. L. Mitchell, R. P. Lin, J. E. P. Connerney, H. Rème, P. A. Cloutier, N. F. Ness, and D. Winterhalter. Magnetic field draping enhancement at the Martian magnetic pileup boundary from Mars global surveyor observations. *Geophysical Research Letters*, 30(2):71 (1–4), CiteID: 1099, doi: 10.1029/2002GL015713, 2003.

[19] C. Bertucci, C. Mazelle, J. A. Slavin, C. T. Russell, and M. H. Acuña. Magnetic field draping enhancement at Venus: Evidence for a magnetic pileup boundary. *Geophysical Research Letters*, 30(17):SSC 1 (1–4), CiteID: 1876, doi: 10.1029/2003GL017271, 2003.

[20] C. K. Birdsall and A. B. Langdon. *Plasma Physics via Computer Simulation*. McGraw-Hill Book Company, New York, 1985.

[21] J. A. Bittencourt. *Fundamentals of Plasma Physics*. Springer-Verlag, New York, third edition, 2004.

[22] M. Blanc, S. Bolton, J. Bradley, M. Burton, T. E. Cravens, I. Dandouras, M. K. Dougherty, M. C. Festou, J. Feynman, R. E. Johnson, T. G. Gombosi, W. S. Kurth, P. C. Liewer, B. H. Mauk, S. Maurice, D. Mitchell, F. M. Neubauer, J. D. Richardson, D. E. Shemansky, E. C. Sittler, B. T. Tsurutani, P. Zarka, L. W. Esposito, E. Grün, D. A. Gurnett, A. J. Kliore, S. M. Krimigis, D. Southwood, J. H. Waite, and D. T. Young. Magnetospheric and Plasma Science with Cassini-Huygens. *Space Science Reviews*, 104:253–346 (doi:10.1023/A:1023605110711), 2002.

[23] X. Blanco-Cano, N. Omidi, and C. T. Russel. Hybrid simulations of solar wind interaction with magnetized asteroids: Comparison with Galileo observations near Gaspra and Ida. *J. of Geophysical Research*, 105(A5):11,1–11,13, 2003.

[24] X. Blanco-Cano, N. Omidi, and C. T. Russell. Magnetospheres: How to make a magnetosphere. *Astronomy and Geophysics*, 45(3):3.14–3.17, 2004.

[25] A. T. Bogdanov, K. H. Glassmeier, and U. Motschmann. From comets to planetary satellites: specific problems in 3D bi-ion fluid simulations of Titan's plasma environment. In Copernicus-Gesellschaft, editor, *Proceedings of ISSS-6*. 2001.

[26] A. Bößwetter. Plasma-Grenzschichten am Mars – Eine 3D-Simulationsstudie. Master's thesis, Technische Universität Braunschweig, 2004.

[27] A. Bößwetter, T. Bagdonat, U. Motschmann, and K. Sauer. Plasma boundaries at Mars: A 3D simulation study. *Ann. Geophys.*, 22(12):4363–4379, 2004.

[28] S. H. Brecht and J. R. Ferrante. Global hybrid simulation of unmagnetized planets – Comparison of Venus and Mars. *J. of Geophysical Research*, 96:11,209–11,220, 1991.

[29] S. H. Brecht, J. R. Ferrante, and J. G. Luhmann. Three-dimensional simulations of the solar wind interaction with Mars. *J. of Geophysical Research*, 98(A2):1345–1357, 1993.

[30] S. H. Brecht, J. G. Luhmann, and D. J. Larson. Simulation of the Saturnian magnetospheric interaction with Titan. *J. of Geophysical Research*, 105(A6):13,119–13,130, 2000.

[31] T. K. Breus, E. M. Dubinin, A. M. Krymskii, R. Lundin, and J. G. Luhmann. The solar wind interaction with Mars – Consideration of Phobos 2 mission observations of an ion composition boundary on the dayside. *J. of Geophysical Research*, 96:11165–11174, 1991.

[32] F. Cap. *Lehrbuch der Plasmaphysik und Magnetohydrodynamik.* Springer-Verlag, Berlin/ Heidelberg/ New York, 1994.

[33] L. A. Capone, R. C. Whitten, J. Dubach, S. S. Prasad, and W. T. Huntress, Jr. The lower ionosphere of Titan. *Icarus*, 28:367–378, 1976.

[34] A. J. Coates. Ion pickup at comets. *Advances in Space Research*, 33:1977–1988, 2004.

[35] A. J. Coates, N. André, H. J. McAndrews, F. J. Crary, D. T. Young, T. W. Hill, K. Szegö, Z. Bebesi, and A. Eviatar. Plasma structure during the 26 December 2005 Titan (T9) encounter: electron results. Presentation at 32th CAPS team meeting, Budapest, Hungary, April 10-12, 2006.

[36] J. Comas Solà. Observations des satellites principaux de Jupiter et de Titan. *Astronomische Nachrichten*, 179:289, 1909.

[37] R. Courant, K. Friedrichs, and H. Lewy. Über die partiellen Differenzgleichungen der mathematischen Physik. *Math. Ann.*, 100:32–74, 1928.

[38] F. J. Crary, R. Baragiola, A. J. Coates, A. Eviatar, T. W. Hill, R. E. Johnson, K. Szegö, and D. T. Young. Ion flows and composition in Titan's wake: Ion measurements from the December 26 Cassini encounter. Presentation at the European Geosciences Union General Assembly, Vienna, Austria, 2–7 April 2006, and at the 32th CAPS team meeting, Budapest, Hungary, 10–12 April 2006 .

[39] T. E. Cravens, C. J. Lindgren, and S. A. Ledvina. A two-dimensional multifluid MHD model of Titan's plasma environment. *Planet. Space Sci.*, 46(9/10):1193–1205, 1998.

[40] T. E. Cravens, I. P. Robertson, J. Clark, J.-E. Wahlund, J. H. Waite Jr., S. A. Ledvina, H. B. Niemann, R. V. Yelle, W. T. Kasprzak, J. G. Luhmann, R. L. McNutt, W.-H. Ip, V. De La Haye, I. Müller-Wodarg, D. T. Young, and A. J. Coates. Titan's ionosphere: Model comparisions with Cassini TA data. *Geophysical Research Letters*, 32:L12108(1–5), 2005.

[41] T. E. Cravens, J. Vann, J. Clark, J. Yu, C. N. Keller, and C. Brull. The ionosphere of Titan: an updated theoretical model. *Advances in Space Research*, 33:212–215 (doi:10.1016/j.asr.2003.02.012), 2004.

[42] Z. Dobe and K. Szegö. Wave activity above the ionosphere of Titan: Predictions for the Cassini mission. *J. of Geophysical Research*, 110(A9):A03224(1–13), doi:10.1029/2004JA010548, 2005.

[43] Z. Dobe, K. Szego, K. B. Quest, V. D. Shapiro, R. E. Hartle, and E. C. Sittler Jr. Nonlinear evolution of modified two-stream instability above ionosphere of Titan: Comparison with the data of the Cassini Plasma Spectrometer . *J. of Geophysical Research*, 112:A 03203 (1–18), doi: 10.1029/2006JA011770, 2007.

[44] M. K. Dougherty, S. Kellock, D. J. Southwood, A. Balogh, E. J. Smith, B. T. Tsurutani, B. Gerlach, K.-H. Glassmeier, F. Gleim, C. T. Russell, G. Erdos, F. M. Neubauer, and S. W. H. Cowley. The Cassini Magnetic Field Investigation. *Space Science Reviews*, 114:331–383, doi:10.1007/s11214–004–1432–2, 2004.

[45] M. K. Dougherty, K. K. Khurana, F. M. Neubauer, C. T. Russell, J. Saur, J. S. Leisner, and M. E. Burton. Identification of a Dynamic Atmosphere at Enceladus with the Cassini Magnetometer. *Science*, 311:1406–1409, 2006.

[46] C. Elachi, S. Wall, M. Allison, Y. Anderson, R. Boehmer, P. Callahan, P. Encrenaz, E. Flamini, G. Franceschetti, Y. Gim, G. Hamilton, S. Hensley, M. Janssen, W. Johnson, K. Kelleher, R. Kirk, R. Lopes, R. Lorenz, J. Lunine, D. Muhlemann, S. Ostro, F. Paganelli, G. Picardi, F. Posa, L. Roth, R. Seu, S. Shaffer, L. Soderblom, B. Stiles, E. Stofan, S. Vetrella, R. West, C. Wood, L. Wye, and H. Zebker. Cassini Radar Views the Surface of Titan. *Science*, 308(5724):970–974, 2005.

[47] A. Eviatar and J. D. Richardson. Corotation of the Kronian magnetosphere. *J. of Geophysical Research*, 91(A3), 1986.

[48] F. M. Flasar, R. K. Achterberg, B. J. Conrath, P. J. Gierasch, V. G. Kunde, C. A. Nixon, G. L. Bjoraker, D. E. Jennings, P. N. Romani, A. A. Simon-Miller, B. Bézard, A. Coustenis, P. G. Irwin, N. A. Teanby, J. Brasunas, J. C. Pearl, M. E. Segura, R. C. Carlson, A. Mamoutkine, P. J. Schinder, A. Barucci, R. Courtin, T. Fouchet, D. Gautier, E. Lellouch, A. Marten, R. Prangé, S. Vinatier, D. F. Strobel, S. B. Calcutt, P. L. Read, F. W. Taylor, N. Bowles, R. E. Samuelson, G. S. Orton, L. J. Spilker, T. C. Owen, J. R. Spencer, M. R. Showalter, C. Ferrari, M. M. Abbas, F. Raulin, S. Edgington, P. Ade, and E. H. Wishnow. Titan's Atmospheric Temperatures, Wind and Composition. *Science*, 308(5724):975–978, 2005.

[49] L. Gan, C. N. Keller, and T. E. Cravens. Electrons in the Ionosphere of Titan. *J. of Geophysical Research*, 97(A8):12,137–12,151, 1992.

[50] P. Garnier, I. Dandouras, D. Toublanc, P. C. Brandt, E. C. Roelof, D. G. Mitchell, S. M. Krimigis, N. Krupp, D. C. Hamilton, and H. Waite. The exosphere of Titan and its interaction with the kronian magnetosphere: MIMI observations and modeling. *Planet. Space Sci.*, 55:165–173, 2007.

[51] G. Giampieri and M. K. Dougherty. Rotation rate of Saturn's interior from magnetic field observations. *Geophysical Research Letters*, 31:L16701 (1–4), doi:10.1029/2004GL020194, 2004.

[52] R. Goldston and P. Rutherford. *Plasmaphysik – Eine Einführung*. Friedrich Vieweg & Sohn Verlagsgesellschaft mbH, Braunschweig/Wiesbaden, 1998.

[53] T. I. Gombosi and K. C. Hansen. Saturn's Variable Magnetosphere. *Science*, 307(5713):1224–1226, 2005.

[54] E. W. Greenstadt. Conditions for Magnetic Interaction of Asteroids with the Solar Wind. *Icarus*, 14:374–381, 1971.

[55] D. A. Gurnett. On a remarkable similarity between the propagation of whistlers and the bow wave of a ship. *Geophysical Research Letters*, 22(14):1865–1868, 1995.

[56] D. A. Gurnett. The whistler-mode bow wave of an asteroid. *J. of Geophysical Research*, 100(A11):21,623–21,629, 1995.

[57] D. A. Gurnett, F. L. Scarf, and W. S. Kurth. The Structure of Titan's Wake From Plasma Wave Observations. *J. of Geophysical Research*, 87(A3):1395–1403, 1982.

[58] K. C. Hansen, T. I. Gombosi, D. L. Dezeeuw, C. P. T. Groth, and K. G. Powell. A 3D Global MHD Simulation of Saturn's Magnetosphere. *Advances in Space Research*, 26:1681–1690, 2000.

[59] K. C. Hansen, A. J. Ridley, G. B. Hospodarsky, N. Achilleos, M. K. Dougherty, T. I. Gombosi, and G. Tóth. Global MHD simulations of Saturn's magnetosphere at the time of Cassini approach. *Geophysical Research Letters*, 32(20):L20S06 (doi:10.1029/2005GL022835), 2005.

[60] R. E. Hartle, E. C. Sittler, F. M. Neubauer, R. E. Johnson, H. T. Smith, F. Crary, D. J. McComas, D. T. Young, A. J. Coates, D. Simpson, S. Bolton, D. Reisenfeld, K. Szego, J. J. Berthelier, A. Rymer, J. Vilppola, J. T. Steinberg, and N. Andre. Preliminary interpretation of Titan plasma interaction as observed by the Cassini Plasma Spectrometer: Comparisons with Voyager 1. *Geophysical Research Letters*, 33(8):L08201 (1–5), doi:10.1029/2005GL024817, 2006.

[61] R. E. Hartle, E. C. Sittler, K. W. Oglivie, J. D. Scudder, A. J. Lazarus, and S. K. Atreya. Titan's Ion Exosphere Observed from Voyager 1. *J. of Geophysical Research*, 87(A3):1383–1394, 1982.

[62] S. Hendricks, F. M. Neubauer, M. K. Dougherty, N. Achilleos, and C. T. Russel. Variability in Saturn's bow shock and magnetopause from Pioneer and Voyager: Probabilistic predictions and initial observations by Cassini. *Geophysical Research Letters*, 32(20):L20S08 (1–4), 2005.

[63] D. W. Hewett. Elimination of electromagnetic radiation in plasma simulation: The Darwin or magnetoinductive approximation. *Space Sci. Rev.*, 42:29–40, 1985.

[64] T. W. Hill. Inertial limit on corotation. *J. of Geophysical Research*, 84(A11):6554–6558, 1979.

[65] P. L. Israelevich, F. M. Neubauer, and A. I. Ershkovich. Titan magnetosphere revisited. Unpublished manuscript, 1995.

[66] G. H. Jones, E. Roussos, N. Krupp, C. Paranicas, J. Woch, A. Lagg, D. G. Mitchell, S. M. Krimigis, and M. K. Dougherty. Enceladus' Varying Imprint on the Magnetosphere of Saturn. *Science*, 311:1412–1415 (doi:10.1126/science.1121011), 2006.

[67] K. Kabin, T. I. Gombosi, D. L. DeZeeuw, K. G. Powell, and P. L. Israelevich. Interaction of the Saturnian magnetosphere with Titan: Results of a three-dimensional MHD simulation. *J. of Geophysical Research*, 104(A2):2451–2458, 1999.

[68] K. Kabin, P. L. Israelevich, A. I. Ershkovich, F. M. Neubauer, T. I. Gombosi, D. L. DeZeeuw, and K. G. Powell. Titan's magnetic wake: Atmospheric or magnetospheric interaction. *J. of Geophysical Research*, 105(A5):10,761–10,770, 2000.

[69] E. Kallio. Formation of the lunar wake in quasi-neutral hybrid model. *Geophysical Research Letters*, 32:L06107 (1–5), doi:10.1029/2004GL021989, 2005.

[70] E. Kallio, A. Fedorov, E. Budnik, T. Säles, P. Janhunen, W. Schmidt, H. Koskinen, P. Riihelä, S. Barabash, R. Lundin, M. Holmström, H. Gunell, K. Brinkfeldt, Y. Futaana, H. Andersson, M. Yamauchi, A. Grigoriev, J.-A. Sauvaud, J.-J. Thocaven, J. D. Winningham, R. A. Frahm, J. R. Sharber, J. R. Scherrer, A. J. Coates, D. R. Linder, D. O. Kataria, J. Kozyra, J. G. Luhmann, E. Roelof, D. Williams, S. Livi, C. C. Curtis, K. C. Hsieh, B. R. Sandel, M. Grande, M. Carter, S. McKenna-Lawler, S. Orsini, R. Cerulli-Irelli, M. Maggi, P. Wurz, P. Bochsler, N. Krupp, J. Woch, M. Fränz, K. Asamura, and C. Dierker. Ion escape at Mars: Comparison of a 3-D hybrid simulation with Mars Express IMA/ASPERA-3 measurements. *Icarus*, 182:350–359 (doi: 10.1016/j.icarus.2005.09.018), 2006.

[71] E. Kallio and P. Janhunen. Atmospheric effects of proton precipitation in the Matrian atmosphere and its connection to the Mars-solar wind interaction. *J. of Geophysical Research*, 106(A4):5617–5634, 2001.

[72] E. Kallio and P. Janhunen. Ion escape from Mars in a quasi-neutral hybrid model. *J. of Geophysical Research*, 107:1–1 (doi: 10.1029/2001JA000090), 2002.

[73] E. Kallio and P. Janhunen. Modelling the solar wind interaction with Mercury by a quasi-neutral hybrid model. *Ann. Geophysicae*, 21(11):2133–2145, 2003.

[74] E. Kallio, I. Sillanpää, and P. Janhunen. Titan in subsonic and supersonic flow. *Geophysical Research Letters*, 31(15):L15703/1–L15703/4 (doi: 10.1029/2004GL020344), 2004.

[75] C. N. Keller, V. G. Anicich, and T. E. Cravens. Model of Titan's ionosphere with detailed hydrocarbon chemistry. *Planet. Space Sci.*, 46(9/10):1157–1174, 1998.

[76] C. N. Keller and T. E. Cravens. One-dimensional, multispecies hydrodynamic models of the wakeside ionosphere of Titan. *J. of Geophysical Research*, 99(A4):6527–6536, 1994.

[77] C. N. Keller, T. E. Cravens, and L. Gan. A Model of the Ionosphere of Titan. *J. of Geophysical Research*, 97(A8):12,117–12,135, 1992.

[78] C. N. Keller, T. E. Cravens, and L. Gan. One-dimensional multispecies magnetohydrodynamic model of the ramside ionosphere of Titan. *J. of Geophysical Research*, 99(A4):6511–6525, 1994.

[79] R. Kippenhahn and C. Möllenhoff. *Elementare Plasmaphysik*. B.I.-Wissenschaftsverlag, Bibliographisches Institut Mannheim/Wien/Zürich, 1975.

[80] M. G. Kivelson. Moon-magnetosphere interactions: A tutorial. *Adv. Space Res.*, 33:2061–2077, 2004.

[81] M. G. Kivelson, L. F. Bargatze, K. K. Khurana, D. J. Southwood, R. J. Walker, and P. J. Colemann Jr. Magnetic Field Signatures Near Galileos Closest Approach to Gaspra. *Science*, 261:331–334, 1993.

[82] M. G. Kivelson and C. T. Russell. The Interaction of Flowing Plasmas With Planetary Ionospheres: A Titan-Venus Comparison. *J. of Geophysical Research*, 88(A1):49–57, 1983.

[83] M. G. Kivelson and C. T. Russell. *Introduction to Space Physics*. Cambridge University Press, 1995.

[84] A. Kopp and W.-H. Ip. Asymmetric mass loading effect at Titan's ionosphere. *J. of Geophysical Research*, 106(A5):8323–8332, 2001.

[85] P. Kuehs. Entwicklung, Implementierung und Test von Analysewerkzeugen für einen Hybrid-Simulationscode. Master's thesis, Technische Universität Braunschweig, 2002.

[86] G. P. Kuiper. Titan: a Satellite with an Atmosphere. *Astrophysical Journal*, 100:378–383, 1944.

[87] S. A. Ledvina and T. E. Cravens. A three-dimensional MHD model of plasma flow around Titan. *Planet. Space Sci.*, 46(9/10):1175–1191, 1998.

[88] S. A. Ledvina, T. E. Cravens, and K. Kecskemety. Ion distributions in Saturn's magnetosphere near Titan. *J. of Geophysical Research*, 110(A06211):1–16, 2005.

[89] S. A. Ledvina, T. E. Cravens, A. Salman, and K. Kecskemety. Ion trajectories in Saturn's magnetosphere near Titan. *Adv. Space Res.*, 26(10):1691–1695, 2000.

[90] S. A. Ledvina, J. G. Luhmann, S. H. Brecht, and T. E. Cravens. Titan's induced magnetosphere. *Advances in Space Research*, 33(11):2092–2102, 2004.

[91] S. A. Ledvina, J. G. Luhmann, and T. E. Cravens. Ambient ion distributions in Saturn's magnetosphere near Titan during a non-Voyager type interaction. *Adv. Space Res.*, 33:221–226, 2004.

[92] E. Lellouch, D. M. Hunten, G. Kockarts, and A. Coustenis. Titan's thermosphere profile. *Icarus*, 83:308–324 (doi:10.1016/0019–1035(90)90070–P), 1990.

[93] A. S. Lipatov. Hybrid codes with finite electron mass. In J. Büchner, C. T. Dum, and M. Scholer, editors, *Space Plasma Simulation – Proceedings of the Sixth International School/ Symposium ISSS-6*, pages 66–69, 2001.

[94] R. Lorenz and J. Mitton. *Lifting Titan's Veil: Exploring the giant moon of Saturn.* Cambridge University Press, 2002.

[95] J. G. Luhmann. A model of the ion wake of Mars. *Geophysical Research Letters*, 17:869–872, 1990.

[96] J. G. Luhmann. Titan's ion exosphere wake: A natural ion mass spectrometer? *J. of Geophysical Research*, 101(E12):29.387–29,393, 1996.

[97] J. G. Luhmann, C. T. Russell, K. Schwingenschuh, and Y. Yeroshenko. A comparison of induced magnetotails of planetary bodies: Venus, Mars and Titan. *J. of Geophysical Research*, 96(A7):11,199–11,208, 1991.

[98] Y. Ma. *Three-dimensional multispecies global MHD studies of the solar wind interaction with Mars and Saturn's magnetospheric plasma flow with Titan.* PhD thesis, University of Michigan, United States – Michigan, 2006.

[99] Y. Ma, A. F. Nagy, T. E. Cravens, I. V. Sokolov, K. C. Hansen, J.-E. Wahlund, F. J. Crary, A. J. Coates, and M. K. Dougherty. Comparisons between MHD model calculations and observations of Cassini flybys of Titan. *J. of Geophysical Research*, 111:A05207 (doi:10.1029/2005JA011481), 2006.

[100] Y. J. Ma, A. F. Nagy, T. E. Cravens, I. V. Sokolov, J. Clark, and K. C. Hansen. 3-D global MHD prediction for the first close flyby of Titan by Cassini. *Geophysical Research Letters*, 31(L22803):1–4, 2004.

[101] C. G. MacLennan, L. J. Lanzerotti, S. M. Krimigis, R. P. Lepping, and N. F. Ness. Effects of Titan on Trapped Particles in Saturn's Magnetosphere. *J. of Geophysical Research*, 87(A3):1411–1418, 1982.

[102] P. R. Mahaffy. Intensive Titan Exploration Begins. *Science*, 308(5724):969–970, 2005.

[103] A. P. Matthews. Current Advance Method and Cyclic Leapfrog for 2D Multispecies Hybrid Plasma Simulations. *J. of Computational Physics*, 112:102–116, 1994.

[104] R. L. McNutt, Jr. and J. D. Richardson. Constraints on Titan's ionosphere. *Geophysical Research Letters*, 15:709–712, 1988.

[105] D. G. Mitchell, P. C. Brandt, E. C. Roelof, J. Dandouras, S. M. Krimigis, and B. H. Mauk. Energetic Neutral Atom Emissions from Titan Interaction with Saturn's Magnetosphere. *Science*, 308(5724):989–992, 2005.

[106] R. Modolo. *Modélisation de l' interaction du vent solaire, ou du plasme Kronien, avec les environnements neutres de Mars et de Titan.* PhD thesis, L' université de Versailles Saint-Quentin-en-Yvelines, 2004.

[107] R. Modolo, G. M. Chanteur, E. Dubinin, and A. P. Matthews. Influence of the solar EUV flux on the Martian plasma environment. *Ann. Geophysicae*, 23(2):433–444, 2005.

[108] R. Modolo, G. M. Chanteur, E. Dubinin, and A. P. Matthews. Simulated solar wind plasma interaction with the Martian exosphere: influence of the solar EUV flux on the bow shock and the magnetic pile-up boundary. *Ann. Geophysicae*, 24(12):3403–3410, 2006.

[109] U. Motschmann. *Wellen und Diskontinuitäten in kosmischen Multi-Ionen-Plasmen.* PhD thesis, Akademie der Wissenschaften der Deutschen Demokratischen Republik, 1990.

[110] U. Motschmann and E. Kührt. Interaction of the solar wind with weak obstacles: Hybrid simulations for weakly active comets and for Mars. *Space Science Rev.*, 122:197–208 (doi:10.1007/s11214–006–6218–2), 2006.

[111] U. Motschmann and J. Raeder. A simulation study of multiple ion wave generation downstream of low Mach number quasiperpendicular shocks. *Geophysical Research Letters*, 19(15):1619–1622, 1992.

[112] U. Motschmann, K. Sauer, T. Roatsch, and J. F. McKenzie. Subcritical multiple-ion shocks. *J. of Geophysical Research*, 96(A8):13,841–13,848, 1991.

[113] J. Müller. Entwicklung eines numerischen Modells zur Untersuchung der Wechselwirkung leitfähiger Objekte mit dem Sonnenwind. Master's thesis, Technische Universität Braunschweig, 2007.

[114] A. F. Nagy and T. E. Cravens. Titan's ionosphere: A review. *Planet. Space Sci.*, 46:1149–1155, 1998.

[115] A. F. Nagy, Y. Liu, K. C. Hansen, K. Kabin, T. I. Gombosi, M. R. Combi, and D. L. DeZeeuw. The interaction between the magnetosphere of Saturn and Titan's ionosphere. *J. of Geophysical Research*, 106(A4):6151–6160, 2001.

[116] N. F. Ness, M. H. Acuna, K. W. Behannon, and F. M. Neubauer. The induced magnetosphere of Titan. *J. of Geophysical Research*, 87(A3):1369–1381, 1982.

[117] F. M. Neubauer. Possible strengths of dynamo magnetic fields of the Galilean satellites and of Titan. *Geophysical Research Letters*, 5(11):905–908, 1978.

[118] F. M. Neubauer, H. Backes, M. K. Dougherty, A. Wennmacher, C. T. Russell, A. Coates, D. Young, N. Achilleos, N. Andre, C. S. Arridge, C. Bertucci, G. H. Jones, K. K. Khurana, T. Knetter, A. Law, G. R. Lewis, and J. Saur. Titan's near magnetotail from

magnetic field and plasma observations and modelling: Cassini flybys TA, TB and T3. *J. of Geophysical Research*, 111:A10220 (1–15), doi:10.1029/2006JA011676, 2006.

[119] F. M. Neubauer, D. A. Gurnett, J. D. Scudder, and R. E. Hartle. Titan's magnetospheric interaction. In T. Gehrels and M. S. Matthews, editors, *Saturn*, pages 760–787. University of Arizona Press, Tucson, Arizona, 1984.

[120] N. Omidi, X. Blanco-Cano, C. T. Russel, H. Karimabadi, and M. Acuna. Hybrid simulations of solar wind interaction with magnetized asteroids: General characteristics. *J. of Geophysical Research*, 107(A12):12,1–12,10, 2002.

[121] N. Omidi and D. Winske. Steepening of kinetic magnetosonic waves into shocklets – Simulations and consequences for planetary shocks and comets. *J. of Geophysical Research*, 95:2281–2300, 1990.

[122] C. Othmer. *Numerical simulation of ion thruster-induced plasma dynamics*. PhD thesis, Technische Universität Braunschweig, 2001.

[123] T. Owen. The composition and origin of Titan's atmosphere. *Planet. Space Sci.*, 30:833–838 (doi:10.1016/0032–0633(82)90115–5), 1982.

[124] C. Paty and R. Winglee. Multi-fluid simulations of Ganymede's magnetosphere. *Geophysical Research Letters*, 31:L24806 (1–5), doi:10.1029/2004GL021220, 2004.

[125] J. L. Phillips, J. G. Luhmann, C. T. Russell, and K. R. Moore. Finite Larmor radius effect on ion pickup at Venus. *J. of Geophysical Research*, 92:9920–9930, 1987.

[126] A. Roboz and A. F. Nagy. The energetics of Titan's ionosphere. *J. of Geophysical Research*, 99(A2):2087–2093, 1994.

[127] K. Sauer, A. Bogdanov, and K. Baumgartel. Evidence of an ion composition boundary (protonopause) in bi-ion fluid simulations of solar wind mass loading. *Geophysical Research Letters*, 21(20):2255–2258, 1994.

[128] K. Sauer, E. Dubinin, and K. Baumgärtel. Nonlinear MHD waves and discontinuities in the Martian magnetosheath. Observations and 2D bi-ion MHD simulations. *Earth, Planets and Space*, 50:793–801, 1998.

[129] K. Sauer, T. Roatsch, U. Motschmann, D. Moehlmann, and K. Schwingenschuh. Plasma boundaries at Mars discovered by the PHOBOS 2 magnetometers. *Ann. Geophysicae*, 8:661–670, 1990.

[130] J. Saur, B. H. Mauk, A. Kassner, and F. M. Neubauer. A model for the azimuthal plasma velocity in Saturn's magnetosphere. *J. of Geophysical Research*, 109(A05217):1–8, 2004.

[131] A. W. Schardt, K. W. Behannon, R. P. Lepping, J. F. Carbary, A. Eviatar, and G. L. Siscoe. The outer magnetosphere. In T. Gehrels and M. S. Matthews, editors, *Saturn*, pages 416–459. University of Arizona Press, Tucson, Arizona, 1984.

[132] R. Schwenn. Der Sonnenwind. In K. H. Glaßmeier and M. Scholer, editors, *Plasmaphysik im Sonnensystem*, chapter 2, pages 17–46. B.I.-Wissenschaftsverlag, Mannheim/Wien/Zürich, 1991.

[133] D. E. Shemansky, A. I. F. Stewart, R. A. West, L. W. Esposito, J. T. Hallett, and X. Liu. The Cassini UVIS Stellar Probe of the Titan Atmosphere. *Science*, 308(5724):978–982, 2005.

[134] H. Shimazu. Three-dimensional hybrid simulation of solar wind interaction with unmagnetized planets. *J. of Geophysical Research*, 106(A5):8333–8342, 2001.

[135] I. Sillanpää, E. Kallio, P. Janhunen, W. Schmidt, K. Mursula, J. Vilppola, and P. Tanskanen. Hybrid simulation study of ion escape at Titan for different orbital positions. 2006. in press.

[136] I. Sillanpää, E. Kallio, R. Jarvinen, P. Janhunen, J. Vilppola, K. Mursula, C. Bertucci, M. K. Dougherty, and F. M. Neubauer. Advanced Hybrid Simulation on the Magnetic Interaction at Titan. *AGU Fall Meeting Abstracts (11-15 December 2006, San Francisco)*, 2006.

[137] S. Simon. Zur Interaktion leitfähiger und magnetisierter Objekte mit dem Sonnenwind. Master's thesis, Technische Universität Braunschweig, 2004.

[138] S. Simon, T. Bagdonat, U. Motschmann, and K.-H. Glassmeier. Plasma environment of magnetized asteroids: A 3D hybrid simulation study. *Annales Geophysicae*, 24(1):407–414, 2006.

[139] S. Simon, A. Boesswetter, T. Bagdonat, and U. Motschmann. Physics of the Ion Composition Boundary: A comparative 3D hybrid simulation study of Mars and Titan. *Ann. Geophysicae*, 25(1):99–115, 2007.

[140] S. Simon, A. Boesswetter, T. Bagdonat, U. Motschmann, and K.-H. Glassmeier. Plasma environment of Titan: a 3-d hybrid simulation study. *Ann. Geophysicae*, 24(3):1113–1135, 2006.

[141] S. Simon, A. Boesswetter, T. Bagdonat, U. Motschmann, and J. Schuele. Three-dimensional multispecies hybrid simulation of Titan's highly variable plasma environment. *Ann. Geophysicae*, 25(1):117–144, 2007.

[142] K. H. Spatschek. *Theoretische Plasmaphysik*. B. G. Teubner, Stuttgart, 1990.

[143] D. F. Strobel and D. E. Shemansky. EUV emission from Titan's upper atmosphere – Voyager 1 encounter. *J. of Geophysical Research*, 87:1361–1368, 1982.

[144] K. Szegö. Private correspondence.

[145] R. L. Tokar, R. E. Johnson, T. W. Hill, D. H. Pontius, W. S. Kurth, F. J. Crary, D. T. Young, M. F. Thomsen, D. B. Reisenfeld, A. J. Coates, G. R. Lewis, E. C. Sittler, and D. A. Gurnett. The Interaction of the Atmosphere of Enceladus with Saturn's Plasma. *Science*, 311:1409–1412 (doi:10.1126/science.1121061), 2006.

[146] D. Toublanc, J. P. Parisot, J. Brillet, D. Gautier, F. Raulin, and C. P. McKay. Photochemical modeling of Titan's atmosphere. *Icarus*, 113:2–26 (doi:10.1006/icar.1995.1002), 1995.

[147] P. Travnicek, P. Hellinger, and D. Schriver. A global three dimensional hybrid simulation of the interaction between a weakly magnetized obstacle and the solar wind. Unpublished manuscript, 2003.

[148] P. Travnicek, P. Hellinger, and D. Schriver. Structure of Mercury's magnetosphere for different pressure of the solar wind: Three dimensional hybrid simulations. *Geophysical Research Letters*, 35:L05104 (1–5), doi: 10.10292006GL028518, 2007.

[149] P. Travnicek, P. Hellinger, D. Schriver, and S. D. Bale. Structure of the lunar wake: Two-dimensional global hybrid simulations. *Geophysical Research Letters*, 32:L06102 (1–4), 2005.

[150] M. I. Verigin, K. I. Gringauz, and N. F. Ness. Comparison of induced magnetospheres at Venus and Titan. *J. of Geophysical Research*, 89(A7):5461–5470, 1984.

[151] J.-E. Wahlund, R. Boström, G. Gustafsson, D. A. Gurnett, W. S. Kurth, A. Pedersen, T. F. Averkamp, G. B. Hospodarsky, A. M. Persoon, P. Canu, F. M. Neubauer, M. K. Dougherty, A. I. Eriksson, M. W. Morooka, R. Gill, M. André, L. Eliasson, and I. Mueller-Wordag. Cassini Measurements of Cold Plasma in the Ionosphere of Titan. *Science*, 308(5724):986–989, 2005.

[152] J. H. Waite, H. Niemann, R. V. Yelle, W. T. Kasprzak, T. E. Cravens, J. G. Luhmann, R. L. McNutt, W.-H. Ip, D. Gell, V. De La Haye, I. Mueller-Wordag, B. Magee, N. Borggren, S. Ledvina, G. Fletcher, E. Walter, R. Miller, S. Scherer, R. Thorpe, J. Xu, B. Block, and K. Arnett. Ion Neutral Mass Spectrometer Results from the First Flyby of Titan. *Science*, 308(5724):982–986, 2005.

[153] Z. Wang and M. G. Kivelson. Asteroid interaction with solar wind. *J. of Geophysical Research*, 101(A11):24,479–24,493, 1996.

[154] D. Winske and N. Omidi. Hybrid codes: Methods and Applications. In H. Matsumoto and Y. Omura, editors, *Computer Space Plasma Physics: Simulations and Software*, pages 103–160. Terra Sci., Tokyo, 1993.

[155] D. Winske and N. Omidi. A nonspecialist' s guide to kinetic simulations of space plasmas. *J. of Geophysical Research*, 101(A8):17,287–17,303, 1996.

[156] D. Winske, L. Yin, N. Omidi, H. Karimabadi, and K. Quest. Hybrid Simulation Codes: Past, Present and Future – A Tutorial. In J. Büchner, C. T. Dum, and M. Scholer, editors, *Space Plasma Simulation*, pages 136 – 165. Springer-Verlag, Berlin/ Heidelberg/ New York, 2003.

[157] D. A. Wolf and F. M. Neubauer. Titan's Highly Variable Plasma Environment. *J. of Geophysical Research*, 87(A2):881–885, 1982.

[158] D. T. Young, J. J. Berthelier, M. Blanc, J. L. Burch, A. J. Coates, R. Goldstein, M. Grande, T. W. Hill, R. E. Johnson, V. Kelha, D. J. McComas, E. C. Sittler, K. R. Svenes, K. Szegö, P. Tanskanen, K. Ahola, D. Anderson, S. Bakshi, R. A. Baragiola, B. L. Barraclough, R. K. Black, S. Bolton, T. Booker, R. Bowman, P. Casey, F. J. Crary, D. Delapp, G. Dirks, N. Eaker, H. Funsten, J. D. Furman, J. T. Gosling, H. Hannula, C. Holmlund, H. Huomo, J. M. Illiano, P. Jensen, M. A. Johnson, D. R. Linder,

T. Luntama, S. Maurice, K. P. McCabe, K. Mursula, B. T. Narheim, J. E. Nordholt, A. Preece, J. Rudzki, A. Ruitberg, K. Smith, S. Szalai, M. F. Thomsen, K. Viherkanto, J. Vilppola, T. Vollmer, T. E. Wahl, M. Wüest, T. Ylikorpi, and C. Zinsmeyer. Cassini Plasma Spectrometer Investigation. *Space Science Rev.*, 114:1–112, 2004.

[159] Y. L. Yung. An update of nitrile photochemistry on Titan. *Icarus*, 72:468–472, 1987.

[160] Y. L. Yung, M. Allen, and J. P. Pinto. Photochemistry of the atmosphere of Titan – Comparison between model and observations. *Astrophysical Journal Supplement Series*, 55:465–506 (doi:10.1086/190963), 1984.

Danksagung

Die vorliegende Arbeit entstand während meiner Tätigkeit als wissenschaftlicher Mitarbeiter am Institut für Theoretische Physik der Technischen Universität Braunschweig. Ich möchte mich bei allen Professoren, Mitarbeitern und Freunden bedanken, die mich in dieser Zeit unterstützt haben.

Mein ganz besonderer Dank geht an *Prof. Dr. Uwe Motschmann*, der diese Arbeit als Mentor betreut hat. Einerseits hat mir Herr Motschmann in zahllosen Diskussionen nicht nur viel Wissen vermittelt; oftmals regten mich seine Hinweise und Kommentare auch dazu an, meine Ergebnisse kritisch zu überdenken. Nicht selten deuteten sich gerade dabei neue, interessante Problemkreise an, die es zu untersuchen galt. Am meisten profitiert habe ich von seinem unbedingten Bestreben, die Physik stets bis ins Detail zu durchdringen und sich niemals mit einem oberflächlichen Verständnis zufriedenzugeben. Andererseits schätze ich an Herrn Motschmann, daß er sich für seine Mitarbeiter in einer Weise einsetzt, die weit über die Bewältigung der täglichen Geschäfte in einem Hochschulinstitut hinausgeht. Nicht nur durch seine kompromißlose Zuverlässigkeit, vor allem auch durch seine beispiellose Gelassenheit, Toleranz und Fairness, ist er für mich in jeder Hinsicht ein unerreichtes Vorbild geworden.

Herrn *Prof. Dr. Karl-Heinz Glaßmeier* gilt mein Dank für die fachliche Unterstützung und für seine Bereitschaft, die vorliegende Arbeit als Zweitgutachter zu betreuen. Durch zahlreiche Kommentare, Fragen und Verbesserungsvorschläge half er insbesondere dabei, die Qualität der gemeinsamen Publikationen an vielen Stellen zu verbessern. Nicht unerwähnt bleiben soll auch die finanzielle Unterstützung meiner Tagungsreisen. Speziell die Reise zur EGU nach Wien im Jahr 2006, die mich sehr vorangebracht hat, wurde von Herrn Glaßmeier ermöglicht. Zahlreiche aufschlußreiche Gespräche gewährten nicht nur einen Einblick in aktuelle wissenschaftliche Probleme, sondern ebenso in den Bereich der Wissenschaftspolitik. Herrn Glaßmeiers Engagement ist es auch zu verdanken, daß wir eine gute und erfolgreiche Zusammenarbeit mit dem Cassini-Magnetometer-Team etablieren konnten.

Trotz hoher Arbeitsbelastung durch einen Forschungsaufenthalt im Ausland war *Prof. Dr. Andreas Eichler* spontan bereit, Mitglied meiner Promotionskommission zu werden. Auch ihm gilt mein herzlicher Dank. Wenngleich sich das Thema dieser Arbeit nicht mit Herrn Eichlers Forschungsschwerpunkten überschneidet, so hoffe ich doch, daß das Studium meiner Ergebnisse auch für ihn interessant war.

Mit *Alexander Bößwetter* arbeite ich nun seit fast vier Jahren gemeinsam im Institut für Theoretische Physik. Im Gegensatz zu mir brachte Alexander bei zahllosen Gelegenheiten die Ruhe und Geduld auf, die notwendig sind, um über die Tücken von Computer-Graphikprogrammen zu triumphieren. Die meisten Abbildungen in dieser Arbeit entstanden mit einer modifizierten Fassung der Gnuplot-Software, die Alexander während seiner Diplomarbeit entwickelt hat. Nicht nur für seine Unterstützung in diesem Bereich bin ich ihm zu Dank verpflichtet, sondern vor allem auch für seine Dienste als Computer-Administrator unseres Instituts. Beim Auftreten von Netzwerkproblemen und defekter Hardware hat Alexander bei zahllosen Gelegenheiten die undankbare Aufgabe übernommen, sich um die notwendigen Reparaturen zu kümmern. Auch die Tatsache, daß die Parallelisierung unseres Simulationscodes mittlerweile nahezu vollendet ist, geht nicht zuletzt auf Alexanders Einwirken zurück. Neben der gemeinsamen Arbeit haben aber auch zahlreiche humorvolle und interessante Gespräche zu einem durchweg angenehmen Arbeitsklima beigetragen.

Wenngleich seit 2004 nicht mehr in unserem Institut tätig, so leistete *Dr. Thorsten Bagdonat* doch entscheidende Beiträge zum Gelingen dieser Arbeit. Die maßgeblichen Schritte bei der Entwicklung des ursprünglichen Kometen-Simulationscodes wurden von ihm erarbeitet. Auch bei den Titan-Simulationen hatte Thorsten nicht nur stets ein offenes Ohr bei Problemen; dank seines Ideenreichtums konnten diese dann auch meist schnell überwunden werden. Insbesondere bei der Erweiterung des Codes zur Durchführung von Multi-Spezies-Simulationen war Thorsten letztlich der einzige, der im Dschungel der Algorithmen noch den Überblick behalten hat.

Mein Dank gilt auch *Gero Kleindienst* vom Institut für Geophysik und Extraterrestrische Physik. Gero beschaffte mir nicht nur die Daten des Cassini-Magnetometer-Instruments; mit viel Engagement entwickelte er zudem eine Software, die eine einfache Einbindung des Materials in den Simulationscode ermöglicht.

Ich danke allen Mitgliedern des Instituts für das angenehme Arbeitsklima und die gute Zusammenarbeit. Unser Numerik-Genie *Joachim Müller* entwickelte nicht nur zahlreiche Verbesserungen des Simulationscodes, vor allem stand er mir für mehrere Semester mit seiner Unterstützung bei der Betreuung der Übungen zu den Theorie-Vorlesungen zur Seite. Als großem Fan von Star-Trek war es mir eine besondere Freude, *Michael Dorn* als Diplomanden für unsere Arbeitsgruppe gewinnen zu können. Mein Dank gilt ihm nicht nur für interessante fachliche Diskussionen, sondern vor allem dafür, daß er während meiner Dienstreisen stets gerne als Vorlesungsassistent eingesprungen ist und die Studenten tatkräftig unterstützt hat. Von *Dr. Jean-Mathias Grießmeier* lernte ich viel über wissenschaftliche Arbeitstechnik und insbesondere auch über die ansprechende Gestaltung von Tagungsvorträgen. Leider hat mit ihm auch der neben mir einzige Star-Wars und Herr-der-Ringe-Fan unser Institut verlassen. Meinen ehemaligen Kollegen *Dr. Fabian Heidrich-Meisner* und *PD Dr. Andreas Honecker* danke ich für die gegenseitige Unterstützung bei der Betreuung der Übungen; beide haben mir insbesondere durch Bereitstellung der Quellcodes zu ihren Übungsaufgaben viel Zeit und Arbeit erspart. Zudem stand mir Fabian in der Anfangsphase meiner Tätigkeit als Vorlesungsassistent mit zahlreichen Tips und Ratschlägen zur Seite. Die gute Kooperation hat sich mit seinem Nachfolger, *Simon-Nils Großjohann*, reibungslos fortgesetzt; ein großes Dankeschön auch dafür. Ich freue mich auf eine interessante Zusammenarbeit mit unseren neuen Institutsmitgliedern, *Erik Johansson* und *Stefan Wiehle*.

Mein herzlicher Dank gilt auch unserer Institutssekretärin, Frau *Renate Strassek*. Nicht nur zahlreiche homorvolle und interessante Gespräche neben der gemeinsamen Arbeit, vor allem auch ihre Bemühungen bei der Rettung meiner Büropflanzen vor dem Verdursten, werden mir stets in guter Erinnerung bleiben.

Ein besonderer Dank geht an alle Hilfsassistenten, die in den vergangenen drei Jahren mit großem Engagement die Studentenlösungen zu meinen recht umfangreichen Übungsblättern korrigiert haben und den Studenten stets unterstützend zur Seite standen. *Harald Nieber* und *Annette Maria Gattner* waren eine große Hilfe bei der Betreuung des Thermodynamik-Kurses im Jahr 2004; insbesondere Annette hat mir mit ihren aufmerksamen Fragen so manches Mal den Schweiß auf die Stirn getrieben. Die Elektrodynamik im Sommer 2006 wurde durch die tatkräftige Unterstützung von *Joachim Müller*, *Ferdinand Plaschke* und *Andre Ahlbrecht* auch für mich zu einem sehr lehrreichen Rückblick auf die Grundlagen. Andres kunstvoll gestalteter "RoTa DiNo" hat einen Ehrenplatz in meiner Materialsammlung erhalten. Dem aktuellen Team, bestehend aus *Hendrik Kriegel* und *Michael Dorn*, möchte ich ebenfalls für die hervorragende Arbeit und Unterstützung danken; insbesondere in der Endphase dieser Arbeit habe ich dadurch viel Zeit gespart. Ein ganz besonderer Dank geht an *Jörg Duhme*, der sich trotz widriger persönlicher Umstände stets mit herausragendem fachlichen und persönlichen Engagement für seine Studenten eingesetzt hat. Nicht unerwähnt bleiben soll auch die Mitarbeit der Studenten, die mit viel Mühe die LaTeX-Manuskripte zu den Vorlesungen angefertigt haben; insbesondere *Johannes Gütschow*, *Matthias Grzeschik* und *Jochen Bandlow* haben hier mitgeholfen.

Mein Dank gilt auch allen Kollegen, mit denen wir in den letzten drei Jahren erfolgreich zusammengearbeitet haben. *Dr. Norbert Krupp* und *Elias Roussos* vom Max-Planck-Institut für Sonnensystemforschung haben mich oftmals über aktuelle Publikationen auf dem Laufenden gehalten. *Dr. Ronan Modolo*, *Dr. Esa Kallio* und *Ilkka Sillanpää*, die ebenfalls Hybrid-Simulationen für Titan durchführen, danke ich für zahlreiche interessante Diskussionen auf diversen Konferenzen. Den Cassini-Team-Mitgliedern *Prof. Dr. Michele K. Dougherty* und *Dr. Cesar Bertucci* vom Imperial College London, insbesondere jedoch *Prof. Dr. Fritz M. Neubauer*, danke ich für die konstruktive und angenehme Zusammenarbeit. Herrn Neubauer gilt mein Dank auch für hilfreiche Diskussionen auf der AGU-Tagung 2006 in San Francisco. Für seine Unterstützung bei der Analyse der T9-Plasmadaten und für die Bereitstellung von Material danke ich Herrn *Dr. Karoly Szegö* vom KFKI in Budapest.

Nicht zuletzt möchte ich meinen Eltern *Almut und Werner Simon* danken, die mich in den letzten Jahren in jeder nur erdenklichen Hinsicht unterstützt haben. Stets haben sie mir das Gefühl gegeben, einen Rückhalt zu haben, der durch nichts erschüttert werden kann. Durch ihren Zuspruch und ihre Geduld haben sie mir insbesondere dann geholfen, wenn die Arbeit an der Uni mal nicht nach meinen Vorstellungen verlief. Zudem hatten beide Verständnis dafür, daß ich auch bei meinen (viel zu seltenen) Besuchen in Goslar oftmals Arbeit aus dem Institut im Gepäck hatte.

Lebenslauf

Name	:	Sven Simon
Geburtsdatum:	:	20.05.1979
Geburtsort:	:	Goslar
Staatsangehörigkeit	:	deutsch
Familienstand	:	ledig

1985 - 1989	Grundschule Jürgenohl, Goslar
1989 - 1991	Orientierungsstufe Goldene Aue, Goslar
1991 - 1998	Christian-von-Dohm-Gymnasium, Goslar
22.06.1998	Abitur, Leistungsfächer: Mathematik und Physik
Juli 1998	Befreiung vom Wehrdienst aufgrund gesundheitlicher Probleme
Okt. 1998	Beginn des Studiums der Physik an der TU Braunschweig
Okt. 2000	Diplomvorprüfung, Gesamtnote: *Sehr gut (1.0)*
2003 - 2004	Diplomarbeit in der Arbeitsgruppe *Extraterrestrische Plasmaphysik* am Institut für Theoretische Physik der TU Braunschweig. Thema der Arbeit: *Zur Interaktion leitfähiger und magnetisierter Objekte mit dem Sonnenwind.* Betreuer: Prof. Dr. U. Motschmann und Prof. Dr. K.-H. Glaßmeier
Sept. 2004	Diplom in Physik, Gesamtnote: *Mit Auszeichnung bestanden*
seit Nov. 2004	Wissenschaftlicher Mitarbeiter (Promotionsstelle) in der Arbeitsgruppe von Prof. Dr. U. Motschmann am Institut für Theoretische Physik der TU Braunschweig

Wissenschaftliche Veröffentlichungen allgemeiner Art:

- S. Simon, T. Bagdonat, U. Motschmann und K.-H. Glaßmeier. Plasma environment of magnetized asteroids: a 3-d hybrid simulation study, *Annales Geophysicae*, Nr. 24 (1), Seiten 407-414, 2006

- A. Bößwetter, S. Simon, T. Bagdonat, U. Motschmann, M. Fränz, E. Roussos, N. Krupp, J. Woch, J. Schüle, S. Barabash und R. Lundin. Comparison of plasma data from ASPERA-3/Mars-Express with a 3D hybrid simulation, eingereicht bei *Annales Geophysicae*, 2006